Universidade do Porto

Faculdade de Engenharia

FEUP

Fully Resolved Dynamics of Mixing in Confined Impinging Jets Reactors

Master Dissertation
in
Computational Mechanics
by

Hélder Manuel Marques Salvador

Supervisors

Ricardo Jorge Nogueira dos Santos

Co-Supervisor

José Carlos Brito Lopes

Laboratory of Separation and Reaction Engineering - LSRE
Laboratório Associado LSRE/LCM
Departamento de Engenharia Química
Faculdade de Engenharia
Universidade do Porto

September 2015

Acknowledgments

I wish to thank my supervisor, Professor Ricardo Santos, for his guidance, helpful technical discussions, continual availability during the development of my work and for encouraging me to carry out this master thesis at LSRE - Laboratory of Separation and Reaction Engineering, in collaboration with the Computational Mechanics Department.

I am indebted to my co-supervisor, Professor José Carlos Lopes, for his expert support, for his trust on my work and his enthusiasm for this project.

I also acknowledge Professor Madalena Dias, director of the LSRE - Laboratory of Separation and Reaction Engineering, for her availability and for providing me all the necessary facilities to perform my work.

I would also like to express my appreciation for the knowledge all the professors have transmitted throughout these two years. I would like to thank specially to Professor José Sá for his availability and for his efforts in opening the Computational Mechanics master course.

During my time at FEUP the help and support of my friends and the collaboration with my classmates have been indispensable, for which I thank them dearly. In particular, I owe a special thanks to my colleagues Mohamed Lotfi, Behzad Farahani and José Berardo.

My gratitude also goes to the colleagues in the LSRE, particularly the Mixing Group, which made this work possible through their help and support, namely Carlos Teixeira, Gabriela Ruphuy, Joana Pereira, Marcelo Costa, Mónica Silva, Nelson Gonçalves and Rómulo Oliveira.

I also have to acknowledge my brothers in life: Ivo Cardoso, João Faustino, Luís Branco, Marco Pereira and Paulo Correia. I will see you next summer.

Finally, I wish to convey my deepest gratitude to my family, particularly my parents, for their unconditional support.

To my parents, family and friends

"Big whorls have little whorls that feed on their velocity,
and little whorls have lesser whorls and so on to viscosity"

Lewis F. Richardson

"When the present determines the future, but the approximate present
does not approximately determine the future"

Edward Norton Lorenz

Abstract

Confined Impingement Jets mixers (CIJ) have attracted wide interest in the past years because of the efficient micromixing and possible application to nanoparticles production. The Reaction Injection Molding (RIM) technology employs CIJ due to the fast reaction between the two monomers used to create plastic components.

In the present work, the flow scales were calculated for Reynolds numbers 150, 200, 250 and 300 until the smallest hydrodynamic scale, the Kolmogorov scale. From the numerical analyses of the flow field, the oscillatory behaviour of CIJ was studied and the energy containing scales identified. Additionally, the turbulent kinetic energy and the turbulent energy dissipation were calculated for all the numerical studies.

A multiphase VOF model is used for the study of 3D mixing inside this reactor with an edge length equal to the Kolmogorov scale, in order to evaluate the mixing related mechanisms and the adequacy of the numerical grid for a non-diffusive model.

Particle Image Velocimetry (PIV) measurements were carried out in order to compare the flow field behaviour of the front plane with the numerical analyses performed. Additionally, two methods previously developed for the CIJ jets impingement point, the elastic analogue model and the jets pressure model, were tested for a wide range of Reynolds numbers in order to assess their accuracy in predicting the impingement point position under different flow conditions.

The flow field was also visualized with the Planar Laser Induced Fluorescence (PLIF) experimental technique using a high speed camera to capture all the large flow scales. An image processing algorithm was developed to compute the jets impingement point position and the jets angle. The PLIF technique was performed for several Reynolds numbers and the results obtained from the image processing and by the differential pressure transducer were processed using Fast Fourier Transforms (FFT). The frequency of the jets oscillations was then compared with results reported in the literature. In addition, the PLIF technique was used to study the impingement mixing of fluids with different rheological properties. The experimental measurements were subsequently compared with the results provided by the two RIM control models for fluids with different viscosities in each injector, in order to validate them for a wide range of jets' momentum ratios.

Resumo

A mistura por jatos opostos (CIJ) tem atraído grande interesse nos últimos anos devido à eficiente micromistura e à potencial aplicação na produção de nanopartículas. A máquina de moldagem por injeção com reação química (RIM), a qual é utilizada para produzir componentes de plástico, usa a mistura por jatos opostos devido à reação rápida que ocorre entre os dois monómeros.

No presente trabalho, as escalas do escoamento foram calculadas para números de Reynolds de 150, 200, 250 e 300, até à menor escala hidrodinâmica, a escala de Kolmogorov. A partir da análise numérica do campo de velocidades, foi estudado o comportamento oscilatório dos jatos opostos e a energia das escalas identificadas. Além disso, a energia cinética turbulenta e a dissipação de energia turbulenta foram determinadas para todos os estudos numéricos.

O modelo multifásico VOF é usado para o estudo 3D do interior deste reator com uma discretização espacial igual à escala de Kolmogorov, a fim de identificar os mecanismos de mistura e de avaliar a escala de discretização espacial acoplada com um modelo não-difusivo.

A técnica de Velocimetria por Imagem de Partículas (PIV) foi realizada com o intuito de comparar o comportamento do campo de velocidades no plano dos eixos da câmara de mistura e injetores com as análises numéricas realizadas. Além disso, dois métodos desenvolvidos previamente para o controlo do processo RIM, o modelo elástico e o modelo de pressão, foram testados para vários números de Reynolds no sentido de avaliar a sua adequação para a previsão da posição do ponto de impacto dos jatos em condições de escoamento diversas.

O campo de velocidades foi igualmente visualizado por via da técnica experimental de Fluorescência Induzida por Laser (PLIF). Com recurso a uma câmara de alta velocidade, que permite capturar instantaneamente imagens da câmara de mistura, foram obtidas as grandes escalas do escoamento. Foi ainda construído um algoritmo para avaliar a posição do ponto de estagnação e o ângulo formado pelos jatos. As medições experimentais com PLIF foram realizadas para uma vasta gama de números de Reynolds e os resultados obtidos quer pelo algoritmo, quer pelo transdutor diferencial de pressão, foram processados por transformadas rápidas de Fourier (FFT). A frequência de oscilação de cada variável foi em seguida comparada com resultados reportados na literatura. Finalmente, a técnica PLIF foi aplicada no estudo da injeção de fluidos com diferentes viscosidades. Os resultados experimentais obtidos foram comparados com os resultados dos modelos elástico e de pressão, de modo a verificar-se a sua validade nestas condições de operação.

Contents

Notation

a	Amplitude of the perturbation parameter
A	Area [m^2]
b	Duration of the perturbation parameter [s]
cdf	Cumulative distribution function [pixel]
C	Concentration [mol/m^3]
$C_{rodamine}$	Rhodamine 6G concentration [Kg/m^3]]
d	Injector diameter [m]
d_p	Seeding particles mean diameter [m]
D	Chamber diameter [m]
D_m	Molecular diffusivity [m^2/s]
D_T	Turbulent diffusivity [m^2/s]
eh	Histogram equalizer [pixel]
$E(t/\tau)$	Residence time distribution
$\dot{E}_k$	Kinetic energy rate (W)
$\dot{E}_{k,in}$	Kinetic energy rate at injector (W)
f_{laser}	Laser pulsing frequency [Hz]
$f_{laser,max}$	Maximum laser pulsing frequency [Hz]
$F_{i\rightarrow j}$	Force from i to j [N]
h_l	Head loss from reduction [Pa]

h_f	Head loss from friction [Pa]
h_k	Head loss from opposite impingement jet [Pa]
H	Chamber height [m]
$I(t/\tau)$	Internal age distribution
I	Pixel grey scale intensity
I_s	Intensity of segregation
k	Chemical reaction kinetic constant or spring constant [N/m]
l	Injector length [m]
l'	Distance from the moment source point to the chamber inlet [m]
l_s	Striation thickness [m]
$\dot{m}$	Mass flow rate [Kg/s]
M	Mass [Kg]
n	Outside normal unitary vector to a control volume
n	Wave number or number of pixels
$N_{particles}$	Number of particles
N_{xyz}	Number total of nodes in 3D simulation
p	Pressure [Pa]
p_0	Reference pressure [Pa]
$p(x)$	Probability density function
Pe	Peclet number
Q	Volumetric flow rate [m^3/s]
R	Orthogonal tensor
R	Injector radius [m]
Re	Reynolds number
$\bar{s}$	Average distribution thickness [m]
S_s	Scale of segregation [m]
S_c	Shmith number
S_s	Scale of segregation
t	Time [s]
T	Temperature [ºC]
t_0	Initial time [s]
$t_{simulation}$	Simulation time [s]
u	Velocity field [m/s]
u	Axial velocity [m/s]
$u_{chamber}$	Average velocity in the mixing chamber [m/s]

u_{inj}	Average velocity at the injectors [m/s]
V	Volume [m^3]
$V_{dissipation}$	Volume where dynamic impingement mixing occurs [m^3]
W	Dimensionless weight
x	Position vector [m]
X	Initial position vector [m]
x_i	Component of **x** in i-direction
$X_{glicerine}$	Mass fraction of glycerine in the glycerol solution
x_{IP}	Impingement point position [m]

Greek letters

α_i	Volume fraction of phase i
$\bar{\alpha}$	Spatial volume fraction average
Δt	Integration time step [s]
Δt_{beams}	Interval between consecutive laser flashes in the PIV experiments [s]
Δx	Numerical grid element length [m]
$\Delta x_{int,region}$	Length of the interrogation region in PIV experiments [m]
Δp	Differential pressure [Pa]
ΔE_p	Storage potential energy [J]
$\dot{\gamma}$	Strain rate [s^{-1}]
ε	Turbulent energy dissipation rate [m^2/s^3]
ϕ	Frequency [H_z]
K	Turbulent kinetic energy [J/kg]
λ	Wave length [m]
λ_B	Batchelor Scale[m]
λ_k	Kolmogorov Scale [m]
ξ	Impingement point position [m]
ρ	Fluid density[kg/m^3]
ρ_p	Particles density[kg/m^3]
$\bar{\rho}$	Average fluid density weighted by the flow rate [kg/m^3]
σ	Standard deviation
σ^2	Variance
σ_α^2	Spatial variance of the volume fraction
μ	Viscosity [$Pa.s$]

$\bar{\mu}$	Average fluid viscosity weighted by the flow rate [$Pa.s$]
τ	Passage time in the mixing chamber [s]
τ_{ii}	Normal Stress [Pa]
τ_{ij}	Shear stress tensor [Pa]
ϕ_K	Kinetic energy rate ratio
ϕ_M	momentum rate ratio
ϕ_{FR}	Flow rate ratio
Ω	Volume or area domain
$\partial\Omega$	Domain boundary surface or perimeter
$\widehat{\omega}$	Non-dimensional vorticity
χ^*	Normalized impingement point position

Mathematical operations

$\langle \ \rangle$	Spatial Average
$\partial_i(\cdot)$	Differential operator
$\hat{\mathbf{e}}_i$	Normalized vector
x	Cross Product
·	Dyadic product
$\nabla(\cdot)$	Gradient operator
$\nabla_x(\cdot)$	Differentiation with respect of x
$\nabla^2(\cdot)$	Laplacian operator
$(\cdot)^T$	Transpose
$\overline{(\cdot)}$	Average

Indices

$*$	Dimensionless variable
‘	Fluctuating term
$2D$	For 2D of the chamber
$3D$	For 3D of the chamber
A	Chemical specie A
B	Chemical specie B
C	Chemical specie C
i	Index of the counter
inj	At injector

j	Index of the counter
k	Index of the counter
max	Maximum of a variable
min	Minimum of a variable
R	Chemical specie R
S	Chemical specie S
x	x-component of the variable
y	y-component of the variable
z	z-component of the variable
1	Left injector
2	Right injector
0..10	Probe points

Abbreviations

2D	Two-dimensional
3D	Three-dimensional
CFD	Computational Fluid Dynamics
CIJ	Confined Impinging Jets
CPU	Central Processing Unit
DIP MODA	Digital Image Processing Multiobjective Optimization Deterministic Algorithm
GPU	Graphics Processing Unit
DFT	Direct Fourier Transform
DNS	Direct Numerical Simulation
FFT	Fast Fourier Transform
LDA	Laser Doppler Anemometry
LES	Large Eddy Simulation
LIF	Laser Induced Fluorescence
NAJ	Narrow Axisymmetric Jets
NS	Navier-Stokes
PDF	Probability Distribution Function
PIV	Particle Image Velocimetry
PLIF	Planar Laser Induced Fluorescence
RAM	Random Access Memory
RANS	Reynolds Averaged Navier-Stokes
RIM	Reaction Injection Moulding

RTD	Residence Time Distribution
TKE	Turbulent Kinetic Energy
VOF	Volume-Of-Fluid
GUI	Grafical User Interface

List of Figures

List of Tables

1 Introduction

1.1 Relevance and Motivation

In the second half of the 20th century, plastic became a most universally-used and multipurpose material in the global economy. From the beginning of production in 50's it was boosted with an increasing rate of almost 9% per year from 1950 to 2012 (PlasticsEurope, 2015). Nowadays plastic is globally used in components which require low weight, excellent finishing and low cost.

Depending on the conditions necessary to produce a plastic component, two major groups emerge to classify those plastics, thermoplastic and thermoset. Thermosoftening (thermoplastic) plastics is a material which requires a specific temperature to be mouldable, weakening the intermolecular bound forces, fulfilling the mould and obtaining their shape upon cooled. Thermosettting plastics is a petrochemical material which requires a chemical reaction to create permanent intermolecular bounds fusing inside the mould and therefore obtaining their shape.

A wide range of industrial processes to produce plastic components exist in the industry in order to adapt for the materials used due to chemical transformation, number of parts to be produced, size and parameters which constrains the mould and process. One of this process is Reaction Injection Moulding (RIM) that uses confined impingement jets mixers

(CIJ), which are the topic of the present thesis. This method have a set of advantages being used particularly to produce component for the aeronautic and automotive industries.

In Section 1.2 will be introduced the process of mixing for the particular case study, followed by a description of the RIM process in the Section 1.3 where will be introduced the process of producing plastic components in CIJ reactors. In the end, in the Section 1.5 will be presented an overview of the thesis layout and objectives.

1.2 Mixing Process, an Introduction for the Case Study

Mixing is a critical stage in any chemical industry and it is used to combine two or more material (fluids or solids) into a homogenous solution. A detailed study of the mixing process is necessary due to limitations such as space, material and operation cost which strongly contribute for the performance of the industrial process. In the early ages, mixing was performed using a continuous flow stirred-tank reactor (CSTR), based on a tank containing the solution to be homogenized and an impeller to perform the mixing. This methodology is still used nowadays for some specific process, but due to energy costs and poor distribution of residence time, it starts to be converted into other mixing techniques more environmentally friendly, with lower production cost and better control of the mixing process.

The work presented in this thesis introduces the study of the flow in Confined Impingement Jets (CJI) where two fluids are injected in a confined chamber though opposed jets. In the impingement zone where the two jets contact a rapid deceleration occurs, dissipating energy radially across the chamber. In this methodology two different geometries emerge: T-Jets with a rectangular section for the injectors and chamber; CIJ with a cylindrical cross section of the injectors and chamber. Although both geometries used the same technique to mix the fluids, different flow structures emerge along the flow regimes studied in the literature.

This geometry is quite simple to manufacture, with no moving components, but a very low roughness in the chamber and injector walls is required. This mixing technology is very advantageous for rapid chemical processes where small micromixing scales have to be reached in short times, for example in Reaction Injection Moulding (RIM), and in applications such as the production of nanoparticles via wet chemistry routes.

1.3 Reaction Injection Moulding in Confined Impingement Jets

The Reaction Injection Moulding process (RIM) was initially developed in Bayer AG in 1964 in order to produce plastic components initially from polyurethanes, but due to the increasing demand of plastic production was adopted to produce polyureas, polyamides, polyesters and polyepoxides (Fonte, 2012). This method is suited to produce large plastic parts and this is why nowadays is used in the aeronautical and automotive industries.

In this process two fluid streams enter in the mixing chamber as opposed jets and mixing occurs rapidly, meaning low residence times order of 1/10 s. In an industrial machine fluids exit the injectors with a velocity of 10 to 150 m/s but due to high viscosity rate of the polymers, up to 1 Pa.s, the Reynolds number are low from 100 to 500. Due to this factor the process demands powerful pumps to produce pressures in order of 100 to 200 bar and therefore equipment to support such pressures. The industrial mixing chambers range from 3 to 15 mm of diameter, with a height five times the diameter and injectors diameter in range 1 to 3 mm (Oertel, 1985; Santos, 2003). Although such pressures are required in the fluids injection, the mixture enters in the mould at low pressure, requiring low cost moulds with low weight (Teixeira, 2000). Adding to this factor the large flow rates, it means the small machines can produce large plastic parts.

Inside the mixing chamber the instability of the jets creates mechanisms of mixing due to the fast deceleration of the jets towards the impingement point. Although high velocities are produced, the fluid motion is dominated by viscous forces relatively to inertia, meaning no turbulent flow is observed.

Due to the low residence times, there is no meaningful polymerization of the fluids inside the mixing chamber, and also due to the high viscosity no considerable molecular diffusion occurs. The mixture mechanisms consist of the stretching of fluid from the jets, followed by bending and folding, which creates a lamellar structure. It is the thickness of these lamellar structures that contributes to mixing and it is considered that both fluids are mixed when their laminas reach a thickness that is sufficient to allow for a full polymerization to occur inside the mould. The mixture is the most important factor of this machine and due to this factor a precise control of the flow rate is needed to deliver the fluids in stoichiometric proportions (Santos, 2003) and perfectly mixed.

This process is highly adaptive since it can also include a vast number of reinforcements, fibbers and reagents in order to add stiffness to the component. Each combination of reinforcement fibbers and reagents species introduced in the mould changes the

mechanical response to applied forces, and therefore the part produced can be optimized regarding its weight and strength. Due to this feature the author believes in the future this process will be more widely used, due to the demand in the industry, particularly in automotive and aeronautical, by trustful, low weight parts with good mechanical proprieties that enable substituting expensive materials such as aluminium, steel and others.

Figure 1.1 shows a graphical representation of a RIM machine. In this scheme two major circuits are observable, an injection and a recirculation circuit. A circuit represented by the storage tanks (7), heat exchanger (5) and recirculation pumps (4) recirculate the fluid for the thermal stabilization of the fluids. The injection circuit is presented next

1. Monomers and polymers, in this example Polyol and Isocyanate are storaged in separated storage tanks (7).
2. High pressure cylinders (6) are used to deliver fluid into the mixing chamber (1). In this process a good control of the flow rates guaranties control of the process and deliver the fluids with accurate stoichiometric ratios
3. The reactants are injected into the mixing chamber where they are mixed until the mould (2) is filed.
4. In the end of the process a piston is shot into the mixing chamber to remove any remaining material.
5. Curing of the polymer in the mould, which depending on the mould size and formulation used, could be 1 to 30s. The time of this process is the limiting step of the entire RIM process (Santos, 2003)
6. Demoulding

Figure 1.2 shows a RIM machine commercialized by KraussMaffei.

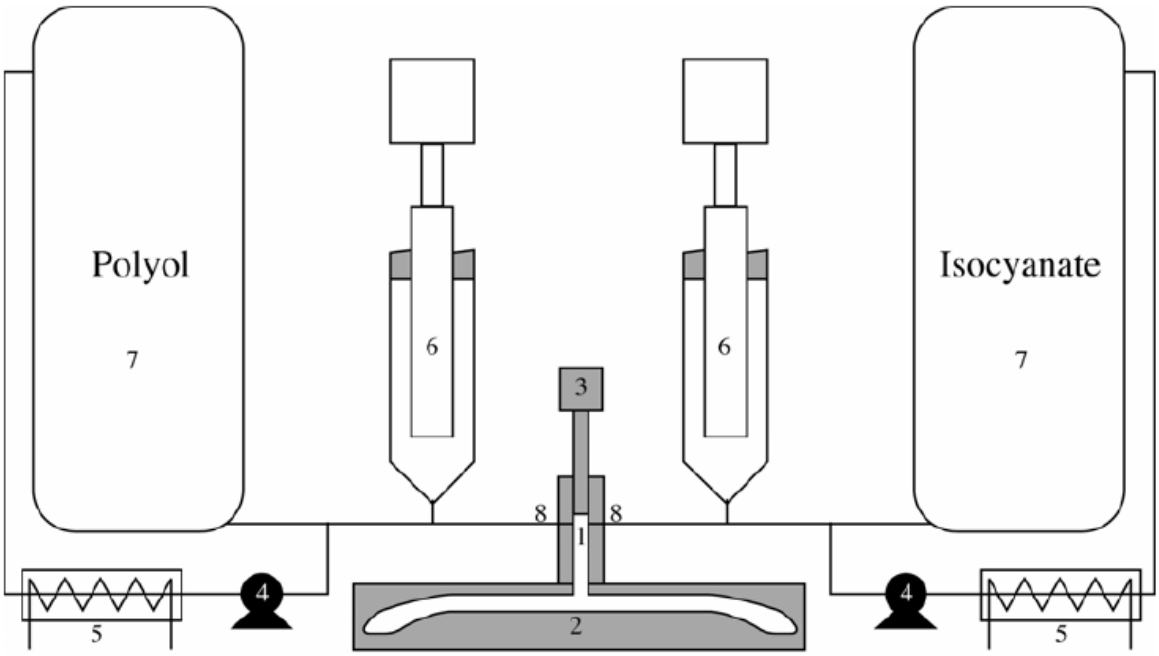

1 – Mixing chamber
2 – Mould
3 – Cleanout piston
4 - Recirculation pumps
5 – Heat exchangers
6 – Lance pistons
7 - Storage tanks
8 – Injectors

Figure 1.1 - Scheme of a RIM machine adapted from Macosko (1989)

Figure 1.2 – RIM machine commercialized by KraussMaffei

According the advantages and disadvantages, it is possible to say

- Advantages
    - Suitable for low quantities. If the cost of production overweights the cost of investment this methodology starts to become inefficient.
    - Low tooling investment, due to low pressure injection it requires lower mould strength and as a consequence this process can be used for prototyping.
    - The RIM process is not dependent of the parts dimensions or weight, being capable to handle complex geometries with thin walls, producing components with excellent finishing allowing high quality painting.
    - By adopting different reaction species it is possible to choose specific mechanical proprieties
- Disadvantages
    - RIM requires excellent control of the environmental conditions and operational variables due to high sensitivity of the process
    - RIM require an excellent know-how to modify/adjust the process variables to different reactors in order to obtain a proper mixture
    - Knowledge in mould designing to archive fast and proper demolding with a good finishing quality

Financial data of the materials for RIM is shown in Table 1, from the annual revenue of the top chemical industries: Bayer AG, Huntsman, BASF (BASF, 2014; Bayer, 2014; Huntsman, 2014). It is separated the global revenue of the companies versus the revenue for polyurethanes, principal RIM material, respectively for the years 2014 and 2013. It is conclude the market for polyurethanes represents an important share of the companies revenue. An average growing rate of polyurethanes market of 4% demonstrates the economic importance of this market in the production of plastic components. The report of Huntsman it was converted from Dollars to Euros by an average exchange in the two years of this study of 0.79 €/$.

Table 1 - Annual revenue in billions of euros of the three major chemical industries

	Global revenue		*polyurethanes*		*Growing rate of polyurethanes (%)*
	2014	2013	2014	2013	
BASF	74.326	73.973	6.135	5.708	6.96
Huntsaman	9.15	8.75	3.76	3.92	1.35
Bayer AG	42.239	40.157	6.285	6.054	3.67

The increasing demand for plastic components allied with the introduction of new capabilities in RIM technology and the poor knowledge of the full resolved fluid flow motion inside the mixing chamber, in order to control the process, constitute the driving forces for the present thesis that pursues a research line that was initiated by Teixeira (2000), and continued with Santos (2003), Fonte (2012) and Gomes (2015).

1.4 Previous work

This work is the follow up of the studies performed by Teixeira (2000), Santos (2003), Fonte (2012) and Gomes(2015) in their PhD thesis. Therefore, before presenting the thesis objective and layout is important to situate the starting point.

Teixeira (2000) performed an experimental and computational studies of the dynamics of the flow field using for the experimental side Laser Doppler Anemometry (LDA) comparing with a 2D model representative of the mixing chamber simulated using the CFD code FIDAP.

In the experimental work, Teixeira (2000) measured the two velocity components normal to the chamber axis for a Reynolds range from 50 to 600. From the LDA experiments the flow variables were computed, namely the Reynolds stresses, turbulence intensity and the distribution of flow field for several planes inside the chamber. From these studies was related the flow field inside the chamber with the Reynolds number in the injector showing the existence of a critical Reynolds for where exist a full segregation of the jets inside the chamber. Also it was observed for the first time the existence of characteristic frequencies of the jets oscillation.

Teixeira (2000) also performed Direct Numerical Simulation (DNS) of the flow field using a 2D computational geometry. This simulation was performed for the same Reynolds range as the experiments, being thoroughly studied the numerical parameters that affect the numerical results. It was proven by comparing with other published works the effectiveness of the numerical simulation to predict the actual behaviour of the flow field.

Santos (2003) performed experiments with LDA for Reynolds numbers ranging from 250 to 600 in which was studied the dynamic behaviour of the flow field and the oscillation frequencies. Using a 2D geometry the flow was modelled using the commercial CFD code FIDAP to correctly replicate the dynamic behaviour of the flow field providing answers for the jets oscillation mechanisms. This was also done using experimental PIV technique.

Santos (2003) work is based in experimental work with LDA and PIV to study the oscillation frequencies and the oscillations mechanism of the flow field. 2D numerical simulation were performed to accurately reproduce the flow field dynamics and the mass transfer mechanism.

LDA was used to study the flow for ranges of Re from 260 to 600, the oscillation frequencies were studied for velocity components with the same direction of the injection in order to compare the results with the 2D numerical simulations, a study made near the impingement region to access the nature of the flow structures is performed. From PIV experimental work the flow field maps were created for Reynolds ranged from 100 to 500 helping to clarify and validate the hydrodynamics of the flow field when compared with numerical data. From experimental work operation parameters such as Reynolds and Froude number and jet's momentum ratio as study helping to provide data for better control of the process.

Using 2D CFD simulations with a commercial software Fluent, Santos (2003) studied the mass transfer mechanisms in the RIM process, where the numerical and physical mechanisms was presented. Also a chemical reaction was perform to better understanding the role played by the flow field in the RIM process.

Fonte (2012) based on 3D numerical simulation made a Lagrangian particle tracking to study the distribution of striation thickness along the chamber using the commercial software Fluent. Also, using numerical simulation it was performed a study using a multiphase model, Volume of Fluid (VOF), coupled with an adaptive mesh refinement based on the gradient of the chemical concentrations for a 2D representation of the mixer chamber with the objective to model the smaller mixing length scales, proven the

applicability of this technique to flow visualization although with extreme computational cost.

In the experimental side PLIF technique was used to qualify the mixing patters of the entire flow field. PLIF experiment results, validate an elastic model, mathematically deduced by Fonte (2012), to predict the position of the impingement point for a different set of flow conditions. It proves the validity of the model handling different flow rates and for different circular injector's cross sections.

1.5 Thesis objective and layout

The present thesis is divided into two main objectives. The first objective is to study the fluid flow and mixing mechanisms in the RIM mixing chamber, using more than one technique. The second objective is to study the jets interaction under balanced and unbalanced flow conditions to evaluate more than one mathematical equation used to developed a robust control for RIM processes.

This thesis is divided into six chapters. The first chapter corresponds to the introduction of the theme and the relevant motivation to study it. The second chapter presents the state of the art of mixing and flow dynamics applied to RIM. The rest of the chapters are divided into different techniques for flow analyses. The main objectives are to investigate and to contribute to widen the knowledge of the governing mixing mechanisms and process control of the RIM machines.

- In Chapter 3 DNS simulation is performed for Reynolds 150, 200, 250 and 300 in order to study the energy containing flow scales where the energy cascades are studied to compare the vortices length in relation to the chamber dimensions. Additionally turbulent quantities such as the turbulent kinetic energy and the turbulent energy dissipation rate are presented for all the Reynolds numbers studied. VOF model is implemented for Reynolds 150 in order to study the advection mechanisms without the effect of diffusion and not considering surface tension.
- In Chapter 4, PIV measurements in a plane passing thought the injector axis are presented in order to perform the study of balanced and unbalanced jets using two mathematical models to predict the impingement point position. The results of the mathematical models to control the mixing process will be compared with the experimental results

- In Chapter 5 was performed the study of the flow field with PLIF experimental technique. In this case a high speed camera was used to record in Real Time the flow field mechanism. An optimization algorithm was used to obtain the impingement point position and the impingement jets angle from the recorded images. Spectral analyses of this two variables was performed in addition to the spectral analyses of the differential pressure between the injectors. The results of this three parameters were performed and compared with experimentally documented data provided from LDA experiments. In the end, process control of the RIM machine was studied, and applied to mixing of fluids with different physical proprieties. For this case two mathematical models were compared with the experiments, and the results were discussed.

Additionally, animations of the experimental and numerical work were included a DVD attached to this dissertation. The animation was prepared to be played with QuickTime Player. Animations where organized in the following folders

- Folder "/Chapter_3/" contains animations of the velocity field, vorticity field for 2D and 3D, in dynamic simulations for different Reynolds number using the following organization
    - Folder "/Chapter_3/Re_150/Velocity_field"
    - Folder "/Chapter_3/Re_150/2D_vorticity"
    - Folder "/Chapter_3/Re_150/3D_vorticity"
- Folder "/Chapter_3/" contains animations of the dynamic behaviour using the VOF model. It is presented as result the fluid volume fraction in the following folder.
    - Folder "/Chapter_3/VOF_Re_150/Volume_fraction"
- Folder "/Chapter_5/" contains animations of the results from PLIF in Real Time, of the flow field for all the Reynolds studied using the following organization:
    - Folder "/Chapter_5/Re_..."

2 State of art of RIM and CIJ

2.1 Introduction

Mixing is an operation present in any physical or chemical industries which requires in this process a contact between two reactants or a homogenation of two or more materials. Therefore mixing is from the middle of the century an important study topic requiring the answer of two important questions. The first question is about the physics and mechanics of the mixing in order to understanding the mixing in a particular process or improving the mixing quality by creating new and innovator process for each particular case. The second question is about the mixing in a chemical way, understand the concept in a molecular level, understanding the chemical reaction and therefore improving by changing reactants and adapting process parameters to better chemical reaction.

In the first part of this section will be introduced concepts of mixing in chemical systems by presenting a global picture of the evolution of mixing studies, starting from the types of mixing, the parameters which influences the mixing and their measurement in practical fluid flow systems, followed by presenting the mechanics and finalising with computational fluid simulation in mixing systems based on hydrodynamic studies.

The second part of this section aim presenting the work perform in RIM, particularly in CIJ, emphases booth numerical and experimental for the biggest topics in this field remainder

the study of the mixing and their characterization and the hydrodynamic studies and their effect in mixing performance.

This overview do not pretend a full detail of all the publish work present in literature, but pretend to contextualize the reader, introducing for the most important publications up to date and which the present thesis represent a progress in this studies. A more detail study in mixing process can be found in (Baldyga & Bourne, 1983, 1984a, 1984c, 1984f, 1989a, 1989d, 1990; Ottino, Ranz, & Macosko, 1979). According the RIM process particular in CIJ's the author recommend (Baldyga & Bourne, 1983; Baldyga, Bourne, & Zimmerman, 1994; Frouzakis, Tomboulides, Lee, & Boulouchos, 2002; Kusch & Ottino, 1992; Kusch, Ottino, & Shannon, 1989; B. S. Lee, Kang, & Lim, 1999; D. Lee & Chen, 2011; J. Lee, Tripathi, & Chauhan, 2014; L. J. Lee, Ottino, Ranz, & Macosko, 1980; R. E. Lee, Finch, & Wooledge, 1957; Wehrmeyer, Cheng, Mosbacher, Pitz, & Osborne, 2002).

The hydrodynamic and mixing study was well study in LSRE, where the author performed the current thesis, where the work publish up to date represent a breakthrough in the studies of CIJ's, and where serve of ground foundation for the present work. Emphasis in the work of A. M. Teixeira (2000), R. J. Santos (2003) and Fonte (2012) in experimental and numerical studies will be made.

2.2 Mixing Study

Due the complexity of mixing a several approaches was perform particularly using experimental method to quantify and qualify the mixing and their mechanism. Nowadays CFD is used to perform the same studies in a numerical way, being possible the study the coupling of hydrodynamics and chemical combined or separated. From this point is important to clearly introduce and define concepts used in the present thesis.

2.2.1 Characterization of the mixtures

Mixing can be classified regarding the type of phases used in the mass transfer. Using Nienow criterion it is possible to identify the following mixing processes

- Single-phase liquid mixing: All the phases present in the mixture are miscible liquids;
- Liquid-liquid immiscible mixing: The phases present in the mixture are liquid incapable to mix, for example oil and water. In this type of mixing the main

objective is to increase the interfacial area between the phases by any means possible.

- Solid-liquid mixing: The main objective of this mixing is suspended the solid particles in a liquid medium.
- Gas-liquid mixing: Similarly to the previous the mixture is perform by the dispersion of gas bubbles into the liquid medium.
- Solid-solid mixing: All the solid phases are mixture until a uniform solid solution is archived.

2.2.2 Residence time distribution RTD

Danckwerts (1953) introduced a method to quantify the distribution of the time in where each particle of fluid remained inside the reactor, provided an idea of the hydrodynamic behaviour of that reactor, in where can be predicted the existence of backmixing, shortcuts and dead zones. A simple test is perform for a certain reactor in where after a steady state of functioning is achieved a marker of ink inject a known concentration in a reactor inlet in time (t=0) and the register of the concentration of the ink in the outlet is performed. The residence time distribution RTD $E(t/\tau)$ is calculated as

$$E\ (t/\tau) = \frac{dF(t/\tau)}{d(t/\tau)} \tag{2.1}$$

Where t/τ is the residence time and $F(t/\tau)$ is the tracer flux in the outflow. Another concept is the distribution of ages of material in the reactor $I(t/\tau)$

$$I(t/\tau) = \ 1 - F(t/\tau) \tag{2.2}$$

Complete segregation is archive when all the particles of fluid have the same age while they cross the reactor.

The main advantage of this method is a simple and efficient practical method with required low knowledge and investment while produce a good quantitative and qualitative measure of the reactor hydrodynamics. Although (Zwietering, 1959)demonstrate for two reactor can have same RTD and complete hydrodynamics in case of kinetic chemical reaction is nonlinear. In the same work was introduce a concept of mixedness, in where exist multiples inlet and a common outlet and was proven this methodology only can predict the upper and lower conversion bounds and in any case can be know the velocity field inside the reactor. As a conclusion a fluid with lower residence time is described by

the complete segregation model and fluid with higher residence times is described by the maximum mixedness model.

2.2.3 Measurement of the degree of mixing

Measure mixing is a critical factor for any reactor design in order to access the quality of the mixing process. Exist in the literature two methods to quantify the mixing quality: physical methods are related to the fluid homogenization and chemical method with quantify the spectrum of products from a chemical reaction.

2.2.3.1 Physical methods

Danckwerts (1952) introduced a set of concepts directly related with the efficiency of a mixing process.

Scale of segregation: This parameter define the mixing texture, quantify the fluid homogeneity or graininess, defined as

$$S_s = \int_0^\infty R(r)dr \tag{2.3}$$

Where $R(r)$ is defined as the correlation coefficient between two separated points in the mixture with distance r

Intensity of segregation: Is defined as the deviation from the mean concentration of a specie by the concentration of the chemical species present in the reactor, defined as

$$I_s = \frac{\sigma_{C_A}^2}{\overline{C_A C_B}} \tag{2.4}$$

Where $\sigma_{C_A}^2$ is the variance of the concentration of specie A C_A, and $\overline{C_A}$ and $\overline{C_B}$ are the mean concentration of specie A and B, respectively. In case of the variation of the concentration of specie A is zero represent a complete homogenization of the mixture since there is complete reacted, and in opposite represent complete segregation

Another method to calculate the intensity of segregation in chemical reactions is using the following equation

$$I_s = 1 - r/r_0 \tag{2.5}$$

Where r_0 is the initial chemical reaction rate, for the case of immediate homogenization, and r is the average chemical rate after leaving the reactor

Nowadays exist others method, more precise, using tomographical technology to predict the scale and intensity of segregation allowing dynamic determination of the concentrations of the tracer at several points in a mixer (Buchmann & Mewes, 1998, 2000; Kling & Mewes, 2004).

2.2.3.2 Chemical methods

Consider a general reaction

$$A + B \rightarrow R \tag{2.6}$$

The velocity of a reaction, produced in a continuous stirred tank reactor, is a function of the mixing quality (Danckwerts, 1958) in the following way:

- Order > 1 implies that the reaction velocity increases by an increasing of the segregation, meaning the increasing of the kinetic term will be produce due worst mixing quality
- Order = 1 indicate the mixing quality is independent of the reaction kinetic constant
- Order < 1 implies the velocity of the reaction is improved by improving in the mixing quality

In the literature exist a set of chemical reaction present a way to address the efficiency of a reactor (Levenspiel, 1962). This reactions can be 1st order, 2nd order our 3rd order.

Weinstein and Adler (1967) study the influence of mixing in a 1st and 2nd order reaction, while Danckwerts (1952, 1958) suggested the using of a 2nd order consecutive reaction to quantify the mixing performance by study the intensity of segregation. 1st order reaction can be represented by:

$$A \xrightarrow{k_1} R \tag{2.7}$$

And 2nd order chemical reaction

$$A + B \xrightarrow{k_2} R \tag{2.8}$$

$$R + B \xrightarrow{k_3} S \tag{2.9}$$

Where A, B, R and S are chemical species and k_1, k_2 and k_3 are chemical reaction kinetic constants. Consider the 1st order chemical reaction: the reactant A will then create R after the time k_1 it is complete. The kinetic constant k_1 access the time required for all A is transform to R, and if this time it is not archived the reaction is incomplete. In a case of a 2nd order reaction two different reactions are parallel created and in case of k_1 is fast enough and B are completely converted to R so, no subproduct S will be created. The full conversion of product A into R for the 1st order reaction or the non-existence the reactant S in the 2nd order chemical reaction is used to measure the micromixing efficiency.

The main conclusions presented by Danckwerts (1952, 1958) and by Weinstein and Adler (1967) show that 1sr order reactions are almost full dependent of the macromixing rather than micromixing wile 2nd order reaction are greatly affected by both micro and macromixing.

In a case of a 1st order reaction segregation can cause the increase of the kinetic reaction constant which can be overpass by increasing the reactor size, but, in case of 2nd reactions it cannot be possible. This reaction is nowadays extremely important to access the distribution of consecutive reactions and due their sensibility to both micro and macromixing to evaluate the mixing performance. Kusch et al. (1989) and Mahajan and Kirwan (1996) used 2nd order reaction to study a wide range of reactors particularly confined impingement jets reactors.

Triplet consecutive reactions (Bourne & Yu, 1994; El-Hamouz & Mann, 1998) allow wide flexibility to characterize the mixing performance, when compared with 2nd and 1st order consecutive reactions.

$$A + B \xrightarrow{k_1} R \tag{2.10}$$

$$R + B \xrightarrow{k_2} S \tag{2.11}$$

$$S + B \xrightarrow{k_3} T \tag{2.12}$$

In this case, perfect mixing is obtained by full conversion of A and B into R. Complete segregation favour creation of T while the creation of S is due complete segregation of A and B from the initial conditions.

Parallel competitive reaction with different constant kinetic reaction coefficient one fast and other slower is study by Bourne, Kut, Lenzner, and Maire (1990) and J. Villermaux, Falk, Fournier, and Detrez (1992)

$$A + B \xrightarrow{k_1} R \tag{2.13}$$

$$A + C \xrightarrow{k_2} S \tag{2.14}$$

In the fast reaction is occur if a past homogenization of the reactant is present, in the other and, the slower reaction helps to compare the mixing efficiency.

2.2.4 Mixing mechanism

By Danckwerts (1952) mixing process can be divided in two main space scales, micromixing and macromixing which is directly related to the scale where the mixing occur. Micromixing is processed in to microscopic level and macromixing is due the effect of large scale eddies in the fluid flow system.

In any fluid flow system exist two mixing mechanisms identified by Bourne (1997) relating how they occur. If two reactants are mixing in a molecular level the mixture is called diffusive mixing in opposite convective mixing occur due the effect of convection in spreading the fluid along the reactor. In the smaller scales, microscale, the fluids are homogenized by diffusive mixing and convective mixing at the lower scales. In bigger scales, macroscales, the fluid is homogenized only due convective mixing but remains full heterogeneous in the lower scales

Although mixing mechanism is not fully understood, Beek (1959) and Jacques Villermaux and David (1983) proposed as a ground foundation three stages in where the mixing is created. This three stages is them directly related for this particular process, RIM.

- Fluid is grossly distributed along the reactor with heterogynous mixing in the macro scale: In a RIM two fluids are injected by opposed jets where a instability region created by the large scale eddies spread the fluid material along the chamber.
- Reduction of the mixing scales: After big eddies distribute the fluids, smaller hydrodynamic scales will homogenized the fluid in a macro and micro scales along is going thought the reactor. In this stage the surface area will exponential increase by stretching increasing and thickness reduction.

- Mixture is produced by diffusion: Due the low residence times, molecular diffusion is not expected to occur significantly inside the reactor. Molecular diffusion will only play a significant role by reaction inside the mould.

2.2.4.1 Lamellar model

In a laminar systems the striation thickness of the fluid is increased along the chamber due viscous forces creating inside the chamber, by bending and folding, lamellar structures of fluid with low thickness and big surface area (Ottino et al., 1979; Ranz, 1979). In turbulent flow systems this elongation of the fluid streams could be break due inertial forces overlapping viscous forces. In the end, inside the mould molecular diffusion enters in place, described by the Fick's law. In fluids as the Schmidt number is big the diffusion is slow and controlled by interfacial area.

Ranz (1979) used a Lagrangian reference frame fixed on a laminae to study the variation of this laminae with the striation thickness, interfacial area and the velocity gradient. A reducing of the striation thickness, consequently and increasing of the surface area augments the direction of diffusion, correspondent to the normal direction with the surface area, decreases improving molecular diffusion and therefore the mixing quality. Ottino et al. (1979) derived and equation, for Newtonian incompressible fluids, to obtained the interfacial area generation as a function of viscous dissipation. Ottino et al. (1979) also presented a set of tools to analyse lamellar structures in a microscale environment without surface tension effects and with instabilities at microscale. Chella and Ottino (1984); Ottino et al. (1979) applied the lamellar model present previously to find concentrations field in a system with multicomponent diffusion and n-linear chemical reactions.

Chella and Ottino (1984) performed a parametric study for a reactor with an arbitrary flow field and segregated feeding with the lamellar model, where the parameters to study was the initial reactant segregation, the ratio of the reactants diffusivities, the first and second Damkõhler number correspondent to the relation between the mixing and reaction times for the first and the relation of mixing and diffusional time for the second number. The reactive schemes used was a second order bimolecular reactions, parallel competitive reactions and consecutive competitive reactions.

Fields and Ottino (1987) used lamellar model to predict the effect of striation thickness distribution on the polymerisation. A competitive-parallel reaction scheme was used to evaluate the formation of soft and hard segments were was tested two distributions of

striation thickness: uniform and one obtain by Kolodziej (1980). The author reported the best result was obtained by the uniform distribution rather than the Kolodziej (1980) distribution.

Fields and Ottino (1987) used a limped competitive-parallel reaction scheme to study the effect of stretching of two fluids, combining the polymerization model with the lamellar model. The authors study the stretching effect where the flow is driven by shear or elongations. The authors conclude the stretching have a strong effect on the reaction system. As a conclusion the authors observed the elongation flow, when compared with shear flow, have a higher mixing efficiency

Due high viscosities of the flow stream the main mixing mechanism present is the reduction of the thickness to a point where diffusion can enter to a level where polymerization can be archived.

2.2.4.2 Engulfment Deformation Diffusion Model

Baldyga and Bourne (1989a, 1989b) proposed a mixing model where the mixing is produced in three steeps: Engulfment caused by vorticity followed by elongation due shear stresses and in the end diffusion. Consider two elongate different fluids in layers A and B with scales equal to the Kolmogorov scale λ_k, Baldyga and Bourne (1984c) proposed the velocity of the reduction of the lamina thickness is a function of the energy dissipation rate and viscosity of the fluids. To model the chemical species transport is used the diffusion-convection-reaction equation. The engulfment is caused by a vortices with lamina thickness of order λ_k which are initially twisted in vortices with λ_k of diameter, but increasing until twice the size when the two fluids are incorporated.

2.2.4.3 The E Model

Baldyga and Bourne (1989a, 1989b) introduced the E model assuming Schmidt number lower than 4000 and more than two engulfment are needed for complete mixing. The author proved experimental and theoretical that deformation and diffusion it is not a limiting steps of the mixing process. Experiments revel the E and EDD model can be used for calculating the product distribution for the consecutive competitive reaction schemes with no differences, although in a numerical component

2.2.5 Mixing and hydrodynamics simulation

In a numerical model the only way to study the fluid structure and the reaction mechanics is to describe the domain, in three-dimension form and discretize into small control volumes, where in each one the Navier-Stokes time dependent equation is calculated

$$\rho \frac{D\vec{v}}{Dt} = -\nabla p + \mu \nabla^2 \vec{v} + \rho \vec{g} \tag{2.15}$$

And the continuity equation

$$\nabla . \vec{v} = 0 \tag{2.16}$$

Coupled with advection-diffusion reaction equation

$$\frac{\partial C}{\partial t} + \vec{v} - \vec{\nabla} C = D_m \nabla^2 C + r \tag{2.17}$$

Where $\vec{v}$ is the three dimensional flow field $\vec{v} = u_1 \hat{\mathbf{e}}_\mathbf{1} + u_2 \hat{\mathbf{e}}_\mathbf{2} + u_3 \hat{\mathbf{e}}_\mathbf{3}$, ρ the fluid density, p is the pressure, $\vec{g}$ is the gravity vector, C is the concentration of a chemical species, $D_m$the molecular diffusivity and r it is the net rate of creation or destruction of a specie by chemical reaction.

The solving of the Navier-Stokes, in a three dimension time dependent resolution for a certain domain and boundary conditions is called Direct Numeric Simulation DNS (Baldyga & Bourne, 1999). Some authors take the liberty of calling DNS of a simulation, both 2D or 3D flow field where all the scales are calculated until the lower scales, Kolmogorov scaled. Although this method can obtain all the scales present inside a reactor, the used of a fine computation grid to discretize the domain make almost impractically, due time limitations, any study until this scale. The grid points required to perform this study is proposition of the ratio off all the scales and the Reynolds number, given by

$$N_{xyz} \approx \left(\frac{L}{\lambda_k}\right)^3 \propto (Re)^{\frac{9}{4}} \tag{2.18}$$

L is The largest length scale of the problem (Baldyga & Bourne, 1999; Givi, 1989) and λ_k is the smallest scale in a turbulent flow, in which the viscosity overtakes the problem and turbulent kinetic energy is dissipated into heat and is function of kinematic viscosity ν and the average rate of dissipation of turbulent kinetic energy per unit mass ε

$$\lambda_k = \left(\frac{\nu^3}{\varepsilon}\right)^{\frac{1}{4}} \tag{2.19}$$

Due to high computation coast of a DNS, nowadays only was possible to study small and moderate Reynolds number, and for higher Re common is the industry and atmosphere the computation cost required will largely exceed the capability of the most powerful computer currently available

If now consider the computational coast required to perform a DNS of the flow field but now considering also the mixing effect. It is know the scale of mixing in turbulent flows is the Batchelor scale

$$\lambda_N = \frac{\lambda_k}{\sqrt{Sc}} \tag{2.20}$$

And Sc is the Schmidt number defined as

$$Sc = \frac{\mu}{\rho D_m} \tag{2.21}$$

Where $D_m$is the molecular diffusivity of a chemical species, ρ is the density and μ is the viscosity. If is considered the mixture is liquid-liquid then the Schmidt number is order of 10^3 and the mixing scale is one order of magnitude smaller than the smallest hydrodynamic scale, Kolmogorov scale. Coupling this parameters in a 3D simulation considering mixing the grid scales required to perform this study is

$$N_{xyz} \propto (Re)^{\frac{9}{4}} Sc^{\frac{3}{2}} \tag{2.22}$$

For $Sc > 1$ it will be necessary a gird refining. In case of liquids, where the Schmidt is ranged of 10^3 then to perform a DNS to a mixing problem the grid nodes will increase in a factor of 3×10^4

Due to high computation coast of a DNS other methods was developed to study the flow and mixing mechanics up to fully turbulent flows. This methodologies used is the Reynolds average Navier –Stokes equation (RANS) now Large Eddy Simulation LES is highly used in turbulent flows to perform computation until low hydrodynamic scales

2.2.5.1 RANS Simulation

In the study of Reynolds-Average Navier-Stokes equation provide a methodology is compute turbulent flows in a certain range for the majority engineering applications. In this method the smaller scales are not computed and the flow is average in each time required. This provided a good stability in the progress of the time integration whit minimum computational cost. In this method all the variables, such as velocity field v_i, are divided on time average term, $\overline{v_i}$, and the fluctuation term v_i'

$$v_i = \overline{v_i} + v_i \tag{2.23}$$

In this method the governing equation is solved, by replacing each variable as their average plus fluctuations in the Stokes equation. A new apparent stress emerge, known as Reynolds stress, by adding a second order tensor in the equation, which from that is possible deduce various models and adding new variables to access different engineering problems, resulting in:

$$\rho\left(\frac{\partial \overline{v_i}}{\partial t} + \overline{v_j}\frac{\partial \overline{v_i}}{\partial x_j}\right) = -\frac{\partial \bar{p}}{\partial x_i} + \mu\frac{\partial^2 \overline{v_i}}{\partial x_j^2} - \rho\frac{\partial\overline{\left(v_i{}'v_j{}'\right)}}{\partial x_j} + \rho\vec{g}_i \tag{2.24}$$

Was refer early the term $\overline{v_i v_j}$ is referred to incompressible flow and named as the Reynolds stress tensor

$$\tau_{ij} = -\rho\overline{v_i{}'v_j{}'} \tag{2.25}$$

RANS methods can be one or two equation (Pope, 2000). Prantl's, Baldwin and Sparlat-Allmaras are examples of one equation RANS models, while for two equation exist the Realisable, K-omega and the K-Epsilon, which is the most used method in RANS nowadays (Baldyga & Bourne, 1999; Givi, 1989; P. A. W. Libby, F.A., 1994). A insight for each RANS method is given by (Pope, 2000; Speziale, 1991).

The same methodology used in RANS can be applied to the advection-diffusion-reaction equation, where the species concentration is given by C, and their time averaging $\bar{C}$ plus the fluctuation c' resulting in

$$\frac{\partial \bar{C}}{\partial t} + \overline{v_i}\frac{\partial \bar{C}}{\partial x_i} = \frac{\partial}{\partial x_i}\left[-\overline{v_i' c'} + D_m\frac{\partial \bar{C}}{\partial x_i}\right] + \bar{r} \tag{2.26}$$

Similarly with the RANS equation it was adding a second term $\overline{v_i' c'}$ which is related with the turbulent diffusivity D_T

$$\overline{v_i' c'} = D_T \frac{\partial C}{\partial x_i} \tag{2.27}$$

The modelling of the Diffusivity term is mostly perform using the $k - \varepsilon$ model (Baldyga & Bourne, 1999), but others methods exist in the literature.

A second order reaction is also divided into averaging term plus fluctuation of the concentration for a given species

$$\overline{r_1} = k_1\left(\overline{C_A C_B} + \overline{c_A{}' c_B{}'}\right) \tag{2.28}$$

$$\overline{r_2} = k_2\left(\overline{C_R C_B} + \overline{c_R{}' c_B{}'}\right) \tag{2.29}$$

Where $\overline{c_i{}' c_j{}'}$ is the unclosed term and $k_{i,j}$ is the kinetic constant for each reaction. Toor (1969), Vassilatos and Toor (1965) and Kosály (1987) presented a method to closer the second order reaction and validated with experimental data. Bourne and Toor (1977), Brodkey and Lewalle (1985), Dutta and Tarbell (1989), Li and Toor (1986) and Wang and Tarbell (1993), proposed models more closely from the reaction reality and therefore more used nowadays. A study of one of this method is presented which was proposed by Bourne and Toor (1977) and Brodkey and Lewalle (1985), respectively.

$$\overline{c_A' c_B{}'} = I_S \, C_{A0} \, C_{B0} \tag{2.30}$$

$$\overline{c_A' c_B{}'} = I_S \, C_{A0} \, C_{B0} \frac{\overline{C_R}}{\overline{C_A}} \tag{2.31}$$

Where I_S is the intensity of segregation and C_{A0} and C_{B0} are the mean concentration of specie A and B, respectively.

Other method is used to calculate the unclosed terms. The Probability Density Function PDF methods is particularly used in combustion (Givi, 1989; Pope, 1985, 1994) but have also proved their value in chemical reaction engineering (R. O. Fox, 1992, 1998; R. O. G. Fox, M.R., 1993; Tsai & Fox, 1994). The main difference of this method from the other method presented is there is no transport of the variables, but by using a subgrid-scale a PDF of this variable is transported (Tsai and Fox (1994). This approach was employed by Li and Toor (1986) for a consecutive reaction CFD based.

Initially the flow is calculated normally using a generic grid and a method suited for the problem in study, where information of the fields (velocity, pressure, temp and others in interest) are extract to a subgrid domain. From this subdomain the chemical reaction will be transported using PDF for all the subdomain in study similar to a post processing stage. This method requires further development (Baldyga & Bourne, 1999).

2.2.5.2 Large Eddy Simulation

Large Eddy Simulation (LES) it is become a very important tool to simulate turbulent flows. In Kolmogorov (1991) theory indicates the large eddies of the flow field are, for confined flows, function of the geometry, but by reducing the scales their effect start to be reduced until, in the lower scale, the kinetic energy is dissipated due viscosity. This feature allows to explicitly solve large eddies and afterward calculate the small eddies in a subgrid scale. This method is formulated in three major steps (Ghosal & Moin, 1995) The first step consists in filtering small spatial scales less than the computation grid. The result equation is used to describe the temporal and special evolution of the large eddies with the effect of the subgrid scale stress tensor from the unresolved small scales into the resolved scales. The second step is substitute the subgrid stress tensor by a model which can be function of the resolved scales and tuning parameters. The last step will performed numerical simulation of the large scale field into a grid small enough to resolved the smallest scales resulting from the large eddies, but much larger than the lower theoretical Kolmogorov scale. This method is not such computational cost of a DNS, where all the scales of the flow are calculated and it is possible to visualize but also do not provided only information of the flow average behaviour as the RANS method, but instead can give a clear picture of the important scales, where the large scales are accurate simulated while also present spectral characteristics of the flow field presented in the smallest scales. For this reason this method is used in wide engineering problems where a picture of the scales from $6\lambda_k$ up to 60 λ_k is needed. In terms of computational cost this method will requires less effort when compared with DNS but still much larger when compared with RANS. Due to stability issues this method required an excellent initial solution therefore many author's start initially to calculate the large scales using a RANS model and import as initial solution for LES. The same procedure can be by done by resolving in a large grid the Navier-Stokes equation.

For mixing proposes the LES can be used with the advection-diffusion-reaction with a low pass filter resulting in a unclosed problem. In the same way as the eddy viscosity is is

treated in LES it can be used the same way for the diffusivity eddy and therefore solving the advection-diffusion problem (Givi, 1989). For a reaction problem since the reaction scale, correspondent to the Batchelor scale presented previously, produce small scales than the hydrodynamic, it is possible to couple in a sub-grid domain others methods such as PDF or RANS (Givi, 1989) (deBruynKops & Riley, 2001) to solve this issue

2.2.5.3 DNS of turbulent flows

Due to high computational cost off a DNS for turbulent flow this method is still very limited for small domains our low Re as reported previously. This method allow understand and determine the flow structures for all the mixing scales, from largest to the lowest, reproducing faithfully the flow dynamics by directly solving the Navier-Stokes equations for a given domain, without any simplification or model being used and therefore is the only way validate numerically the mixing models used nowadays. (Givi & Mcmurtry, 1988) study a second order bimolecular reaction (Toor, 1969) (Kosály, 1987) revealing when compared with experimental data an advantage of knowing the instantaneous values for the chemical in space and time domain.

Other advantages of a DNS into study the hydrodynamics of a chemical reaction is the parametric study of a particular reaction, in where the factors which affect the mixing can be study singular, or parallel with complex flow dynamics. A particular case is present in Chakrabarti, et al. (1995) where was observed the flow dynamics of a cubical domain with periodic boundary conditions for study the fluid flow inside a Plug Flow Reactor PFR, (Gerlinger, Schneider, Falk, and Bockhorn (2000), a 2D DNS simulation using a pseudo-spectral method to for Re equal to 2000 with different flow structures, where 2 and 3 vortices and fully turbulent flow existent in the domain. The replication of exact conditions for the flow structures, creation of vortices, structured flow, and the position distribution and dimension of such structures creates a big advantage in using numerical methods to study such flows, where due to unpredictable behaviour of such flows their replication in laboratory will be extremely difficult being basically a lucky experiment.

2.2.5.4 DNS of chaotic flows

In mixing process a chaotic flow it is a flow which under a tracer experiment and subjected to flow field will produce complex and unpredictable fractal structures with a time dependent exponential growing. In fact the term chaotic flow is often used to indicate a flow, below the turbulent flow regime and where in mixing process can be an alternative

process (Muzzio & Liu, 1996).for high viscosity fluids where inducing turbulence is very cost-expensive, to ensure mixing in two or more flow streams and it is why a very study topic due to the complex nature of the flow and their wide applicability in the industry.

Practical application of the chaotic mixing in the industry process can be expressed in a wider ways as in those generated by channel with obstacles, impingement jets or other situation where the fluid is forced to generate self-sustainable flow patterns ensuring mixing of the fluid flow streams. One of this process it was study by Howes, Mackley, and Roberts (1991) is the flow around a 2D baffled channel, simulated in Re equal to 300, where a transition to self-sustainable chaotic system is achieve, and much lower than turbulent regimes starting from Re equal to 2000 to 3000. The chaotic nature of the flow was study under particles injection and the mixing mechanism was studied. This work it was limited by the computational resources where it was impossible to simulate the smallest scales of mixing and where the particles injection only could identify the mixing mechanics in macro scale being computed over the velocity field. Another work for the same geometry was perform by Roberts and Mackley (1995) where the mixing performance was study using stretching rates which is a mixing quantity in a Eulerian flow field where was study the stretching of a particle, by conservation of volume, and the rate of separation between two particles.

Static mixers is one of the most study type of mixer existing in industry. For them a set of authors studied the flow field using different methodologies in CFD which are resumed here:

- Muzzio and Liu (1996) study a chemical reaction in a 2D chaotic flow for bimolecular and multiple competitive-consecutive reaction. This study was perform for three level of chaos, regular, chaotic and full chaotic where Poincaré maps was created and conclude presence of heterogeneities in the concentration field for consecutive-competitive reactions.
- Zalc and Muzzio (1999) used the same strategy used in the previous point for parallel reactions.
- Mickaily-Huber et al. (1996) simulate a 3D static mixer injected in half of the inlet one phase and in the other half other phase. By progressing the reactor the phases will then achieve different degrees of interpenetration and by divide the outlet into several sub-domains the intensity of segregation was calculated from the variance of the species concentration.
- Hobbs and Muzzio (1997) compute stretching rates of a 3D reactor using a Eulerian

- Mackley and Saraiva (1998) compared the two methods described early where, for the same reactor and flow conditions conclude the stretching rate of a particle injection test and the intensity of segregation due to tracer experiment will produce essentially the same results.
- Byrde and Sawley (1999) study using an Eulerian particle injection the effect of the mixing elements twisted angle on the effectiveness of mixing. The quality of the mixing it was calculated considered as the distance of one species without a presence of another species which correspond to the scale of segregation
- Lamberto, Alvarez, and Muzzio (2001) used PDF of the stretching rate computed from the particle injection trajectory in a CSTR for different functioning regimes.

Giona, Adrover, Muzzio, and Cerbelli (2000)study in the effect of numerical diffusion on a simulation of mass transfer with diffusion. It was conclude $(Pe/2)^n$, where n is the number of cells and Pe the Peclet number is the minimum number of nodes where physical realistic concentration is obtain. As it is known numerical diffusion greatly affect numerical codes to predict a concentration in a tracer experiment, since unit concentration is assumed in cell-based. To overcome this problem for CFD or FEM methods a denser grid points can be used with a consequent memory limitation, or an increase of the order of the finite differences for CFD method or the order of the interpolated function weighted based for FEM with cost in the speed of the calculations. Both methods can be used to overcame this problem but with high computational cost. To overcome this problem (Adrover, Cerbelli, & Giona, 2002) proposed a spectral method for FEM based on the eigenfunction of the Laplacian operator with greatly effect on the reduction of the computational cost with a reduction of the diffusion problems for convection-diffusion-reaction equations.

In the computational perspective by the Moore's law it is expecting an exponential grow of the computational capabilities present nowadays with also advance in the modelling mathematical methods to integrate the Navier-Stokes in the domain and therefore DNS simulation start to become a valid hypotheses to compute in larger Reynolds and reacting flows allowing the study the mixing mechanics in a reaction system with greatly practical interest in improving industrial process

2.3 Mixing in Confined Impinging Jets

2.3.1 Hydrodynamics in CIJ - Experimental Studies

2.3.1.1 Flow Visualization

Imaging the flow field was the earliest method applied by researchers in order to characterize the mixing mechanisms in impinging jets reactors. There are several flow imaging techniques, with the simplest being to employ a coloured tracer in one of the jets and to take pictures of the formed patterns (Bierdel & Piesche, 2001; L. J. Lee et al., 1980; C.L. Tucker & N.P. Suh, 1980). This method can be further improved if the tracer fades with mixing, allowing for a clearer observation of the flow patterns, as regions of poor mixing will be seen as coloured, while well mixed regions become limpid (Sandell, Macosko, & Ranz, 1985). Other techniques that have been used for visualising impingement mixing include particle tracing (Wood, Hrymak, Yeo, Johnson, & Tyagi, 1991), in which the paths of particles seeded to the fluid are recorded, and more recently LIF, abbreviation for Laser Induced Fluorescence (Johnson, Wood, & Hrymak, 1996; Unger & Muzzio, 1999); Unger, Muzzio, and Brodkey (1998). In LIF, a fluorescent tracer is present in one of the jets and the flow is illuminated by a laser light sheet, so that flow pattherns in specific planes within the mixing chamber can be visualised.

In the following sections, flow visualisation studies performed in impinging jets reactors using the aforementioned techniques will be reviewed.

A. Colored Tracer

L. J. Lee et al. (1980) carried out visualisation studies with coloured tracers in a mixing chamber having the typical dimensions of a RIM mixhead. In their work, the momentum ratio between the jets was 2.25 which prompted the higher velocity stream to penetrate further into the mixing chamber. L. J. Lee et al. (1980)studied various Reynolds numbers between 50 and 150 in order to characterize mixing quality. In all cases, they observed the formation of vortices that exhibited higher intensity around the impingement point but that dissipated entirely further downstream. L. J. Lee et al. (1980) were unable to obtain clear images of the flow field at a Reynolds number of 150 given the rapid formation of vortices that moved at velocities higher than the flash speed.

Charles L. Tucker and Nam P. Suh (1980) also realised flow visualisation experiments in a RIM machine mixing chamber. They studied the flow patterns produced when impinging an inky fluid with a clear one with a momentum ratio of 1 between the jets, for Reynolds numbers in the range of 50 to 600. However, only the flow patterns with a Reynolds number between 58 and 259 were depicted in their paper. Charles L. Tucker and Nam P. Suh (1980) found that at a Reynolds number of 58 the flow is parallel and there is no mixing of the jets' fluid. They reported that, if the Reynolds number is increased, the interface of the two streams becomes increasingly unstable and small eddies begin to form. Ultimately, for higher Reynolds numbers, large eddies are produced with alternating rotations and oscillatory motion is observed on the interface of the impinging jets.

In addition, Charles L. Tucker and Nam P. Suh (1980) were able to determine the effect of the angle between the injectors on the mixing performance. They noticed that for directly opposed jets chaotic patterns where attained at lower Reynolds numbers, whereas in mixing chambers where the jets were pointing downwards, in the same direction of the flow, the transition to unsteady states occurred at higher Reynolds numbers. Charles L. Tucker and Nam P. Suh (1980) also concluded that smaller jet diameters achieve chaotic states at lower Reynolds numbers.

Sandell et al. (1985) visualised the operation of an impingement mixer by means of a dye that fades with mixing, thus enabling the observation of the tracer paths even at high Reynolds numbers. In Sandell et al. (1985) work, a mixing chamber approximately ten times larger than an industrial RIM mixhead was studied, in which the jets were aligned with the chamber axis and pointed to the top. The fluid used was water and the tracer was injected as a thin filament in both jets. The flow field dynamics was reconstructed through images recorded in a videotape and mixing was assessed by the outlet flow patterns, with darker regions denoting less mixing quality.

Sandell et al. (1985) investigated the influence of the Reynolds number on impingement mixing and established that mixing increases with the Reynolds number, in the 250 to 400 Reynolds number range. However, for higher Reynolds numbers, up to 720, mixing intensifies at a very slow rate. Additionally, Sandell et al. (1985) noticed the effect of varying the Reynolds number on the flow field dynamics. They stated that although the flow oscillates up to Re = 250, the jets do not cross to the opposite side of the mixing chamber. Subsequently, at Re = 400 the jets cross the chamber impinging in the opposite wall and surrounding each other and at Re = 560 the jets start to display instabilities prior

to the impingement point. Despite the strong flow field dynamics, the dye streak remains a sharp distinct filament, indicating that the flow is laminar as would be expected from the Reynolds number in the chamber.

Sandell et al. (1985) also considered the effect of the distance of the injection nozzles from the top of the mixing chamber on the flow field dynamics. They concluded that increasing the distance of the nozzles from the top lead to an augmented flow instability. Accordingly, they computed the Strouhal number from the dynamic evolution of the imaged flow field, which describes oscillating flow mechanisms and is defined as the ratio of the product of the oscillation frequency of the jets, ϕ, and the injector diameter, d, to the jets average velocity, v_{inj}.

$$St = \frac{\phi d}{v_{inj}} \tag{2.32}$$

Sandell et al. (1985) measured a Strouhal number of 0.048 for Re = 250 and of 0.12 for Re = 400. Above Re = 400 and similarly to the trend observed for the mixing quality the increase of the Strouhal number was slow, as exemplified by the values measured at Re = 560 (St = 0.15) and at Re = 720 (St = 0.16).

It is worth remarking that in the work of Sandell et al. (1985) a mixing chamber with different geometric dimensions and configuration than typical RIM mixheads was used. Nevertheless, the occurrence of a plateau for mixing quality at Reynolds number below turbulent regime is in agreement with the results reported in previous works with RIM machines mixing chambers. In addition, as previously discussed when addressing the measurement of product distribution from test reactions, the utilisation of water in impingement mixing experiments can affect the flow field transitions to happen at higher Reynolds numbers.

B. Particle Paths

Wood et al. (1991) performed visualisation experiments with particle tracing on a mixing chamber that had twice the characteristic dimensions of the chambers used in industrial RIM machines. They demonstrated that the flow field is steady for Reynolds numbers up to 75. For a Reynolds number of 75, distinct recirculation zones can be detected upstream and downstream of the injectors and the flow field is symmetric at the plane of the injectors and the chamber axis. If the Reynolds number is increased above 75, low amplitude long wavelength oscillations develop in the impingement point and their

amplitude grows with the Reynolds number. At Re = 135 it is seen that the jets impingement point is off-centred. Both from the experimental results of Wood et al. (1991) and from mixing and reaction studies in RIM machines, it can be concluded that the observed critical Reynolds phenomenon stems from the transition from steady flow fields to time dependent flow fields.

C. Laser Induced Fluorescence (LIF)

Johnson and Wood (2000); Johnson et al. (1996) employed the LIF technique to characterise the flow field in RIM machine mixing chambers. In the visualisation experiments, they made the following observations:

i. For Reynolds numbers below 50, the jets do not impinge; they only bend and flow towards the outlet.
ii. For Reynolds numbers between 50 and 90, the jets impinge at the mixing chamber axis. At the impingement point, the fluid spreads in the radial direction and forms a disc, whose diameter is only slightly larger than the injectors diameter.
iii. The flow field is stable and unaffected even by induced perturbations in all cases where the Reynolds number is below 90.
iv. For Reynolds numbers above 90, the impinging disk starts to oscillate with low frequency. The amplitude and frequency of the oscillations increases until the Reynolds number exceeds 150, at which point the disk is no longer detected.
v. At a Reynolds number of 300, which is noteworthy from a commercial point of view, no flow structure could be visualised with LIF.

The works carried out by Johnson and Wood (2000); Johnson et al. (1996) draw attention to the difficulties in imaging the impingement mixing mechanisms with any kind of tracer because of the fast homogenization in RIM machines mixing chambers above Reynolds numbers in the order of 150. Consequently, techniques not sensible to mixing should be utilised to depict the flow structures, such as laser velocimetry techniques that measure the velocity of seeding particles.

Unger and Muzzio (1999) made a visualisation study, based on LIF technique, of the flow field in a mixing chamber typical of precipitators. The fluid used was an aqueous solution of glycerine and one of the jets was coloured with a fluorescent dye. Unger and Muzzio (1999) obtained images of the mixing of the two streams that provided a good

representation of the flow structures formed in this type of mixers. They calculated the intensity of segregation for different Reynolds numbers and found that the intensity of segregation declines abruptly for Reynolds numbers between 100 and 300. From Re = 300 to Re = 500 the intensity of segregation continues to decrease before reaching a bottom. Unger and Muzzio (1999) also compared the mixing performance of two impingement jets geometries: directly opposed jets and the jets pointing to the close end of the chamber with 8º deviation from the vertical axis. They concluded that up to Re = 300 the intensity of segregation was lower for the chamber with opposed jets, whereas for higher Reynolds numbers the intensity of segregation is slightly lower in the asymmetric jet geometry.

In Unger and Muzzio (1999) work, the region of sharp transition was offset to higher Reynolds numbers, most probably due to the differences between the geometry studied and typical RIM mixing chambers, namely the ten times larger dimensions.

The flow visualisation studies based on LIF provided a better understanding of the phenomenon underlying the sharp increase of mixing efficiency at Reynolds numbers between 100 and 200: the flow evolves from a steady symmetric state with high segregation between both streams to complex flow patterns that generate mixing under laminar regimes.

2.3.1.2 Measurement of Hydrodynamic Variables

For an accurate characterisation of the flow field, quantitification of hydrodynamic variables is required, which is not attainable with the visualisation techniques previously described. Moreover, with a quantitative description of the flow field, namely the velocities field, it is possible to gain further insight into the effects of relevant parameters on impingement mixing, such as the Reynolds number.

The following techniques, which will be considered in the next sections, have been applied in experimental hydrodynamic studies in impinging jets reactors: Laser Doppler Anemometry, LDA Johnson (2000a, 2000d); Johnson et al. (1996); R. J. Santos, A. M. Teixeira, M. R. P. F. N. Costa, and J. C. B. Lopes (2002); R. J. Santos, Teixeira, and Lopes (2005); R. J. N. d. Santos (2003); A. M. Teixeira (2000); André M. Teixeira, Santos, Costa, and Lopes (2005); Wood et al. (1991) Particle Tracking Velocimetry, PTVZhao and Brodkey (1998a, 1998d) ,Particle Image Velocimetry, PIV R. Santos, A. Teixeira, M. Costa, and J. Lopes (2002); Ricardo J. Santos, Erkoc, Dias, Teixeira, and Lopes (2008); Unger et al. (1998)

A. Laser Doppler Anemometry (LDA)

LDA is used to measure the fluid velocity at specific single points of the mixing chamber. The spatial distribution of the average velocities and of its statistics, such as the standard deviation, is then assembled from multiple measurements at different locations. Despite allowing high data rates and extensive time series, is not possible to obtain the instantaneous velocity fields or the circulation paths of the fluid inside the chamber under dynamic flow fields with LDA.

Johnson et al. (1996) were not able to characterize the flow field with LIF for a Reynolds number of 300 since the jets were the only observable structure. As a result, they employed LDA to assess the influence of the geometric parameters at this regime. By measuring the vertical velocity at sucessive planes along the chamber axis by LDA and subsequently calculating the averaged velocity component in the chamber axis, Johnson et al. (1996) obtained the average recirculation patterns within the mixing chamber.

R. J. Santos et al. (2002); A. M. Teixeira (2000) reported the detailed flow field characterisation inside a RIM machine mixing chamber by means of LDA measurements and quantified the effect of the Reynolds number on the flow field. From the distribution of the average velocity components, measured in normal planes to the mixing chamber axis within a thin measurement grid, it was found that the averaged flow field exhibited no variation with the Reynolds number. R. J. Santos et al. (2002); A. M. Teixeira (2000) also computed the distribution of higher statistical moments, namely the pdf of the lateral velocities and the Reynolds stresses, from the LDA measurements. They found that the flow fluctuations intensify rapidly with the Reynolds number up to Re = 100 but afterwards display a slight evolution only. Additionally, regions of higher velocity fluctuations were seen to occur near the jets impingement region and to increasingly spread throughout the chamber for higher Reynolds numbers.

Wood et al. (1991) performed LDA measurements to characterise the oscillatory behaviour of the impinging jets in a RIM machine mixing chamber. The axial and lateral velocity components were measured at 4 jets diameters downstream of the impingement point at a data rate of 300 Hz and the Strouhal number was determined at Re = 125 for two different fluids with viscosity of 27 and 55 mPa.s. Wood et al. (1991) showed that, for the same Reynolds number, the Strouhal number is constant, irrespective of the velocity of the jets.

Johnson and Wood (2000) studied the typical frequencies in opposed jets mixing chambers through LDA measurements. Two mixing chambers geometries were considered, one with a circular cross-section and the second with a parallelepiped shape, for which three injectors diameters were also tested. Johnson and Wood (2000) computed the Strouhal number for the Reynolds number at which the flow field becomes time dependent, that is Re ≈ 100, and for the limit Reynolds number where oscillations with distinct frequency still persist, namely for 130 < Re <220. It was not feasible to calculate the Strouhal number for higher Reynolds numbers as the oscillations became markedly random and without a defined frequency. Johnson and Wood (2000) noticed that the Strouhal number increases with the Reynolds number from the lowest values where flow field oscillations occur to the highest values where the oscillations still have a defined frequency. In addition, it was concluded that the Strouhal number is affected both by the ratio of the injectors and the chamber diameter.

Johnson (2000a, 2000d) studied the effect of the jets momentum ratio with LDA and found that, for momentum ratios different from one, the impingement point moves towards the nozzle where the jet has less momentum and the flow field also displays more stability.

R. J. Santos (2003) determined the Strouhal number from LDA measurements for Reynolds numbers ranging from 250 to 600. In addition to a LDA probe with a high area of signal capture that achieves high data rates, data processing was employed to attain defined frequencies at these high Reynolds numbers regimes. In general, researchers have faced difficulties in finding the typical frequency above the critical Reynolds number, due to the intensification of the random behaviour of the jets oscillations (Johnson & Wood, 2000)

However, the technique used by R. J. Santos (2003) made possible to establish that for 250≤Re≤600 the jets oscillate with frequencies around typical values which scale with the Reynolds number, while the Strouhal number is kept almost constant, meaning the main characteristics of the flow field are retained. Accordingly, R. J. Santos (2003) pointed out that the dependence of the Strouhal number on the Reynolds number only occurs at the first transition regimes to dynamic states. R. J. Santos (2003) also showed that the dependence of the Strouhal number on the injectors and chamber diameters ratio stems from the flow structures that are formed for the different geometries, for which specific jet oscillations frequencies develop. Additionally, R. J. Santos (2003) studied the influence of the jets momentum ratio on the flow field dynamic behaviour and concluded that if the

momentum ratio is different from 1 the jets do not oscillate, regardless of the flow regime being above the critical Reynolds number.

B. Particle Tracking Velocimetry (PTV)

PTV is a techique used to compute the velocity, in a Langragian approach, by measuring the location of particles in three-dimensional space as they move under the influence of the flow field.

Zhao and Brodkey (1998a, 1998d) obtained the averaged flow field in an opposed jets precipitator chamber from PTV measurements with water at Re = 200 and Re = 4000. The average velocity field determined by for the unsteady flow in the chamber at Re = 200 was similar to the steady state reported by other authors such as Wood et al. (1991). However, in the velocity maps where time average was done over smaller periods the flow field dependence with time was undoubtedly detected as the flow structures present were not the same as the ones found in the long time averaged sequences. As for the studies at Re = 4000, it can be seen that both the flow patterns and the overall circulation patterns change entirely. The unsteady nature of the flow was evidenced by Zhao and Brodkey (1998d)

C. Particle Image Velocimetry (PIV)

PIV is an Eulerian method that measures the distribution of the instantaneous velocities of the flow field in a 2D plane, allowing to represent the flow structures without the influenced of mixing effects like in the case of tracer techniques.

Unger et al. (1998) characterised the flow field in an opposed jets chamber typical of precipitators with PIV and glycerine aqueous solutions for Re≤80 only, as the flow starts to evolve into unsteady flow for higher Reynolds numbers. From the velocity vectors maps of the flow field, it can be noticed that the jets begin to impinge when the Reynolds number exceeds 10 and recirculation zones are also formed for those regimes.

2.3.2 Hydrodynamics in CIJ - Numerical Studies

Computational fluid dynamics numerical codes have the capability to full characterize a reactor functioning, ranging from the hydrodynamic study to more complex analyses such as reaction studies, multiphase studies and others. CFD is used in RIM machines to major quantify the mixing mechanism from the study of reaction and hydrodynamic as also the reaction parameters such as RTD, pressure drop and other crucial in any project. In the beginning of the development of RIM CFD analyses of a 3D domain of the mixing chamber was impossible due computational limitations and this is why several simplifications and approaches was perform to approximate the experiment to the numeric work.

One big advantage of CFD simulations is the knowledge of all the variables in any single point of the computational domain, making the possibility to study the reactor in a macro and microscopic scale, depending of the discretization used. In this subsection will be presented the studies performed for a steady state flow regime and for a time-dependent flow regime

2.3.2.1 Mixing Models employed in CIJ

The models used to access the mixing performance of a CIJ is a lamellar model, since the flow inside the mixing chamber is driven by viscosity, therefore a way to perform the mixing quantification is by calculate the stretching of particles and their striation thickness

- L. J. Lee et al. (1980) develop an expression to calculate the striation thickness base on a stretching function, where this function correlate the particles stretching versus the viscous energy dissipation. The validation of the equation was perform for a range of Reynolds number and the geometric parameters of the chamber.

$$\bar{s} = \left(\frac{ndD^3}{1 + r_s^{-1}}\right)^{\frac{1}{4}} Re^{-\frac{3}{4}} \tag{2.33}$$

- C.L. Tucker and N.P. Suh (1980) formulate the final particle striation thickness is related to the size of the smallest eddies and therefore function of the Reynolds number for a fix geometry

$$I_s \propto Re^{-3/4} \tag{2.34}$$

And where the striation thickness can be calculated by

$$\bar{s} \propto\propto \frac{d}{Re^{\frac{3}{4}}} \tag{2.35}$$

- Baldyga and Bourne (1983) developed a model to predict the striation thickness for T-Jet's mixer based on the theory of turbulent diffusion and validate the model with experimental work performed by Kolodziej, Macosko, and Ranz (1982). The model reproduced a good agreement for striation thickness less than $10\mu m$, value for which a good mixing is achieve for polymerization can occurs
- Fonte (2012) used a lagrangian approach so study the stretching of particles in a 3D domain and consequently the striation thickness by assuming a conservation of a particle volume. It conclude for the Reynolds in study the CIJ produce a striation thickness small enough to ensure a controlled polymerization in the mould.

2.3.2.2 Steady CFD Simulations

In a steady state regime a 3D mixing chamber used as precipitator simulation was perform by

Zhao and Brodkey (1998a, 1998d), where by presenting the flow vector map for a plane aligned with the chamber axis a recirculation vortex was observed for the top and bottom of the chamber although the main flow it is conducted through the chamber axis.

For the same precipitator described early Unger et al. (1998) the hydrodynamic behavior of the flow field where observed a transition of regime located in Re equal to 80 achieve a self-sustainable chaotic flow regime. Using the methodology of the shear rate the author observed a linear relationship between the Reynolds and the strain rate, even in the zones where high shear stress occur, at the impingement point and outlet. A study of the jets imbalance with the intensity of segregation shows a slight change in the position of the stagnation point in 1° can reduce the intensity of segregation in 80% by increasing the recirculation zones.

2.3.2.3 Unsteady CFD Simulations

Dynamics CFD analyses is used in RIM mixing chamber to study the flow mechanism involved in the mass transfer, simply from advection terms with only resolved Navier-Stokes equation, or when the advection terms are couple with reaction equation, permits a full study, comparing with experimental data the perform and optimization of the mixing chambers. Due the unstable nature of the flow and the necessity to quantify the flow,

steady CFD simulations didn't provide enough tools needed to provide a time-dependent flow characterization.

Wood et al. (1991) perform a 3D CFD simulation for a transient flow and compared with visualization studies and LDA described in the previous subsections. The results of the simulation prove, when comparing with LDA and visualization studies a good agreement. The axial velocity proved consistent with LDA and the flow pattern when compared with visualization studies shows similarity. For the Reynolds in study the oscillatory movement of the jets was study using a frequency spectra and also the Strouhal number was study for different geometries dimensions.

A. M. Teixeira (2000) perform a unsteady 2D CFD simulation of CIJ's for Reynolds range from 100 to 500. The main conclusion was the self-sustainable chaotic regime was archive for Re > 250 and, for Re < 250 the flow tends to be segregated. The study of the flow perturbations bellow the critical Reynolds shows stability even when exited, but with the increasing of Reynolds above the critical value shows the flows will never tend to be segregated.

Johnson (2000a, 2000d) study the effect of the jests momentum imbalance in the flow field. He demonstrate a slight change of the jets momentum will cause a deviation of the stagnation point from the chamber axis. This work proves the conservation of jets momentum with different geometries dimensions. Testing different injector diameters but with the flow rate compensated to maintain the same momentum is proven to maintain the impingent point in the center.

R. J. Santos (2003) presented numerical simulation in CIJ to study the effect of unequal momentum ratio in the mixing performance where ti conclude by study the mass transfer efficiencies using a reaction model it is possible the system is not sensible to slightly changes in the jets momentum ratio.

Bierdel and Piesche (2001) study for a 3D mixing chamber in Reynolds equal to 50, which is know it produces a segregated state. By inducing oscillatory perturbation in the jets velocity unsteady flow field is created for a Reynolds bellow the critical. The mixing quality study was perform using particle tracking, where the author conclude the mixing efficiency increases with the Reynolds number and with the frequency of the time-dependent oscillatory perturbation. In the end this results was compared with visualization and tracer experiments.

2.3.3 Mixing and Chemical Reaction in CIJ

Until now the focus was present the work perform in RIM and their mixing chamber CIJ's, where initially the hydrodynamic behaviour of the flow was study using experimental and numerical tools. It is know the hydrodynamics greatly affect the mixing degree and therefore their study is critical to ensure a good mixing of the fluid flow stream and consequent a good polymerization inside de mould. In this subsection will be addressed the mixing study's in CIJ, studied by experimental and numerical tools.

2.3.3.1 Experimental Studies

A. Tracer Experiments

Tracer experiment is an old technique to quantify the mixing performance of any reactor used nowadays. This technique is very used due their simplicity and reduced cost when compared with another's.

S.C. Malguarnera and N.P. Suh (1977); Salvatore C. Malguarnera and Nam P. Suh (1977) used glycerin as a fluid and acetic acid solution as a tracer in one of the fluid streams where a several samples was perform and the standard concentration was compute and used as mixing quality. The main objective is to perform a dimensional analyses of CIJ understanding the main factor which can affect the mixing mechanism. The author identifies some key aspects:

- The Reynolds number calculate at one injector was ranged from 50 to 500 where the author conclude
    - The standard deviation of the tracer concentration as 2.5 times lower comparing Re=100 with Re=50
    - For Reynolds lower than 50 no mixing occur
    - The moment ration between both streams should be the equal for effective mixing, and calculated as

$$R_M = \frac{\rho_1 v_{inj1}^2 d_1^2}{\rho_2 v_{inj2}^2 d_2^2} \tag{2.36}$$

Where ρ is the fluid density, v the mean injector velocity and d the injector diameter. The subscript 1 and 2 corresponded to the left and right injector respectively

- According the geometrical characteristics of the mixing chamber the author concluded
    - There is no effect of the runner length in the mixing quality
    - The chamber diameter don't affect directly the mixing performance, although the volume of the chamber implies: for bigger chamber have difficulty of expelling the air inside the chamber and for smaller volumes a tight control of the flow is required.
    - The distance of the injector to the top of the chamber cause no impact on the mixing quality

C.L. Tucker and N.P. Suh (1980) measure the mixing quality by quantifying the spatial variance of the absorbance of the tracer on the outlet. From this method it is observed an exponential decreasing of the absorbance with the Reynolds number by a factor -9/4 and regarding the study of the moment ratio it was obtained no changes on the mixing efficiency up to values of 2.5. The author's conclude the decreasing of the scale of segregation would be related with the decrease of the smallest scales on the flow field. From this work some important notes should be said. According the mixing efficiency with the moment rate ratio present a opposition with the previous work form S.C. Malguarnera and N.P. Suh (1977); Salvatore C. Malguarnera and Nam P. Suh (1977). The second note is regarding the decreasing of the scale of segregation with the flow scales by a factor of -9/4. It is know the smaller cases in turbulent flow Tennekes and Lumley (1997) varies as:

$$\lambda_k \propto Re^{-\frac{3}{4}} \tag{2.37}$$

In fact this statement cannot be very accurate since the flow regime is far from turbulent and therefore, in a three dimensional geometry, it cannot relate the flow scales with the smaller scales. In fact (R. J. Santos, 2003) present a power spectra where prove the flow scales did not have such big variation by the Reynolds is increasing. According the study of the moment ratio with the mixing quality it can be said the method did not guaranty the separation of the influence in the practical effect in the mixing mechanism inside the chamber. Face of what is described and because the work present others error which cannot be denied and therefore the conclusions about the influence of the moment rate ratio with the Reynolds number should be carefully attended.

B. Adiabatic Temperature Rise

One process to measure the mixing uses the measurement of the rising temperature in the experiments with the exothermic reactions in case of a mixing constrain reaction.

Lee et all (1980) study the adiabatic temperature rise of the polymerization reaction in where various Reynolds number were studied whit some geometrical parameter. The author conclude according the effect of the Reynolds number it was observed a increase of the temperature rise up to Reynolds 200 although the bigger change had occur between Reynolds 100 and 160. According the second part of the study, the effect of geometrical parameters namely the ratio of the injectors' diameters, the camber diameter and the jets alignment and direction. It was observed for all the geometrical parameter present the same critical Reynolds number in which the adiabatic temperature rise is constant. It was also verified that directly opposed jets present lower efficiently. This study is is very important since present some conclusion where at date it was new, but since the experiment was performed for jets momentum ratio different than one then the is necessary carful attention when compared with the results of this thesis since ratios different than one complete changes the reactor hydrodynamics and therefore the mixing performance.

Sebastian and Boukobbal (1986) studied the stoichiometric reaction between polyol and isocyanate the effect on the momentum ratio in the adiabatic temperature. For the same stoichiometric ratio, where for equal injector diameter the moment ratio is 2.42, it was perform a changing in the moment ratio by changing the injectors diameters. It was observed the rise of the adiabatic temperature is was up to Reynolds 200 where for each Reynolds studies the maximum temperature rise was for equal momentum ratios

Harris, Anderson, and Shannon (1992) a study to quantify the effect on the Reynolds number into the adiabatic temperature of a polymerization reaction. The authors observed a increase in the adiabatic temperature until Reynolds 200, proving the mixing performance is only improve until that Reynolds reinforcement the idea of concentering the study of the mixture efficiency by studding the mixing mechanism and reaction until that particular Reynolds.

C. Physical Characteristics of the Final Polymer

The physical characteristics of the polymer can be used to access the effectiveness of the mixing for RIM process due to the fact of bad mixing will influenciate the reaction in the mold and consequently the characteristic of the part.

Kolodziej et al. (1982) study a polymerization reaction, where in one of the injector was added a carbon black tracer. In the end the final part was visualized to quantify and identify thinner strias, characteristics of an efficient mixing. Reynolds ranged from 80 to 450 was tested but was only visible reduction of the strias thickness until Reynolds 200, where from this number no significant changes occur.

Kolodziej, Yang, Macosko, and Wellinghoff (1986) ranged the Reynolds from 80 to 210 to quantify the mixing of the polymer by using the molecular weight distribution, where higher molecular weight is associated with better mixing. The results shows higher molecular weight is associated with high Reynolds number

Nguyen and Suh (1985) quantified the mixing, for a mixing chamber with three inlet, introducing in one injector Polyol for where the Reynolds number was calculated, for other isocyanate, impinging in a third fluid stream or inert material, for which is removed in the end of the process. Where less strias thickness is associated with better mixing. The Reynolds number was varied from 311 to 4534. This study present some differences between the RIM mixing chambers: The geometry have three inlet separated 120º where RIM mixing chamber have only two, the Reynolds number is far from the used in industry, in which Reynolds number is less than 600, where for polyol is ranges in this study from 311 to 4534 meaning for isocyanate is six time higher. The fluid streams also don't present a unitary momentum ratio. It is observed the holes in the final polymer which decrease with the Reynolds number by a factor of $Re^{-\frac{3}{4}}$, agreeing with turbulent theories (Tennekes & Lumley, 1997). In fact this study don't present an achievement for laminar flows since no hydrodynamic study was perform to predict such behavior, but in opposite it is proven methods in measuring the segregation scales in turbulent flows for CIJ reactors.

D. Product Distribution from Test Reactions

Other method is used in the literature to quantify the mixing quality. The method here presented is used in CIJ measurement the product distribution from a consequtive-competetive reaction

Tosun (1987) studied the a consecutive – competitive reaction proposed by Bourne (1982) in chambers with unequal injector diameters. The chamber 1 have 10.3 mm with one injector with 1.8mm of diameter opposed with 7.1mm. For chamber 2 with a diameter of 20.3 and the second injector a diameter of 11.9 maintain in opposite the diameter of 1.8mm. The experiment was perform with water added with a solution of carboxymeththyl a inert substance for the reaction. It is observed the maximum mixing efficiency in Reynolds up to 10000, but the maximum slope was until Reynolds of 2000. Although this experiment was perform for CIJ did not study with particular detail the mixing scales in laminar flow regimes, meaning the flow hydrodynamics is promoted due production of turbulence and not by laminar flows with complex flow regimes

Kusch et al. (1989) used the test reaction proposed by Bourne (1982) to study the mixing in chamber with geometrical similarities as used in industrial process. The injectors have 1mm of diameter and the chamber of 5mm. it is observed in the results increasing in mixing efficiency up to Reynolds 300, but is for Reynolds up to 200 were biggest change occur. This result it will confirm other experimental analyses in CIJ where prove, by comparing this work with others publish in the literature the maximum mixing is archive until Reynolds of 200 although in this work the Reynolds is set up to 300. This can in fact be explained by the using of water in the test, which can cause for the same Reynolds number values of Froude lower. The Froude number is defined as:

$$Fr = \frac{v_{inj}^2}{dg} \tag{2.38}$$

Where v_{inj} is the mean velocity in the injector, d the injector diameter and g is the gravity acceleration. As comparison reasons this work present a general overall behavior of the mixing efficiency present in (Fonte, 2012; R. J. Santos, 2003; A. M. Teixeira, 2000).

Mahajan and Kirwan (1996) used the consecutive – competitive reaction proposed by Angst, Bourne, and Sharma (1982); Bourne (1982). The geometry in where this experiment was perform is used for precipitator and therefore different than used in RIM mixing chambers, with injectors diameters ranged form 0.5 to 2mm and the distance between them ranges from 5 to 20mm and the mixing camber diameter is 25mm. The Reynolds number is study from 1000 and 2000. As the work of Tosun (1987) turbulence is the main issue in the reduction of scales.

The present work it is a study of the scales in a RIM mixing chamber where the operational conditions is closer to the industrial applications. Based on the previous works where resumed it is conclude, from the chemical reaction studies, the Reynolds for which the process efficiency greatly increased is from 100 to 200, in laminar flow regime. After this Reynolds, and for the same flow regime, it is not visible any further improvement in the mixing. For higher Reynolds, also presented, the main factor of the hydrodynamic behavior is due production of turbulence

E. Numerical Studies

Santos() studied, in a 2D geometry, the effect of the design parameters of CIJ in the mixing using a chemical reaction model and a numerical tracer to perform the study of the mass transfer and reaction inside a typical RIM mixing chamber for the usual Reynolds used in the industry. The author conclude the mass transfer mechanics is greatly increase when the flow reach a self-sustainable chaotic state obtaining full develop vortices thought the mixing chamber. The study of the Schmidt number calculated as

$$Sc = \frac{\mu}{\rho D_m} \tag{2.39}$$

it seam to over predict the mass transfer between both flow streams, and added do the smoothness of the concentrations gradient did not allowed to visualized the striation thickness. According to reaction history, due computational reasons was prohibitive to perform a dynamic numerical simulation but even though this effect was clearly seen in steady state simulation the homogenization of the fluid occur in the regions immediately downstream of the impinging point.

Fonte (2012) perform an 2D dynamic simulation using VOF method with grid adaptive based on the gradients. The influence of the numerical models was used to evaluate one which produce the lower diffusion. The author identifies a new mixing mechanics of rupturing of the strias. From is work it is clear the visualization of the reduction of the scales up to values of 10μm, reported by Lee et all (1980). The author then concluded by using an Eulerian-Eulerian approach with a model which described purely the adventive mixing in the chamber (VOF) clearly reduced the effect of diffusion in the results and by introducing a local grid adaptive the striation thickness of the impingent jests is clear visualized.

3 CFD Model and Simulation of CIJ

3.1 Introduction

This chapter presents the analysis of the dynamic behaviour of the flow field of the complete mixing chamber, following the work in 2D performed by Teixeira (2000), Santos (2003) and Fonte (2012). A DNS[1] simulation is performed in a HPC environment, where for the first time the full hydrodynamic behaviour of the flow field was studied in order to quantify the mixing performance of a real 3D RIM mixing head. The breakthrough results produced in this work are intended to be the starting point for the development of new mixing techniques and for the real time optimization of the RIM process control.

Teixeira (2000) performed parametric analyses in a 2D model of the mixing chamber, studying several numeric parameters and boundary conditions. From his work it was possible to establish the parametric values that produce the most reliable results for the 2D mixing mechanisms in the RIM mixing chamber.

Santos (2003) performed a study of the mechanisms of the jets oscillations presenting for the first time spectral data of the flow field, which allowed the identification of the mixing hydrodynamic scales in 2D simulations. In addition, Santos (2003) carried out parametric studies of the Reynolds number, Froude number, jets momentum ratio, among others. To

[1] Direct Numerical Simulation is considered as all the scales of the flow produced by integration of the Navier Stokes equation in the discrete domain are solved

account for the mass transfer, Santos (2003) used an isothermal reaction model to simulate the mixing mechanics by means of a passive tracer.

Fonte (2012) employed a 3D geometry to study the mixing performance and quantified the mixing length scales and the stretching properties of the flow using the Lagrangian particle tracking. To account for the mass transfer, the author applied a multiphase VOF model to quantify the lamellar structures of the flow, using an adaptive grid algorithm based on the phase gradient.

In this work, the dynamic behaviour of the flow field is studied by means of the analysis of the mechanisms of the jets oscillations in a 3D simulation and at Reynolds numbers where the mixing performance is strongly affected by the hydrodynamic behaviour of the flow field.

- In section 3.2, a description of the model used to simulate the flow field will be presented, with focus on the geometrical characteristics of the chamber, the governing equations, the boundary conditions and the numerical methods employed to calculate the variation of the quantities in the domain. The parametric variables used in the present study, which were also investigated by Teixeira (2000), Santos (2003) and Fonte (2012), will also be considered.
- In section 3.3, the results of the numerical simulation will be discussed. The power spectra analysis of the simulations will be introduced and the contour maps of the physical variables that contribute to the study of the mixing mechanisms will be examined, as well as the evolution of these variables in time and in the spatial domain.

The mixing performance is then modelled with a multiphase VOF model using an Eulerian-Eulerian approach in order to evaluate the mixing scales of the lamellar structures of the flow. For the first time, the VOF model will be applied to analyse the advective mixing without taking into consideration the effect of diffusion in the fluid flow streams for the complete mixing chamber.

- In section 3.4, the multiphase model used to evaluate the mixing performance will be introduced, namely the governing equations, the boundary conditions and the numerical methods employed.
- In section 3.5, the results of the multiphase model and the mixing related quantities are presented, in order to assess the mixing performance.

Finally, the main conclusions drawn from the numerical studies, concerning the mixing mechanisms, the flow behaviour and the mixing performance, will be discussed in section 3.6.

3.2 Model Description

3.2.1 Physical Domain

The RIM machine mixing head modelled in this work has the same physical dimensions as the mixing chamber that was previously experimentally and numerically studied by Teixeira (2000), Santos (2003) and Fonte (2012), which are dimensions usually employed on the industrial processes. In Figure 3.1 is shown a schematic representation of the mixing chamber, which consists of a cylindrical chamber with two cylindrical injectors normally aligned with the chamber axis and forming a 180º with respect to one another. The chamber diameter is D=10 mm and the chamber height is H=50 mm. The injectors are positioned at a distance of h=2.5 mm from the top of the mixing chamber and their diameter and length are d=1.5 mm and l=5 mm, respectively.

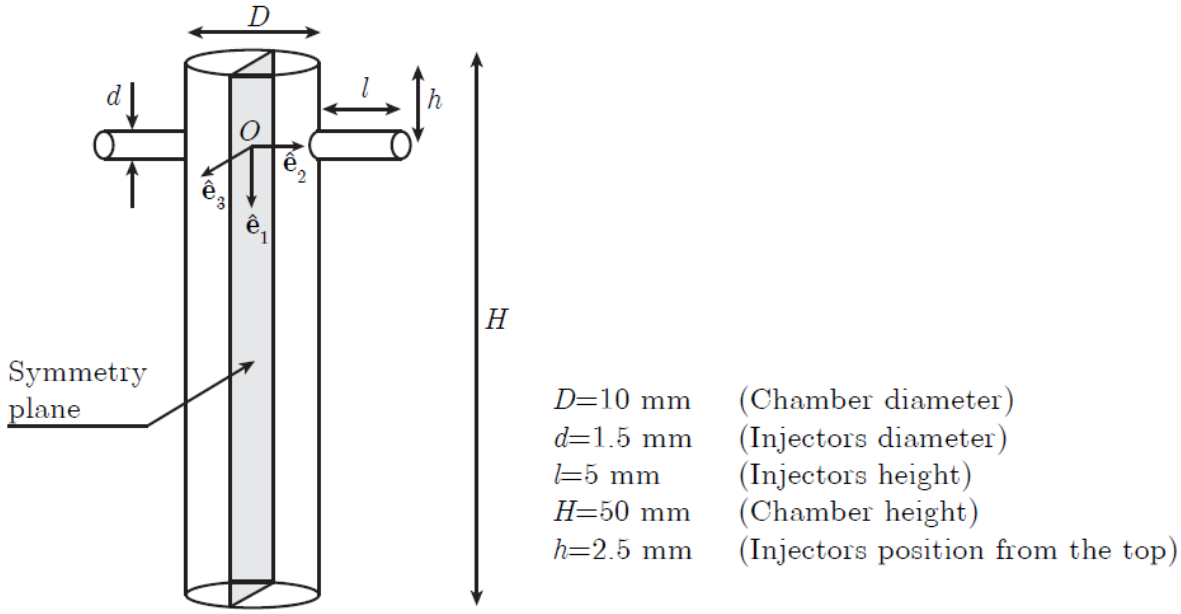

Figure 3.1 - Schematic representation of the CIJ mixing chamber and related physical dimensions. Retrieved from Fonte (2012)

For modelling purposes, it is assumed that the coordinates' axes are centred with respect to the mixing chamber axis and aligned with the injectors' axis and that the origin of the geometrical domain is where the two axes encounter each other. Additionally, it is considered a plane normal to the injectors' axis that divides the mixing chamber in half. The implementation of this symmetry plane will greatly reduce the computational cost when a

steady state simulation is performed since it is known from previous works that a fully segregated flow without any chaotic flow motion is obtained in these conditions. Therefore, for the steady state flow regime the symmetry plane is activated and set with zero shear forces in each direction allowing free flow motion in one half of the mixing chamber. Conversely, when a transient simulation is performed the symmetry plane is removed, thus allowing flow motion in the whole chamber domain.

3.2.2 Domain Discretization

The physical domain is discretized into small control volumes where the NS equation will be solved. The construction of the geometrical domain and its discretization to create a simulation grid were performed using the *DesignModeler* and the *Meshing* software included in the ANSYS® v15 suite. The entire domain was discretized into small sections in order to manually ensure mesh control, both in cell size and meshing method, generating 2.3 million uniformly sized hexahedral finite volumes with the maximum edge length of $\Delta x = 100\ \mu m$. The mesh generator automatically adapts the mesh to discretize curved surfaces as well as maps the face cell between each section so that a perfect cell match is attained. A few triangular cells are used in order to match the injector hexahedral cells with the chamber hexahedral cells.

Figure 3.2 shows a plane along the chamber and the injectors axes of the 3D hexahedral mesh in a cut passed in the injector's axis. It can be observed the presence of matching quadrilateral cells along the domain, which means a good information transfer between each cell since there are not present discontinuities the mesh domain. Triangular cells is used to match the cell region form the injectors with the cell region form the chamber due to the fact a no using of this element's will force high distorted elements in the region which is worse than have non align face cells with the primary direction of the flow. This effect is clearly visualize in the velocity contour where small numeric diffusion of the velocity is observed, particularly align with the injector's walls. Since a parabolic profile exist in the injector, meaning high velocity in the center of the injector's, then the consequence for the oscillatory movement of the jets is primarily due the high velocities, correspondent in the injector axis, rather than low velocities, and therefore the using of this cells will not have a big impact in the end results

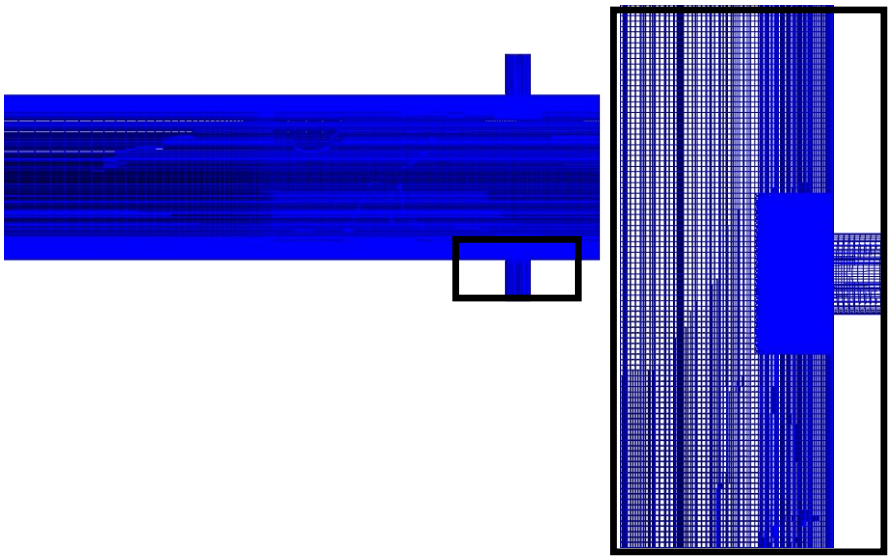

Figure 3.2 – Hexahedral mesh with 100 μm used in the simulations (left). Detail of the triangular cells used to couple both meshes avoiding distorted elements (right)

3.2.2.1 Grid size

The choice of the maximum edge length is chosen according to the Kolmogorov length scale which corresponds to the lowest scale in a turbulent flow and varies with Reynolds number as $Re^{-3/4}$. Despite the Reynolds in study is laminar and far beyond the transition region choosing the lower scale as the Kolmogorov ensures all the hydrodynamics length scales are being simulated without a need of a sub-grid turbulence modelling as the one used in LES. Since the Navier-Stokes equation are directly simulated for all the possible length scales existent for a particular hydrodynamic simulation this is referred in the literature as Direct Numerical Simulations (DNS). The Kolmogorov length scale λ_K in isotropic and homogeneous turbulent flow can be estimated as

$$\lambda_K = \left(\frac{\upsilon^3}{\varepsilon}\right)^{-\frac{1}{4}} \tag{3.1}$$

Where υ is the kinematic viscosity and ε the turbulent energy dissipation rate which can be calculated by integrate over a boundary surface $\partial\Omega$ neglecting the contribution of the friction in the walls, resulting in:

$$\varepsilon \approx \oiint_{d\Omega} \frac{|\boldsymbol{u}|^2}{2} \rho \, (\mathbf{u}.\mathbf{n}) \, dS \tag{3.2}$$

Where the vector $\mathbf{n}$ represent the normal vector's to the geometry axis. Consider the chamber volume where dissipation occur as

$$V_{dissipation} = \left(\frac{\pi}{4} D^2\right)(nD) \tag{3.3}$$

Where nD correspond the distance between the top of the chamber until the point where dynamic mixing occur, which can take value as $nD \approx 2D \text{ to } 3D$ (kolodziej et all.,1982). A new variable can be assumed as the average density weighted by the volumetric flow rate Q, defined as

$$\bar{\rho} = \frac{Q_1\rho_1 + Q_2\rho_2}{Q_1 + Q_2} \tag{3.4}$$

Where the indices 1 and 2 correspond to the left and right injector. This weighted density can be also extended for the average viscosity, $\bar{\mu}$, defined as:

$$\bar{\mu} = \frac{Q_1\mu_1 + Q_2\mu_2}{Q_1 + Q_2} \tag{3.5}$$

The variation of kinetic energy can be neglected since due to the areas ratio, the average velocity in the outlet is about 5% of the average velocity in inlet. Consider the flow in the injector is laminar resulting in a parabolic velocity profile, and the introduced new variables, the turbulent energy dissipation rate can be now expressed as:

$$\varepsilon = \frac{\int_0^{\frac{d_1}{2}} \left[2\, u_{inj,1} \frac{\left(\frac{d_1}{2}\right)^2 - r^2}{\left(\frac{d_1}{2}\right)^2}\right] \rho_1 \, \pi \, r \, dr \; + \; \int_0^{\frac{d_2}{2}} \left[2\, u_{inj,2} \frac{\left(\frac{d_2}{2}\right)^2 - r^2}{\left(\frac{d_2}{2}\right)^2}\right] \rho_2 \, \pi \, r \, dr}{\bar{\rho}\, V_{dissipation}} \tag{3.6}$$

Where $r \in \left[0, \frac{d}{2}\right]$ is the radial position at the injector's circular cross section. This equation can be introduced in the Kolmogorov length scale formulation, resulting in:

$$\lambda_K = \left(\frac{D^3 nd}{1 + \frac{1}{\emptyset_K}}\right)^{\frac{1}{4}} Re^{-\frac{3}{4}} \tag{3.7}$$

Where the kinetic energy rate ratio can be calculated as:

$$\emptyset_K = \frac{\rho_1 d_1^2 u_{inj,1}^2}{\rho_2 d_2^2 u_{inj,2}^2} \tag{3.8}$$

For a isotropic and homogeneous turbulent flow, meaning there is no mean shear due rotational our boundary effect or there is no flow gradients, the Kolmogorov scale correspond to the lower hydrodynamic scale in the flow and if the grid spacing is lower than this value for Navier-Stokes can be applied means a full DNS with all the flow scales is numerically calculated.

Libby (1996) say acceptable accuracy in DNS is obtain if grid spacing is between four to six times greater than the Kolmogorov scale. In the present work and for the largest Reynolds in study, 300, it is obtain for n=3 Kolmogorov scales a value closer to 95 μm which is a bit lower than the computational grid used but inside the Libby theory range. In this particular case only the lower scales will not be accurate calculated but, as it will be seen forward this scales represent to the dissipation range which don't affect he major effect in study which occur for lower space scales. For the lower Reynolds in study, [150, 200 and 250] it produces scale values bigger than the computational mesh meaning in this case all the scales it will accurate calculated. The mesh size chosen it guaranties a full representation of the hydrodynamic phenomena for all the Reynolds number in study.

3.2.3 Governing equations

Mathematical equations which describe the flow motion was originally introduced by Euler (18th century) described the conservation of mass (continuity) and balance of momentum and energy for incompressible fluid (or compressible if the divergence of the flow field is zero) without viscosity. Latter Navier-Stokes equation (19th century) described the rate of change of momentum at each point in a viscous fluid with constant density ρ and constant kinematic viscosity ν

$$\frac{\partial \mathbf{u}}{\partial t} + \mathbf{u} \cdot \nabla \mathbf{u} = -\frac{\nabla p}{\rho} + \mu \nabla^2 \mathbf{u} \tag{3.9}$$

With $\nabla \cdot \mathbf{u} = 0$, representing the conservation of mass equation evaluated for the boundary of the problem consider incompressible fluid. $\mathbf{u}(\mathbf{X}, \mathrm{t})$ is the fluid velocity field in a Lagrangian reference frame. $\mathbf{P}(\mathbf{X}, \mathrm{t})$ is the pressure field resulting from the preservation of incompressibility of the fluid. This equation is similar to the Newton's law in which force is equal to mass times acceleration. In the left hand side of the equation represent the

acceleration of the fluids particles and on the right hand side is the sum of the forces per unit mass in a control volume: the pressure force and the viscous forces arising from momentum diffusion though molecular collision (Ecke, 2005). The nonlinear term $\mathbf{u} \cdot \nabla \mathbf{u}$ describes the adjective transport of the fluid momentum which produce a particular phenomenon.

The Navier Stokes equation due the non-linearity of their equation are very sensible to the initial conditions which can translate into complete different solutions by s slight change in the initial conditions. This effect was visualized by Edward Lorenz (1972) in atmospheric flows introducing a new field: the Chaos theory. Changing the flow regime can produce smooth laminar flow to more complex flow motions quantified by their length or time scale. Reynolds study this concept in a pipe flow where visualize the concept of the non-linear term of the equation and by introducing a new flow parameter, the Reynolds number, could according to this an-dimensional number predict the dominance of the non-linear term over the viscous term, which is the case of turbulent flow motion. The Reynolds number is calculated as

$$Re = \frac{inertial\ forces}{viscous forces} = \frac{\rho v L}{\mu} \tag{3.10}$$

For CIJ's is defined as

$$Re = \frac{\rho v_{inj} d}{\mu} \tag{3.11}$$

Where *v* is the average velocity of the fluid, L the characteristic linear dimension and ρ and μ the fluid density and dynamic viscosity, respectively. For CIJ's the characteristic dimension is the internal diameter of the injector and the velocity is the average velocity for that injector. In the case in study the flow is far from turbulent and situate in the laminar region meaning in the fluid flow the viscous forces over dominates the inertial forces produced by the non-linear term. The work perform so far clearly illustrate that fact Santos (2003) and therefore as it can be seen from previous studies (Teixeira, 2000; Santos, 2003; Fonte, 2012) after a certain Reynolds, critical Reynolds number, exist in time and spatial domain a big variation of the flow field inside the mixing chamber which since the flow is driven by viscosity is not caused by turbulence effects but only caused by the highly chaotic nature of the flow.

3.2.4 Boundary conditions and initial conditions

3.2.4.1 Injectors

The fluid enter in the chamber in a normal direction of the chamber axis in the injector's section. The injectors have a small length which will going to allow the introduction of a steady full developed, laminar flow with a parabolic velocity profile, Couette flow, in a cross section of the injector. The equation to describe the parabolic profile is

$$\mathbf{u} = -2u_{inj}\left(\frac{\left(\frac{d}{2}\right)^2 - r^2}{\left(\frac{d}{2}\right)^2}\right)\mathbf{n} \tag{3.12}$$

Where u_{inj} stands for the mean velocity in the cross section, $\mathbf{n}$ the normal direction of the flow and r is defined as

$$r = r(x,z) = \sqrt{x^2 + z^2} \tag{3.13}$$

Additionally the velocity gradient is assumed as null in each injector resulting in introducing zero pressure to not include addition flow forces which will going to affect the flow behaviour.

3.2.4.2 Walls

For all the wall of the mixing chamber the velocity component are set as zero producing a non-slip wall. In this problem the walls are consider without roughness

3.2.4.3 Outlet

The outlet boundary condition is used assuming parallel flow in the boundary with velocity gradient null resulting in

$$v_{x,z} = 0 \tag{3.14}$$

$$\tau_{yy} = -p_0 \tag{3.15}$$

Where τ_{yy} is the normal total shear stress in the direction of the chamber axis and p_0 the pressure at outlet. For a Newtonian fluid τ_{yy} is defined as

$$\tau_{yy} = 2\mu\frac{dv_y}{dy} - p \tag{3.16}$$

Where μ is the fluid viscosity and p the pressure. In the outlet $p = p_0$ and $\tau_{yy} = -p_0$ resulting in

$$\frac{dv_y}{dy} = 0 \tag{3.17}$$

3.2.4.4 Steady state

Steady state solution is archive in order to obtain an initial solution for transient flow regime. This simulation is obtain by setting the time dependent term of the NS equation as zero which is allowed iterate until the residuals set minimum as 10^{-6} in the continuity and momentum equation. To ensure a fast process and since in a steady state flow regime both fluids streams remains segregated, as previous studies demonstration, then a symmetry plane, demonstrated in Figure 3.1, is set as "on" with no shear stress between the flow and each face of the symmetry plane

3.2.4.5 Transient state

The previous steady state simulation provide an initial for the transient nature of the flow, by introducing in the Stokes equation the time derivative term. The symmetry plane used in the previous run was disable allowing passage of the bow between one side of the chamber to another side.

To start a transient simulation a *non-symmetric perturbation* is introduced in one injector while the opposite injector remained the same flow rate. Such perturbation is directly introduced in the velocity profile, using a User Defined Function (UDF) increasing the injector's velocity. In the right injector the velocity profile was replaced by

$$\mathbf{u} = -2u_{inj}\left(\frac{\left(\frac{d}{2}\right)^2 - r^2}{\left(\frac{d}{2}\right)^2}\right) f(t/\tau)\,\mathbf{n} \tag{3.18}$$

Where $f(t/\tau)$ is the *perturbation time function*, depending on the flow time t and the chamber mean residence time, τ, defined as:

$$\tau = \frac{D^2 H}{2u_{inj}d^2} \tag{3.19}$$

The methodology of implementing a perturbation time function was previously performed by Teixeira (2000), Santos (2003) and Fonte (2012) where it was study in order to ensure a

introduction of a discontinuity in the flow field. Therefore a smooth time function with a continuous first order derivative was chosen

$$f\left(\frac{t}{\tau}\right) = 1 + \frac{a}{2}\left(1 - H\left(\frac{t}{tau} - b\right)\right)\left(1 - \cos\left(\frac{\frac{2\pi}{b}t}{\tau}\right)\right) \tag{3.20}$$

Where $H\left(\frac{t}{tau} - b\right)$ represent the Heaviside function. The parameter a is defined as the maximum amplitude of the perturbation, set as a=0.1. Parameter b represent the time, according the chamber mean residence time in where the perturbation is applied, set as b=0.121.

Figure 3.3 represent graphically the perturbation function where it can be observed the perturbation have very small effect on the solution since $v_{inj\,perturb}$ is set as maximum correspondent to $10\%\ v_{inj}$. After $0.1\ \tau$ no further perturbation is introduced on the domain and the velocity parabolic profile is set as equal in both fluids streams. Santos evaluate the influence of the perturbation on the flow dynamics and observed there is no influence of the initial perturbation after a transitory state, where the system evolves into chaotic or into segregated. From the results it was observed for all the Reynolds in study the transition region always lies prior than 1τ, therefore all the numeric results presented is was perform form for $\tau = 2 \text{ and } \tau = 3$.

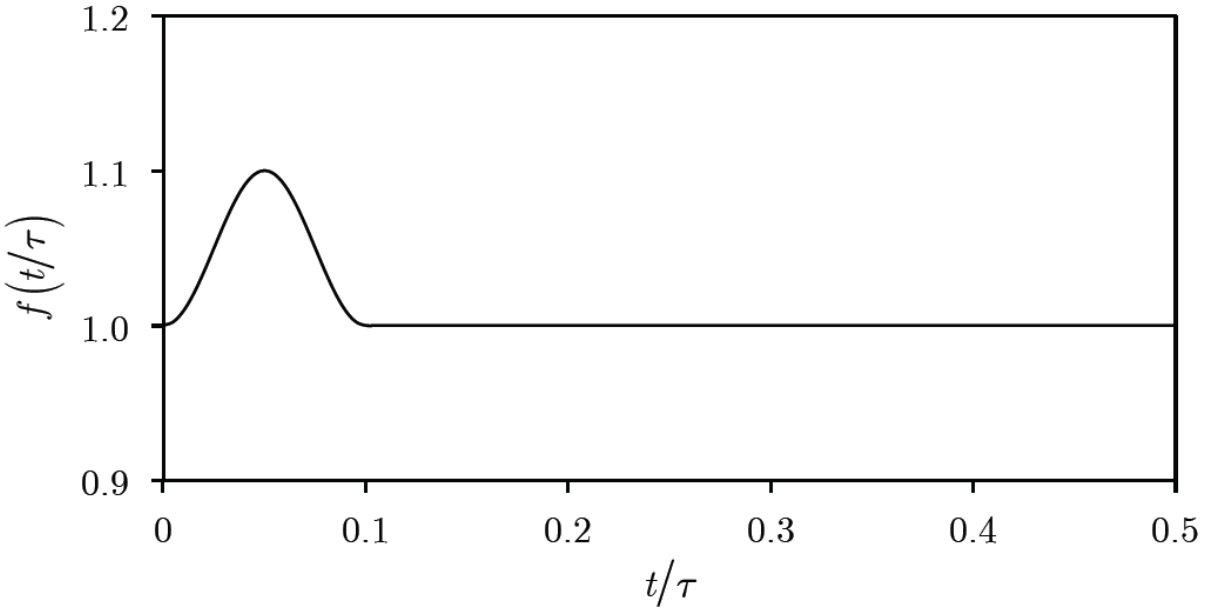

Figure 3.3 - Perturbation time function on the right injector affecting the normal velocity to the injector's cross section

Courant number emerges of solving partial differential equations using finite differences as approximation. In CFD time dependent problem the advance is time is major dependent of

the advective term, which dominates the solution. Therefore is necessary a progressed time less than a certain time for explicit time-marching method. Courant-Friedrichs-Lewy (CFL) is defined as

$$C = \frac{u\,\Delta t}{\Delta x} \leq Cmax \tag{3.21}$$

Where u in the magnitude of the velocity, correspondent in this case of u_{max} of the parabolic profile, Δt the incremental time step and Δt the length of the interval, in this case correspond to the mesh size. If explicit (time-marching) solution is used then $Cmax < 1$ to ensure numerical stability, while implicit method usually don't required so lower values of $Cmax$. To guaranty uniformity in the results, the time step marching is calculates based on $Cmax = 0.5$ for each Reynolds in study

3.2.5 Discretization and Numerical methods

The numerical implementation of the mathematical techniques used for temporal and spatial discretization of the flow equations along with the gradients discretization into the discrete domain is presented in Appendix A.

3.2.5.1 Steady and Unsteady Numerical Methods

In a steady state flow regime the pressure-velocity coupling is used SIMPLEC since low gradient pressure field exists in the mixing chamber resulting in fast convergence and accurate results particularly in low-Reynolds flows. For the momentum discretization a third-Order MUSCL scheme is used because the flow behaviour naturally exhibit discontinuities in the flow field, particularly in areas of interest, therefore the using of a high accurate numerical scheme is required. The areas of interest also required higher interpolation of the pressure and therefore a second order discretization is used. In the end the gradients are evaluated using Least Squares Cell based scheme since is the best suited method to be used in structure polyhedral grids. When transient state is used it was chosen to have a second order implicit formulation to avoid temporal discontinuities.

3.2.6 Computational performance

The DNS simulation was performed in a HPC environment using Dell PowerEdge R420 chassis connected with 40 Gbpds InfiniBand network, each node have 2 Intel E5-2450 CPUs, 68GB of DDR3 RAM clocked at 1600MHz and SATA HDD disk with 500GB 7.2K. For each Reynolds in study two full nodes was used where the computation cost of each one present in Table 3.1

Table 3.1 - Computational cost of each simulation performed in HPC environment

Reynolds	Hours	CPU h
150	521	16675
200	595	19057
250	670	21440
300	744	23822

3.3 Results of Numerical Simulation

In this section will be presented and discuss the results provided by the numerical simulation for Reynolds 150, 200, 250 and 300. The choice of the Reynolds lies on previous numerical and experimental results, presented in chapter 2, which clear conclude the mixing reach their maximum efficiency at Reynolds 300. Since the flow is driven by viscosity over inertia, the shear force of fluids laminae will stretch the particle of fluid into even smaller thickness allowing diffusion and reaction in the mould enter in place and create a uniform plastic component. The aim of this chapter is then identify the hydrodynamic scales which leads to the striation of the particles of fluid, provided emphasis in the location where the hydrodynamic scales are created and dissipated allowing in the future a tighter and efficient control of the process with the lower production cost possible. Additionally this works present a new alternative to study mixing in a laminar chaotic environment leading to a new world of possibilities in field of mixing.

3.3.1 Flow visualization

Results from transient simulation for each Reynolds in study is presented in terms of velocity and vorticity maps to allowed better understanding of the flow dynamic behaviour. As introduced early the chaotic flow motion is initialized using a perturbation, increasing the velocity in one injector in a specific time. Previous study Santos (2003) prove the flow is independent form this initial perturbation after one residence time. Therefore for all the simulations performed will be study ranging from $\tau = 1$ to $\tau = 3$. For better visualization of the flow, animations is provided in a DVD, were is observable the velocity maps, 2D vorticity maps and 3D vorticity maps, allowing a better visualization of the impinging jets iteration with the direction of the flow rotation

3.3.1.1 Instantaneous flow field velocity maps

From previous works it is know the flow from each injectors feeding streams impinging impinge align with the injector axis where the flow rapidly decelerate spreading radial the flow in a form of ellipsoid pancake. Oscillation of this impinging surface, observe upstream

and downstream, of the injector' axis will spread fluid material between the left and right side of the chamber improves the distribution of particle material, reducing interfacial are of the fluid stream and as consequence improve mixing performance.

Conventionally will be assumed when the impinging surface is aligned with the chamber axis the angle is null and when the top of this surface moves for right side then the angle is positive and in opposite where it shifts for the left side the angle is negative. Whit this convention is mind and when observed the velocity field it is observable in the from plane occur bigger variations of the angle comparing with the top view of the chamber. Therefore this effect will mean the fluid are transfer for all the chamber mainly due this motion, meaning the 3D flow can have similarities when compared with 2D simulation. Previous work Santos (2003) proved this concept when the author compared 2D simulation with experimental work where it was observed same flow behaviour when

$$Re_{3D} = \frac{1}{2} Re_{2D} \tag{3.22}$$

High angles of the jets, this can be visualized for Reynolds 150, usually produce the destabilization of the impinging surface angle producing often a breaking of the oscillatory movement. This effect is produce by bending of the jets where the fluid coming from on injector goes downstream while the other go upstream of the mixing chamber. After the breaking of the oscillatory movement the flow will recovery from this state until impinge properly whit the jets' aligned with the injector axis. The main driven force of this breaking is an increase of the frequency of the motion with an increase jets angle. When the jets angle cannot recovery fast enough to follow the frequency of the motion then breaking occurs. The breaking of oscillatory movement will cause a fast displacement of the impinging point position where gradually will tend to origin position.

Generally speaking was not observed a correlation between the frequency of motion and the angle of motion between the front plane with the top plane. Spite this fact it was observed a 3D movement of the impinging point particularly when breaking of the oscillatory movement happen. Comparing booth planes it is clear the bending of the jets is mainly in the front plane due the bigger area allowing bigger angles rather than in the top plane which is confined in smaller area equal to diameter of the chamber. Therefore it can be said the movement of the front plane is the mainly driven force for distributing and spread material along the chamber improving mixing performance.

Observing the full dynamics of the flow from the numerical simulation it is clear that when Reynolds is increasing from 150 to 300 this will cause a increasing of the breaking of the jets

per residence time. This effect will form in the area close the impingement point a region with increasingly complex flow structures which will cause a harder recovery of the oscillatory movement. An accumulation of this complex structures will difficulty the recovery and increase the breaking of the oscillatory movement, which in higher Reynolds will not be just due bending but will be also because of small deviation of the impingement point position. An increasing of the Reynolds number will consequent increase the frequency of the jets oscillatory movement, maintaining the same patter where the oscillatory movement is mainly in the front plane rather than in the top plane. It is observable, for higher Reynolds an lower tolerance of the impinging point variation without breaking occur, but if jets oscillatory movement breaking occur will produce larger displacements in the impinging point and a much higher difficulty, in terms of time, to restore the normal spreading of material along the chamber. It is clear large changes in impinging point, approximating this to the wall will greatly reduce the oscillatory behaviour in this region reducing considerable the mixture. This pattern was also described in Santos *et al.* (2010).

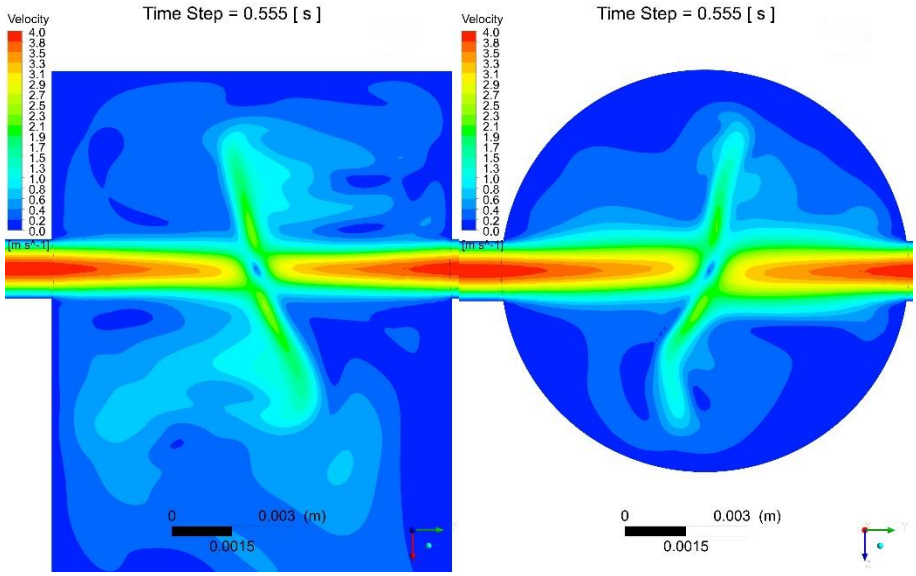

Figure 3.4 - Velocity maps for Reynolds 150 at time $t/\tau = 1$

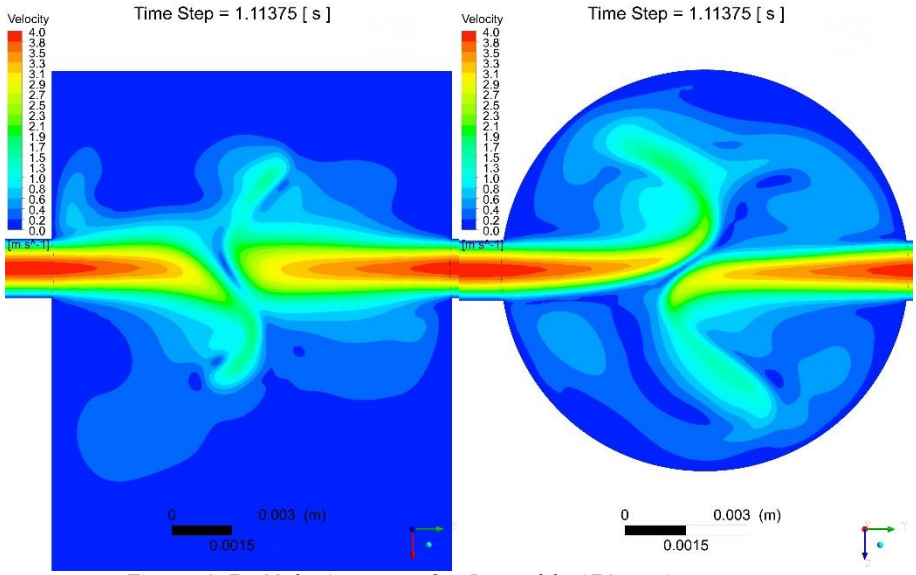

Figure 3.5 - Velocity maps for Reynolds 150 at time $t/\tau = 2$

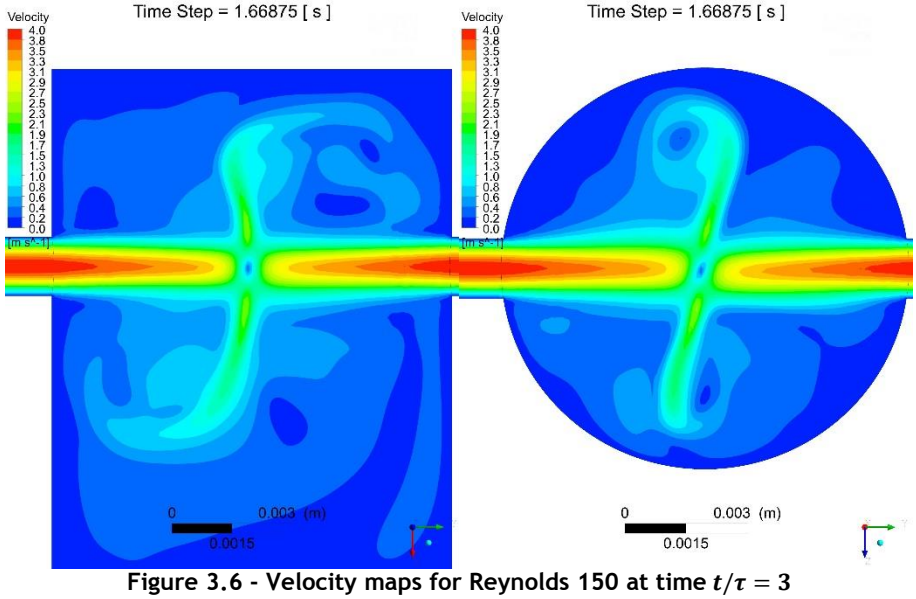

Figure 3.6 - Velocity maps for Reynolds 150 at time $t/\tau = 3$

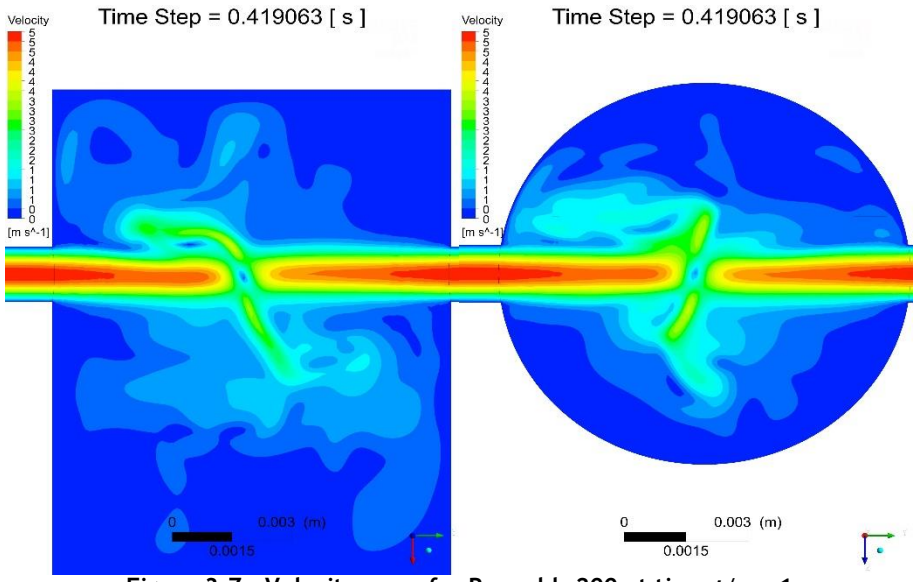

Figure 3.7 - Velocity maps for Reynolds 200 at time $t/\tau = 1$

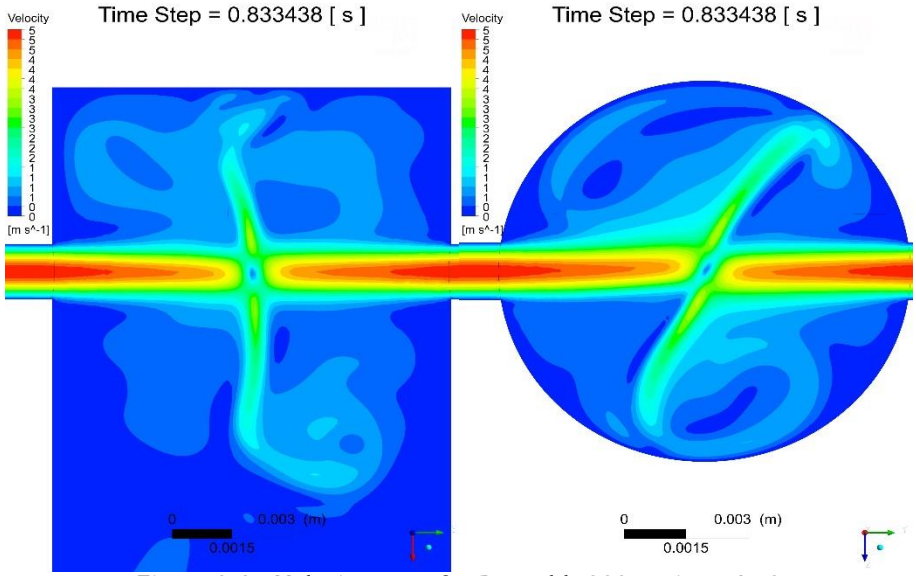

Figure 3.8 - Velocity maps for Reynolds 200 at time t/τ=2

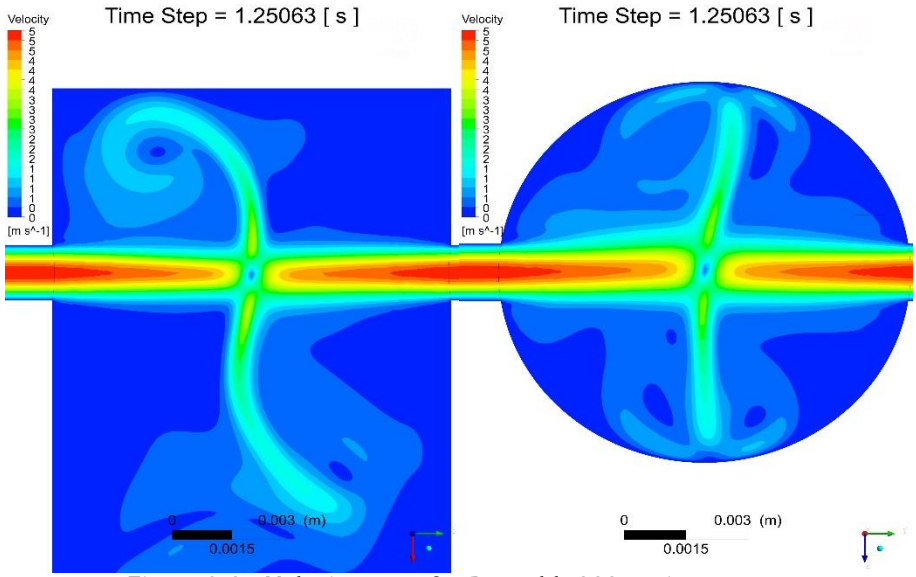

Figure 3.9 - Velocity maps for Reynolds 200 at time $t/\tau = 3$

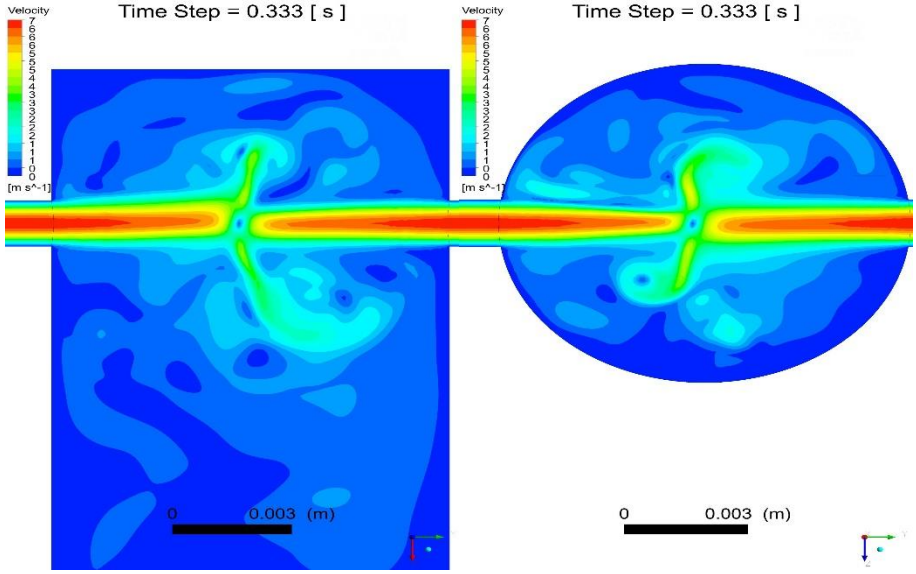

Figure 3.10 - Velocity maps for Reynolds 250 at time $t/\tau = 1$

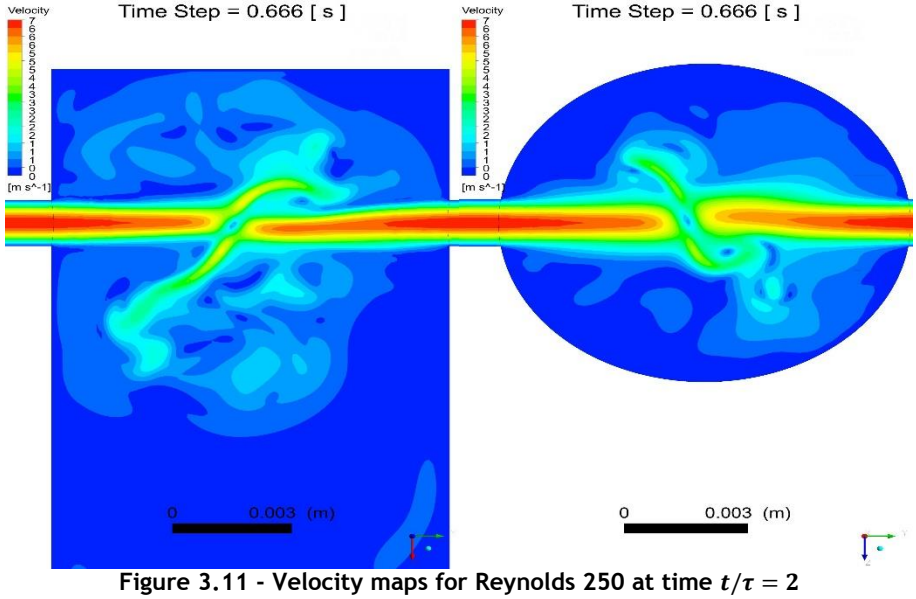

Figure 3.11 - Velocity maps for Reynolds 250 at time $t/\tau = 2$

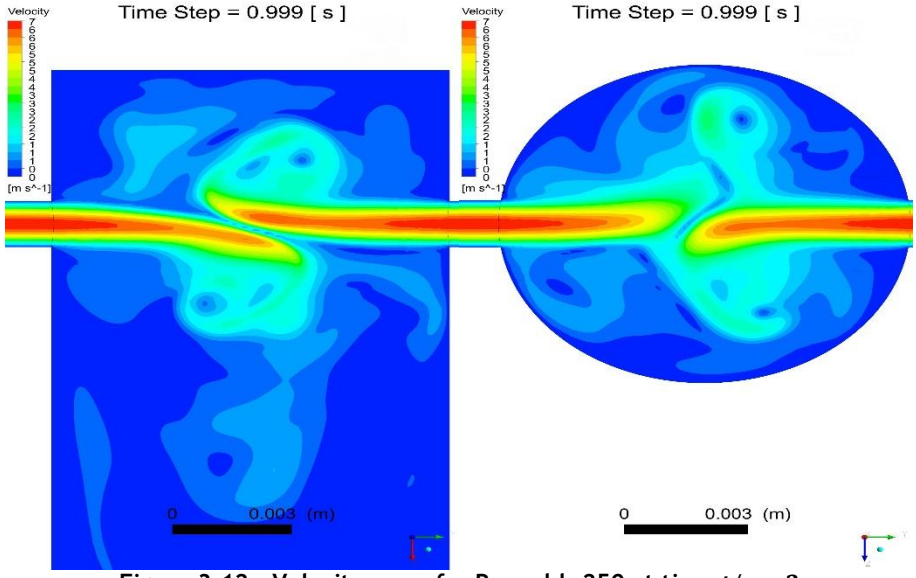

Figure 3.12 - Velocity maps for Reynolds 250 at time $t/\tau = 3$

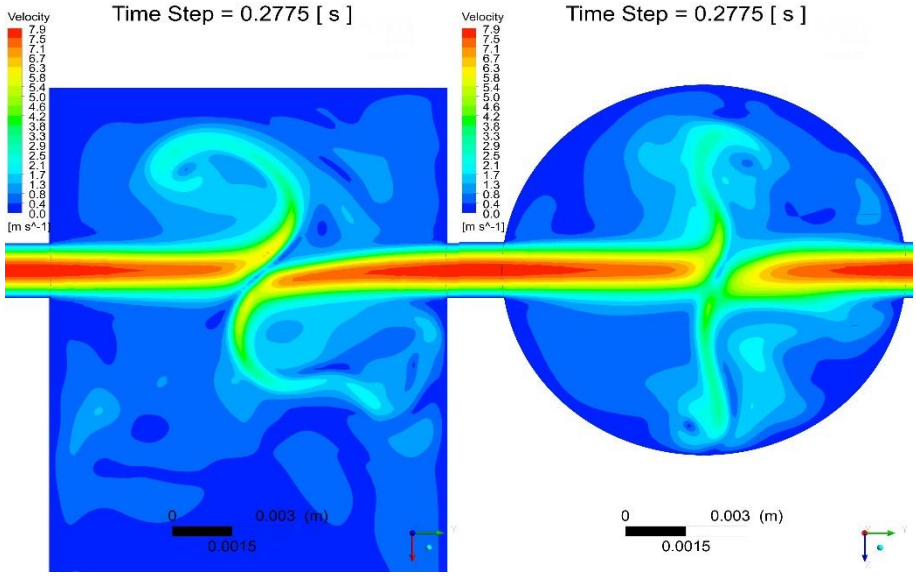

Figure 3.13 - Velocity maps for Reynolds 300 at time $t/\tau = 1$

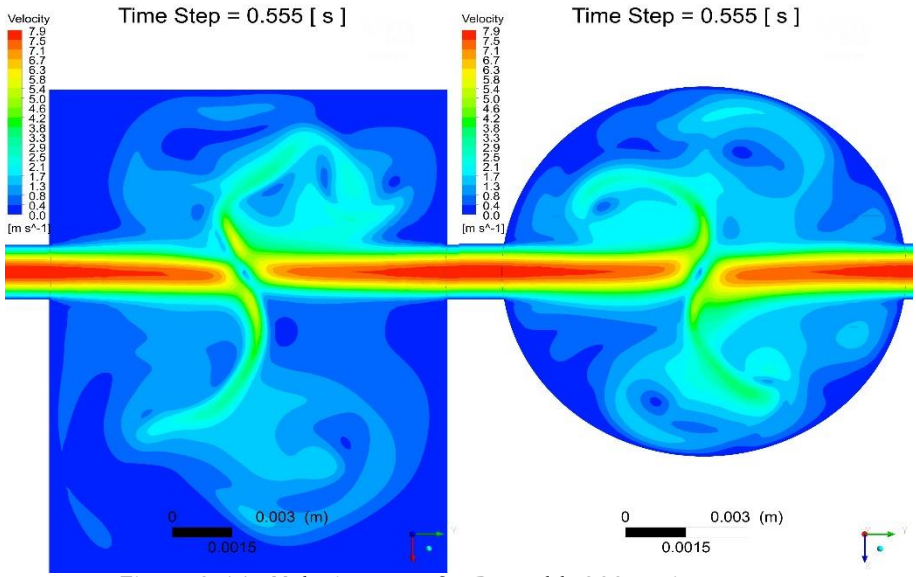

Figure 3.14 - Velocity maps for Reynolds 300 at time $t/\tau = 2$

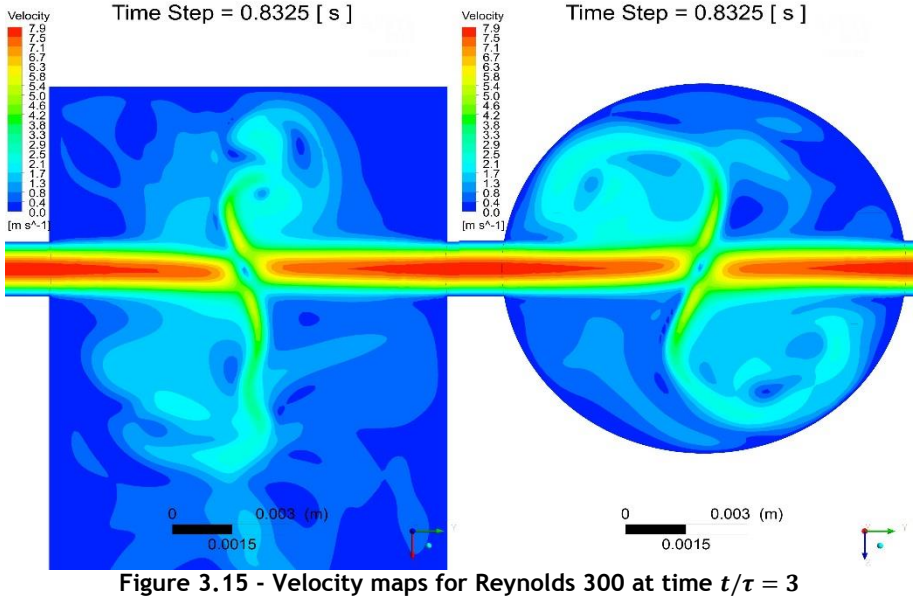

Figure 3.15 - Velocity maps for Reynolds 300 at time $t/\tau = 3$

3.3.1.2 Instantaneous flow field Vorticity map

In this section will be presented 3D vorticity maps for each Reynolds in study. The movies correspond to this figures are presented in (FOLDER). Each figure represent a representation of the impinging surface by setting a constant value of vorticity enough to allowed clear visualization of the oscillatory motion patterns. Additionally in this figure is presented the vorticity normal to the front plane calculated as

$$\vec{\omega} = \nabla \times \vec{v} = \left(\frac{\partial}{\partial x}, \frac{\partial}{\partial y}, \frac{\partial}{\partial z}\right) \times \left(v_x, v_y, 0\right) = \left(\frac{\partial v_y}{\partial x} - \frac{\partial v_x}{\partial y}\right)\vec{z} \tag{3.23}$$

The two dimensional voticity is defined as the cross product of the gradient ∇ with the flow field $\vec{v}$. It represent the rotation of the flow parallel to the $\vec{z}$ direction. When coupled with the study of the strain rate It is a value tool to access phenomena of stretching of fluid particles since represents the areas where increasing both interfacial area (area between two fluid flow streams for mixing) and local gradients in fluid proprieties (driving potential for mixing across this interface).

For this case the impingement surface is created with two colours. Orange is associated with positives values of vorticity while the blue colour represents negative vorticity values.

By observing the normal impingement surface oscillation is observed when the angle of this surface go in clockwise then the region downstream the impingement point is filled with positive values and otherwise, when the impingement surface go anticlockwise then the same region is filled with negative values. The oscillatory behaviour of this surface will then create regions with a certain thickness and different rotations which will improving the stretching of the fluid particles. The thickness of this regions and the intensity of this rotation will have a huge influence in the mixing performance, and it was observed the thickness reduces with the increasing of the Reynolds number as opposite the intensity of the rotation will increase with the increasing of the Reynolds. It was observed some disconnections of small structures of high vorticities from the impingement surface with this small structures moving downstream to the chamber outlet. Visualization studies suggests with the increasing of the Reynolds number will increase the number of vorticity regions loosen and their intensity and size. The loosen of this regions will then transform the flow behaviour along the chamber.

By observing the oscillatory behaviour the impingement surface it is clear the high angle of the vorticity will cause the breaking of the jets movement. This can be cause since there is two jets with different direction but the same rotation direction which can cause an intensification of the jets bending by repelling each other. When occur then a large number of smaller structures with high intensity vorticity values is created in the impingement region. The small regions with high intensity but with different directions will couple together and create complex flow patterns. This small structures will then flow downstream of the chamber, significantly impacting the mixing performance. This small structures when loosen from the main structure and hit the jets can cause a local deformation of the jets with severe impact in the impingement point position and/or jets angle and oscillation.

If breaking occur can cause the rupture of the fluids lamina Fonte (2012) which can cause the stop of the stretching of the fluids particle. Additionally the smalls regions with high intensity will travel along the chamber and perturb the flow behaviour. It is know this small regions usually carry along their path zones with very concentrate fluids phase, which in terms of mixing will reduced the performance. Alongside is it unknown the effect of this small vortex regions when travel along the chambers, but it is know this small structures are the main feature in reactors type (4 inlets), in terms of mixing performance, where the main feature is the confining the mixing in the top of the reactor while the phases are fully dissipated by small and high intensity vorticities regions

It is important focus all of this visualization studies were performed for the same fluid with same momentum in each side. Different types of fluids in each side, especially if the viscosity and density differs allied with different stoichiometric ratios will produce a far more complex flow pattern which need be carefully study and could differ from those study in this section

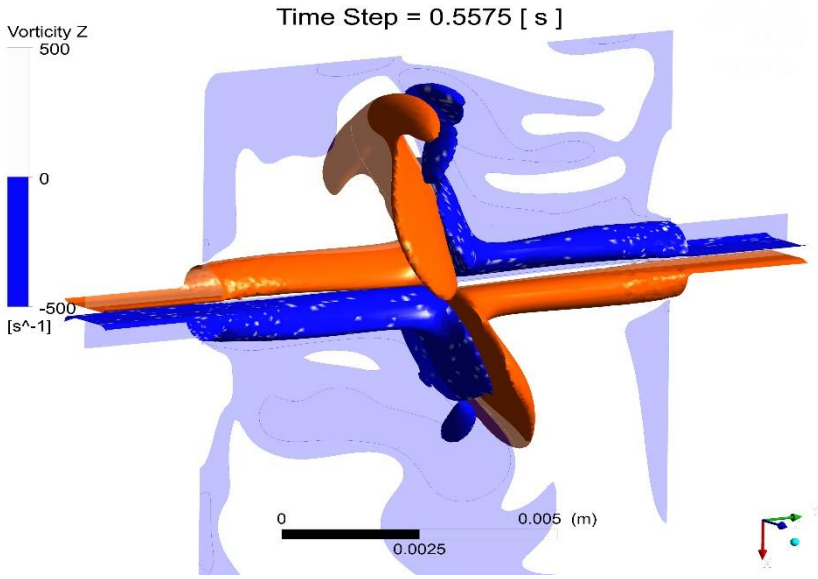

Figure 3.16 - Vorticity map for Reynolds 150 at time $t/\tau = 1$

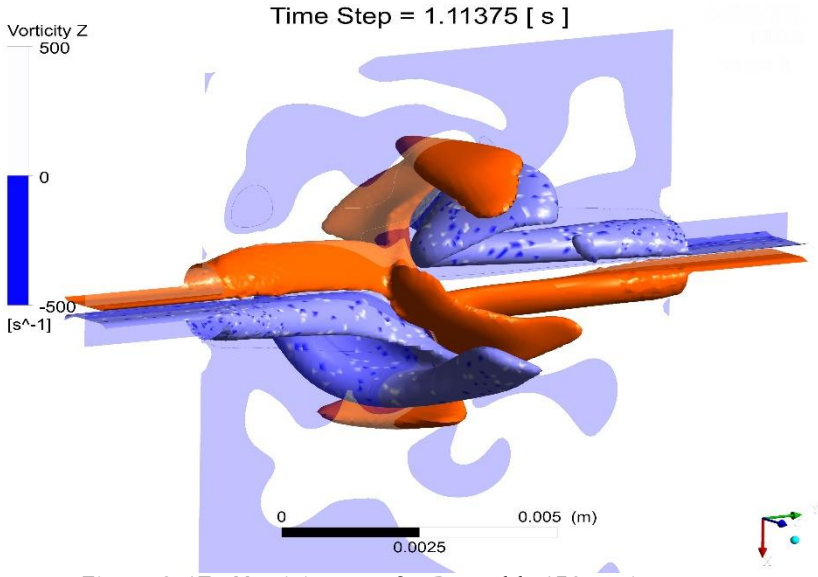

Figure 3.17 - Vorticity map for Reynolds 150 at time $t/\tau = 2$

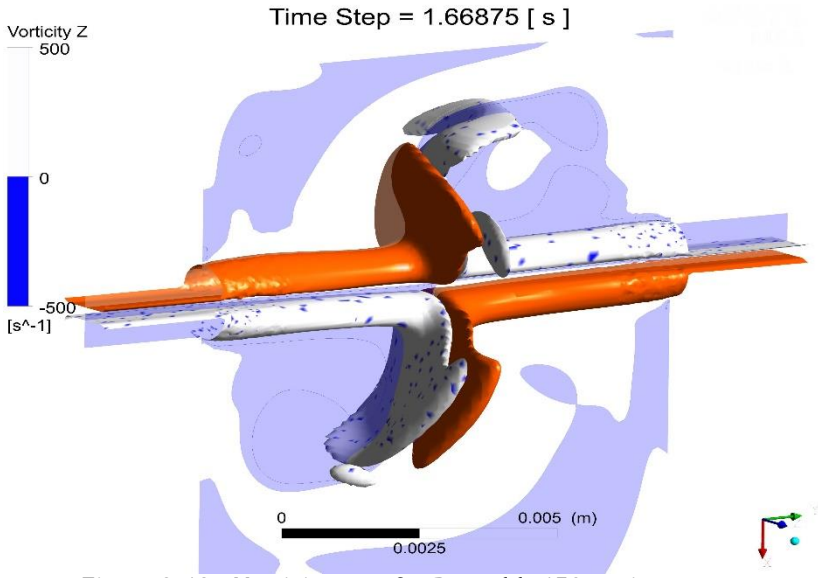

Figure 3.18 - Vorticity map for Reynolds 150 at time $t/\tau = 3$

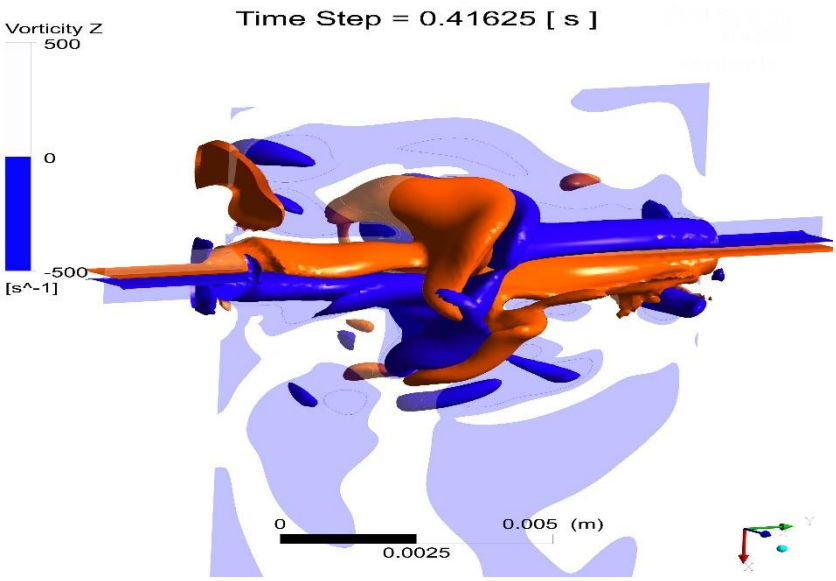

Figure 3.19 - Vorticity map for Reynolds 200 at time $t/\tau = 1$

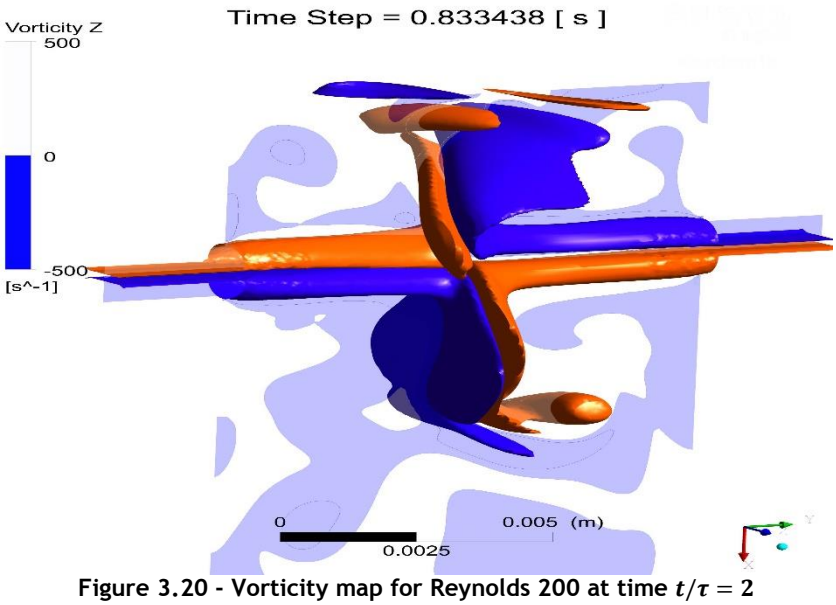

Figure 3.20 - Vorticity map for Reynolds 200 at time $t/\tau = 2$

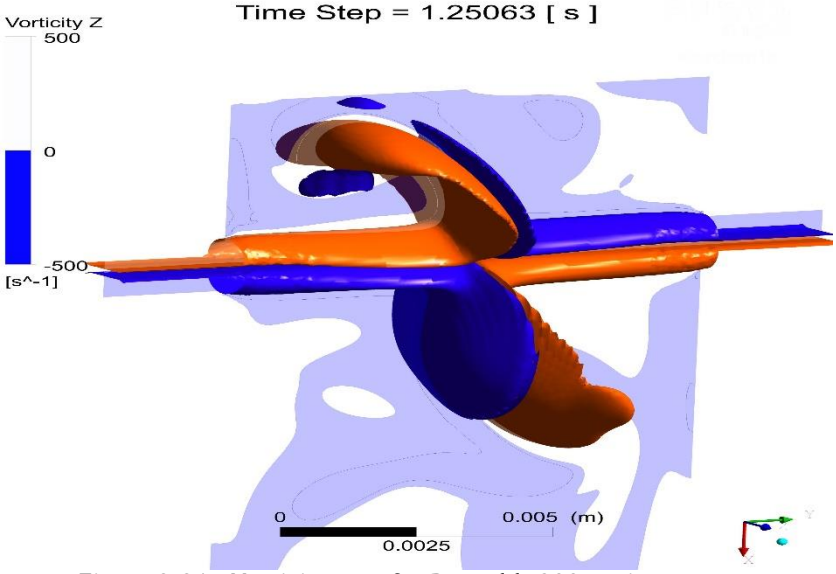

Figure 3.21 - Vorticity map for Reynolds 200 at time $t/\tau = 3$

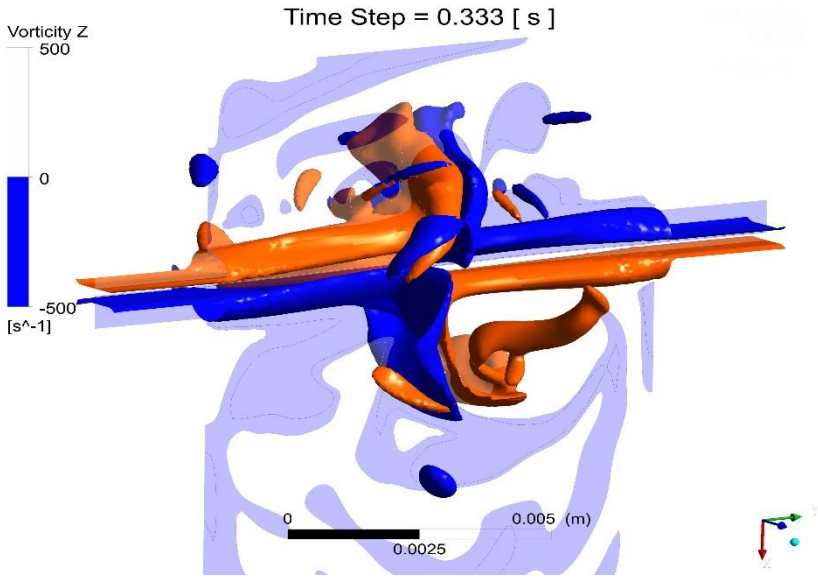

Figure 3.22 - Vorticity map for Reynolds 250 at time $t/\tau = 1$

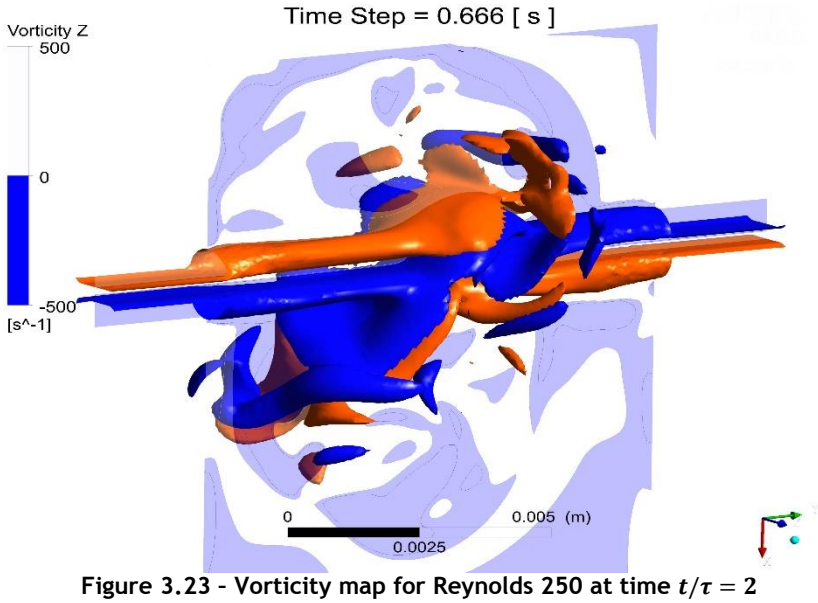

Figure 3.23 - Vorticity map for Reynolds 250 at time $t/\tau = 2$

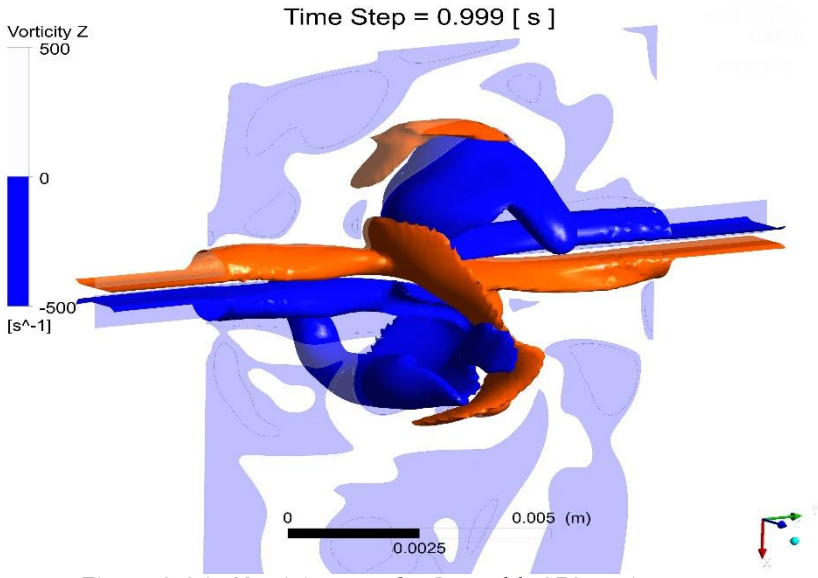

Figure 3.24 - Vorticity map for Reynolds 250 at time $t/\tau = 3$

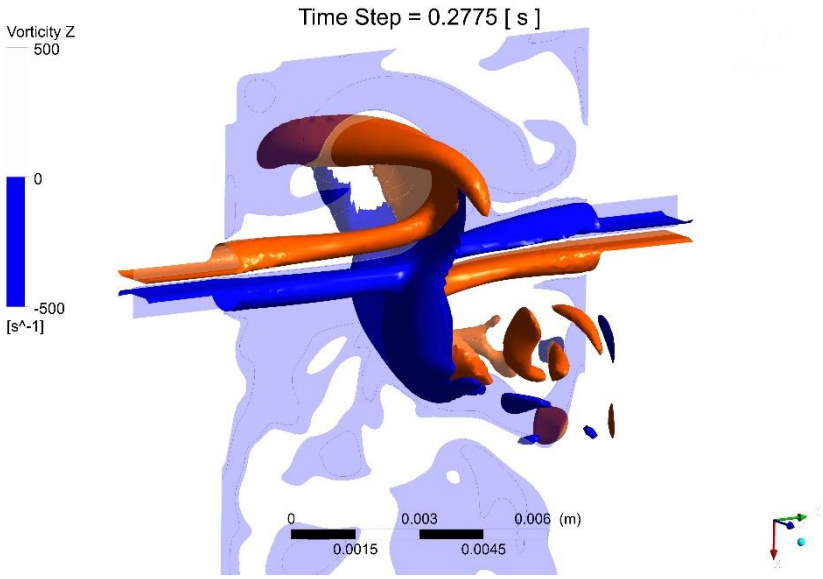

Figure 3.25 - Vorticity map for Reynolds 300 at time $t/\tau = 1$

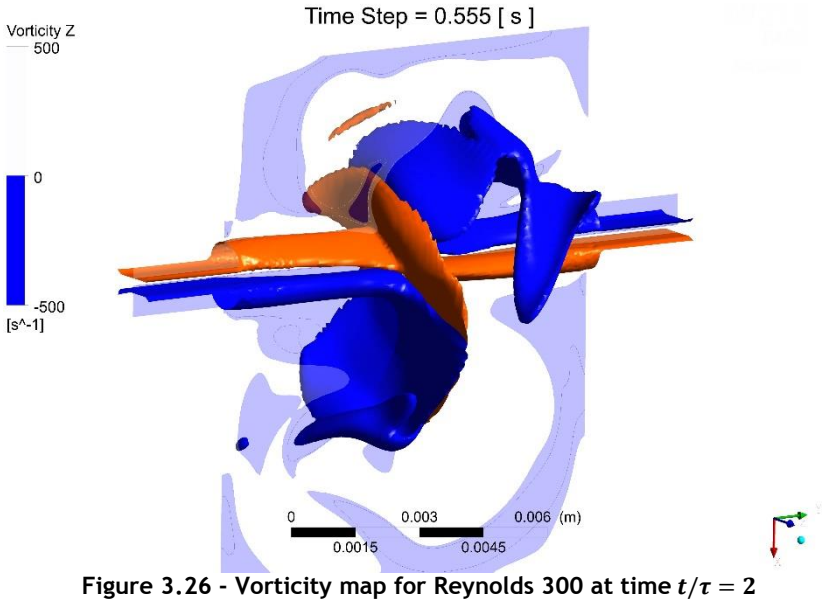

Figure 3.26 - Vorticity map for Reynolds 300 at time $t/\tau = 2$

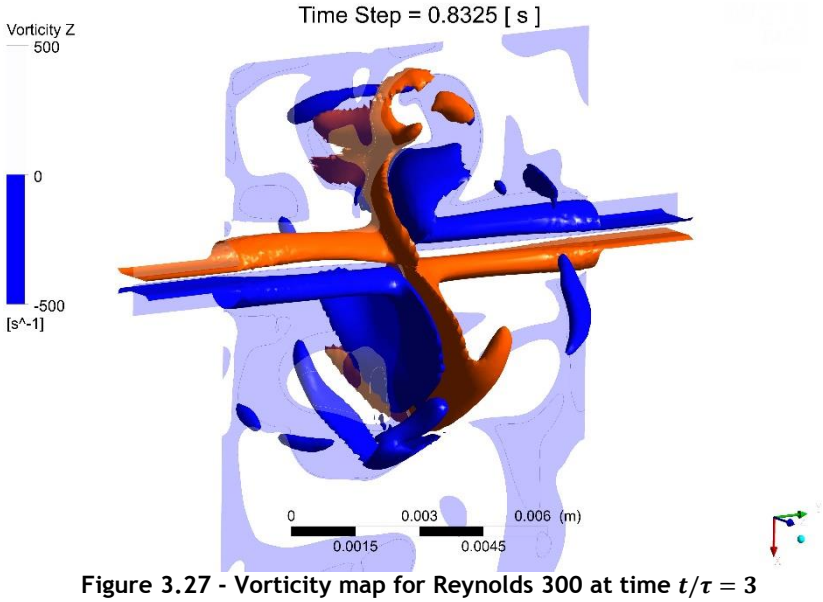

Figure 3.27 - Vorticity map for Reynolds 300 at time $t/\tau = 3$

3.3.2 Spatial evolution of the flow

In the present case the flow is mainly driven by viscosity forces rather than inertial forces, which indicates the flow are laminar. The non-linearity of the NS equation produces an uncertainty flow behaviour, which can cause the chaotic nature or turbulent nature. Chaotic is defined by a set of non-linear equation which with a slightly change in the initial condition will greatly affect the flow behaviour in the next time steep. A succession of sight differences in each time step would greatly differ the results in the end of the simulation.

Exist in the literature tree main approaches to measure chaotic systems (Argyris, Faust, & Haase, 1993; Froehling, Crutchfield, Farmer, Packard, & Shaw, 1981; Lester, Smith, Metcalfe, & Rudman; Y. C. Li, 2013; Narasimha, 1986; Ngan & Vanneste, 2011; Research, 2003; Sommerer, Ott, & Tél, 1997; Southerland, Frederiksen, Dahm, & Dowling, 1994; Stroock et al., 2002; Voth, Saint, Dobler, & Gollub, 2003; Wong, 2010):

- Stochastic approach – This is a probabilistic method to characterize to the behaviour of the flow field. Exist two main methods. The first is the Lyapunov exponents which quantifies the rate of separation of an infinitesimal close trajectories. The second is the correlation length and time scales which measure the dimensionality of the space and time occupied by a set of random points. Roughly speaking the Lyapunov exponents is the same as the inverse of the correlation length and time. This methods are generic and don't provide relevant informations.
- Chaotic advection approach – This method focus in specific features of the flow. The main methods used to calculate are spatial distributions of Lyapunov exponents and stable and unstable manifolds. Those methods are incredible hard to implement and don't provide such important quantification tools and this is why are often used as diagnostic tool.
- Eigenfunction approach – This method solve infinite-dimensional eigenvalue problem for advection-diffusion problems, by calculate the Eigenmodes of the data series and only focus in the dominant Eigenmodes. This method is very hard to implement and focus in special characteristics of the problem.

All of the methods used to quantify and qualify the results from chaotic systems don't provided enough practical information to access to main problem, thus is required to use other methods to study spatially to access the flow hydrodynamic temporal and spatial scales. Turbulent methods in other hand ensure quality of the result this relevant and practical information therefore will be used in the present work.

Along the domain a set of point, align with the axis of the chamber is positioned to record each time step, the velocity components of the flow in each point. The points was chosen based on the following equation. Data series provide the simulation is then treated where is only consider 1 to 3 τ data, since the first τ is used to create the oscillatory behaviour.

$$0, d, d + 2^{-6}D, \ldots, d + 2^{2}D \tag{3.24}$$

In order to quantify the flow, turbulent methods of investigating the flow behaviour was used. Initially is assumed the flow can be characterize by their mean velocity and the fluctuations

$$v^{*} = \bar{v} + v' \tag{3.25}$$

Where $\bar{v}$ is the average velocity, $v(t)$ is the instantaneous velocity and v^{*} is the velocity which contain the velocity variation along the time series. The oscillatory time dependent velocity is shown in Appendix B. It is observed in this appending an irregular behaviour with different magnitude and frequency passing through the point monitor. Such region is referred to as an eddy or turbulent structure which simply pass by this monitor. The size of the region and its representative velocity are namely the length scale and the velocity scale. The Appendix B contain the time series used in the analysis of this problem. It is observable a vanishing of the velocity magnitude and a slightly increase of the length scale as the point is progress towards the chamber outlet.

Figure 3.28 to Figure 3.31 show the each velocity component against the position of the point normalized by the chamber diameter. Being v_y the velocity of the injector and v_x the velocity parallel with the chamber axis and v_z the velocity normal to boot of them. As expected the v_y take in the point zero, the velocity close to the injector axis velocity, with fluctuations corresponding to the side of the impingement point position with a fast vanishing of those fluctuations in the downstream points. The impingement will then convert velocity in y direction to velocity in z direction thus is observable by the bigger z velocity in the impingement point. According to the x velocity is observable a higher value in point 1 due the spreading of material from the impingement point.

Generally speaking is possible to conclude the following. Fluctuations in y-velocity is mainly driven by the oscillation in the impingement point position and his velocity almost don't lose kinetic energy from the injection to the chamber to impingement. The magnitude of the x-velocity when compared with z-velocity, prove the spreading of fluid is mainly parallel with the chamber axis rather than opposite direction.

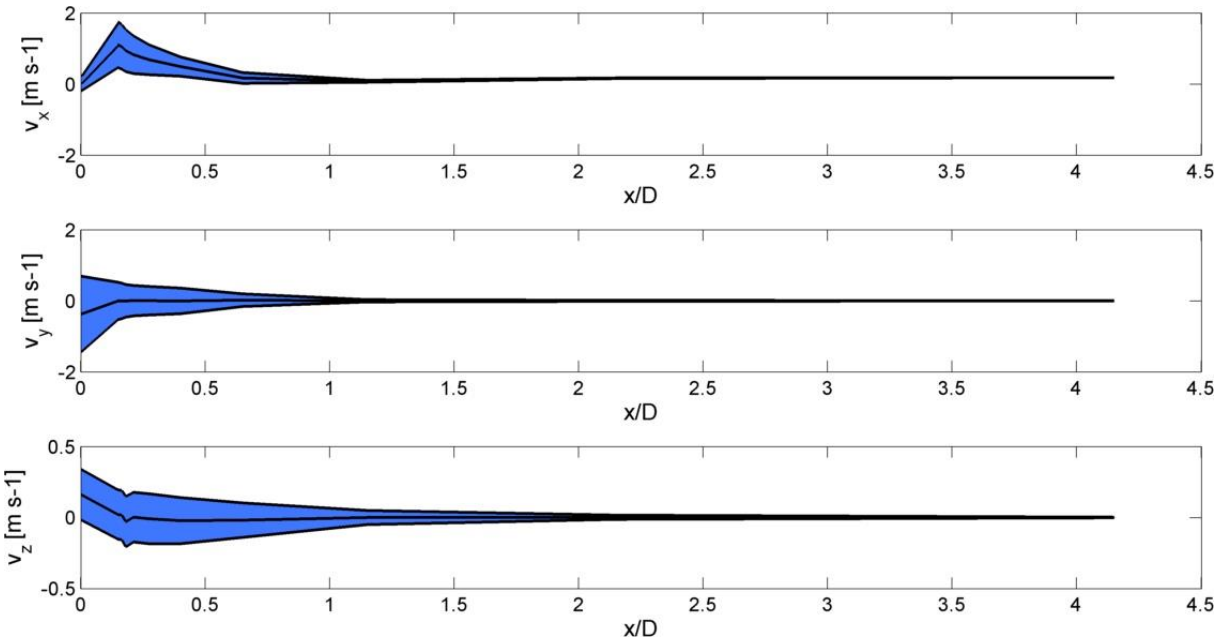

Figure 3.28 - Mean and fluctuations velocities components toward the chamber outlet, for Reynolds 150

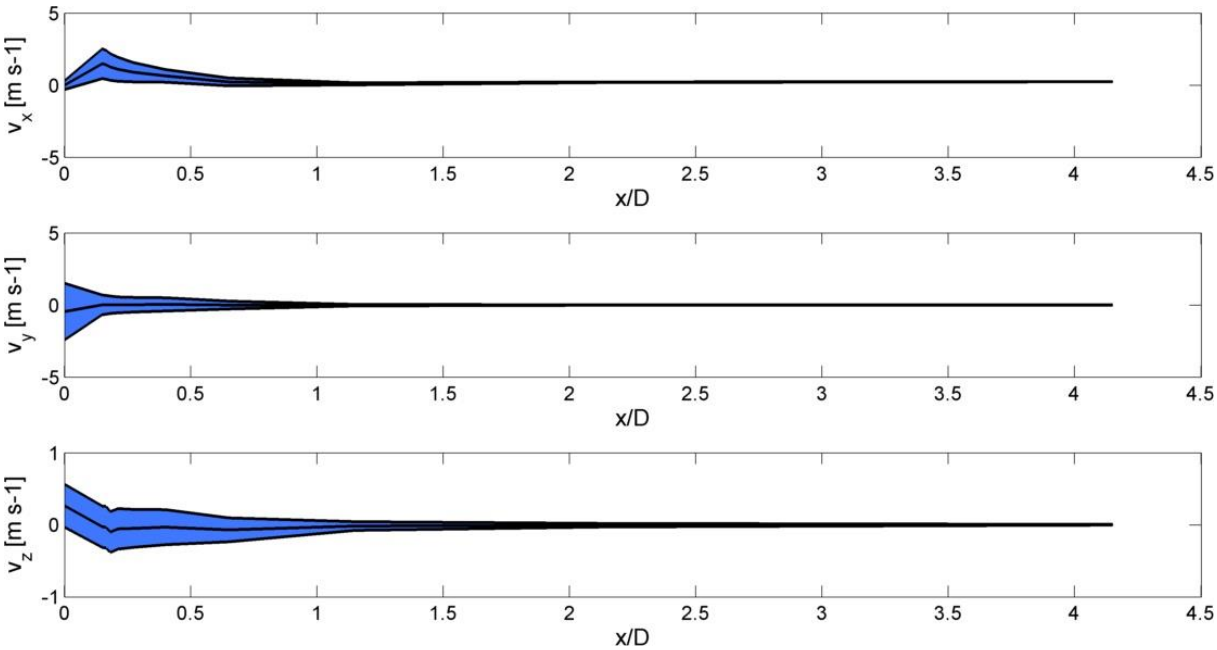

Figure 3.29 - Mean and fluctuations velocities components toward the chamber outlet, for Reynolds 200

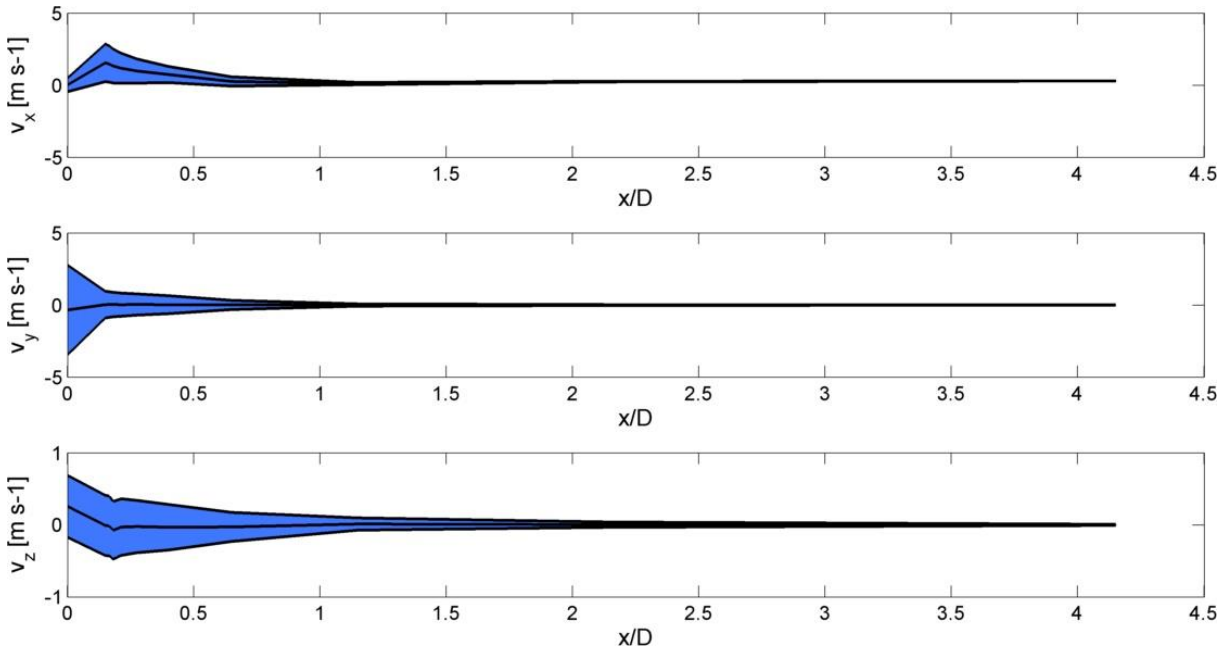

Figure 3.30 - Mean and fluctuations velocities components toward the chamber outlet, for Reynolds 250

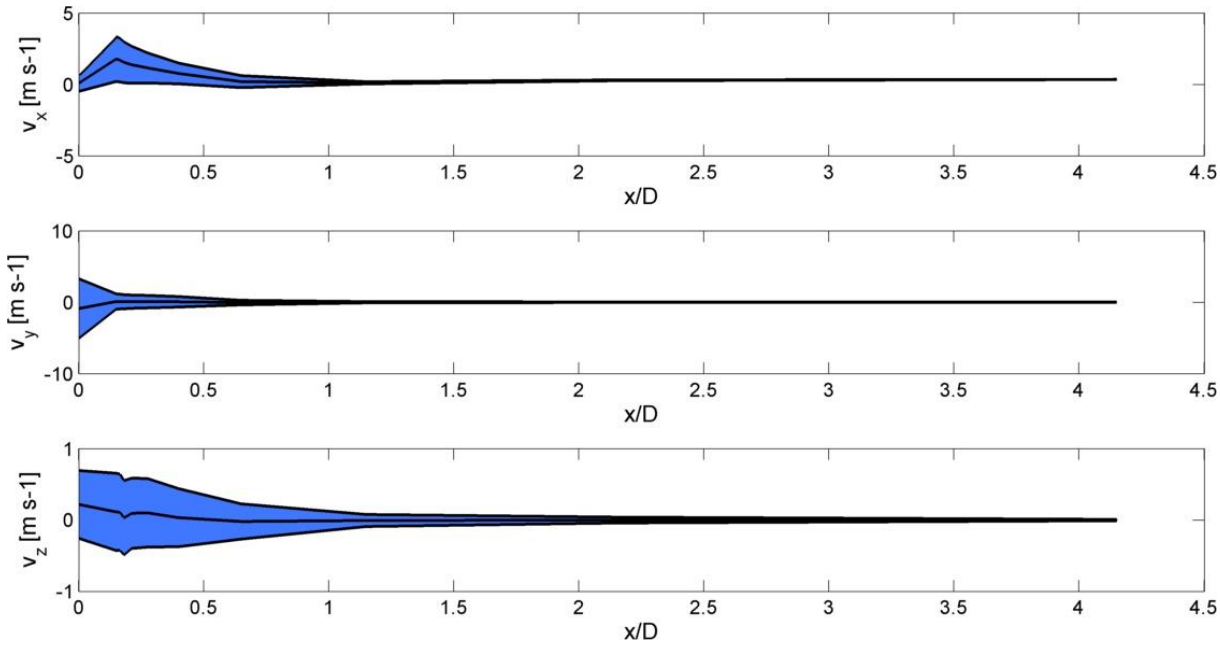

Figure 3.31 - Mean and fluctuations velocities components toward the chamber outlet, for Reynolds 300

The Reynolds number is a constant which correlates the length and the velocity scales. The energy of such scales are, by turbulent theory, transport energy from the larger scales to the lower scales by an energy cascade, with in the smaller scale known as Kolmogorov scale are dissipated into heat by viscosity.

As DNS simulation the flow is solve until the lower hydrodynamic scale. The Kolmogorov scale is defined as

$$\lambda_k = \left(\frac{\nu^3}{\varepsilon}\right)^{\frac{1}{4}} \tag{3.26}$$

Where ν is the kinematic viscosity and ε the turbulent energy dissipation. It is expected the results contain all the scales except for Reynolds 300 the mesh is a bit larger than the hydrodynamic scale. Spite this fact would be expected the lack of resolution act as a filter for the lower scales. The main importance of this study is not quantify exactly the flow behaviour, from the scales point of view, but it is observe and identify which scales are associated with a certain behaviour, and therefore it is expected a good resolution in this case. Other scales are inherent to describe the flow, namely the length scale, the time scale and the velocity scale

$$\eta = \left(\frac{\nu^3}{\varepsilon}\right)^{\frac{1}{4}} \tag{3.27}$$

$$\tau = \left(\frac{\nu}{\varepsilon}\right)^{\frac{1}{2}} \tag{3.28}$$

$$v = \left(\frac{\nu}{\varepsilon}\right)^{\frac{1}{2}} \tag{3.29}$$

Where ν is the kinematic viscosity and ε the turbulent energy dissipation. Kolmogorov scales decrease as the Reynolds number increases. Turbulent kinetic energy (TKE) is defined as:

$$k = \frac{1}{2}\left(\overline{u'^2} + \overline{v'^2} + \overline{w'^2}\right) \tag{3.30}$$

Turbulent kinetic energy (TKE) is a measurement of the energy containing in turbulent eddies thus measure the intensity of turbulence, where is provided due the velocity fluctuations of the flow field. In a fluid flow system exists a large number of eddies, from all sizes, each one containing a certain amount ok TKE. Normally large eddies contain the most amount of

TKE. Large eddies are then stretched, deformed and destructed into small eddies without any loss of energy in this passage.

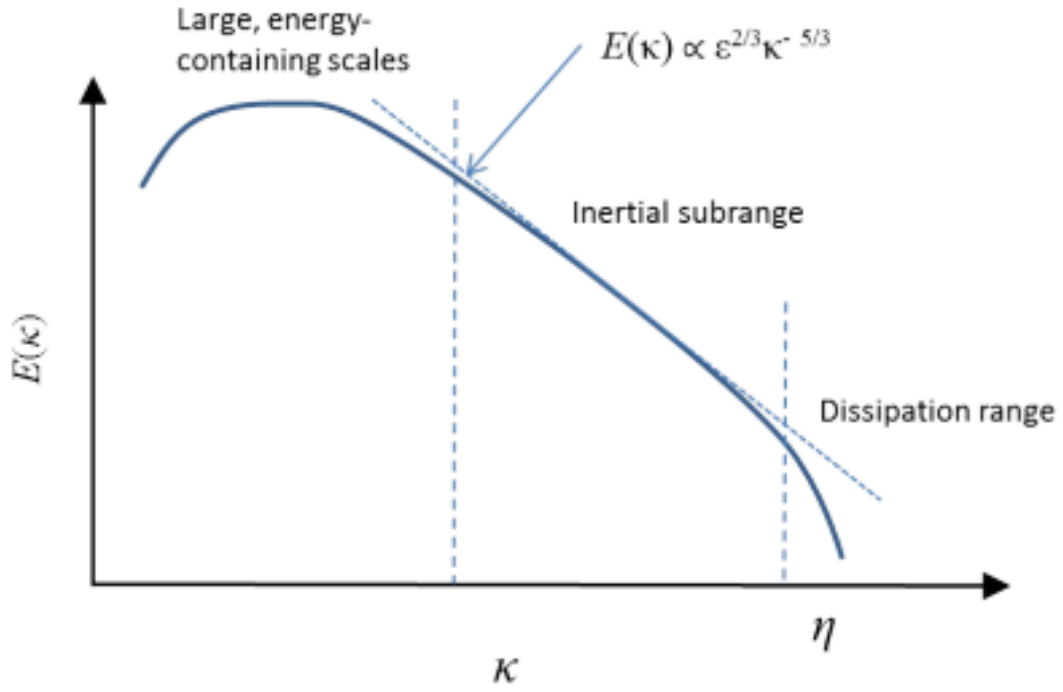

Figure 3.32 - Schematic illustration of the energy cascade. It shows the amount of turbulent energy E associated with different wave number k

As shown in Figure 3.32 larges eddies scales are associated with low wave numbers with high energy. This region is where the most energy is created or conserved. In the inertial subrange, which have a -5/3 relation, but this will be explained latter, is where the energy is transfer from larger to smaller vortices. The slope presents the rate in which the energy is transfer and for each case different relations emerge. In the dissipation rage, associated with high wave numbers the energy will be dissipated until vanish due viscous effects.

TKE is associated with velocity fluctuations. Figure 3.33 shows the TKE along the normalized dimension along the chamber outlet. In point 0 exist a small value of TKE due mainly by the y-velocity component. The peak of maximum production of TKE is obtain in point 1 since it is where is located the maximum velocity fluctuations for spreading of material along the chamber axis. After this point and moving towards the outlet the TKE decays.

Reynolds 150 correspond to the lower value of TKE while opposite Reynolds 200 corresponded to larger value. It is expectable the increasing of TKE with the Reynolds number. Spite this fact it is observable for Reynolds 200 and 250 almost the same value of TKE, which could mean both Reynolds have similar flow hydrodynamics.

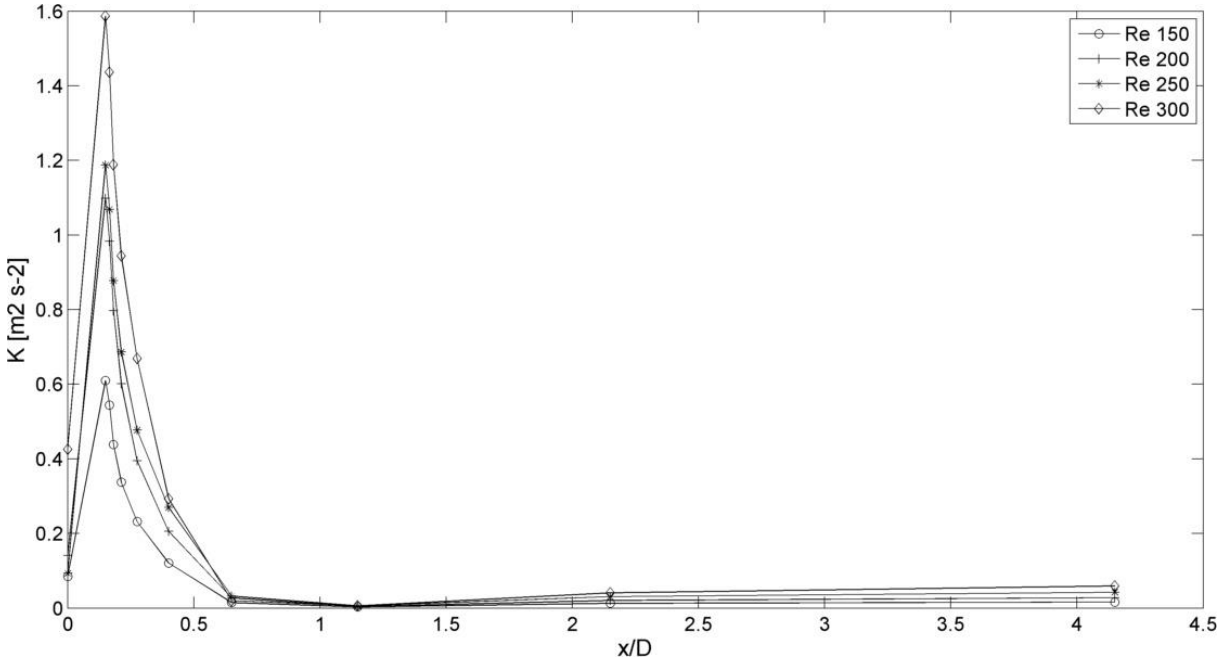

Figure 3.33 - Turbulent kinetic energy along the chamber axis

Kolmogorov's hypothesis says for homogenous turbulence, the kinetic energy k is the same everywhere and for isotropic turbulence the eddies also behave the same in all directions. This fact is true since this hypothesis is valid for local isotropy, this mean the scales are in the energy transport range, or in other words low small scale. This hypotheses consider the larger scales of turbulence can be anisotropic.

In the intermediate scales the length scale is relatively large then the flow will not be affected by the dynamic viscosity, therefore the statistic of the motions of scale is uniquely determined by the rate of dissipation of kinetic energy ε, defined as.

$$\varepsilon = 2v < s_{i,j} \cdot s_{i,j} \cdot > = 2v\left(s_{1,1}^2 + s_{1,2}^2 + s_{2,1}^2 + s_{2,2}^2 + s_{1,3}^2 + s_{2,3}^2 + s_{3,3}^2\right) \tag{3.31}$$

Where the derivatives are calculated as

$$s_{i,j} = \frac{1}{2}\left(\frac{\partial u_i^*}{\partial x_j^*} + \frac{\partial u_j^*}{\partial x_i^*}\right) \tag{3.32}$$

In the process of conversion of turbulence from large eddies to smaller eddies two main scales emerge, as show in Figure 3.34.

- The inertial sub range where the motions are determined only by inertial effect. From this range a well know relations between energy content, rate of dissipation and wave number in this range

$$E(k) = C\varepsilon^{\frac{2}{3}}k^{-\frac{5}{3}} \tag{3.33}$$

- The dissipation range where turbulent effects are dissipated by viscous effect by the fluid

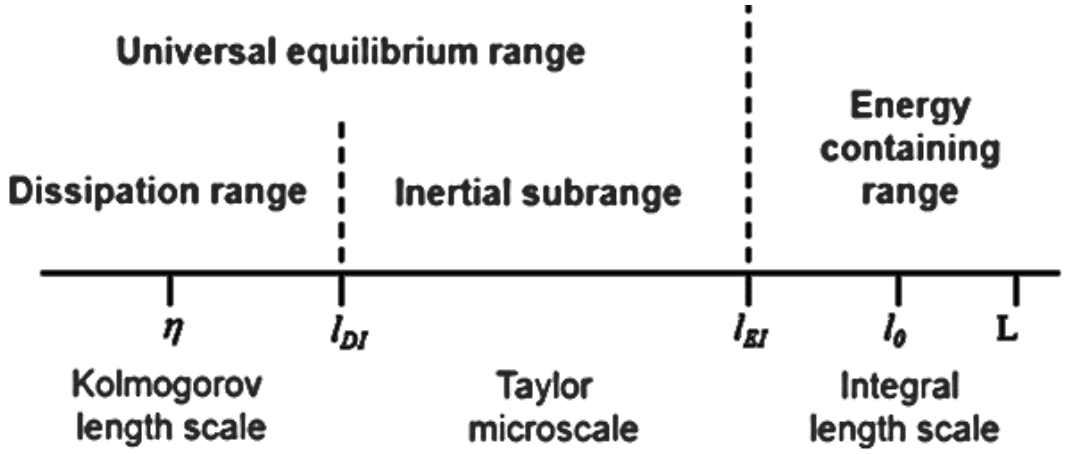

Figure 3.34 - Cascade of transport and dissipation of turbulent energy

3.3.3 Average flow field

From the results of the numeric simulation a specific number of time steps chosen randomly along all the time domain was used to perform an average flow field. This average will be explained in detail in the next sub-chapter. The average was perform using user defined scalars in order to create new variables with the results from the velocity field. Those velocities will be latter treated to obtain the most important tools to evaluate the flow field, namely the rate of creation and dissipation of turbulent kinetic energy.

The starting point will be evaluate numerically the position of the stagnation point position, which is know their location being aligned with the chamber axis and injector axis, although none test was perform to quantify. This meaningful analyses will be necessary for experimental part of the present thesis

3.3.3.1 Stagnation Point Position

From the previous works there is no evidence of a numerical study to evaluate the impingement point position in 3D. From 2D experiment it is know the stagnation point is align with the chamber axis but bend according to the injector axis a distance correspondent to 2d.

Experimental work does not provide enough information, with reliable data to ensure a proper measurement of the position, thus the importance of this test. The present test aim comparing the impingement point position for each the Reynolds in study by a change of direction of the velocity. Three lines, each one represent the orthogonal axis, centred in the point align with the injector axis and chamber axis are created. Average velocity directions will then be evaluated for each line in order to identify the impingement point position

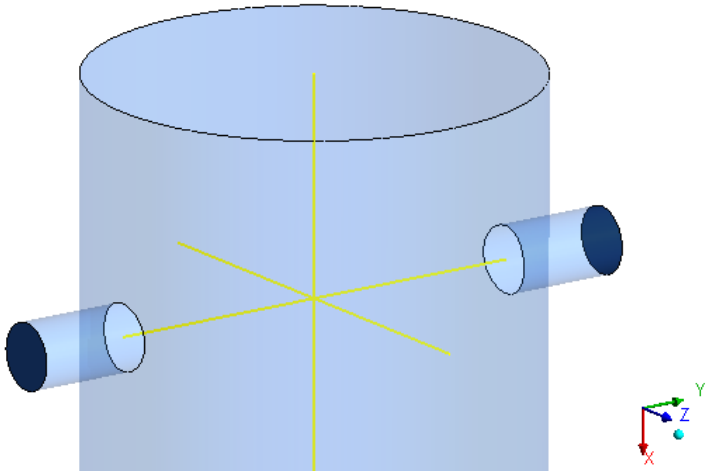

Figure 3.35 - Lines aligned with origin of the chamber

Each velocity component are ploted against a proper axis (Figure 3.36 to Figure 3.38). Each orientation provide in a smaller plot a closer look to [0, 0] coordinate.

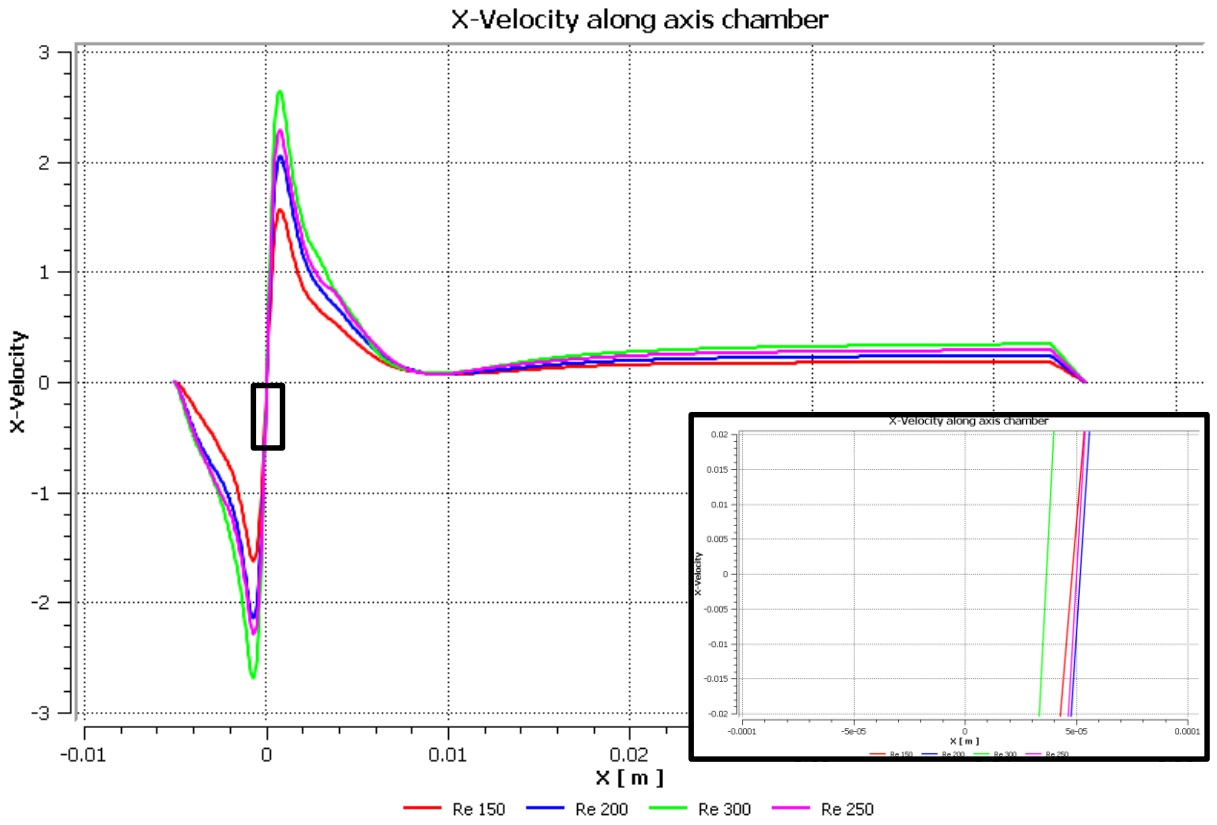

Figure 3.36 - Impingement point position, X-velocity along the chamber axis

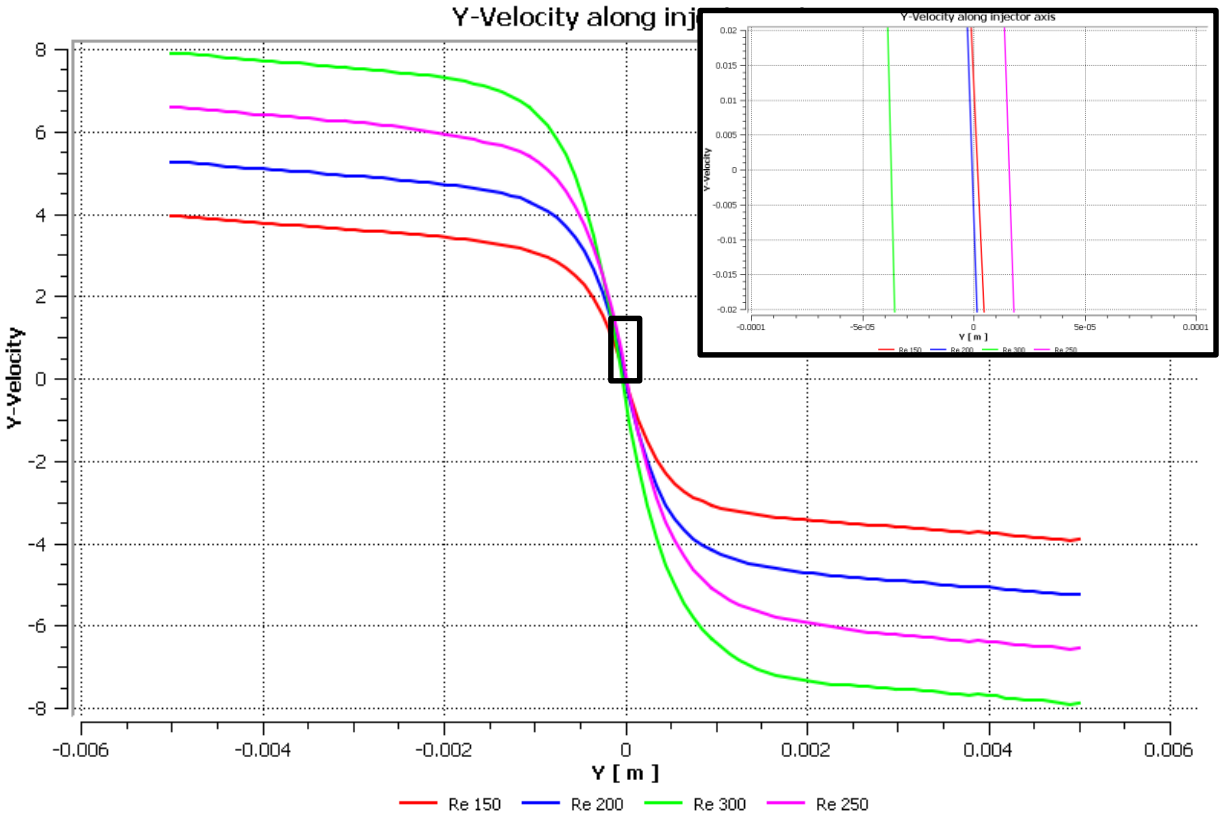

Figure 3.37 - Impingement point position, Y-velocity along the injector axis

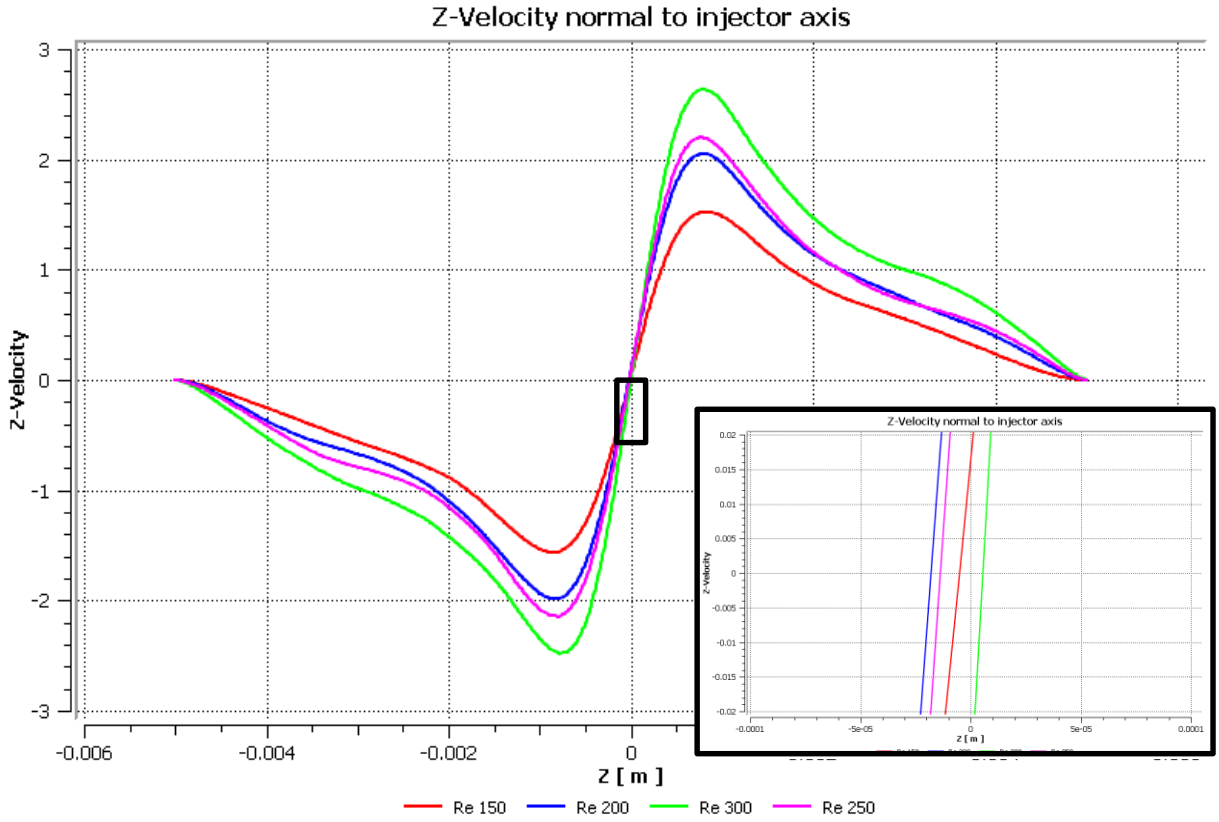

Figure 3.38 - Impingement point position, Z-velocity along the injector axis

The maximum edge size for all the simulation are 100 μm. Consider all the values bigger than the resolution of the mesh. It is concluded, face of the error in resolution and averaging, the impingement point position, in other words, the location where the velocity change in direction is in [0, 0, 0] m, which means the impingement point position are centred with the origin. This prove will be used when was develop a deterministic algorithm to obtain the stagnation point position and the jets angle.

Important fact to refer is the highest rate of change in the velocity, in order words, the higher partial derivative, is in all representations around the stagnation point position, being for higher Reynolds number a slight increase in this value. Higher derivatives are in y and x direction, namely the injector axis direction and the chamber axis direction. This conclusion will later held to understand the rate of dissipation of turbulence

3.3.3.2 Velocity

The average velocity component is show in Figure 3.39 to Figure 3.42 for each Reynolds in study. In the left side is shown the top plane contour of the velocity and on the right side is show the velocity along a line aligned with the injector axis and which cross the points used to record the velocity (Equation 3.24).

For all the Reynolds in study is observable the same behaviour:

- In the plot correspondent to the x velocity the point 0 have an inverse direction of the velocity, since the position of the stagnation point, obtained in the simulation is around $50\ \mu m$ from the origin tending downstream. Although there is not resolution to confirm this value numerically this produce a shift in the sign. The adjacent point p1 have the maximum x-velocity since all the volume contained energy provided by the injectors are directionally downstream. The following point have consequently a reduced velocity since there is a spreading of material in more than one direction thus is clearly observable an cone with high velocity, being this cone formatted due the oscillatory behaviour of the impingement surface. Downstream of the jets a negative sigh of the x-velocity is observable since it correspond to a low speed recirculation zone. Along the chamber a vanishing of the high central located velocity into a more spread distribution, being in the end almost uniform x-velocity in the chamber outlet meaning in the total height of the chamber a vanishing of high velocity and high intensity fluctuations into a uniformly distributed velocity profile translating no more mixing advection mechanics close to the outlet of the chamber.
- The y-velocity profile presents in the injector axis, p0, the maximum velocity magnitude. It is clear from this graphic the reduction of the velocity since enter in the chamber don't lose its kinetic energy, meaning, the spreading of the fluid due impingement is mainly influence by the injector's velocity. In impingement the velocity quickly decays in very low distance, producing a fast deceleration of the fluid which is the mainly cause of the spreading and oscillatory motion of the impingement surface. After the impingement point and progress towards the chamber outlet there is low value of velocity, slightly vanishing until the chamber outlet.
- The z-velocity in the Reynolds in study present to have a random behaviour without any common reference. Generally speaking the magnitude of this velocity don't present a relevant factor in the advection mixing since the value is low. Is observable an homogeneous and uniform velocity in the chamber outlet for all the Reynolds. The low value and random pattern could be due averaging, since velocity in this component is mainly driven by the location of the impingement point and the oscillatory motion of the impingement surface.

All the comments was perform for all the Reynolds in study in a general sense. An important note, which was referred previously the averaging of the velocity component was necessary to compute the rate of creation and dissipation of turbulent kinetic

energy, thus the stabilization value of this variables in the whole was consider to limiting number of time steeps for averaging due space limitations. The values and contours present was averaged from the instantaneous velocity field considering this limiting factor, which could cause a lack of resolution in some locations or, in case of low values and shifting velocity directions each time step.

A. Reynolds 150

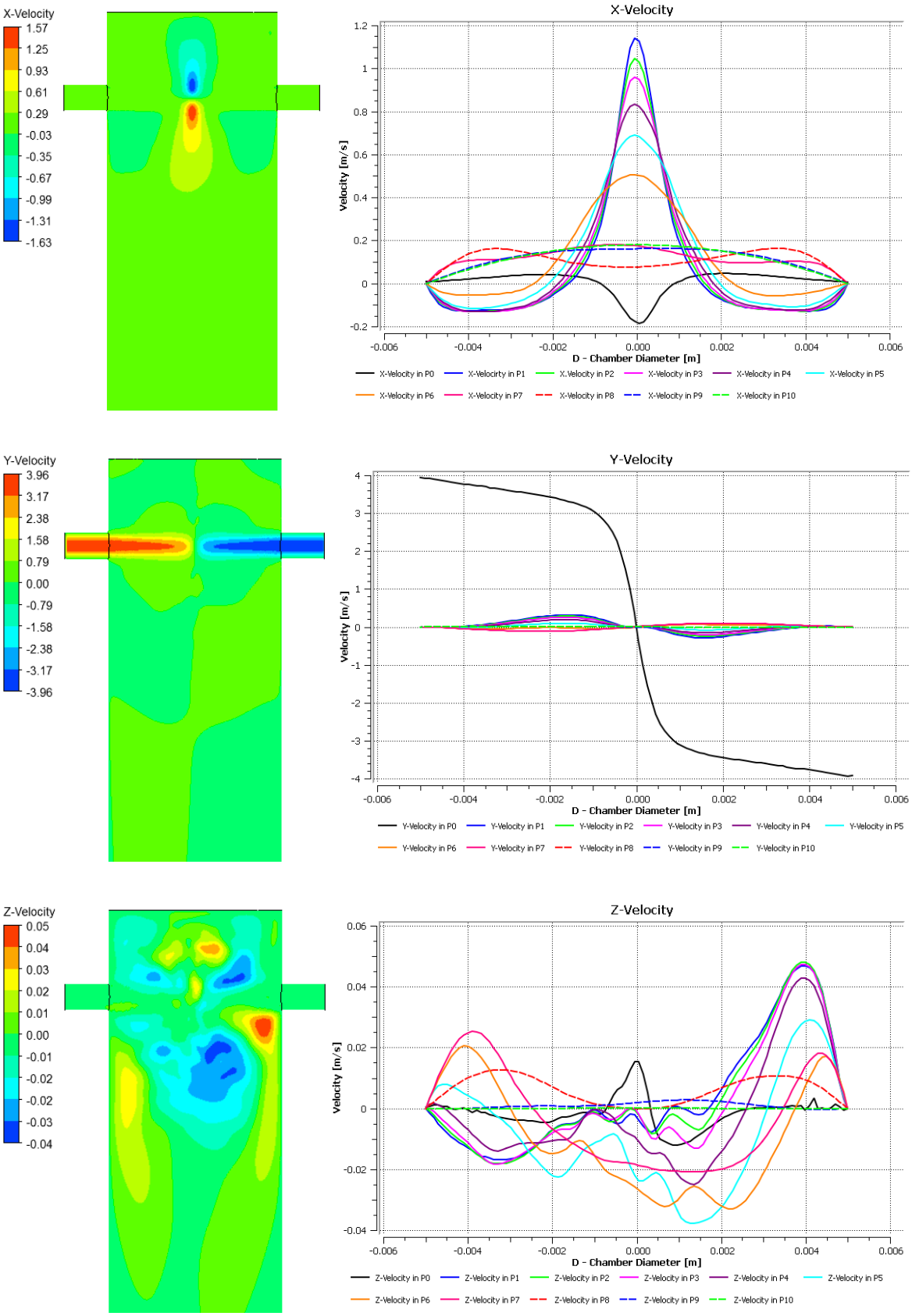

Figure 3.39 - Contour of the velocity components in the front plane (left). Velocity components along the probe points in a line aligned with the injectors axis (right). Reynolds 150

B. Reynolds 200

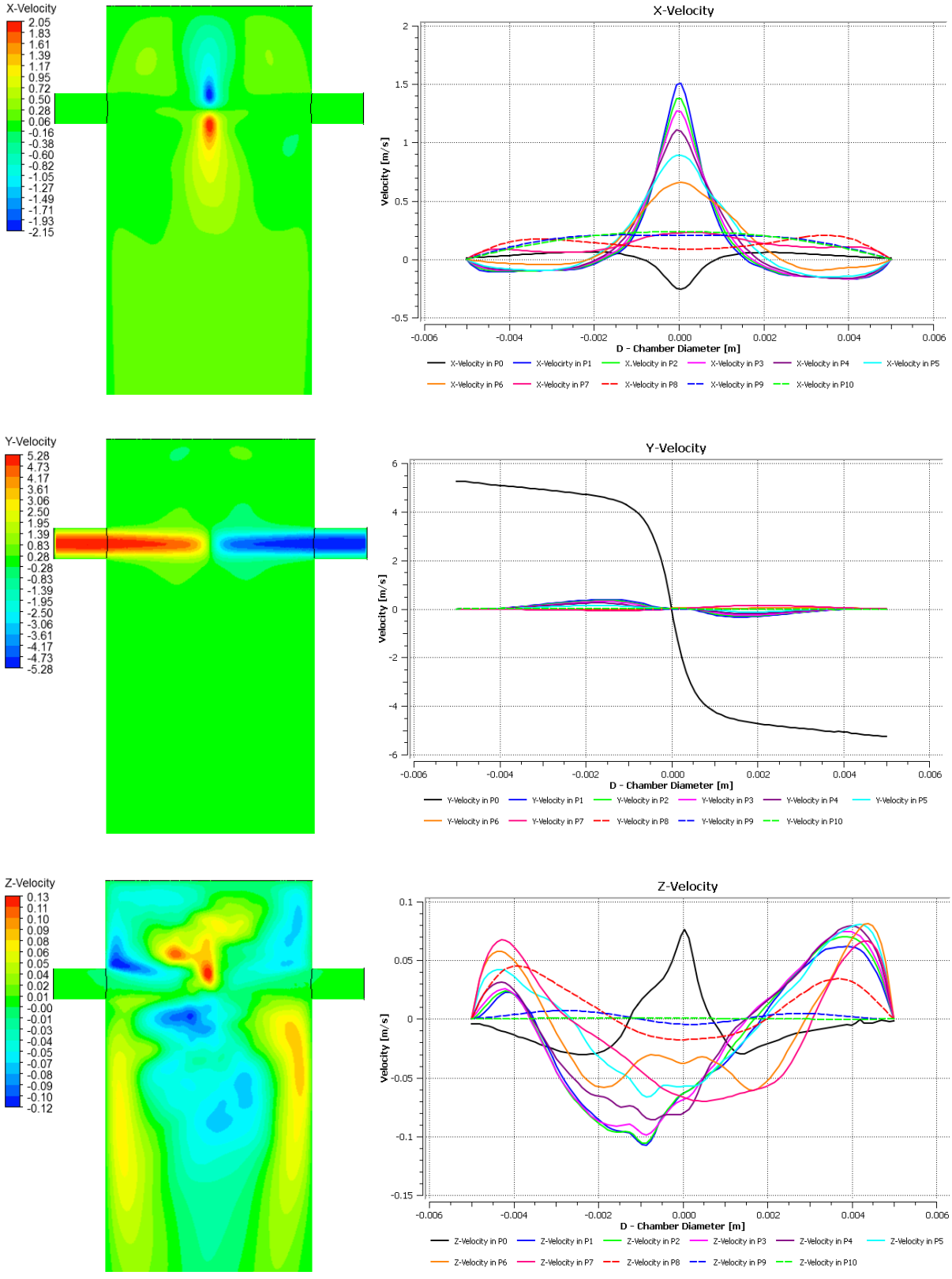

Figure 3.40 - Contour of the velocity components in the front plane (left). Velocity components along the probe points in a line aligned with the injectors axis (right). Reynolds 200

C. Reynolds 250

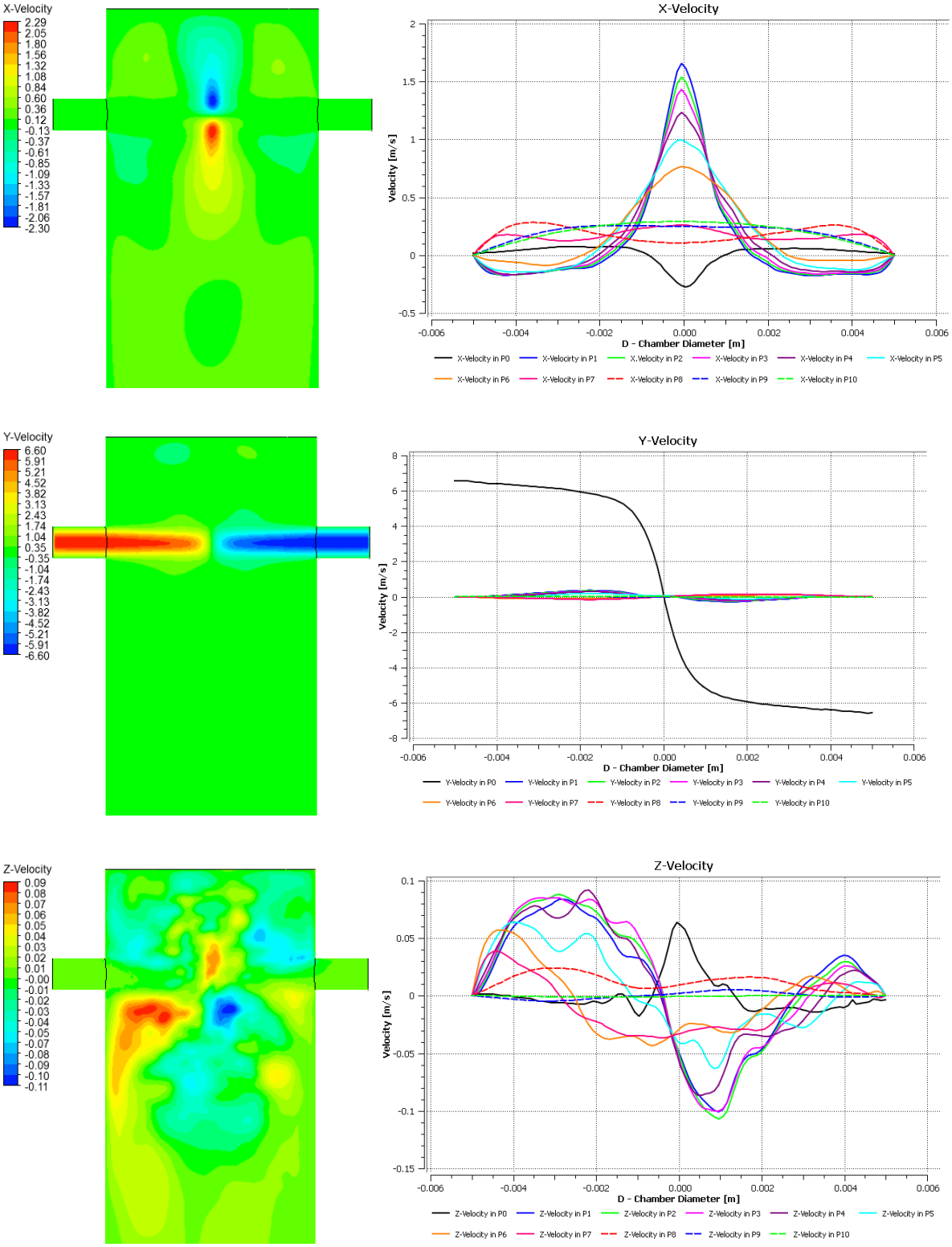

Figure 3.41 - Contour of the velocity components in the front plane (left). Velocity components along the probe points in a line aligned with the injectors axis (right). Reynolds 250

D. Reynolds 300

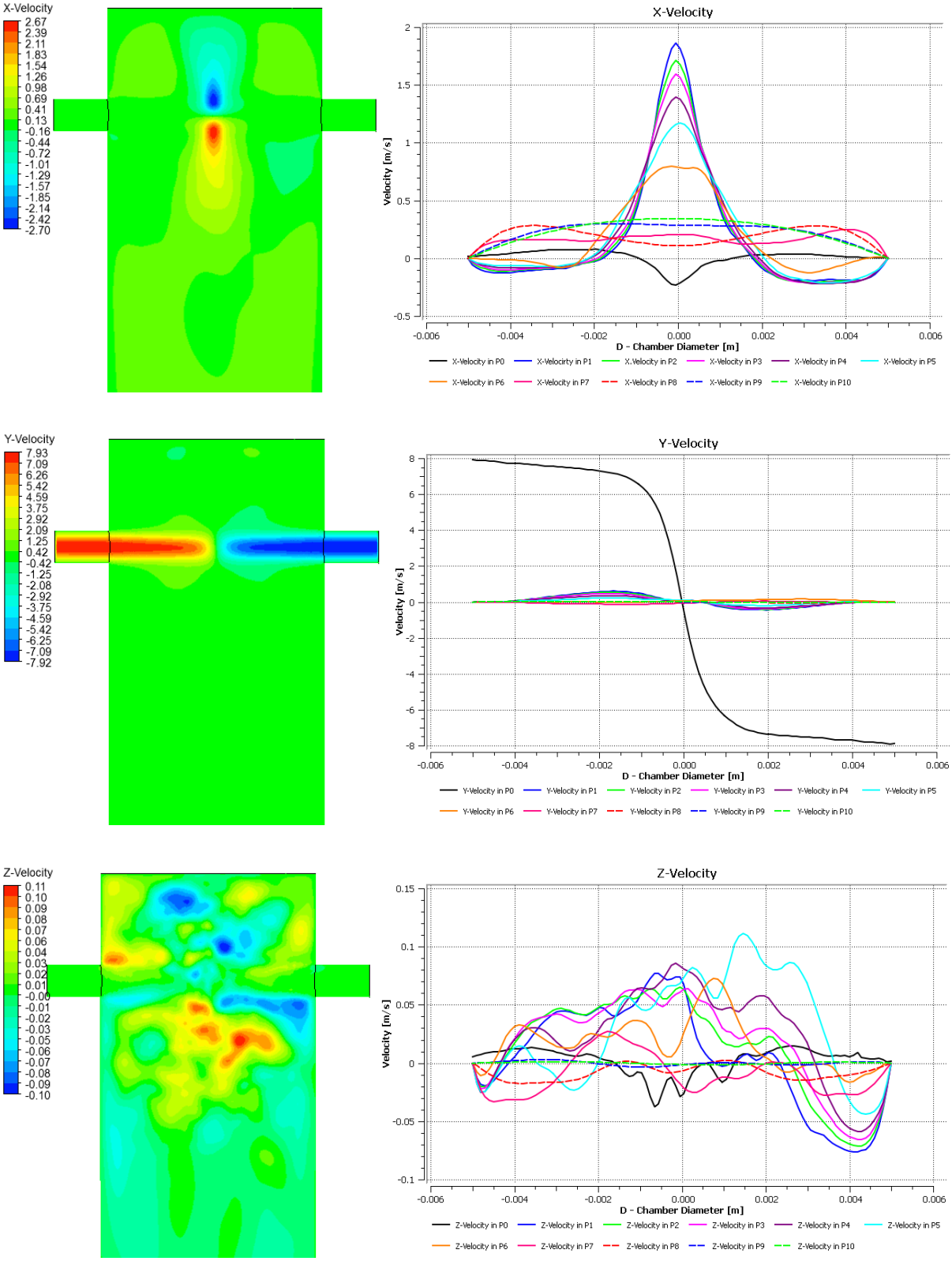

Figure 3.42 - Contour of the velocity components in the front plane (left). Velocity components along the probe points in a line aligned with the injectors axis (right). Reynolds 300

3.3.3.3 Rate of creation and dissipation of turbulent kinetic energy

The rate of creation and dissipation or turbulence was calculated based on the following scheme:

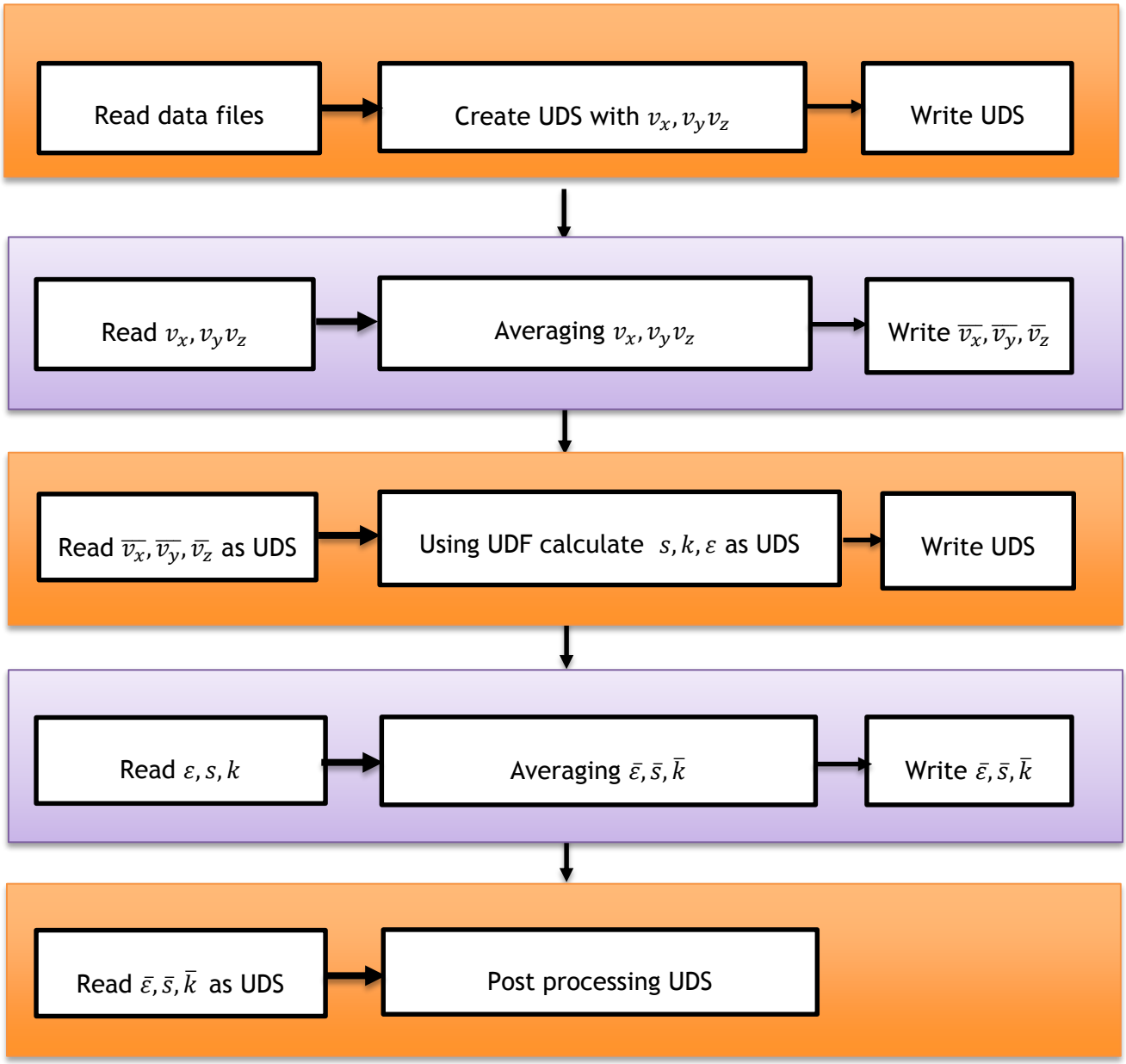

Figure 3.43 - Algorithm to obtain fluid flow variables k and ε

Initially was read a specific number of data files, each one correspondent to a certain time step. The choice of the time step was used as quasy-spaced time step along 1τ to 3τ of data files, with a random choice of the time step according the mutation rate, in other words was chosen data files correspondent even distributions which after wards will be randomly

chosen data file in a certain range (more and less) the specific time step. This method help to prevent stroboscopic effects of the fluid in the results, particularly in the averaging, if it happens. Additionally after all the process being repeated help to analyse the stability of the method and the accuracy of the result.

The previous scheme is set with colours to represent each step used, being the orange colour associated with fluent process and grey as of the side created code in c to run in windows OS. First using fluent the selected time steps are read and the velocities are exported using a UDS (used-defined scalar). After a set number of time steps are read the UDS's are written in a text file. A code is created in c language to read the text file, containing all the time steps for each variable and calculate the averaging of each cell in the domain. The averaged values are then written into a text file to be used in the third phase. A UDF (user-defined function) is created to calculate the rate of creation of turbulent kinetic energy and the spatial derivatives which is necessary to calculate the rate of dissipation of turbulence. Using the same process all of this this variables are averaged. In the end all the variables are read and set as UDS and all the essential post-processing is perform.

Since exist close to three million cells in the domain and each one individual cell and their correspondent variable are save in the hard drive, an increasing of the time steps used in the calculation will greatly affect the available space needed for the calculations. Since this physical constrain then was necessary to proceed to a study of the strict necessary number of time steps used in the calculations. Because of this restriction was perform a test to evaluate the essential number of time steps

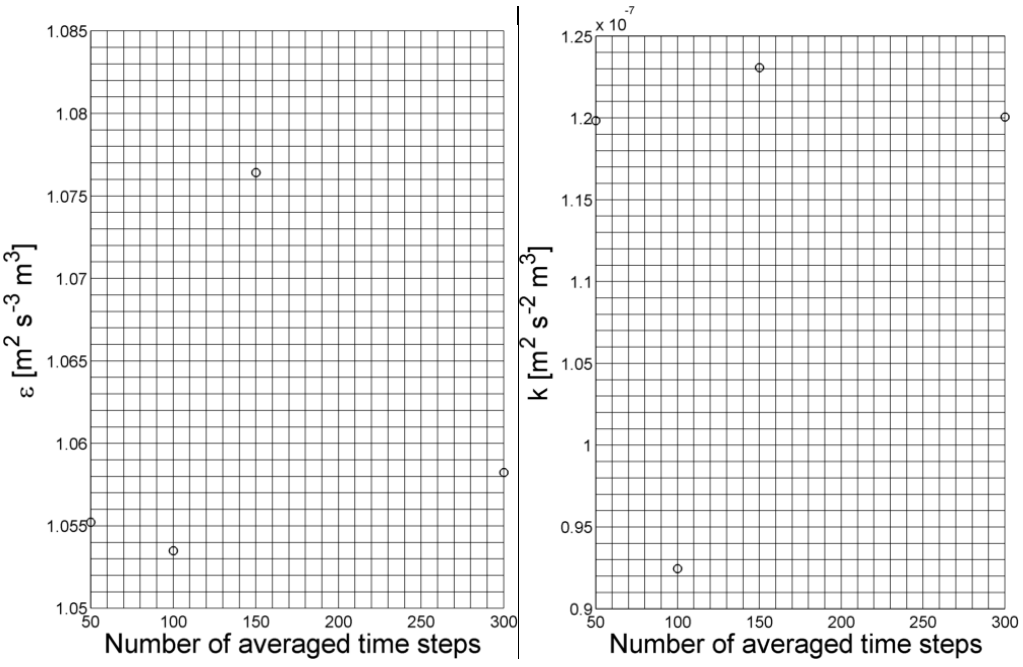

Figure 3.44 -Convergence due averaging time steps for k and ε

In Figure 3.44 is presented the convergence history for ε, k. Both of them were calculated based the volume integral of this scalar in the whole domain. Those convergence histories is presented for one set of averaging, spite the fact that more than one averaging was perform and the results seem to agree with the current presentation. Due lack of space it was impossible run for more than 300 averaged results. It is observed for an averaged time steps of 100 and 150 the values seem to have a big difference from averaged values. Although this is true the relative difference of the error is not so high. For a trustful results was chosen that an average of 300 time steps guaranties in both high number of time steps to averaged, low relative error from the previous averages and with reasonable space to perform the calculations.

Recall the physical meaning of the creation and dissipation of turbulence. k, creaction of turbulent kinetic energy is the variable which count the fluctuation of velocity of the flow field, meaning an local increase of those fluctuations will then concentrate the production of turbulence in that area. In opposite ε stands for the dissipation of turbulence, which is calculated by the partial derivatives of the flow field, meaning high local derivatives will then create a local area where occur turbulent dissipation.

The results shows contours of both variables and also a plot of those variables in lines parallel with the injector axis along the chamber crossing the points chosen to record the velocity each time step. The importance of this work lies in identification of the zones exhibiting local production and dissipation of turbulence which physically represent the creation of vortices and their transformation into small vortices by turbulent cascade, which are the main phenomena of advection mixing in turbulent flows. This technique is widely used in full turbulent flow systems although for the first time will be applied into a laminar chaotic internal flow.

In some publish works some authors prefer to use turbulence modelling for modelling a laminar chaotic system (Icardi et al., 2011). Those modelling are by using RANS, LES to model the flow field. RANS consider a time space averaging without scales resolving, as opposite LES uses a sub-grid to compute scales up to a certain level, and therefore only compute larger and medium scales. It is true both techniques perform better than DNS, when only computational cost is considered, although they are not considered the quality of the results. All the results presented with this techniques only show the effect of the larges scales modelling of the problem to identify factors such as impingement point position and local velocities. But when medium and lower scales are modelled the author don't agree with the using of such tools. In part it is know that turbulence model are statistically created for

modelling full homogenous and isotropic turbulence and therefore the equations are only valid for those cases, and not valid accurate for laminar flows, because their add terms in the N-S equation which will going to affect the full dynamics of the problem. A simple example is consider RANS modelling for this problem. In a full turbulent motion, where the flow is only driven by inertia rather than viscous forces, a introduction of an simple fictitious viscosity to converge the problem will not affect full turbulent flows because the contribution of the viscous effect is almost null, but for a laminar flow this is not true since the flow is only driven by viscous forces, and therefore can cause a completely different behaviour than the experimental visualization of the flow motion.

For this reason the author perform a DNS. First to identify the hydrodynamic scales which contributes to the problem, the second to not change the dynamic modelling of the flow. If the flow is laminar and incompressible then the mathematical equation to model those flows are the N-S with simplification for incompressible flows. In computational terms modelling low Reynolds number is nowadays possible without a need for the fastest and more advance HPC.

Techniques to study turbulent flows are then use to assess the flow hydrodynamic behaviour, since in practical terms chaotic tools don't provide valuable information of the flow field only for academic proposes as for example to calculate the fractal characteristic of the flow (Baldyga & Bourne, 1995).

A. Reynolds 150

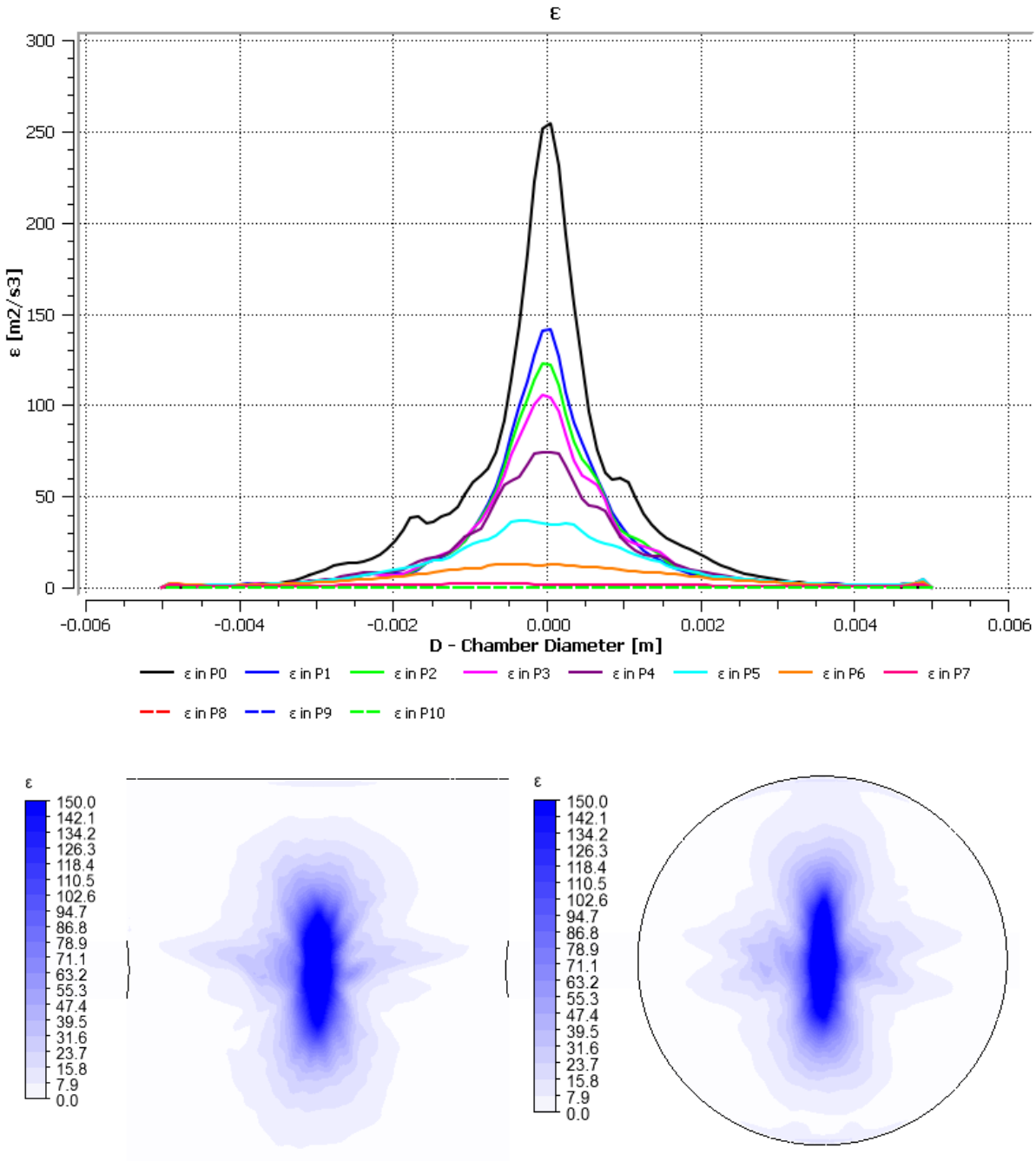

Figure 3.45 - Variation of ε along the chamber for lines parallel with the injector axis and passing in the probe point (top), Contour of ε for the top part of the chamber (bottom). Reynolds 150

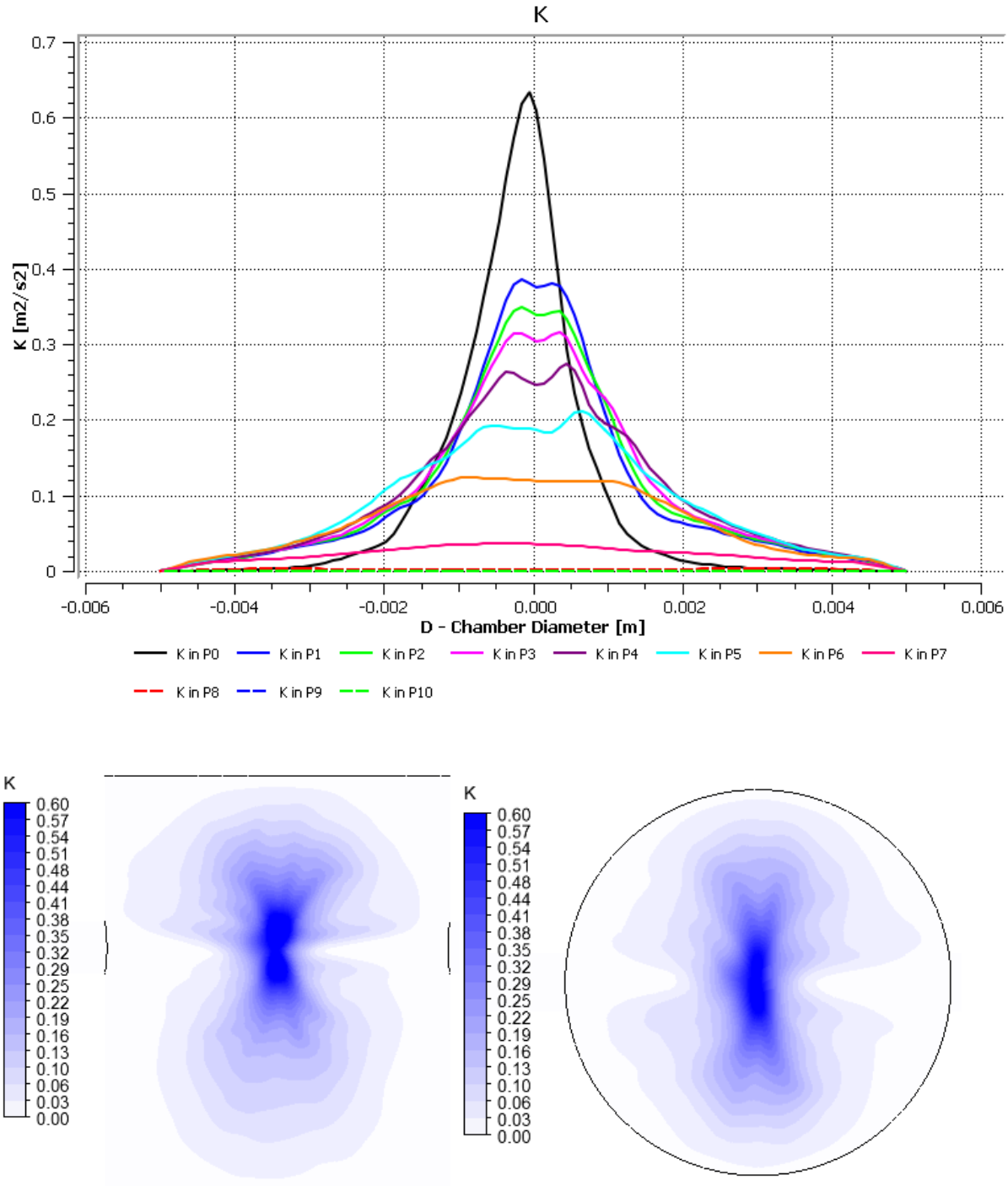

Figure 3.46 - Variation of k along the chamber for lines parallel with the injector axis and passing in the probe point (top), Contour of k for the top part of the chamber (bottom). Reynolds 150

B. Reynolds 200

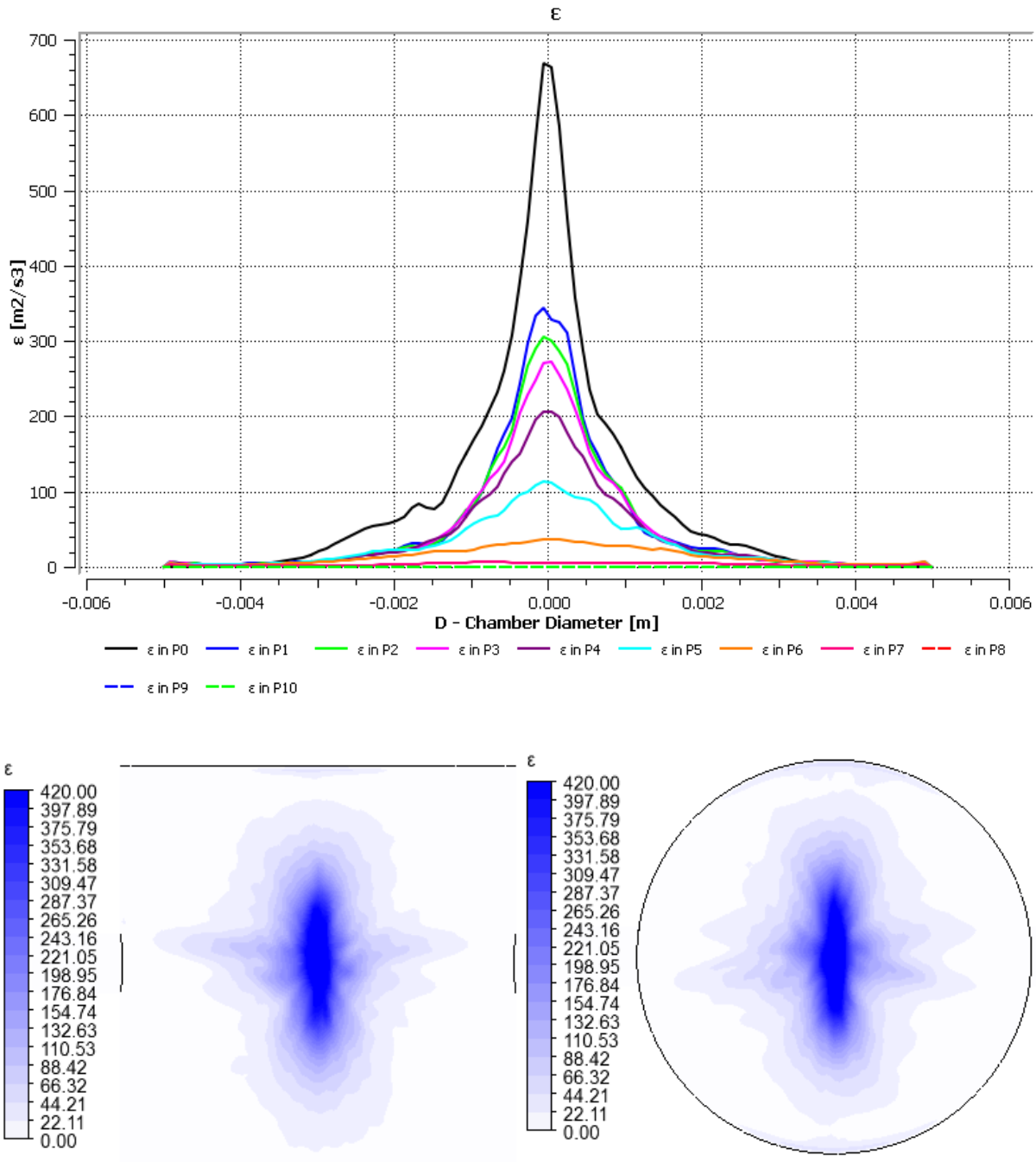

Figure 3.47 - Variation of ε along the chamber for lines parallel with the injector axis and passing in the probe point (top), Contour of ε for the top part of the chamber (bottom). Reynolds 200

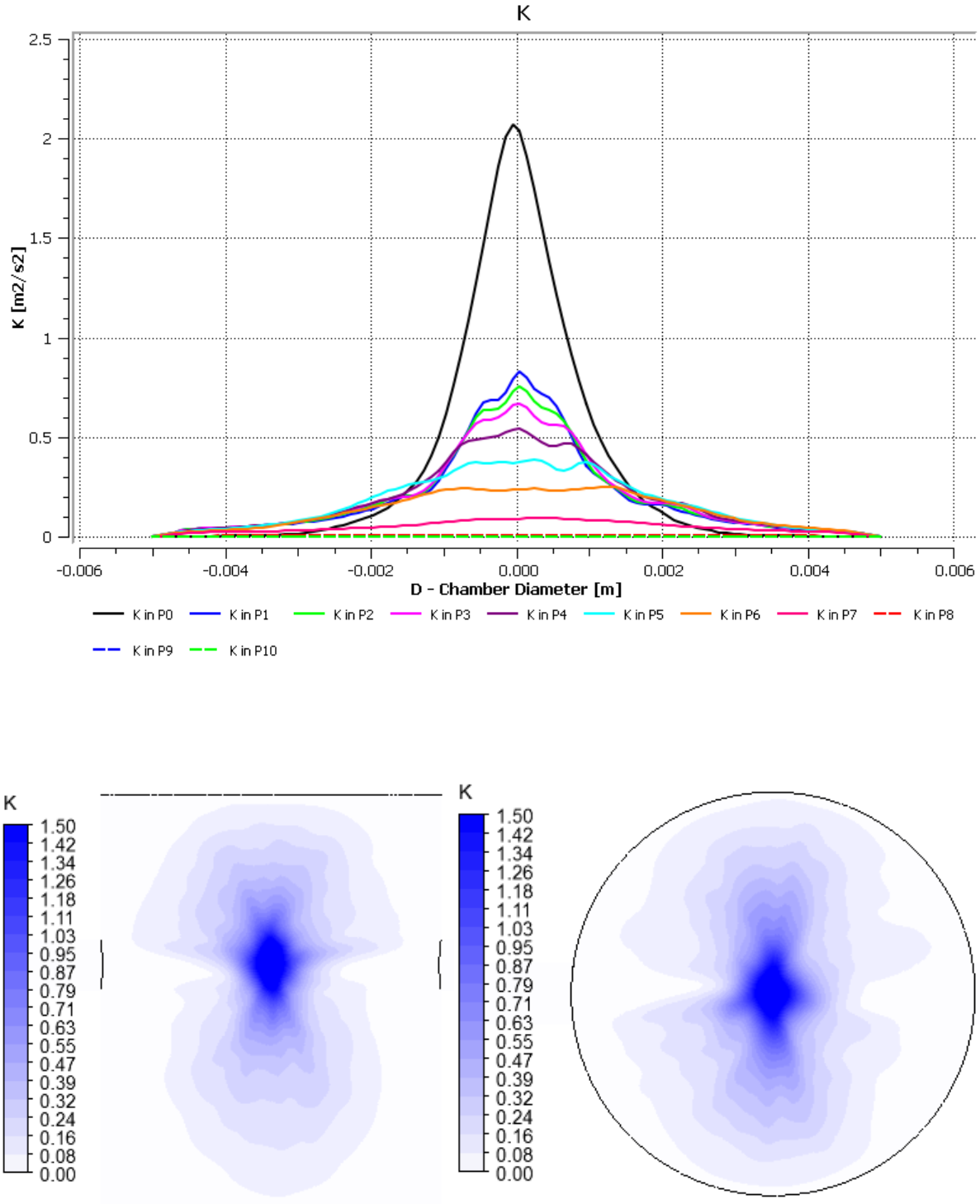

Figure 3.48 - Variation of k along the chamber for lines parallel with the injector axis and passing in the probe point (top), Contour of k for the top part of the chamber (bottom). Reynolds 200

C. Reynolds 250

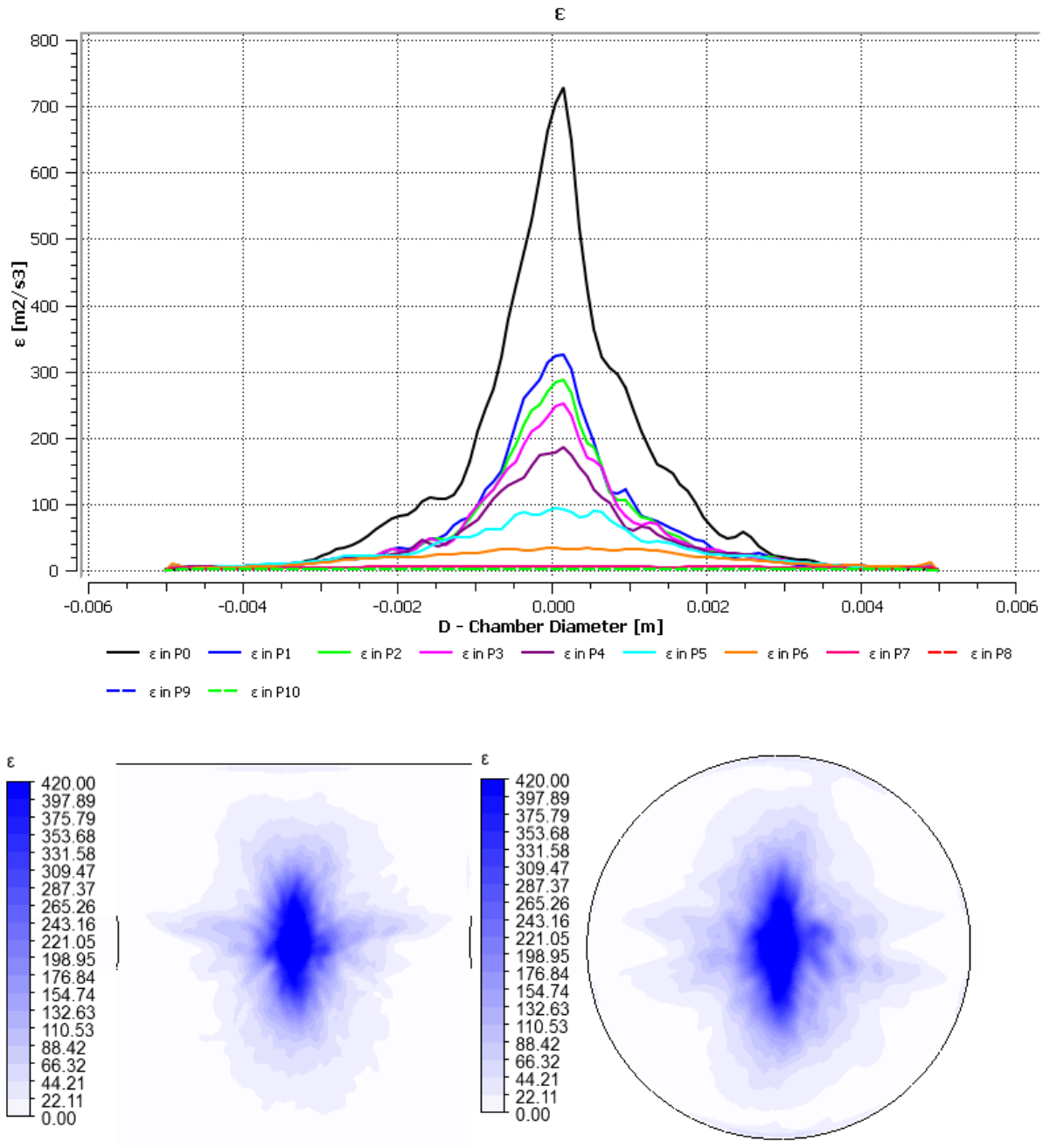

Figure 3.49 - Variation of ε along the chamber for lines parallel with the injector axis and passing in the probe point (top), Contour of ε for the top part of the chamber (bottom). Reynolds 250

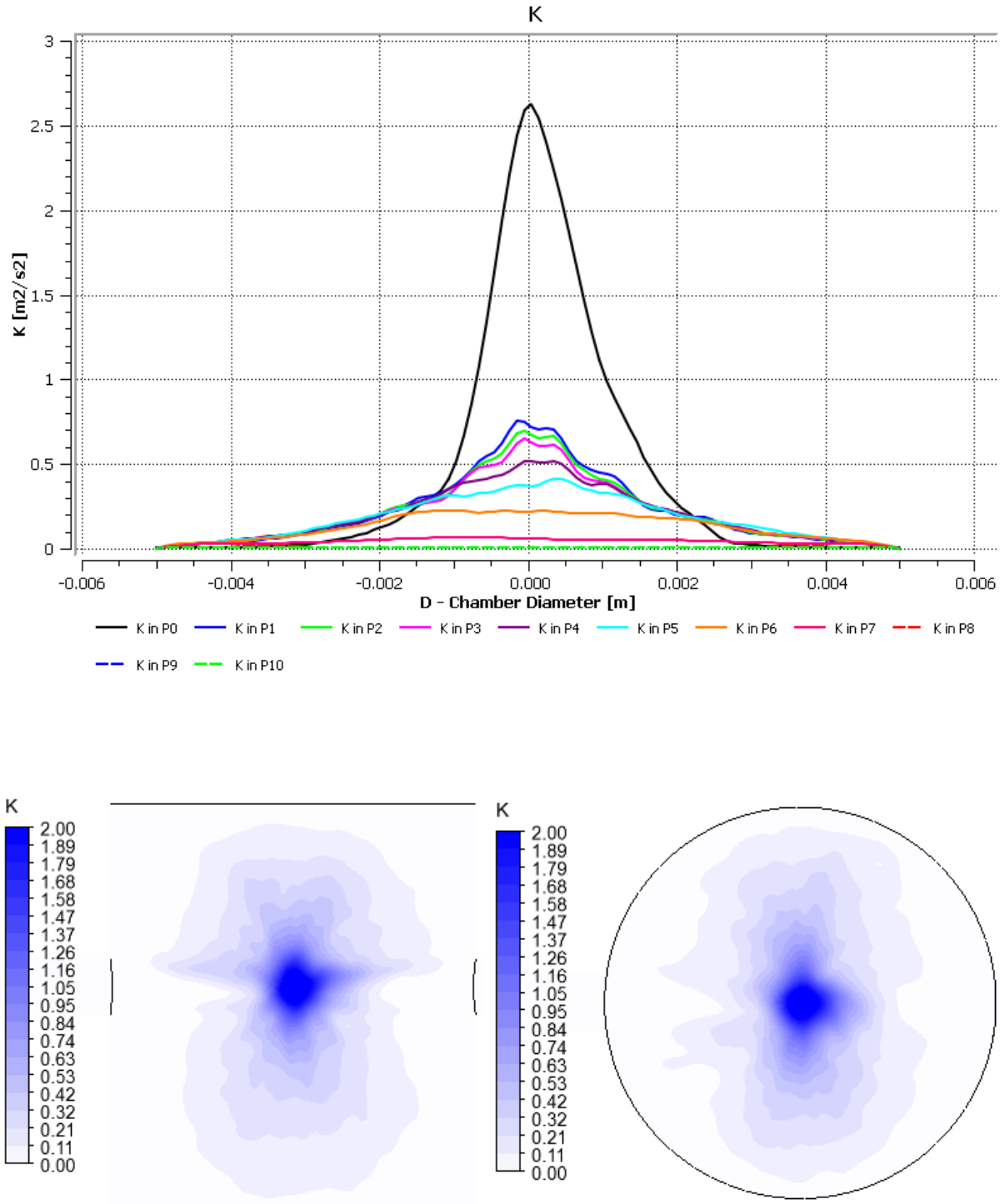

Figure 3.50 - Variation of k along the chamber for lines parallel with the injector axis and passing in the probe point (top), Contour of k for the top part of the chamber (bottom). Reynolds 250

D. Reynolds 300

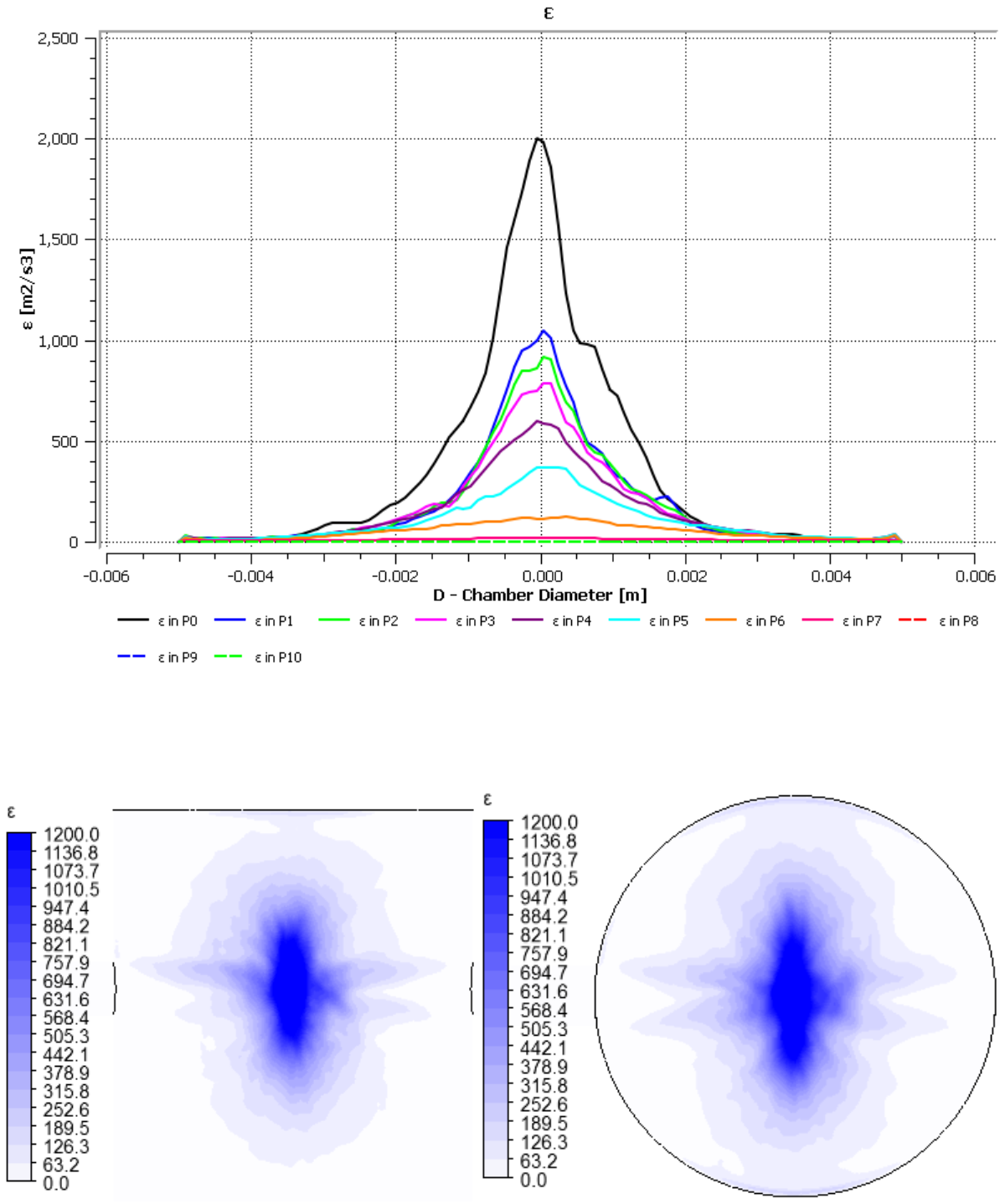

Figure 3.51 - Variation of ε along the chamber for lines parallel with the injector axis and passing in the probe point (top), Contour of ε for the top part of the chamber (bottom). Reynolds 300

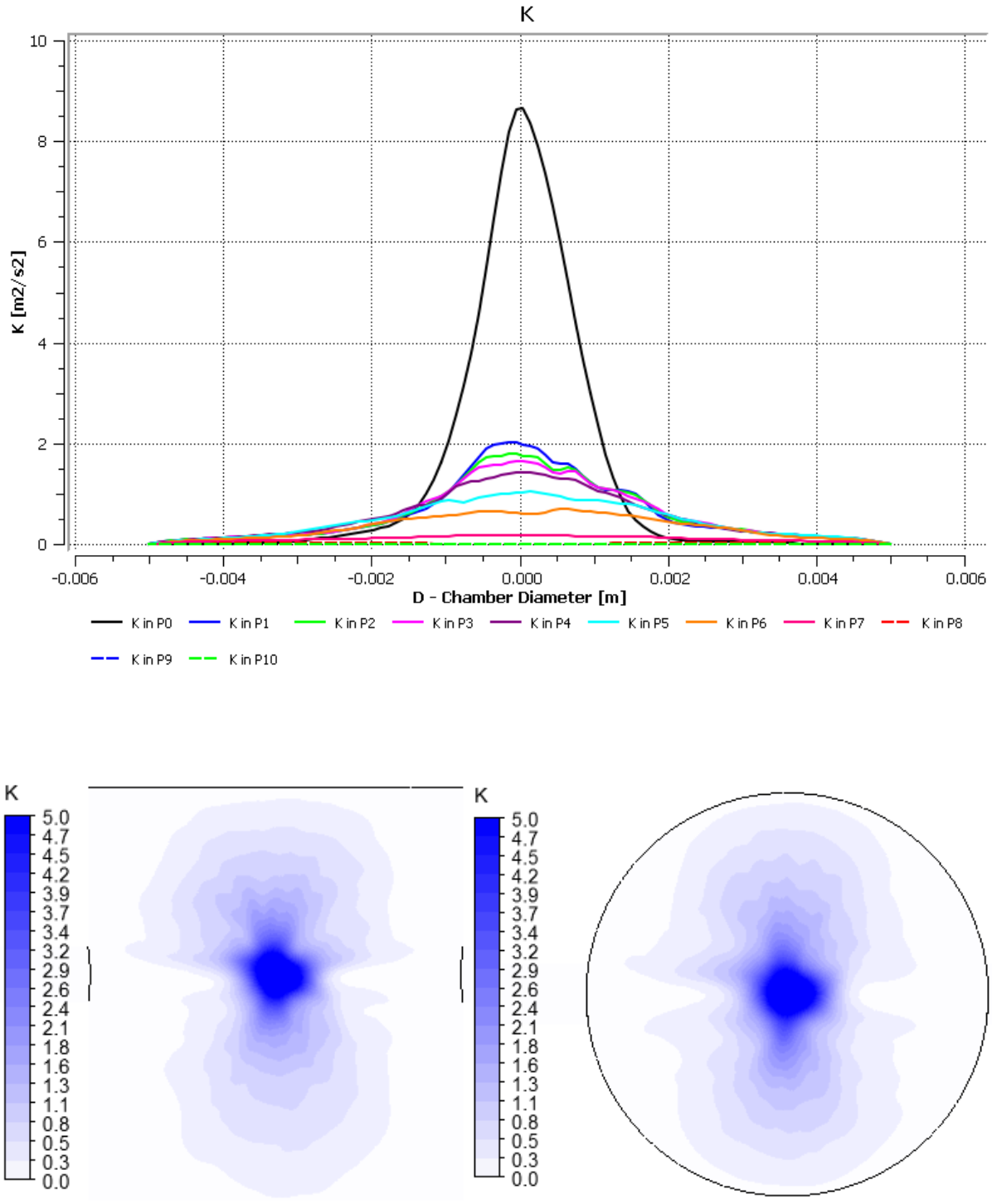

Figure 3.52 - Variation of k along the chamber for lines parallel with the injector axis and passing in the probe point (top), Contour of k for the top part of the chamber (bottom). Reynolds 300

For all the Reynolds number in study it is clear the results tends to be symmetric regarding the centre of the chamber. Non perfect symmetry is only due lack of more averaging time steps. Spite this fact it is only present the important variables for a averaging of 300 time steps, others averaging such as 50, 100 and 150 was visualized, and qualitatively have the same shape although with slightly different values. In the present work don't focus in the value itself but in the shape of interesting variables.

According the creation of turbulent energy it is clear that a cone without turbulent emerges. This is due the jet´s don't carry turbulent energy and its high kinetic energy don't allowed any creation in this region. Is the perimeter of the jets with low velocity which in contact with the flow create this conical structure. All the turbulent energy is created in the impingement point and the dissipated trough the pathline of the flow due the oscillatory mechanics of the impingement surface (translation of the impingement point and rotation of the surface).

From the contour of this variable it is clear the main creation of turbulent energy in the front plane fulfil in height approximately six times the injector diameter and in width 4 times the injector diameter. In the top plane similar relation emerge, begin the height almost fulfil the entire chamber diameter and the width have the same relation, 4 times the injector diameter. This relations are in the same range for all the Reynolds in study.

It is observed for Reynolds 150 the production of turbulent energy have a large planar structure for production of such energy. An increasing of the Reynolds number will then tend to reduce the size of such structure into a format of a boll. It is observable than for high Reynolds number this high energy region will tend to locate the production into a single point, where opposite for low Reynolds number, the pancake form will help to distribute the region where this energy is created almost fulfil the top of the entire chamber.

The dissipation of turbulent energy create some structures which go from the high intensity dissipation into the camber walls by following the path of the low velocity of jet's, particularly in the top of the jets. Recalling the mathematical expression of this variable, it is directly correlated by the high velocity gradient. Therefore is normal to have high dissipation where each component of the velocity fast changes, which is normal close the jet's and in the impingement point.

Regarding about the location where the energy is dissipated it is clear almost the same relationship between height and width for the top and front surface. Even that it is observable more complexes patterns than k.

A careful attention should be made when is comparing the contour for k and ε. For Reynolds 150 the contour of ε is cropped to the half oh the maximum value while for k the contour almost present all the values. For Reynolds 200 booth contours are cropped for almost 2/3 of the maximum value for each variable. For the other Reynolds the contour of ε is almost cropped to ½ of the maximum value while k is only 1/3. To better analyse this effect a comparison between k, ε is presented by comparing the difference between the maximum value for the point 0 with the maximum value of the point 5, which closely correspond the end of the impingement surface for the average Reynolds in study.

Defining

$$\Delta\varepsilon = \varepsilon_{p_0} - \varepsilon_{p_5} \tag{3.34}$$

Similar for k

$$\Delta k = k_{p_0} - k_{p_5} \tag{3.35}$$

And

$$\Delta p/p_0 = \Delta\varepsilon/\varepsilon_{p_0} \tag{3.36}$$

$$\Delta p/p_0 = \Delta k/k_{p_0} \tag{3.37}$$

Based on the previous definitions is possible to identify the behaviour of those variables ε, k by representing into a plot which is in Figure 3.53.

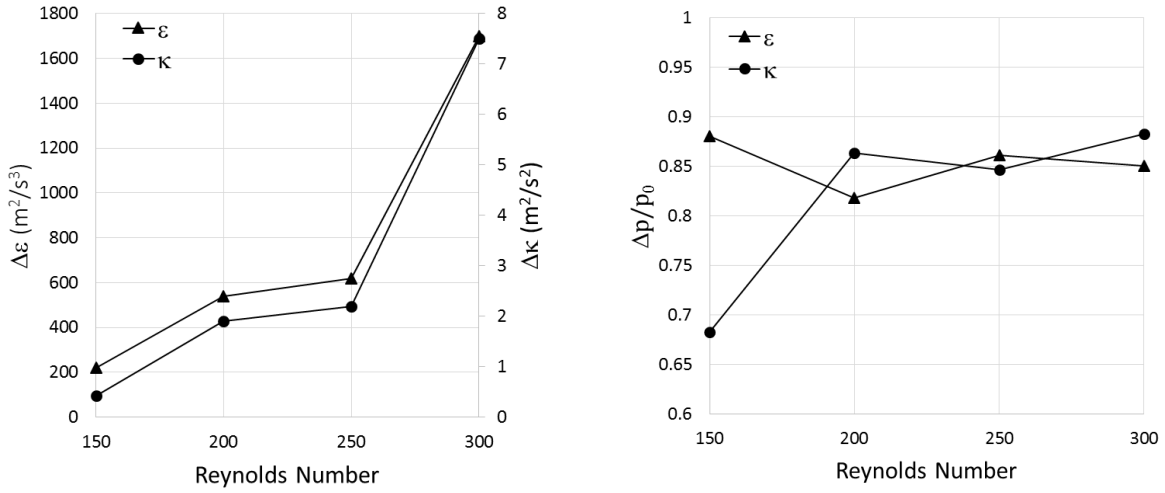

Figure 3.53 - Variation of k and ε along the numerical experiments. Observation energy containing inside the impingement structure (left). Normalization of this energy with energy containing in the central area (right)

According to Figure 3.53 it is possible to observe a constant growing by an increase of the Reynolds number. What is surprising and was observed in k obtaining from the points is a almost stagnation of the flow behaviour from 200 to 250 in both k and ε. It is unknown what mechanism produce such stabilization of the flow behaviour but this means in terms of both variables an increasing of the Reynolds number don't produce such advantage in the increasing of the hydrodynamic mixing in the range 200 to 250. An increasing is observable in the range 150 to 200 and from 250 to 300, being this range where the main growing is visualized with more than 250% of increasing of the value for each variable in study.

About the Figure 3.53 if it obtain the average between k and ε for the increasing Reynolds number is observable a small increase of both relationship variables when the Reynolds number is increased. After Reynolds 200 is observed a fluctuation of this relationship for both k and ε with a small difference between each one. For Reynolds 150 the difference is much higher, where the area for the dissipation overhauls the area of the production of turbulent energy

Knowing the length scale relationship for isotropic and homogenous turbulence is defined as

$$l \sim \frac{k^{\frac{2}{3}}}{\varepsilon} \tag{3.38}$$

Then for an increasing in Reynolds is observable a decreasing of the length scale for the range 200 to 300, while in observable an increasing of the length scale from 150 to 200. This effect indicate than Reynolds 250 makes the transition from an incremental length scale to a reduction of length scale which allied with a fast growing rate of those variable have as consequence the reduction of the eddies sizes and the amount of eddies created which facilitate the transfer of energy by energy cascade and the mixing overall performance.

3.3.4 Spectral analysis

Time series provided by the sampling points usually don't provide direct information about the flow behaviour, then is necessary to use other tools to quantify the flow. As previous turbulent methods was used to quantify the flow field using spectral analysis methods to transform the data points into the energy-containing-frequency domain. In Appendix C is presented all the power spectra for all the points and velocity components for each Reynolds in study.

Small conclusions was presented in Appendix B was the influence of the Reynolds number in the flow regime, the non-random velocity oscillation, an increase of the frequency of such oscillations with the increasing of the Reynolds number and the vanishing of such velocities and oscillation when the flow go downstream the mixing chamber.

The transformation from time into frequency domain was done using the Discrete Fourier transform DFT, defined as

$$G = \left(\phi = \frac{k}{N\Delta t}\right) = \sum_{i=1}^{N-1} v_y(i\Delta t) e^{-j\,2\,\pi\,ik/N},\ k = 0,1,2,..,n-1 \tag{3.39}$$

Where $v_y(i\Delta t)$ correspond to the velocity time series, Δt is the time interval, ϕ is the frequency, N is the total number of points existent in the time series and $e^{-j\,2\,\pi\,ik/N}$ is the complex number where j is the imaginary part. Fast Fourrier Transformers, FFT, substitutes DFT, in terms of implementation since improve the computational effort to produce such calculations.

FFT provides the complex number series, which to translate into power spectrum is necessary to calculate the modulus $|G(\phi)|$.The power spectra presented in this chapter and in the appendix (xxx) is normalized by the outlet velocity for each simulation performed. The outlet velocity is calculated based on the conservation off mass in the control volume

$$\dot{m}_{inj_1} + \dot{m}_{inj_1} = \dot{m}_{out} \tag{3.40}$$

Where inj represent in injector and the indices 1 and 2 represent the left and right injector. Since the is an incompressible fluid with the same characteristics in each boundary and each injector have the same velocity then the previous equation can be simplified into

$$2Q_{inj} = Q_{out} \tag{3.41}$$

$$\frac{2\pi d^2}{4} \cdot v_{inj} = \frac{\pi D^2}{4} \cdot v_{out} \tag{3.42}$$

$$\frac{d^2}{D^2} \cdot v_{inj} = v_{out} \tag{3.43}$$

Yielding the normalization of the frequency series to obtaining the power spectrum $G'(\phi)$ is performed by

$$G'(\phi) = \frac{|G(\phi)|}{v_{out}} \tag{3.44}$$

3.3.4.1 Power spectra

Using MATLAB an automated code was created to read the data sampling and compute FFT and in the end plotting the respective data. From this results will be investigated the results provided by the point 0 and point 1, correspondent to the point align with the injector axis and the first point after this following downstream the chamber. Although all the results is presented in the Appendix C, only go to be presented this two points for they-velocity component just to latter being possible to compared with experimental data.

By turbulent theory it is know the power spectra have three range of scales:

- Energy containing scales: is where most of the energy is containing into large length scales associated to large eddies
- Inertial range: is where the energy is transfer. In this range two main slopes can emerge if the case of an injection of energy is observed. -5/3 slope is where an inversion of the energy cascade, where smaller scales feed up the larger scales. -3 slope represent the direct entrosphy cascade where the direction of the scales is positive, meaning the larger scales are dissipated into smaller ones and the process continue until the dissipation range. Is the injection where the shift between these two slopes emerge
- Dissipation range is where the scales reach the “final destination” and are transform into heat

This knowledge found the ground base to access the problem in hand, where will be discussed

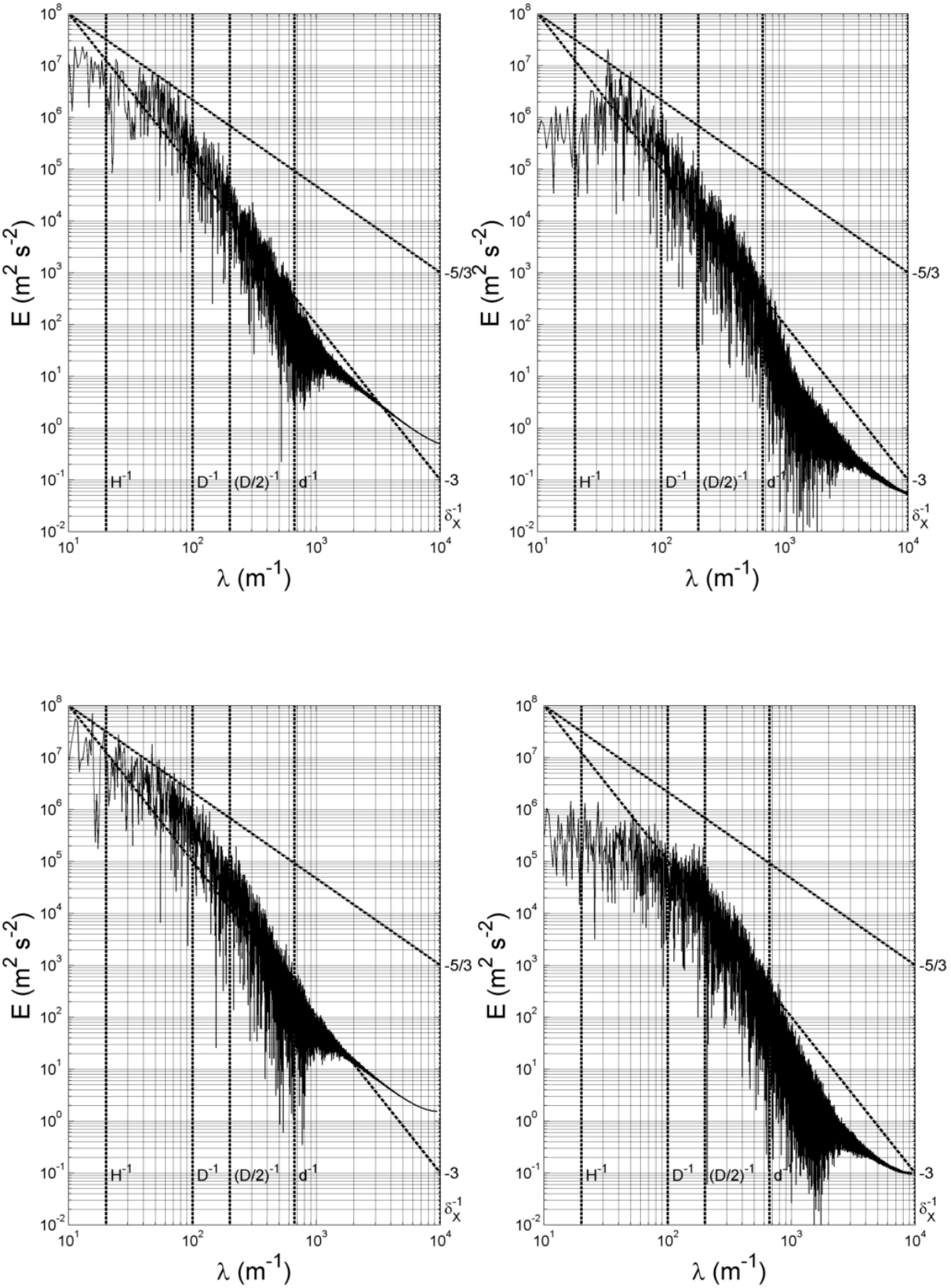

Figure 3.54- Power spectra form all the Reynolds number performed [150, 200, 250, 300] for the probe p_0

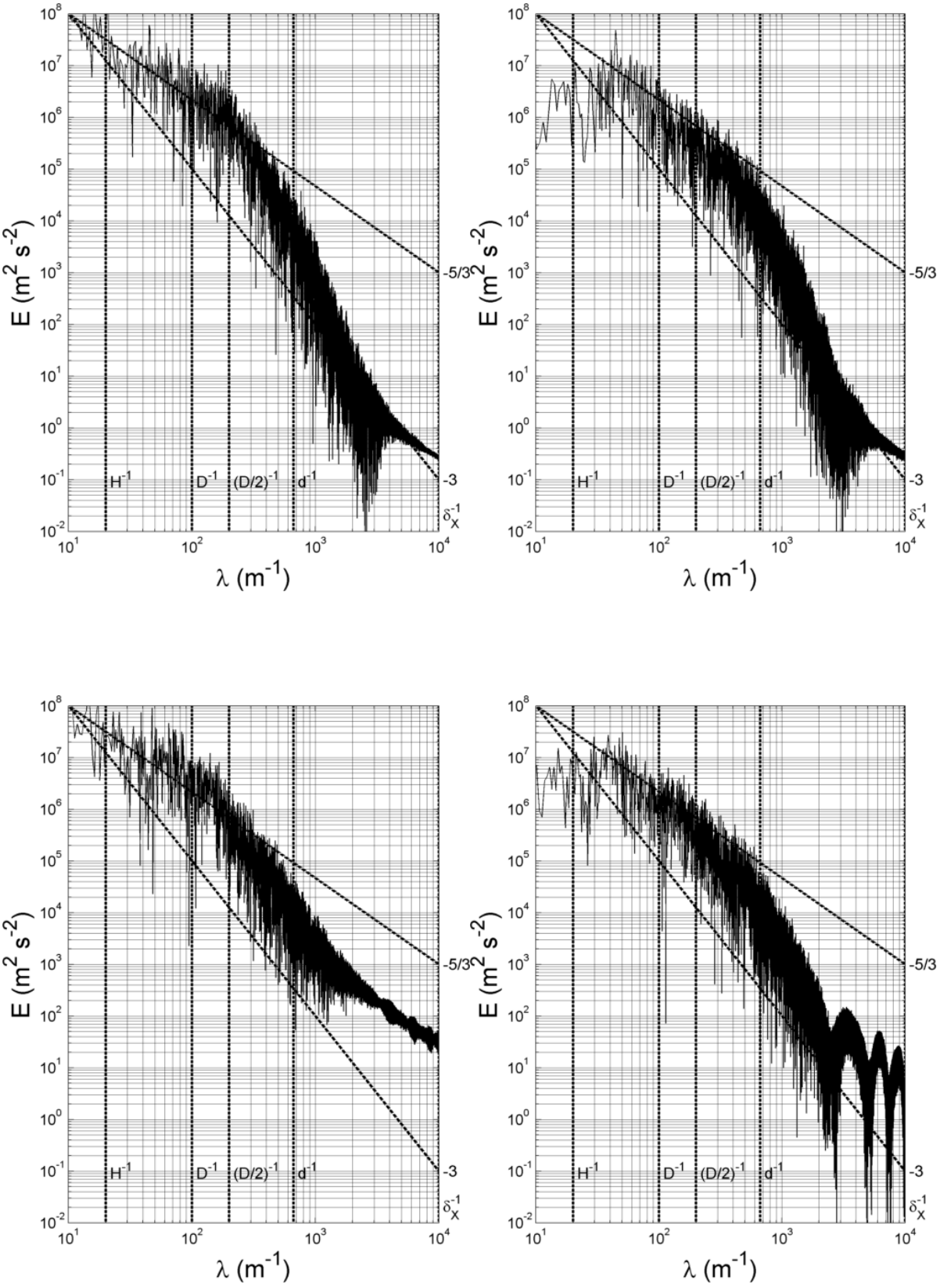

Figure 3.55- Power spectra form all the Reynolds number performed [150, 200, 250, 300] for the probe p_1

This comments will about the power spectrum for each Reynolds and in both point. The energy is injected at the scale of half the chamber diameter, with width D/2, which afterwards grows until between D and H in a inertial sub range. The energy is transfer from the large scales until the large scales by an inverse energy cascade with slope -5/3.

The inflation point which marks the injection of energy separates an inertial sub-range in an inverse energy cascade to a dissipation sub-range in an direct entrosphy cascade which follow the direct direction, meaning the large scales feed up the smaller scales. This inversion is located in eddies of the size of half the camber diameter D/2. The transformation of energy from larger eddies into smaller eddies ends in the dimension as the injector diameter, d, where starts the dissipation range. After this point all the energy is converted into heat.

Geometrical this mean the larger energy scale is not contained in the chamber diameter but in a dimension bigger than this. Meaning that the biggest scale is located aligned with the chamber axis which are feed up for scales no smaller than half the chamber diameter. Interpreting the amount of data in this range translate in a conclusion very small amount of eddies are created. A reduction of small eddies in point close to the origin of the chamber and comparing with the creation and dissipation rate of turbulent energy, means a large amount of small eddies, larger than the injector diameter are created and immediately dissipated in this small region meaning a lot of energy dissipated in this small region. So the “game changer” in new technologies for RIM cannot be in increase locally the creation and dissipation but create new alternatives to create large eddies which can travel the entire length of the chamber improving mixing efficiency

The concept of allying the dimensional characteristic of chamber with the turbulent characteristics of a laminar chaotic flow is new concept and when relate this with the mixing performance proves there is a relationship between both sides.

By observing the Appendix C is observable in the point containing the oscilatory motion of the impiging surface the maximum energy is located in the same length size. After this set of points and progressing downstream the mixing chamber it is observable the energy containig scales tend to containg eddies with increasing length size when more downstrem is in the chamber. All the others velocity components, x-velocity and z-velocity, have the same caracteristic behaviour of increasing length. Is is important to refer the moust energy connatining scales is in the x and y direction of the mixing chamber. Such conclusion was corraborated previousllu when the flow behavior was analized.

3.4 Mixing dynamic's using VOF

Previous works in study the mixing dynamic failed into study a complete domain 3D due tremendous computational cost required. Then for the first time was tried to simulate mass transfer without reach the lower mixing scale in the flow. The mixing will be analysing using flow visualization of the results.

3.4.1.1 Discrete domain

The domain for considerer was the same used in section 3.2.1, with exactly the same geometrical dimensions and the symmetry plane.

3.4.1.2 Grid size

It is know the lower hydrodynamic scale present in a flow is the Kolmogorov scale. Although in mixing the lower mixing scale know is the bachelor scale defined as

$$\lambda_N = \frac{\lambda_k}{\sqrt{Sc}} \tag{3.45}$$

Since this scale is extremely small and the computational effort to simulate the all the mixing scales is tremendous, then is necessary increase the order of magnitude of the length scale to comprehensible values. Therefore was chosen to use an grid size element a bit lower than the Kolmogorov scale, for Reynolds number 150, thus was chosen as grid size the same as in section 3.2.2.1 in order to reduce the time spend in preparation the computational domain and the meshing.

3.4.1.3 Governing equations

The incompressible flow used in this simulation has the same physical characteristics as the used in the experiments in chapter 4. The mathematical model used in this simulation to govern the hydrodynamic behaviour was the Navier-stokes equation presented in section 3.2.3. Additionally, the mass transfer equation is necessary to model the volume of fluid method.

$$\rho(\partial_t \mathbf{u} + \mathbf{u} \cdot \nabla \mathbf{u}) = -\nabla p + \mu \nabla^2 \mathbf{u} \tag{3.46}$$

Where $\mathbf{u}$ is the 3D flow field, t is the flow time and p the pressure. The VOF model allows the tracking of the interface between two immiscible fluids (phases) only allowing advective effects on the mixing. Mathematically the model is developed for only calculating the

concentration of one phase, as a scalar, defined as α_A, meaning is the concentration of a passive fluid A. In a control volumes it need to guaranty the conservation of phases in the following way

$$\alpha_B + \alpha_B = 1 \tag{3.47}$$

And considered

$$\alpha_B = (1 - \alpha_A) \tag{3.48}$$

Resulting in

$$\alpha_A + (1 - \alpha_A) = 1 \tag{3.49}$$

Which can be rewriting to be implemented in the mass conservation equation

$$\partial_t \alpha_A + \mathbf{u}\nabla\alpha_A \tag{3.50}$$

In a control volume the sum of concentration of phases should be equal to one. In the case of in one control volume $\alpha_A = 1$ mean that control volume is filled with only one hase and this phase is A, and opposite if the concentration of $\alpha_A = 0$ means the control volume is filled with phase B. Then the concentration of each phase is in the range $0 < \alpha_{A,B} < 1$.

Additionally was not considered any surface tension between the two fluid stream, meaning there is no additional terms to be added in the mass conservation equation

3.4.2 Boundary conditions and initial conditions

3.4.2.1 Injectors

In each injector a parabolic velocity profile, as presented in section 3.2.4.1 was implemented with the velocity correspondent to Reynolds 150. Additionally was considered in each injector is enter different phase, as expressed:

$$\begin{cases} \alpha_A = 0, & \text{at right inlet} \\ \alpha_A = 1, & \text{at left inlet} \end{cases} \tag{3.51}$$

3.4.2.2 Outlet

The outlet boundary condition is split in half and extended to avoiding problems if backflow occurs, this means, $\mathbf{u}.\mathbf{n} < 0$. The following boundary conditions was implemented in each half of the outlet

$$\begin{cases} \alpha_A = 0, & \text{at right side } [-\mathrm{D}/2, 0] \\ \alpha_A = 1, & \text{at left side } [0, \mathrm{D}/2] \end{cases} \tag{3.52}$$

3.4.2.3 Steady State

For fast convergence the flow was initialize by setting zero velocity and zero pressure in all the domain and in the right side of the domain the concentration of phase A was set as zero and in the other side of the chamber was set as one.

At a steady state the flow is allow to converge until all the equations reach a minimum of 10e-6 for all the residuals. Additionally the same technique of the symmetry plane was used to segregate the flow into two equal parts

3.4.2.4 Transient state

In the transient state and similar to the section 3.2.4.5, the oscillatory motion was initialized by a perturbation using a velocity-time function.

3.4.3 Discretization and numerical methods

3.4.3.1 Steady and Unsteady Numerical Methods

The flow is solved using a laminar solver, by calculating the NS equation and the mass transfer equation. A coupled pressure-velocity model was used. The gradients where calculated using last squares cell based. Presto discretization was used for the pressure and for the momentum the quick. The volume fraction discretization used was the first order implicit. For the time discretization was used the second order implicit scheme. The advantages of using this methods was described in 3.2.5.1. The mathematical implementation of this methods is described in Appendix A.

3.4.4 Computational performance

The simulation was perform using 3 nodes with the same HPC hardware described in 3.2.6. A study was perform to evaluate the best combination with computational time and hardware required reaching the conclusion the 3 nodes provided this best combination. An important note should be referred. The limiting factor was not in terms of processor but in the communication between the three nodes. The computational cost is described in Table 3.2.

Table 3.2 - Computational cost of the VOF methodology comparing with previous simulation for the same Reynolds number

Reynolds	Hours	CPU h
150	521	16675
VOF	1861	59555

Comparing with the same Reynolds number an increasing of almost 4 times the computational time /CPU required to do a mass transfer simulation.

3.4.5 Results

The results provided by the numerical simulation is divided in two types. The first type if the hydrodynamic behaviour which seem to agree in both numerical velocity sample and vorticity maps. This proves the hydrodynamic behaviour don't rely on the mass transfer but rather in the continuity equation from the N-S. The flow visualization, based on the mass transfer mechanism from the VOF method will be presented following.

3.4.5.1 Flow visualization

Front view and top view of the concentration of phase A is presented. Dark red and dark blue represent the zones where the concentration of phase A is 1 and 0, respectively. Intermediary colours represent zones where the concentration of phase a is different than zero and one.

From the presented contours of the concentration of phase A an fast mixture is possible to see immediately the breaking of the larger vortice which indicate a presence of good mixing mechanism. Unfortunately it is not possible to verify the reduction from the larger scales to the medium scales since the mesh resolution is extremely big, but otherwise will be impracticable using lower edge size required ti model all the mixing scales

As it is possible to see there is diffusivity mixing and only the advective term is consider, since in the impingement surface a very thin gradient is observed. Unfortunately the numerical diffusion is extremely high. The numerical diffusion of phases is not due the low order discretization used, first order upwind, but from the larger computational control volume. In the result of such high value it is not possible to visualize the reduction of hydrodynamics scales, or either, the complete mixing mechanics existent in the mixture of this two phases.

Although for $t/\tau = 3$ it is clear the oscillatory motion of the impingement surface create zones where the concentration of phase 1 is maximum and others where the concentration is minimum. Since the flow frequency of the jets this pattern can create zones with

unreacted reagent in the mould and therefore the study of the mixing mechanism is such a valuable tool. Hydrodynamic speaking this high eddy will be subjected to stretching bending and folding when go downstream of the mixing chamber. The mixing consequence is a reduction of the filament of phase A, as it can be seen in Fonte (2012).

As proposed by Fonte (2012) the usage of an adaptive mesh based on the phase gradients will allowed to model all the mixing scales without a full refinement of the mixing chamber but only located in the interface between the two phases. This method was tested for the present simulation, but much before the refinement of the domain stagnated in a certain value of cells the simulation become extremely heavy to hardware to support and then was need to be cancel.

For the next chapter, when a computational optimization algorithm is created it is required to know a priory the size of the impingement surface in order to track the impingement surface. Then from the present contours it take the conclusion the best choice will be a dimension equal to the injector's diameter and aligned with the injector's axis to compensate the bending of the jets.

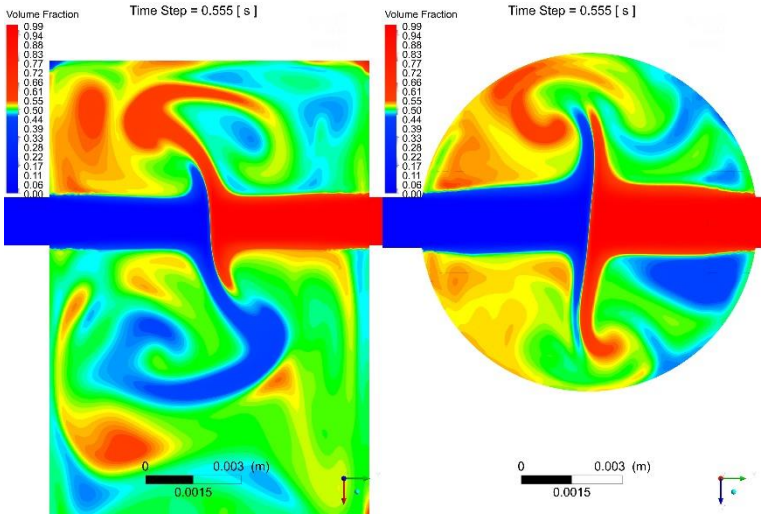

Figure 3.56 - Phase maps for Reynolds 150 at time $t/\tau = 1$

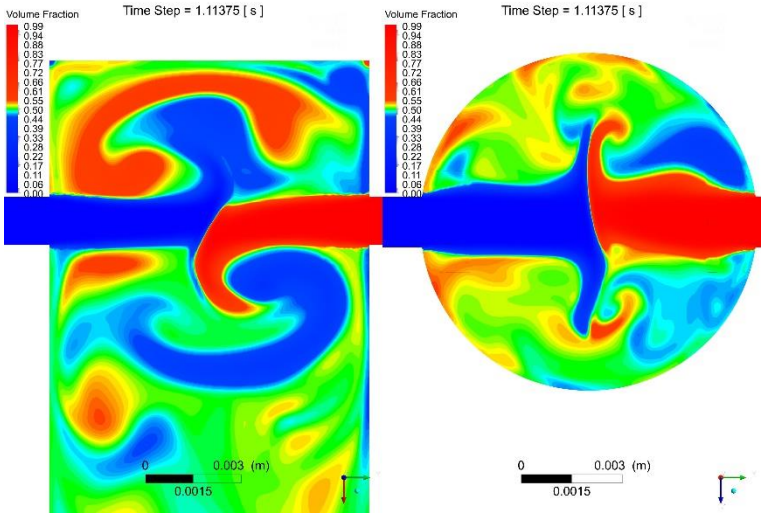

Figure 3.57 - Phase maps for Reynolds 150 at time $t/\tau = 2$

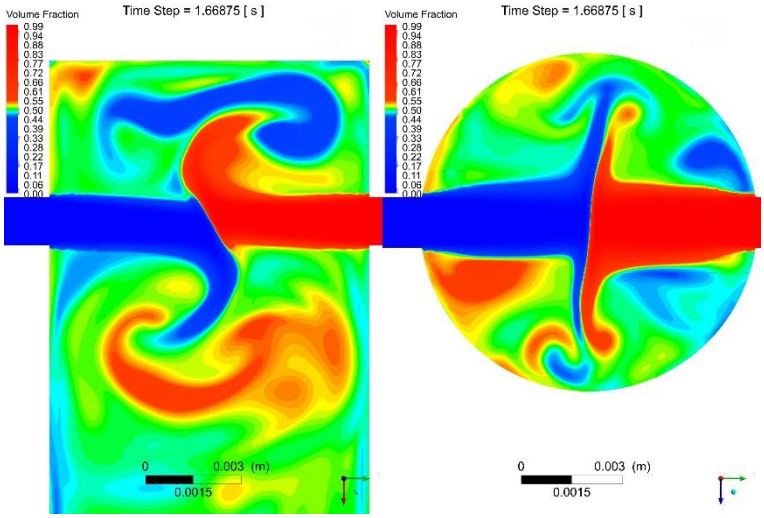

Figure 3.58 - Phase maps for Reynolds 150 at time $t/\tau = 3$

3.5 Conclusions

From the hydrodynamic behaviour is concluded the following

- DNS simulation was perform for Reynolds number 150, 200, 250, 300 since it is necessary to evaluate the hydrodynamic behaviour to create and develop new technologies to improve the mixing dynamics.
- The breaking of the oscillatory movement of the impingement surface due jets bending or high angles, cause complex behaviour in the impingement region with biggest changes in the flow field, particularly in the vorticity.
- The impingement point and a impingement surface have a 3D motion but the main variations are in the front plane.
- Turbulent quantitative methods was successful applied to study laminar chaotic flows with emphases in the creation and dissipation of turbulent energy and correlation with the geometrical location of such variables and the relation between both for each Reynolds in study. Additionally was successful study the correlation between the eddies size with the geometrical characteristics of the chamber.
- The author recommends the development of new technologies for low Reynolds number since it reduces the equipment costs due high pressures and tight control of the flow dynamic. New works tend to progress in study the flow using mechanisms to induce oscillation in the jets. The author believe the usage of such technology in low Reynolds number will greatly affect positively the flow dynamics and consequently improve mixing performance.

From the mixing dynamics it is concluded the following:

- For the first time was perform a representation of the mixing dynamics in a 3D environment using VOF for interface tracking and without molecular diffusion.
- Mesh resolution was not enough to calculate the smaller mixing scales and therefore the results appear to have a big numerical diffusion thus only was possible to verify the larger vortices.
- The author recommends in the future, when computer make accessible a creation of the same method VOF for the 3D domain but with interface taking based on the gradients of the phases (Fonte, 2012) Note: this was test but due the large necessity to refinement is practice impossible nowadays, with the resources available to tackle this problem.

4 Development of a Real-time Control System for the CIJ Flow Field with PIV

4.1 Introduction

Over the past years, researchers have used the flow visualization technique based on the Particle Image Velocimetry (PIV) to study the flow field behaviour in several industrial and academic applications and the same holds true for studies in Reaction Injection Moulding.

The PIV technique was used in the present work to compute the 2D velocity field from the displacement in 2 consecutive images of a small point which flows with the current. The method will be explained later in section 4.4 and the essential hardware and software employed will be described in subsection 4.4.1. This method has proved to be extremely useful to compare the experimental results with the CFD data.

Although the hydrodynamics of the CIJ flow field was already investigated in previous works (Santos, 2003; Fonte, 2012; Gomes, 2015), it was necessary to replicate some parts of the work performed in order to ensure the quality of the results. Based upon the results of this hydrodynamic study, it was possible to analyse and validate other tools that can be used to establish operational and design parameters of the CIJ mixer. First, the elastic model proposed by (Bird et al., 2002; white, 2006) and further developed by (Fonte, 2012)was considered. To allow validation of the model, when possible similar conditions to those of (Fonte, 2012) work were employed. In addition, a Reynolds number dependence study was

performed. Next, the pressure model proposed by (Gomes, 2015) was examined and, for the first time, it was validated against experimental data.

This chapter is structured as follows. Section 1.2 defines the hydrodynamic variables that are relevant to describe the operating conditions in the system. Section 1.3 describes the main characteristics of the experimental facility. Section 1.4 explains the PIV technique and includes a description of both the hardware and the software used. Section 1.5 concerns the study of the turbulence intensity within the mixing chamber. Section 1.6 gives an overview of the elastic model, presenting its validation and an extension of the model for different Reynolds numbers. Section 1.7 introduces the pressure model and discusses its ability to reproduce the experimental measurements. Section 1.8 addresses the main conclusions that can be drawn from this chapter.

4.2 Hydrodynamic variables

The hydrodynamic variables introduced (Malguarnera and Suh, 1977; Macosko, 1989) to carry out the dimensional analysis of impingement mixing in RIM machines will be adopted hereafter to describe the designated operating conditions.

Initially, the Reynolds number is used to describe the flow motion. In impinging jets mixers, the Reynolds number is defined at the injectors as

$$Re = \frac{\rho v_{inj} d}{\mu} \tag{4.1}$$

where ρ is the fluid density, v_{inj} is the velocity at the injectors, d is the injectors diameter and μ is the fluid viscosity. The fluid properties are highly dependent on the operating temperature, therefore, in addition to a careful data acquisition during the experiment, a good knowledge of the fluid rheology is necessary.

Additionally, several parameters can be employed to express the jets' flow unbalancing in impinging jets mixers (Macosko, 1989). The jets' momentum rate ratio, ϕ_M, is defined as

$$\phi_M = \frac{\rho_1 d_1^2 u_{inj,1}^2}{\rho_2 d_2^2 u_{inj,2}^2} \tag{4.2}$$

Where the indices 1 and 2 represent the left and the right injector, respectively. The kinetic energy rate ratio between the two jets, ϕ_K, is defined as

$$\phi_K = \frac{\rho_1 d_1^2 u_{inj,1}^3}{\rho_2 d_2^2 u_{inj,2}^3} \tag{4.3}$$

As for the jets' mass flow rate ratio, it is defined as

$$\phi_{FR} = \frac{\rho_1 d_1^2 u_{inj,1}}{\rho_2 d_2^2 u_{inj,2}} \tag{4.4}$$

All of these definitions will be mentioned later when the analysis of the flow regime is coupled with the identification of the impingement point by means of two new methods that were developed in previous works (Fonte, 2012; Santos, 2003). The first method to be considered is an elastic analogue model. Then, at the end of this chapter, a pressure model will be discussed. These two models are extremely important in order to perform real-time control of the system as their application makes it possible to select operational and geometrical conditions that set the impingement point at the centre of the chamber, promoting maximum oscillatory motion of the impingement surface and thus enhanced mixing.

4.3 Domain

4.3.1 Physical characterization of the mixing chamber

To allow visualization of the flow behaviour, the mixing chamber was machined from a Plexiglas block and the internal walls were polished to remove defects caused by the manufacturing process.

Figure 4.1 shows a schematic image of the chamber. The injectors are perfectly aligned with each other and with the chamber axis. The chamber diameter, D, is 10 mm and the injectors diameter, d, is 1.5 mm. The injectors have a length of 6D to allow a fully developed parabolic flow and are positioned 5 mm below the top of the chamber. The chamber height, H, is 50 mm.

The fluid enters in the chamber through the opposed injectors and is mixed by impingement prior to the disposal in the mold. The liquid is then discarded from the mold to the exterior and it will go on to be reused during the experiments. The fluid physical properties do not suffer significant variations during the recirculation since the tanks, the chamber, the mold and the storage vessel were clean and dry before the experiments took place.

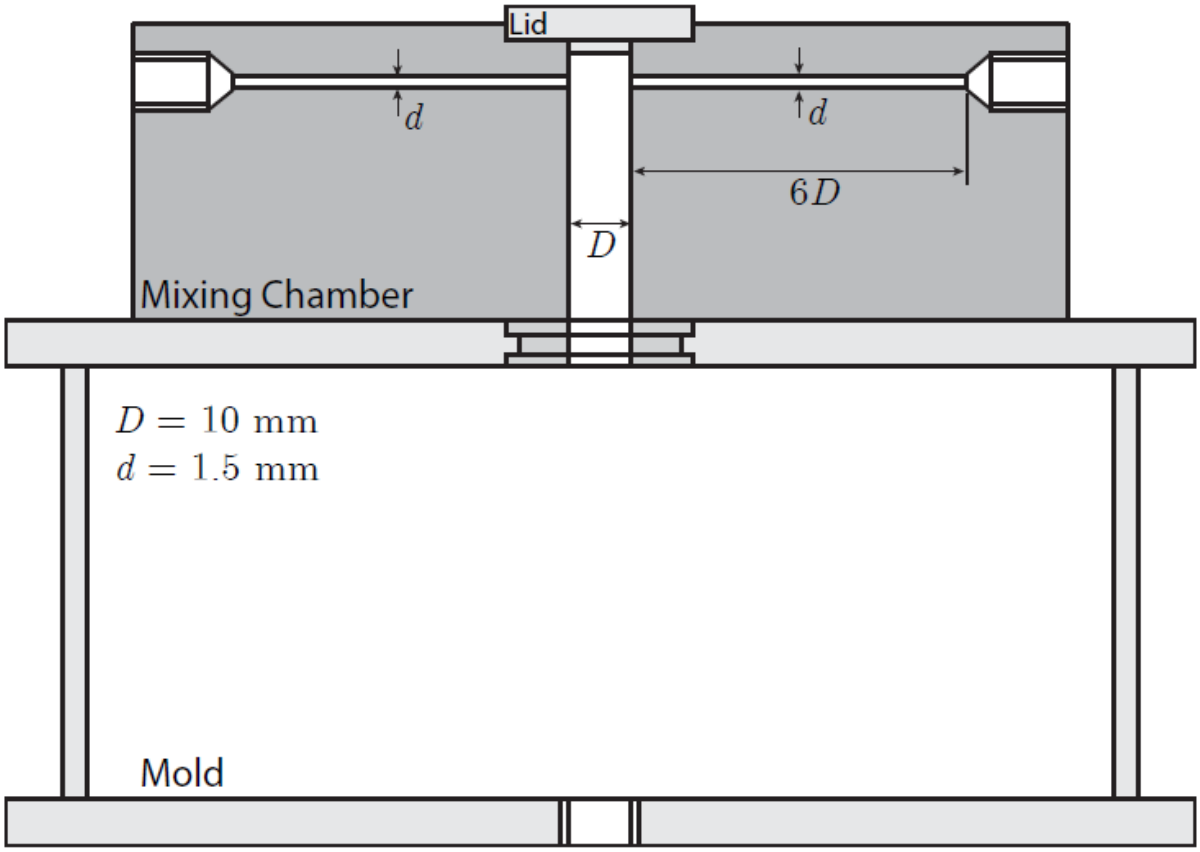

Figure 4.1 – Schematic of the transparent mixing chamber and the mold

4.3.2 Schematic representation of the RIM machine

The Reaction Injection Moulding (RIM) machine where the experiments were carried out comprises the equipment depicted in Figure 4.2. Two containers (1) feed the working fluid to each injector whereas the additional container (6) is used to collect the fluid discharged from the mould. A hydraulic loop feeds each container (1) with the working fluid that is collected in the disposal container (6). The two containers (1) are air pressurized in order to guarantee a smooth injection of the fluid without pulsation, which occurs if the fluid injection is done with pumps, causing pressure spikes. This ensures total control of the RIM process and allows making direct comparisons between the results of the PIV technique and those of the CFD simulation.

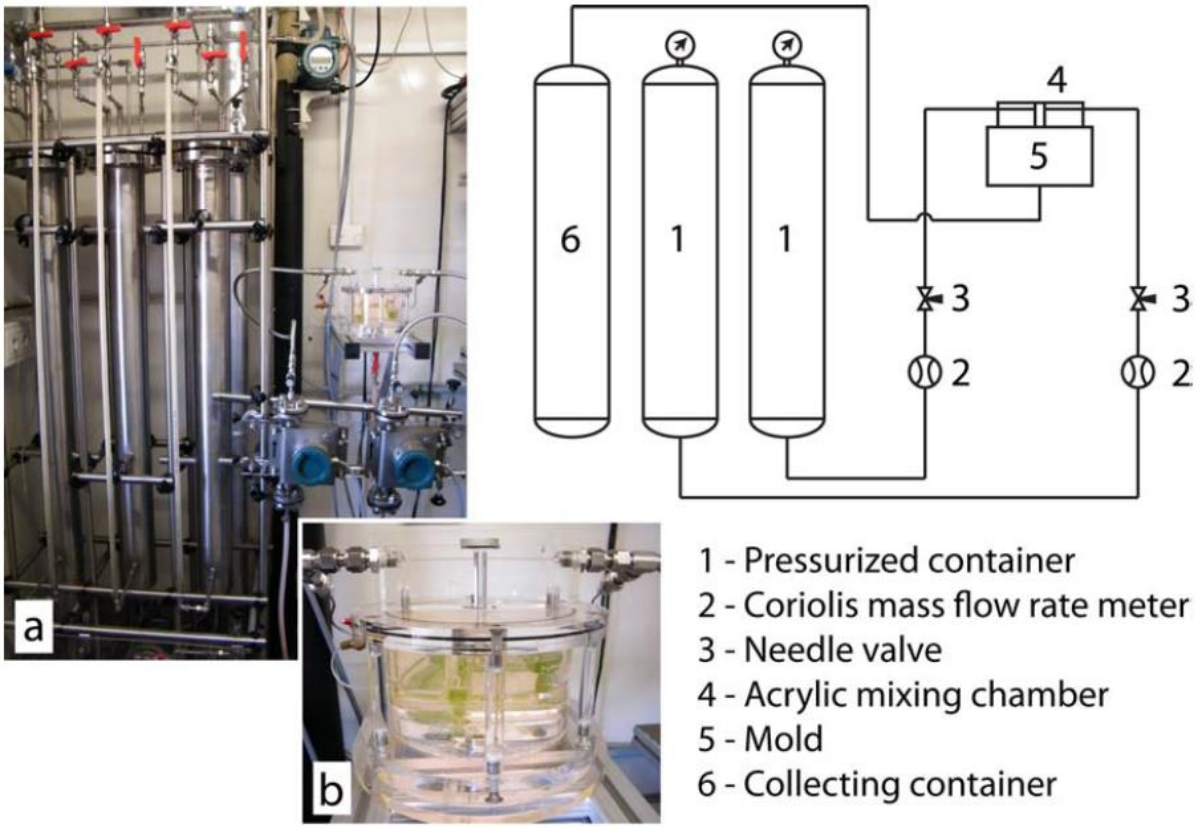

Figure 4.2 – Representation of the RIM equipment: a) hydraulic loop, b) transparent mixing chamber and mold

4.3.3 Physical characterization of the working fluid

A tight control of the working fluid composition is required since the process variables, namely the Reynolds number and the jets' kinetic energy rate ratio, which is a function of both the density and the viscosity, are highly dependent on the fluid properties. A further issue that arises is that those properties change drastically with the operating temperature. Therefore, it is necessary to determine the density and the viscosity of the fluid as a function of temperature in the designated operating conditions, which range from 20º to 30º.

The liquid used in the experiments is a glycerin (99%) solution in water. The mass fraction of the glycerine solution, defined as

$$\chi_{glicerine} = \frac{M_{glicerine}}{M_{solution}} \tag{4.5}$$

where $M_{glicerine}$ Is the mass of glycerol in the solution and $M_{solution}$ is the total mass of the solution, was set at 73%.

The density of the solution is determined by

$$\rho = (1 - \chi_{glicerine})\rho_{water} + \chi_{glicerine}\rho_{glicerine} \tag{4.6}$$

where ρ_{water} and $\rho_{glicerine}$ (kg/m^3) are the water and the glycerine densities, respectively. The variation of the water and the glycerine densities with temperature $\theta(K)$ is given by (Santos, 2003)

$$\rho_{water} = 1064.6 - 0.23\theta \tag{4.7}$$

$$\rho_{glicerine} = 1440.5 - 0.61\theta \tag{4.8}$$

In addition, the viscosity of the solution is computed by the following expression

$$\mu = \left((1 - \chi_{glicerine}) \left(A_{water} e^{\frac{B_{water}}{\theta}} \right) + \chi_{glicerine} \left(A_{glicerine} e^{\frac{B_{glicerine}}{\theta}} \right)^{\alpha} \right)^{\frac{1}{\alpha}} \tag{4.9}$$

where μ is the viscosity in $mPa.s$, $A_{water} = 5.17x10^{-4}\, mPa.s$, $B_{water} = 2.22x10^3\, K$, $A_{glicerine} = 7.06x10^{-9}\, mPa.s$, $B_{glicerine} = 57.64x10^3 K$ and $\alpha = -0.32$. This theoretical curve was compared with viscosity measurements made with a rheometer (Paar Physica UDS 200) with a plane (MK24) and plate in the temperature range of 20º to 30º.

Figure 4.3 demonstrates the dependence of the working fluid viscosity with temperature.

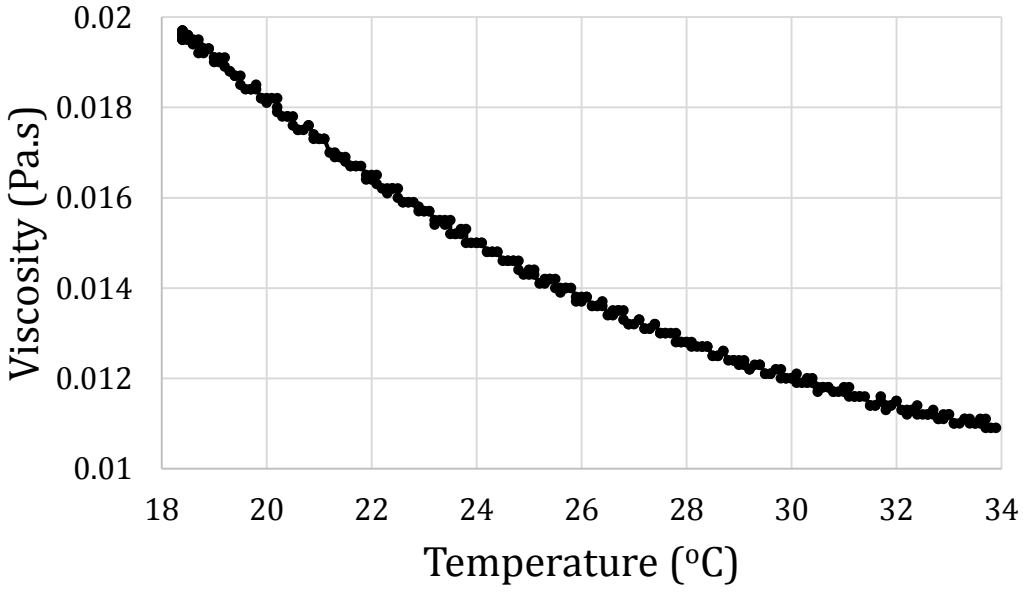

Figure 4.3 - Variation of the glycerine-water solution with temperature

4.3.4 Recording hardware

The flow is controlled with two needle valves, one in each injector line, and adjusted through two ROTA-Yokogama Coriolis mass flow meters (model RCCCS33 M01A1SH) with a precision of $\pm 0.05 g/s$ in the range of 1.2g/s to 13.2 g/s. For the lowest flow rate (0.5 g/s) this corresponds to a relative error of 10%. Additionally, the mass flow meters enable the measurement of the fluid temperature and density for a single experiment, thus allowing a more precise control of the experimental variables. For each run, the pressure is recorded by a calibrated differential pressure transducer (Validyne P305D) fitted at the start of the injectors. The signal is processed through a data acquisition system (GW Instruments MacADIOS II) connected to an external board (GW Instruments MacADIOS ABO) with a computer using a program written in LABVIEW. The same recording system is employed for the mass flow readers. The data acquired is then processed in MATLAB to quantify the results obtained.

4.4 PIV technique

In the late 90's, developments in the acquisition of high-quality digital images allowed new techniques for flow visualization to emerge, one of them being Particle Image Velocimetry (PIV) (Westerweel, 2008; Westerweel, Elsinga, and Adrian ,2013).

The PIV technique requires a sequence of snapshots of the flow field in order to correlate seeding points in consecutive images and create a displacement vector for the domain under study. These points are created experimentally by seeding the fluid with particles that reflect the light. By adjusting a beam planar laser it is possible to obtain the displacement field in any 2D plane in the mixing chamber. 3D PIV is also possible with the implementation of an additional camera, but was not performed in the present work.

A charge-coupled device (CCD) camera with a high transfer rate allows taking shots at the plane illuminated by the beam laser. From two consecutive frames the displacement field is computed using a cross-correlation method that consists of a digital image processing technique to identify high gradients in the image created by the seeding particles. This is performed for each division of the target area on the chamber, known as interrogation spot.

The capture time is chosen according to the size of the interrogation spot and the velocity field passed by. It should be assured that the particle moves less than a fourth of the interrogation spot size between two frames. Due to the low acquisition rate of the CCD cameras relative to the instantaneous velocity this method can only be applied when low

velocity fields are expected. In order to overcome this limitation, a laser beam is pulsed close to the camera shutter is almost closing and the second beam is pulsed as soon as the camera shutter opens again. This reduces the time between the capture of two consecutive pictures drastically and therefore boosts the technique capabilities.

At the experimental facilities available in the LSRE laboratory, a TSI PIV system is used to perform 2D analyses of the flow field. To carry out the PIV measurements it is necessary to employ a pulsed Yag laser, a CCD camera and a synchroniser, as well as a computer to control each component, acquire the images and post process them with in-build software to yield the instantaneous velocity vector maps. The image acquisition was done in an Intel Xeon CPU at 2.33 GHz with 2GB of RAM. Additionally, a PCI card was utilised to transfer the images from the camera to the computer prior to their analysis. A photograph and a schematic of the apparatus are shown, respectively, in Figure 4.4 and in Figure 4.5.

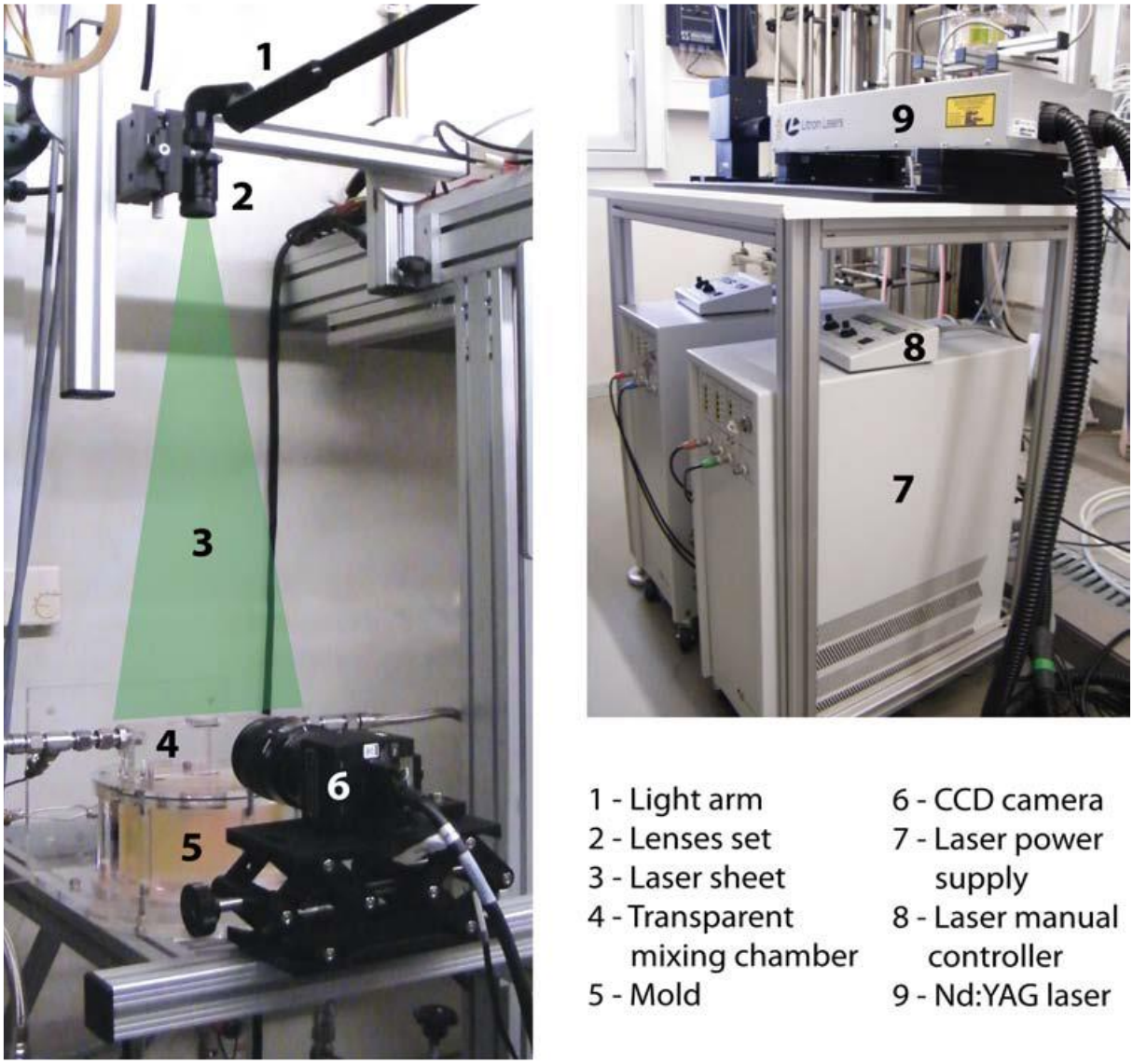

Figure 4.4 – PIV experimental setup

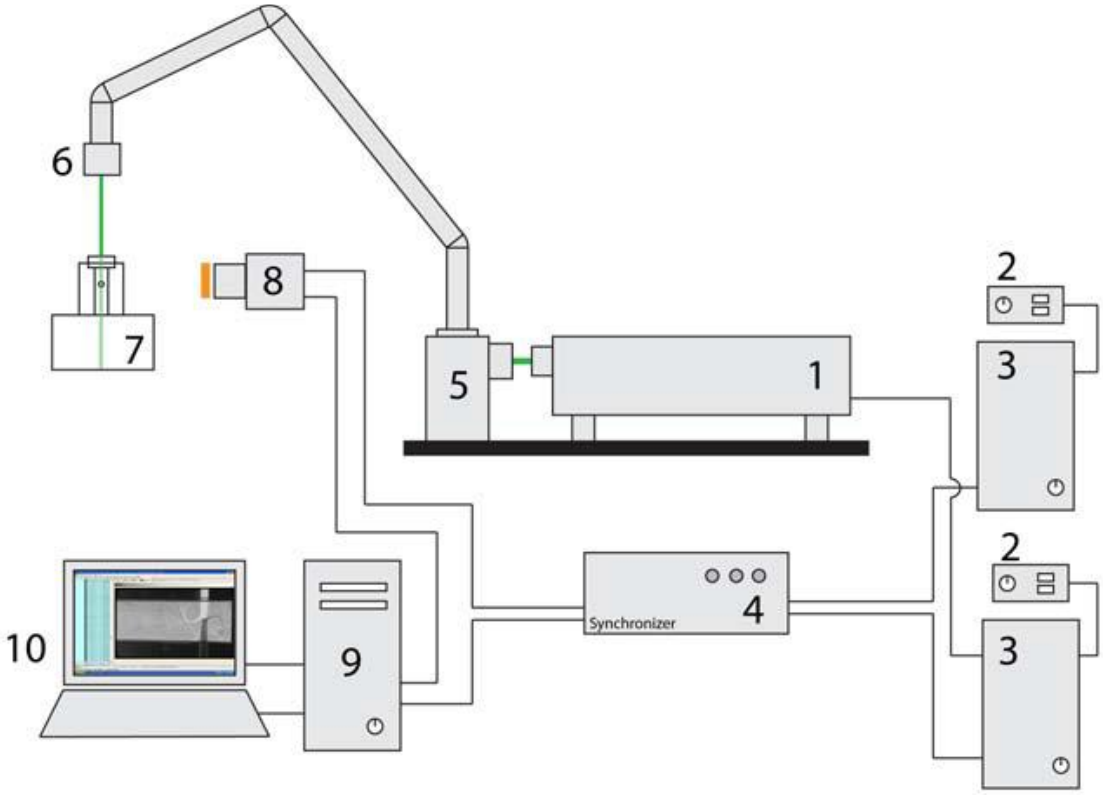

1 - Nd:YAG laser (532 nm)
2 - Laser manual controller
3 - Laser power supply
4 - Synchronizer
5 - Light arm
6 - Set of lenses
7 - Side view of the mixing chamber
8 - PIV camera with orange glass filter
9 - Data acquisition PC
10 - Monitor and software interface

Figure 4.5 – Schematic of the PIV experimental setup

In the next sections, is offered a brief description of the components required to perform 2D PIV.

4.4.1 PIV hardware and software

4.4.1.1 CCD Camera

The PIV camera used is a TSI PIVCAM 10-30, which has a resolution of 1016x1024 pixels and a frame rate of 30Hz. The camera is connected to the computer through a Frame Grabber (TSI 600067).

4.4.1.2 Synchroniser

A TSI 610032 synchroniser was used to control the image acquisition process. The synchroniser has the functionality of regulating the camera shutter opening and closing, according to the acquisition settings defined in the software, hence allowing real-time

control of the laser impulse. The acquisition parameters setup enables the user to specify the instant where each component acts separately, such as the time interval between images and the interval of time between the laser beam and the closing or opening of the camera shutter. This process is known as shutter feedback mode and is the most advisable for image acquisition.

4.4.1.3 Laser source

The laser is a double Nd:Yag laser (model MiniLase-15). The two lasers emit beams with 12 mJ pulses and, as a result, the time between a pair of lasers can be set until $1\mu s$. Each pulse can be pulsed until 15 Hz for each pair of consecutive frames. First, each laser is fed through a cavity, resulting in a beam with a diameter of 2.5 mm. Next, the laser is transported by means of a TSI light arm (model 610015). Then, the laser is transformed into a thin sheet by a combination of one cylindrical and one spherical lens. The cylindrical lens expands the beam generating a sheet whereas the spherical lens narrows the sheet thickness to avoid capturing particles in different planes. In the present work, a 200 mm spherical lens and a -25mm cylindrical lens were used, creating a thin sheet of 17.5mm height and 50.9 μm thickness at a distance of 20 mm from the lenses. The last lens is placed at 500 mm from the top of the mixing chamber ensuring a laser thickness of 1 mm.

4.4.1.4 Control, acquisition and post processing software

The control of the process parameters, the acquisition of the images and the processing of the results into vector maps was performed by means of the *Insight* (version 9.0) software using the graphical user interface (GUI). The software allows the user to input the acquisition settings which are then transmitted to the synchronizer through the RS232 port. The images from the experiment are recorded by the camera and transferred by a Frame Grabber which allocates them in the computer disk, improving the acquisition rate. Finally, the images are processed and the displacement field and subsequently the instantaneous velocity field are converted into vector maps.

During the post processing stage, the software will detect spurious vectors, characterized by a small correlation peak, which can be caused by insufficient seeding, strong velocity gradients or three-dimensional motion of the particles of the laser sheet. This will cause a discontinuity in the vectors and therefore a simple filter can easily identify such errors. The tolerance used to filter the errors was equal to three times the standard deviation computed from all the vectors in that map.

4.4.2 Seeding

In the present work, spherical TSI nylon particles (model 10084) were seeded to the working fluid with a sufficient concentration to ensure 5 to 15 particles per interrogation spot, which is a common rule of thumb for this PIV technique. The seeding particles have a nominal diameter of $d_p = 4\ \mu m$ and a density of $\rho_p = 1.14\ g\ cm^{-3}$.

According to Tropea *et al.*(2007) it is necessary to guarantee that the particles flow passively with the flow field. For that purpose, the Stokes number, St, was maintained at a value below 0.1 for all the experiments as it assures that the particles follow the flow with errors smaller than 1%.

The Stokes number is defined as the ratio between the particles characteristic response time and the characteristic flow time scale:

$$St = \frac{\dot{\gamma}\rho_p d_p^2}{12\mu} \tag{4.10}$$

where $\dot{\gamma}$ is the characteristic strain rate of the flow. To ensure conservative results, the maximum strain rate existent in the domain, which is located at the injectors, was used in the calculations, as given by

$$\dot{\gamma} = \frac{8u_{inj}}{d} \tag{4.11}$$

4.4.3 PIV settings

In the present chapter, the PIV technique is used to quantify the flow near the impingement point position. Santos (2003) performed an analysis of the distortion produced by PIV and identified extreme optical distortions occurring near the chamber walls. Consequently, in this work, the region of interest was chosen in the range of $-0.4 \leq \frac{x}{D} \leq 0.4$ to avoid such effects. Accordingly, the interrogation region was chosen to be 32x32 pixels.

After discerning the displacement field by cross-correlation between two sequential pictures, the velocity field is calculated dividing the displacement field by the time interval between two sequential pictures which corresponds to the time between two consecutive laser pulses, Δt_{beams}, defined as

$$\Delta t_{beams} = \frac{\Delta x_{int.\ region}}{2\max\{u_{inj,1}, u_{inj,2}\}} \tag{4.12}$$

where $\Delta x_{int.\ region}$ corresponds to the physical length of each interrogation region, calculated by converting pixels into physical length. For the time interval between two consecutive laser pulses the minimum velocity detected by the PIV technique is determined by the equation

$$u_{min} = \frac{1}{8}\max\{u_{inj,1}, u_{inj,2}\} \tag{4.13}$$

which corresponds to the particle moving 1 pixel in the image. The average velocity inside the mixing chamber $u_{chamber}$ has the smallest value given by

$$u_{chamber} = \frac{d^2}{D^2}\left(u_{inj,1} + u_{inj,2}\right) \tag{4.14}$$

The main focus in the present work is to investigate the impingement region, where high velocity gradients occur, hence the minimum detectable velocity is not a significant factor in the scope of the present work.

The resolution of the images recorded in the PIV experiments can be improved either by decreasing the pulse time delay or by increasing the number of pixels per search area. Whilst in the first option the particles may present a high displacement and as a result not be detected in the cross-correlation process, in the latter, the coarser grid can filter the small flow structures. For that reason, a sensitivity analysis of the acquisition settings should be conducted and such was the approach applied in this work. The acquisition parameters were tested and selected in order to ensure a good description of the main flow, more specifically in the proximity of the impingement region, while also allowing a visualization of the smaller flow structures which otherwise could be indiscernible.

4.5 Flow Field Visualization

The velocity field was computed using the PIV software as a post processing tool. The displacement field was calculated from the images obtained in the PIV experiment with the methods and parameters described in the previous sections. Due to a bug in the computer concerning its memory only 20 pictures were obtained for each set of experiments.

The experiments were conducted by setting the right injector flow rate according to the desired Reynolds, whereas the flow rate of the left injector was increased until a variation of the impingement point was noticeable. After this step and while maintaining the specified flow rate at the right injector, the left injector flow rate was increased at a rate of 0.1 g/s.

A MATLAB code was created to evaluate each individual velocity field for each frame of the experiment in order to calculate the impingement point position. This was performed by means of the identification of the changing in the sign of the velocity field in the injector axis centre, followed by the detection of an increase in the modulus of the vertical component of the velocity in the interrogation spot upstream and downstream of the impingement region. Additionally, the contours of the non-dimensional kinetic energy of the velocity fluctuations, $k/u_{inj,1}^2$, were plotted against the average velocity vector field. The kinetic energy of the velocity fluctuations is defined as

$$k(x) = \frac{1}{2}\overline{\left(u_x(\mathbf{x},t) - \overline{u_x(\mathbf{x})}\right)^2} + \frac{1}{2}\overline{\left(u_y(\mathbf{x},t) - \overline{u_y(\mathbf{x})}\right)^2} \tag{4.15}$$

where x and y correspond to the horizontal and vertical coordinates of the 2D mixing chamber, then u_x and u_y correspond, respectively, to the x-velocity and y-velocity components of the velocity field.

The flow field behaviour is presented next for the Reynolds numbers studied (45, 111, 159, 220 and 313), from Figure 4.6 to Figure 4.28.

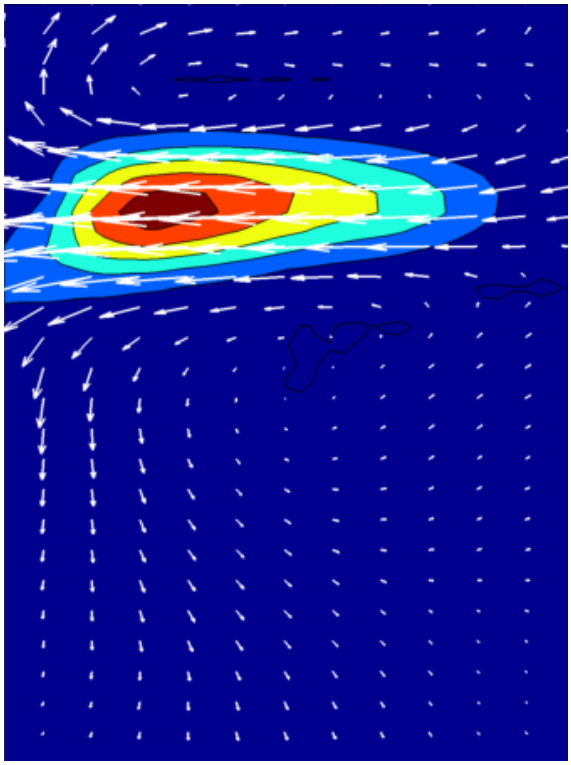

$\phi_k = 0.0947$

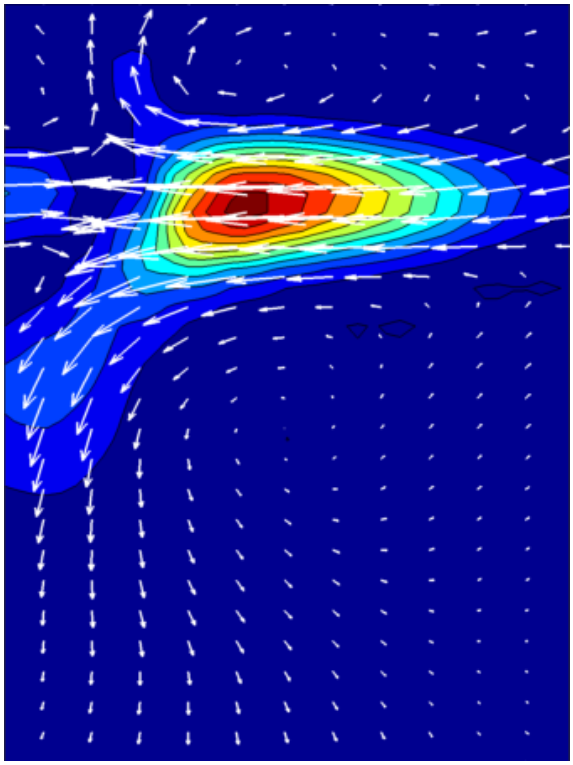

$\phi_k = 0.2887$

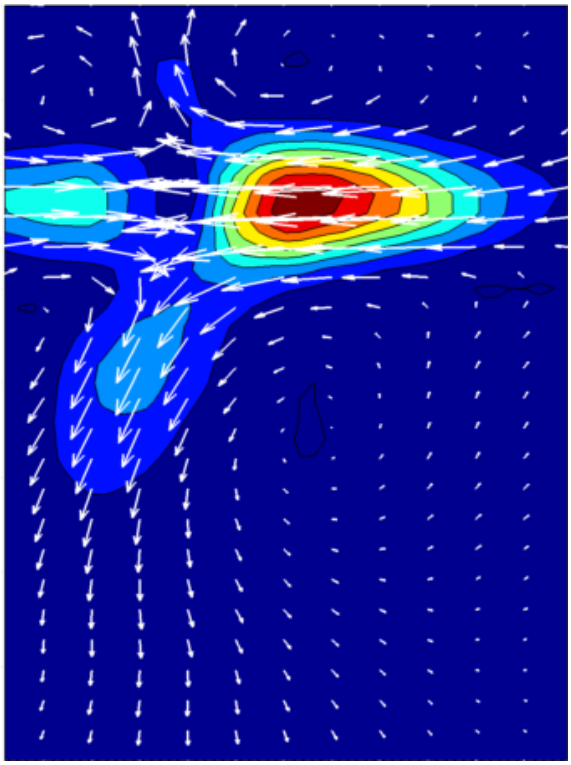

$\phi_k = 0.6179$

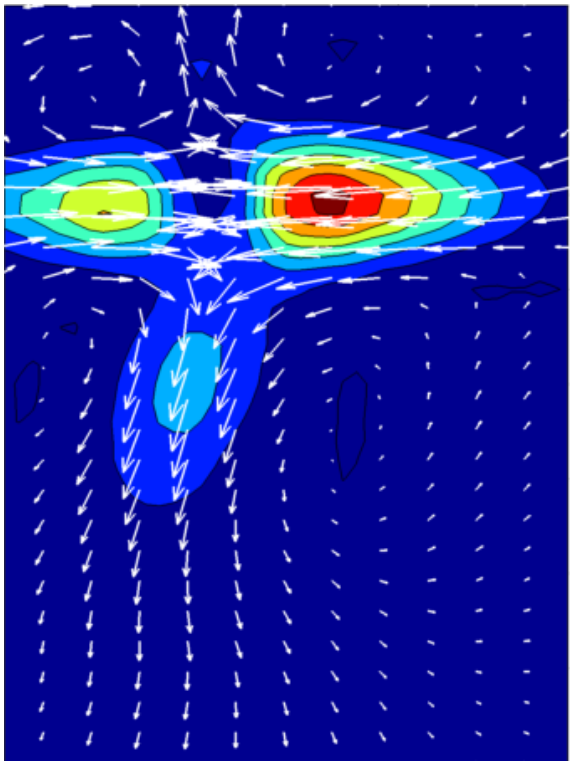

$\phi_k = 0.7100$

Figure 4.6 - Velocity field vector maps and non-dimensional velocity fluctuations contours for jets' kinetic energy rate ratios ϕ_k = [0.0947, 0.2887, 0.6179, 0.7100] at Reynolds 45

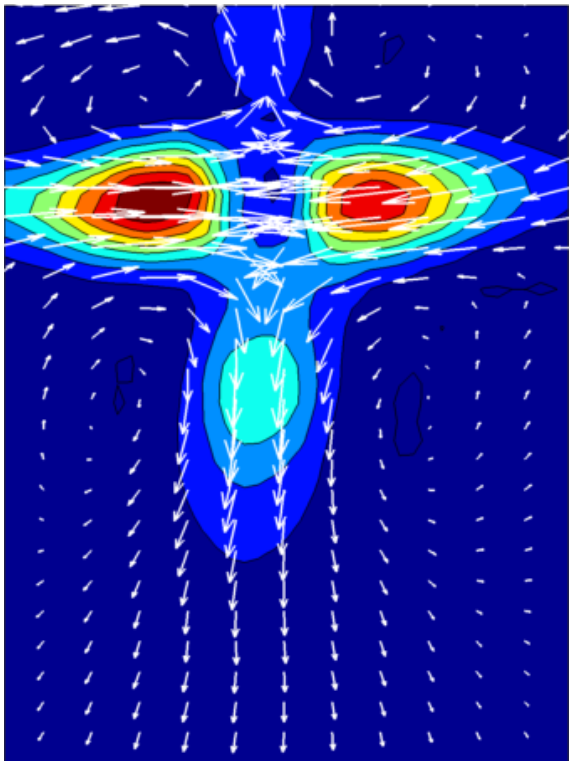

$\phi_k = 0.7733$

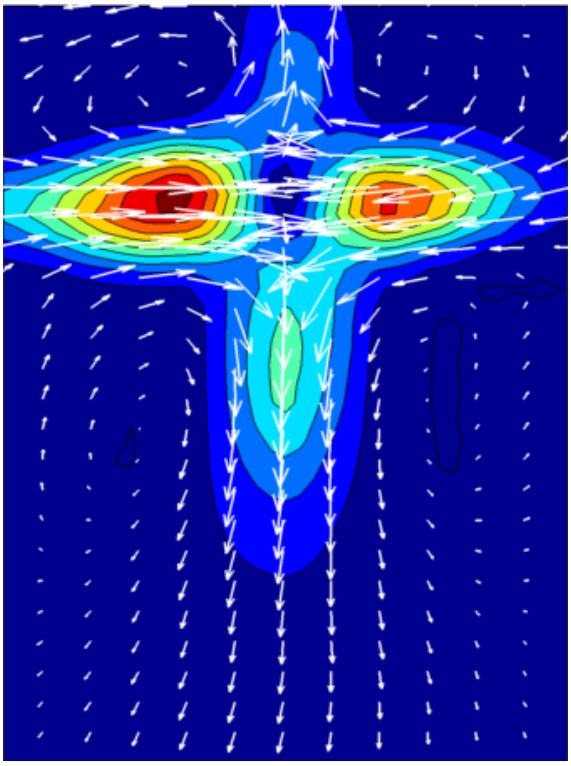

$\phi_k = 0.8658$

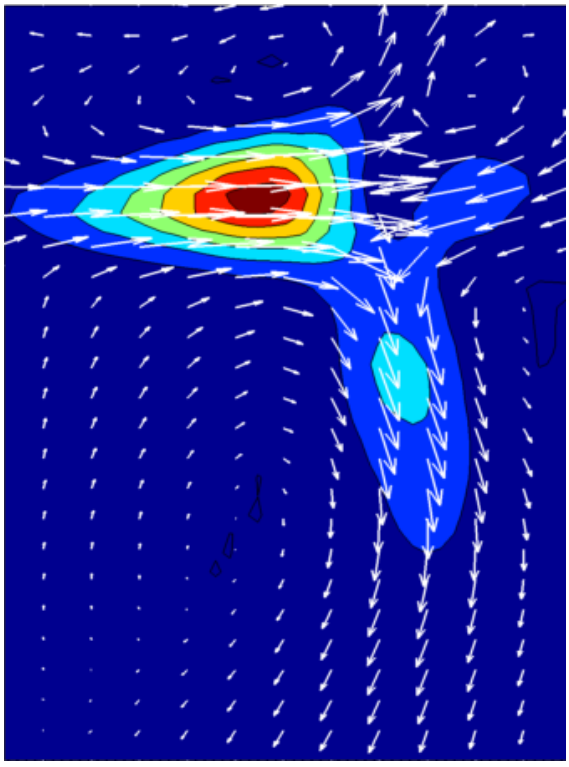

$\phi_k = 2.1929$

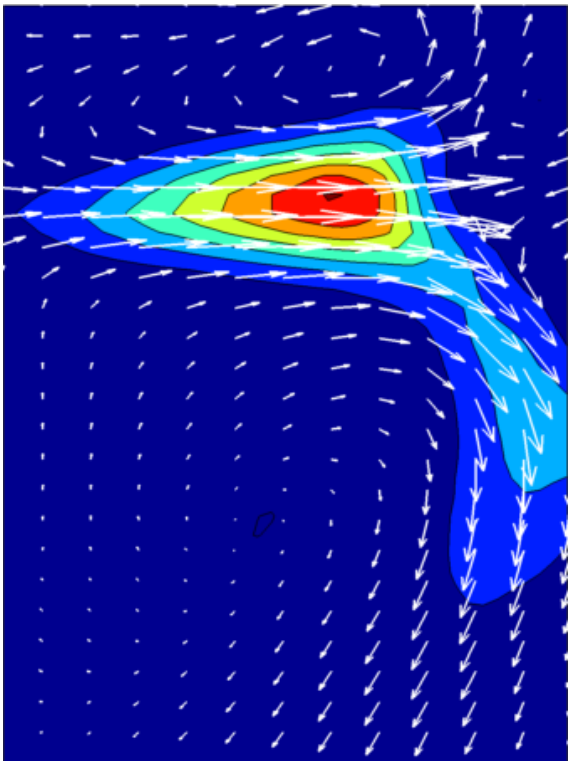

$\phi_k = 2.2919$

Figure 4.7 - Velocity field vector maps and non-dimensional velocity fluctuations contours for jets' kinetic energy rate ratios ϕ_k = [0.7733, 0.8658, 2.1929, 2.2919] at Reynolds 45

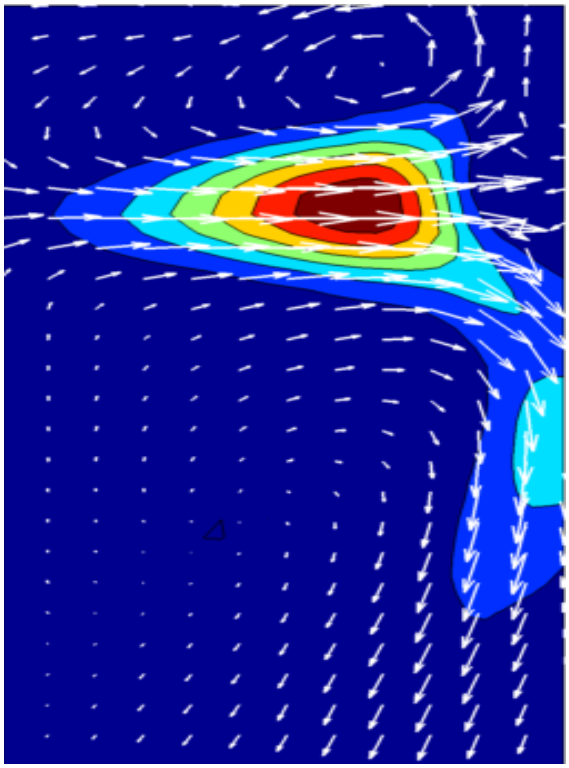

$\phi_k = 2.7689$

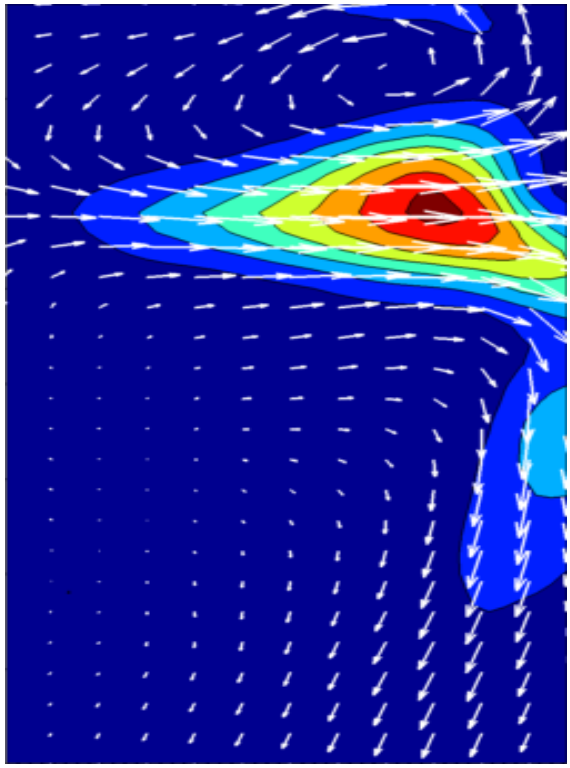

$\phi_k = 3.7194$

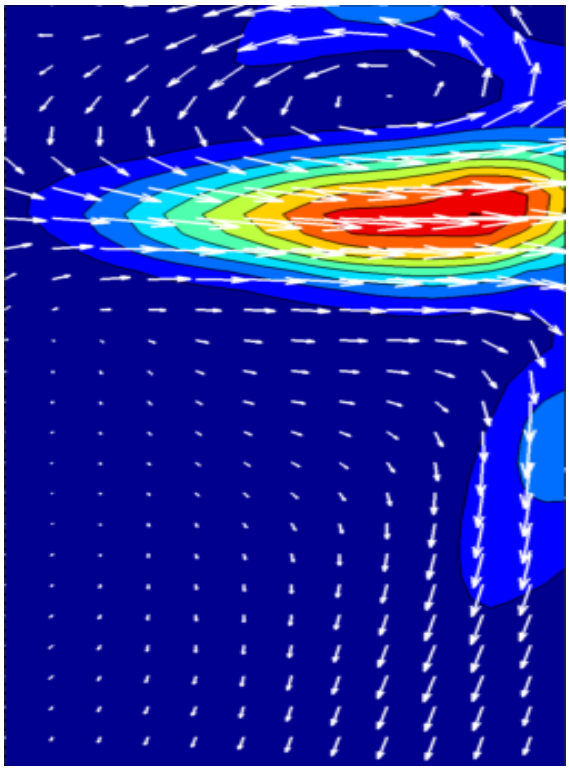

$\phi_k = 4.4879$

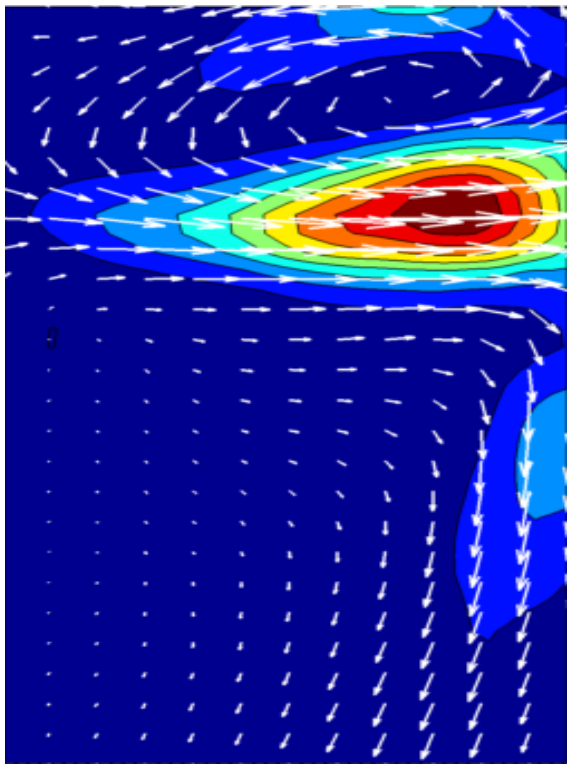

$\phi_k = 5.5027$

Figure 4.8 - Velocity field vector maps and non-dimensional velocity fluctuations contours for jets' kinetic energy rate ratios ϕ_k = [2.7689, 3.7194, 4.4879, 5.5027] at Reynolds 45

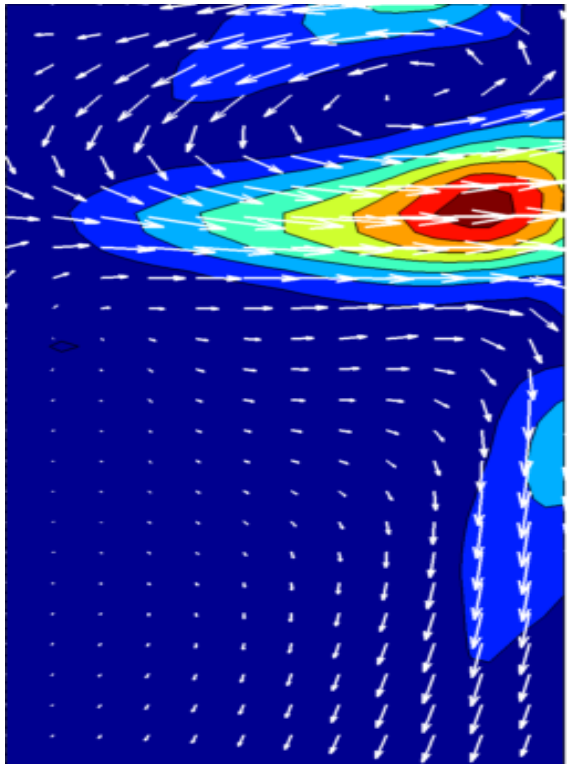

$$\phi_k = 8.0014$$

Figure 4.9 – Velocity field vector maps and non-dimensional velocity fluctuations contours for jets' kinetic energy rate ratio ϕ_k = 8.0014 at Reynolds 45

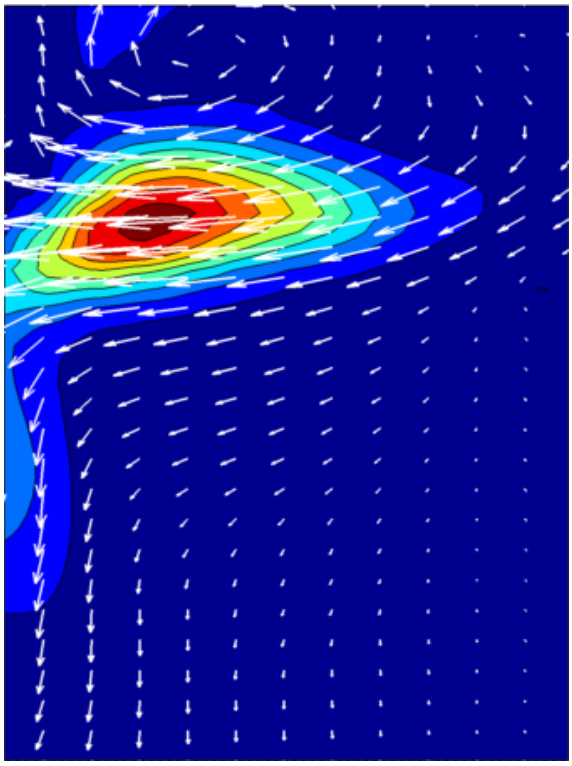

$\phi_k = 0.2912$

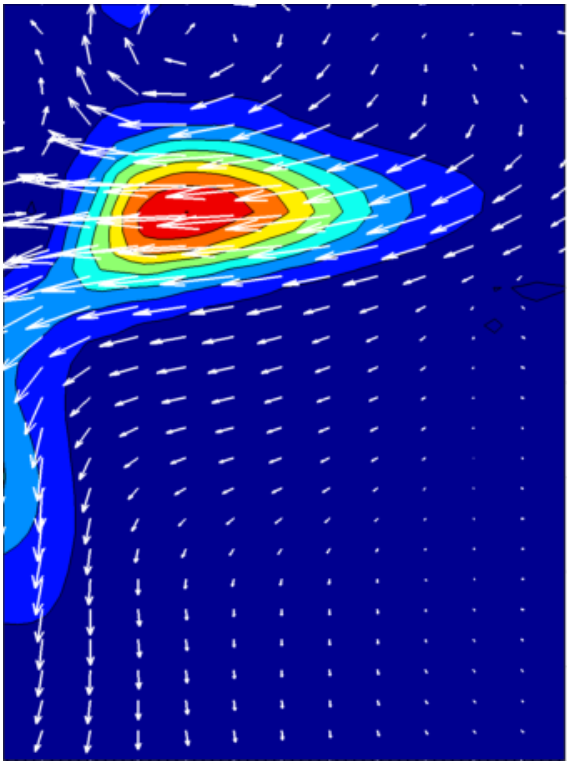

$\phi_k = 0.3329$

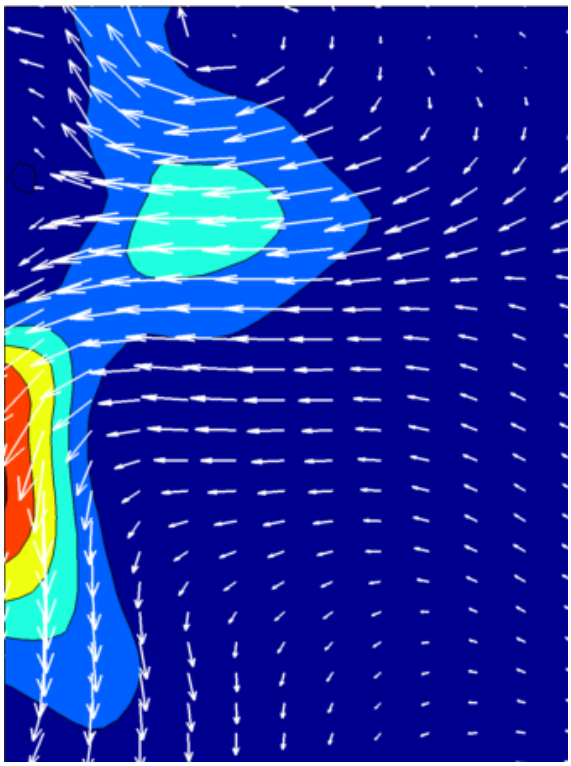

$\phi_k = 0.3879$

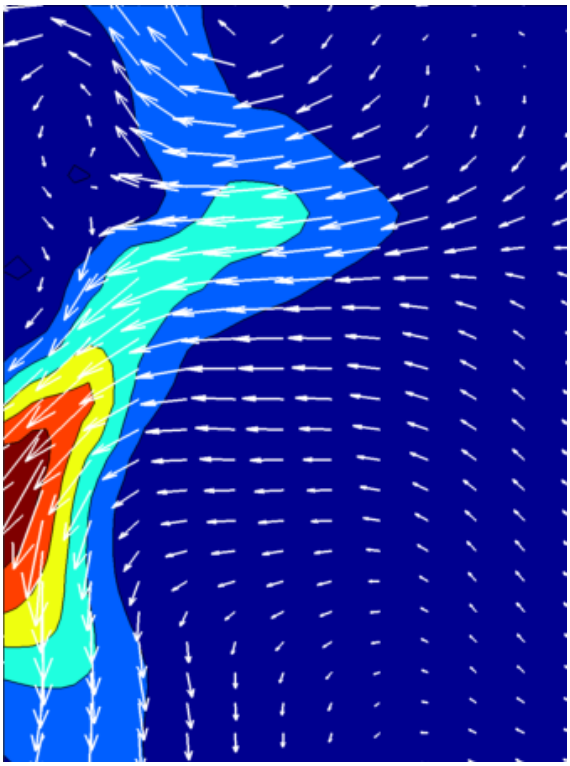

$\phi_k = 0.4581$

Figure 4.10 - Velocity field vector maps and non-dimensional velocity fluctuations contours for jets' kinetic energy rate ratios ϕ_k = [0.2912, 0.3329, 0.3879, 0.4581] at Reynolds 111

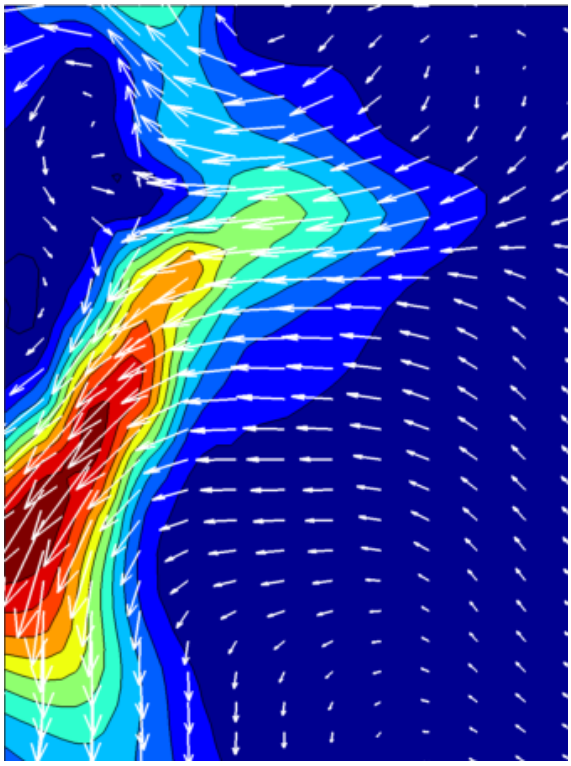

$\phi_k = 0.4713$

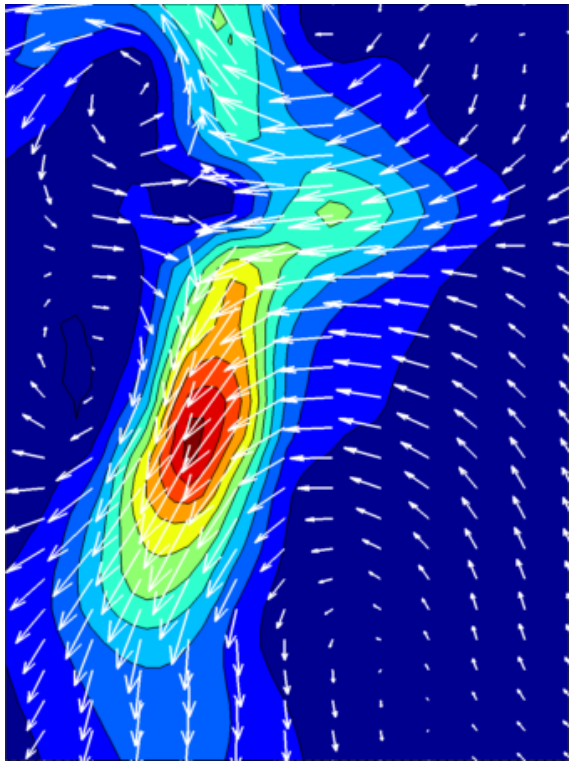

$\phi_k = 0.6601$

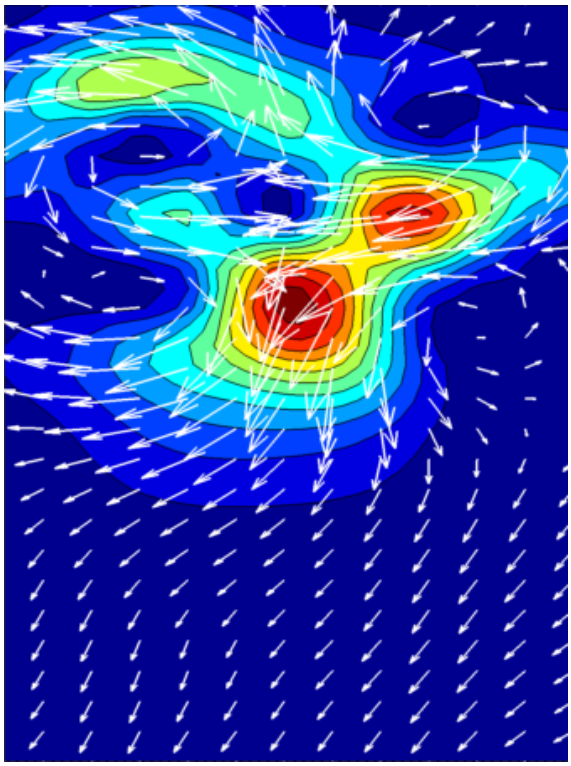

$\phi_k = 0.8378$

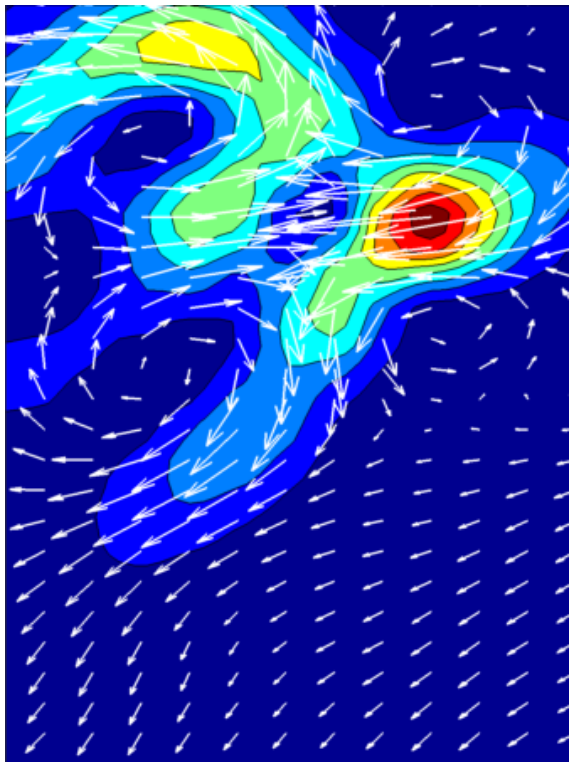

$\phi_k = 0.9315$

Figure 4.11 - Velocity field vector maps and non-dimensional velocity fluctuations contours for jets' kinetic energy rate ratios ϕ_k = [0.4713, 0.6601, 0.8378, 0.9315] at Reynolds 111

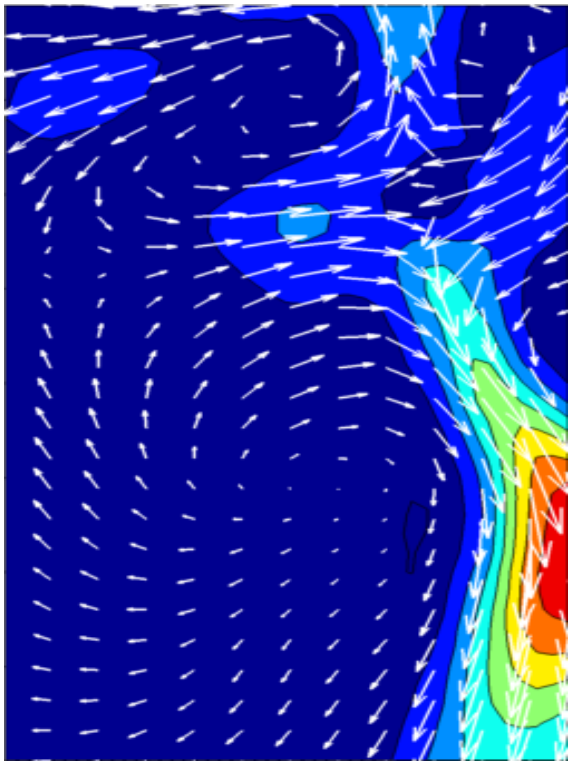

$\phi_k = 1.0962$

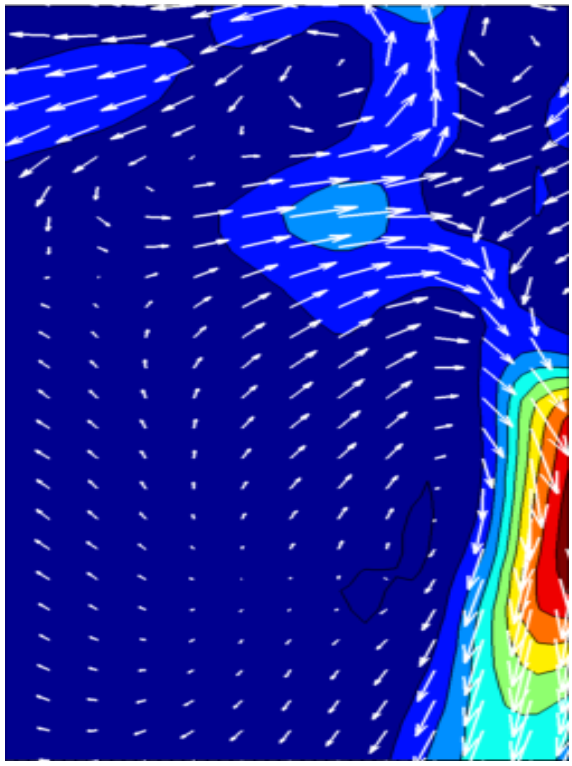

$\phi_k = 1.0476$

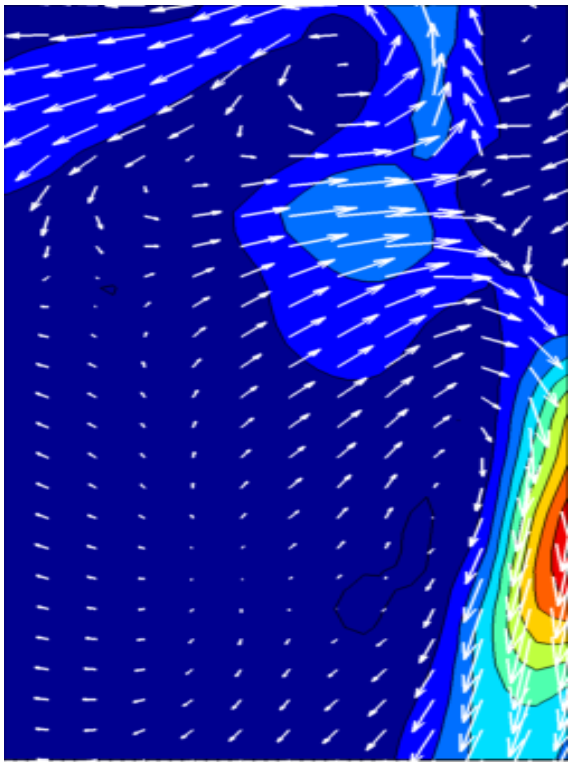

$\phi_k = 1.2268$

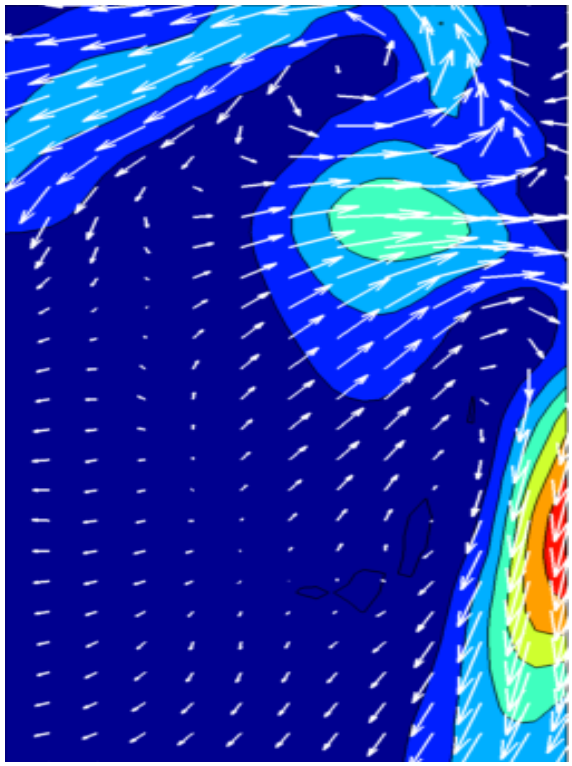

$\phi_k = 1.4630$

Figure 4.12 - Velocity field vector maps and non-dimensional velocity fluctuations contours for jets' kinetic energy rate ratios ϕ_k = [1.0962, 1.0476, 1.2268, 1.4630] at Reynolds 111

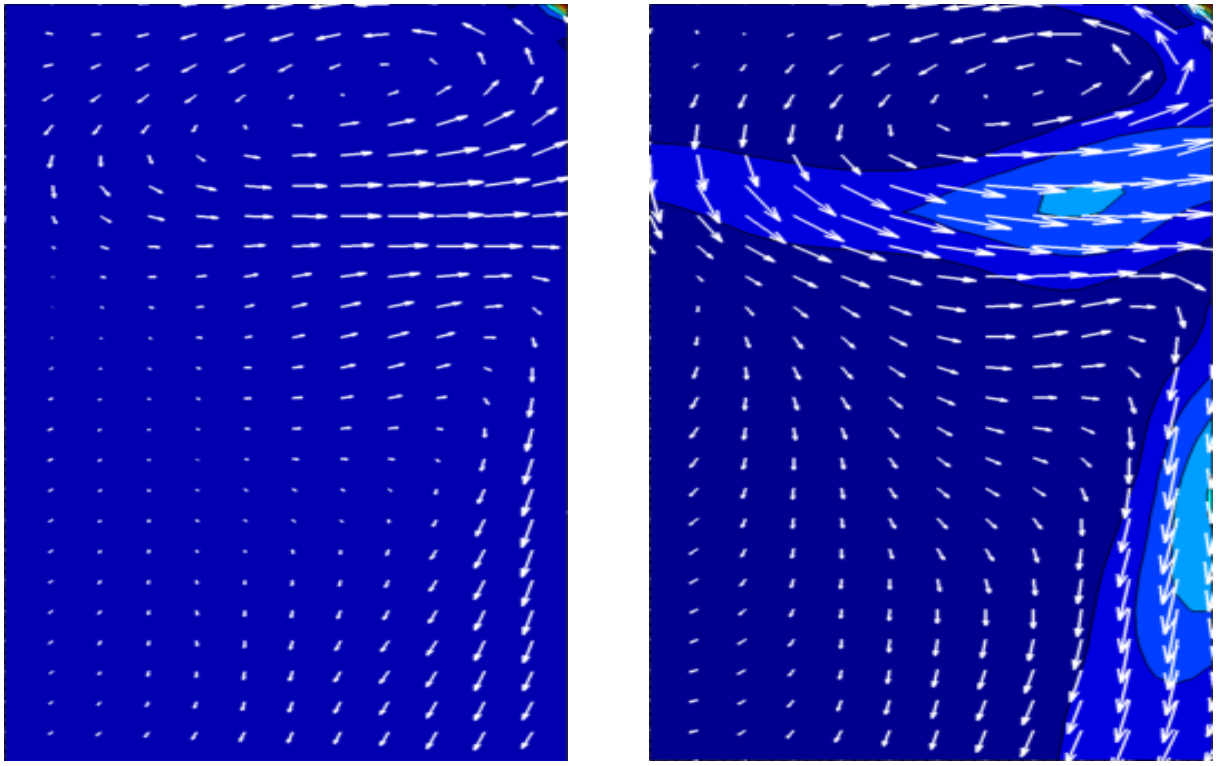

$\phi_k = 1.7108$ $\phi_k = 1.9148$

Figure 4.13 - Velocity field vector maps and non-dimensional velocity fluctuations contours for jets' kinetic energy rate ratios ϕ_k = [1.7108, 1.9148] at Reynolds 111

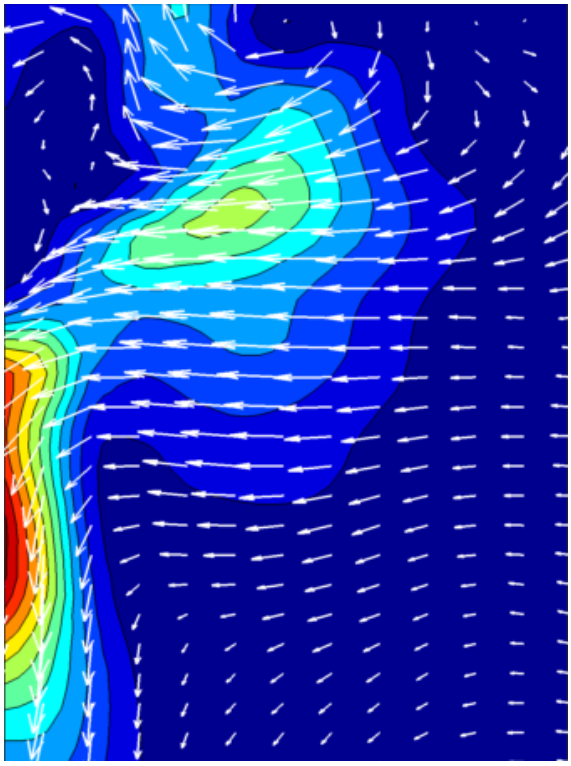

$\phi_k = 0.4362$

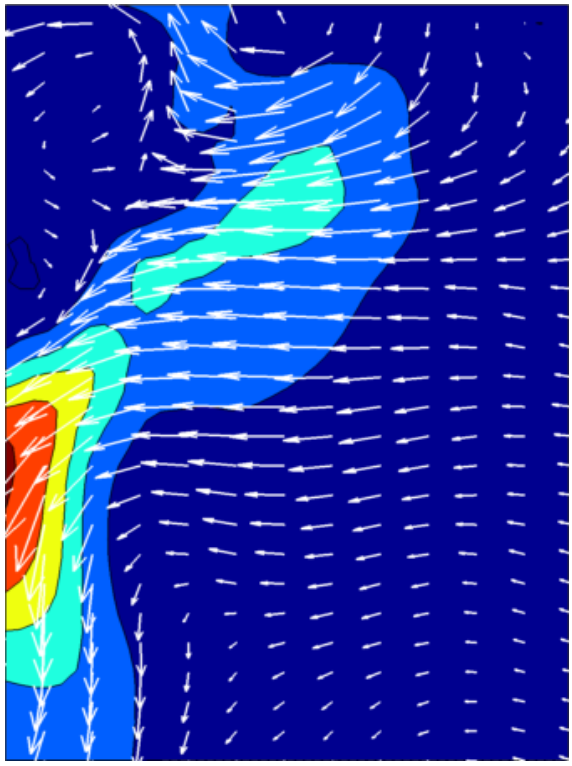

$\phi_k = 0.4914$

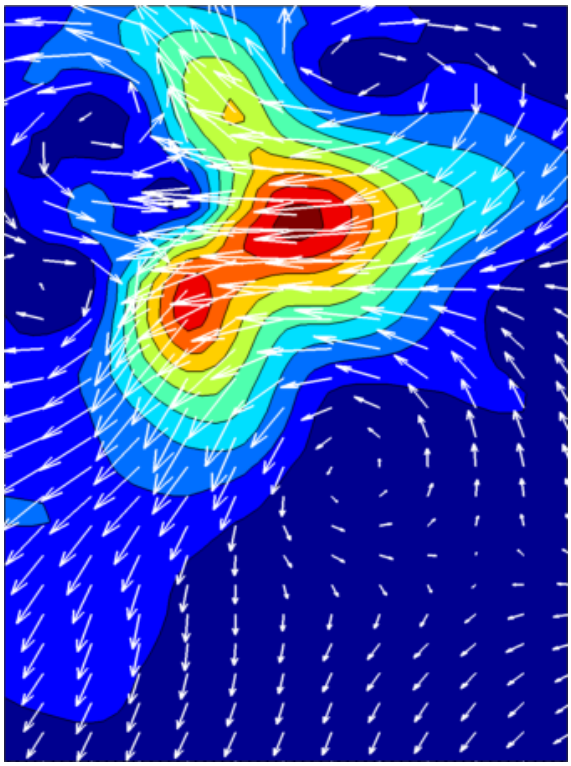

$\phi_k = 0.5353$

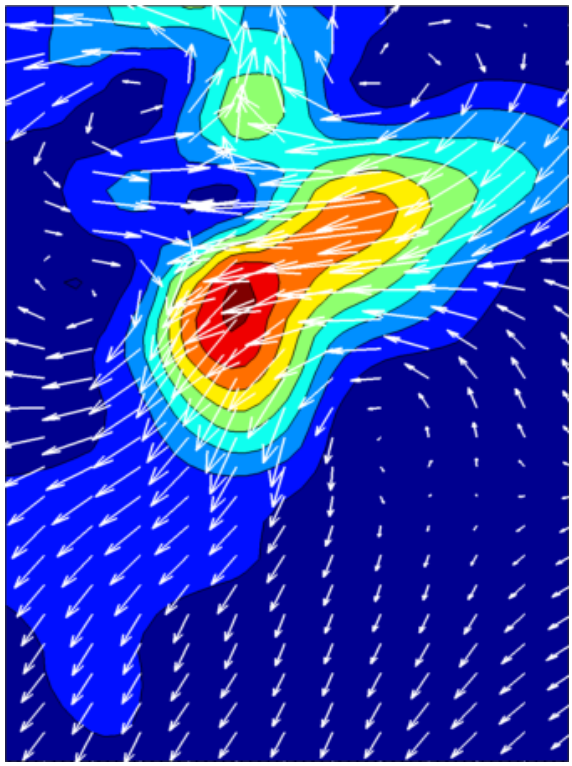

$\phi_k = 0.5842$

Figure 4.14 - Velocity field vector maps and non-dimensional velocity fluctuations contours for jets' kinetic energy rate ratios ϕ_k = [0.4362, 0.4914, 0.5353, 0.5842] at Reynolds 159

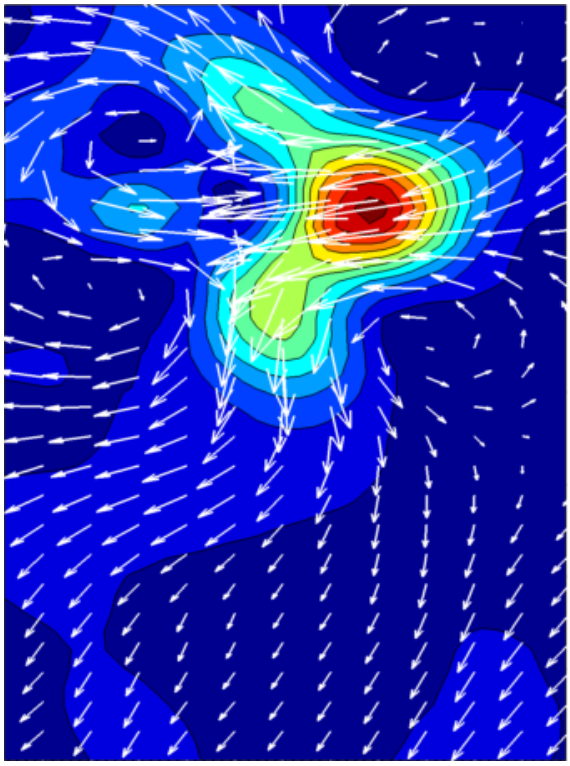

$\phi_k = 0.6851$

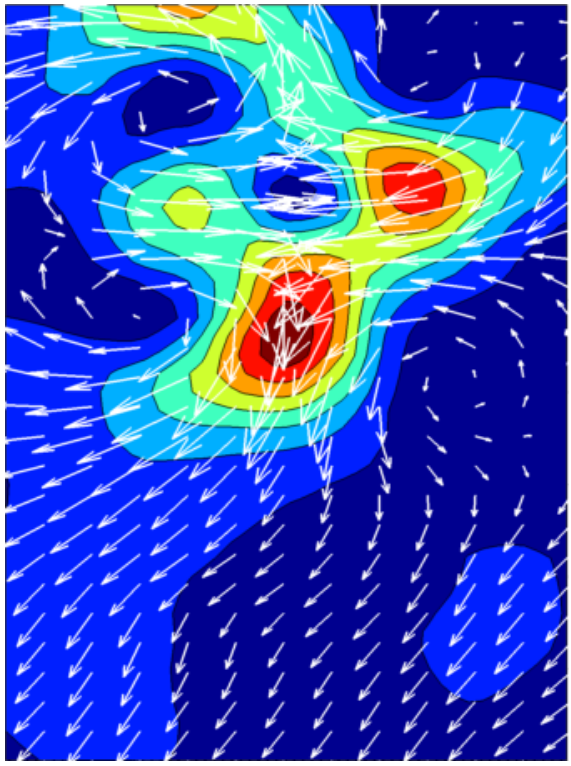

$\phi_k = 0.8136$

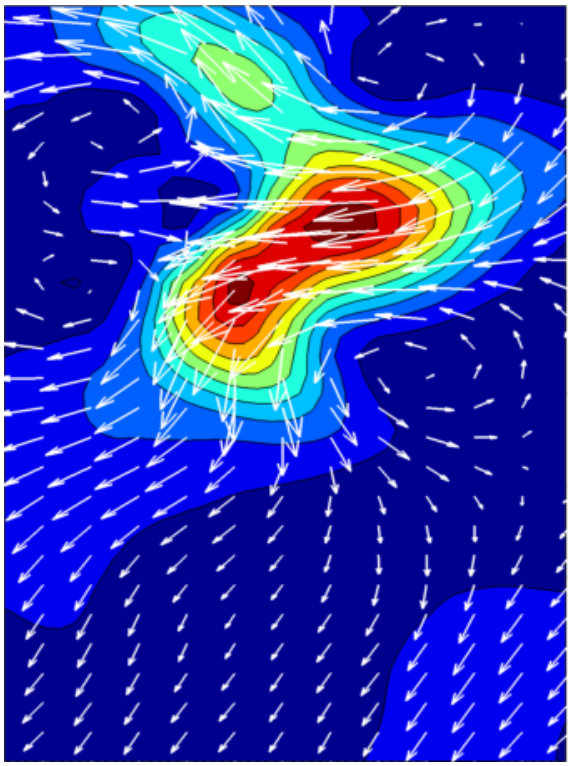

$\phi_k = 0.8528$

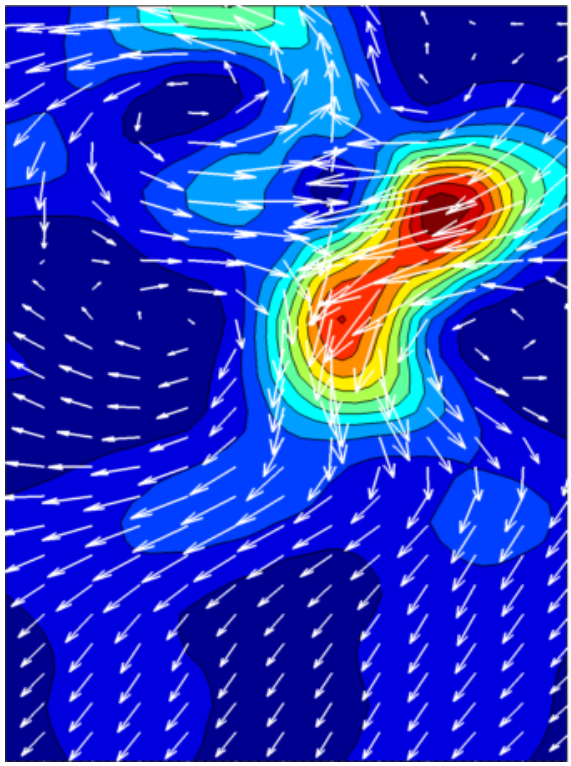

$\phi_k = 0.9291$

Figure 4.15 - Velocity field vector maps and non-dimensional velocity fluctuations contours for jets' kinetic energy rate ratios ϕ_k = [0.6851, 0.8136, 0.8528, 0.9291] at Reynolds 159

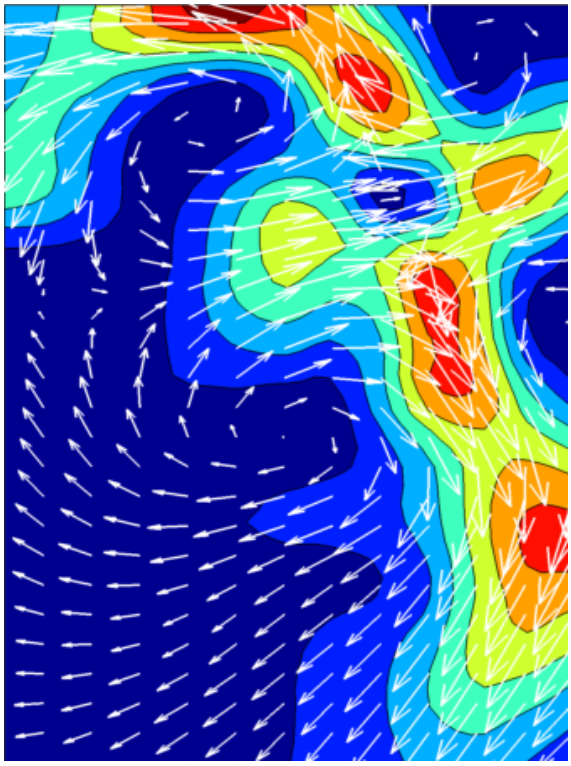

$\phi_k = 1.0300$

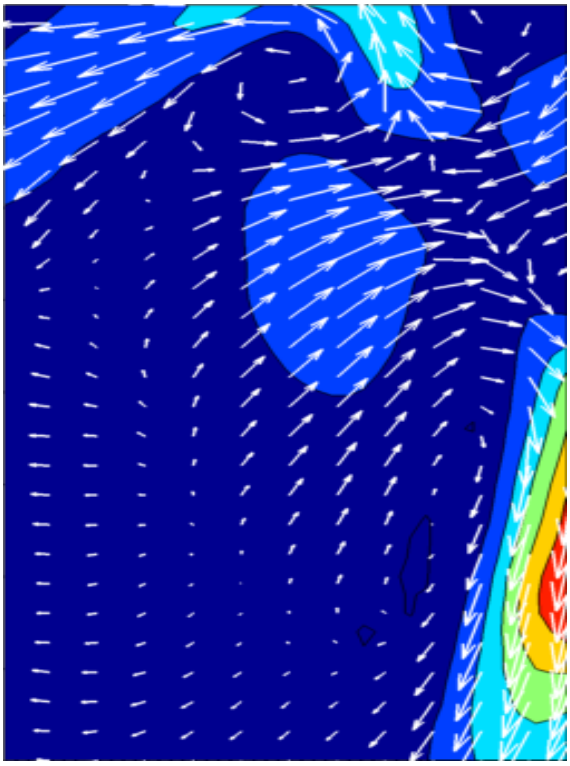

$\phi_k = 1.1645$

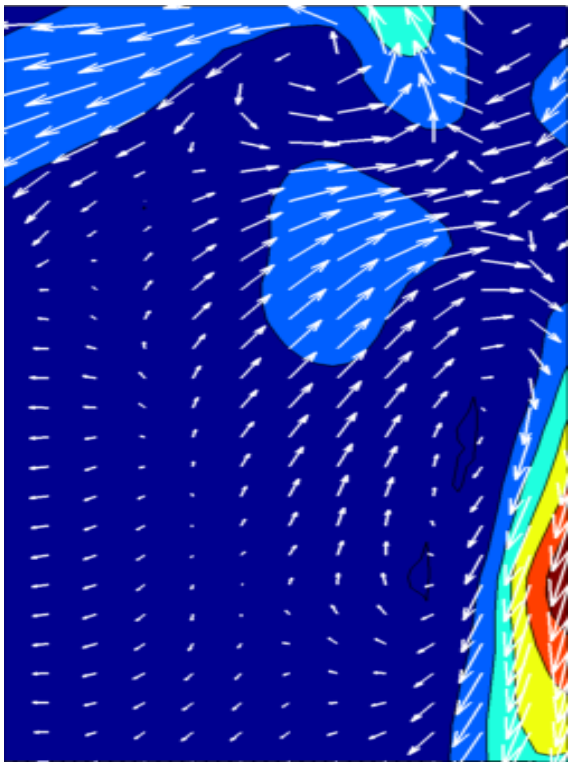

$\phi_k = 1.3170$

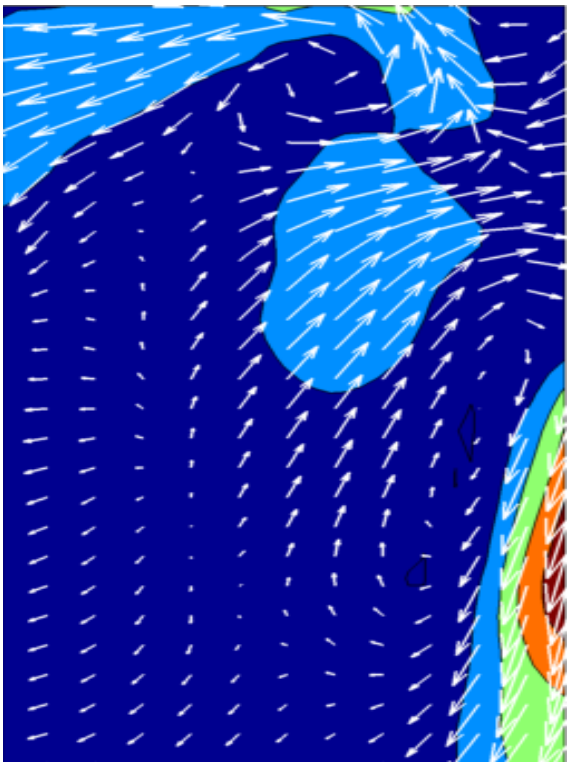

$\phi_k = 1.4438$

Figure 4.16 - Velocity field vector maps and non-dimensional velocity fluctuations contours for jets' kinetic energy rate ratios ϕ_k = [1.0300, 1.1645, 1.3170, 1.4438] at Reynolds 159

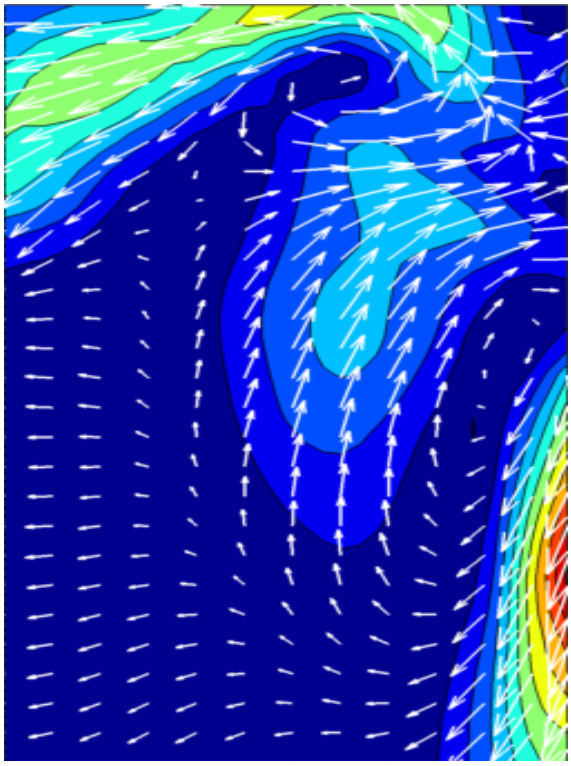

$\phi_k = 1.6544$

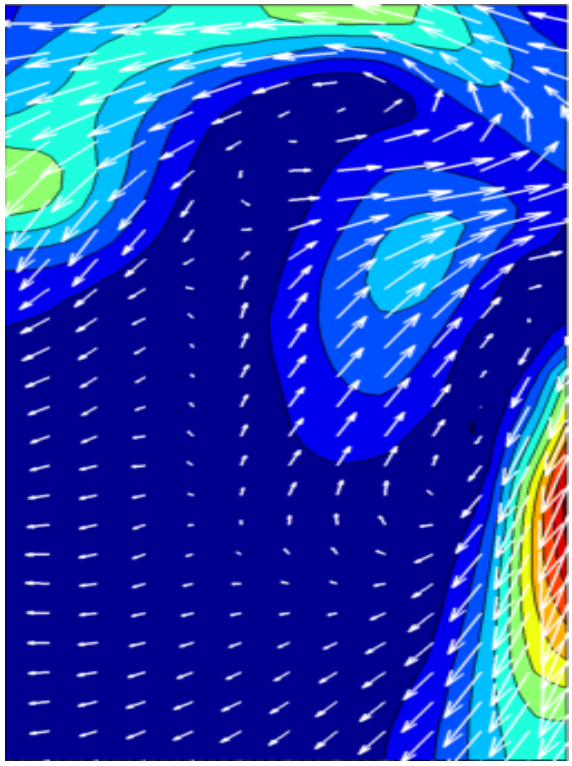

$\phi_k = 1.7219$

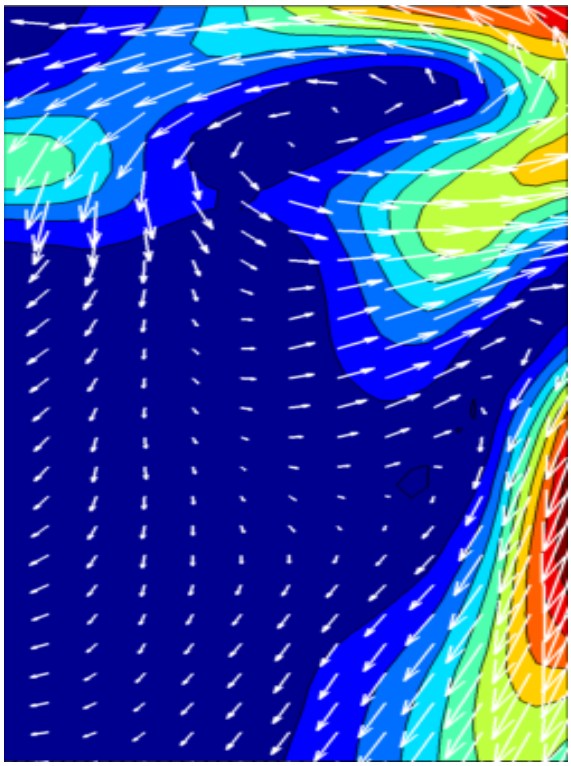

$\phi_k = 1.7849$

Figure 4.17 - Velocity field vector maps and non-dimensional velocity fluctuations contours for jets' kinetic energy rate ratios ϕ_k = [1.6544, 1.7219, 1.7849] at Reynolds 159

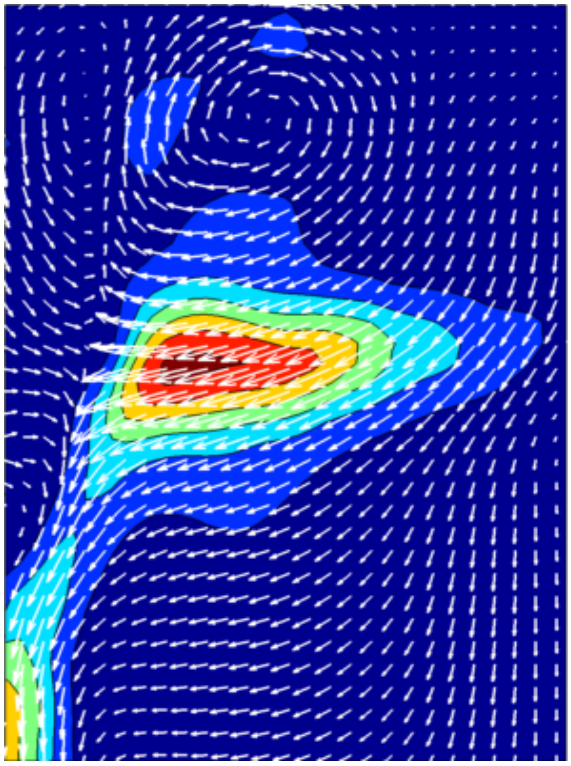

$\phi_k = 0.4201$

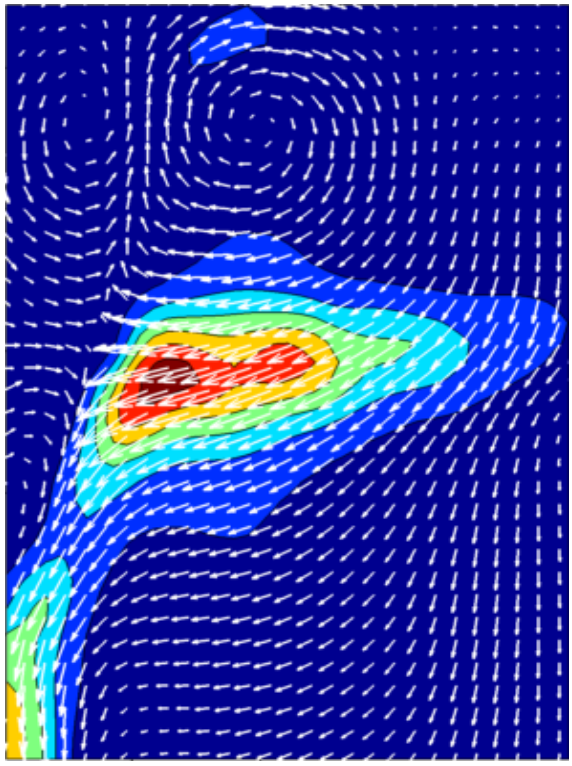

$\phi_k = 0.5154$

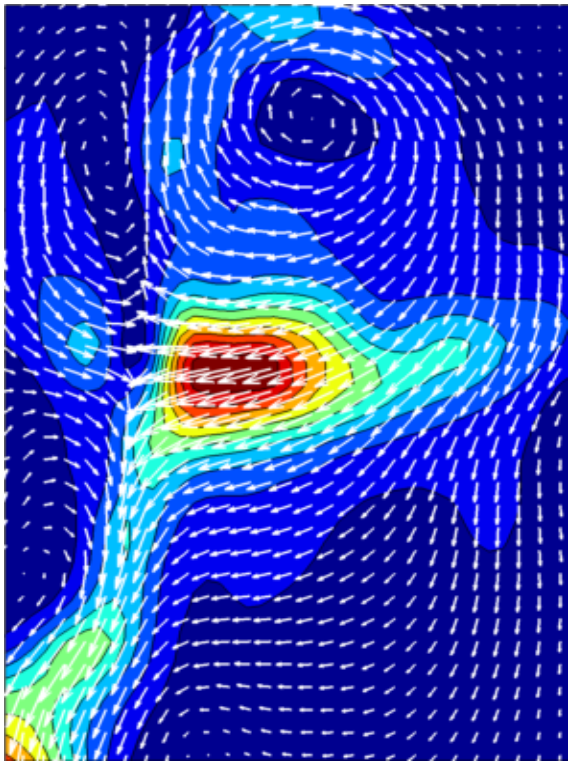

$\phi_k = 0.5300$

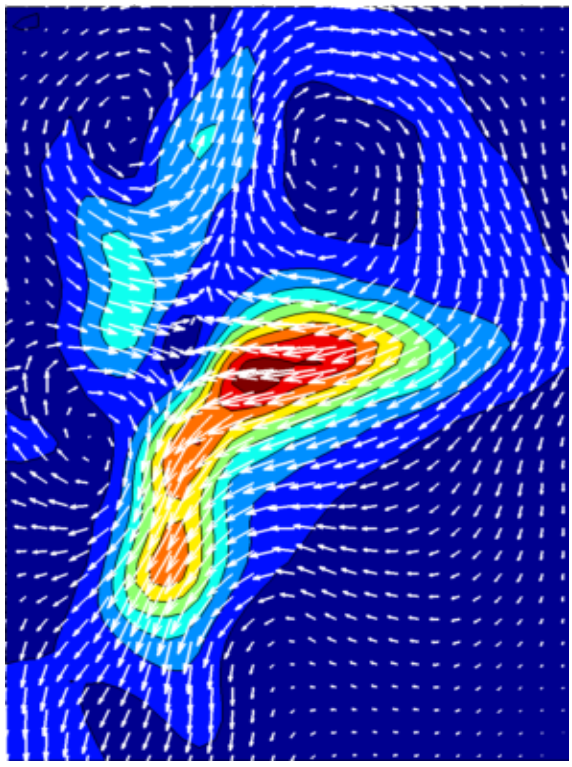

$\phi_k = 0.5517$

Figure 4.18 - Velocity field vector maps and non-dimensional velocity fluctuations contours for jets' kinetic energy rate ratios ϕ_k = [0.4201, 0.5154, 0.5300, 0.5517] at Reynolds 220

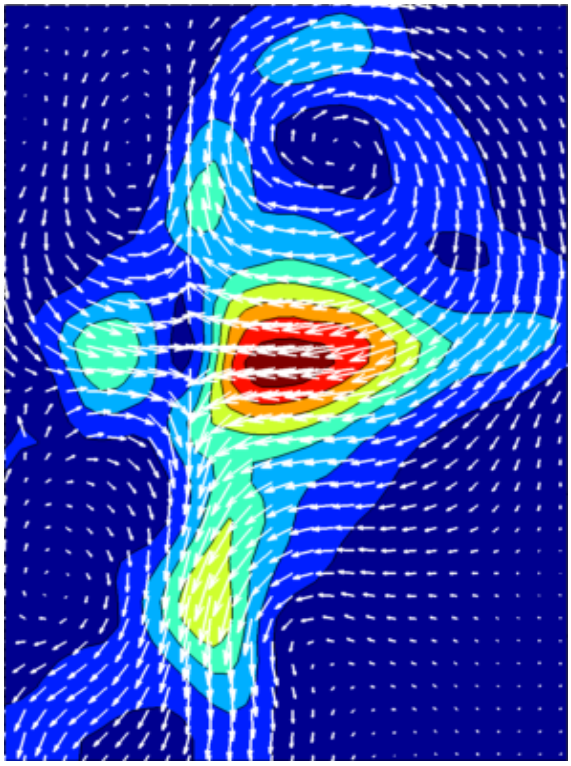

$\phi_k = 0.5877$

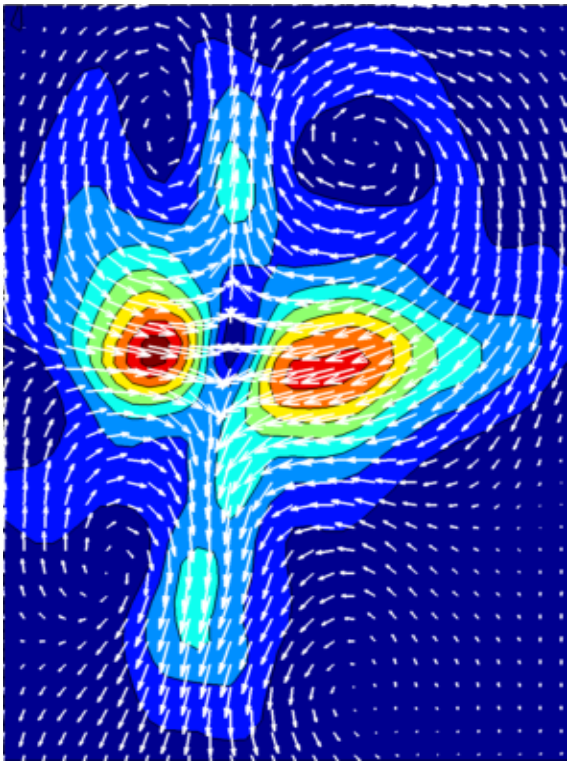

$\phi_k = 0.6925$

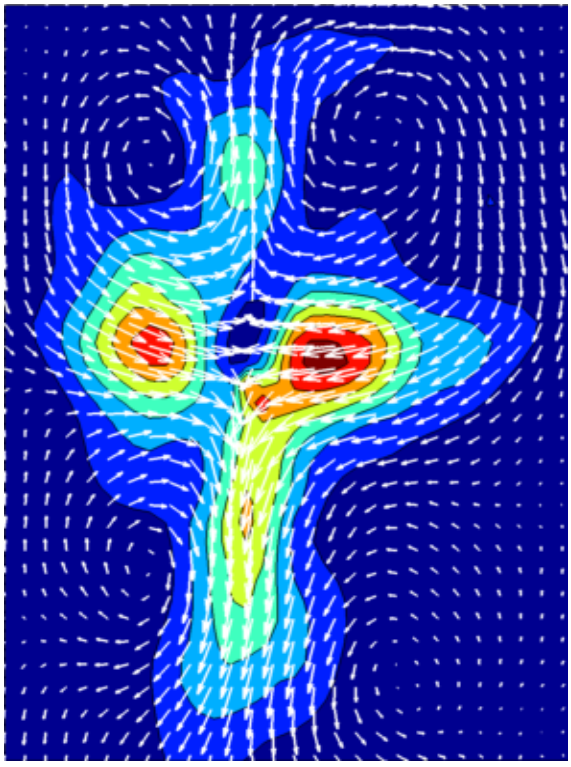

$\phi_k = 0.7333$

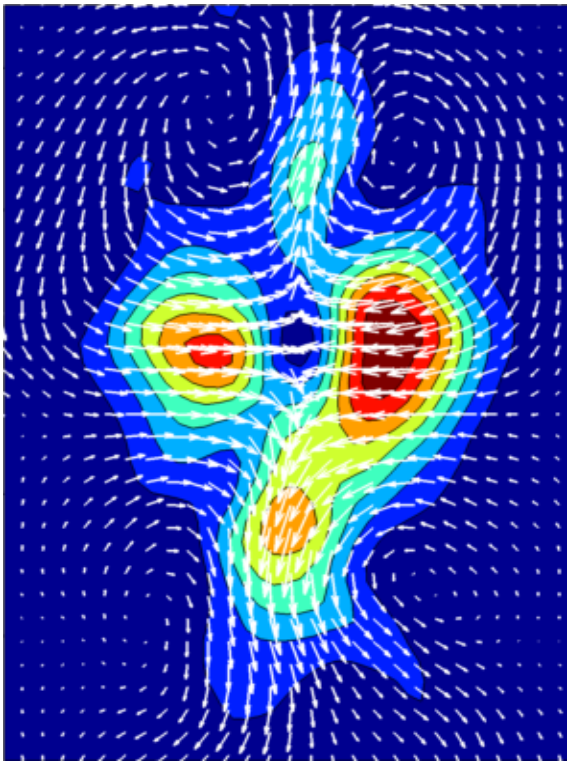

$\phi_k = 0.7704$

Figure 4.19 - Velocity field vector maps and non-dimensional velocity fluctuations contours for jets' kinetic energy rate ratios ϕ_k = [0.5877, 0.6925, 0.7333, 0.7704] at Reynolds 220

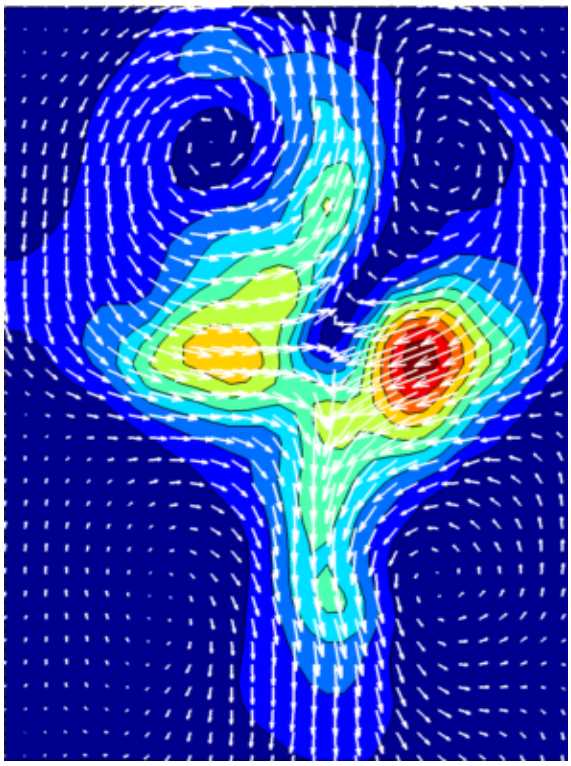

$\phi_k = 0.8126$

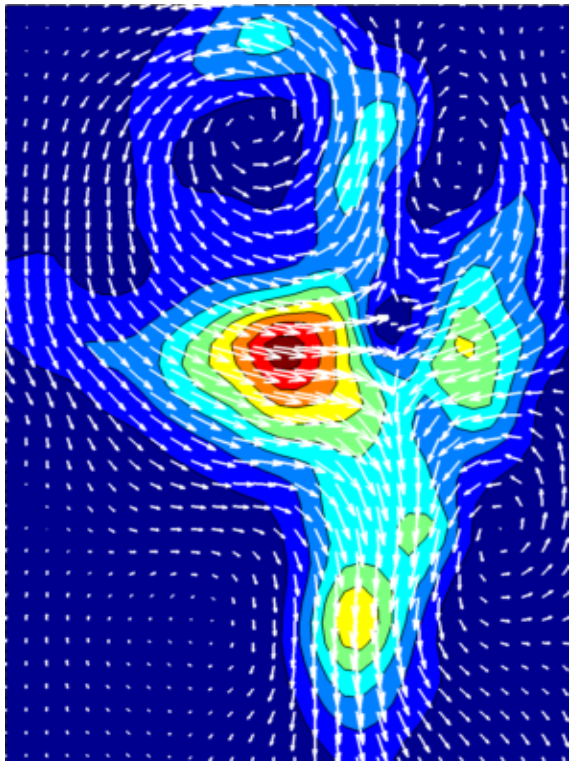

$\phi_k = 0.9023$

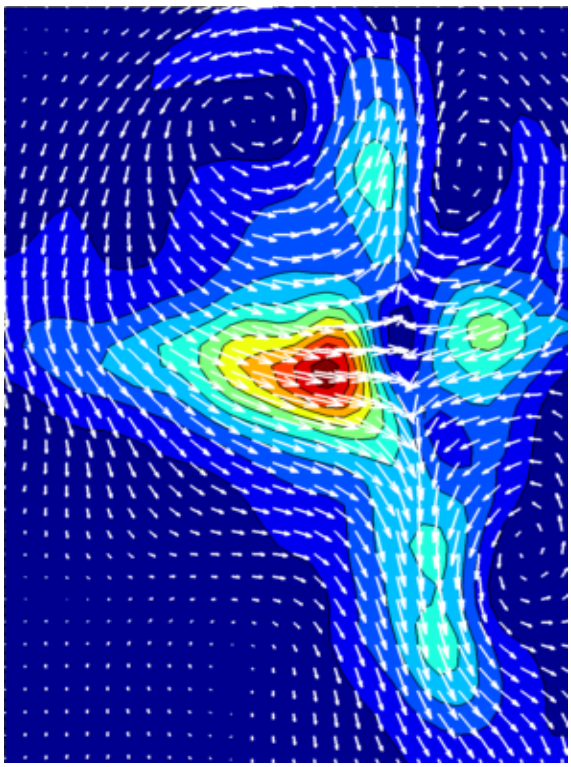

$\phi_k = 0.9537$

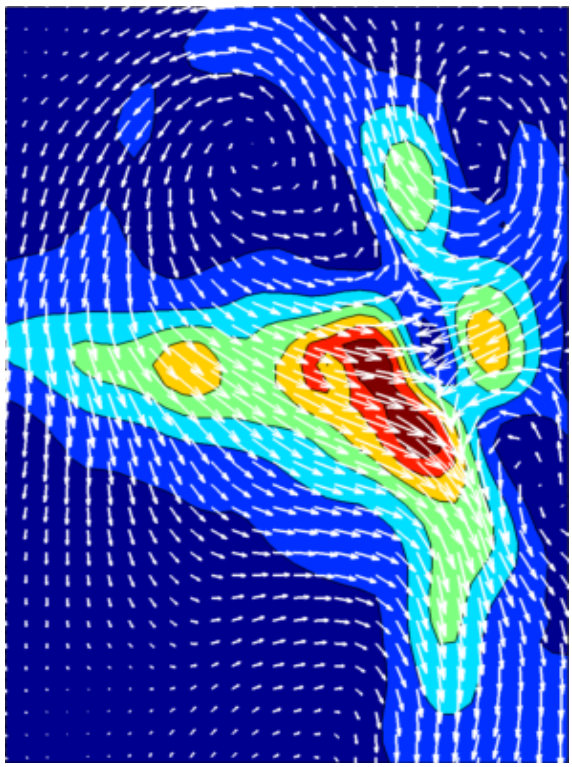

$\phi_k = 1.0729$

Figure 4.20 - Velocity field vector maps and non-dimensional velocity fluctuations contours for jets' kinetic energy rate ratios ϕ_k = [0.8126, 0.9023, 0.9537, 1.0729] at Reynolds 220

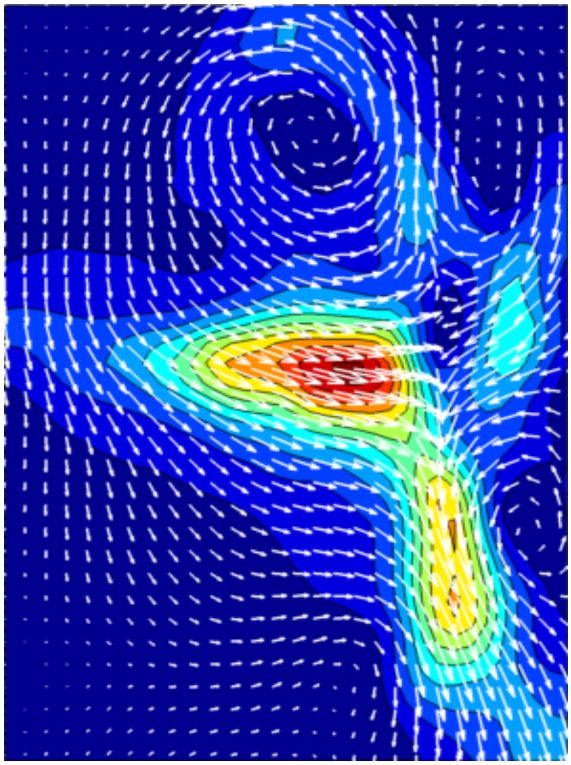

$\phi_k = 1.0899$

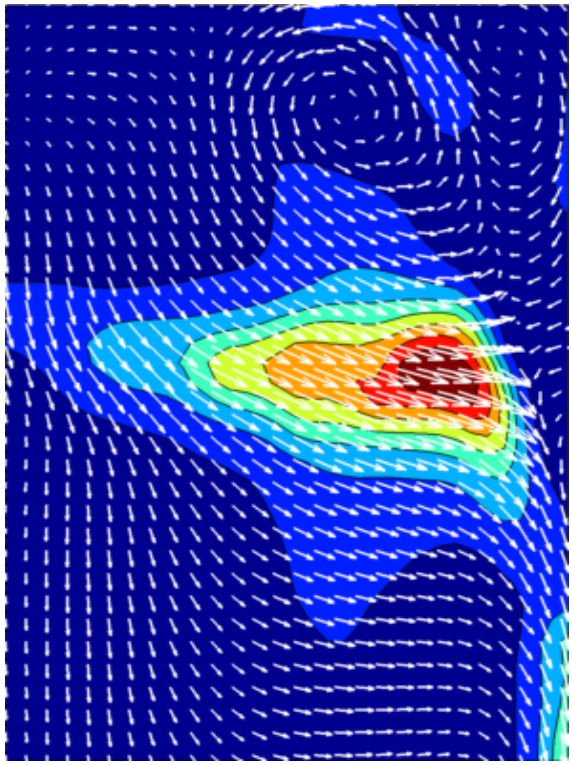

$\phi_k = 1.2069$

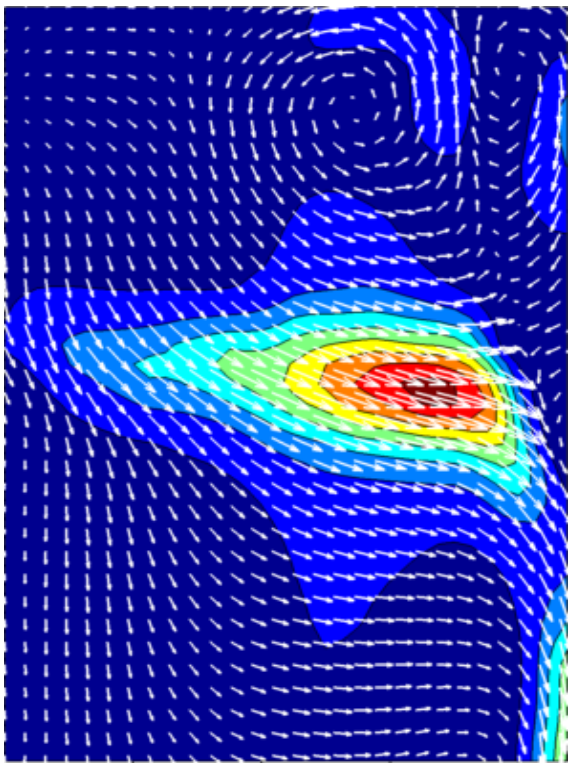

$\phi_k = 1.2496$

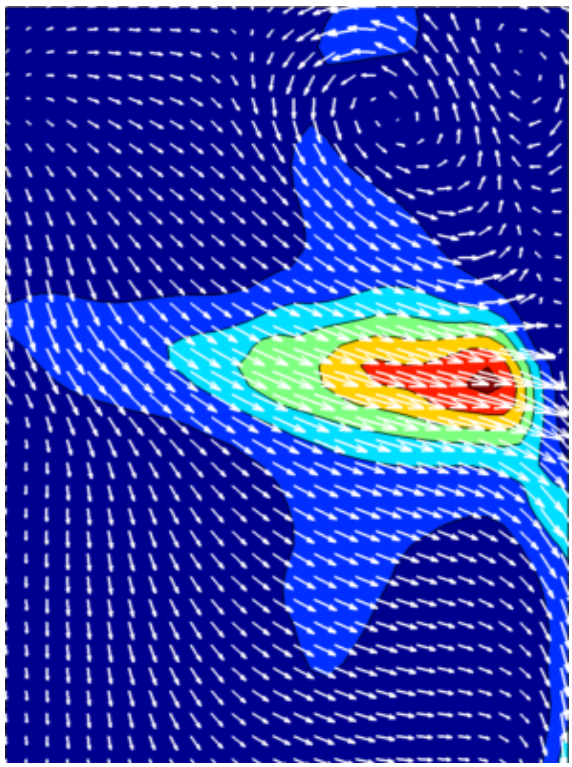

$\phi_k = 1.4791$

Figure 4.21 - Velocity field vector maps and non-dimensional velocity fluctuations contours for jets' kinetic energy rate ratios ϕ_k = [1.0899, 1.2069, 1.2496, 1.4791] at Reynolds 220

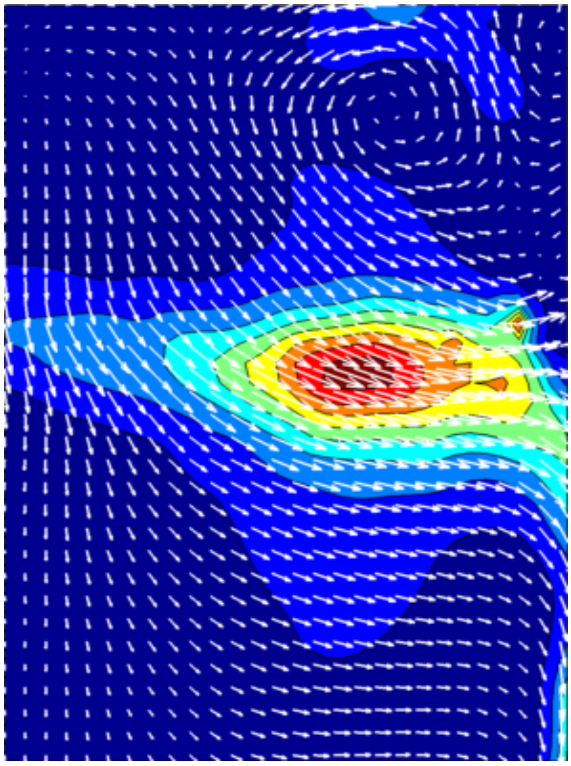

$\phi_k = 1.4855$

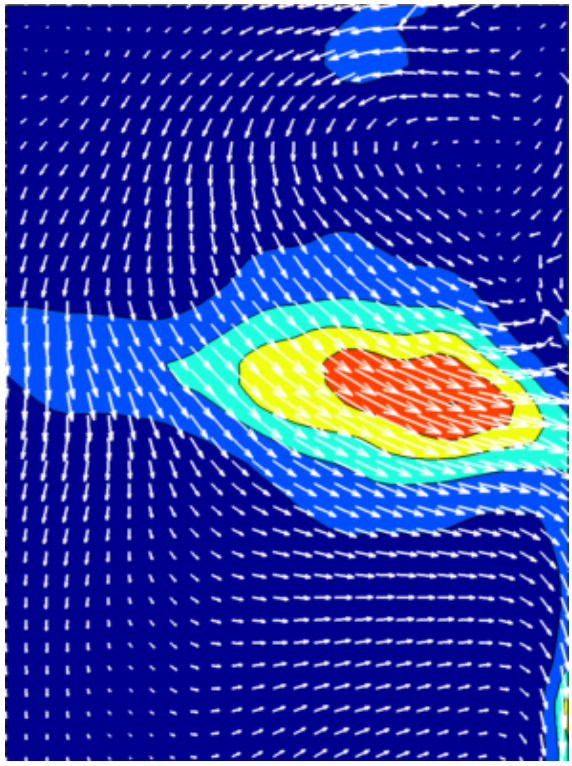

$\phi_k = 1.5350$

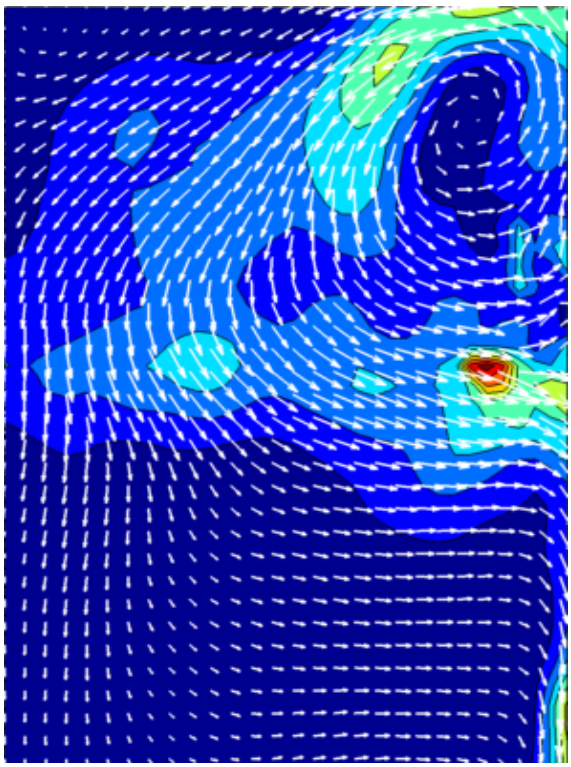

$\phi_k = 1.7452$

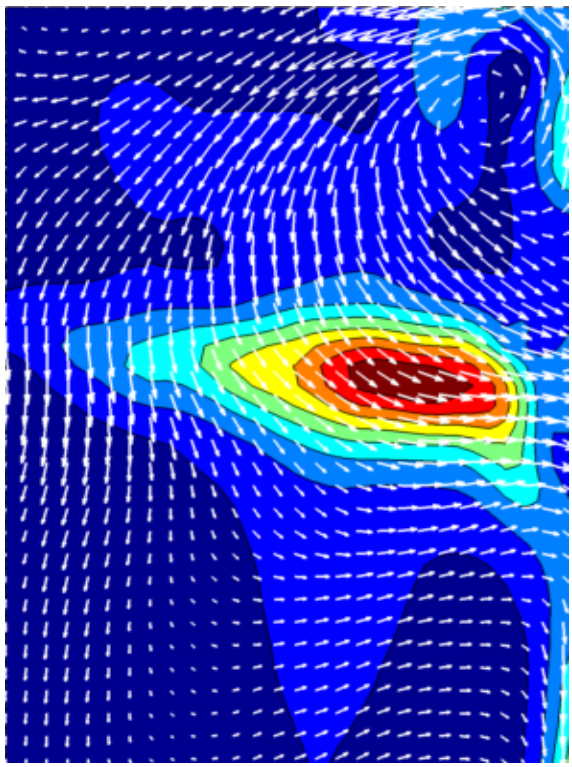

$\phi_k = 1.9899$

Figure 4.22 - Velocity field vector maps and non-dimensional velocity fluctuations contours for jets' kinetic energy rate ratios ϕ_k = [1.4855, 1.5350, 1.7452, 1.9899] at Reynolds 220

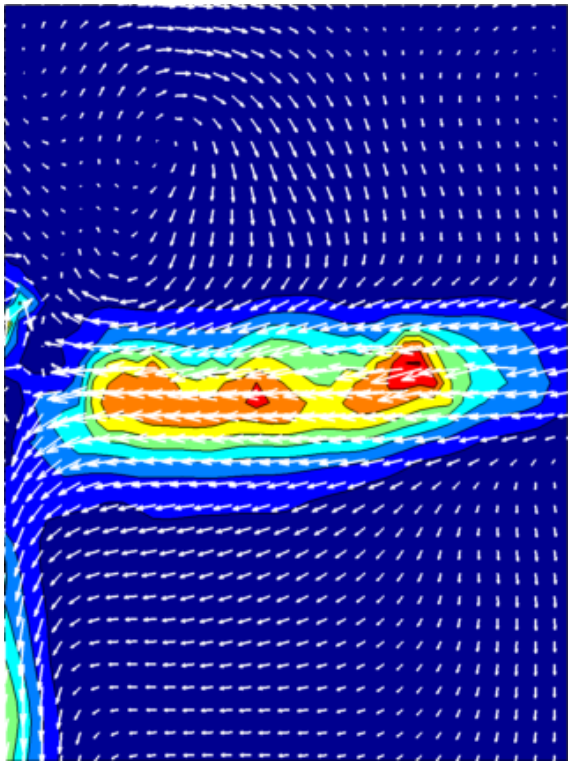

$\phi_k = 0.5634$

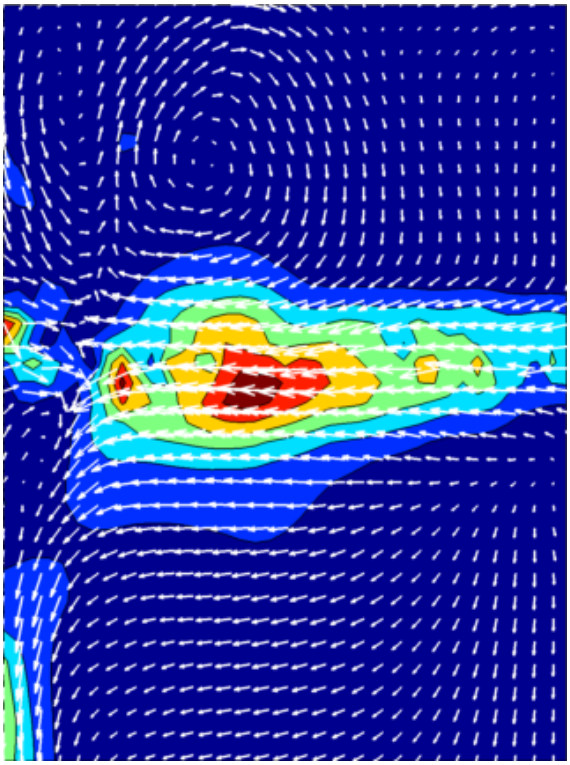

$\phi_k = 0.6439$

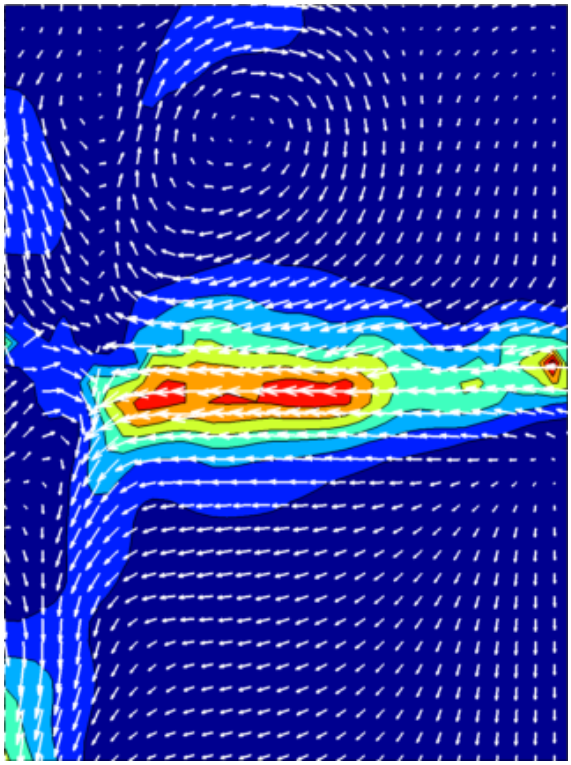

$\phi_k = 0.6509$

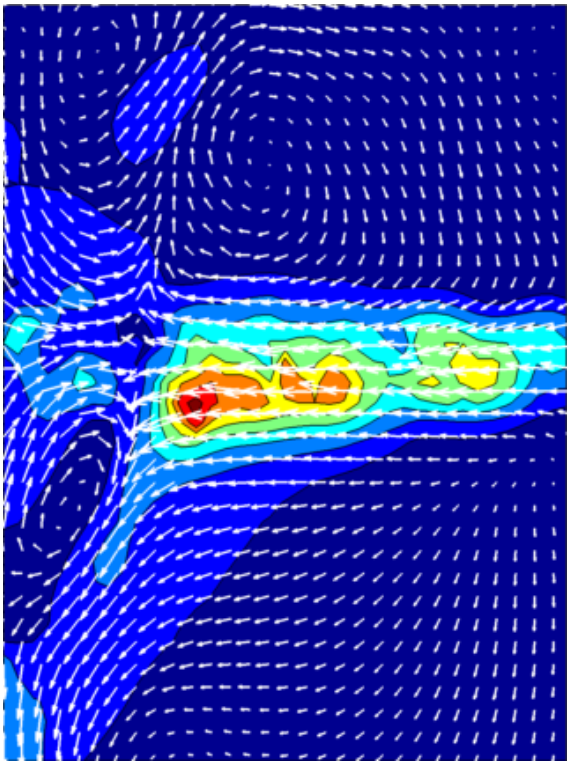

$\phi_k = 0.6704$

Figure 4.23 - Velocity field vector maps and non-dimensional velocity fluctuations contours for jets' kinetic energy rate ratios ϕ_k = [0.5634, 0.6439, 0.6509, 0.6704] at Reynolds 313

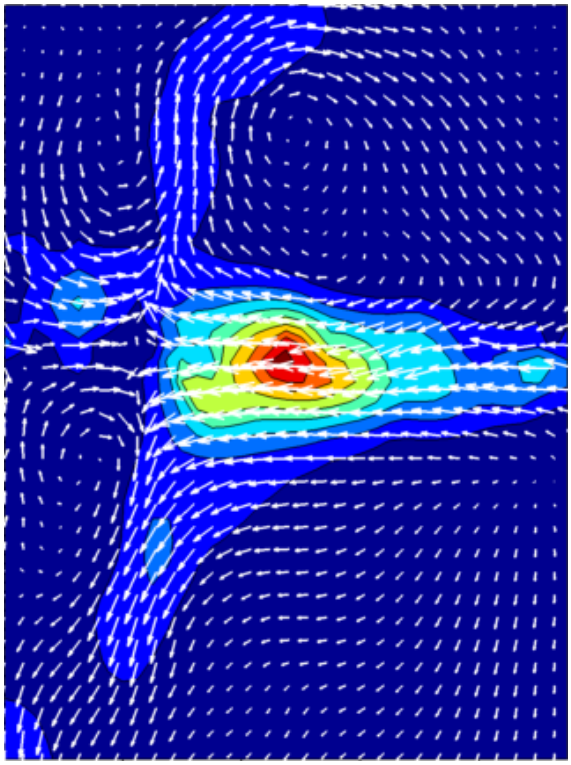

$\phi_k = 0.7141$

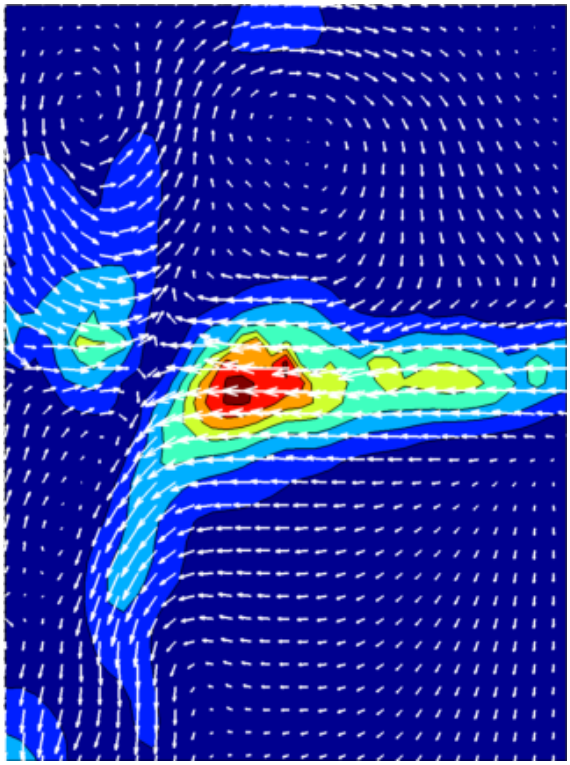

$\phi_k = 0.7169$

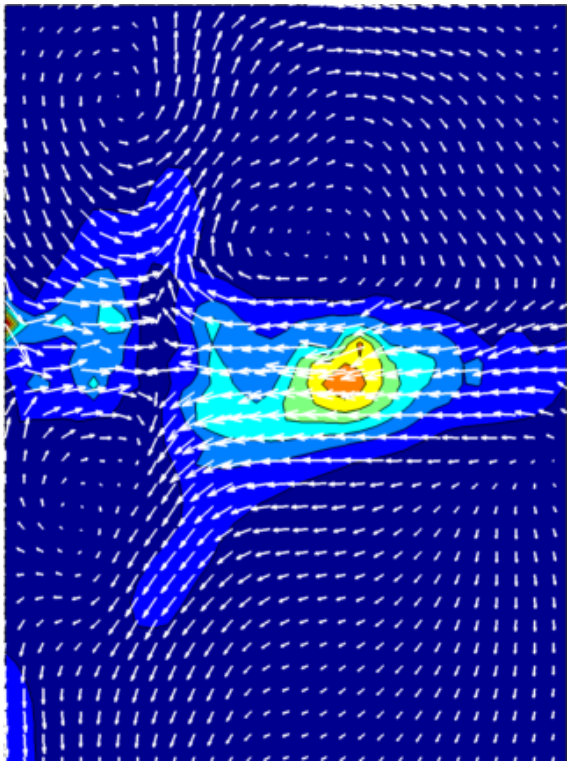

$\phi_k = 0.7660$

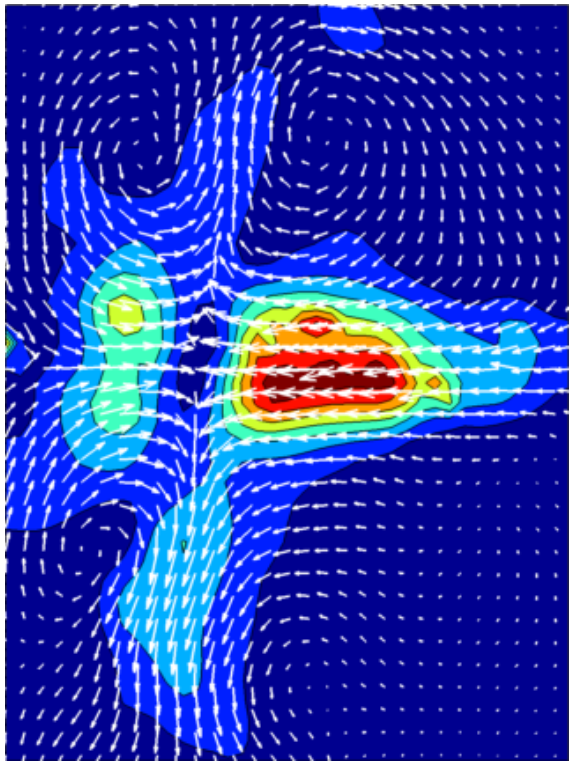

$\phi_k = 0.8258$

Figure 4.24 - Velocity field vector maps and non-dimensional velocity fluctuations contours for jets' kinetic energy rate ratios ϕ_k = [0.7141, 0.7169, 0.7660, 0.8258] at Reynolds 313

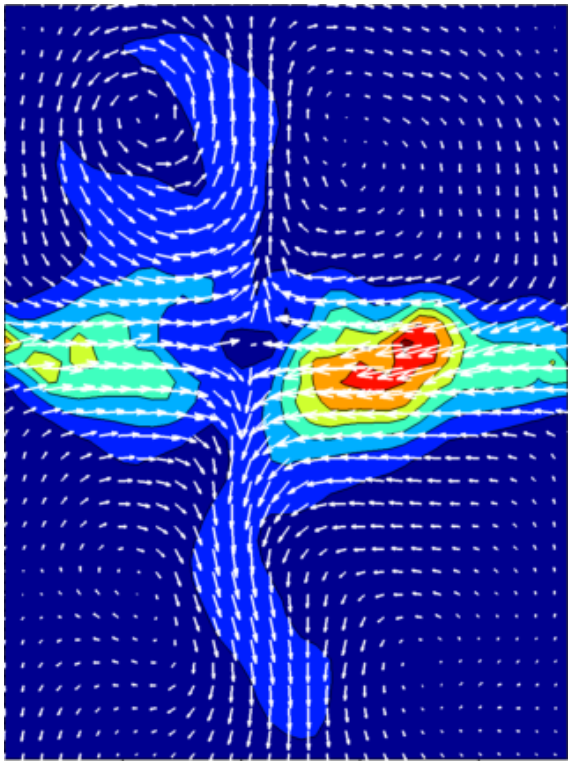

$\phi_k = 0.8754$

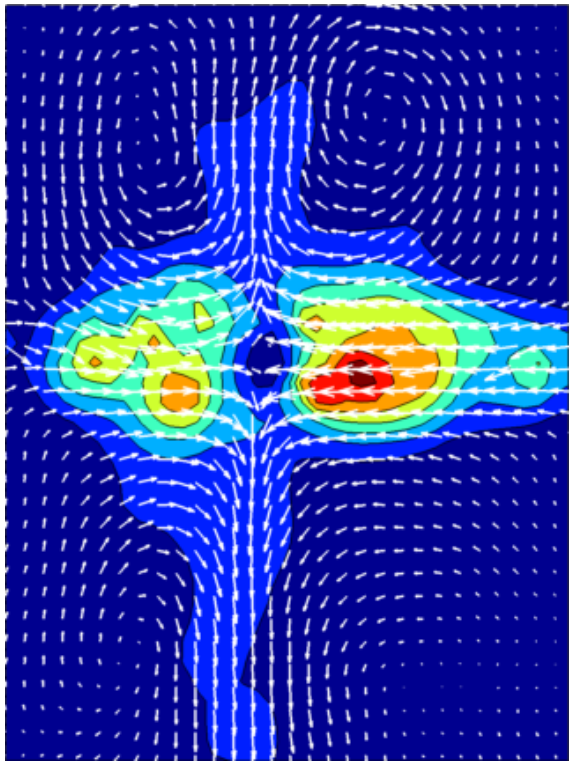

$\phi_k = 0.9001$

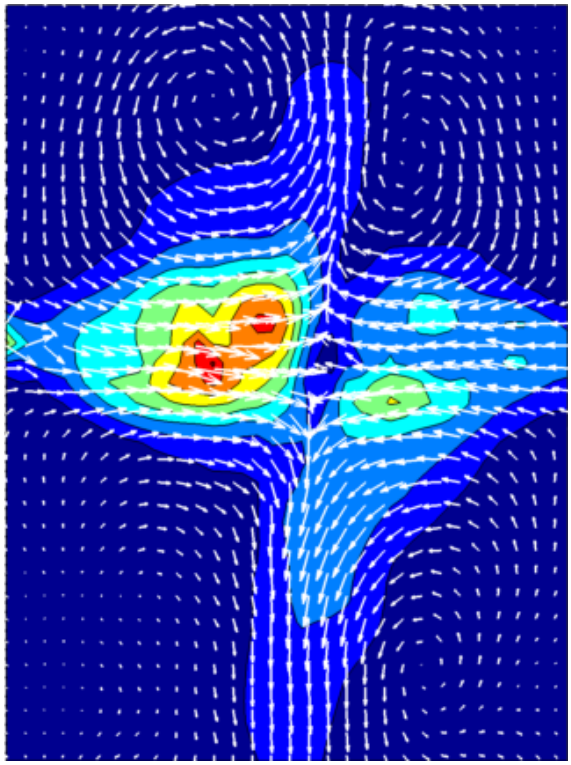

$\phi_k = 0.9770$

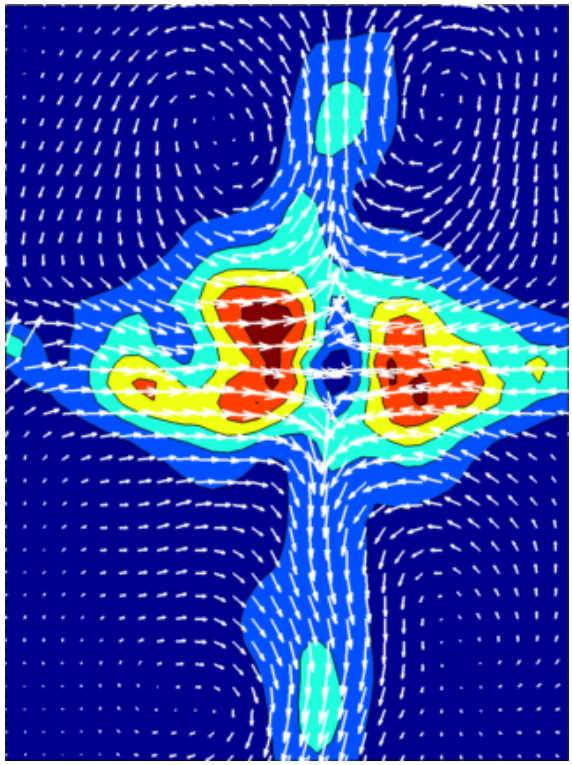

$\phi_k = 1.0046$

Figure 4.25 - Velocity field vector maps and non-dimensional velocity fluctuations contours for jets' kinetic energy rate ratios ϕ_k = [0.8754, 0.9001, 0.9770, 1.0046] at Reynolds 313

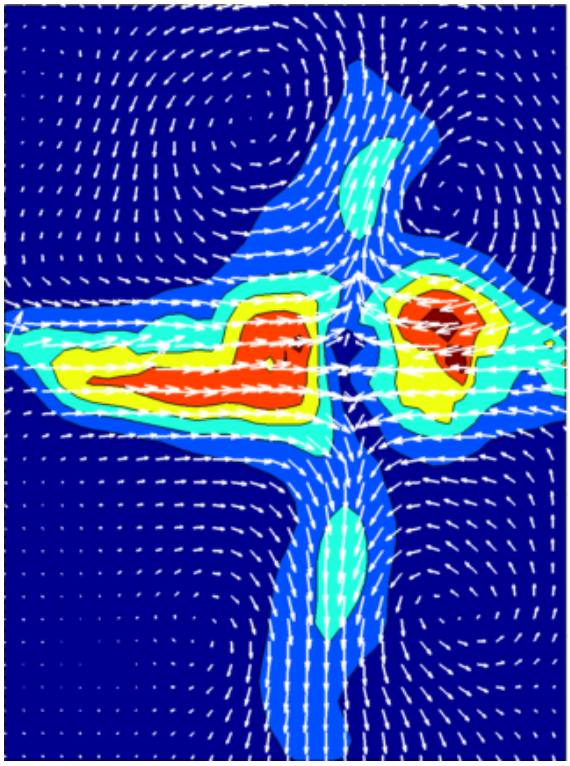

$\phi_k = 1.0529$

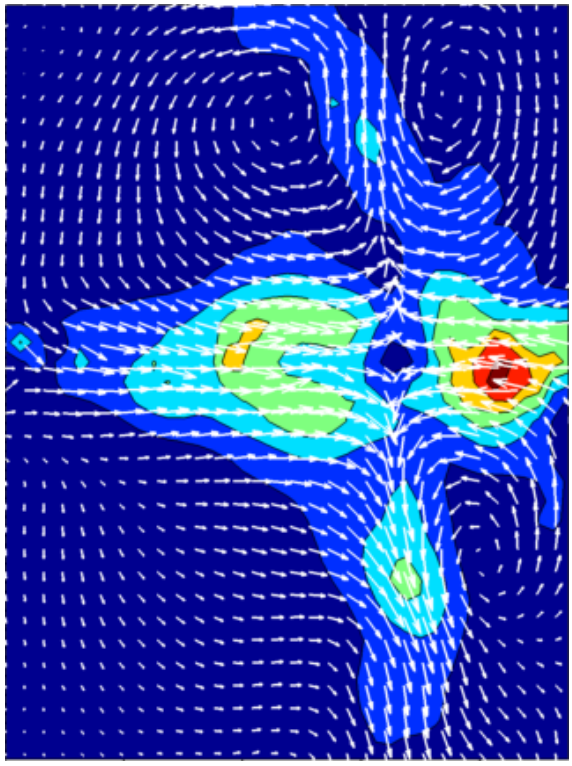

$\phi_k = 1.0974$

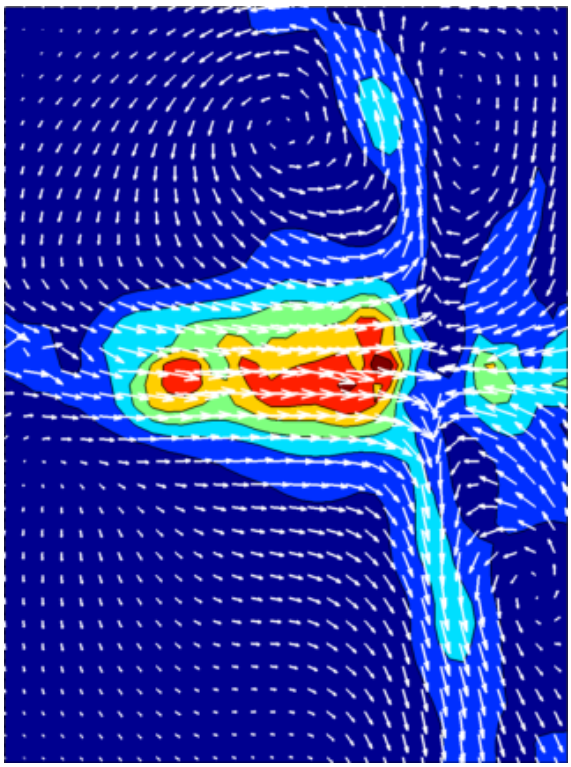

$\phi_k = 1.1339$

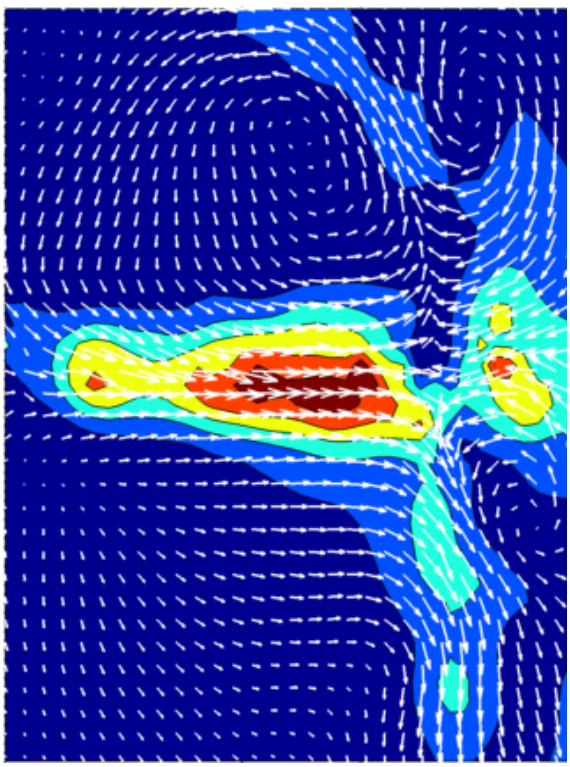

$\phi_k = 1.1929$

Figure 4.26 - Velocity field vector maps and non-dimensional velocity fluctuations contours for jets' kinetic energy rate ratios ϕ_k = [1.0529, 1.0974, 1.1339, 1.1929] at Reynolds 313

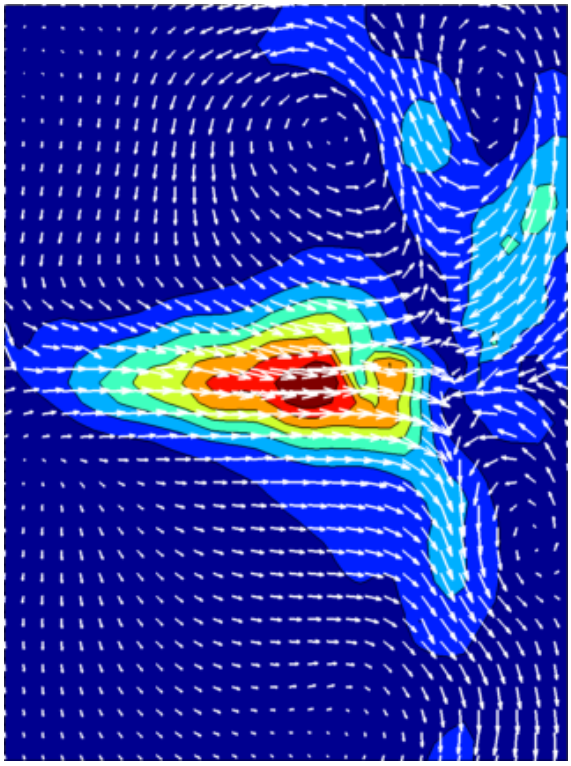

$\phi_k = 1.1621$

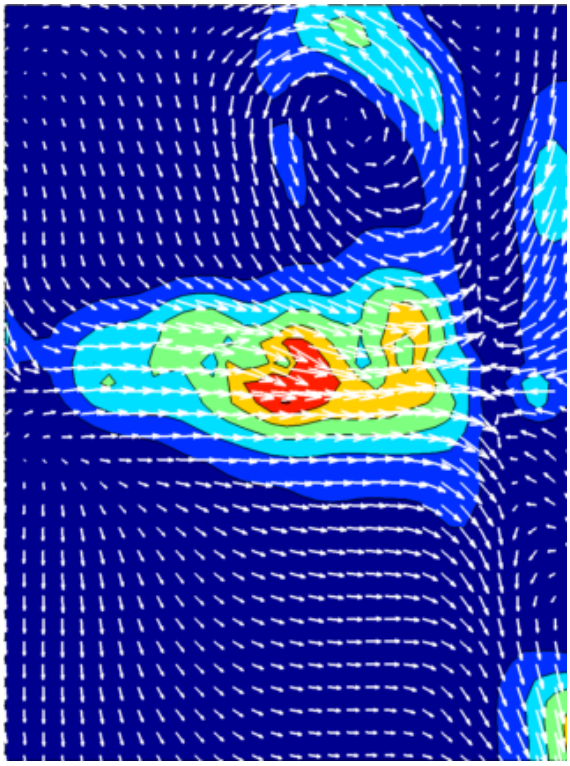

$\phi_k = 1.2989$

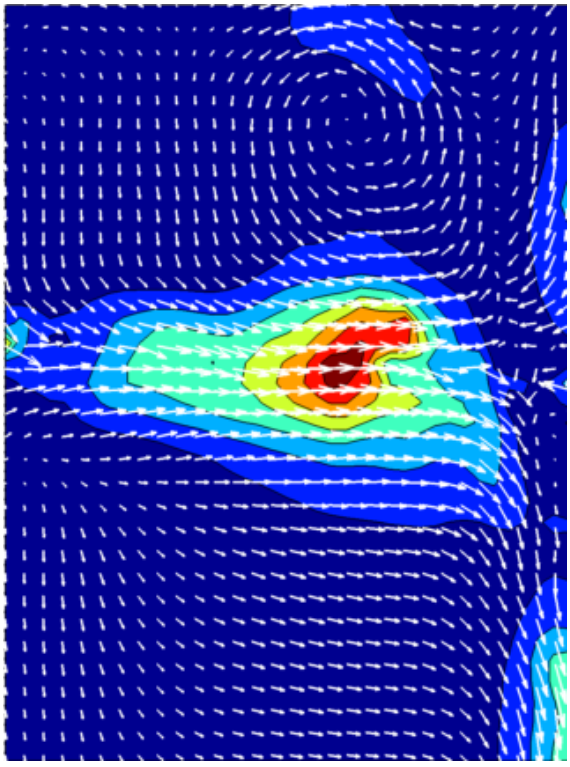

$\phi_k = 1.3310$

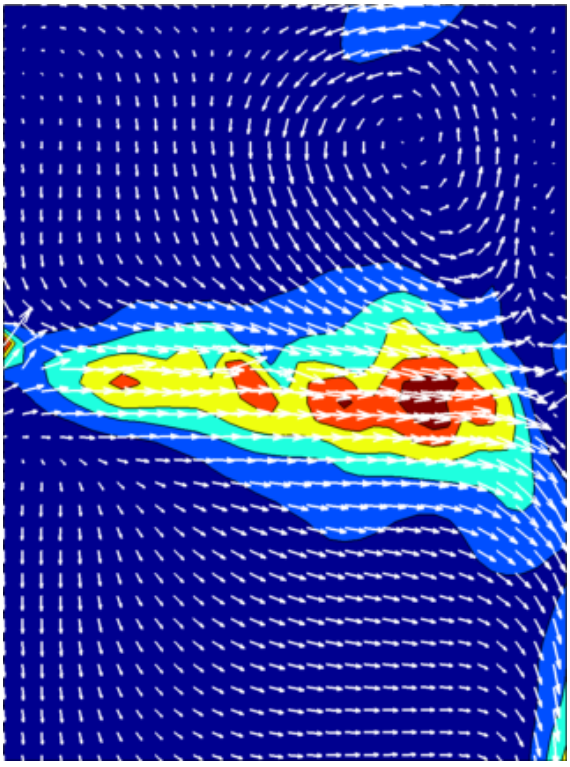

$\phi_k = 1.3626$

Figure 4.27 - Velocity field vector maps and non-dimensional velocity fluctuations contours for jets' kinetic energy rate ratios ϕ_k = [1.1621, 1.2989, 1.3310, 1.3626] at Reynolds 313

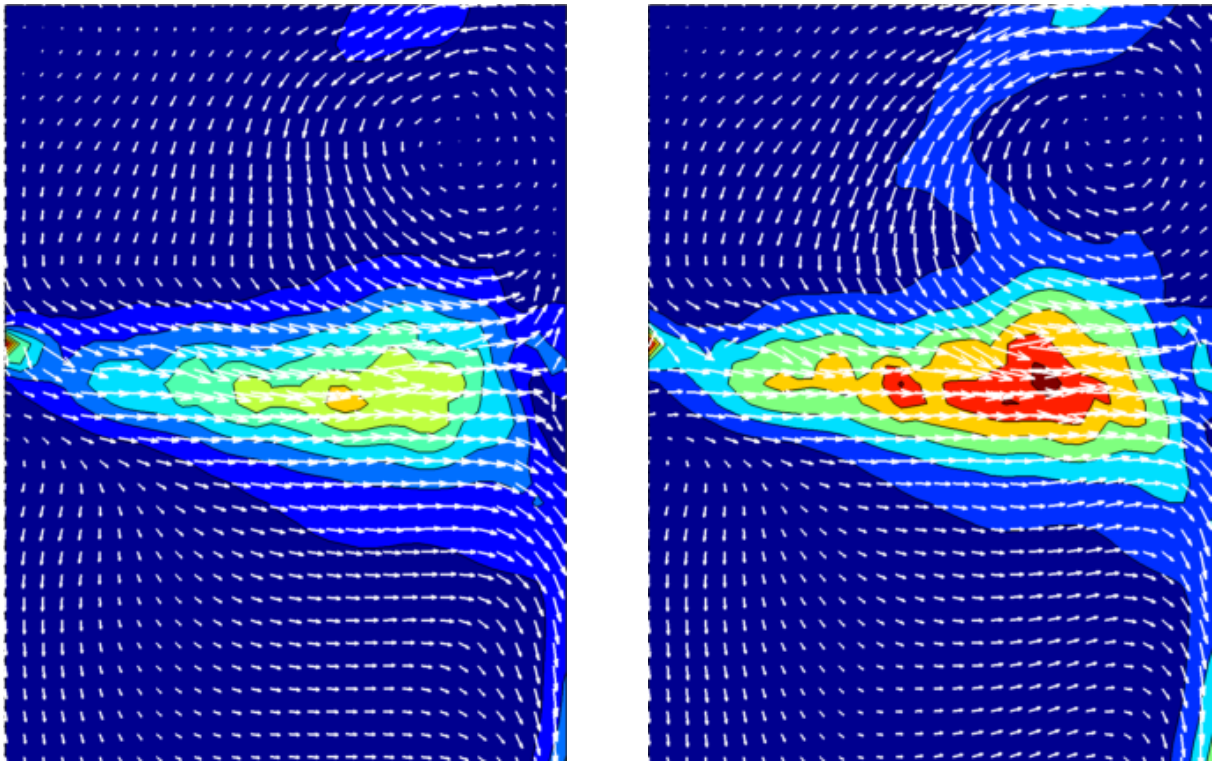

$\phi_k = 1.4389$ $\phi_k = 1.4888$

Figure 4.28 - Velocity field vector maps and non-dimensional velocity fluctuations contours for jets' kinetic energy rate ratios ϕ_k = [1.4389, 1.4388] at Reynolds 313

For the lower Reynolds studied, 45, it is observed a linear behaviour regarding the impingement point position and the kinetic rate ratio. When this value is closer to one and since the Reynolds number in study is below the critical Reynolds, then the kinetic energy variation of the velocity field is only aligned with the injectors and the spreading of the fluid downwards and upwards the jets impingement does not present such variation. From Reynolds 45 is clearly seen the four recirculation zones, one in each side of the jets streams and impingement point position. A general comment is that the largest velocity components are, as expected, in the jets streams and downwards and upwards the impingement point. Additionally, when the jets tend to one side of the chamber it is clear the attachment of the lower part of the impingement surface to the chamber walls. In this case, the flow lost all its dynamic capabilities and mixing is considered stagnated.

For Reynolds 111, it occurs a displacement of the jets alignment and therefore the image presented is in a plane not aligned with the injector's axis. Generally speaking, it is observed a region in the impingement zone where large velocity variations occur and also, when the impingement tends to dislocate to the right side of the chamber, it is observed that the main variation of the flow field is close to the chamber walls.

For Reynolds 159, the same conclusions can be drawn as the ones for Reynolds 111. Additionally, since there is more flow dynamics an additional area with high velocity variations appears. When the jets tend to the right side the fluid tends to attach to the wall and recirculate in the top of the mixing chamber.

Due to the high complexity of the flow structures for larger Reynolds number, the resolution of the PIV method was increased for the last Reynolds in study, namely 220 and 313.

For Reynolds 220 and 313, like for lower Reynolds, it is observable a high variation of the velocity fluctuations in the impingement zones, particularly aligned with the injectors and downstream and upstream the mixing chamber.

Since a greater resolution is used, it is possible to visualize that when the impingement point is close to the walls a recirculation zone appears downstream of the jets. It is this recirculation zone that acts as an attachment of the jets to the walls and destroys the oscillatory motion of the impingement surface, thus reducing the area where the impingement mixing can occur. When the jets unbalancing is 10%, the oscillatory motion of the impingement surface is completely destroyed (Santos, 2010).

4.6 Elastic model

The elastic model proposed by (Fonte, 2012) will now be briefly introduced, followed by the comparison and validation of this model with the PIV measurements performed. Although the elastic model was already validated for a simple case, in which the injectors had different diameters from each other, it was never validated for different fluid properties and for a different set of Reynolds numbers. The latter will be the focus of attention in the following sections.

4.6.1 Overview of the elastic analogue model

The elastic model aims at predicting the impingement point of two opposed jets in a RIM machine for a variety of geometries, fluid properties and operation conditions. This is accomplished by drawing a parallel between the two opposed jets and two connected springs. Consider Hooke's law for an ideal spring:

$$F = k.x \tag{4.16}$$

where F is the force of the spring, k is the rigidity constant and x the displacement of the spring. It is known that the impingement point occurs when the force of the jets balances out, so that an analogy can be done with the rigidity and displacement of one spring.

Additionally, the jet's kinetic energy with the position inside the chamber can be estimated by the simplified model of a narrow axisymmetric jet (NAJ) proposed by (Bird, Stewart, and Lightfoot 2002; White, 2006). This model neglects both the effect of the walls and the additional kinetic energy dissipation due to unsteady vortex formation and detachment in the unsteady chaotic regime.

Fonte (2012) coupled the NAJ model with the elastic analogue model of impingement jets. The spring length, analogue to the jets length, to a certain point source until the impingement point position, x_{IP}, is defined as

$$\begin{cases} l_1 = \dfrac{D}{2} + x_{IP} + l_1' \\ l_2 = \dfrac{D}{2} - x_{IP} + l_2' \end{cases} \tag{4.17}$$

where l is the total spring length and l' is the distance to the source point momentum. Applying the NAJ model gives

$$\frac{\frac{D}{2} + x_{IP} + l_1'}{\frac{D}{2} - x_{IP} + l_2'} = \sqrt{\phi_K \frac{Re_1}{Re_2} \frac{d_1}{d_2}} \tag{4.18}$$

The previous equation can be transformed in order to calculate the impingement point position $\left(\text{in its non-dimensional given by } \chi^* = \frac{x_{IP}}{D/2}\right)$, yielding

$$\boldsymbol{\chi^* = \frac{\left(\frac{Re_2}{10}\frac{d_2}{D} + 1\right)\sqrt{\phi_K \frac{Re_1}{Re_2}\frac{d_1}{d_2}} - \left(\frac{Re_1}{10}\frac{d_1}{D} + 1\right)}{\sqrt{\phi_K \frac{Re_1}{Re_2}} + 1}} \tag{4.19}$$

This equation is constrained by the chamber wall, which bounds all the mixing mechanisms, and is only valid for $|\chi^*| \leq 1$.

To validate Equation 4.19, Fonte (2012) carried out CFD simulations and PIV measurements with the same working fluid used in this work, but only for different injectors' diameter ratio and for a constant Reynolds number below the critical value, meaning there were no jets oscillations that could cause the impingement point position to fluctuate. The specific

objective of (Fonte, 2012) work was to study the optimal operating conditions for when the stoichiometric ratios between both fluids are different, which can be achieved by adjusting the injectors' diameters to guarantee that the impingement point position lies on the centre of the mixing chamber.

The focus of this work is the validation of the elastic analogue model for a wider range of working Reynolds numbers, considering the same working fluids and the same injector diameter employed by (Fonte, 2012). This was performed using the PIV technique described in section 4.4 to obtain the experimental data against which the model will be compared. The results will be presented as a function of the main process parameters defined in section 4.2, namely the flow rate ratio, the momentum rate ratio and the kinetic energy rate ratio, for Reynolds 45, 111, 159, 220 and 313.

4.6.2 Flow rate ratio

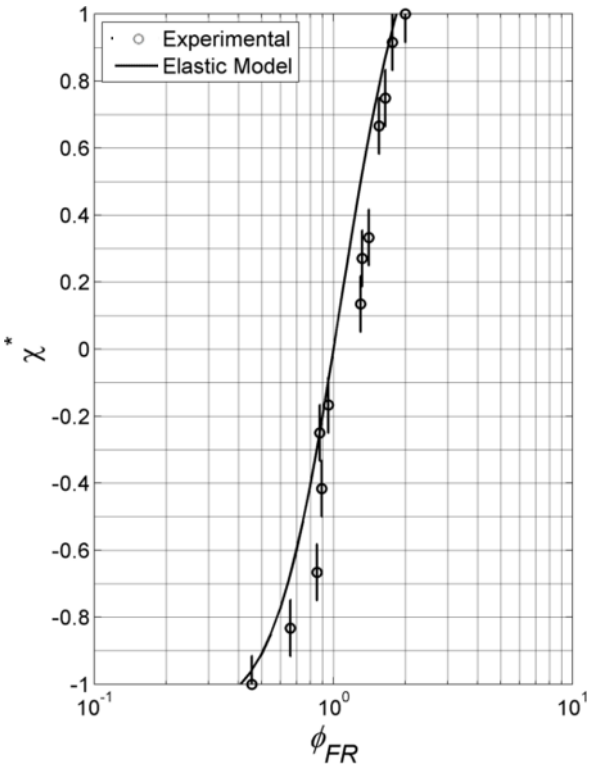

Figure 4.29 - $\chi^*_{exp}(\phi_{FR})$ vs $\chi^*_{model}(\phi_{FR})$ for Re = 45

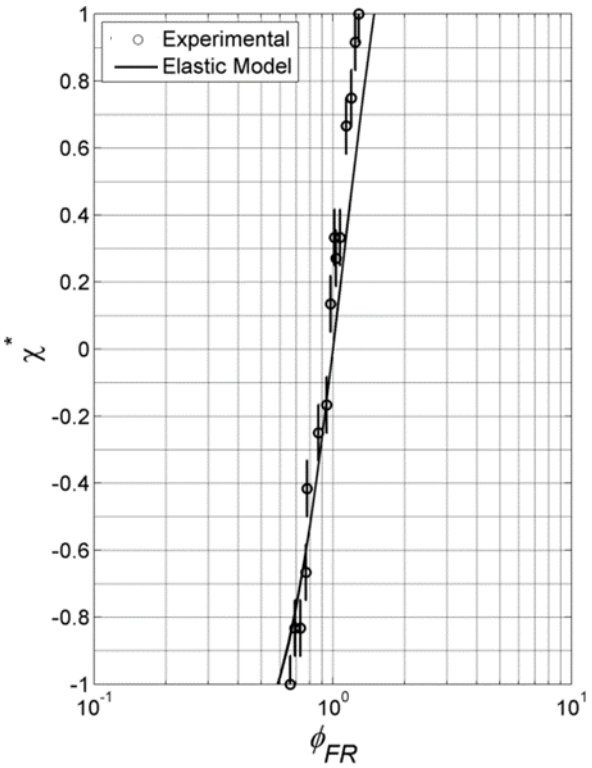

Figure 4.30 - $\chi^*_{exp}(\phi_{FR})$ vs $\chi^*_{model}(\phi_{FR})$ for Re = 111

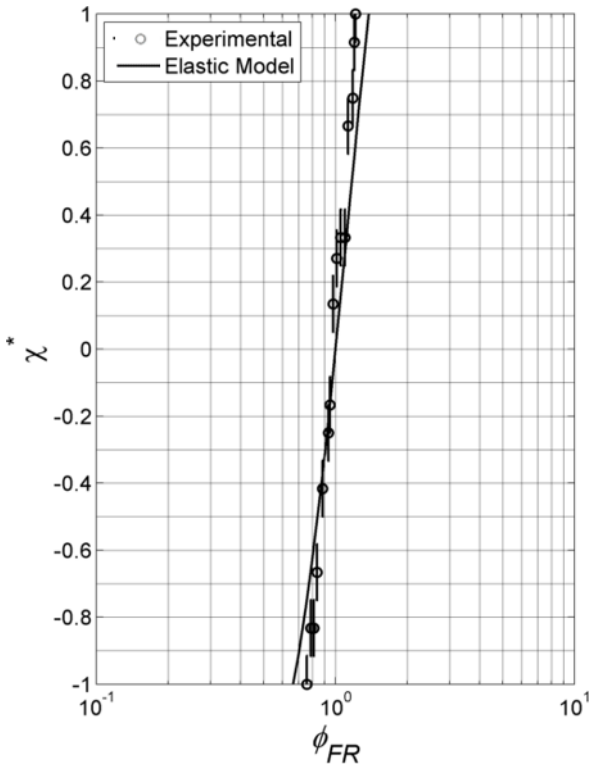

Figure 4.31 - $\chi^*_{exp}(\phi_{FR})$ vs $\chi^*_{model}(\phi_{FR})$ for Re = 159

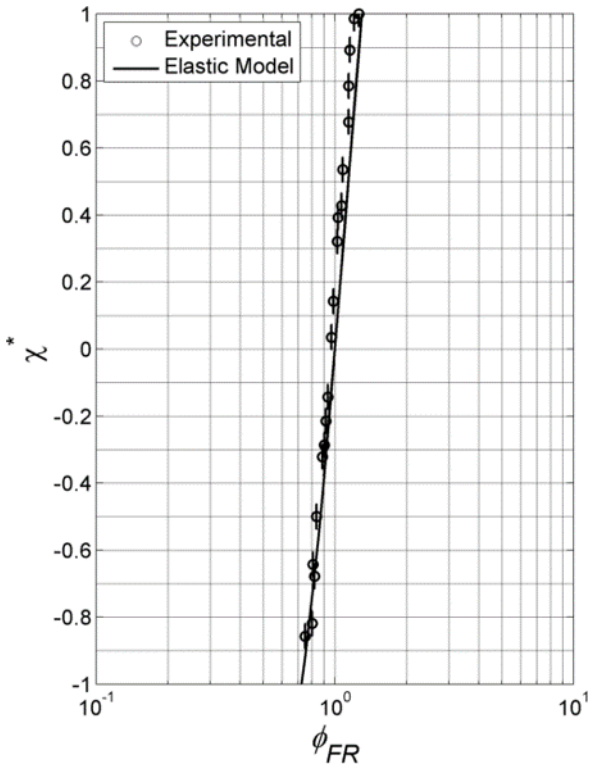

Figure 4.32 - $\chi^*_{exp}(\phi_{FR})$ vs $\chi^*_{model}(\phi_{FR})$ for Re = 220

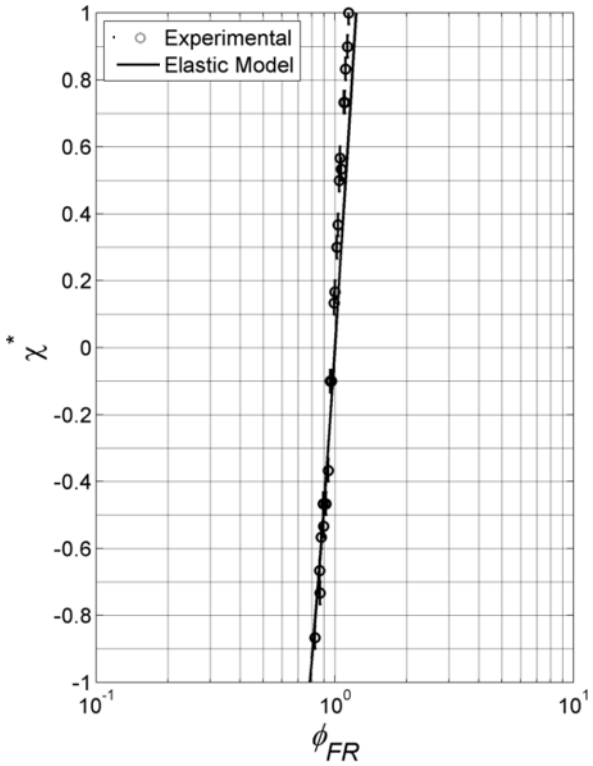

Figure 4.33 - $\chi^*_{exp}(\phi_{FR})$ vs $\chi^*_{model}(\phi_{FR})$ for Re = 313

4.6.3 Kinetic energy rate ratio

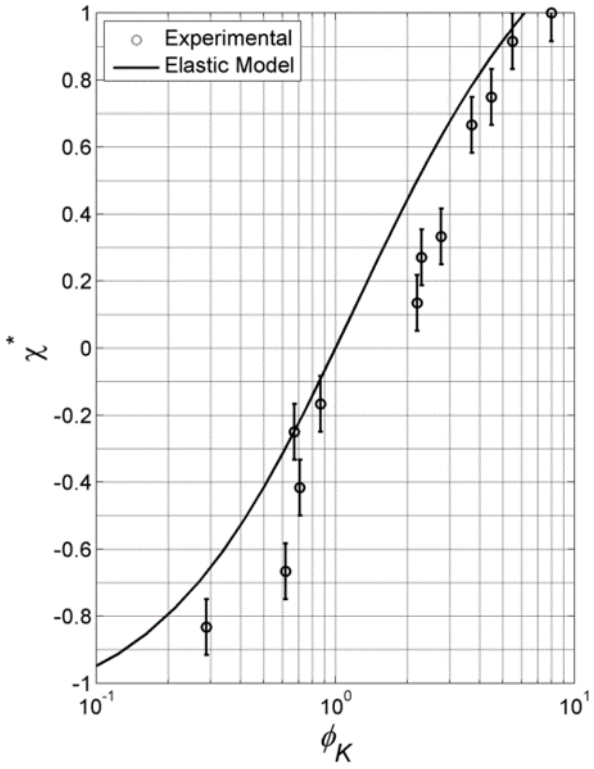

Figure 4.34 - $\chi^*_{exp}(\phi_K)$ vs $\chi^*_{model}(\phi_K)$ for Re = 45

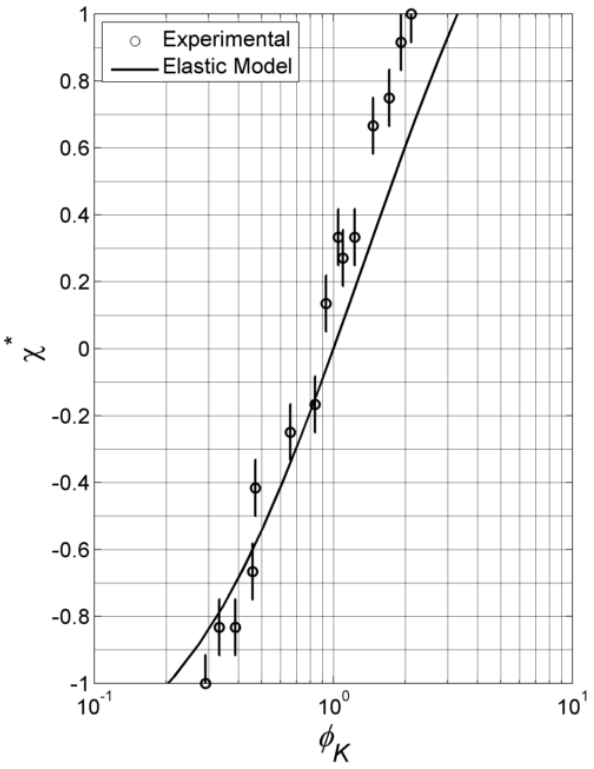

Figure 4.35 - $\chi^*_{exp}(\phi_K)$ vs $\chi^*_{model}(\phi_K)$ for Re = 111

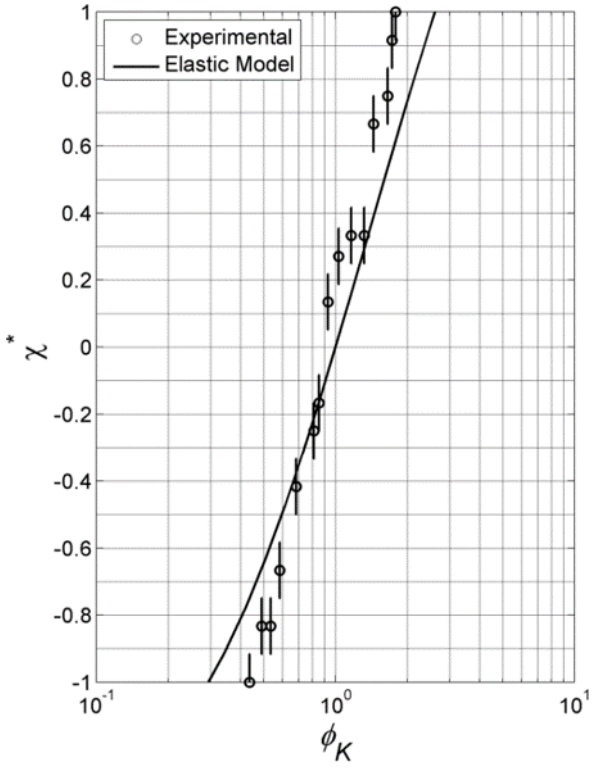

Figure 4.36 - $\chi^*_{exp}(\phi_K)$ vs $\chi^*_{model}(\phi_K)$ for Re = 159

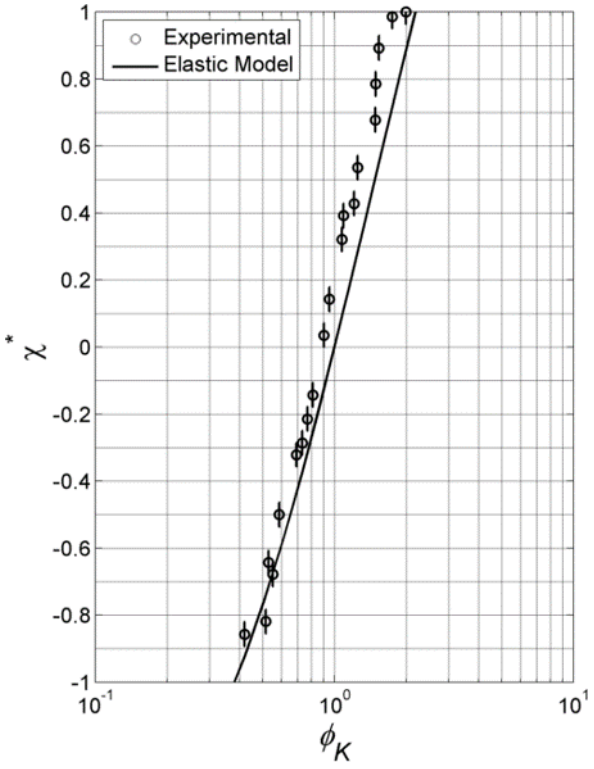

Figure 4.37 - $\chi^*_{exp}(\phi_K)$ vs $\chi^*_{model}(\phi_K)$ for Re = 220

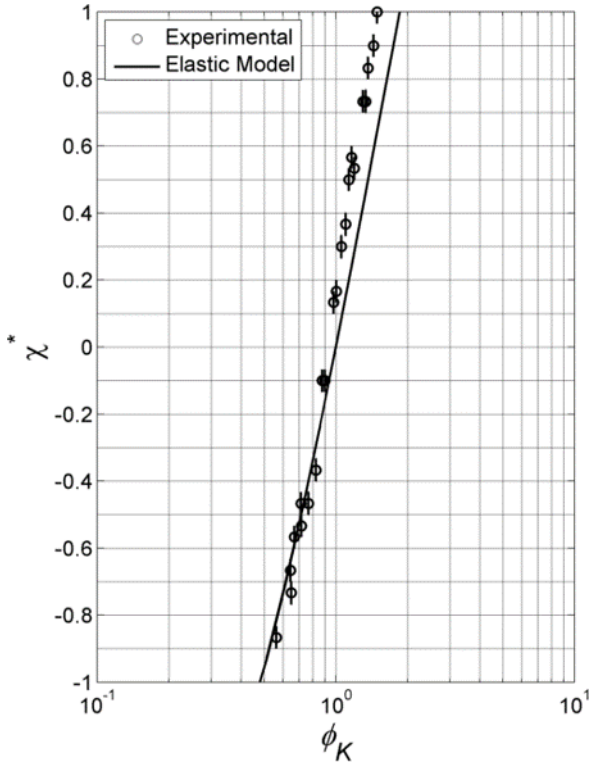

Figure 4.38 - $\chi^*_{exp}(\phi_K)$ vs $\chi^*_{model}(\phi_K)$ for Re = 313

4.6.4 Momentum rate ratio

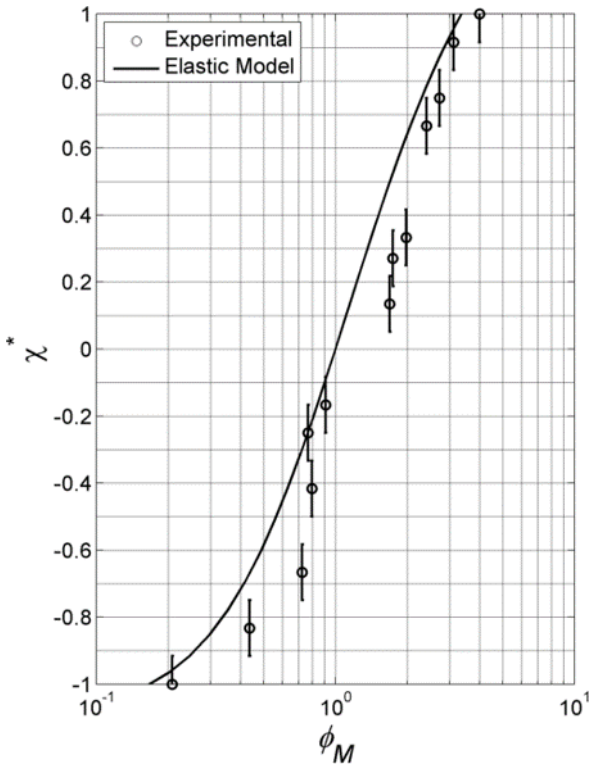

Figure 4.39 - $\chi^*_{exp}(\phi_M)$ vs $\chi^*_{model}(\phi_M)$ for Re = 45

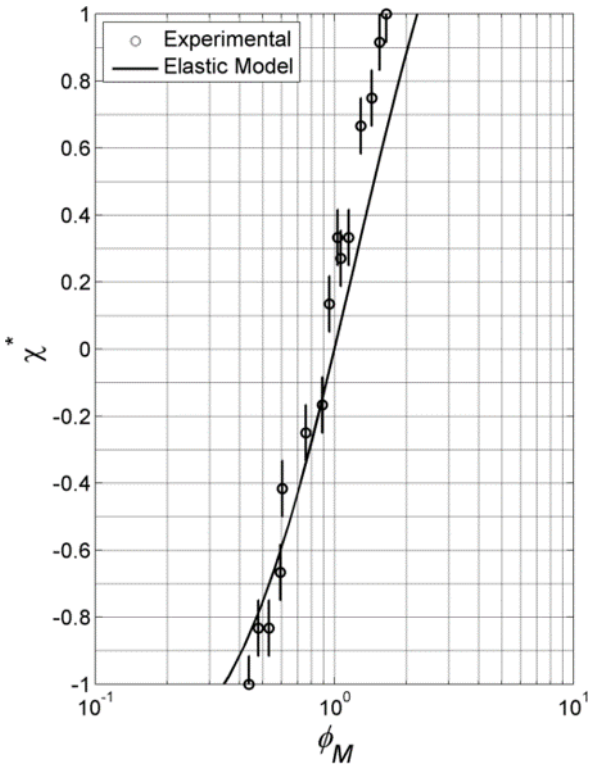

Figure 4.40 - $\chi^*_{exp}(\phi_M)$ vs $\chi^*_{model}(\phi_M)$ for Re = 111

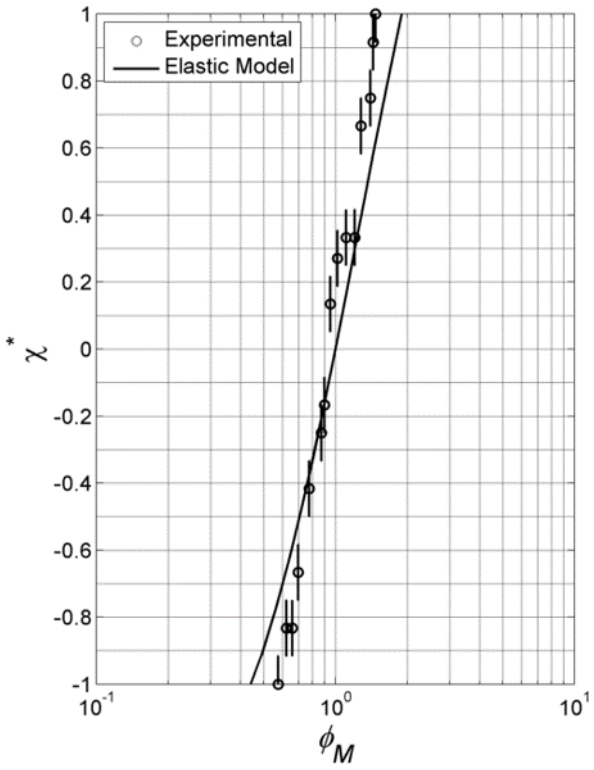

Figure 4.41 - $\chi^*_{exp}(\phi_M)$ vs $\chi^*_{model}(\phi_M)$ for Re = 159

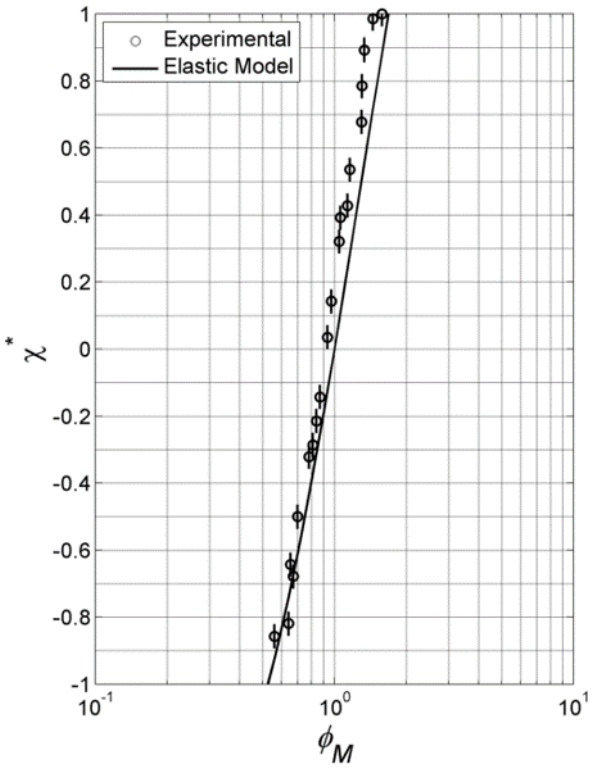

Figure 4.42 - $\chi^*_{exp}(\phi_M)$ vs $\chi^*_{model}(\phi_M)$ for Re =220

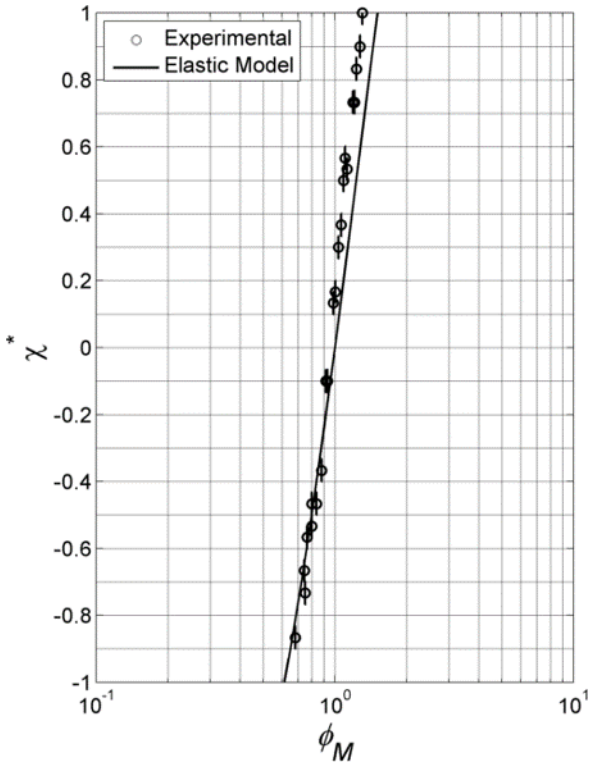

Figure 4.43 - $\chi^*_{exp}(\phi_M)$ vs $\chi^*_{model}(\phi_M)$ for Re = 313

4.6.5 Comments to the elastic analogue model results

The elastic model is plotted against the experimental results obtained from the PIV method. The error associated with each experimental point is, in the vertical direction, related to the size of the interrogation spot through the variance of the average of the 20 pictures. In the horizontal direction the error is mainly due to the variation of the flow rate measurement, thus, as discussed early, this error is very small when compared to the value of the flow rate, becoming imperceptible when plotted, so it was chosen not to represent such a small value in each graph. For low Reynolds numbers, namely 45, 111 and 159, the error associated with the impingement point position is larger than the error recorded for the Reynolds numbers of 220 and 313. This effect is due to the fact the interrogation area decreases, meaning that the pixel/distance increases, giving higher resolutions and decreasing the experimental error.

The MATLAB code created to analyse the impingement point position first calculates the average of the y-velocity component for the interrogation spot immediately in the top and bottom position of the injector axis. With this value, the zones where the following statement is true are identified:

$$y_{velocity_{x_{IP}}} \geq \overline{y_{velocity}} \tag{4.20}$$

Then, the program will search for the zones where impingement occurs by probing locally the variation of the x-velocity using the following constraints:

$$if\ x_i > 0 \wedge\ x_{i+1} < 0\ \ then\ x_{IP} = x_i + x_{i+1} \tag{4.21}$$

$$if\ 0 \leq x_i \leq 0.1 * \overline{x_{velocity}} \wedge\ x_{i+1} < 0\ \ then\ x_{IP} = x_i \tag{4.22}$$

During the experiments, small increments were made in the flow rate in one side of the chamber while in the other side the flow rate was maintained almost constant. It is important to mention that it is extremely hard to manually control the flow rate of each injector, since for low Reynolds numbers the needle valve does not respond with such precision and for larger Reynolds numbers a tighter control is required. Consequently, a great effort is needed to control the flow rate while the experiment is in progress. It is also worth remarking that immediately after manually setting the appropriate flow rate in each injector, both the images and the flow rate were recorded independently by two different acquisition systems, hence a delay can occur between the recording of the flow rate and the imaging, since each equipment has its own delay time, in addition to the delay time caused by the manual start of the acquisition.

Both for the jets' flow rate ratio, the momentum rate ratio and the kinetic energy rate ratio, it is noticeable a decrease in the range of their values when the Reynolds number increases, indicating that, as observed experimentally, it is required a tight control of the flow rate to ensure that small fluctuations do not affect the position of the impingement point.

When the impingement point is aligned with the chamber central axis an excellent agreement between the experimental work and the elastic analogue model is obtained, proving that the model works very well with normal operating conditions. By contrast, when the impingement point is located close to the chamber walls the elastic analogue model seems to have a conservative value, that is, for the same impingement point position the operational variables have smaller experimental values rather than in the elastic model.

Generally speaking, the elastic analogue model revealed a good agreement with the experimental data for the Reynolds range in study, for values either below or above the critical Reynolds number, when the average flow field is used. Therefore, this equation has proved to be very valuable for controlling the impingement point position for a wide range of operating conditions, namely for different injectors' diameter ratios and flow rates. However, it is still necessary to validate the elastic analogue model for when the injected streams have different properties.

4.7 Pressure model

Control the process is always a fundamental question in RIM machines, since a change of less than 1% of the jets balancing can compromise the mixing (Santos, 2003). Moreover, a deviation of 10% can make one of the jets to be pushed way from the other jet, breaking the oscillatory motion of the impingement surface entirely and resulting in damaging consequences for the final plastic product Fonte (2012).

For this reason, controlling the RIM process is essential for the mixing performance and this is why so many resources have been applied into the research and development of new and innovating control methods. One of this methods of controlling the RIM process was developed by the LSRE laboratory and lead to a national and international patent, the RIMcop. In this technology, the differential pressure between each side of the injectors is employed to control the laminar and chaotic flow motion. The idea underlying RIMcop is that the pressure can be read by a differential pressure transducer which is coupled with an electronic device to add other variables that perform the indirect control of the impingement point position by means of slight changes to the injectors flow rate.

Subsequently, it is necessary to develop a mathematical model that allows direct control of the impingement point position for a different set of operational parameters, such as the Reynolds number, the fluid properties and the geometrical parameters. (Gomes, 2015) proposed a new model to predict the impingement point position from the differential pressure but did not perform its validation. Therefore, it is necessary to validate such model for a different set of flow conditions, particularly for different Reynolds numbers.

In the next section, this mathematical model will be thoroughly explained and its limitations will be examined. Later, the model predictions will be compared with the data obtained from the experimental work performed and the results will be discussed. In the next chapter, this model will be further applied to evaluate its ability to reproduce the experimental measurements if different fluid properties are considered in each injector, namely the fluid viscosity and the fluid density.

4.7.1 Pressure mathematic model for jets equilibrium

The main concept of the RIMcop is that small variations of the impingement point position can be directly related with the pressure variation on the impingement jets, which can be read from measurement points at the beginning of the injectors. The pressure measured in one of these measurement points is then subtracted from the pressure measured in the opposed measurement point by a mechanical device which automatically translates this pressure variation into an electrical signal in order to be read by a computer or controller. Based on this approach, (Gomes, 2015) developed a model to correlate the impingement point displacement with the differential pressure between each injector. The model assumes that the injector force is directly proportional to the flow force induced by shear stress in the injector and to the inertial forces caused by the kinetic energy of the injectors:

$$\mathbf{F} = \oiint \mathbf{T}\, d\mathbf{A} + \oiint \mathbf{v}\, (\rho \mathbf{v} \cdot d\mathbf{A}) \tag{4.23}$$

where T is the normal stress in the injector, A is the injector area, v is the velocity flow field. The integration is performed in the control surface from the jets inlet until the impingement point. Neither the drag forces from the vortices around the jets nor the x-velocity after impingement are considered in the evaluation of the integral.

This assumption results in

$$\int_0^{d_1/2} T\ 2\ \pi\ dr = \pi \frac{d_1^2}{4}\ p_1 - F_{1x} \tag{4.24}$$

where F_{1x} is the traction force from the opposed jet. Additionally, the inertial terms are given by

$$\oiint \mathbf{v}\ (\rho \mathbf{v} \cdot d\mathbf{A}) = \int_o^r \rho_1\ v_1^2\ 2\ \pi\ r\ dr - \int_0^{\frac{d_1}{2}} \rho_1\ v_{1x}^2 2\ \pi\ r\ dr \tag{4.25}$$

Where v_{1x} is the parabolic flow profile due to the laminar flow regime and v_1 is the velocity at injector 1. In the impingement point the x-velocity is zero, resulting in

$$\oiint \mathbf{v}\ (\rho \mathbf{v} \cdot d\mathbf{A}) = -\int_0^{\frac{d_1}{2}} \rho_1\ v_{1x}^2 2\ \pi\ r\ dr = -\pi\ \rho_1 v_1^2 \frac{d_1^2}{3} \tag{4.26}$$

From the balance between the traction and inertial terms for each jet, it follows:

$$F_{ix} = \frac{\pi\ d_i^2}{2}\ p_i + \pi \rho_i v_i^2 \frac{d_i}{3} \tag{4.27}$$

In the impingement point, the moment between the jets should balance out:

$$F_{1x} l_1 = F_{2x} l_2 \tag{4.28}$$

where l_1 and l_2 are the distances from the chamber walls to the impingement point, then $l_1 + l_2 = D$. Substituting in Equation 4.28 gives

$$\frac{\pi\ d_1^2}{2}\ p_1 l_1 + \pi \rho_1 v_1^2 \frac{d_1}{3} l_1 = \frac{\pi\ d_2^2}{2}\ p_2 l_2 + \pi \rho_2 v_2^2 \frac{d_2}{3} l_2 \tag{4.29}$$

Consider now the non-dimensional pressure, p^*, defined as

$$p^* = \frac{p}{\rho_1 v_1^2} \tag{4.30}$$

Rearranging Equation 4.29 and introducing the jets' momentum rate ratio yields

$$l_1^* = \frac{\phi_d^2 p_2^* + \frac{4}{3}\phi_R}{p_1^* + \phi_d^2 p_2^* + \frac{4}{3}\phi_R + \frac{4}{3}} \tag{4.31}$$

where l_1^* is the dimensionless distance, given by $l_1^* = l_1/D$. The distance of the impingement point to one side of the chamber is $\chi^* = \frac{1}{2} - l_1^*$. Substituting in Equation 4.31 results in the following pressure equilibrium equation for the jets, which is represented below (Figure 4.44):

$$\chi^* = \frac{p_1^* - \phi_d^2 - \frac{4}{3}\phi_M + \frac{4}{3}}{2p_1^* + 2\phi_d^2 p_2^* + \frac{8}{3}\phi_M + \frac{8}{3}} \tag{4.32}$$

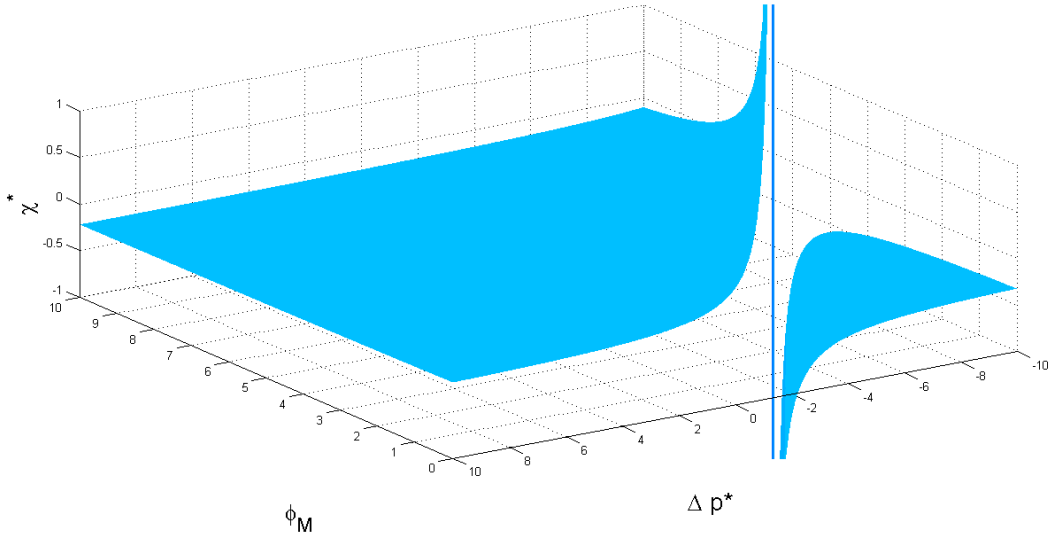

Figure 4.44 -3D Representation of the jets' pressure equilibrium equation

As can be noticed in the previous image, Equation 4.32 yields an asymptote in the middle of the domain, so it is necessary to be careful when implementing this model. By performing some simplifications to the model, Equation 4.32 can be tested for a specific set of operating conditions. Consider $\phi_d = 1$ and $\phi_M = 1$, meaning that the injectors have the same diameter and the jets' momenta are balanced, for fluid streams with the same physical properties, which yields the same Reynolds number in each injector and simplifies Equation 4.32 to

$$\chi^* = \frac{1}{2}\frac{\Delta_p^*}{-\Delta_p + \frac{8}{3}} \tag{4.33}$$

From Equation 4.33, two individual case scenarios were studied, as shown in Figure 4.45 and in Figure 4.46.

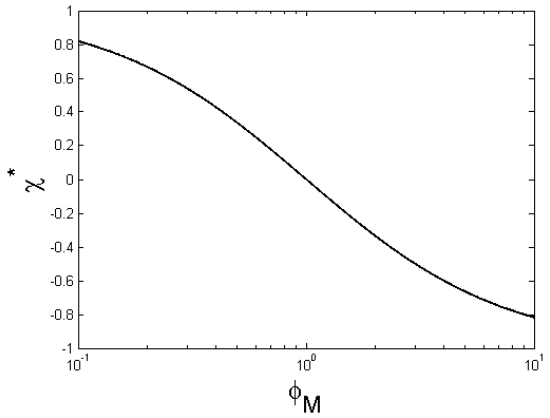

Figure 4.45 - $\chi^*(\phi_M)$ for $\Delta_p^* = 0$

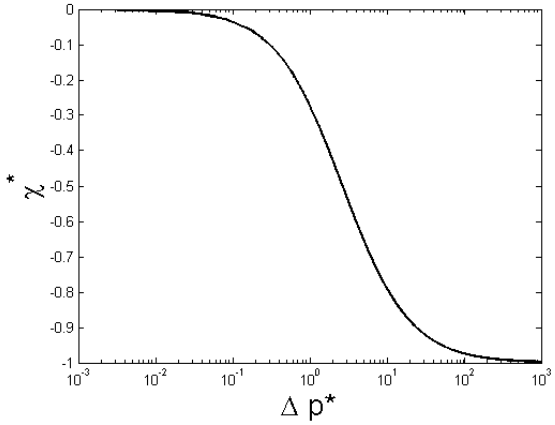

Figure 4.46 - $\chi^*(\Delta_p^*)$ for $\phi_M = 1$

The figure in the left represents the position of the stagnation point, χ^*, as a function of the jets' momentum rate ratio, ϕ_M, for a differential pressure, Δ_p^*, equal to zero. For this case, the equation performs very well when evaluating close to the impingement point position, where $\phi_M = 1$ and $\Delta_p^* = 0$, as it shows a smooth linear variation of the impingement point position when $\phi_M$varies. The figure in the right shows the impingement point position against Δ_p^* for $\phi_M = 1$ in the range of equilibrium. It is worth noting that for this conditions the equation only produces positive values of Δ_p^* when the impingement point position tends for one side of the chamber, reflecting the main limitation of this formulation, which is only valid for half of the chamber. This picture also shows a small initial variation of the Δ_p^* with a small rate of decline of the impingement point position. After a certain value this rate highly increases.

Following the presentation of the mathematical model proposed by Gomes (2015). the validation of this model for a wide range of operating conditions will now be considered. In this work, it will be studied a set of different Reynolds numbers for jet streams with the same physical properties and for the same chamber geometry.

4.7.2 Pressure correction

The mathematical model described earlier will be tested against the experimental work performed using PIV. For this particular case, it is necessary to adjust the results in order to comply with the limitations of the pressure model.

The mathematical equations which rule this model considered a source point at the beginning of the mixing chamber and aligned with the injector axis. As in the experimental setup the differential pressure is only calculated outside the mixing chamber, it is necessary

to perform adjustments in the recorded data. A good illustration of this correction is provided in Figure 4.47.

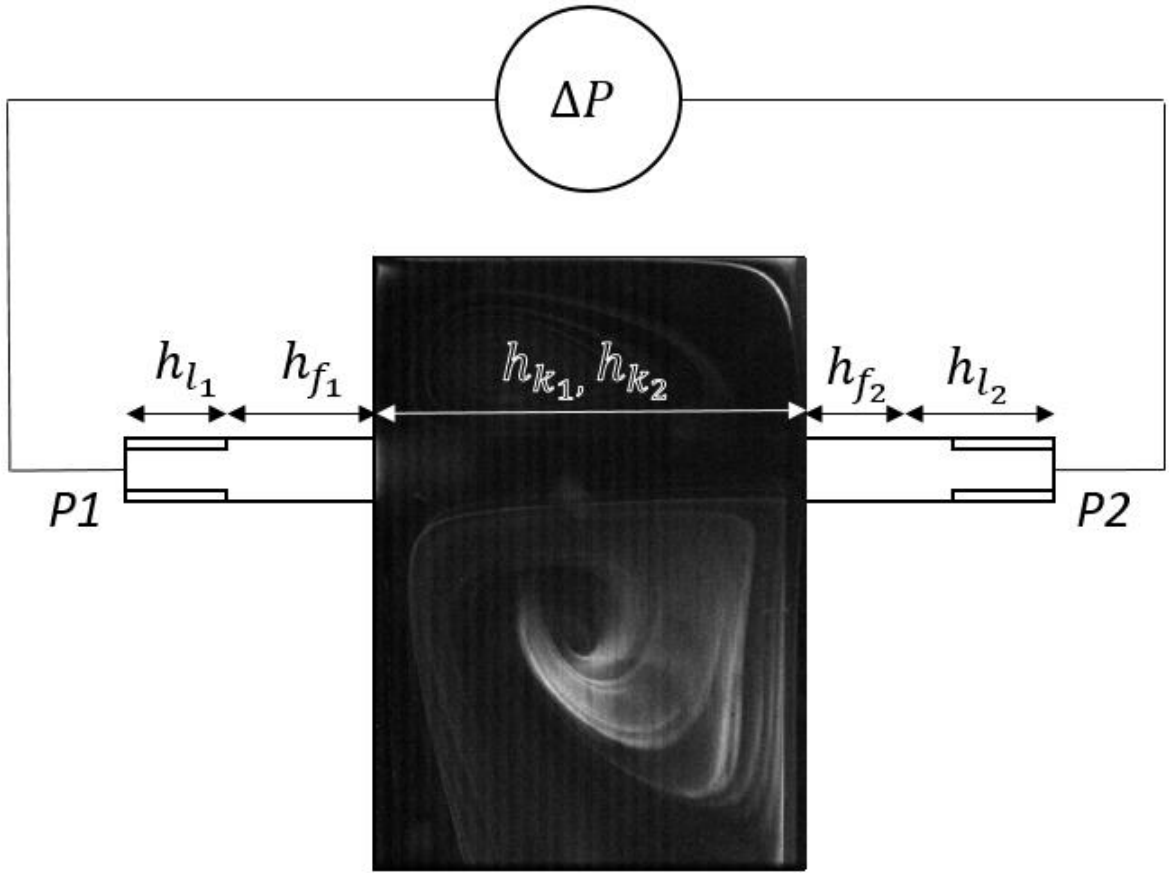

Figure 4.47 - Schematic of the pressure correction

Δ_P is the difference between P_1 and P_2. Consider there is no flow rate between the pressure point and the differential transducer which can cause an additional hidden force in the results. With this in mind, it is know that the difference between p_1 and p_2 is directly related to the local pressure loss due to a connection, h_l, defined as

$$h_l = \rho k v^2 \tag{4.34}$$

where k is a coefficient related to the nature of the local resistance. For this case, the recommended value for k lies between 0.9 and 1.1. It was chosen a k value of 1, as this was the value that fitted best to the experimental data.

The pressure loss in the injectors pipe, h_f, in which the flow regime is laminar, thus a parabolic flow profile is achieved in this smooth tube, was calculated from Poiseuille's law:

$$h_f = \frac{128 * \mu * Q * L}{\pi * d^4} \tag{4.35}$$

where Q is the volumetric flow rate and L the tube length, which is 55 mm.

Additionally, the pressure of the jets is accounted for by calculating its kinetic energy, h_k, since when tested the jets hit the opposite injectors:

$$h_k = \frac{1}{2}\rho v^2 \tag{4.36}$$

Consider the differential pressure Δ_p as

$$\Delta_p = p_1 - p_2 \tag{4.37}$$

Adding each head loss in the previous equation yields

$$\Delta_p = \left(h_{f_1} + h_{l_1} + h_{k_1}\right) - \left(h_{f_2} + h_{l_2} + h_{k_2}\right) \tag{4.38}$$

This equation was tested experimentally. By shutting off one valve and gradually increasing the flow rate while recording the pressure values, it is possible to compare the previous equation with experimental measurements in order to validate it. The results obtained are presented in Figure 4.48.

The fitting curve, mathematical deduced shows an excellent agreement with the experimental data for all the flow rates studied, which were chosen to comply with the Reynolds numbers range used in the experimental work.

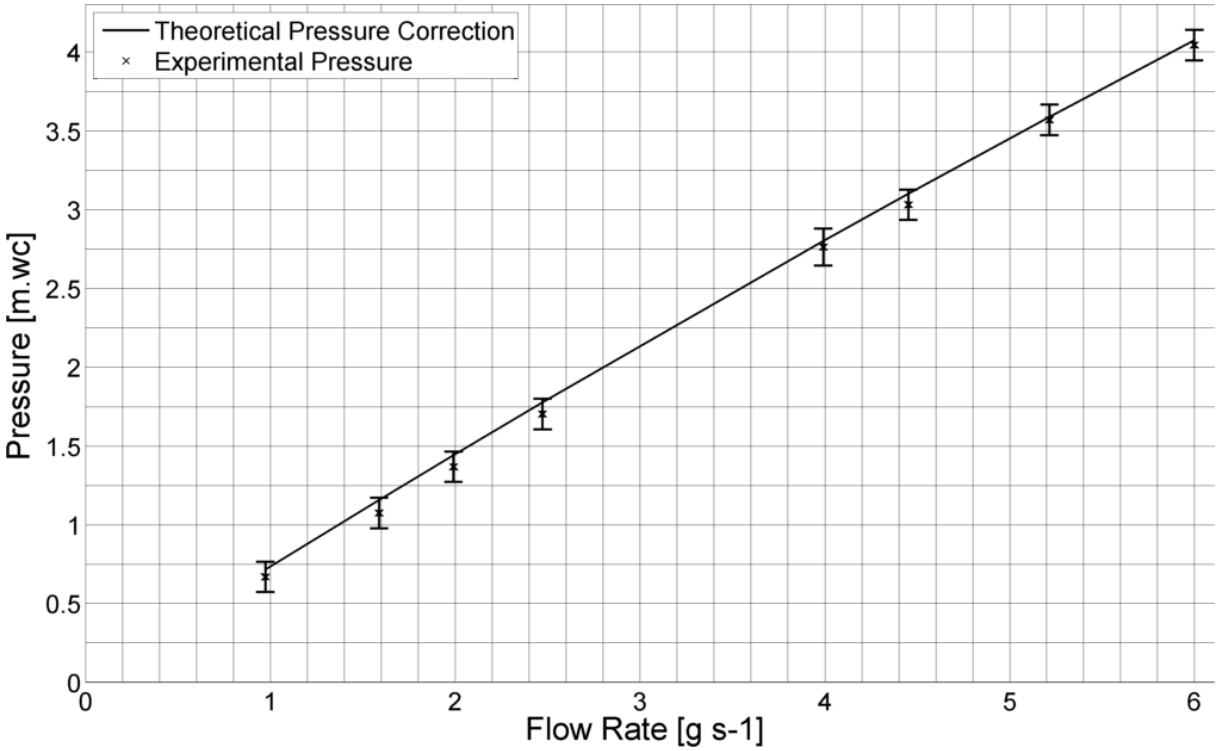

Figure 4.48 - Comparison between the pressure correction model predictions and the experimental data

During the experiments, the pressure data is recorded in $m.wc$ since the pressure transducer was calibrated with a column of water, thus it is necessary to convert it into S.I. units of pressure, Pa:

$$\Delta p = P1 - P2\ [m.cw] = = \Delta p * \gamma\ \text{[Pa]} \tag{4.39}$$

where

$$\gamma = g * \rho_{h_2o} \tag{4.40}$$

The pressure is then corrected using the aforementioned pressure correction model for taking into account the head loss in each injector. The corrected pressure, $\Delta p_{corrected}$, is computed as follows:

$$\Delta p_{corrected} = \Delta p + \left(h_{f_1} + h_{l_1} + h_{k_1}\right) - \left(h_{f_2} + h_{l_2} + h_{k_2}\right) \tag{4.41}$$

Then, the corrected pressure is normalized by the velocity on the right injector, given that the right injector's flow rate is kept at a constant value throughout the experiments:

$$\Delta p^*_{corrected} = \Delta p_{corrected} / \rho v_2^2 \tag{4.42}$$

Using the pressure equilibrium model and considering p_1^* as the reference pressure with $\phi_d = 1$, since there is no difference in the injectors' diameters, the impingement point position is calculated as

$$\xi = \frac{\Delta p^*_{corrected} - \frac{4}{3}\phi_M + \frac{4}{3}}{-2\Delta p^*_{corrected} + \frac{8}{3}\phi_M + \frac{8}{3}} \tag{4.43}$$

Where

$$\phi_M = \frac{\beta^2}{\alpha^2} * \frac{\rho_1}{\rho_2} \tag{4.44}$$

with the constants α and β calculated as

$$\beta^2 = \frac{d_1^2}{d_2^2} \tag{4.45}$$

$$\alpha^2 = \frac{\alpha_2^2}{\alpha_1^2} \tag{4.46}$$

The comparison of this corrected pressure model with the experimental data for Reynolds 45, 111, 159, 220 and 313 is presented in the following section, from Figure 50 to Figure 54.

4.7.3 Results of the pressure model

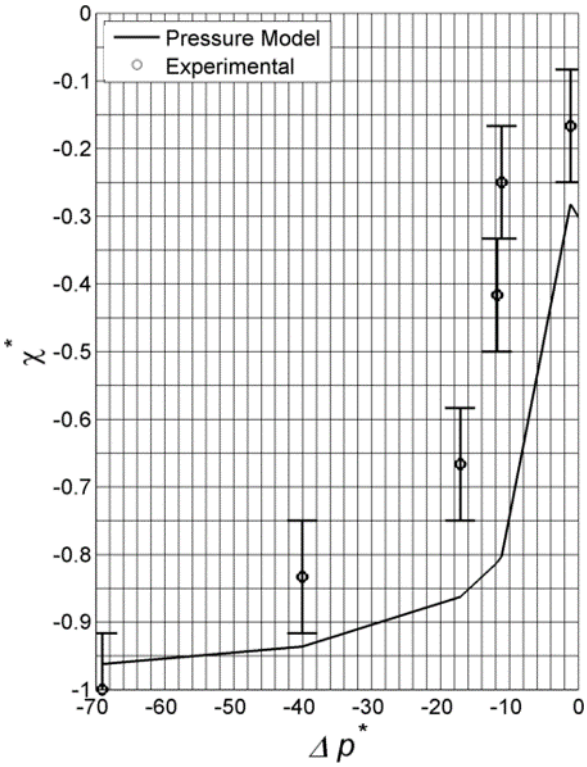

Figure 4.49 - $\chi^*_{exp}(\Delta^*_p)$ vs $\chi^*_{model}(\Delta^*_p)$ for Re = 45

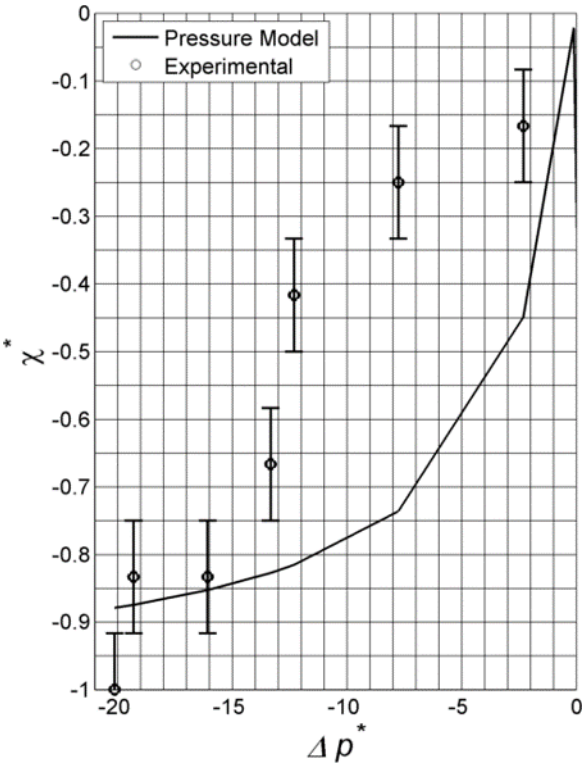

Figure 4.50 - $\chi^*_{exp}(\Delta^*_p)$ vs $\chi^*_{model}(\Delta^*_p)$ for Re = 111

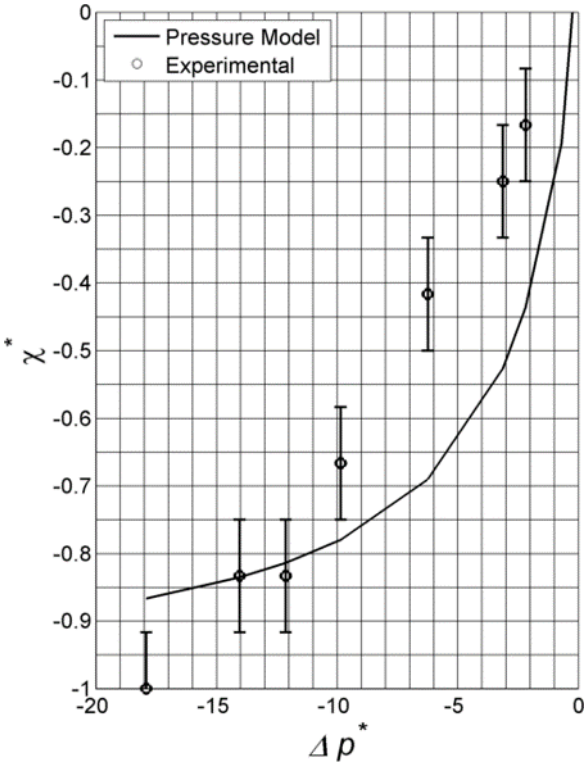

Figure 4.51 - $\chi^*_{exp}(\Delta^*_p)$ vs $\chi^*_{model}(\Delta^*_p)$ for Re = 159

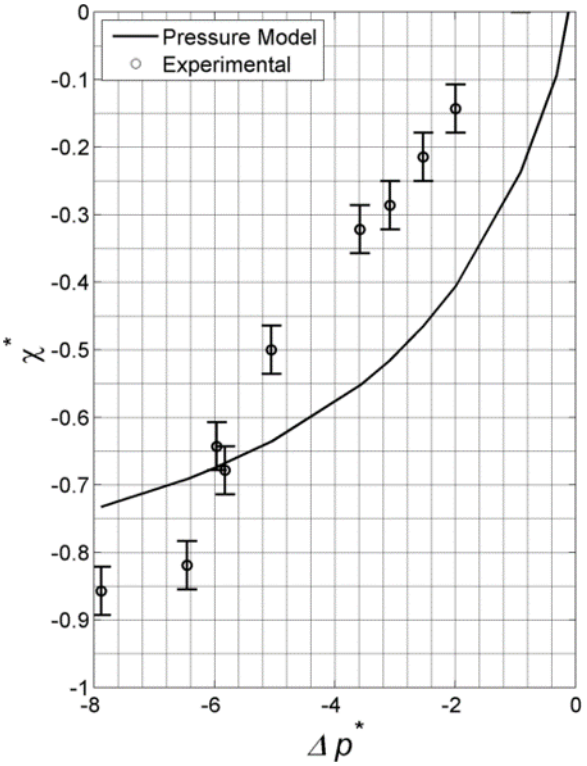

Figure 4.52 - $\chi^*_{exp}(\Delta^*_p)$ vs $\chi^*_{model}(\Delta^*_p)$ for Re = 220

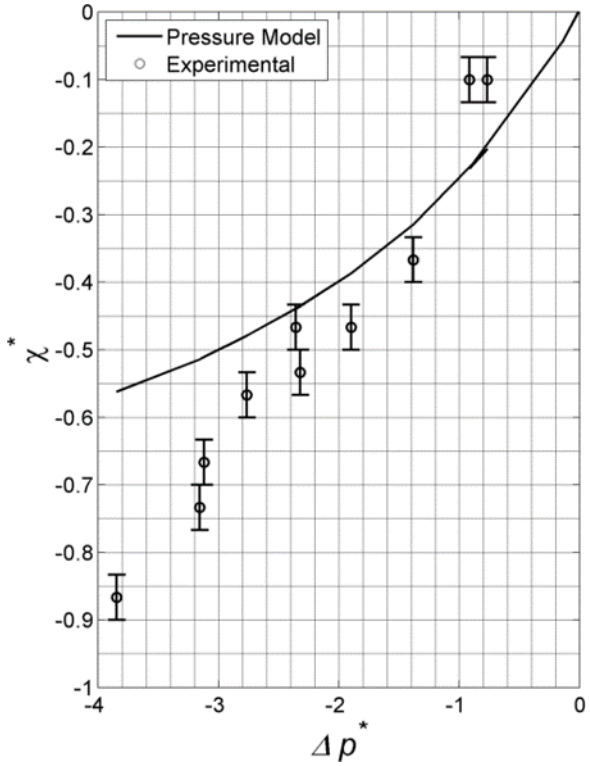

Figure 4.53- Normalized pressure for Reynolds 313

4.7.4 Comments on the pressure model

The work presented here has two main errors, although just one is quantified. The first error is associated with the experimental measurement of the impingement point, which was already explained in the previous section to make comparisons with the elastic analogue model. The second error is related with the quantification of the pressure variation and can be divided in two parts. The first part is associated with the variation of the pressure along the experiment which is almost null, while the second is associated with the measurement of the pressure. This measurement was performed using a differential pressure transducer with a thick membrane that is not sensible to low variations of pressure. Consequently, this translates into rounding errors, which are also small when compared with the pressure values. Therefore, the sum of these two errors was not plotted. Nonetheless, it is observable along the experiment a significant change in the rest position of the pressure value which can affect significantly the measurement of the pressure values.

The domain in study corresponds to the negative values of Δp^*, which is opposite to Figure 4.456 where the domain only contains positive values, since only half of the chamber is presented. Nevertheless, it is important to divide the domain in two separate parts: the first

part is far from the centre of the chamber and the second part is close to the centre of the chamber where the jets impingement should occur.

For Reynolds below the critical value, 45, it is observable a good agreement with the behaviour of the model although the model seems to obtain lower pressure values than the experimental work. When the impingement point is far from the centre it is observable a very good match between both, but when the impingement point tens to the centre of the chamber the difference between the model and the experimental work teds to increase. As it can be seen in the centre of the chamber the model reach is maximum value and values beyond will not have a physical meaning since the equation reach the asymptote.

For Reynolds 111, which represents the start of the self-sustainable chaotic regime, it is observed that the model and the experimental data have an excellent agreement when the impingement point is situated close to the chamber walls. When the impingement point tends to the centre of the chamber the opposite is observed, which cannot be explained by experimental error and must be due to the beginning of the oscillation mechanics of the impingement point. Close to the centre of the chamber both sets of data present similar values and, in the end, the model seems to reach the asymptote.

For Reynolds 159, a good agreement is shown between model and experiments both when the impingement point is close to the chamber walls and close to the centre of the chamber. However, in general, there are considerable differences in the values of the normalized pressure between both series, experimental and mathematical model.

For Reynolds 220, the model predictions are too dissimilar from the experimental data close to the chamber walls and when the impingement point tends do go to the centre of the chamber both sets of results diverge. Still, when the impingement point is close to the centre the experimental results tend to the mathematical model.

As for the last Reynolds studied, 313, when the impingement point is close to the chamber walls both methods seem to diverge, but when it starts to approach the centre of the chamber they tend to agree. In the centre of the chamber, it appears that the variation between the predicted and measured results is small.

Generally speaking, the mathematical model used to describe the pressure along the chamber has as main limitation that it can only predict the pressure in half of the chamber, although it is known that when the jets streams physical properties and the injectors' diameters are the same this symmetry occurs. Nonetheless, the model in general seems to agree with the experimental values when predicting the pressure in the centre of the

chamber and close to the chamber walls, while between this two regions the results sometimes diverge.

4.8 Conclusions

The control of the impingement point position is a crucial operation in order to achieve a good mixing within the chamber. Previous works proved that even a slight change of 1% in the jets balancing can affect mixing performance and that if the jets unbalancing reaches 10% it can destroy per complete the chaotic nature of the flow with damaging consequences for mixing performance.

In the present work, PIV experiments were performed to validate for the first time two different mathematical methods for predict the stagnation point position using two main variables. The first method, the elastic analogue model, used the knowledge of the fluids physical properties, chamber dimensions and working conditions to predict the impingement point position. The second method in study uses the differential pressure in the injectors to predict the impingement point position and is the main driving force for RIMcop technology.

From the visualization studies, it is obtained the velocity field with the non-dimensional velocity fluctuations, where it is observed that the biggest fluctuations of the flow field occur in the impingement zone. In addition, if the Reynolds number is increased, the variations tend to progress forward and downwards the impingement surface. As for when the impingement is close to the chamber walls, it is observed an attachment of the lower part of the impingement surface to the chamber, with this effect being intensified by a small recirculation downstream of the jets streams.

For the first time, the elastic analogue model was evaluated for a wide range of operation conditions, namely for different Reynolds. In general, it was confirmed its validity for all the Reynolds in study: conservative values where obtained close to the chamber walls and a perfect fitting was observed when the impingement point is in the centre of the chamber.

Regarding the pressure model validation, for the first time, this model was compared with experimental work for a wide range of operating Reynolds number. Generally speaking, it was observed a good agreement close to the chamber walls and to the centre of the chamber. Nevertheless, the model lacks for not representing the complete mixing chamber, as due to the existence of an asymptote it only considers half of it. Therefore, it can be concluded that this model requires further work in order to achieve a better fitting with the experimental data and to be reliable to be used with the RIMcop technology.

5 Real time visualization of the flow field using PLIV

5.1 Introduction

Inside a mixing chamber strong dynamics due the existence of large velocity field associated with quick acceleration and deceleration of the fluid in a reduced confined space can achieve high complexity of flow structures, which even in low Reynolds number, in a laminar flow regime mixing of two fluids can occur. In the present work Reynolds number is defined as

$$Re = \frac{\rho\, v_{inj}\, d}{\mu} \tag{5.1}$$

Where ρ and $\mu$is the fluid density and viscosity respectively, v_{inj} is the average injector velocity and d is the injector diameter.

The main objective of this chapter is the study, for the first time, the full resolved flow dynamics inside the mixing chamber. To tackle this problem the full resolved flow was study using a high speed camera with a Planar Laser Induced Fluorescence (PLIF) technique. The present study tends to compare the oscillatory motion of the impingement surface in a 2D cut of the mixing chamber, with the know patterns of the flow dynamics existent in literature.

A deterministic multiobjective optimization algorithm was created to sequentially analyse the image produced by the PLIV technique in order to evaluate the impingement point

position and the jets angle, which is known, by the present and previous works the driven force of inducing a self-sustainable chaotic regime which leads to a strong mixing performance due improving of the hydrodynamic flow regime.

Results from the optimization algorithm created will be verified in order to obtain a pattern between the jets motion with the impingement point position, allowing a understanding of the phenomena of the impingement surface oscillation.

Power spectral analyses will be perform to compare the pattern of the variation of impingement point position and the jets angle with experimental from the pressure fluctuations. The objective is to analyse the influence of the oscillatory motion of the impingement surface in the pressure variation read by the differential pressure transducer

Additionally the two method existent in literature to control the RIM process, the elastic analogue model and the pressure model, will be tested for the first time under different fluids proprieties in each injector, leading to a more profound knowledge of the applicability of such methods into a more robust and wide operational conditions control. This test is of extreme importance since in industry is required to mixing two different fluid proprieties, polyol and isocyanate, in order to produce plastic components even in different stoichiometric proportions.

This chapter starts to present and explain the optimization algorithm created to study the impingement point position and the jets angle by an image resulted from a PLIV technique. After this process the experimental setup and experimental conditions of PLIF technique is explained additionally with the presentation of the results obtain, particularly the visualization studies, the impingement point position and jets angle along the experiment and the power spectra of the study variables. In the end the elastic model and pressure model was study to access the effectiveness of such mathematical models for different jets fluid properties.

5.2 Digital Image Processing Multiobjective Optimization Deterministic Algorithm

5.2.1 Introduction

Digital Image Processing (DIP) is a method developed in the 60s by USA space relate industries and academies as Jet Propulsion Laboratory, MIT, Bell laboratories and others, in order to developed new strategies to process information provided by satellite images, espionage photos, medical imaging, character recognition and others.

Wide methodologies of DIP existent in literature to a manipulation of digital images using signal processing analyses theory to transform and adapt images. In the present work will be used image manipulation in order to obtain a proper image to be input as function in the optimization algorithm implemented. The main objective of this manipulation is reducing noise in the image and create a sharper image to improve the optimization.

Optimization algorithms is a technique used to minimize or maximize a mathematical functions. In the present work a Multiobjective Optimization Deterministic Algorithm (MODA) was created to identify the location of the stagnation point and the jets angle by searching in the image obtain by PLIV technique. The optimization algorithm created identify more than one variable (multiobjective) and coupled all in order to mathematically determinate the position of the stagnation point. This is perform using a set of mathematical equations (Deterministic) meaning in each search only one solution is obtained, which could lead a errors, but highly reduced the computational effort required to solve the problem. Therefore was necessary to introduce more than one variable to reduce the error of the optimization algorithm created.

The literature present more than one technique to improve image processing, particularly for PIV form micro-mixing, but none algorithm was created to measurement of PLIV variables as required in this task. Additionally there is none optimization algorithm to identification of mixing-relate proprieties from a set of images, emphasising the contribution of the present work to expand the knowledge of science for coupling for the first time digital image processing methods with optimization algorithm to study mixing relate proprieties using PLIV and DIPMODA

5.2.2 Implementation

The implementation of a DIP MODA is separated in two main subroutines. The first subroutine have the objective of obtaining the physical dimensions of the chamber, particularly the diameters and the canters of the injector and chamber. Additionally this subroutine is equipped, if required, with a method to identify rotations of the chamber by analysing the centre of each injector and compute the angle between them. For the variable in used are not directly influenced by small rotation of the image and since the camera was proper calibration before each test no need for this step be used.

The second subroutine computes the stagnation point of each individual image by processing the images using DIP techniques and using MOPA to provide each value, namely the stagnation point and the jets angle. During the creating of the algorithm to compute the stagnation point was required to analyse the some possible values as impingement point and compared with others variables in order to choose the proper suitable position of the stagnation point.

One of the main advantages of a deterministic algorithm is the possibility of succession of error's which could lead to a very wrong set of data. To tackle this problem is was required to put some limitations in the code. The biggest limitation is the stagnation point are confined close to the centre of the chamber, although don't required to be exactly in the centre because it was allowed bigger variation along the chamber diameter. This don't mean if the impingement point is very close the chamber walls the optimization don't chose this point but the probability to choose is lower than if the impingement is located in the centre of the chamber. Additionally limitations to the operation are presented in the sequence of the presentation of the algorithm.

All of the techniques used and presented was required to tackle this problem for a wide range of Reynolds number, being each Reynolds introduced a new complex problem which need to be solve independent of the flow regime. Problems such as low motion of the impingement point presented for low Reynolds number opposite of fast, complex and unpredictable motion of the same variable for high Reynolds number, fast and slow motion of the impingement structure angle aligned with bending and consequent breaking of such structure impose a wide and complex problems which need to be solved.

Figure 5.1 shows the complexity of the problem in hand. The optimization algorithm always find the best point, given the restrictions but in some cases is impossible to ensure quality of the results if there is no quality of the input and the figures show this.

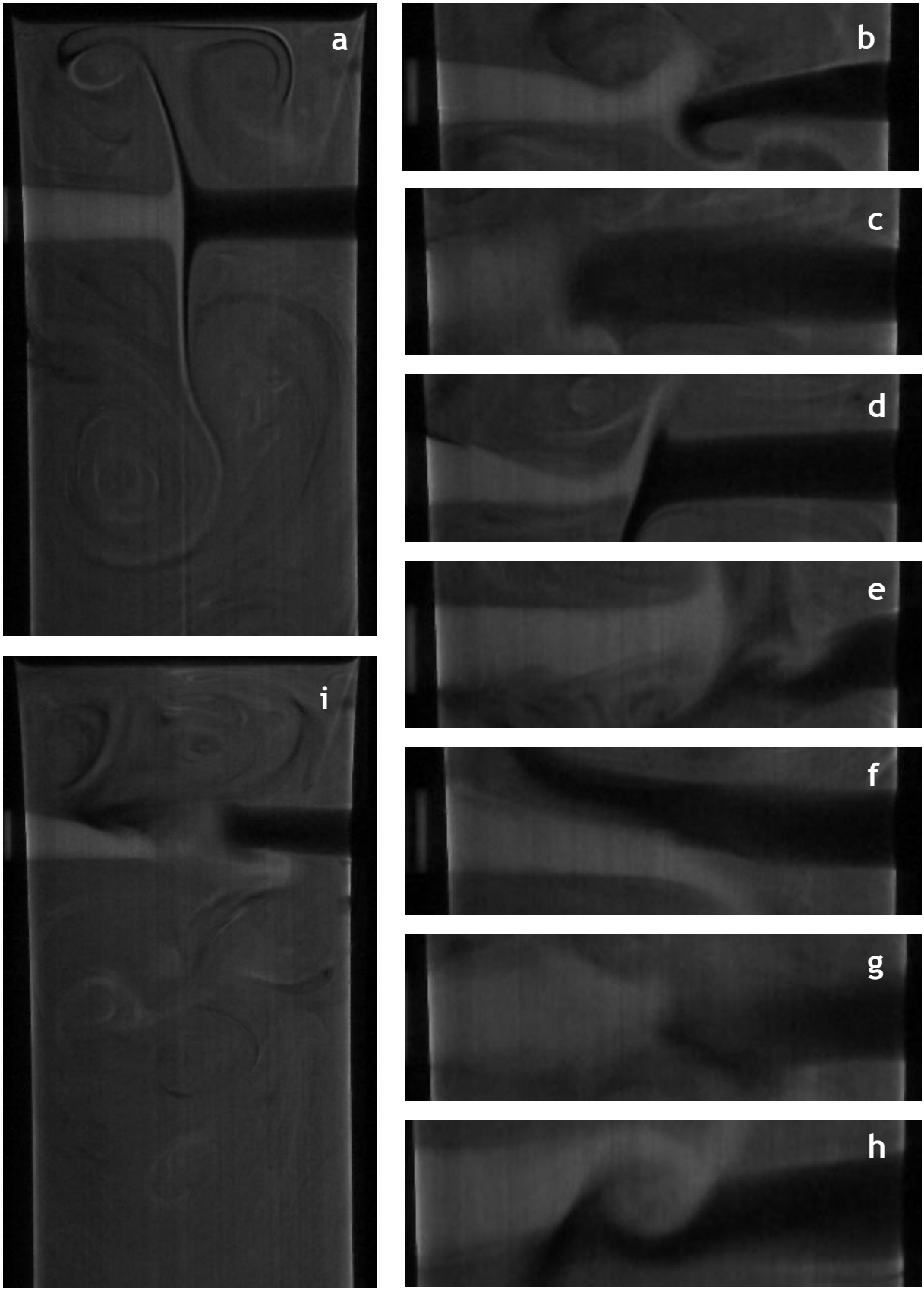

Figure 5.1 - Examples of instantaneous jets impingement: a) Ideal image, b) Complex impingement with weak interface, c) Unknown surface, d) Destruction of one jet due to vortex impact, e) Destruction of one jet associated with weak interface, f) Jets bending, g) Unknown interface, h) Formation of two possible interfaces, i) Disappearance of impingement

The DIP MODA flowchart is presented in Figure 5.2. The program is start by clear the memory and allocating space for the variables. Following the subroutine of calculating the chamber dimensions is run for one single image for each Reynolds in study. Although it was perform a calibration image in the beginning of each day of practical work it was chosen to calibrate the program for the physical dimensions in each time to reduce errors which can result by the operation. This was possible since the images was storage using 8 bits, meaning each pixel have 256 colours.

After the chamber dimensions was calculated the program progressed to calculate the stagnation point and jets angle. This step was done in a subroutine to ensure the maximum performance of the program, since in some steps parallelisation of the problem is possible. In the present work all the calculation was perform using Central Processing Unit (CPU), although is possible an advisable using, particularly for the image processing Graphics Processing Unit (GPU), allowing fast processing due high parallelization.

For the stagnation point two know image processor filters was used to adapt the image for the optimization program. Initially was performed a histogram-based filter to sharp the contrast of such picture allowing better identification of the flow strias, and since low strias are visible intensify the visualization of bigger strias and consequently better definition of the impact region. Additionally to capture only the interface between both jets it was calculated the gradient of the image and followed by the normalization. This will help to identify the location of the interface by tracking the jets diameter range inside de mixing chamber. This two methodologies will be introduced in follow with the correspondent equations.

The optimization algorithm will then use the processed images to obtain a simple point in the figure which correspond to the stagnation point, additionally with the jets angle by repeating almost the same methodology for finding the stagnation point. All the points correspondent to a change of phase in a vertical domain equal to the chamber diameter will be then filtered using statistical analyses and consequently a polynomial fitting curve will interpolate all of this values in the domain in order to obtain the slope of the line which corresponds to angle of the jets.

In the end the program will normalize all the obtained values in order to be comprehensive to the user and write and plot the important variables. This process is repeated for all the Important Reynolds in study which the results will be presented in the results section.

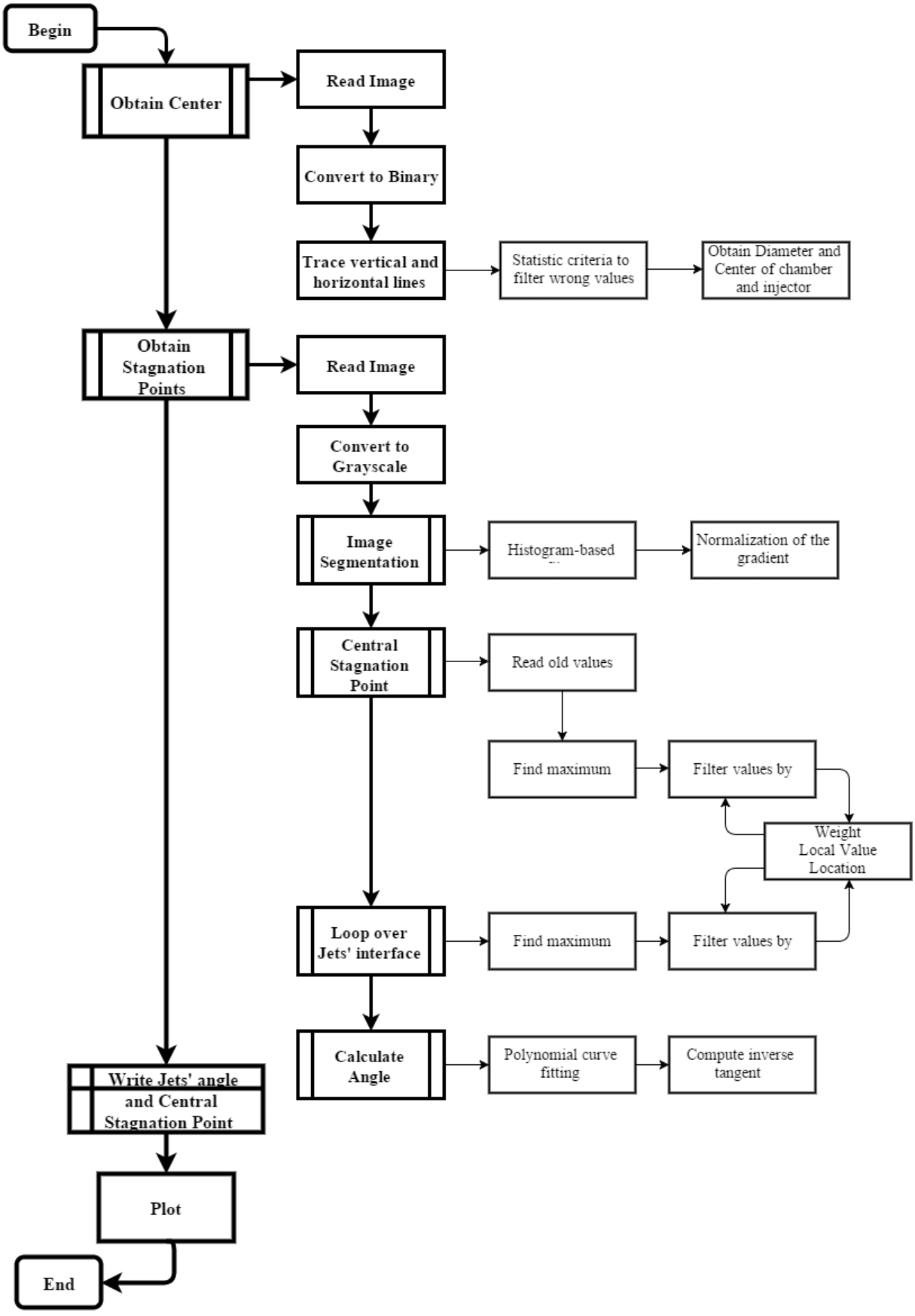

Figure 5.2 - Schematic procedure of implemented algorithm

5.2.2.1 Image adaptation

An image is mathematical point of view a function $f(x,y)$, defined by two variables in space and one additional to defined the brightness of the picture. In practical terms in a case of a greyscale image a 2D matrix defined by and x and y coordinates where in each cell a number represent a colour. For this particular case in image of 8 bits was produced, meaning each cell of the matrix can have a number between 0 and 256, where 0 corresponds the black colour and 256 correspond the white colour and all the number between both extremes represent a brightness in greyscale colour.

In a colour image the 2D matrix is then extended into a 3D, where in each block of 3 cells in a (x,y) direction a brightness exist for the three principal colours red, green and blue. The high speed camera used recorded in RGB mode and after transfer the data into a computer it was possible to convert into a greyscale in order to reduced storage space. One of the most well know conversion of a RGB into a greyscale image is by weighted averaging the each 3 brightness of the picture in a (x,y) direction, using the following equation

$$Image_{greyscale} = 0.3^{R} + 0.59^{G} + 0.11^{B} \tag{5.2}$$

Where R,G,B represent the colour initials red, green and blue. Figure 5.3 and Figure 5.3 shows the difference between a RGB image and a greyscale image. The most important is in the averaging the jets interface didn´t lose their sharpness and as it can be seen in the figures this statement is true

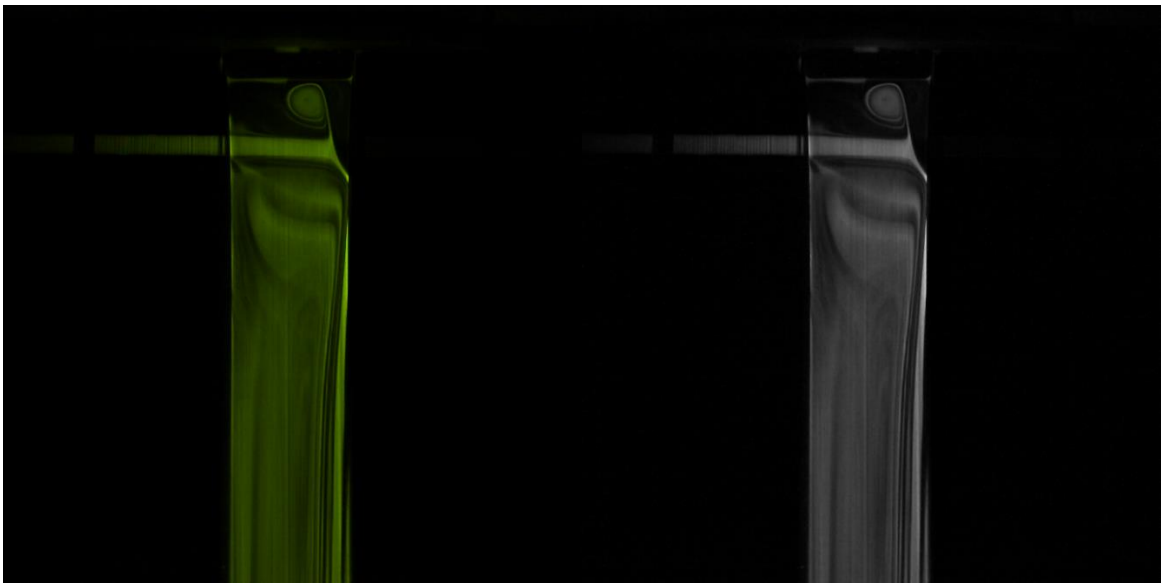

Figure 5.3 - RGB image

Figure 5.4 - Greyscale image

In the second subroutine in order to obtain the impingement point and the jets angle the image enhance was perform to allow clear visualization of the impingement structure formed due jets impinging. This step is crucial so ensure the optimization algorithm obtain a good sharp edge of the impingement, therefore more than one step was necessary to adjust the original image into an image which can be processed.

From the original image, Figure 5.3, a histogram based transformation is performed to ensure a sharp edge in the impinging zone. It can be seen in the original image some blurry but the histogram transformation a sharp edge, from white immediately to black is obtained. The histogram transformation spread the most used values into all the domain by creating and histogram almost flat, and it works by measuring the number of occurrences n_i of a grey level i in a grayscale image$x$. The probablitity of occurrence of a grey level is defined as

$$p_x(i) = p(x = i) = \frac{n_i}{n}, 0 \leq i < L \tag{5.3}$$

Where L is the total number of gray levels, in this particularly case 256, and n the total number of pixel in a image. Consider the comulative distribution function cdf_x defined as

$$cdf_x(i) = \sum_{j=0}^{i} p_x(j) \tag{5.4}$$

The general histogram equalization is calculated using

$$eh(i) = round\left(\frac{cdf(i) - cdf_{min}}{M \cdot N - cfd_{min}}(L-1)\right) \tag{5.5}$$

Where $M \cdot N$ is the number of rows multiplid the number of coloms whitch consequentlly correspond the number of pixel in the image. cfd_{min} is the miminum-non-zero value of the comulative distribution

Followed this step was necessary to ensure a more steep gradient in the image in case of a blurry impingement. Therefore was only consider the values after the histogram transformation inside a tolerance. This tolerance was set just to ensure the location of the impingement point are not influence in case of a good interface, but in case of a very blurry interface create an sharp edge.

Followed this step it was calculated the gradient of the image provided by the histogram transformation. The image gradient represent the direction change of the intensity of a greyscale in the image and it is calculated using the following equation.

$$\nabla f = \frac{\partial f}{\partial x}\hat{x} + \frac{\partial f}{\partial y}\hat{y} \tag{5.6}$$

Where $\frac{\partial f}{\partial x}, \frac{\partial f}{\partial y}$ represent the gradient of in the x and y direction respectively. Following the flip the colour in the image and improve the sharpness of the image the gradient of the image ∇f^* was calculating using the following equation

$$\nabla f^* = \frac{\nabla f - \nabla f_{min}}{\nabla f_{max} - \nabla f_{min}} \tag{5.7}$$

All of this steps was necessary to ensure a sharp and well defined interface without inducing errors in the location. The author emphasis more than one technique can be used to ensure the same conditions for the optimization algorithm use but due to the lack of information in the literature which can be used in the case of a blurry interface this sequence was of image processing was created.

An important note the last image treatment used ensure the image is numerically inside the range [0,1], meaning the zero represent the black colour and the one the white colour. This is vital since the optimization algorithm created is a weighted-based algorithm and an increase in this range will giving more weight in the image than in other variables which are essential to a smooth and error prove method.

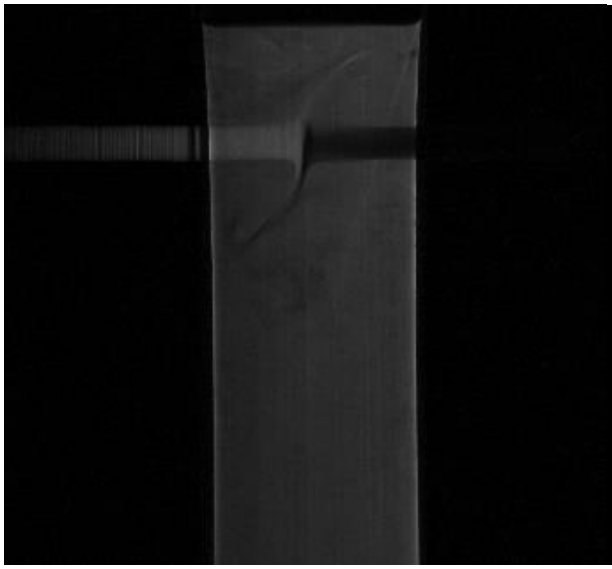

Figure 5.5 - Original image

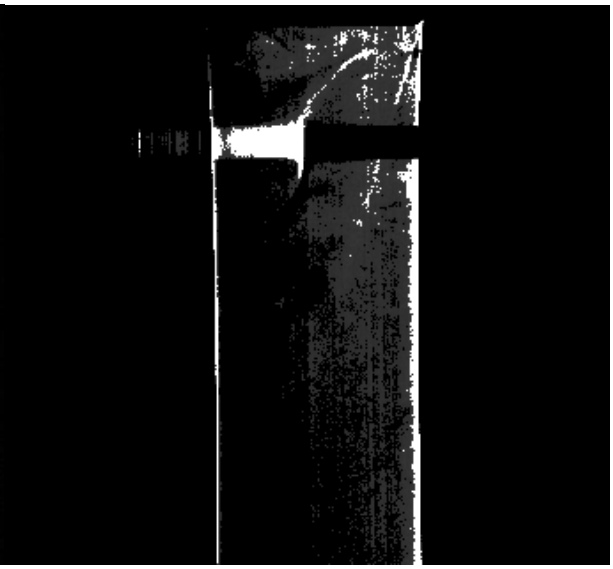

Figure 5.6 - Histogram based transformation

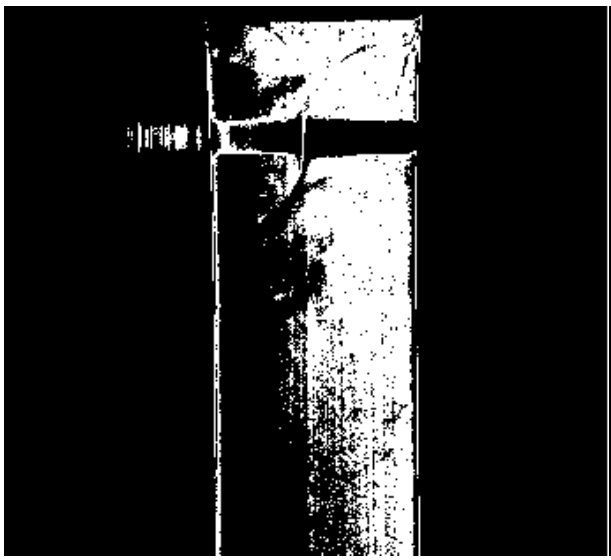

Figure 5.7 - Image gradient transformation

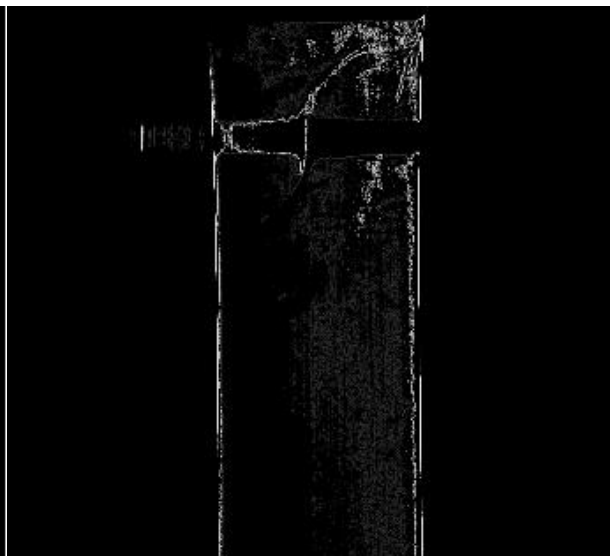

Figure 5.8 - Normalized gradient transformation

5.2.2.2 Determination of physical dimensions of the mixing chamber

To obtain the chamber dimensions the image from a unknown time step was chosen and followed transform from a greyscale image into a binary image. As it can be seen in figure xxx the blank spaces presented in the image are consequent the chamber dimensions. Just need to reefer here is a unknown and small error due the refraction of the light close to the walls of the chamber, although it was verified this error don't affect the results in study. The vertical red lines and horizontal blue lines correspond to a representation of the brute-force method to determine the chamber dimensions.

The blank space are then converted into physical dimensions in the intersection of the lines with the value of one, corresponding to the white colour, in the image matrix. After averaging the results of vertical and horizontal separated, they are filterer to obtain in the end a set of pixels in the horizontal and vertical direction witch correspond to the chamber and injector diameter, and the middle position is referred to the centre of each one.

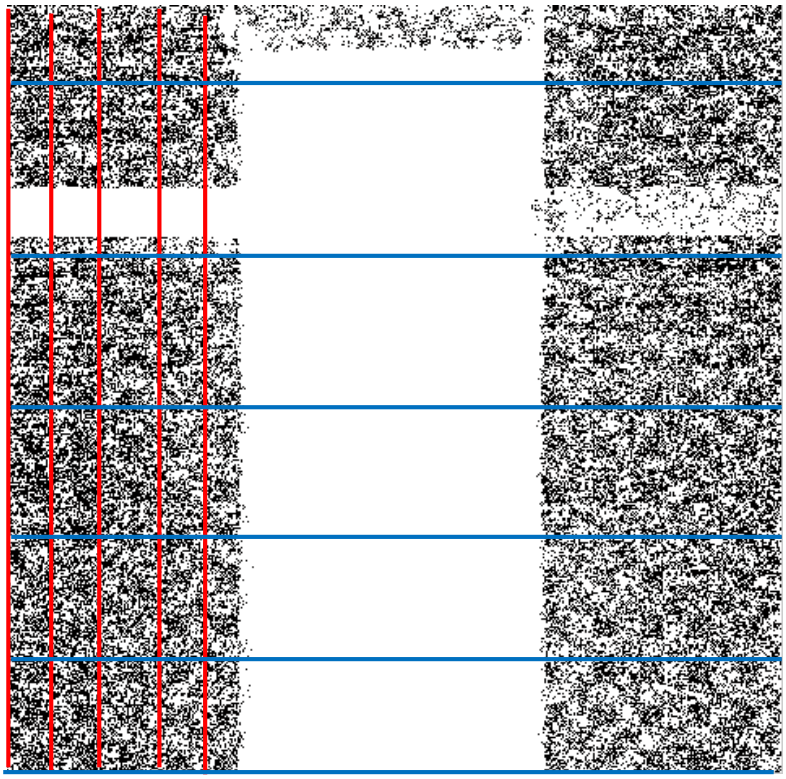

Figure 5.9 - Binary image to obtain physical geometrical dimensions of the chamber

This process is perform for one picture in each test perform. The results are then displayed for the user to ensure an acceptance due the proper measurement of the chamber dimensions.

5.2.2.3 Determination of the central stagnation point

After the process of ensuring a good quality image the optimization algorithm use the picture treated in order to determine the impingement point position. Following the injectors centre the program will verify the location of the high brightness values, associated to the white colour, which in the picture due the normalization is close to the value one.

Multiobjective optimization was essential to guaranty the location of the stagnation point is archived. Using a bell shape weighted method and controlling specific the shape, using the following mathematical expression

$$W_i = \frac{1}{1 + \left(\frac{x - c}{a}\right)^{2b}} \tag{5.8}$$

Where a represent the wide in the bottom, b the wide in the top and c the location of the central maximum point. Figure 5.10 shows the weighed method used to optimize the location with the stagnation point with more than one variable. The figure show the location of the stagnation point in the left of the chamber close to the walls in the top plot and the location of the stagnation point in the centre of the chamber

The weight 1 corresponds to the weight due the location of the old stagnation point correspondent to the immediately time step before the current calculation. Using this method it give more weight to neighbour values rather than far values. The weight 2 correspond to the location of the stagnation point inside the chamber, favouring locations in the middle of the chamber.

The weight are averaged using the following equation

$$W^* = \left(\left(\frac{W_1}{2}\right)^2 + W_2^2\right)^{\frac{1}{2}} \tag{5.9}$$

As it can be seen the average weight and the weigh 1 was tuned and chosen to ensure the choice of the stagnation point even for fast displacements, larger than the weight 1 domain.

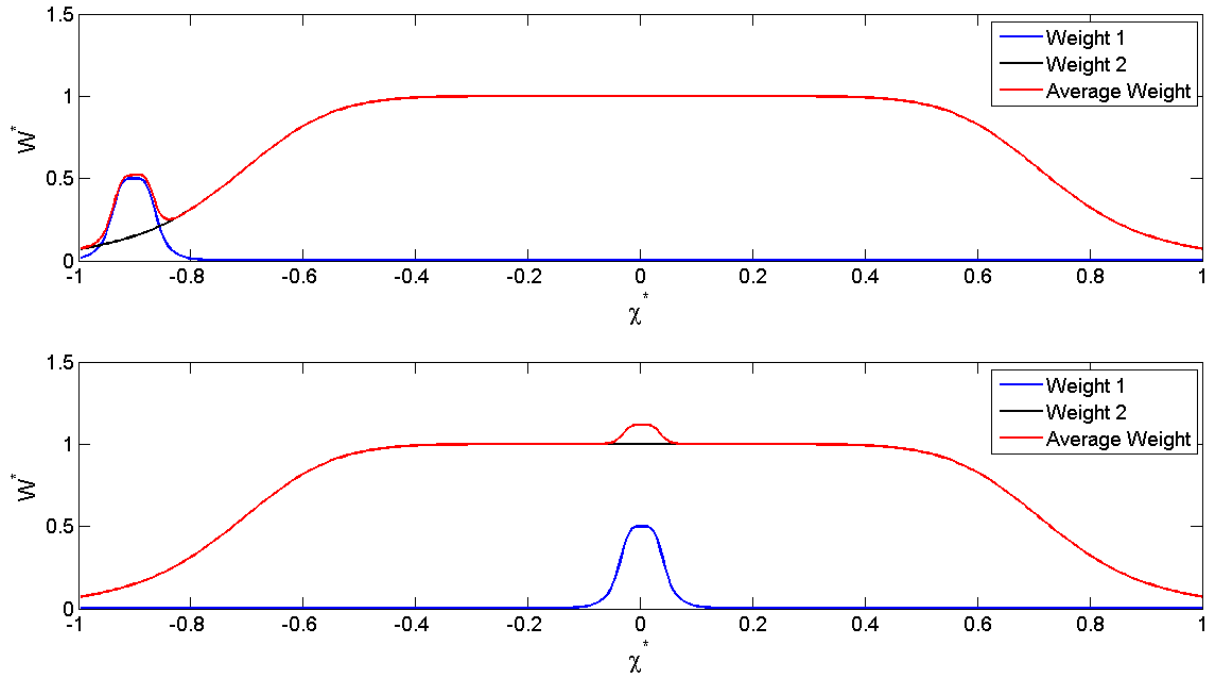

Figure 5.10 - Weighted method response for two different cases. The previous impingement point position is on the left side of the chamber (top) and in the centre of the chamber (bottom)

Additionally the average weight are then chosen also according to the location of the stagnation point position using the following mathematical equation

$$x_{IP} = \mathrm{X}_{\nabla f^*} \cdot W^* \tag{5.10}$$

This equation will lead, the chosen of the maximum value considering the cell value of the normalized image gradient, pondered by the location of the previous stagnation point and the position insider the mixing chamber.

This multiobjecive optimization will ensure quality of the result by guaranty low error succession between each frame, a ponderable choice of the impingement point favouring the result obtained by the image and also with the multiobjective variables described. As it can be seen in the results section a coherent and realistic displacement of the impingement point, by comparing with the patter in the movies, is obtained.

A bad choice of the impingement point will lead to a unrealistic and incoherent value of the jets angle, which going to be presented next, and will be easily seen in the result for this new variable.

As it was refereed this technique it works error-proof in a case of a good image is obtain and a proper impingement section is observed. In a case of both conditions isn't verified could lead to a bad calculation of the impingement point position and jets angle

5.2.2.4 Evaluation of jets angle

Using the same strategy was used to calculate the impingement point position, the jets angle will used the previous calculate value as a starting point. A loop will sequentially identify the stagnation point along it search downwind and upwind the mixing chamber in a injector diameter range.

The same methodology multiobjective weighed method was used but with refinement. Since the maximum angle is obtain due the jets bending it was ensure the location of the point inside the mixing chamber don't interfere with the decreasing in weight due this variable.

Followed the weighted 1 in now change to consider the stagnation point in the previous vertical point calculated in the same time step image. Additionally as it goes up and down, get farther than the central stagnation point, alight with the jets centre, the wide's of the weight 1 are progressively reduced to the reduction of thin lamina of fluid, particularly obtain in a case of high angle of the impingement jets or other irregular phenomena.

After the points location (x,y) of the impingement surface is obtained the results are then filtered and only consider in a case of

$$\overline{x_{ip}} - 2\ desv(x_{ip}) \leq x_{ip} \leq \overline{x_{ip}} + 2\ desv(x_{ip}) \tag{5.11}$$

Where $\overline{x_{ip}}$ is the averaging of the position of the set of impingement point's position in the jets angle and $desv(x_{ip})$represent the standard deviation of the result. This methodology was used to discarded the possibility of the low angle affect the solution due high angles of slope obtain, which correspond to zero degrees normalized angle.

After filtering and order one polynomial function interpolate the result into the following formula

$$y = mx + b \tag{5.12}$$

Where m represent the slope. The angle is then calculated using

$$Angle = \operatorname{atan}(m) \tag{5.13}$$

The result angle is the normalized and in case of the impingement rotates clockwise it is consider positive angle and anticlockwise negative angle.

5.3 Real time flow visualization

Previous works focus in the study of the mixing mechanics using images obtained from a sequence of frames which didn't allowed to study in detail all the process of the impingement surface moving in a real time flow. For the first time a sequence of images was obtained in order to visualize the principal mixing mechanics inside the mixing chamber, which is known to be in the impingement area. This study will further improve the knowledge of the oscillatory motion of the impingement surface for a large set of Reynolds number.

Additionally using the DIP MODA the behaviour of the impingement surface will be study, particularly the impingement point position in a 2D frame and the jets angle in the same plane. Will be draw relations and conclusions regarding the pattern of this both variables and the relationship between the Reynolds number and measurement devices for RIM control.

In the present subsection will be stat to present the experimental equipment and technique used to obtain the real time flow images of a RIM machine. Additionally will be presented the working fluid rheology and the error analyses of the measurement equipment and experimental technique

In the end the results will be presented, start by an analyses of the visualization studies, where the instantaneous 2D flow field will be presented for each Reynolds in study, and after the results provided by the DIP MODA correspondent to the angle and stagnation point for all the domain in study also will be analyse. Spectral analyses comparing the stagnation point position, the jets angle and the displacement of the differential pressure transducer will be presented and discussed.

This is the first time where real time flow visualization is perform for RIM machine were due their importance will be possible to study the flow for all the spectra, which will allowed a comparison with the DNS performed. In the present case only will be study the injection of energy, which is known to be due of the oscillatory motion of the impingement surface, but latter other techniques could emerged to analyse other characteristic of the flow, particularly the dimension of the laminate thickness entre others.

5.3.1 Experimental setup

Planar Lased Induced Fluorescence PLIF is an experimental technique which allow visualization of the flow field in a giving plane. For this happen a fluorescent dye marker is added to the flow entering in one side of the mixing chamber, where when contact with the

laser sheet the die marker will emit a light which will going to be latter being possible to identify using an digital camera. The intensity of emitted light will be possible identify and quantify the concentration of the flow in a given area. This technique is not invasive, meaning don't intervene with the flow field and additionally don't change the proprieties of the fluid injected with the die marker.

In the present work PLIF technique was used to for the first time perform real time visualization of the flow field allowing better understanding of the mixing mechanics of the impingement jets and the consequences of the breaking of the oscillatory motion of the impingement surface for the flow field behaviour.

5.3.1.1 The RIM machine

The RIM machine in two main groups. The first group is composed by pumps, tanks, valves, etc, everything which is needed to control and maintain the fluids. The second is the mixing chamber. In the present work the mixing chamber was created from a Plexiglas block which is cut in order to create the injector's and the mixing chamber with the physical dimensions similar to an industrial mixing chamber and presented in Figure 4.1. The choice of Plexiglas is to allow internal visualization of the flow field using different experimental techniques.

One of the main problems when construction of the mixing chamber in order to don't affect the mixing performance is ensuring the injectors are perfectly aligned with each one and perpendicular to the chamber centre. Additionally the injectors have enough length to ensure the development of a parabolic velocity profile due the flow regime is in laminar.

As it can be seen in the Figure 4.1, the injectors have 1.5mm of diameter, and are placed 5mm from the top of the mixing chamber. The injectors are position normal to the mixing chamber axis, which have a diameter of 10mm and a length of 50mm. The downstream of the mixing chamber is connected to a spherical container with 150 mm of diameter and 80 mm of height, which replicated the mould filing.

Additionally the processes equipment, presented in figure xxx, contain two tanks where the working fluid is storage, being one with pure working fluid and other with dyed fluid. The dyed fluid is injected in the left side of the mixing chamber while the pure fluid is injected in the right side. After mixing the fluids go for the mould recipient and after for an additional storage tank which will storage the fluid for proper disposal. The tanks are pressurized with air, to prevent fluctuations of the pressure due pumping, and are controlled with a needle valve.

The fluid temperature, density and flow rate are measured with a coriolis mass flow rate meter and storage in a computer with addition with the differential pressure provided from the differential pressure transducer which reads the difference of pressures between both sides of the chamber.

5.3.1.2 PLIF Setup

The PLIF requires two main components. The first component is a laser system to produce, conduct and create a sheet which will illuminate the dyed fluid and the second is a camera to record this illuminate flow dyed. The experimental setup is presented in Figure 5.11 and in Figure 5.12.

A thin laser sheet of 1mm of thickness, which cut the mixing chamber axially through the injectors, illuminated the dyed fluid, is created allowing the 2D fluid flow visualization. The Laser source (model: 543-TSI-A01) emits a continues laser with maximum 400mW energy at a wavelength with 454 to 514 nm which are transported to the top of mixing chamber by a TSI light arm (Model 610015) which consist in a articulated hollow tube with 1.8m with reflective mirrors. In the end of the light arm a spherical 500 mm lens concentrate the beam and afterwards -15mm cylindrical lens create a laser sheet which a focal distance of 500mm resulting in 1mm thickness laser sheet.

The flow field is recorded using a high speed camera model Photron FastCam (Model: SA5) with the ability of recording 1024 x 1024 pixels in a 16 bits of RGB. In each sequence the camera is setting to record at 1000 FPS with a shutter rate of 2000 FPS. The capture image is then save in the camera internal storage and after that transferred into a computer using a RJ45 cable where the images are treated and storage. The camera software will then create the experimental video which will be going to be save additional with the individual images to be processed using the DIP MODA program. When experiment it was ensure a proper position and alignment of the camera additional to focus into the laser sheet to observe the flow patterns.

It is know from the manufacture the Rodamine 6G, used as a dye marker, have the maximum absorption of light close to 526 nm and emits fluorescence in a wavelength around 564 nm (Magde et al., 2002). To filter any reflections of the green laser light and orange glass filter with 545 was adapted into the camera lens. During the experiment no additional light source was available in the experiments.

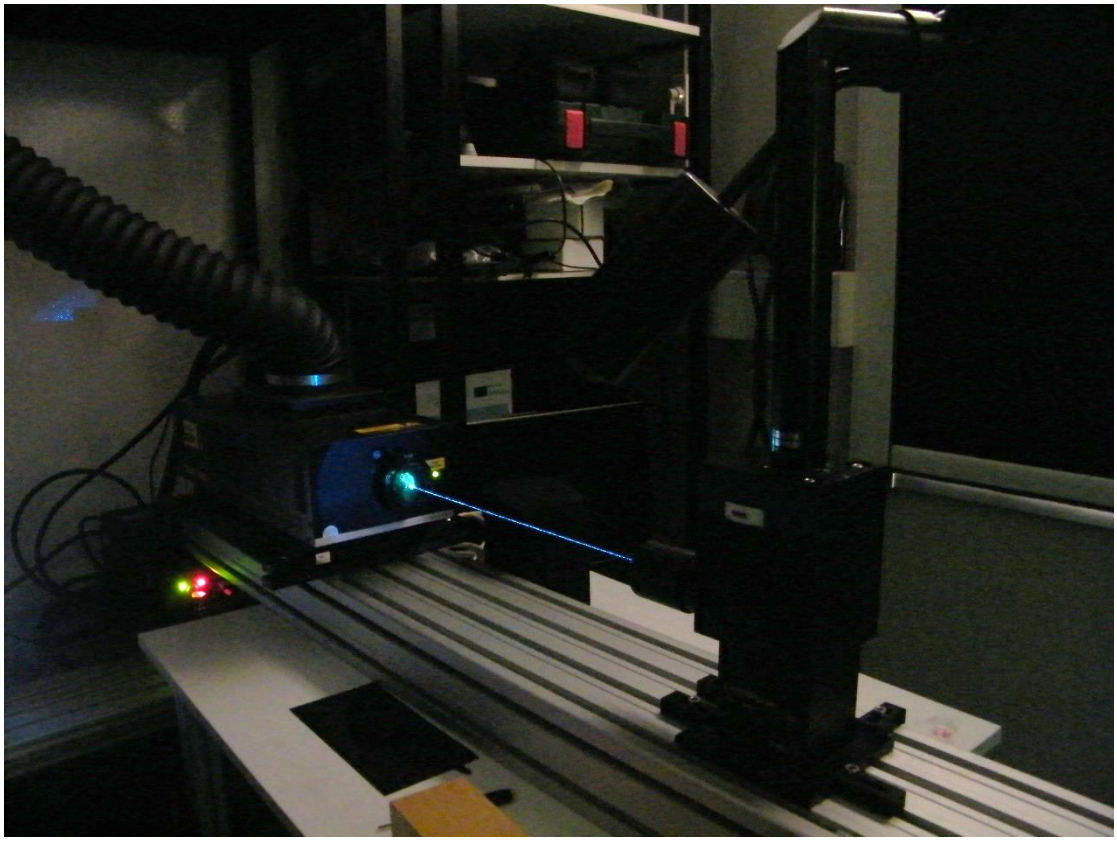

Figure 5.11 - Experimental setup. The laser source and the light arm.

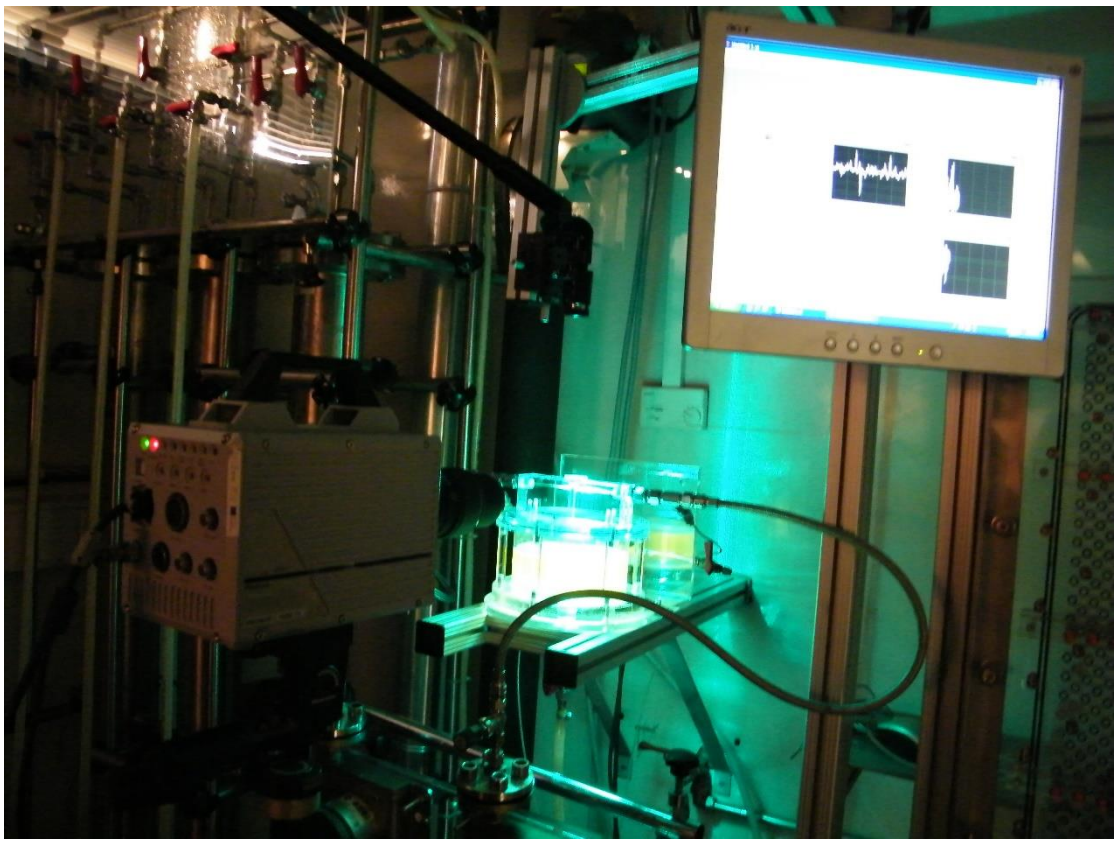

Figure 5.12 - Experimental setup. Fast camera, light arm, mixing chamber and computer for acquisition of the differential pressure and flow rate in each injector

5.3.2 Experimental conditions

The fluid is a mixture of glycerol and water at a percentage of 72.5% as defined in section 4.3.3. in order to obtain a 0.02 Pa.s of viscosity in the working temperature. The fluid was mixture in batch and was insert into the tanks during the experiment. In each batch the fluid rheology was performed.

During the experiments the fluid density flow rate and temperature additional with the pressure provided by the differential pressure transducer was recorded at 1000 Hz

5.3.2.1 Rheology of the solution

In each batch the fluid proprieties was calculated using a rheometer (Paar Physica UDS 200) with a plane (MK24) and plate in the temperature range 20 to 30º. In Figure 5.13 is present the working fluid. The mathematical expressions and the fitting curve for viscosity temperature dependent was introduced earlier in section 4.3.3. It was considered in the calculation of the experiment Reynolds number the averaging of the viscosity of the four batch as the viscosity standard for the present work.

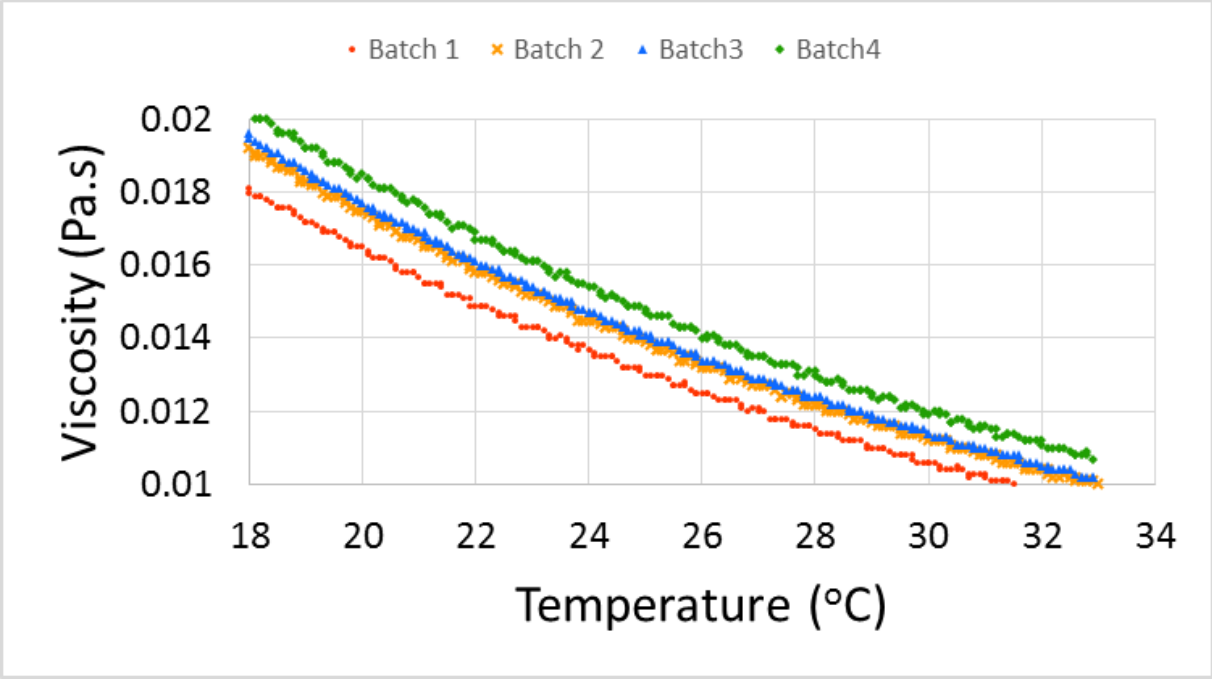

Figure 5.13 - Rheology of each batch working fluids

5.3.2.2 Calibration

The fluid temperature, density and flow rate was recorded by the Coriolis mass flow meter (model RCCCS33 M01A1SH) with precision of $\pm 0.05 g/s$ in the range of 1.2g/s to 13.2 g/s, and for the minimum flow rate in this work as 0.5 g/s correspond to a relative error of 10%.

The pressure for each simulation is recorded by a differential pressure transducer (Validyne P305D) mounted in the beginning of the injection of the mixing chamber which are calibrated externally using a column of water and the signal is recorded using a data acquisition system (GW Instruments MacADIOS II) connected to a external board (GW Instruments MacADIOS ABO) with a computer and recorded using a LABVIEW developed program. Same recording is used for the mass flow readers. All of variables are then latter processed using MATLAB to postprocess and quantify the results obtained.

The concentration of rhodamine 6G used in all experiments was $C_{rhodamine} = 0.4g/l$. Claudio perform a study to verify the linear response between the light intensity and concentration of rhodamine in the solution. This simple test consists in illumined various concentrations of the solution with rhodamine 6G and obtain the pixel light intensity I. It is know the pixel light intensity have a linear relationship with the concentration of rhodamine in a following form

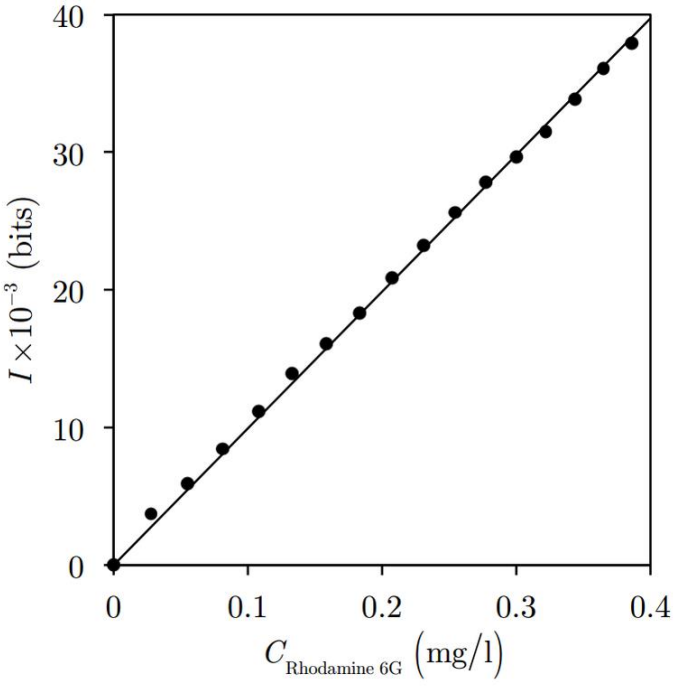

Figure 5.14 – Pixel light intensity as a function of rhodamine 6G concentration in the working fluid

5.3.3 Results

Consider the mean passage time τ, defined as

$$\tau = \frac{D^2 H}{2 u_{inj} d^2} \tag{5.14}$$

Where H is the hight of the mixing chamber, d the injector diameter and u_{inj} the mean velocity in the injector. The normalized impingement point position is defined as

$$\chi^* = \frac{x_{IP}}{\frac{D}{2}} \tag{5.15}$$

Where x_{IP} is the impingement point position, in mm normalized by the chamber radios $D/2$

The results from the high speed camera are presented for a large set or Reynolds number. For each case will be visualized the instantaneous flow field, the impingement point and jets angle using DIP MODA and the spectral analysis comparing this both flow variables with the variation of pressure reader by the differential pressure transducer.

5.3.3.1 Diffusion study

The study of the diffusion between two fluids was performed. After introduced in the chamber randomly proportion between the two fluids to form thin thickness laminas it was observed mainly three images, each one separated by 5000 ms.

As it can be seen in Figure 5.15 the thin laminas presented in the top of the mixing chamber will allowed visualize the diffusion between both fluids. In this region is clearly visualized imperceptible diffusion of the thin laminas for t=0 ms and t=10000 ms by a small reduction of the sharpness of this laminas.

This work documenters the assumption using until now of the both fluid, due their high viscosity, don't mix due diffusion inside the mixing chamber and it is necessary some oscillatory motion to perform advective mixing.

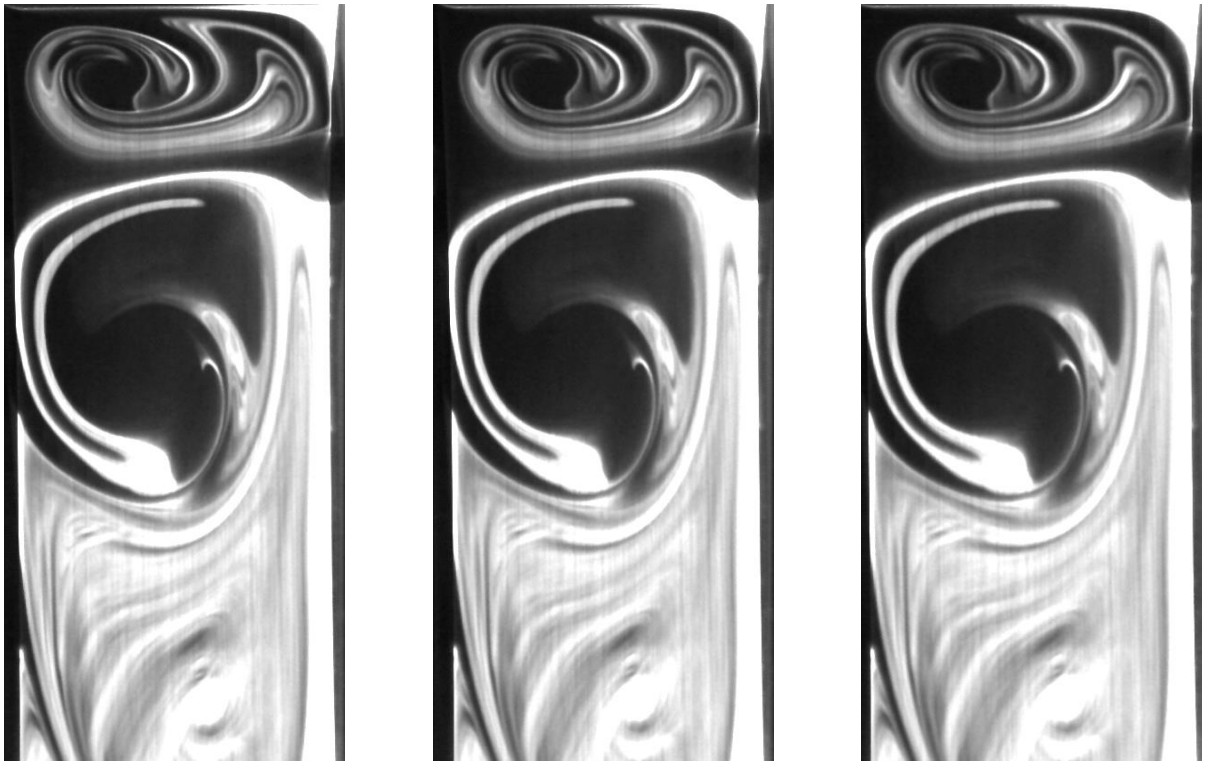

Figure 5.15 - Diffusion study for t=0ms (left) for t=5000 ms (meddle) and t=10000 ms (right)

5.3.3.2 Instantaneous flow field visualization

The instantaneous flow field visualization is presented from Figure 5.16 to Figure 5.32, which correspond to all the Reynolds in study. In the CD folder is present the movies correspondent to each experiment. Before present the main conclusions of the flow field is necessary to highlight the flow regime from previous works.

In the latest work, Fonte (2012) performed visualization study to analyse the beginning of the oscillatory movement of the impingement surface in where he conclude:

- For Reynolds less than 103 the flow is segregated, meaning there is no distribution of material along the chamber and half of the chamber is fulfilled with the fluid injected by the injector
- For Reynolds equal to 104 the flow evolves into a oscillatory periodic laminar regime characterized by small disturbance of the impingement jets interface with the formation of alternated vortices downstream the inlet. In this configuration the flow is segregated for each side of the chamber
- For Reynolds bigger than 111 occur formation of vortices earlier in the flow field, meaning closer to the impingement point, with this interaction develop a self-sustained chaotic laminar regime with strong mixing dynamics.

Other works, both numerical and experimental, situate the critical Reynolds, value in a self-sustainable chaotic regime occur in the range 110 to 120.

In the present work it was used more than one batch working fluid, and as it was documented exist a big variation in rheology between each batch performed. This will then will result in a small variation of the Reynolds calculated associated with this uncertainty. Spite this fact the conclusions of the instantaneous flow field visualization will be perform for the current experimental work.

In Reynolds number 26 and 65 the flow is fully segregated as it can be seen due the complete separation of colours in each side of the chamber. In this conditions no mixing of the fluids exist since the flow leave the chamber with a very low contact region, only exist in the interface. This flow regime is identified due existence of two big recirculation vortices in the top of the mixing chamber followed with parallel path lines downstream the mixing chamber after the impingement.

For Reynolds 83 a oscillatory periodic regime is obtain with formation of small vortices detaching in the downstream the mixing chamber. This vortices is very large and don't provoke mixing, remaining the flow segregated

Above Reynolds 90 self-sustainable chaotic regime is obtain, meaning due the oscillatory motion of the impingement surface spread of material along the chamber will exist and foment advective mixing mechanisms. For this Reynolds the impingement surface present an almost periodic motion provoke bending and stretching of the fluid particles along downstream the mixing chamber. The strias will then folder into a horizontal plane after the impingement point and flowing downstream the mixing chamber until a length where start to parallelise the flow with direction of the chamber axis. This effect is mainly due viscous shear on the walls which after will be going to be transmitted into the fluid. This pattern in maintained until Reynolds 123 but with difference is during the range the oscillatory motion of the impingement surface is fully chaotic and unpredictable.

In Reynolds 134 two main flow dynamics is observed. One is similar with the previous explanation where the spreading of material occupies all the chamber diameter with horizontal pathlines downstream the impingement region with a halt of the flow afterwards. Additionally is observed a stopping of the oscillatory motion in the front plane but without any segregation of the flow. This is due the additional planes of motion will spread the fluid particles with addition of small detaching l vortices downstream impingement point. This

small vortices will not spread material along all the chamber diameter but will focus in the centre of the chamber

The incremental increasing of the Reynolds number will tend to reduce the lamina thickness and the size of the main vortices with increasing in the frequency in where the vortices is created.

Above Reynolds 171 the previous mechanics will start to vanish and new will emerge. It is observed an increasing of the breaking of the oscillatory motion of the impingement point, which will going to create tinny vortices in the region close the impingement point position and concentrate the mixing in this region. This breaking will create big destabilization of the impingement point position along the diameter of the chamber. Additionally the reduction of the jet's angle is observed. The main lamina of fluid created due impingement tends, whit the increasing of the Reynolds number reduce the thickness and length. All of this patterns occurs with a going reduction of length scales, increasing frequency of the impingent motion and concentrate the mixing mechanics in area of the impingement point position.

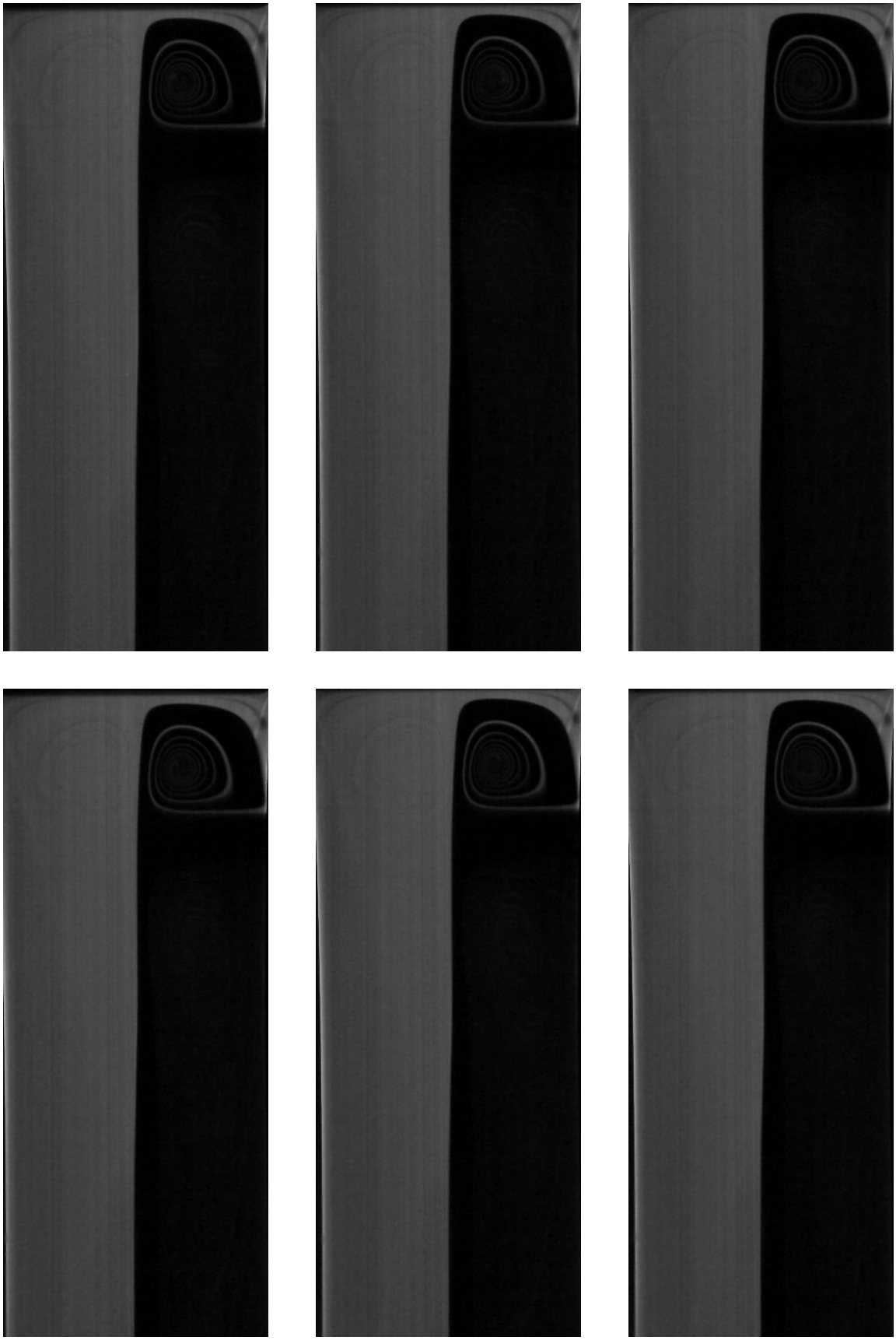

Figure 5.16 - Instantaneous flow field in the front plane for Reynolds 26

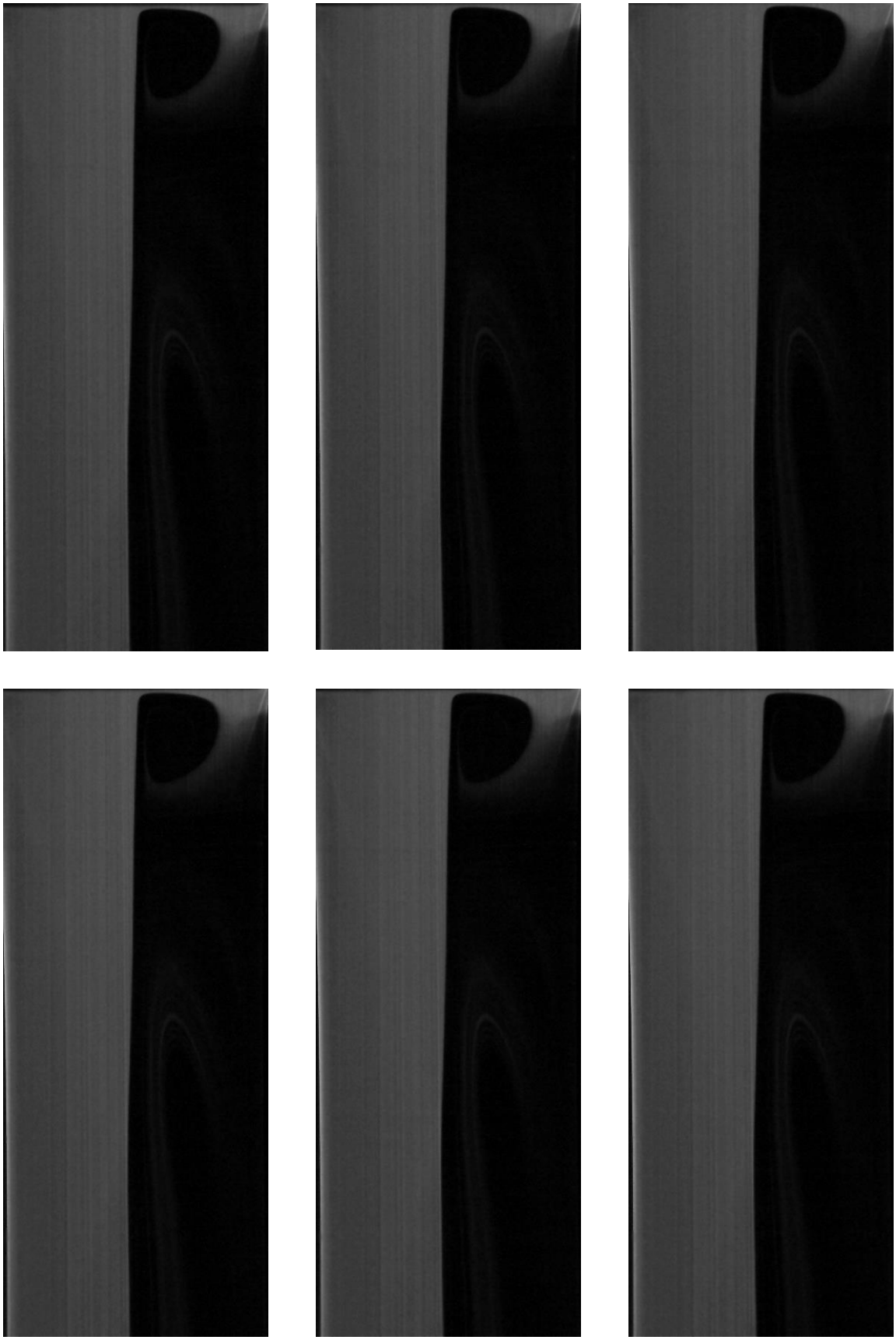

Figure 5.17 - Instantaneous flow field in the front plane for Reynolds 65

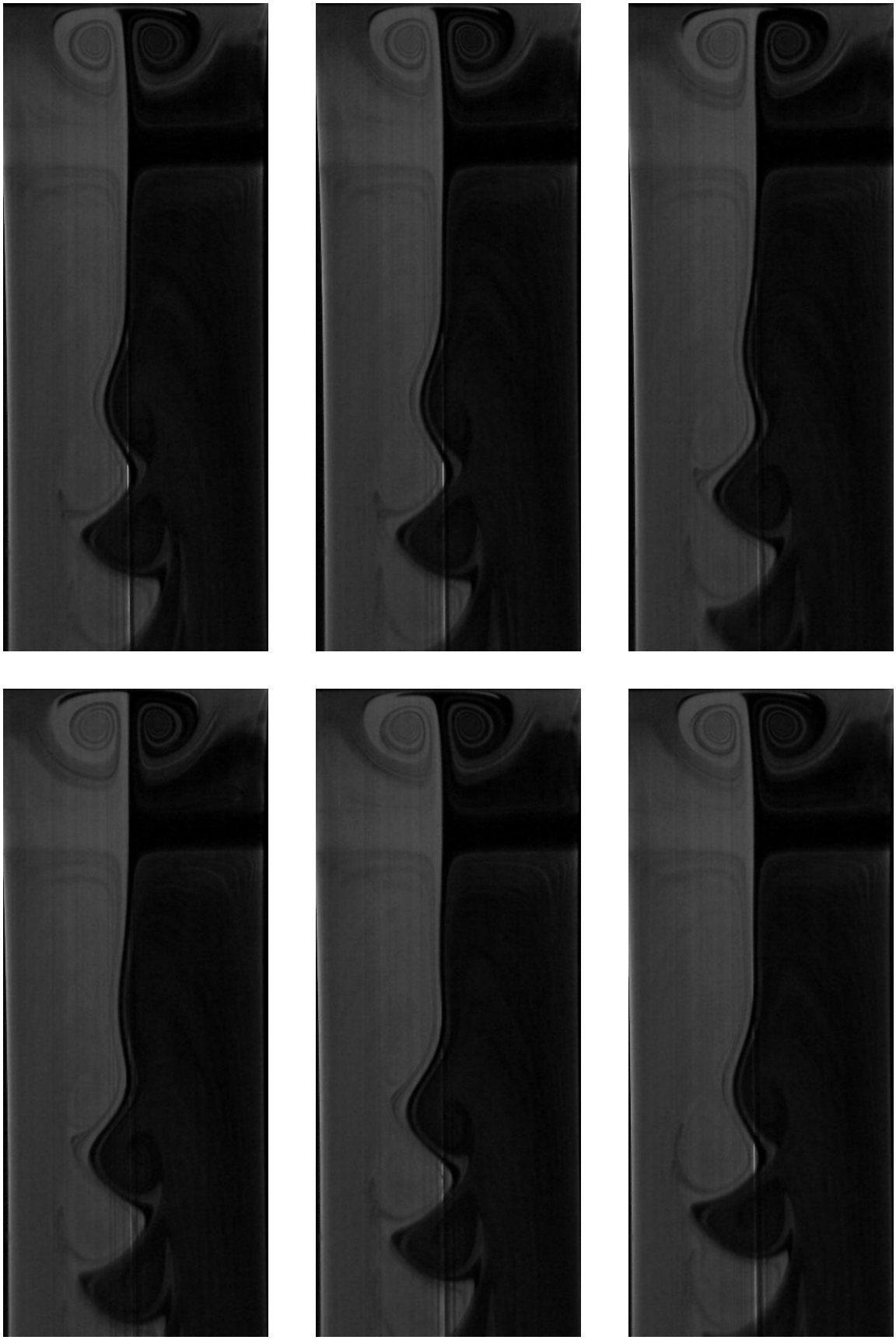

Figure 5.18 - Instantaneous flow field in the front plane for Reynolds 83

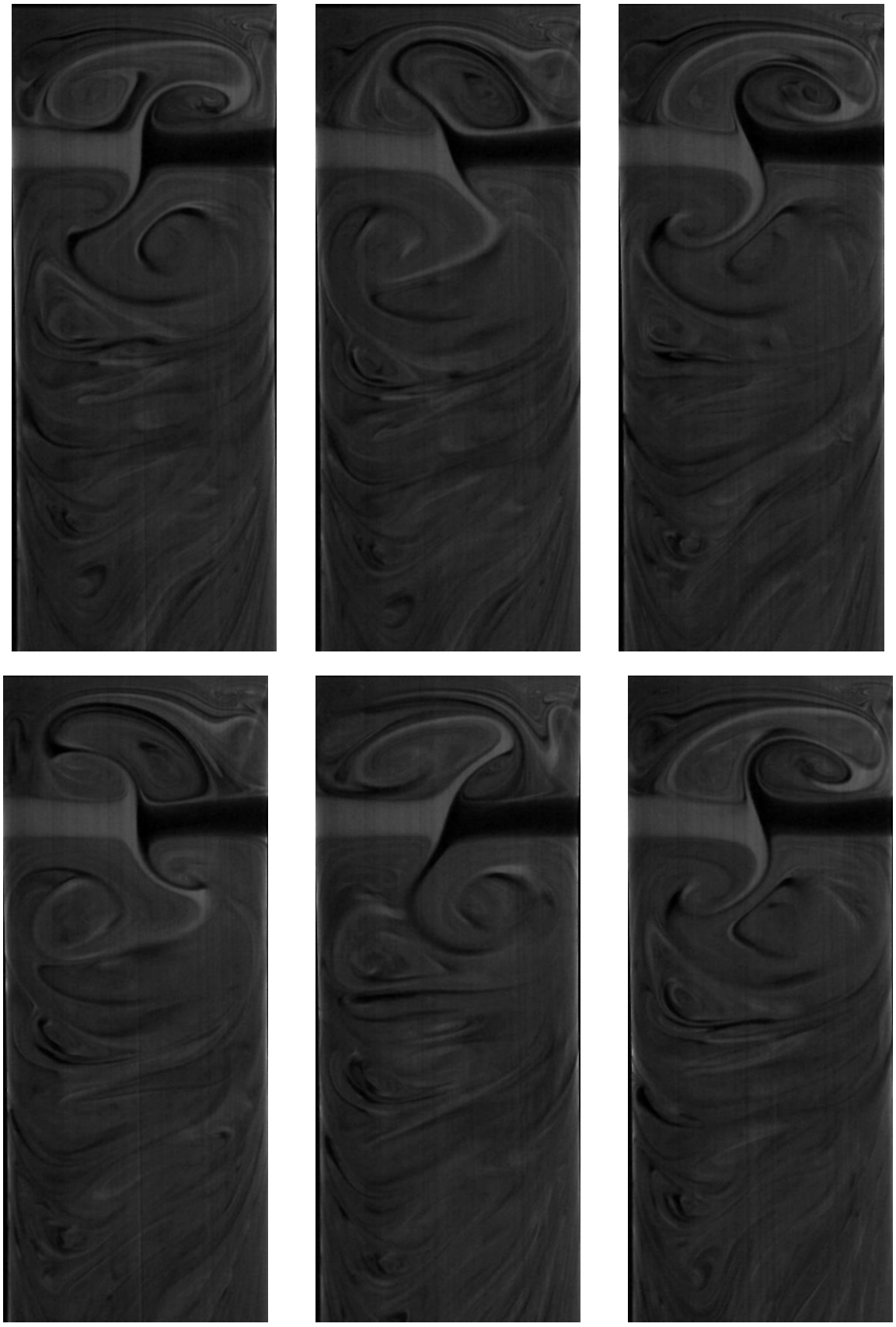

Figure 5.19 - Instantaneous flow field in the front plane for Reynolds 90

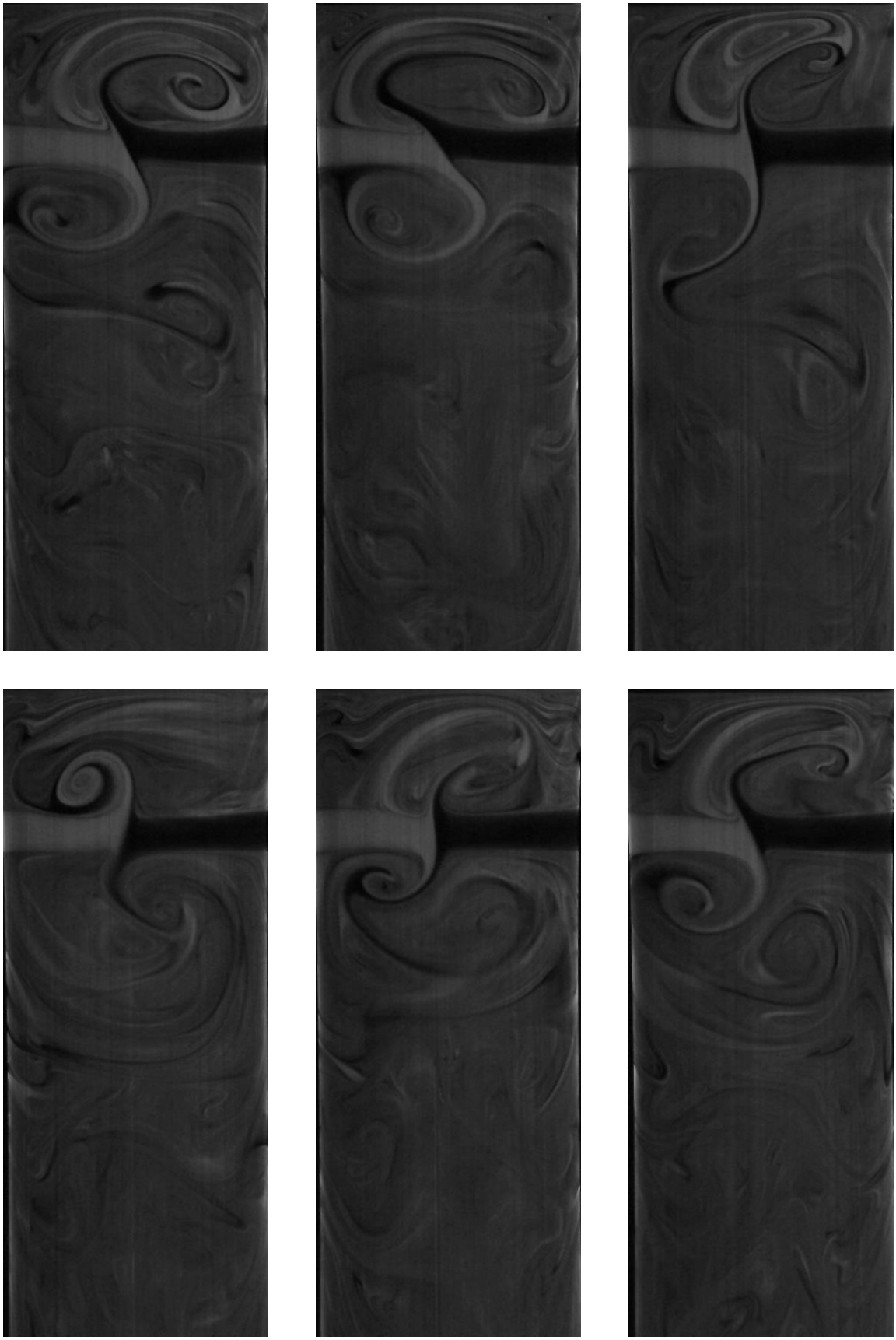

Figure 5.20 - Instantaneous flow field in the front plane for Reynolds 100

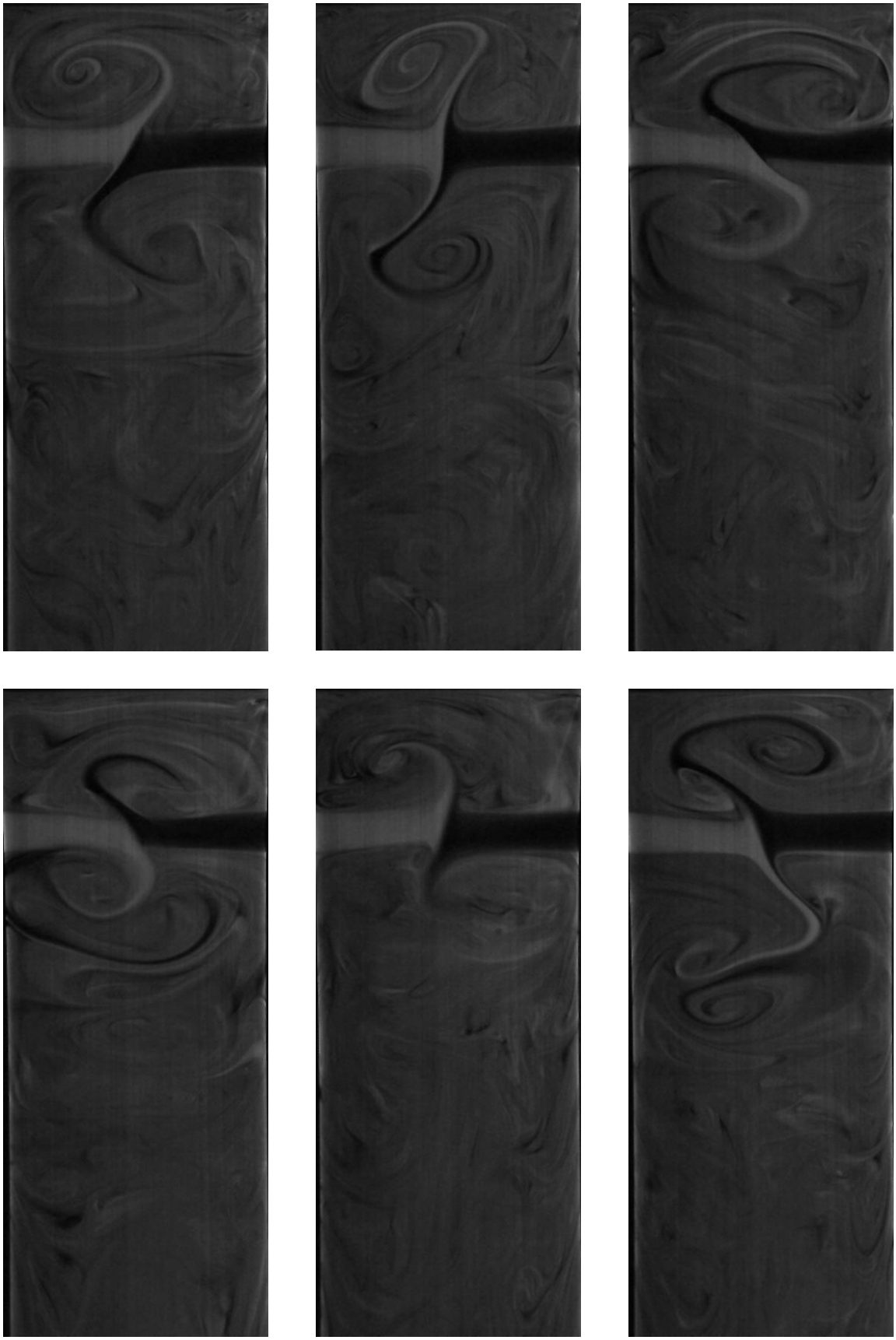

Figure 5.21 - Instantaneous flow field in the front plane for Reynolds 123

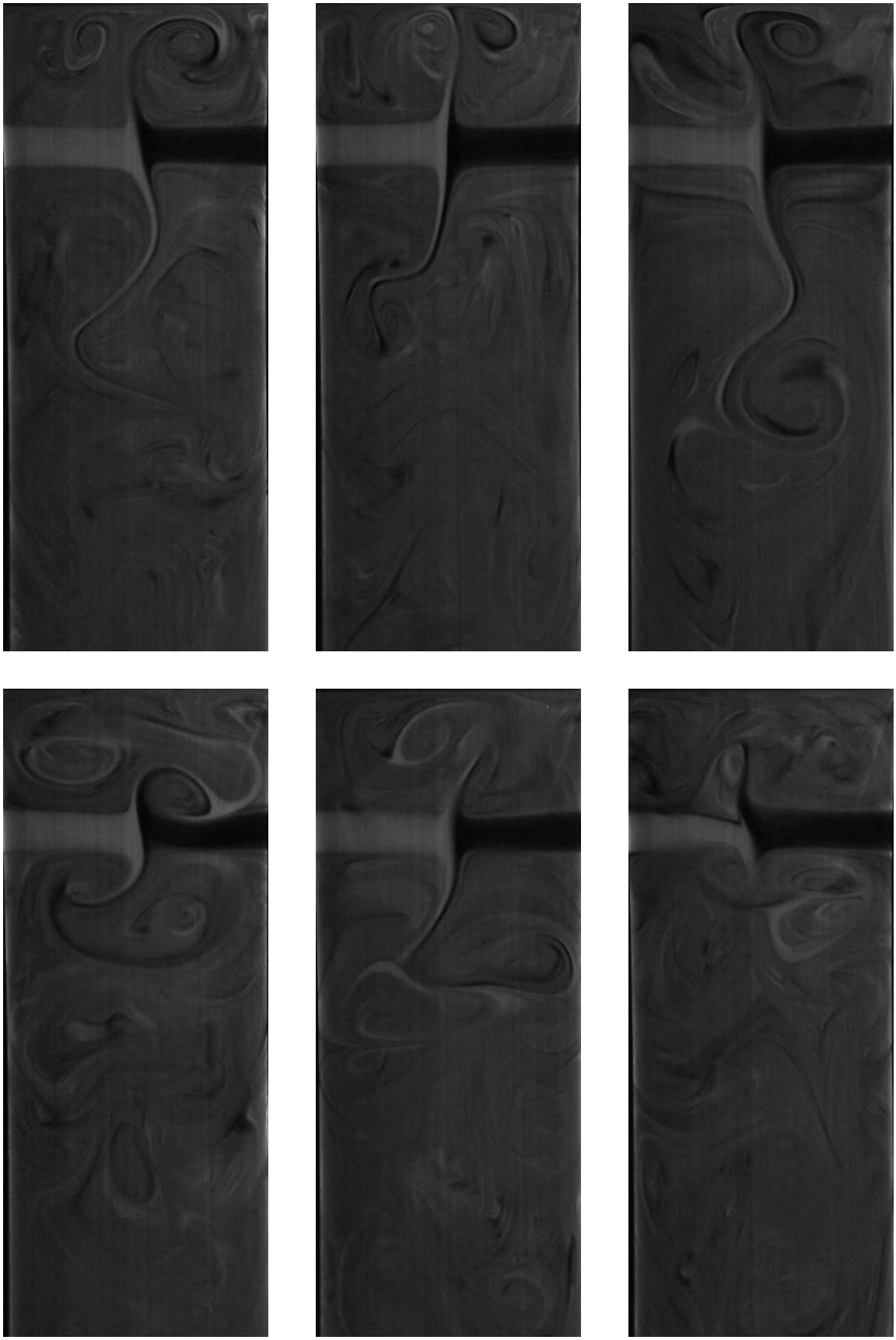

Figure 5.22 - Instantaneous flow field in the front plane for Reynolds 134

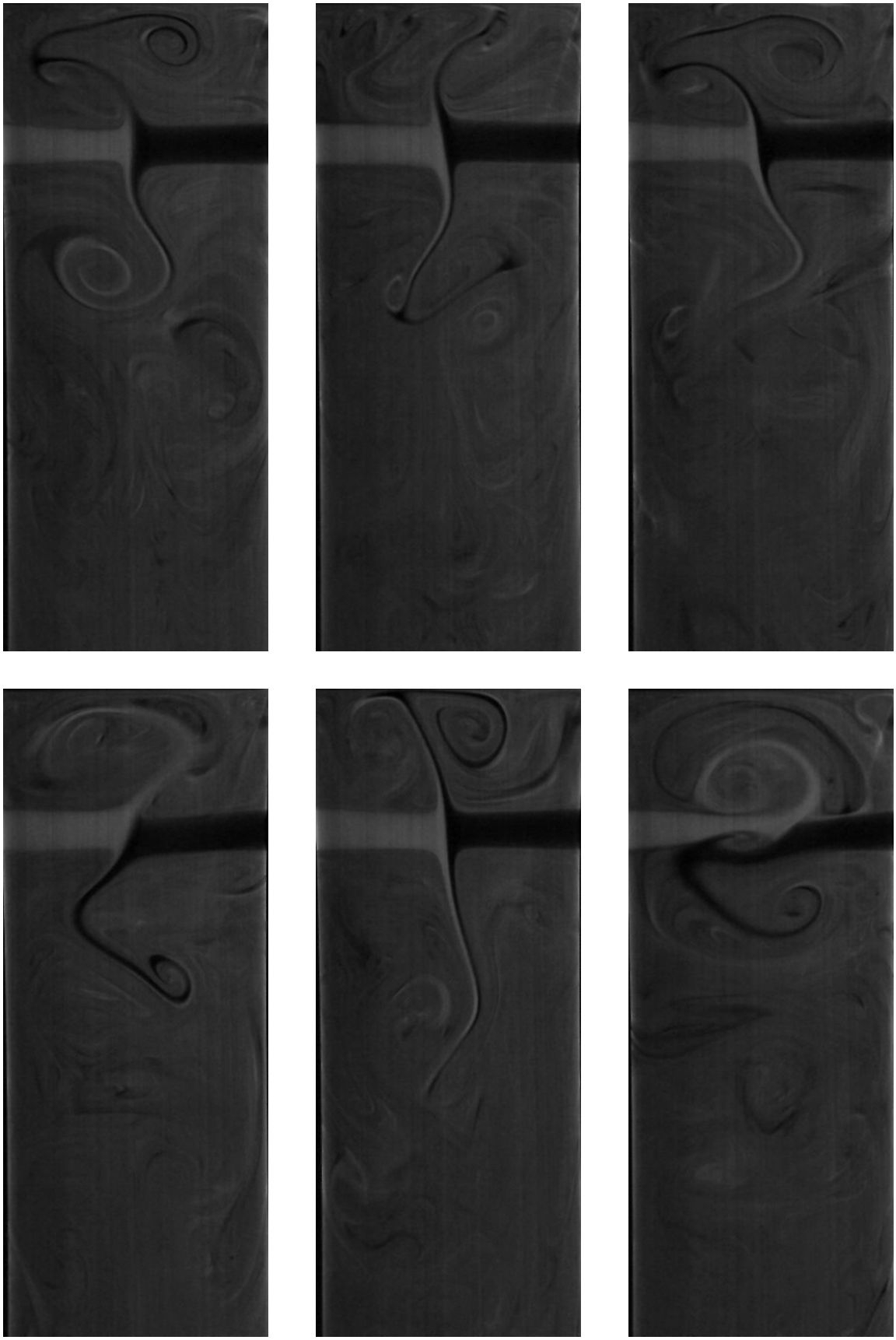

Figure 5.23 - Instantaneous flow field in the front plane for Reynolds 171

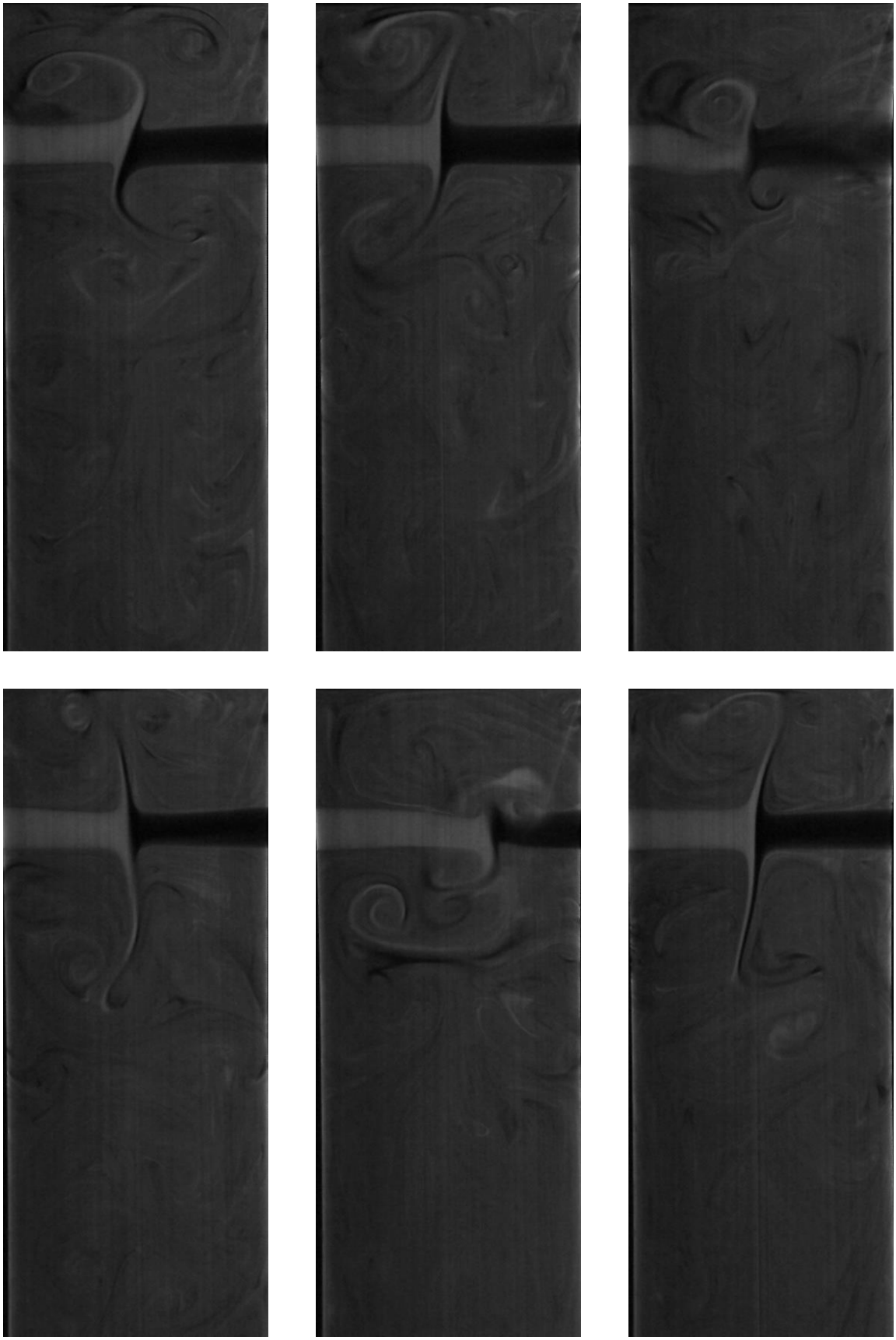

Figure 5.24 - Instantaneous flow field in the front plane for Reynolds 205

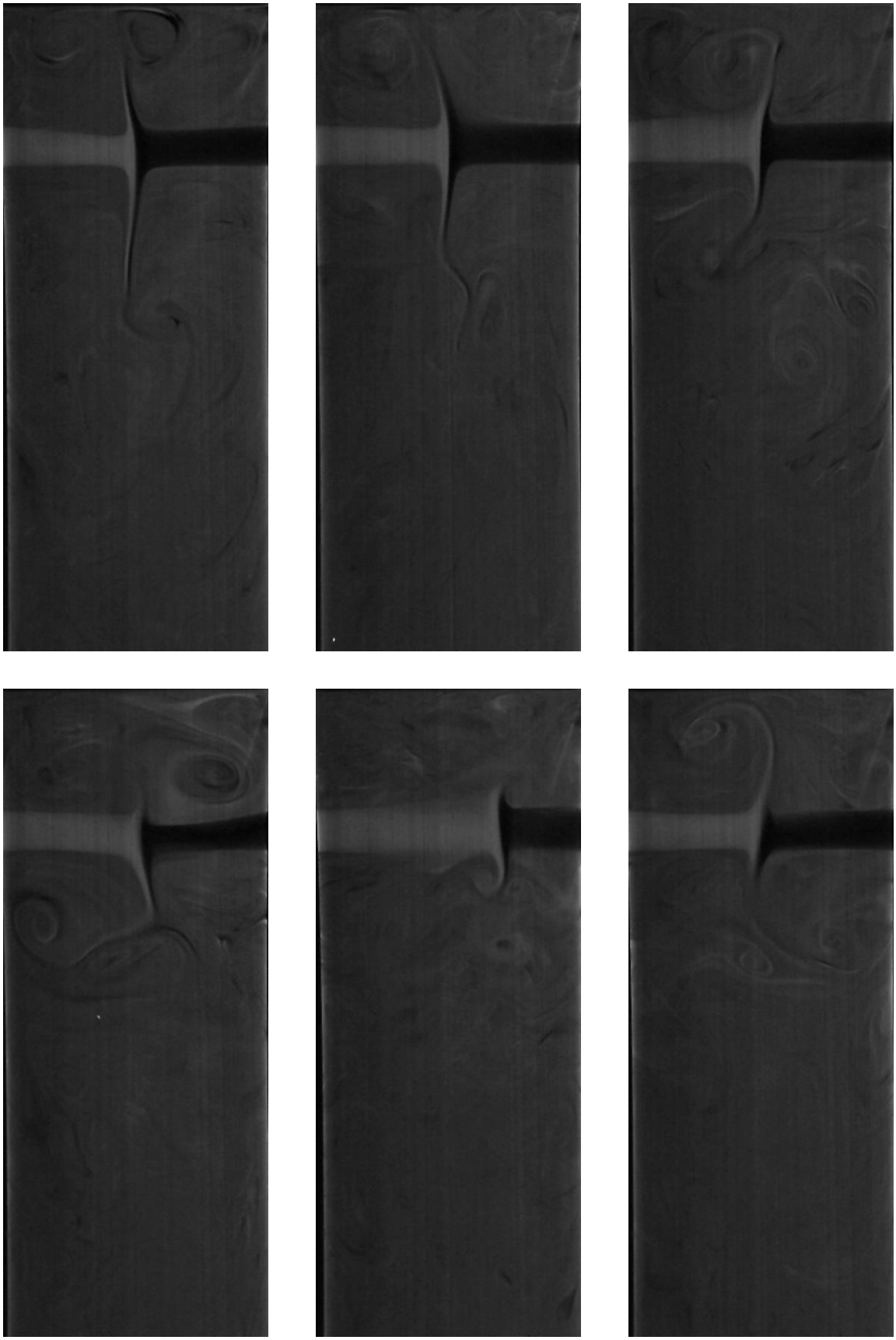

Figure 5.25 - Instantaneos flow field in the front plane for Reynolds 270

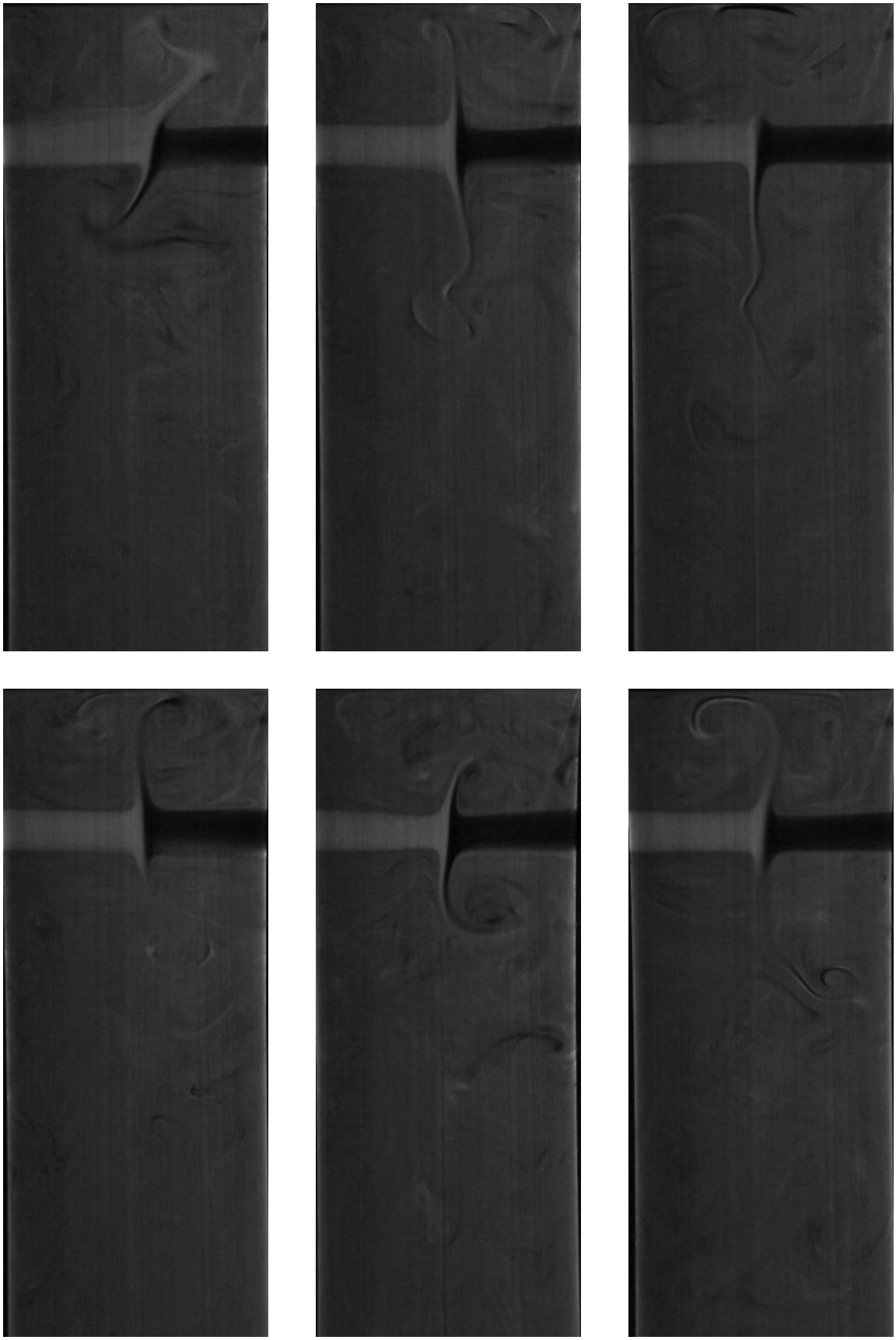

Figure 5.26 - Instantaneos flow field in the front plane for Reynolds 273

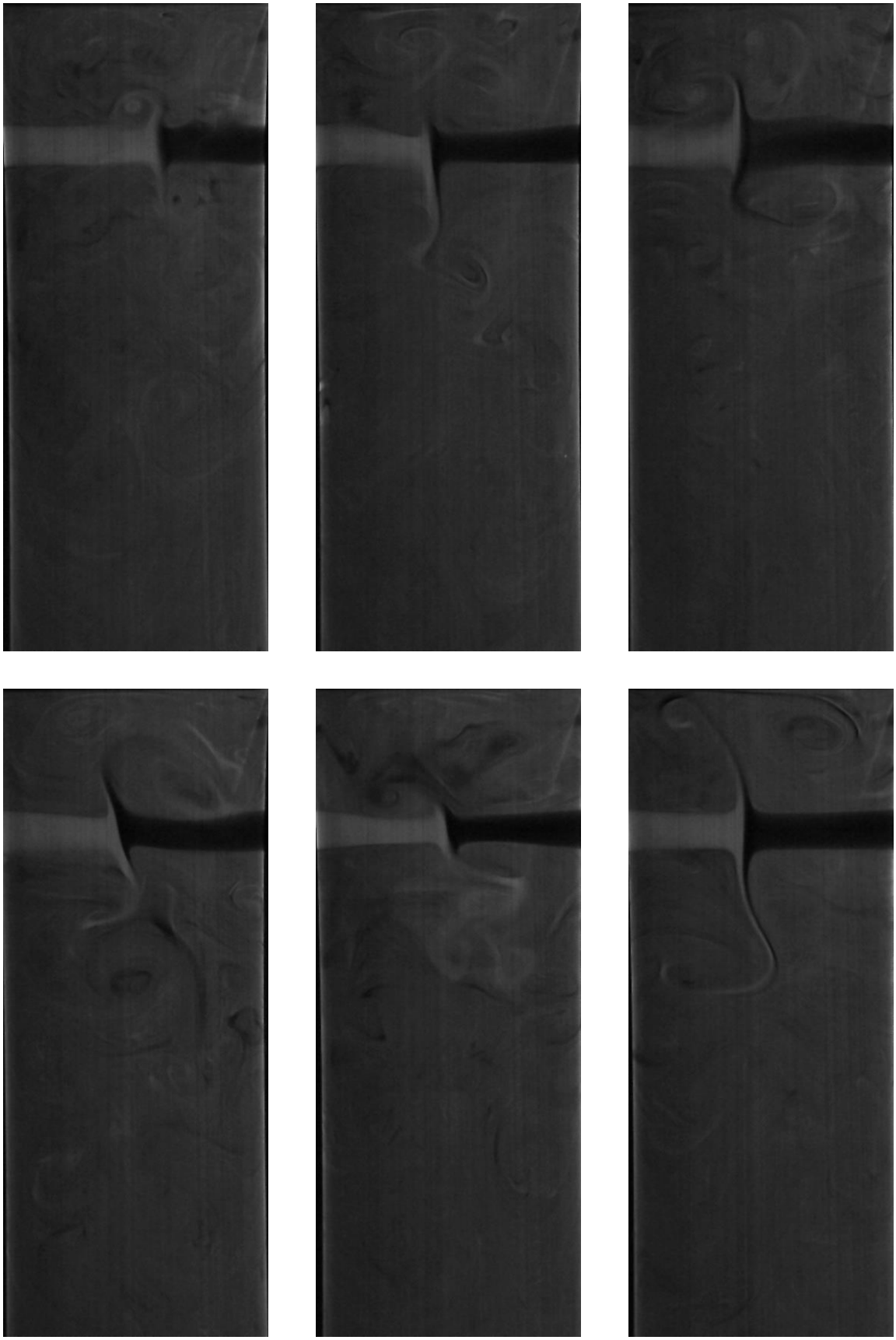

Figure 5.27 - Instantaneos flow field in the front plane for Reynolds 275

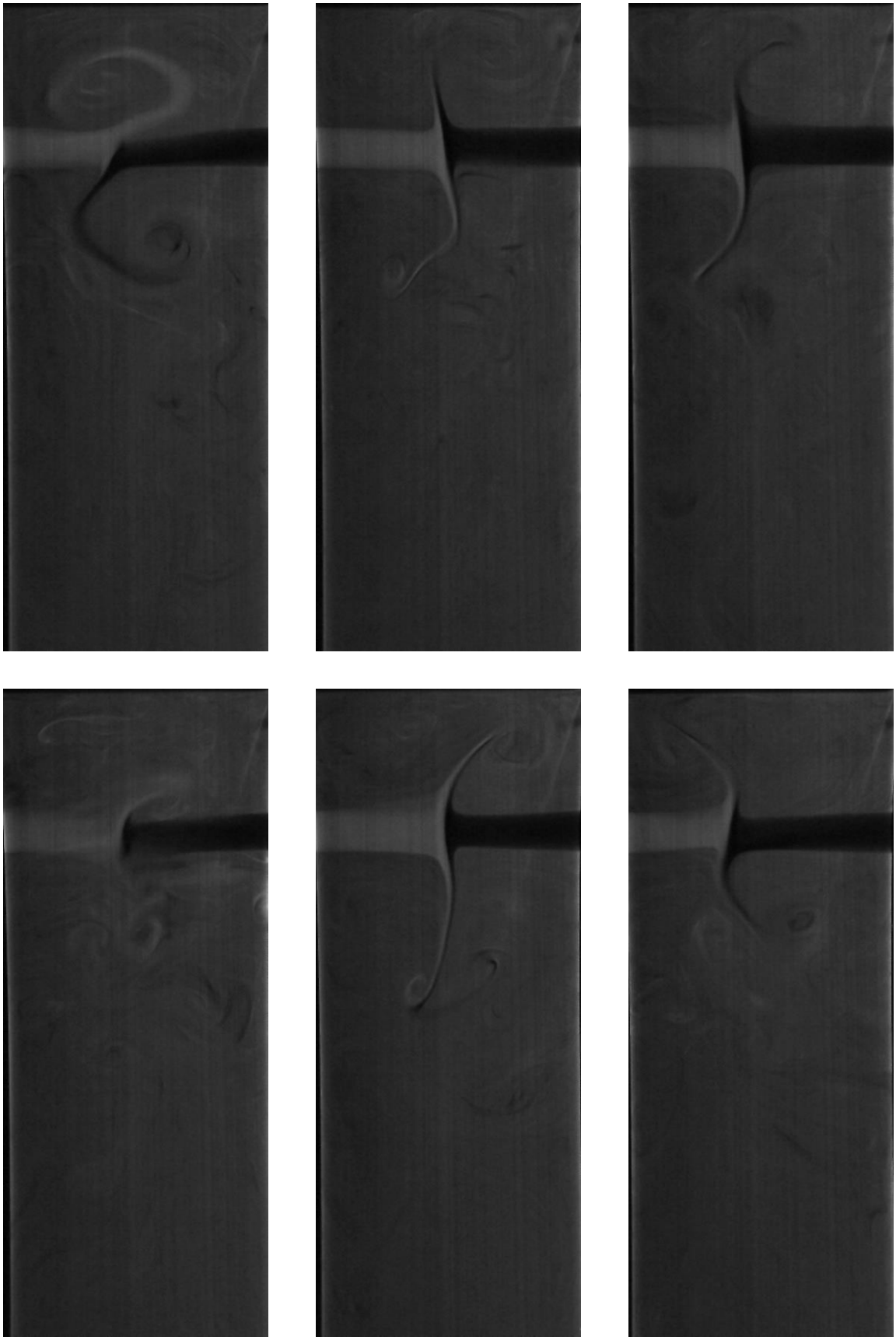

Figure 5.28 - Instantaneos flow field in the front plane for Reynolds 344

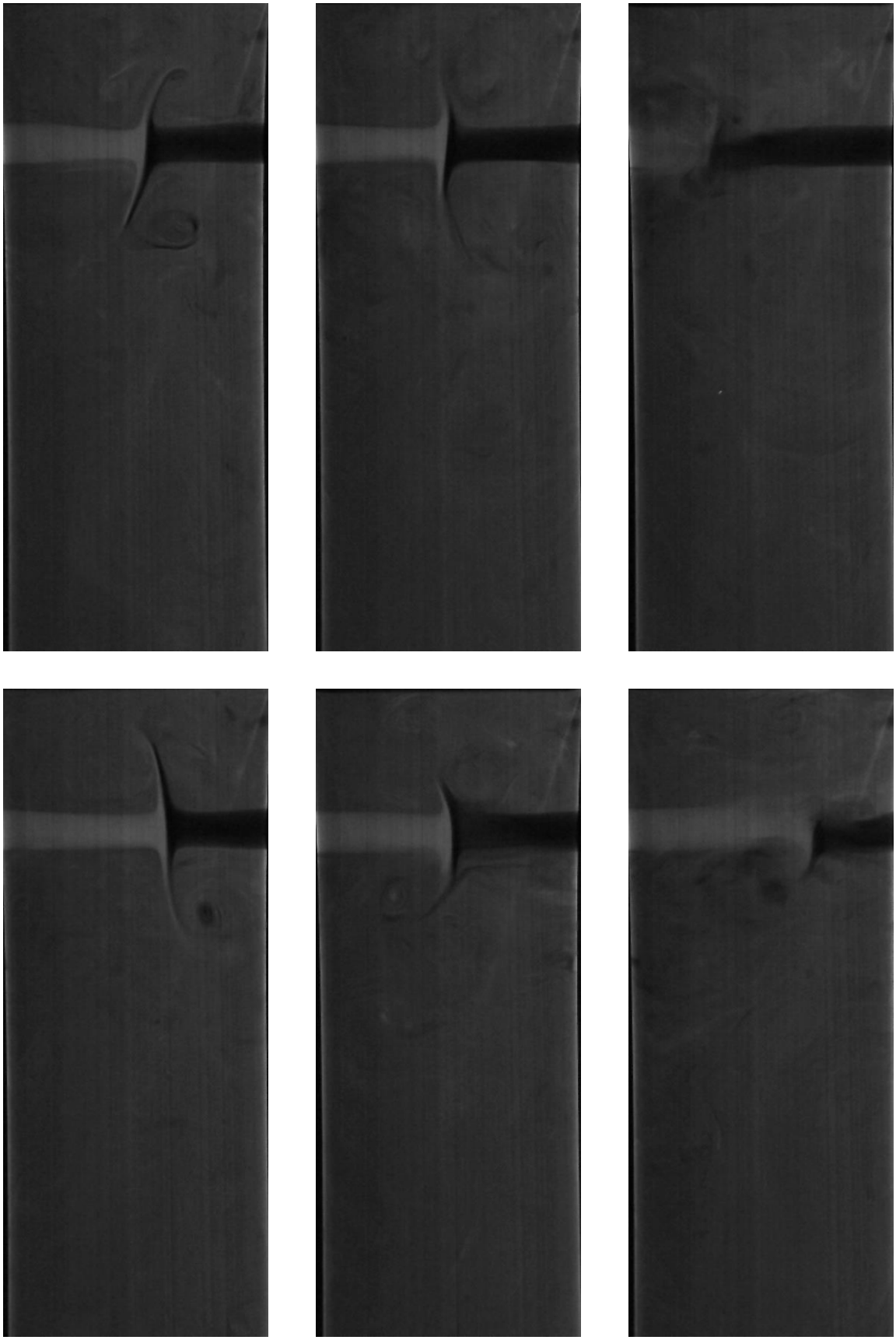

Figure 5.29 - Instantaneos flow field in the front plane for Reynolds 421

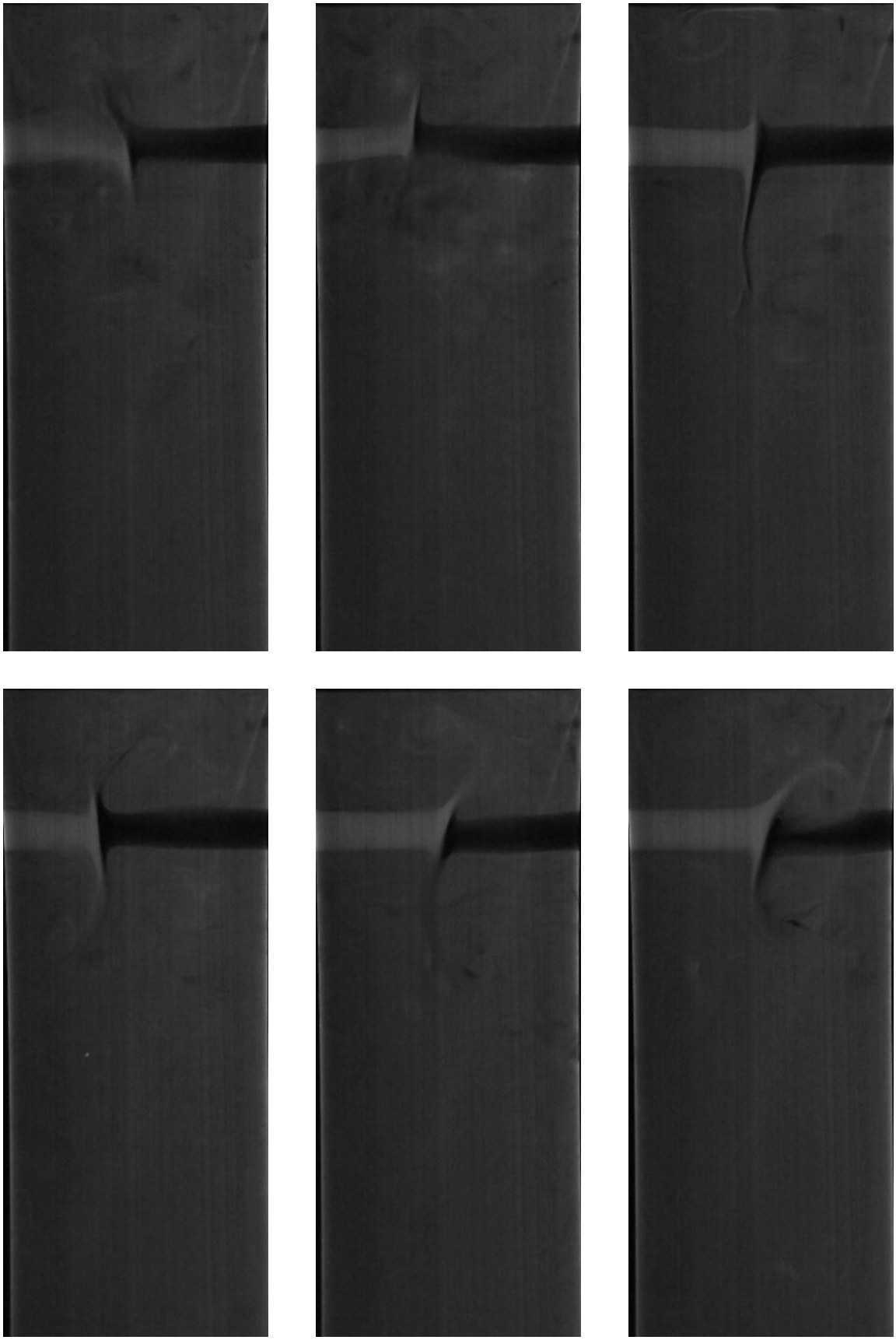

Figure 5.30 - Instantaneos flow field in the front plane for Reynolds 568

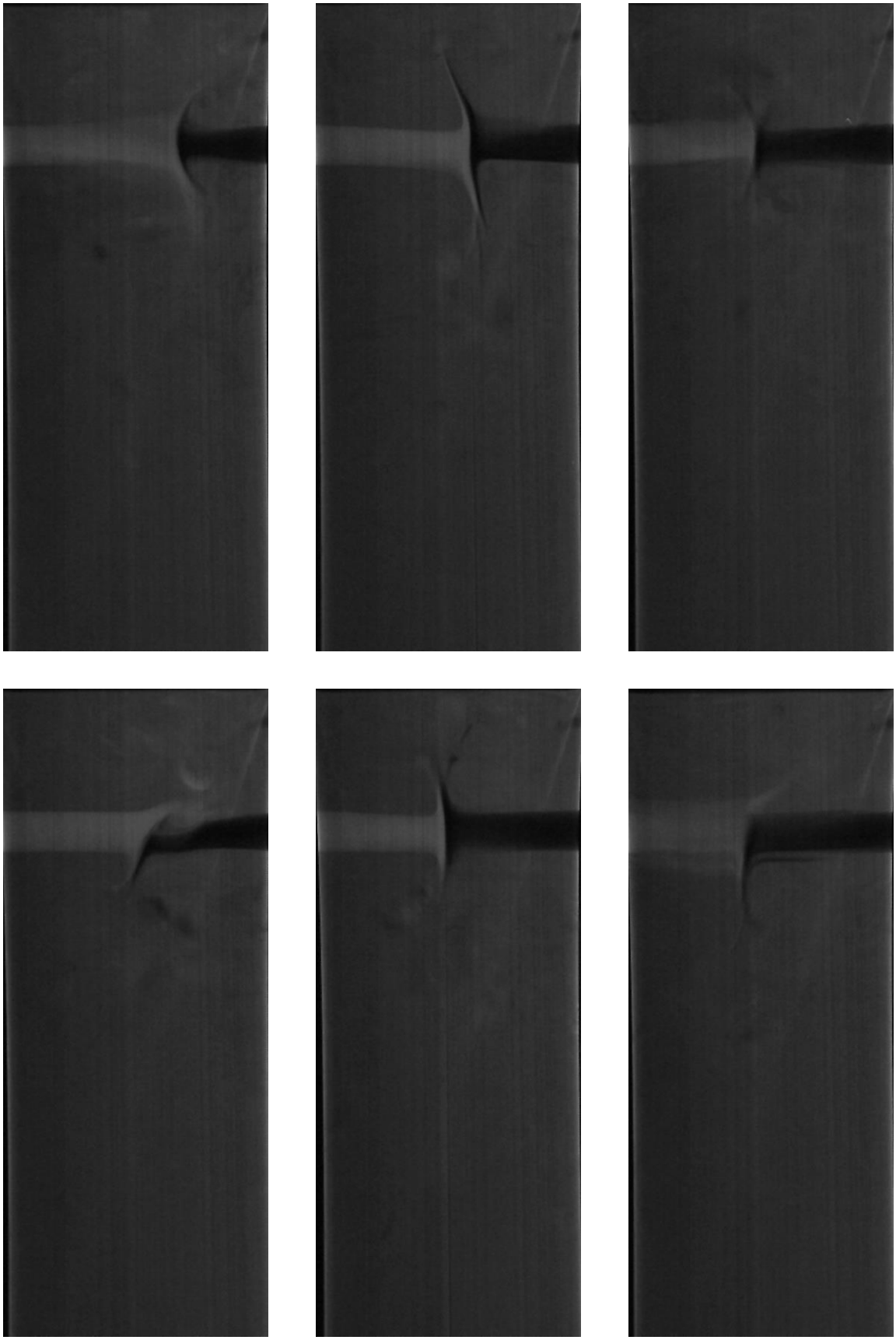

Figure 5.31 - Instantaneos flow field in the front plane for Reynolds 723

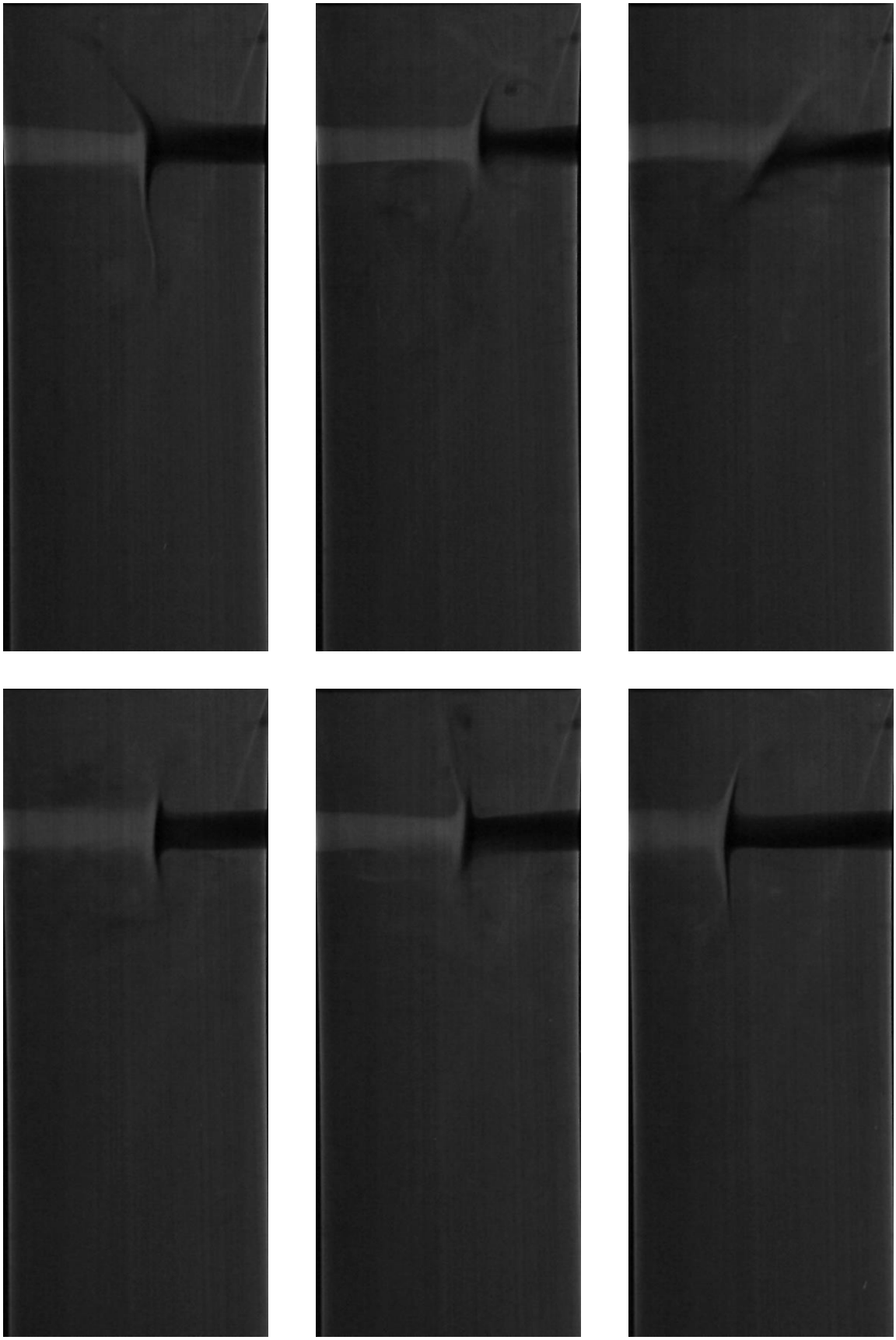

Figure 5.32 - Instantaneos flow field in the front plane for Reynolds 857

5.3.3.3 Impingement point position and jets angle

The impingement point position and the jet's angle was calculated from the real time experiments for each Reynolds in study by using the DIP MODA algorithm developed for this particular case. For each individual image the program obtain this two variables which will going to be presented and discussed.

As it can be seen in the segregated flow regime there is no impingement point and jet's angle variation along the experimental domain which corresponds to the recorded image sequence.

For the oscillatory periodic regime, correspondent to Reynolds 83, it can be seen a very small displacement of the impingement point position and no variation in the jet's angle. Although in the experiment it can be seen a very small variation of angle, the algorithm didn´t detected. This is since the filter introduced to filter wrong results and the minimum tolerance acceptable don't allowed such small variation of the jets angle, since it will correspond to large slope of the fitting curve and could emerge problems into converted into angle due asymptote in the arc tangent.

For Reynolds where self-sustainable chaotic regime is archive is observed for Reynolds 90 a periodic repetition of the jet's angle and impingement point position. Additionally is observed the impingement point position, which is consider align with the injector axis, a maximum displacement into the right instants before the top tip of the impingement surface tends to the maximum angle in a clockwise direction. This displacement of the impingement point position for the same direction of the angle could be due the bending of the jets, where the right side jet went downstream and the left side upstream the mixing chamber. This pattern is repeated inverted when the jet's angle is anti-clockwise.

In the next study Reynolds, 100, is observed the periodic pattern it start to vanish into a random motion of the jets angle which held an increase in the impingement point displacement. The next Reynolds, 125, this periodic pattern is fully dissipated into a full chaotic and unpredictable motion of the jets angle and impingement point position.

The phenomena already mentioned of the freezing in the jets angle, observed in Reynolds 134, is clear quantitate where occupied 0.1τ to 0.15τ without any oscillatory motion in the front plane and without any significant displacement of the impingement point position in this region. It is also observed for this particular Reynolds peaks in the displacement of the impingement point correspond to bigger jet's angles.

From Reynolds 171 is observable a appear of high local jets angle with addition to a chaotic motion of the jets. With the increasing of the Reynolds number this peeks of high angle with addition of an reduction of the oscillatory motion with lower angle into peeks low angle peeks appears. Additionally is observing in a certain time the impingement point position a big displacement from the average followed by a gradually reduction into the centre of the chamber. After in the centre this process is repeated again without any observable pattern. This pattern is intensified with the increasing of the Reynolds number.

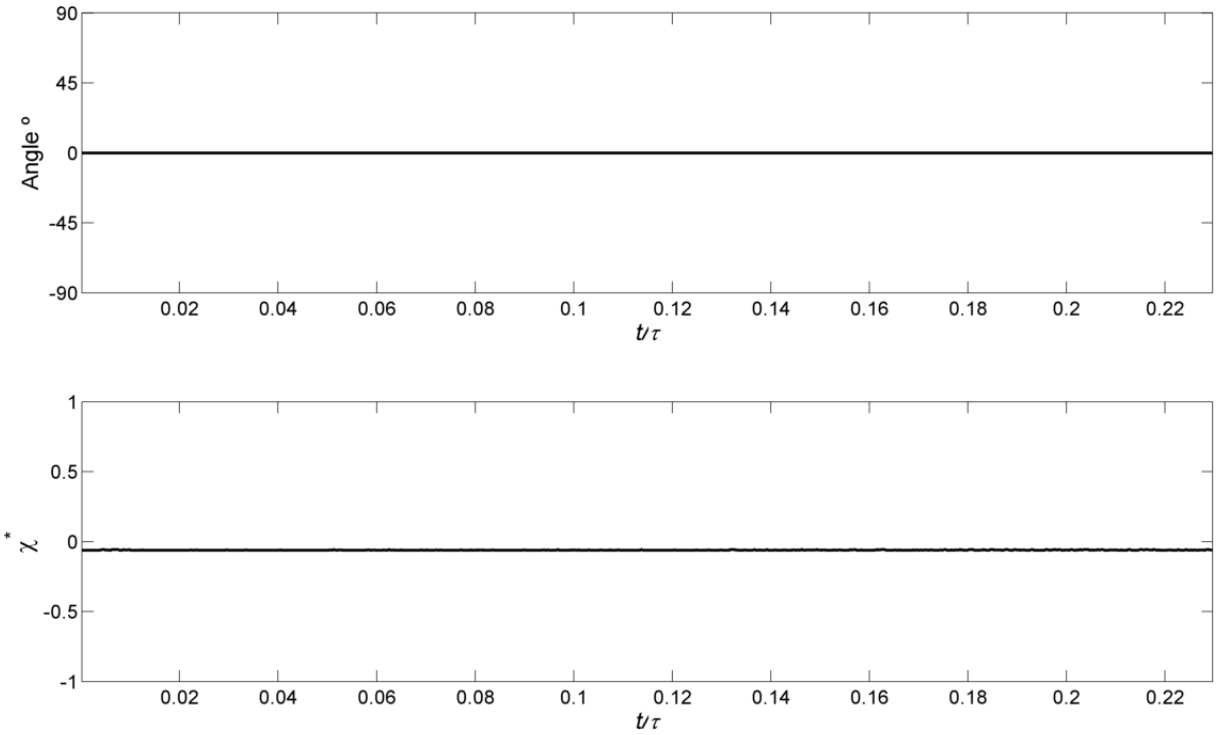

Figure 5.33 - Jets angle and impingement point position for Reynolds 26

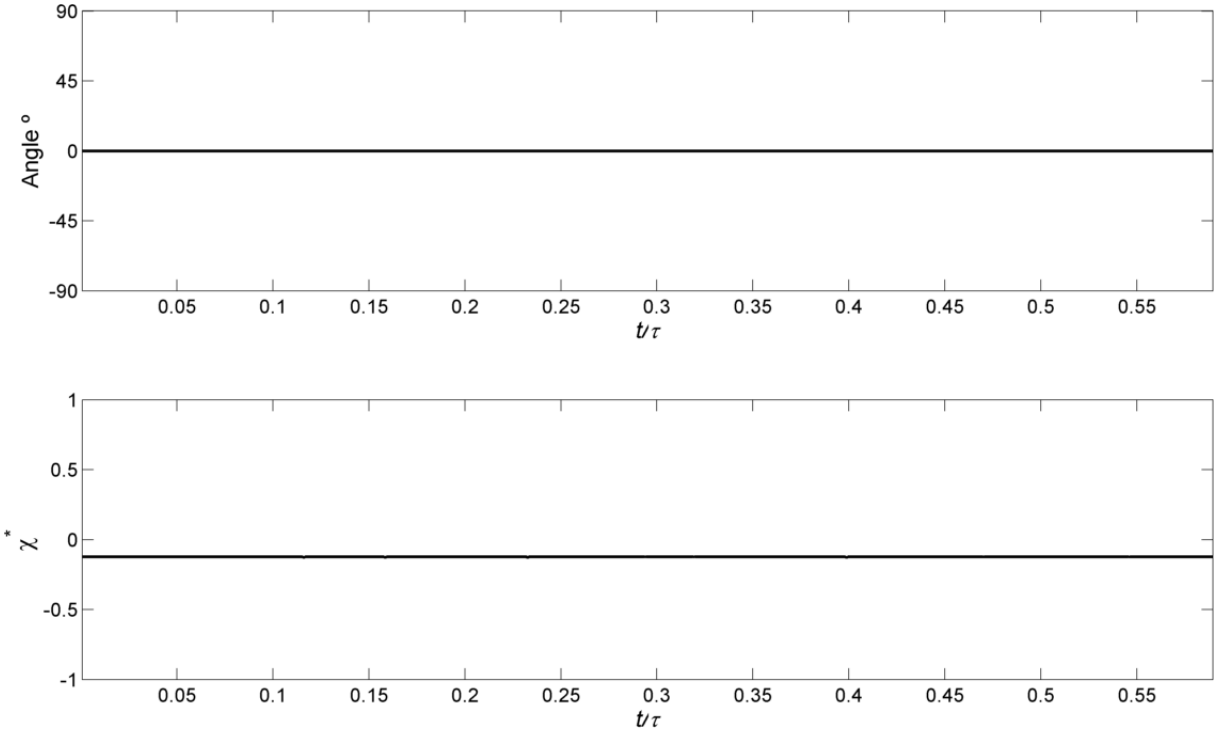

Figure 5.34 - Jets angle and impingement point position for Reynolds 65

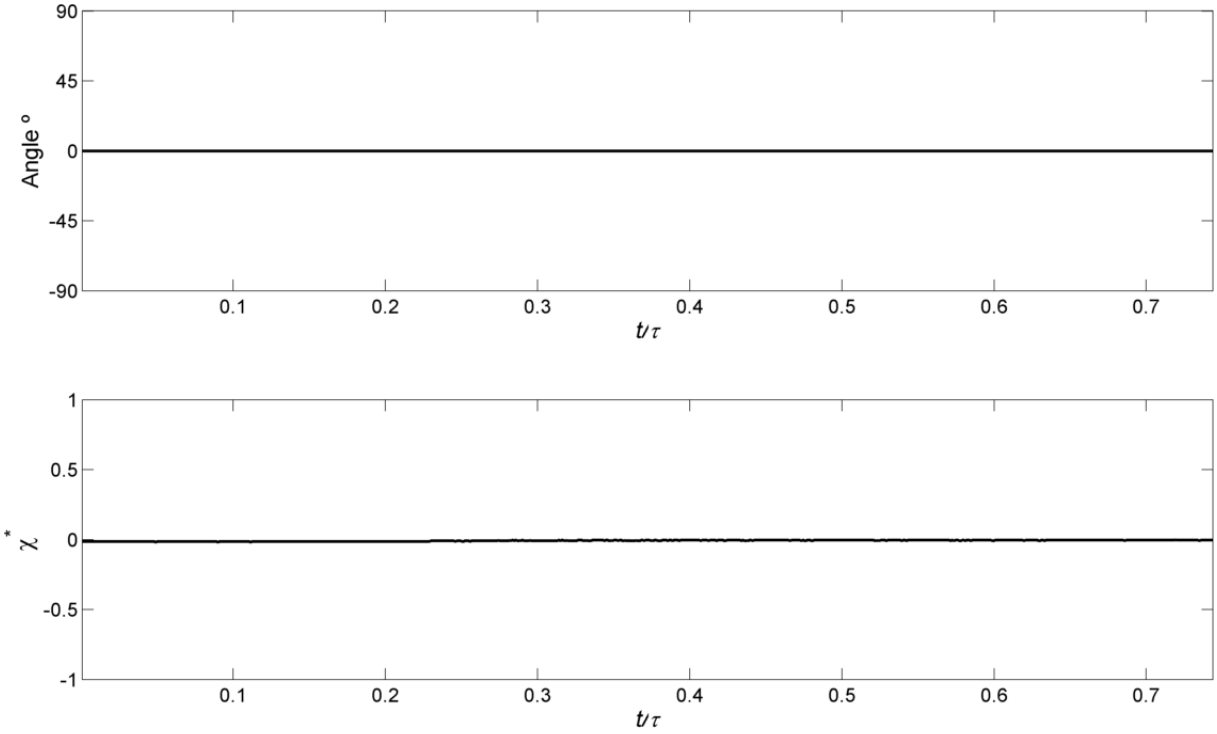

Figure 5.35 - Jets angle and impingement point position for Reynolds 83

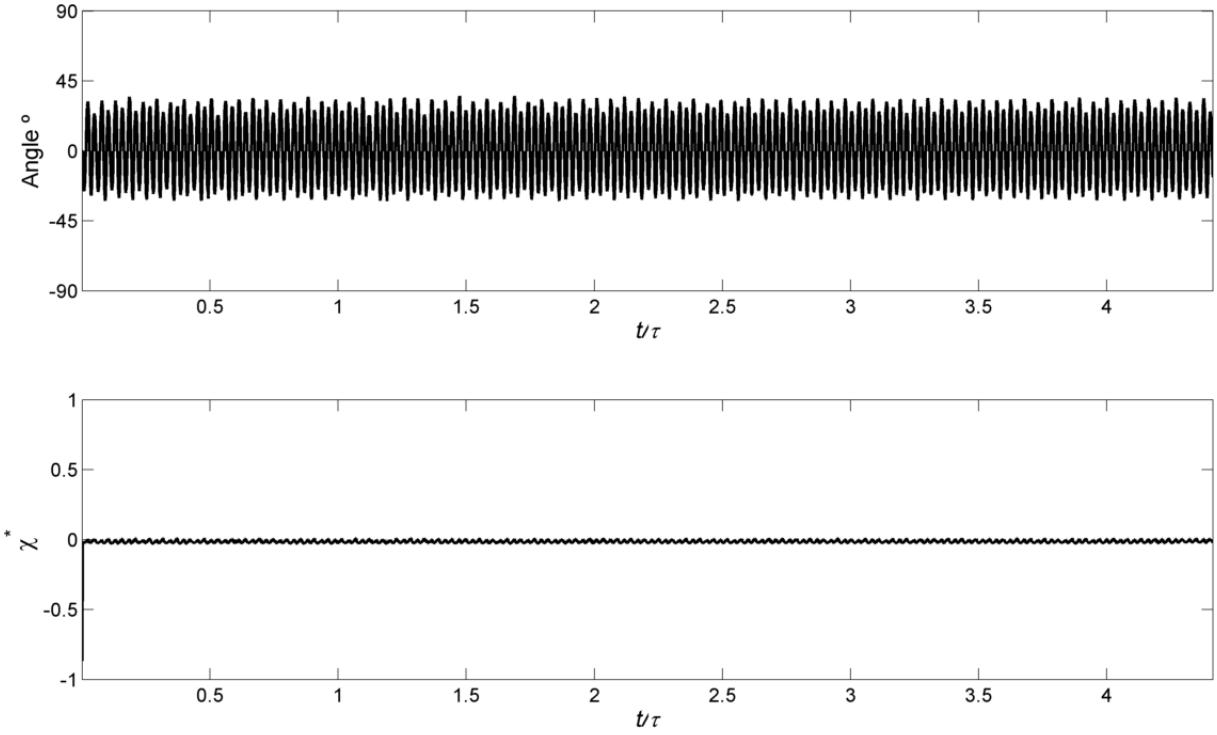

Figure 5.36 - Jets angle and impingement point position for Reynolds 90

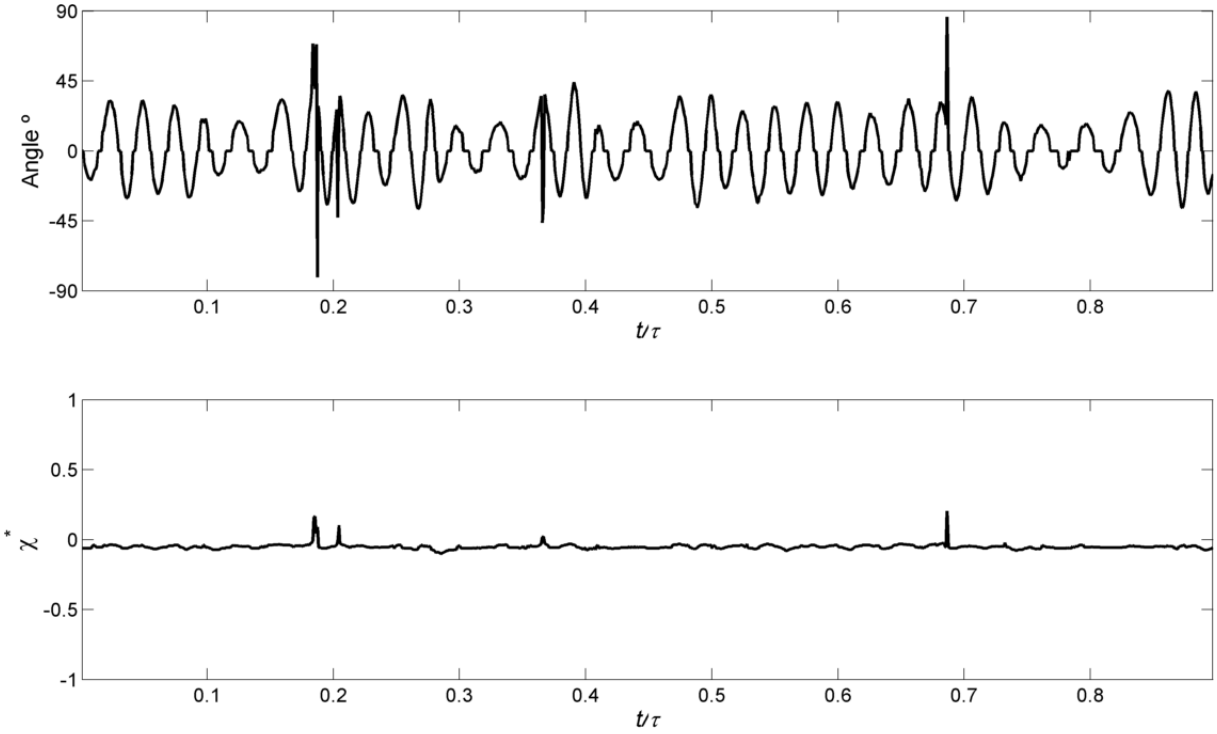

Figure 5.37 - Jets angle and impingement point position for Reynolds 100

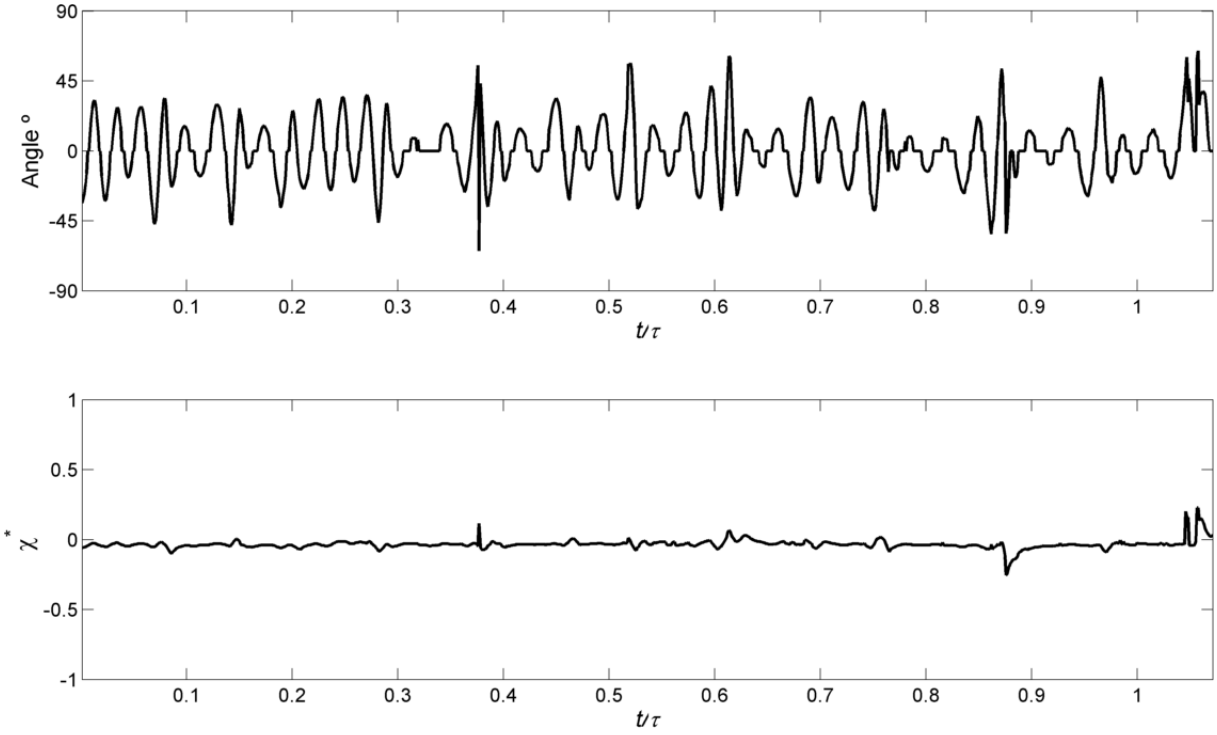

Figure 5.38 - Jets angle and impingement point position for Reynolds 123

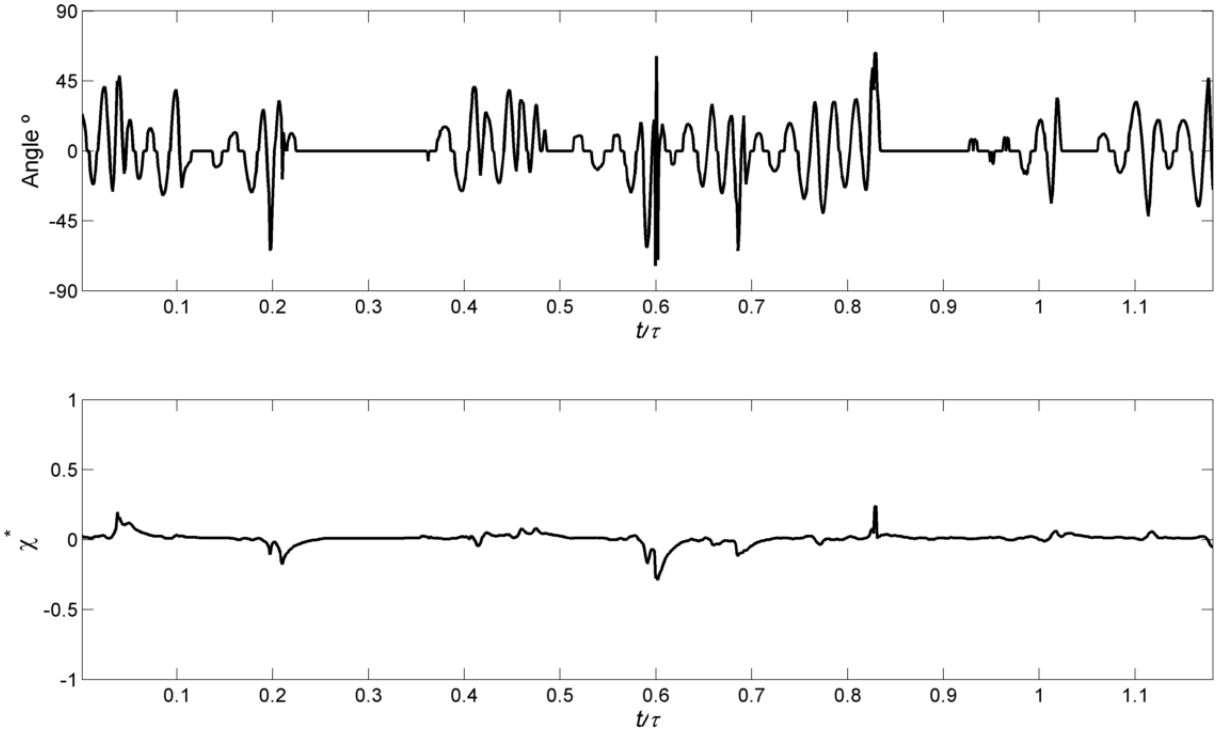

Figure 5.39 - Jets angle and impingement point position for Reynolds 134

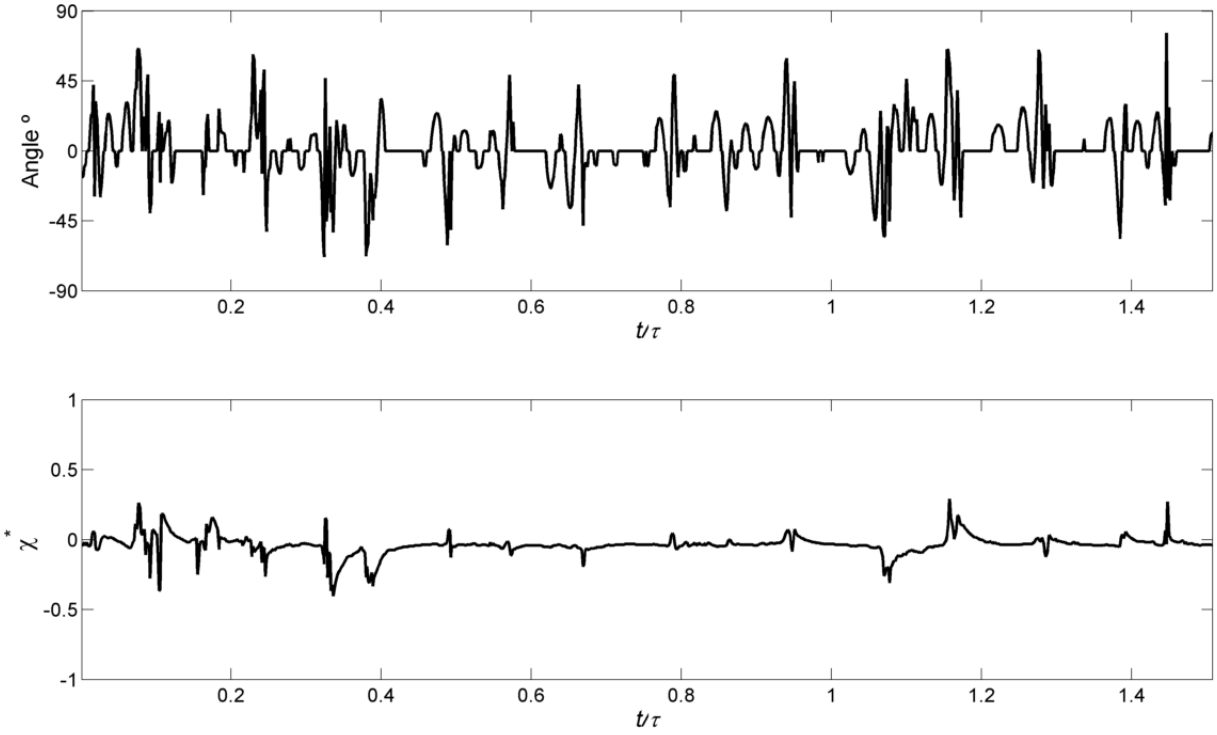

Figure 5.40 - Jets angle and impingement point position for Reynolds 171

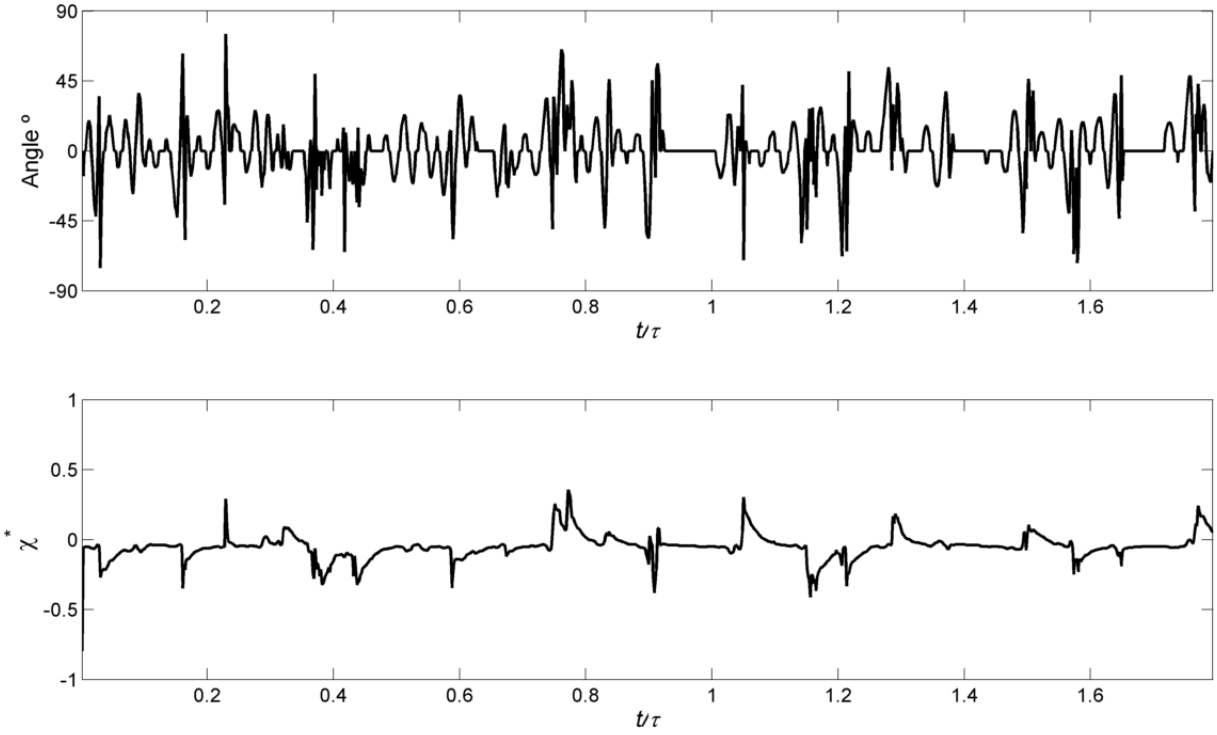

Figure 5.41 - Jets angle and impingement point position for Reynolds 205

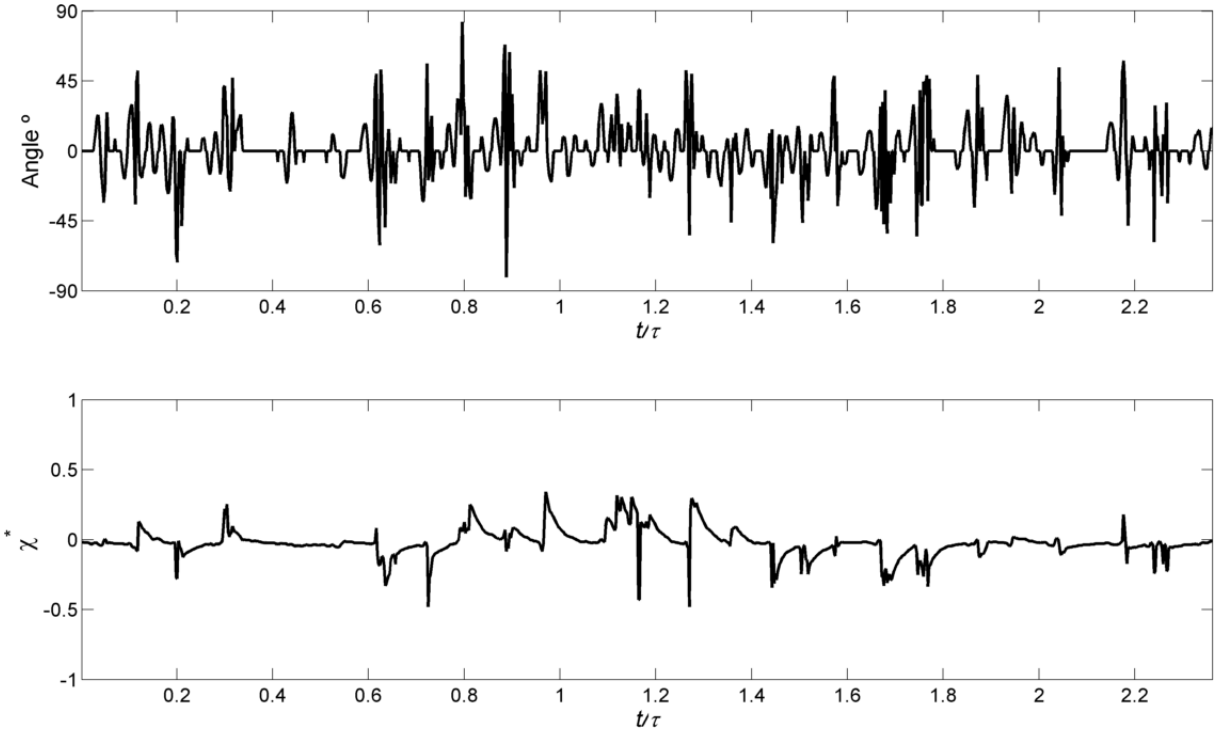

Figure 5.42 - Jets angle and impingement point position for Reynolds 270

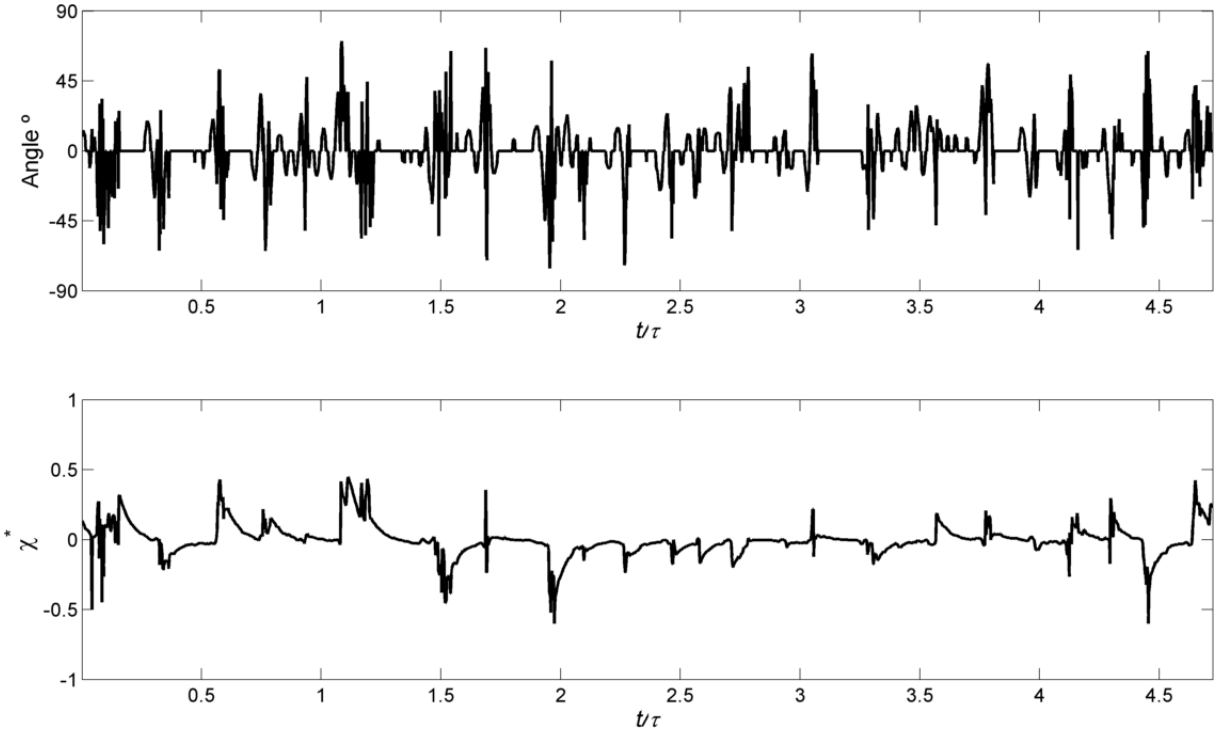

Figure 5.43 - Jets angle and impingement point position for Reynolds 273

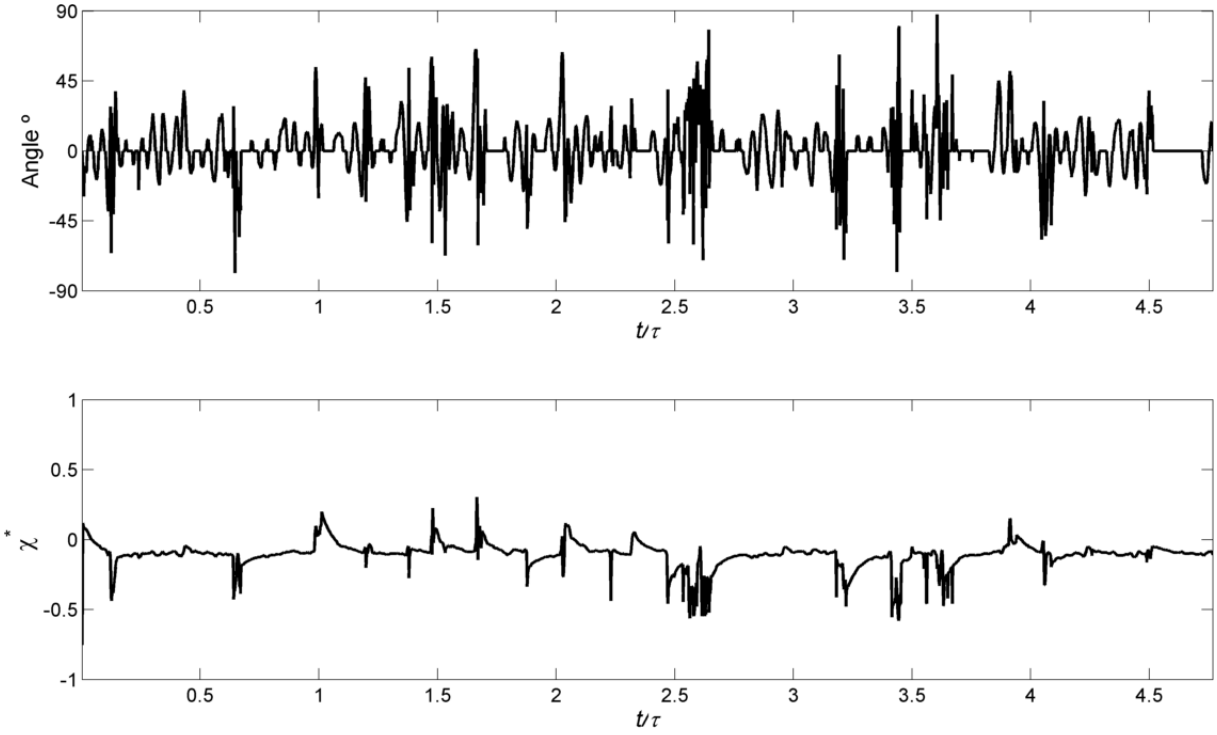

Figure 5.44 - Jets angle and impingement point position for Reynolds 275

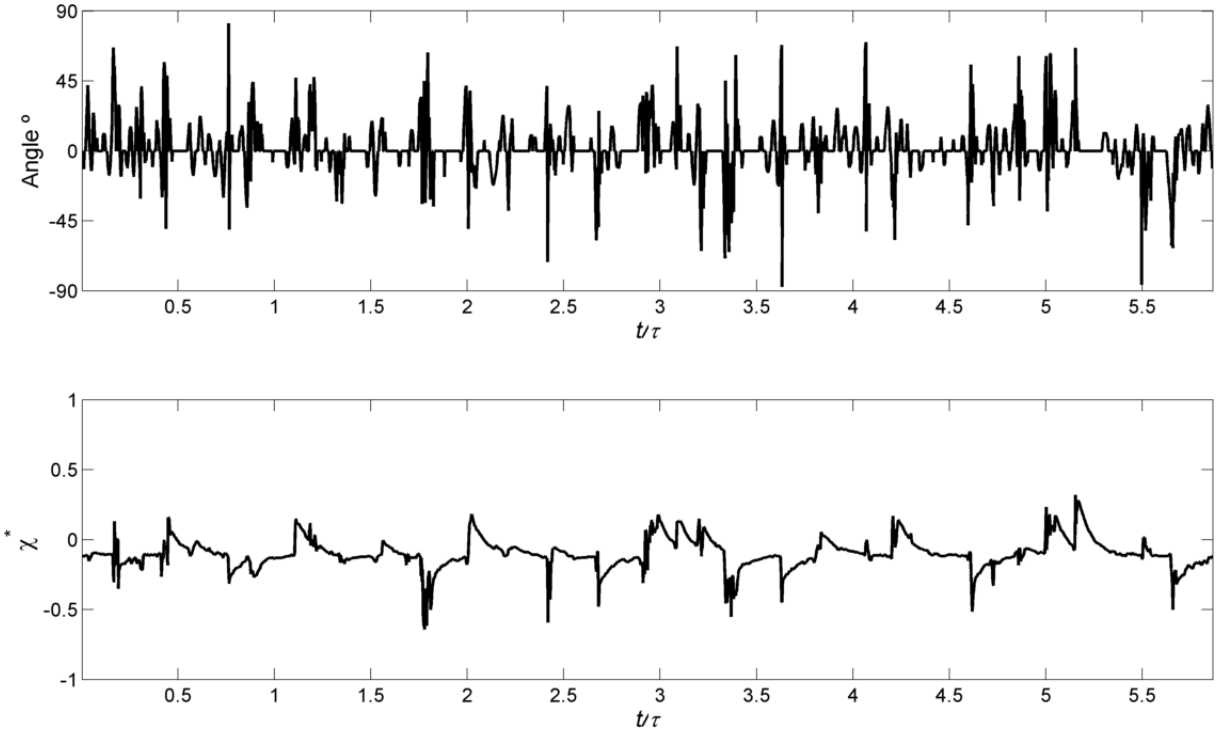

Figure 5.45 - Jets angle and impingement point position for Reynolds 344

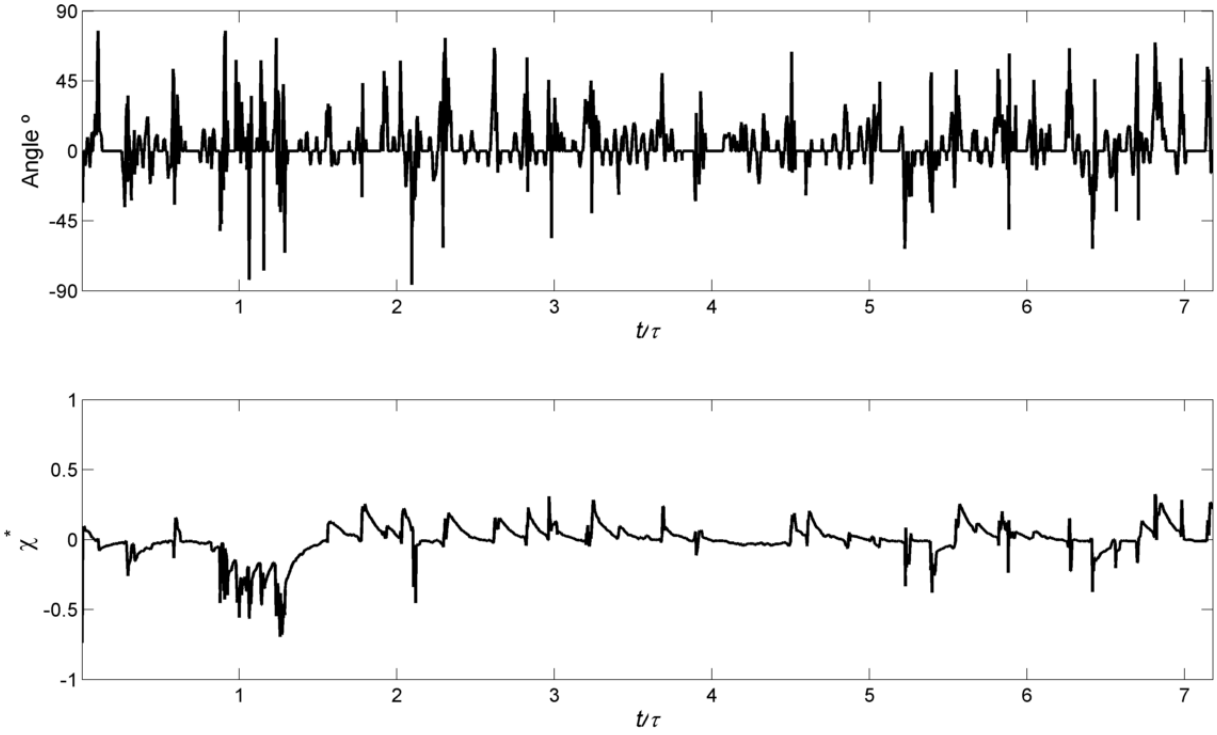

Figure 5.46 - Jets angle and impingement point position for Reynolds 421

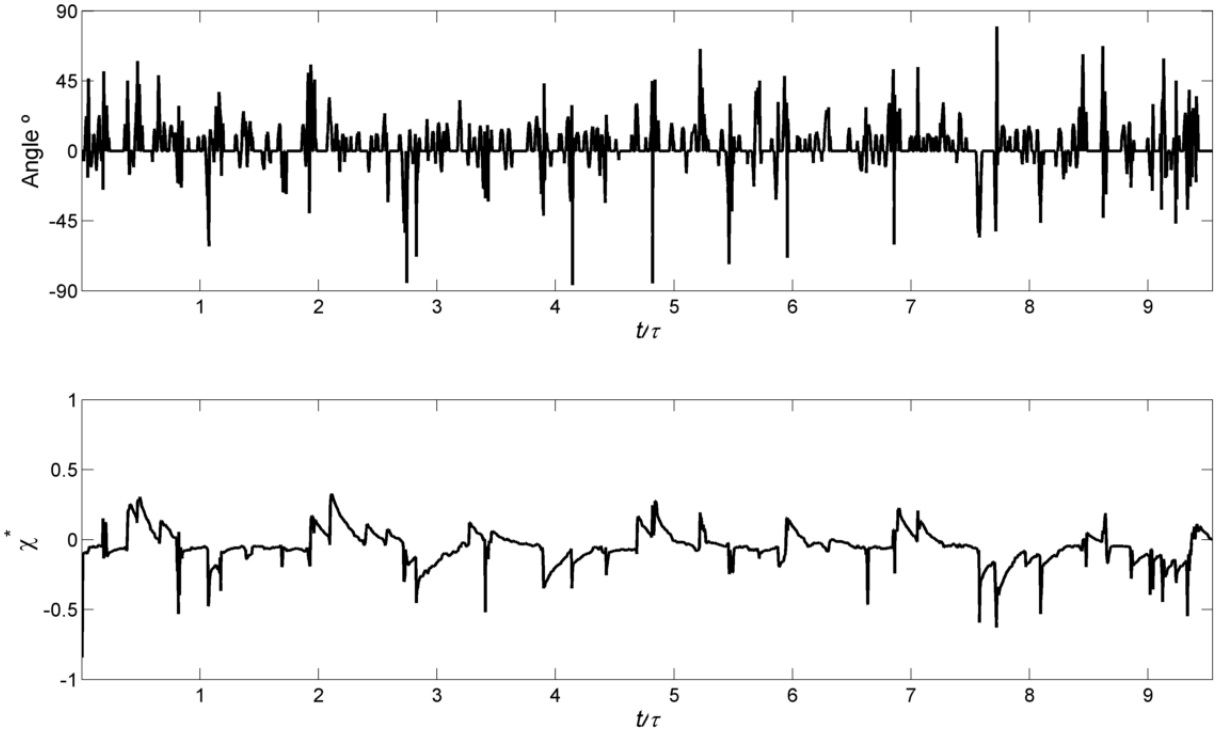

Figure 5.47 - Jets angle and impingement point position for Reynolds 568

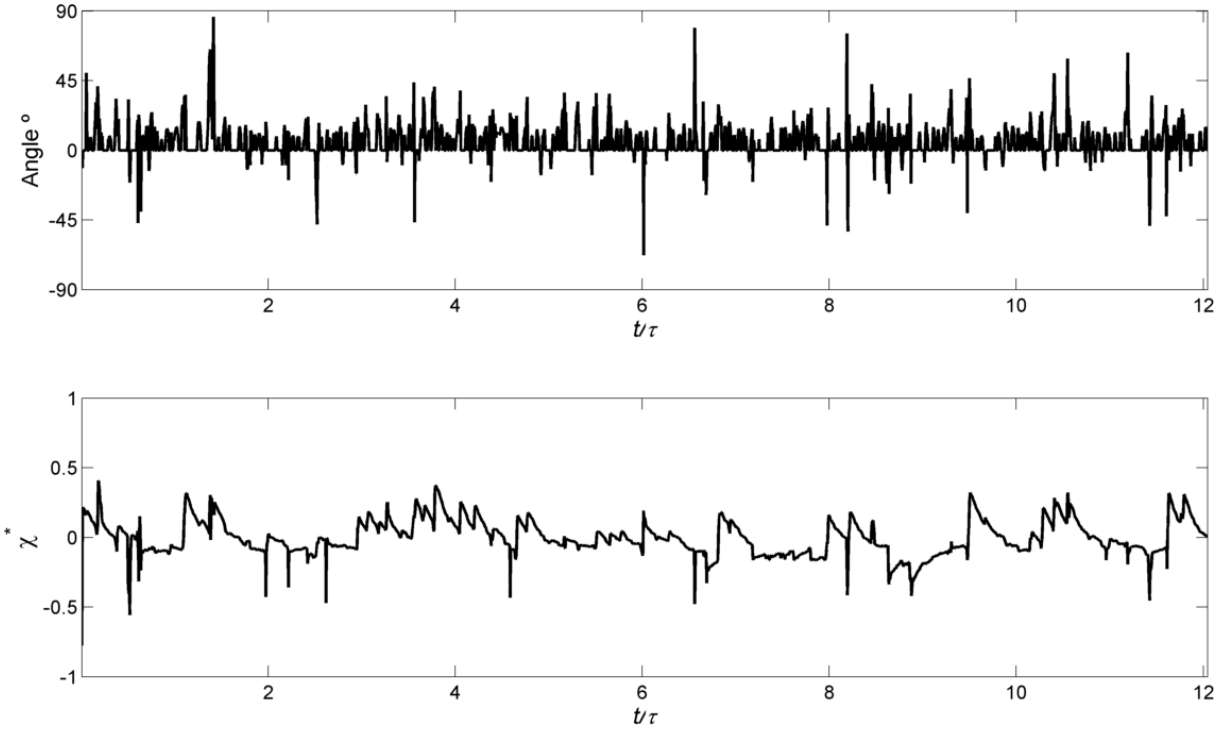

Figure 5.48 - Jets angle and impingement point position for Reynolds 723

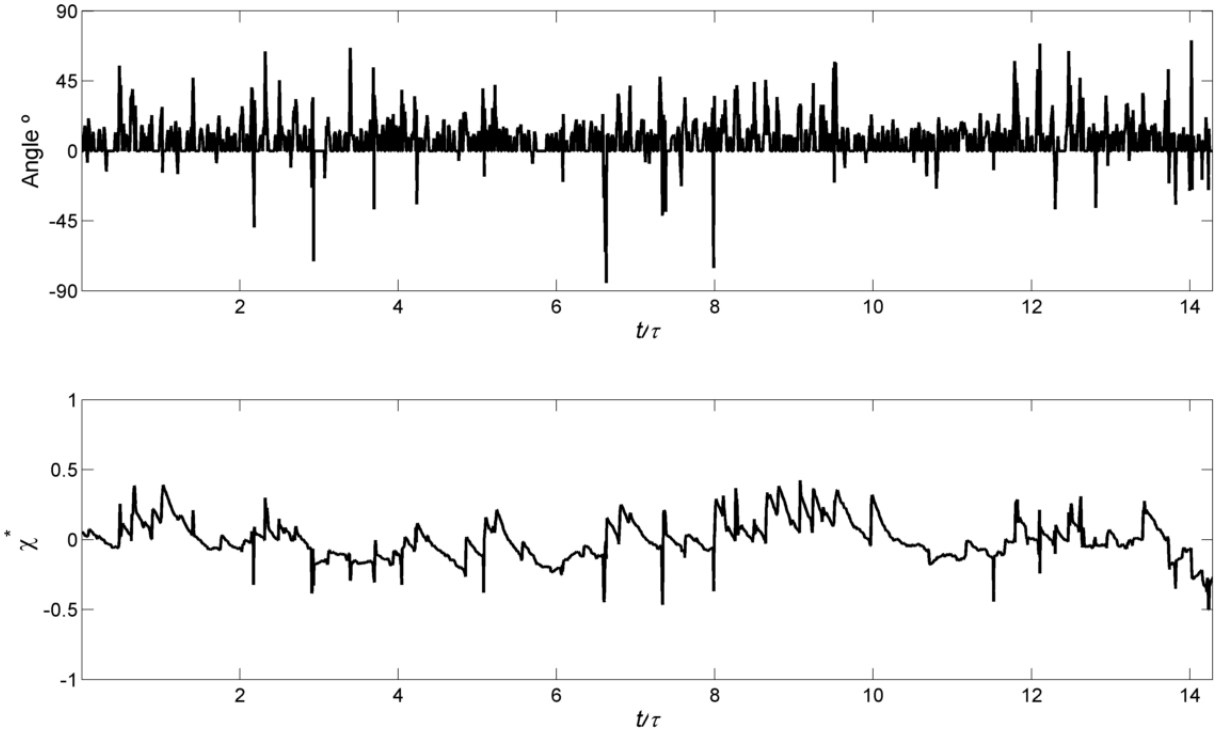

Figure 5.49 - Jets angle and impingement point position for Reynolds 857

5.3.3.4 Spectral analyses

Fast Fourier Transform is used to perform analyses in the results where will be identify the value of energy in the containing scale. Will be compared the results from the jet's angle, impingement point position and the differential pressure variation provided by the pressure traducer and recorded in each experiment.

Previous works (Santos, 2003) performed a LDA visualization of the energy containing scales of the fluctuated flow field in a set of planes. In a plane passing by the injector's axis the main frequency was recorded for a set of Reynolds and an extrapolation was perform. The results of this work are presented in Figure 5.50.

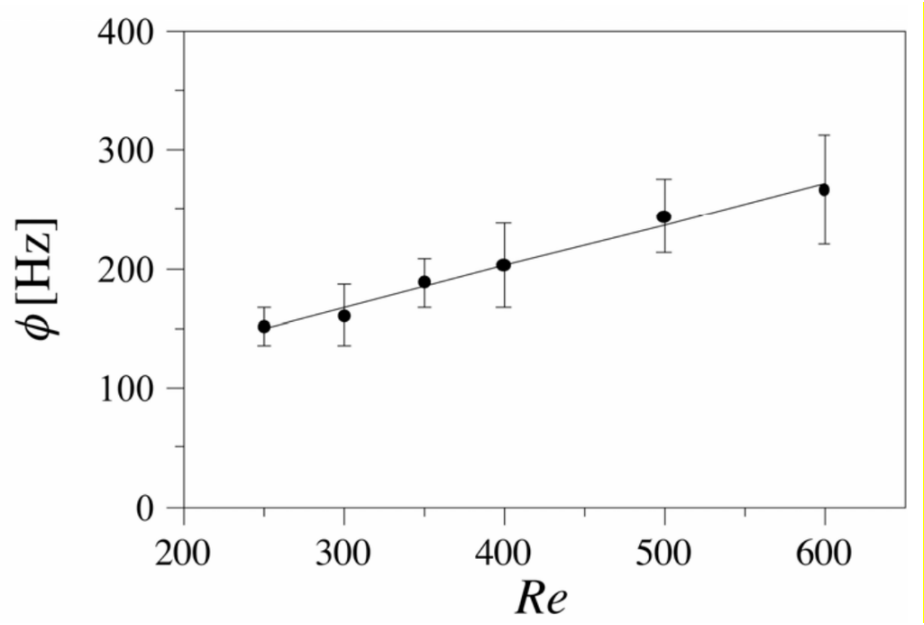

Figure 5.50 – Evolution of the average typical frequency

Before start to comment the results some notes of the hydrodynamic behaviour should be reminder. As it was observable from chapter 3 the impingement point position and the impingement surface have a 3D motion, where the mainly oscillation is observed in the front plane, passed in the injectors axis and chamber axis. The differential pressure transducer recorded the variation of pressure between each injector, which varies due the oscillatory 3D motion of the impingement surface being directly translate into a linear motion which is recorder and presented.

The main driven force of the present work is to compare the results provided by Santos (2003) with the three different variables, namely, the injectors angle, the impingement point position and the differential pressure transducer recorded by the pressure transducer. The results are presented and discussed individually.

Starting by analysing the frequency recorded by the differential pressure transducer. For the case of segregated flow dynamic is observable some noise in the range of 60/70 Hz, which could indicate some electromagnetic interference which could be introduced by external equipment such as computer monitor or the high speed camera. This hypotheses is give more weight to validate since when the self-sustainable chaotic regime is obtained this value vanish. When the Reynolds is increase it would be expected the maximum frequency of the system increase as documented by Santos (2003) but this value tend to fluctuate far away from the expected frequencies.

For the stagnation point position it is observable similar values such in the documented range until Reynolds 123. Far from this Reynolds this variable don't present physical reliability to predict the main frequencies in the flow field.

For the jets angle same analyses was conducted. It is observable a very good agreement was obtain until Reynolds 273 which indicates the driving force of the flow field is directly related with the jets angle rather than the impingement point position. For Reynolds above this value there is not observable any correlation with documented expectable frequency.

Above Reynolds 273 and due the combination of small angle of the impingement jets, associated with succession of breaking of the impingement surface and fast displacement of the impingement point would not allowed record the frequencies existent in the impingement surface

An inverse energy cascade, represented by the slope -5/3 is observable for all the variables in all the Reynolds in study, meaning it was capture the regime where injection of energy is obtain until the large energy containing scale, which is only due the strong dynamics of the impingement surface.

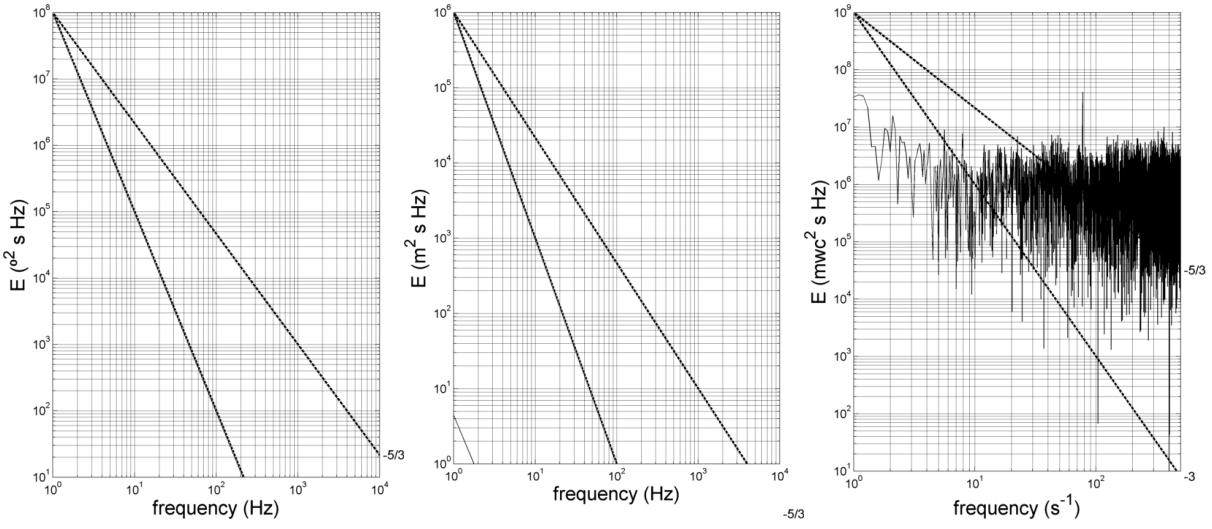

Figure 5.51 – Power spectra for Jet's angle (left), impingement point position (middle) and pressure transducer (right) for Reynolds 26

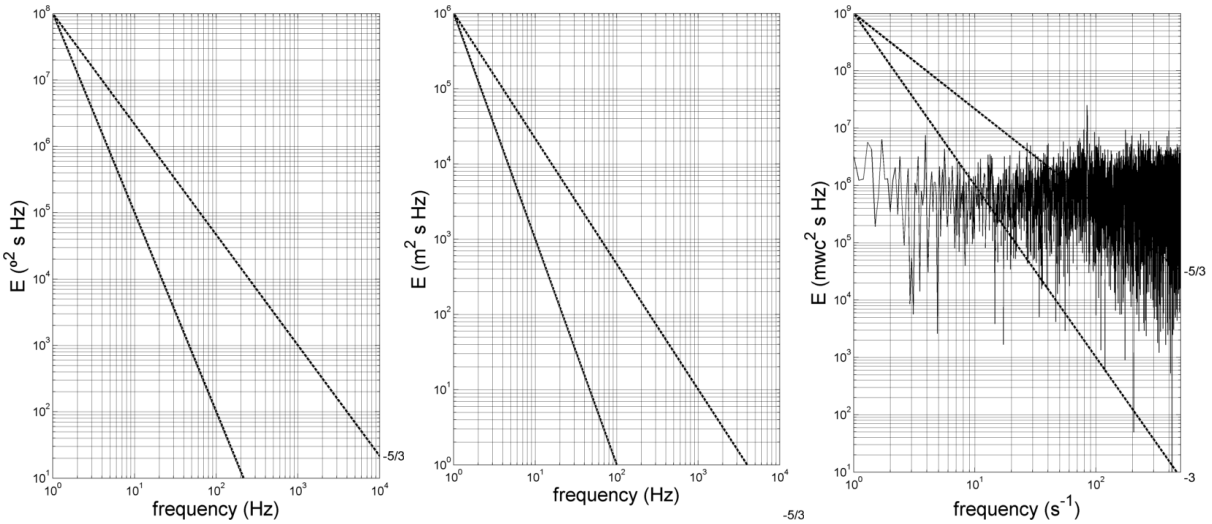

Figure 5.52 – Power spectra for Jet's angle (left), impingement point position (middle) and pressure transducer (right) for Reynolds 65

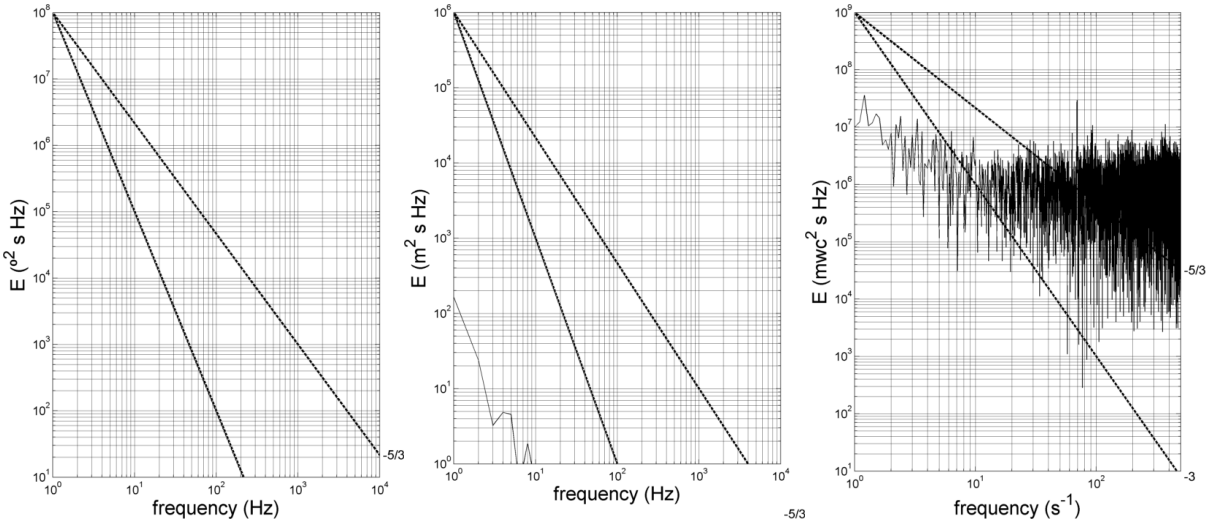

Figure 5.53 – Power spectra for Jet's angle (left), impingement point position (middle) and pressure transducer (right) for Reynolds 83

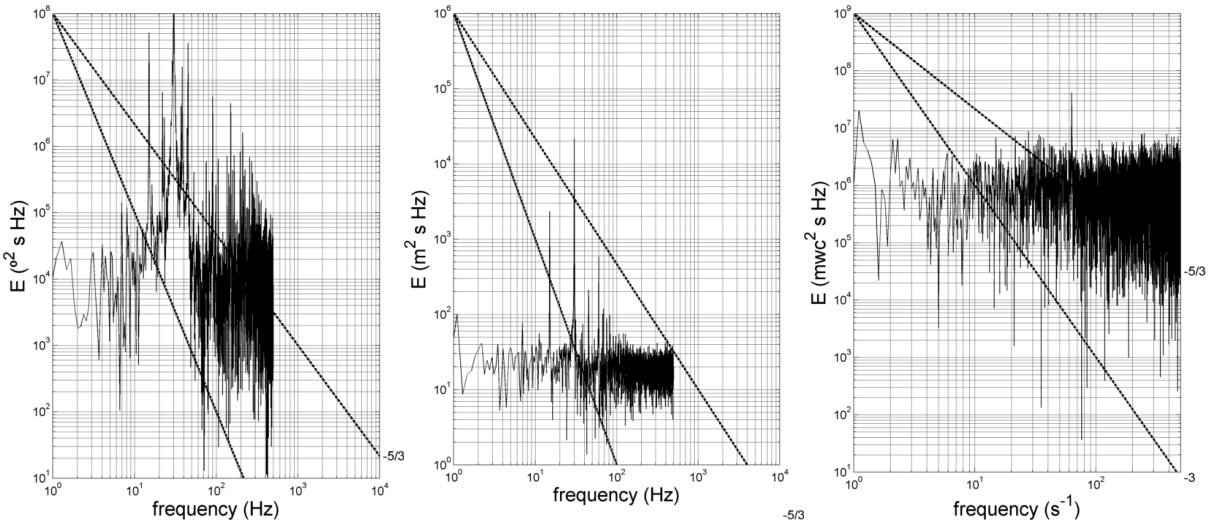

Figure 5.54 – Power spectra for Jet's angle (left), impingement point position (middle) and pressure transducer (right) for Reynolds 90

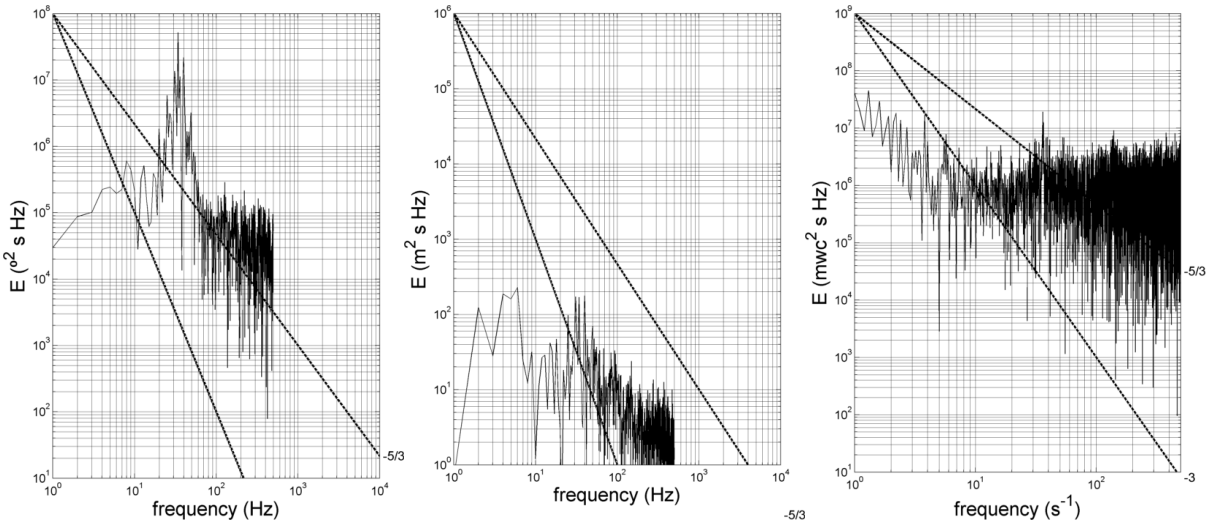

Figure 5.55 – Power spectra for Jet's angle (left), impingement point position (middle) and pressure transducer (right) for Reynolds 100

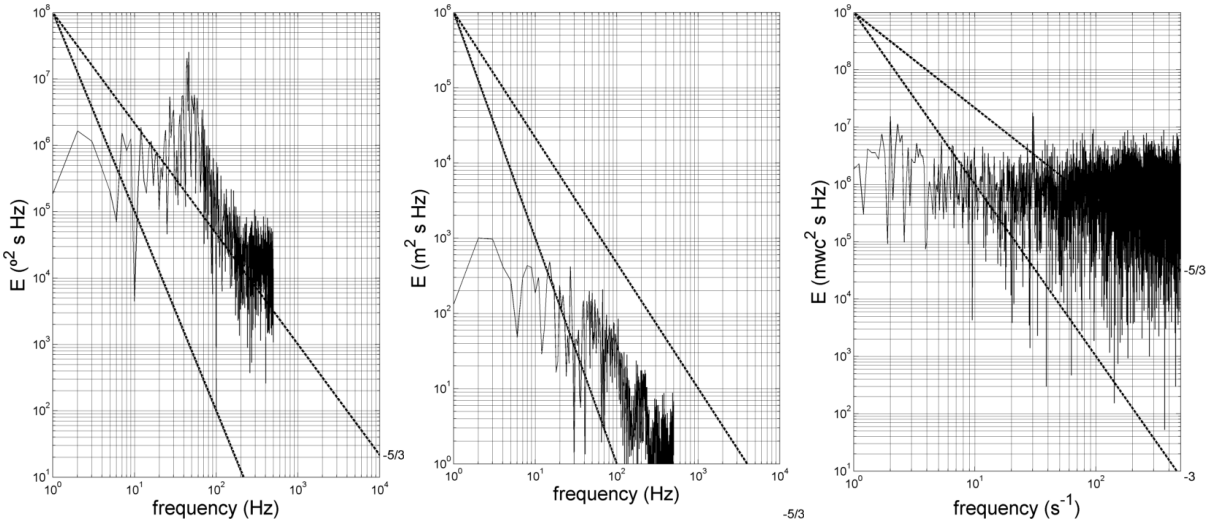

Figure 5.56 – Power spectra for Jet's angle (left), impingement point position (middle) and pressure transducer (right) for Reynolds 123

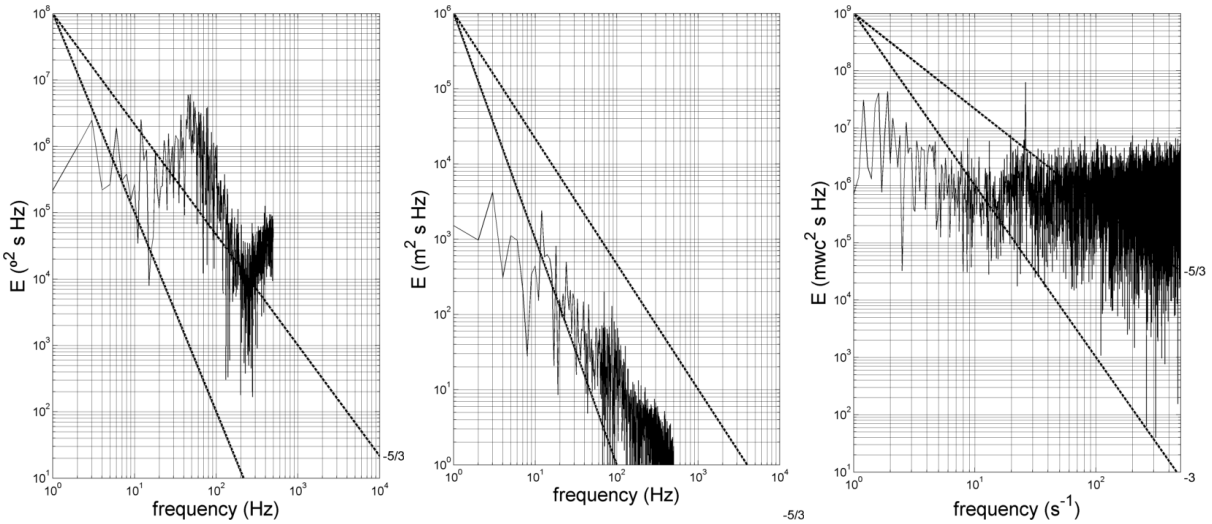

Figure 5.57 – Power spectra for Jet's angle (left), impingement point position (middle) and pressure transducer (right) for Reynolds 134

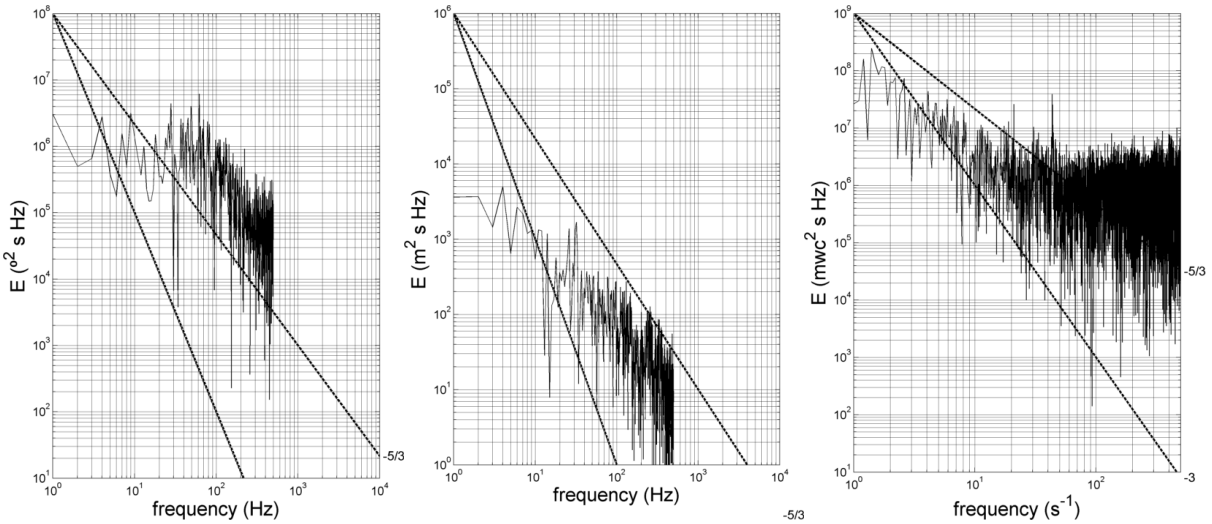

Figure 5.58 – Power spectra for Jet's angle (left), impingement point position (middle) and pressure transducer (right) for Reynolds 171

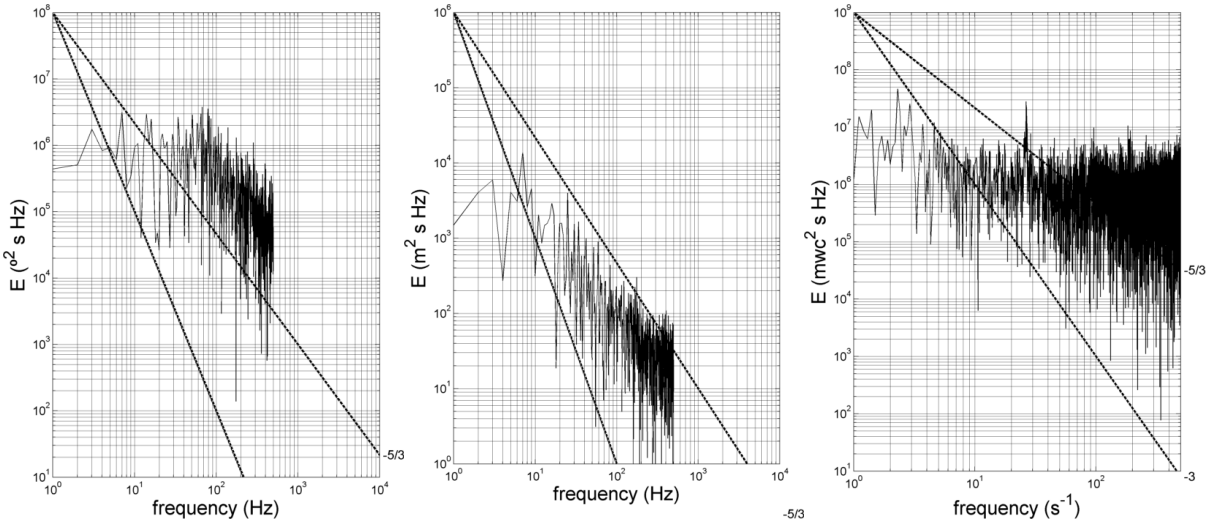

Figure 5.59 – Power spectra for Jet's angle (left), impingement point position (middle) and pressure transducer (right) for Reynolds 205

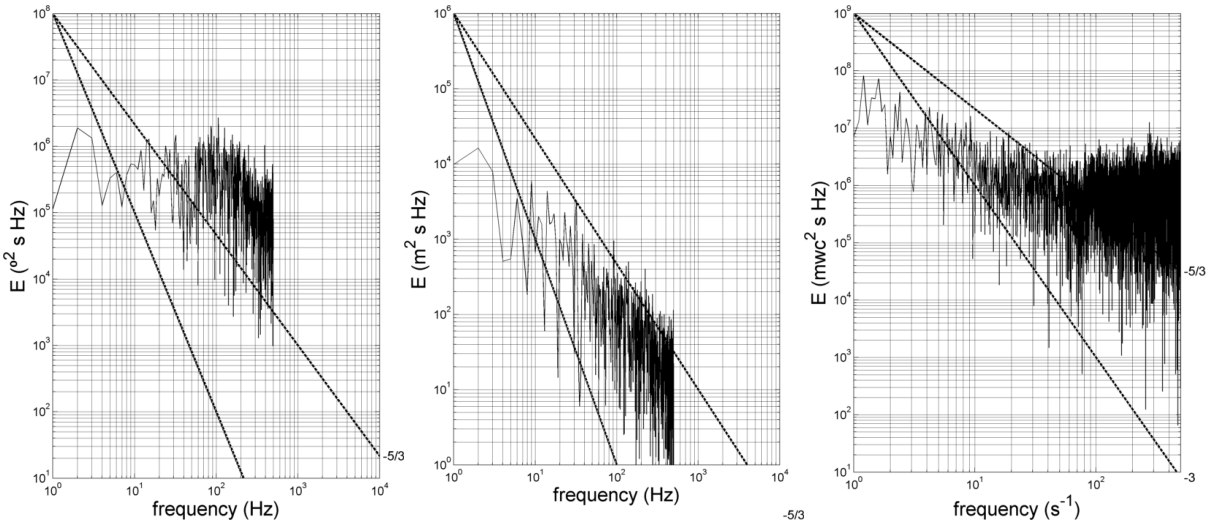

Figure 5.60 – Power spectra for Jet's angle (left), impingement point position (middle) and pressure transducer (right) for Reynolds 270

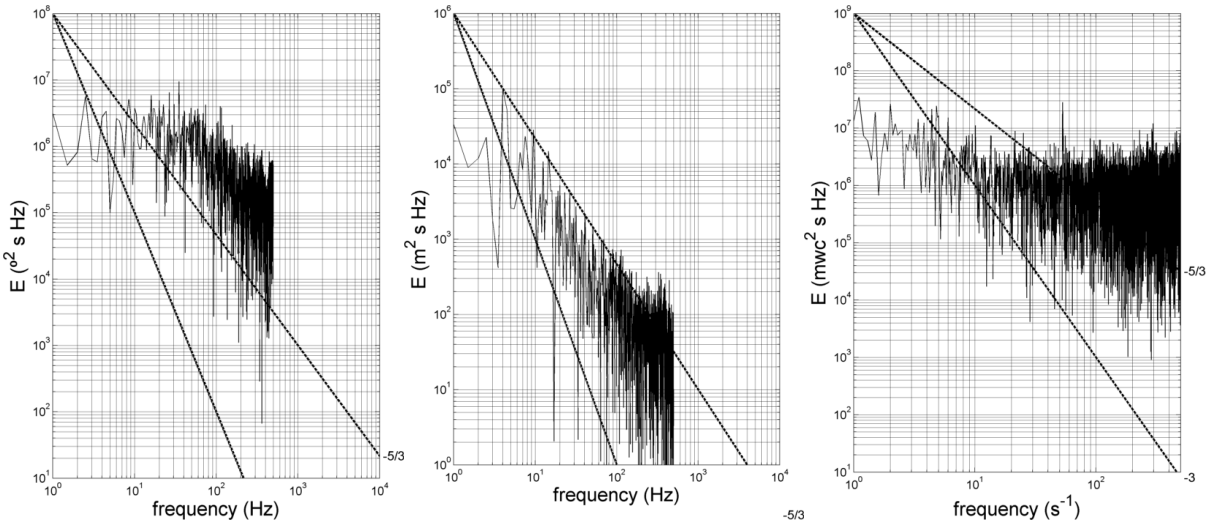

Figure 5.61 – Power spectra for Jet's angle (left), impingement point position (middle) and pressure transducer (right) for Reynolds 273

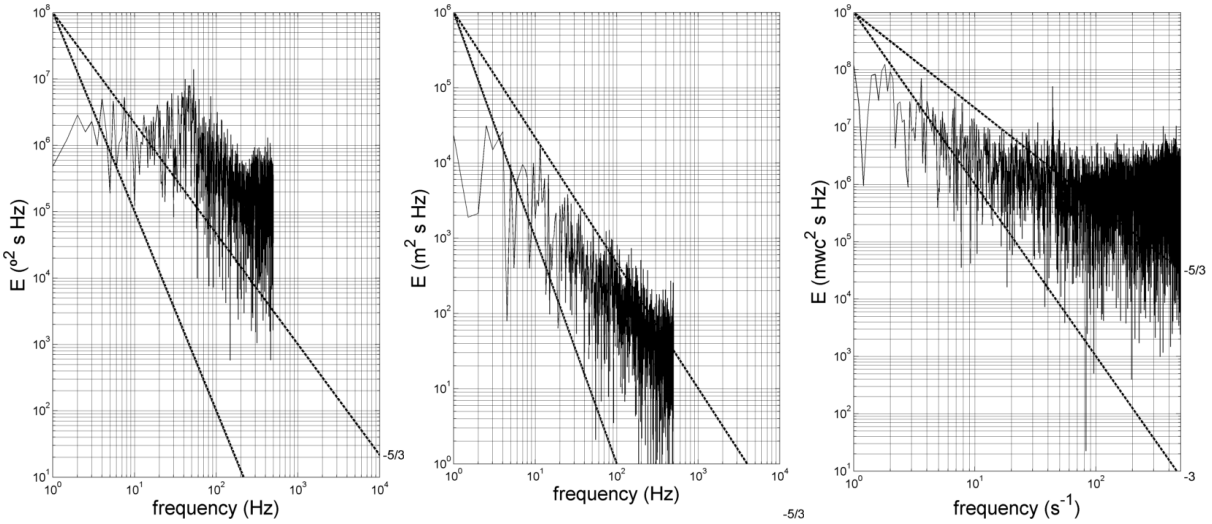

Figure 5.62 – Power spectra for Jet's angle (left), impingement point position (middle) and pressure transducer (right) for Reynolds 275

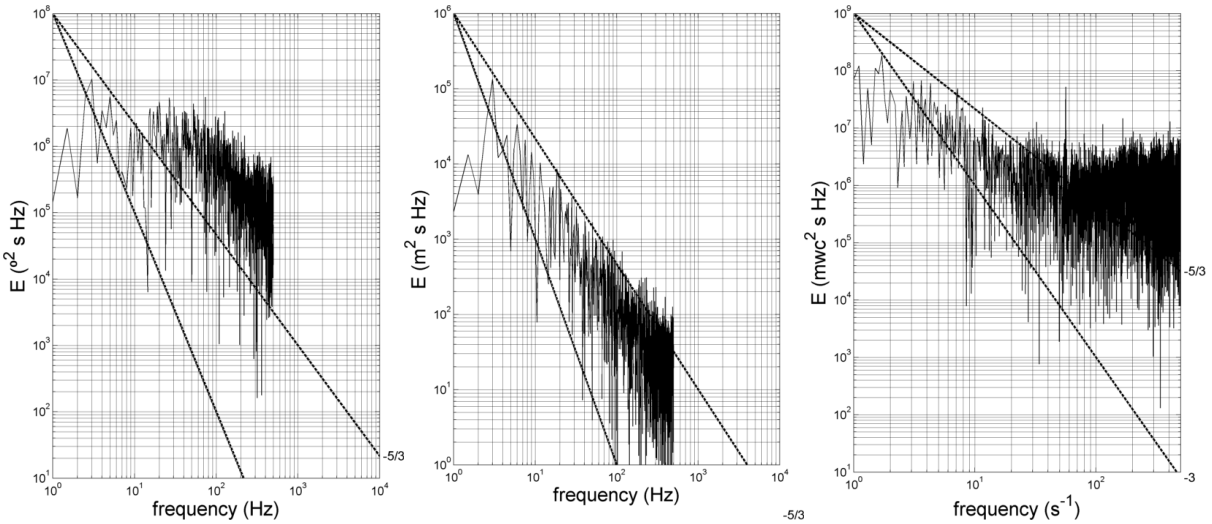

Figure 5.63 – Power spectra for Jet's angle (left), impingement point position (middle) and pressure transducer (right) for Reynolds 344

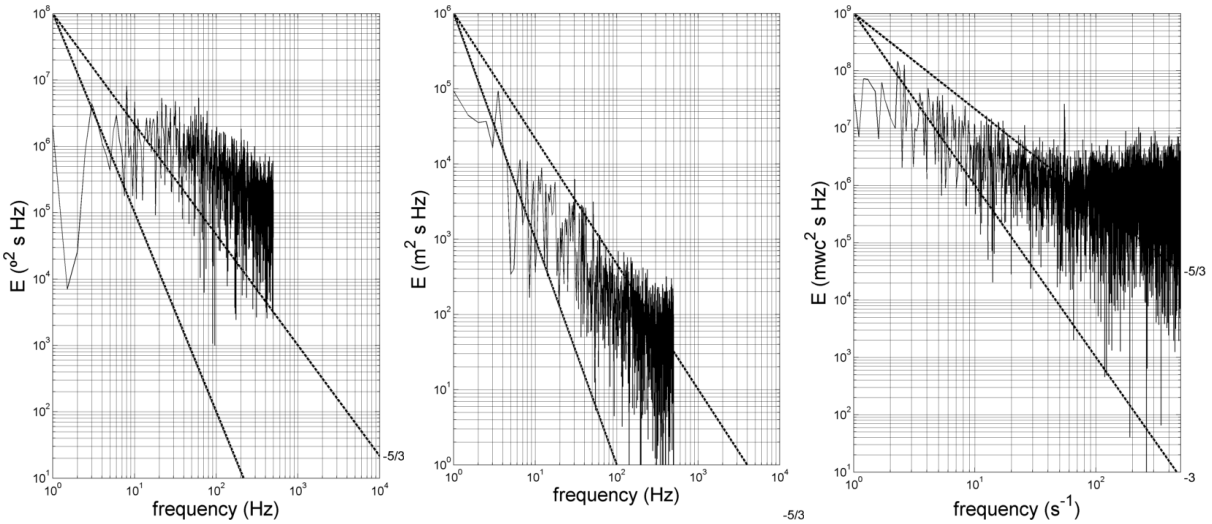

Figure 5.64 – Power spectra for Jet's angle (left), impingement point position (middle) and pressure transducer (right) for Reynolds 421

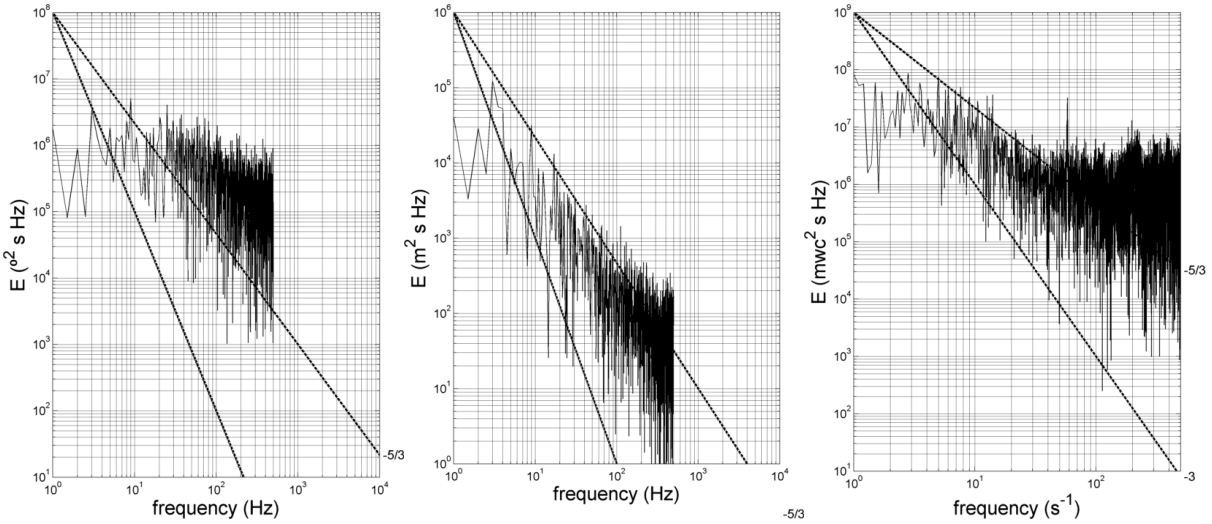

Figure 5.65 – Power spectra for Jet's angle (left), impingement point position (middle) and pressure transducer (right) for Reynolds 568

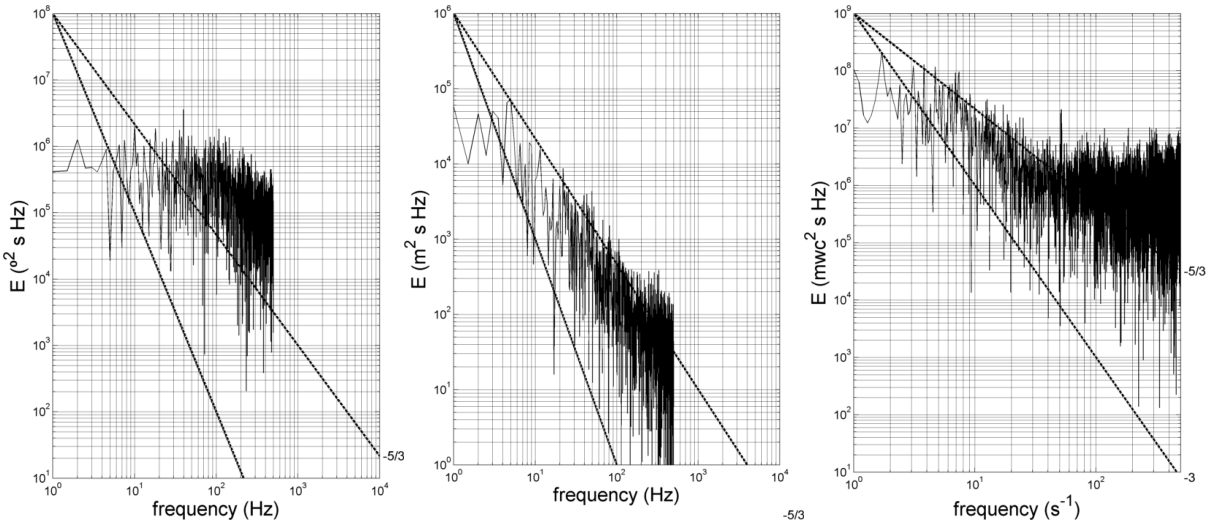

Figure 5.66 – Power spectra for Jet's angle (left), impingement point position (middle) and pressure transducer (right) for Reynolds 723

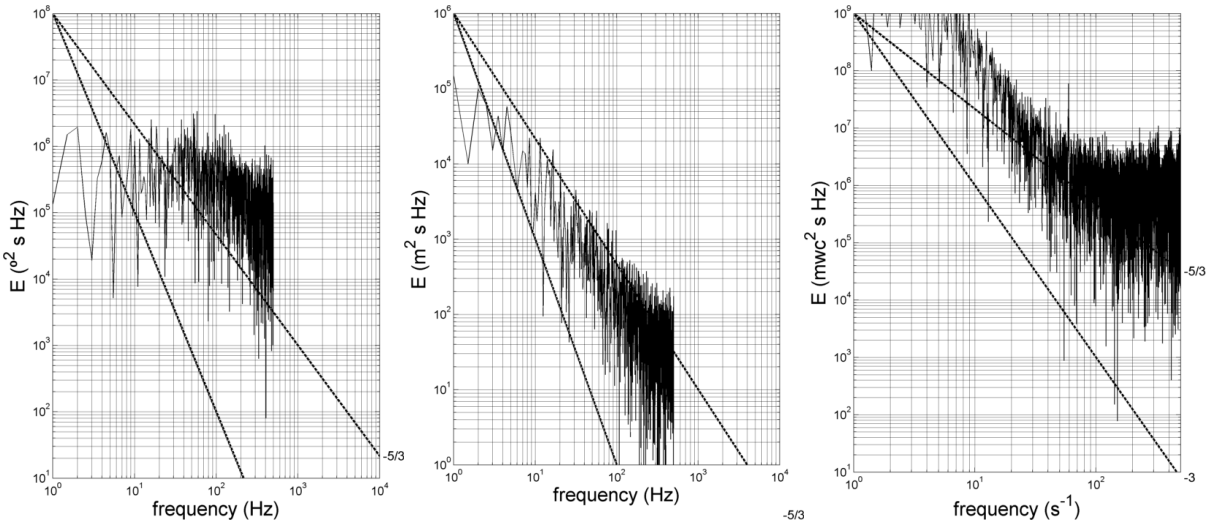

Figure 5.67 – Power spectra for Jet's angle (left), impingement point position (middle) and pressure transducer (right) for Reynolds 857

5.4 Parametric analyses of the flow field using two different viscosity fluids

Maximising the flow dynamics requires the impingement point position lie in the middle of the mixing chamber allowing the bending and stretching of the fluid laminas occupied all the chamber diameter. Ensuring the flow dynamics occur in the centre of the chamber requires thigh control of the flow rate in order to ensure not only this condition but others more problematic as it is different stoichiometries and different fluid proprieties. This is only possible with advance techniques to control the mixing process and expensive equipment not just for operating in high pressure but also so ensure low operation errors.

In the present work the flow parameters are study using two different viscosity fluids each one entering in one side of the chamber in order to validate some mathematical models existent in the literature

The importance of the present chapter is not only to validate some control models but to access their efficacy in a wide range of possible operation conditions, which is known to be one of main difficulty to control different fluids proprieties, which could be used to design and construct a multipurpose RIM machine.

In the present section will be study two main mathematical models. The first model study is the elastic analogue model proposed by Fonte (2012) which due their versatility will be

tested against experimental data. This step is new in literature since there is no prove of existence of this test for this model or similar models for RIM machine.

Additionally the pressure model developed by Gomes (2015) which is the main driven force in the RIMcop technology into create a multipurpose machine which can allowed different wide range of fluid proprieties.

This section is separated in two main parts. The first is presented the experimental PLIF setup and additional with the experimental conditions which going to be introduced all the tools and equipment used for this testing and also the conditions for each individual experience. In the end the results will be presented with addition of a brief description of the models and the sequence performed in the experiments.

5.4.1 Experimental setup

5.4.1.1 The RIM machine

In the present subsection the RIM machine used in experiments is equal to the RIM present in section 5.3.1.1 in both mixing chamber and additional components, but with a small difference in the operation, in which in the present case the two fluids are storage in different reservoir tanks in order to feed different injectors

5.4.1.2 PLIF Setup

In the PLIF setup big changes were performed, now combining the CCD camera used for PIV and a generator of laser beams.

The transparent mixing chamber is illuminated with a laser sheet cur the chamber axially through injectors, as previous experiments, with a thin slice of 1mm. In the present work the laser source used is a Nd:YAG double-head pulsed laser from Litrom Lasers (model NanoL50-100), which emits 4ns pulsed beams with maximum energy of 400 mJ/pulse at a maximum rate of 100 Hz and correspondent wavelength of 532 nm. The transport and conversion of the laser beam into a laser sheet is the same as previously reported.

Due existence of errors in the hardware, particularly in the computer memory only was possible to obtain 50 pairs of laser-synchronized frames of the illuminated flow. The record of the flow field was performed using a CCD camera (model TSI 630157) with the ability of capturing 11192 x 1600 pixels with 16 bit of greyscale at a maximum acquisition rate of 30

Hz. The transport of the images into a computer was performed through a frame grabber (model TSI 600067). A filter was adapted into the camera lens as explain in chapter xxx to avoid reflections.

The frequency of the be used in the experiments f_{laser} as defined as function of the Reynolds number (Re) and the maximum allowed frequency of the PLIF system $f_{laser,max}$, defined as

$$f_{laser}(RE) = \frac{Re}{600} f_{laser,max} \tag{5.16}$$

The default exposure time of 405 μs is it sufficient low to ensure a freezing flow into images. The TSI software (Insight 3G version 9.0) is responsible input the experimental parameters into a synchronizer (model TSI 610035) which is used to coordinate the image shutter with the input laser beams. The image acquisition was done using a Dell Precision 690 PC with a dual core Intel Xenon CPU at 2.33 GHz and 2 GB of RAM

5.4.2 Experimental conditions

In the present experiments it was set during each Reynolds in study, a constant flow rate for the right side injector while small increments of 0.1 g/s was introduced in the left side of the injector in order to dislocate the impingement point position from the left side of the chamber until the right side on the chamber.

5.4.2.1 Rheology of the solution

The main objective presented in this chapter is study the parameters which directly affected the flow impingement point. Therefore it was chosen as working fluids, fluids with complete different rheology. In the left side of the chamber fluid close to 20 cPA of viscosity was used, and for the other side of the chamber a fluid with three times more viscosity was chosen in order to access the efficacy of such control models.

The fluids rheology was perform for a temperature range between 20 and 34 °C. Figure 5.68 shows the reduction of viscosity with temperature for each working fluid.

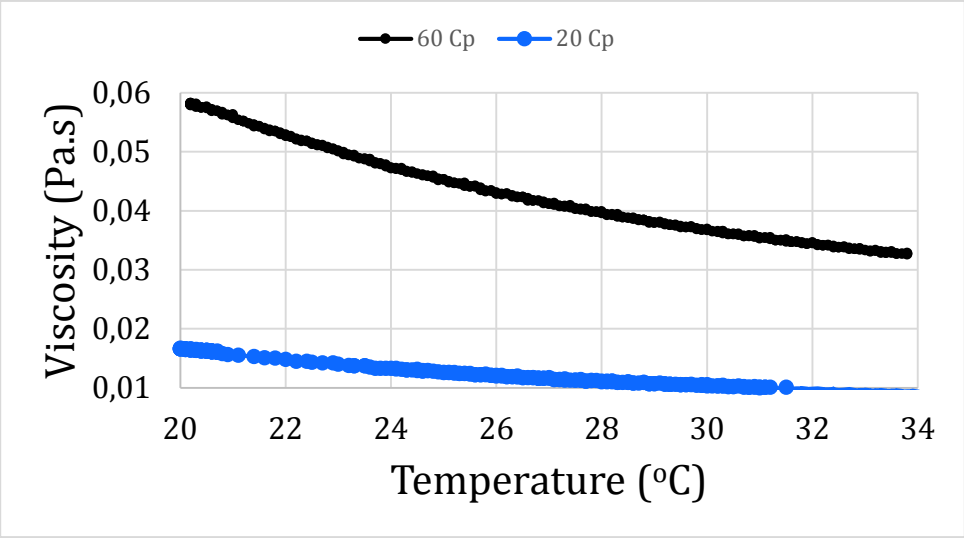

Figure 5.68 -Rheology of both working fluids

5.4.2.2 Calibration

Since the control equipment, and data acquisition system was the same used in the previous PLIF experiment, such as the Coriolis mass flow meter and the differential pressure transducer, the calibration and assessment of the error was already performed in the previous part of the present chapter. This results will then be used to evaluate the location of the impingement point in function of the control parameters of the RIM system.

In the fluid with higher viscosity is added a dye marker of rhodamine 6G at the concentration of 0.4 g/l. No need for calibration of the concentration of dye marker in the solution since will be only interested for the impingement point position.

5.4.3 Results

The images obtained from the PLIF technique are averaged for each experiment. Using the average image will be presented and visualization study is performed. Additionally and using the DIP MODA program the impingement point position is obtain and the results are used to compare with both mathematical models in study.

Before initialize the comment of the results is necessary to define some parameters which going to be used for this validation. This parameters was already explained in previous chapter and therefore will going only be presented the mathematical equations

Defining the momentum rate ratio as

$$\phi_M = \frac{\rho_1 d_1^2 u_{inj,1}^2}{\rho_2 d_2^2 u_{inj,2}^2} \tag{5.17}$$

Where ρ is the fluid density, d the injectors diameter and u the injectors velocity. The indices 1 and 2 represent the left and the right side injectors respectively. In the present case the left side injector have the lower fluid viscosity while the right side have the higher fluid viscosity.

The kinetic energy rate ratio is defined as

$$\phi_K = \frac{\rho_1 d_1^2 u_{inj,1}^3}{\rho_2 d_2^2 u_{inj,2}^3} \tag{5.18}$$

And the jets mass flow rate ratio

$$\phi_{FR} = \frac{\rho_1 d_1^2 u_{inj,1}}{\rho_2 d_2^2 u_{inj,2}} \tag{5.19}$$

5.4.3.1 Average Flow field visualization

The average flow field visualization is presented in Appendix D, which correspond of the average from 50 images obtained from the PLIF experiments for each individual increment of flow rate.

Initially should be commented the position of the stagnation point is only visible for half of the chamber diameter, and with the displacement of the impingement point into the right the images appears to become blurry and in some cases is possible to observe bending of the jets, being the right injector tends to the top of the mixing chamber.

Additionally, is clearly observed, when there is no oscillatory motion of the impingement surface, the strias of the fluid is clearly observed due the immiscibility of both fluids streams. This highlights the importance of a proper advective mixing since not only the fluids are immiscible as it is harder for the particles of fluid bending and folding inside the mixing chamber and reducing is thickness until polymerization can occur.

It is visible close the chamber wall a difficulty in the displacement of the impingement point position with increments of the flow rate in the left side of the chamber. This effect is extremely important since introduce new difficulty into the control of the flow rate for each injector due existence of a small region of flow rate combination where mixing can occur.

By observing the equation of the kinetic energy rate ratio for the centre of the chamber, i.e $\phi_k = 1$, requires a direct relationship between the density and the velocity. In the average images is observed a tendency of the flow field embrace the jets with higher viscosity and density. This phenomena is caused since the flow entering in the left side injector have higher velocity and consequent higher momentum than the fluid entering in the right side. This effect is of major interest of study since the oscillatory mechanics which create advection is highly influenced by the shape of the impingement surface and consequent frequency.

5.4.3.2 Elastic analogue model

The mathematical formulation of the elastic analogue model proposed by Fonte (2012) was previously described in the chapter 4. In the present section will be used this model for different fluid viscosities entering in each side of the mixing chamber. The mathematical equation of the elastic analogue model is

$$\chi^* = \frac{\left(\frac{Re_2}{10}\frac{d_2}{D} + 1\right)\sqrt{\phi_K \frac{Re_1}{Re_2}\frac{d_1}{d_2}} - \left(\frac{Re_1}{10}\frac{d_1}{D} + 1\right)}{\sqrt{\phi_K \frac{Re_1}{Re_2}} + 1} \tag{5.20}$$

Where χ^* is the normalized impingement point position in the range [-1, 1] where zero correspond to the centre of the chamber, Re correspond of the Reynolds number and D the chamber diameter. The indices 1 and 2 represent the left side and the right side injector respectively.

Respecting the assessment of the error of the impingement point position, it was obtained from the average flow field and was it was visualized the interface have a sharp contrast, which mean there was not variation of the impingement point position along the experiments. Additionally the impingement point position was obtain using the DIP MODA algorithm where it was analyse individual pixels in a line correspondent to the injectors centre which consequently reduced substantial the error into negligible values. Also the error and the variation associated with the measurement of the flow rate was very small and also considered negligible regarding the magnitude of the results. Additional note should be refer into previous statement. When the position of the impingement point passes the centre of the chamber it was visualized some oscillations into the impingement position which appears into experimental results as a higher deviation of the mathematical model

It was performed experiment in 5 different Reynolds number and the results will be plotted against the main RIM parameter used in control. As it can be seen in Figure 5.69 to Figure 5.74 all the control parameters the experimental results tends to match the elastic analogue model in a region close to the chamber centre. Close to the walls the model tends to unpredicted the impingement point position being this difference higher with the increasing of the Reynolds number.

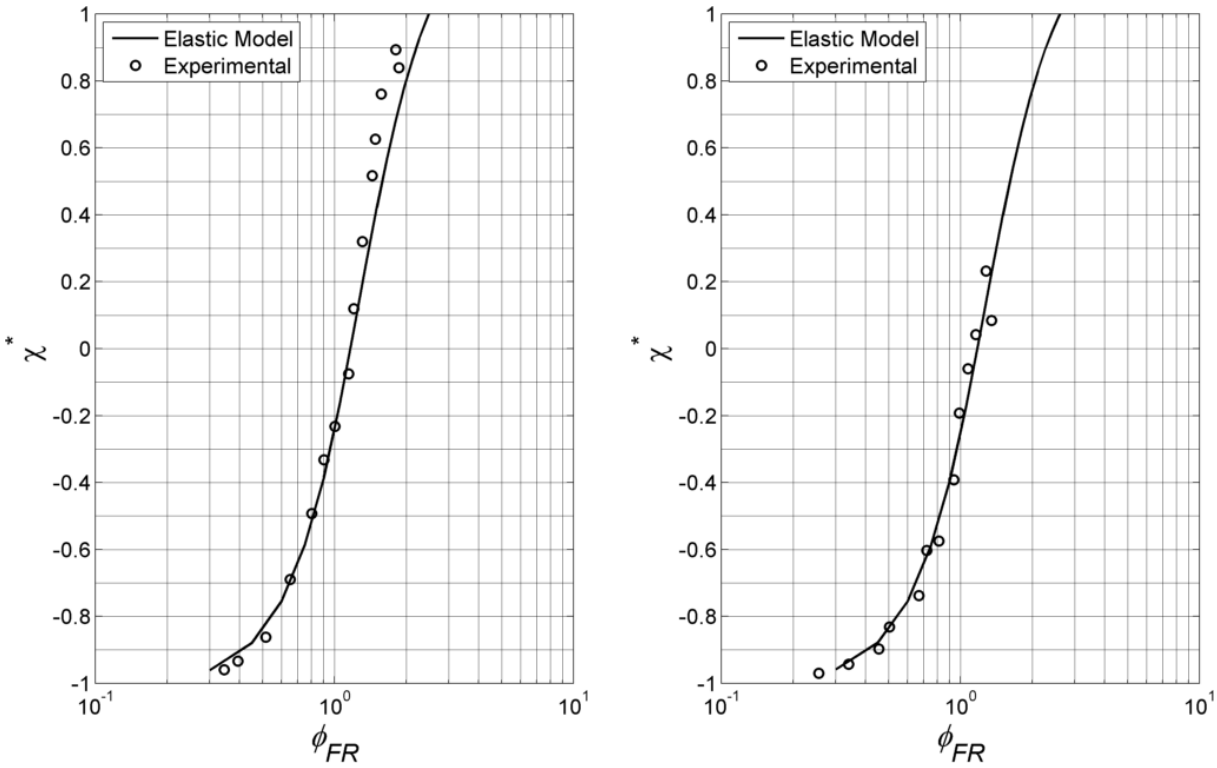

Figure 5.69 - Flow Rate Ratio for Reynolds 72 (left) and Reynolds 81 (right)

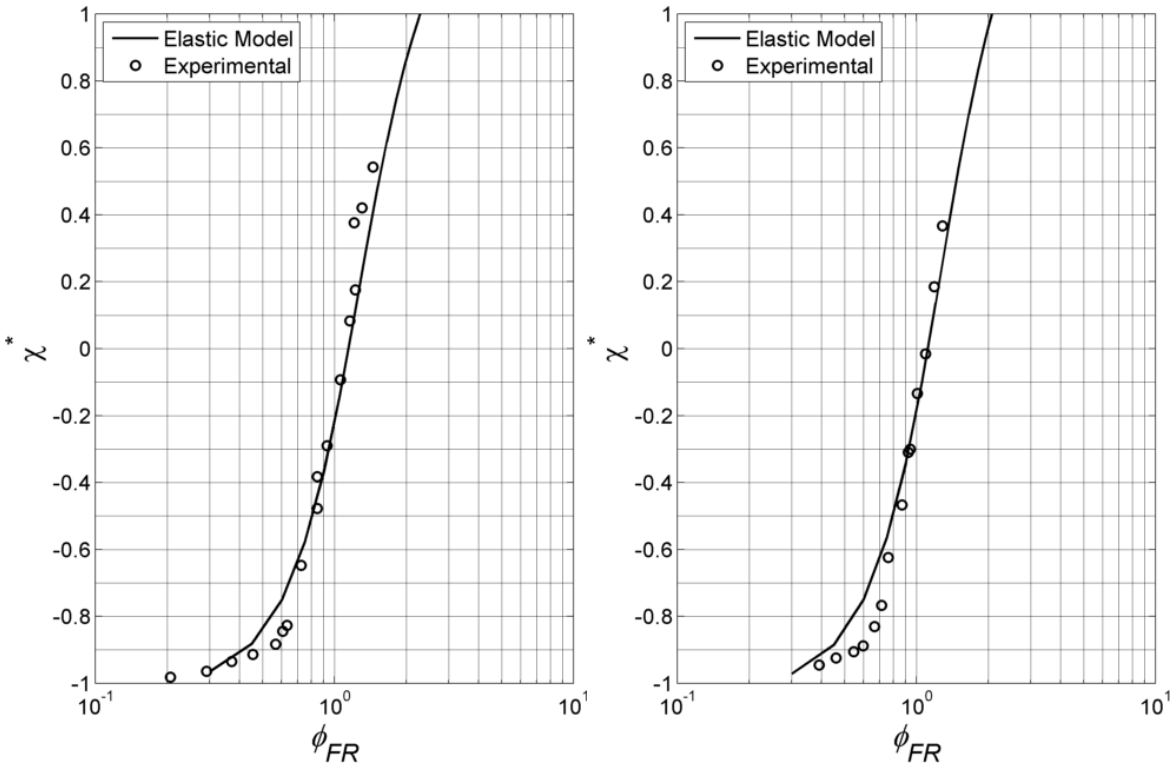

Figure 5.70 - Flow Rate Ratio for Reynolds 118 (left) and Reynolds 138 (right)

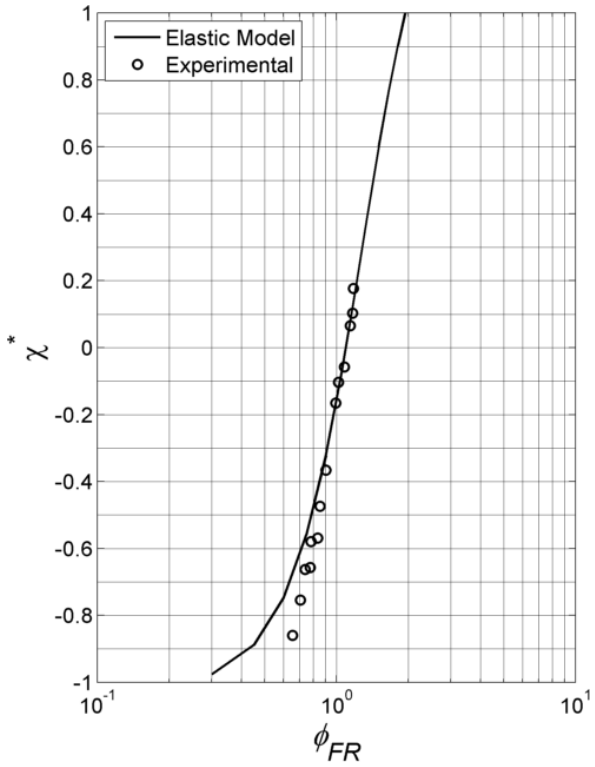

Figure 5.71 - Flow Rate Ratio for Reynolds 162

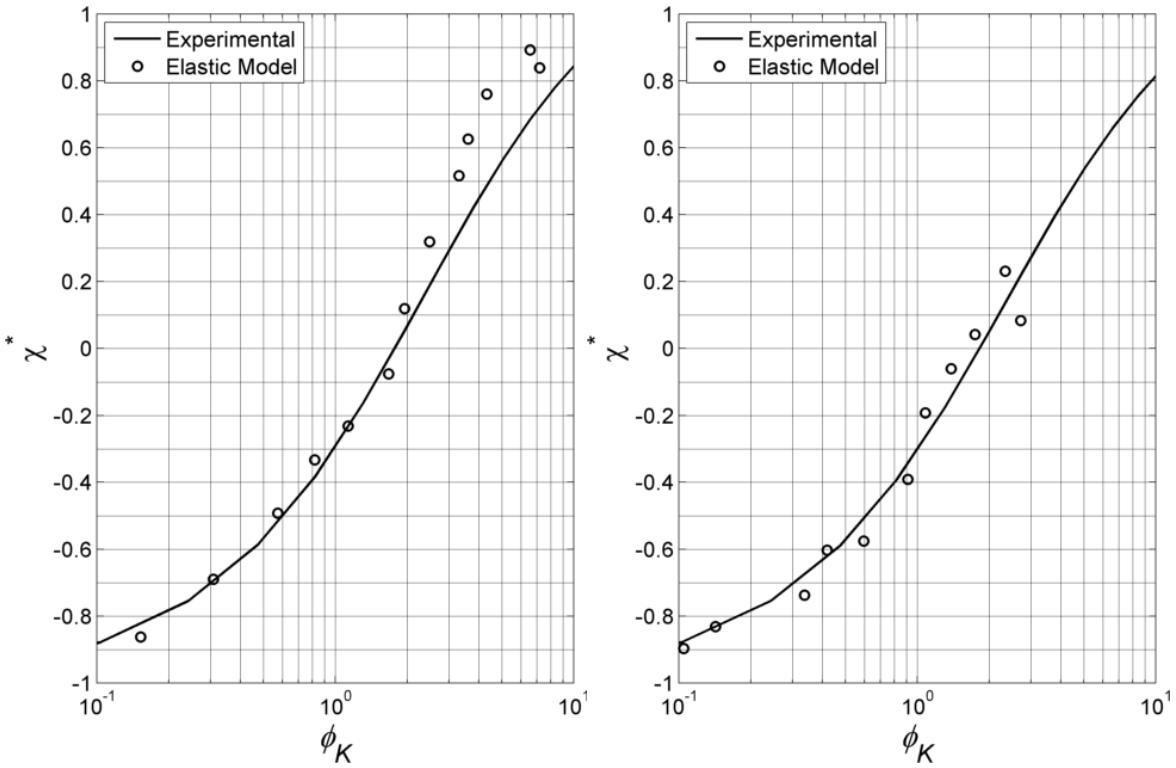

Figure 5.72 - Kinetic energy rate for Reynolds 72 (left) and Reynolds 81 (right)

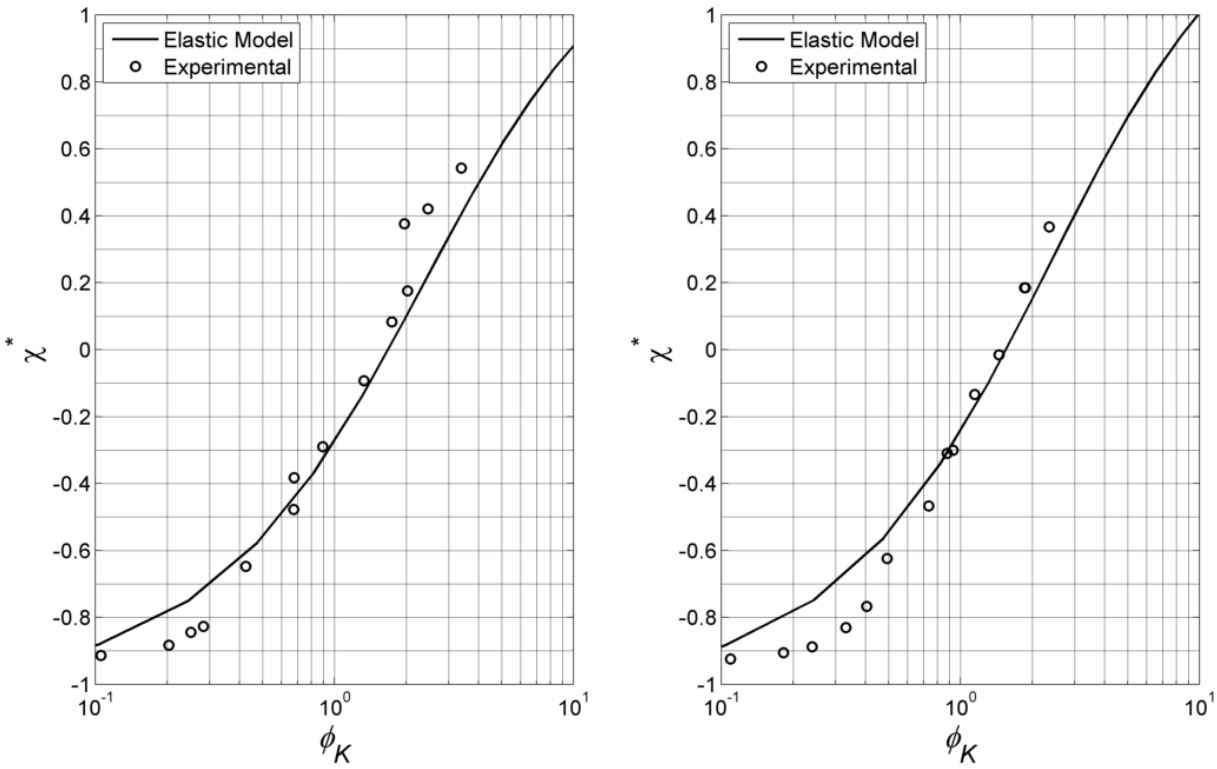

Figure 5.73 - Kinetic energy rate for Reynolds 118 (left) and Reynolds 138 (right)

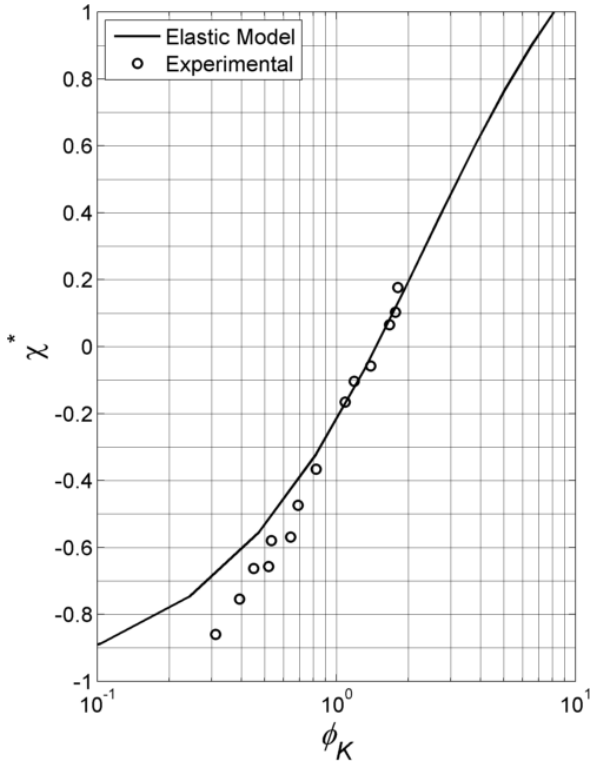

Figure 5.74 - Kinetic energy rate for Reynolds 162

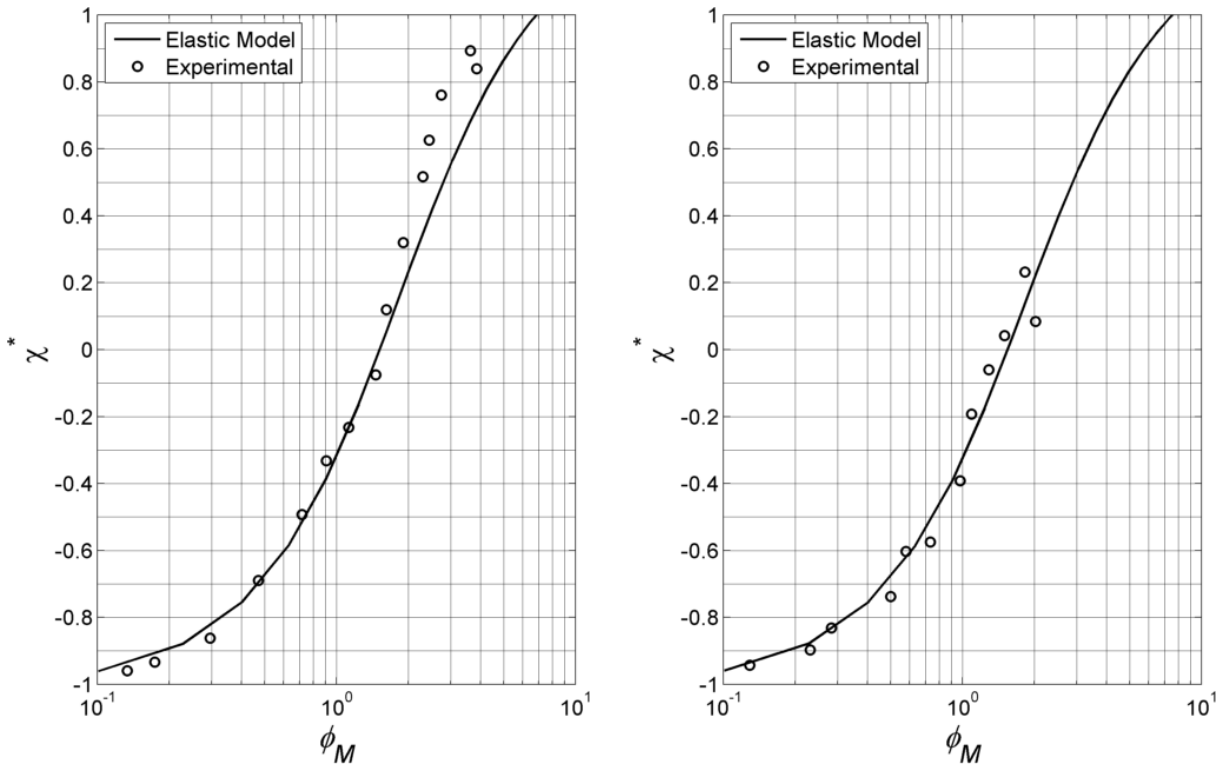

Figure 5.75- Momentum rate ratio for Reynolds 72 (left) and Reynolds 81 (right)

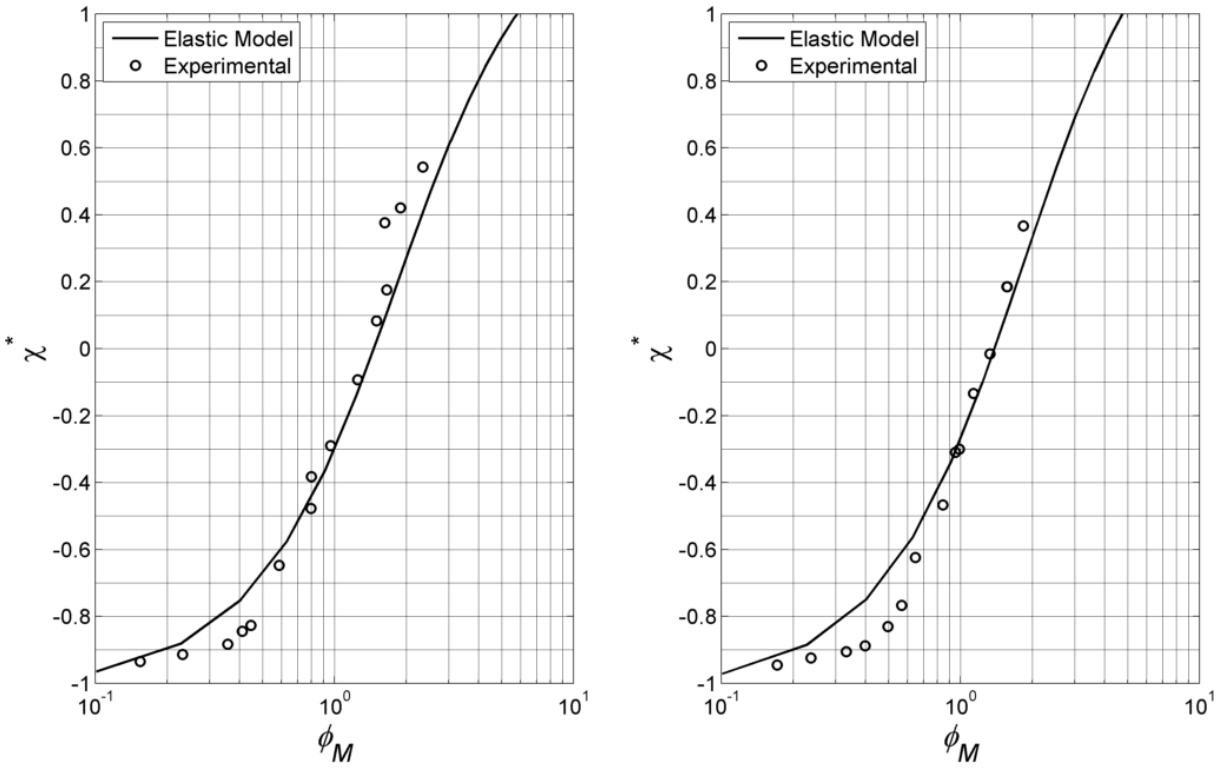

Figure 5.76- Momentum rate ratio for Reynolds 118 (left) and Reynolds 138 (right)

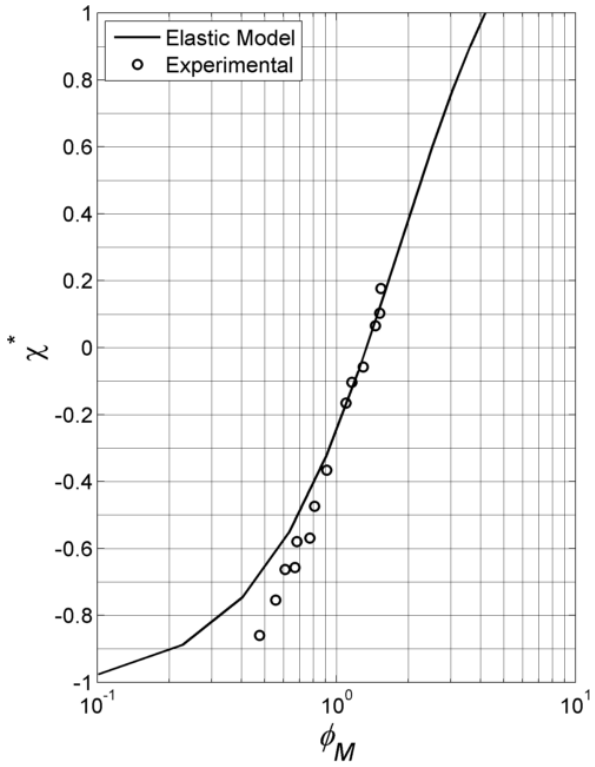

Figure 5.77- Momentum rate ratio for Reynolds 162

5.4.3.3 Pressure model

The pressure model presented in chapter 4 will be tested for a case of two different fluid viscosities.

The mathematical model present a decreasing of the pressure when the stagnation point is increase, being this increase be exponential for low values of normalized pressure. The experimental work present a impingement point position situated in high values of the normalized pressure, which is perform for the more viscosity fluid.

As a conclusion the mathematical model which describes the pressure variation don't present any match with the experiments for fluids with different viscosities, and therefore the author recommends in new works the study of this methodology of control the process by developing a new fitting mathematical model which can be used for a wide range of operational conditions such as different diameters, different fluid proprieties and which can be used for a variety of Reynolds number.

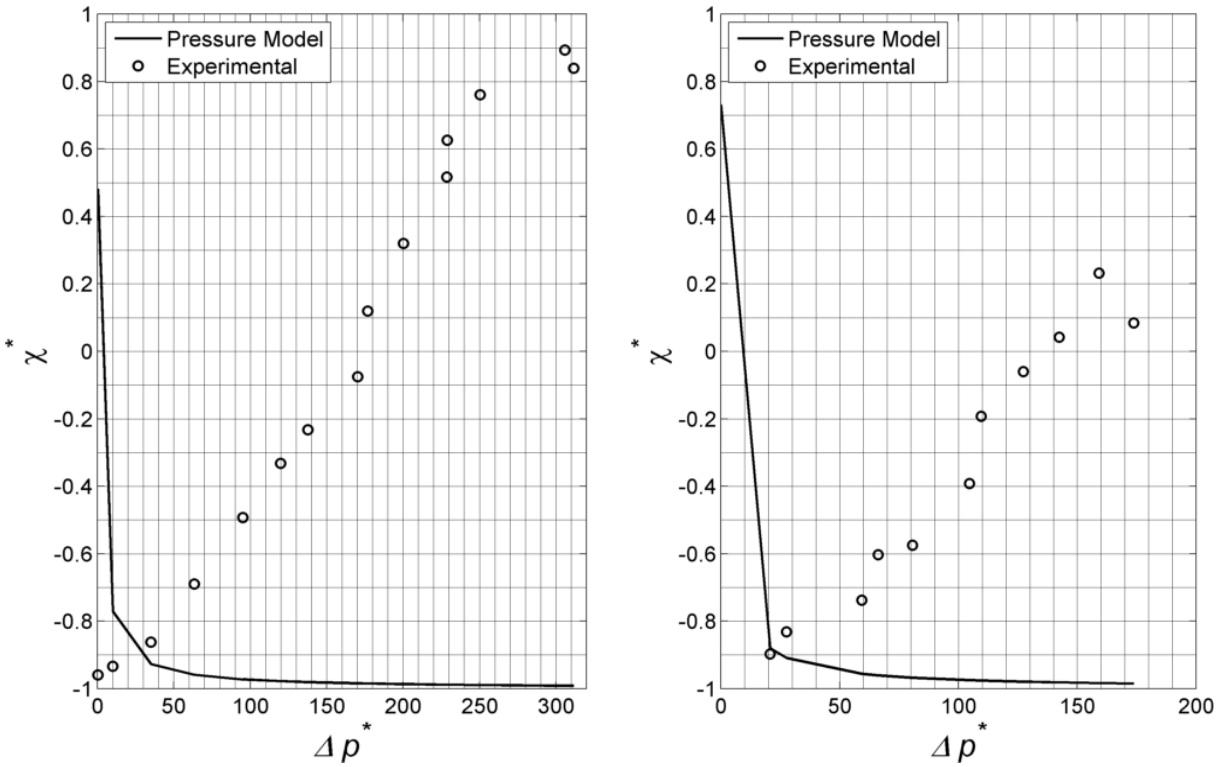

Figure 5.78- Pressure model validation for Reynolds 72 (left) and Reynolds 81 (right)

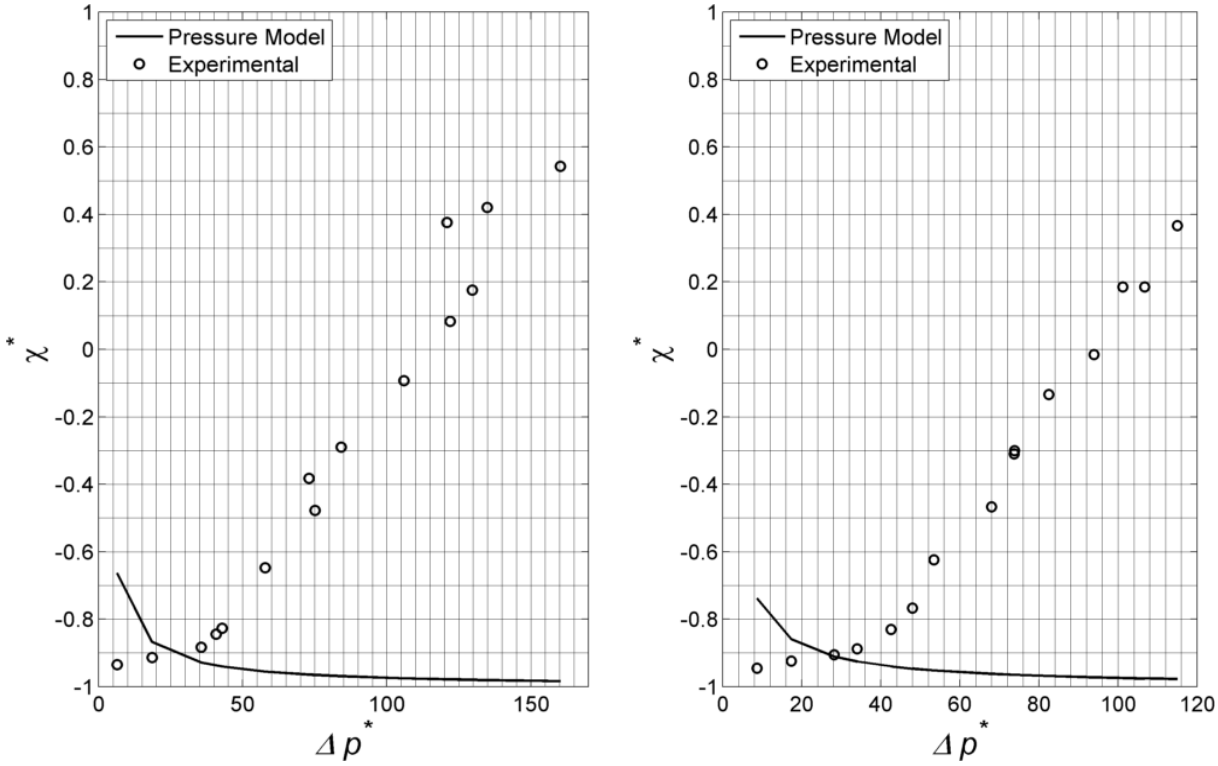

Figure 5.79- Pressure model validation for Reynolds 118 (left) and Reynolds 138 (right)

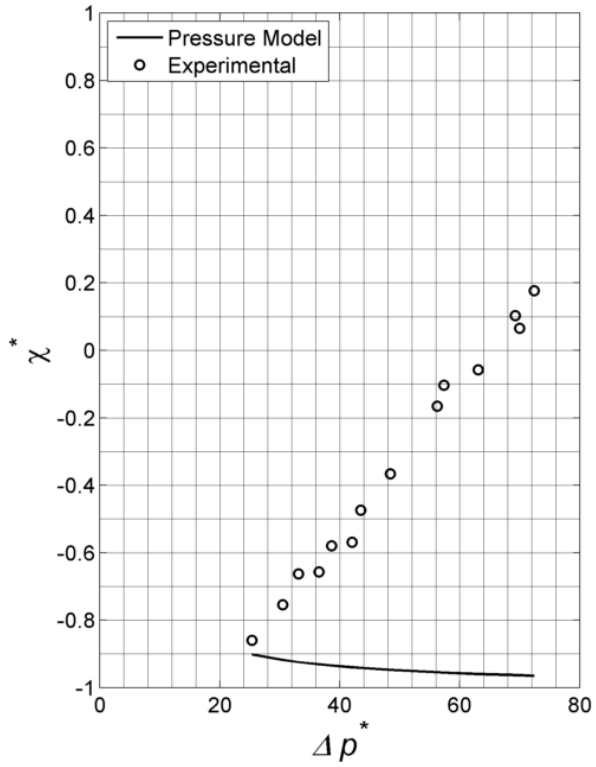

Figure 5.80- Pressure model validation for Reynolds 162

5.5 Conclusions

The main presented in the present chapter is divided into two main sections. The first section analyse the results provided by PLIF experiments using a high speed camera to record the main flow scales. The second work tends to analyse the two main mathematical models to predict the impingement point position by knowing two different parameters, namely the mass flow rate and the Reynolds number in each injector for the elastic analogue model, and the differential pressure between both injectors for the pressure jets model.

According the first part of the work it was observed the FFT of the pressure transducer didn't obtain any physical meaning of the frequencies of the main flow scale and therefore it was necessary to go to previous works where this frequency was already obtain for a set of Reynolds number. It became clear with this work the main flow scale correspond to the impingement surface rotation rather than the impingement point position, which could be due the magnitude of both variables or the tracking of the flow, while the impingement point position is 1D compared with the 2D for the jets angle.

Instantaneous flow field visualization identified three main flow dynamics: segregated flow, periodic segregated flow and self-sustainable chaotic regime. The present work identify for the self-sustainable chaotic regime three main different flow conditions: the periodic, flow frequency random oscillation and high frequency random oscillation.

Using fluids with different viscosities entering the mixing chamber by different jets two mathematical models was used to access the viability of such techniques in order to be used as control model for a wide variety of operating conditions such as different stoichiometry, different fluids rheology's and geometrical conditions. Therefore the elastic analogue model and the pressure model was tested. It was conclude the elastic analogue model suited perfectly in the results provided by the experimental data. In the other hand the jets pressure model, which is the main concept of the RIMcop technology, didn't fit in the results since completely different curves was obtain for each case which proves the complexity and difficulty of modelling the impingement point position with this technology and therefore improvement is necessary to be made.

6 Final remarks

6.1 Conclusions

The present work is divided into three main chapters according to the type and methodology to access different aspects of the flow field in RIM mixing head. First results chapter access using numerical tools the flow field in a RIM machine which was study in order to quantify and qualify the scales of the flow. In the second results chapter experimental technique, PIV, was perform in a front plane of the mixing chamber. This allowed to quantify and qualify the flow field behaviour and the access the effectiveness of two main mathematical equations models to predict the impingement point position base on a various flow parameters. In the last results chapter the experimental technique, PLIF, was performed for the same front plane of the mixing chamber. By using an algorithm, DIP MODA, the impingement point position and the jets angle was calculated for the domain of each experiment. Additionally using the same technique it was access the effectiveness of the same mathematical equations models, using different fluid viscosities entering opposed in the mixing chamber.

In the present chapter will be resumed the main conclusions for each topic studied, for the first time in the literature, presented by the present work. The main topics are the flow hydrodynamic behaviour and scale containing eddies, frequency of the larger eddies, the mixture using a non-diffusivity model (VOF) and using an large size grid and in the end

mixing control using two different mathematical models the elastic analoge model and the pressure model.

6.2 DIP MODA for tracking impingement point and jets angle

Digital Image Processing Multiobjective Optimization Deterministic Algorithm (DIP MODA) was created in order to obtain the jets impingement point and the jets angle. This code is divided into two parts, where the first part is the image processing of the images obtained from the PLIF experiments for a defined set images. It was used a high speed camera which allowed to track, in real time, the flow behaviour. A multiobjective optimization algorithm allowed to track the impingement point position, by searching in a line central to the jets centre, the value of the interface, combined by others variables using a bell shape weighted method. The same idea was performed for the jets angle, where different variables used and the interface was track and the angle calculated using a linear regression. This code prove to be very effective by tested against a benchmark test and afterwards applied to the real problem in study.

6.3 Hydrodynamic behaviour

6.3.1 Visualization studies of the hydrodynamic flow behaviour

Numerical studies was performed for Reynolds 150, 200, 250 and 300. All the flow hydrodynamic scales was calculated since the flow was solved until the Kolmogorov scale. The visualization studies shows with an increasing of the Reynolds number an increase of the oscillation of the impingement surface due impingement jets. Also with this increasing it is observable a breaking of the normal oscillatory motion of the impingement surface which cause a creation of small vortices in the impingement region rather than vortices flowing along the chamber height. This indicate a large energy dissipation in this small region and with an increasing of this region the size of this dissipation tends to small due increasing of the creation of this small vortices.

Generally speaking it is observable a large oscillation, in terms on angle in the front plane rather than the top plane. Additionally is observable the large size eddies is majority contain in the front plane since the top plane the eddies are containing in the chamber diameter while the front plane allowed bigger area available to jets motion.

6.3.2 Qualitative and quantitative analyses of k and ε

The turbulent kinetic energy and the turbot energy dissipation was calculated for each numerical studies performed. It is visualized for each variable the location is in the impingement area since it is here exist the biggest fluctuation velocity field and the higher velocity gradients of the flow field.

In term of the vertical dimension of the higher concentration of this variables it is observed a small growing in terms of the magnitude from 150 to 200 while in the range 200 to 250 remain almost constant. The biggest rate of growing is observed in range 250 to 300. By normalizing this variables by the value in the central point it is observed a fast growing rate for k with a high decreasing of ε for the range 150 to 200. Generally speaking is observed a opposed variation of this variables with a slight increasing of the Reynolds number

6.3.3 Scales containing eddies

Using Fast Fourier Transformed was used to calculate the scale containing eddies which was compared with the chamber dimensions. Two main cascades was obtain: the inverse energy cascade with slope -5/3 which means the larger low scales are feed with low dimension scales and the direct entrosphy cascade which means the flow flows in a positive direction where the larger scales give energy to the lower scales. In the dissipation range all the flow scales are dissipated into heat in the size equal as the kolmogoroff scale.

In the inertial subrange the inversion of cascades from a slope -5/3 into -3 is a point where the energy is injected which correspond a size equal the injector's diameter. The larger energy containing scale have an eddy size between the chamber diameter and the height of the chamber size.

6.3.4 Frequency analyses

Using the DIP MODA the jets angle and the impingement point position was obtain for each set of capture images referred to and experiment. Additionally was also recorder the value differential pressure between each injector. FFT was perform for each case and the results compared with documented work. It was proven the frequency of the jets angle matches the documented work frequency until Reynolds close to 300. After this value it was not observed any significant match, since complex phenomena's in impingement jet iteration.

All the others variables such as the impingement point position and the differential pressure didn't obtained any relevant data

6.4 Mixture using a non-diffusivity model (VOF)

In the present work Volume of Fluid (VOF) model was used to access the study of mixing mechanism using a non-diffusivity model. Due the high computational effort of such method it was choose to setup a mesh length equal to the Kolmogorov rather than the bachelor scale. In the present work it was clear after the large scale vortices created due impingement the reduction of scale was more than the mesh size and therefore numerical diffusion dominate the entire domain. An adaptive grid gradient based was performed to effectiveness obtain smaller scales but the tremendous computational effort was necessary to abort such technique due computational limitations.

6.5 RIM process control

6.5.1 Elastic analogue model

The elastic analogue model was verified for a variety of Reynolds number with equal fluids rheology's, with 20 mPa.s in each injector using PIV and with different fluid rheology's with 20 and 60 mPa.s of viscosity respectively in each injector using in this case PLIF technique. The elastic analogue model was proven to successful determine the impingement point position for a wide fluid proprieties and Reynolds number. Previous works was already validate for different injectors diameters which concludes this model to be one of the most well adapted model in the literature

6.5.2 Pressure jets model

The pressure jets model was tested in the same conditions as the elastic analogue model and using the same methodologies. The present work concludes this model, which only model half of the chamber, didn't perform very well with the same fluid theologies in each injector but it was acceptable for the impingement point close the walls and the centre of the chamber. For the test with different fluid proprieties the model didn't pedict and even behave opposite as the experimental work. The author then conclude further investigation in the development of such model in order to be used with RIMcop technology for a wide range of control conditions.

6.6 Future work recommendations

The present work is divided into two main research. For the first research related to study the hydrodynamics mixing mechanism for the fluid flow system. For this case some suggestions for future work are presented.

- Create a mechanical/electromechanical system to oscillate the flow rate in the jets. New works in the field of combustion uses this methodology to improve the mixing efficiency. In the present work this methodology can improve the formation of large eddies, which going to break into small eddies for a longer distance inside the mixing chamber, improving the overall mixing performance particularly at low Reynolds number.
- Further investigate, using experimental and numerical techniques, the mixing between fluids com different rheology's, particularly with high viscosity ratios which is usually found in RIM process.
- Implement a non-diffusive dynamic adaptive grid to model the flow field inside a 3D model of the mixing chamber in order to obtain the full hydrodynamic behaviour, and the full mixing behaviour by model the flow field until the bachelor scale.

The second research theme it was the validation of some mathematical models to be used as control the mixing process. For this case some suggestions for future work is presented

- Improvement of the control of the mixing process using the RIMcop technology for a wide variety of situations requires a development of a new mathematical model which can be used for more than one control variable, such as Reynolds number, impingement point position, jets ratio and others.
- Development of a multi-variable control using the elastic analogue model to predict the position of the impingement point, which can be coupled with the differential pressure of the impingement jets and can be validated by a real time image processing technique with the same concept used to calculate the impingement point position using the DIP MODA algorithm

References

Adrover, A., Cerbelli, S., & Giona, M. (2002). A Stectral Approach to Reaction/Diffusion Kinetics in Chaotic Flows. Computers and Chemical Engineering, 26, 125-139.

Angst, W., Bourne, J. R., & Sharma, R. N. (1982). Mixing and Fast Chemical Reaction - V. Influence of Diffusion Within the Reactor Zone on Selectivity. Chemical Engineering Science, 37(8), 1259-1264.

Baldyga, J., & Bourne, J. R. (1983). Distribution of Striation Thickness from Impingement Mixers in Reaction Injection Molding. Polymer Engineering and Science, 23(10), 556-559.

Baldyga, J., & Bourne, J. R. (1984a). A Fluid Mechanical Approach to Turbulent Mixing and Chemical Reaction Part Iii Computational and Experimental Results for the New Micromixing Model. Chemical Engineering Communications, 28(4-6), 259-281. doi: Doi 10.1080/00986448408940137

Baldyga, J., & Bourne, J. R. (1984c). A Fluid Mechanical Approach to Turbulent Mixing and Chemical Reaction PartII Microming in the Light of Turbulence Theory. Chemical Engineering Communications, 28, 243-258.

Baldyga, J., & Bourne, J. R. (1984f). Mixing and Fast Chemical Reaction-VIII. Initial Deformation of Material Elements in Isotropic, Homogeneous Turbulence. Chemical Engineering Science, 39(2), 329-334.

Baldyga, J., & Bourne, J. R. (1989a). Simplification of Micromixing Calculations. I. Derivation and Application of New Model. The Chemical Engineering Journal, 42(2), 83-92. doi: 10.1016/0300-9467(89)85002-6

Baldyga, J., & Bourne, J. R. (1989d). Simplification of Micromixing Calculations. II. New Applications. The Chemical Engineering Journal, 42, 93-101.

Baldyga, J., & Bourne, J. R. (1990). Comparison of the Engulfment and the Interaction-by-Exchange-with-the-Mean Micromixing Models. The Chemical Engineering Journal, 45, 25-31.

Baldyga, J., & Bourne, J. R. (1995). Interpretation of Turbulent Mixing Using Fractals and Multifractals. Chemical Engineering Science, 50(3), 381-400.

Baldyga, J., & Bourne, J. R. (1999). Turbulent Mixing and Chemical Reactions. New York: John Willey & Sons.

Baldyga, J., Bourne, J. R., & Zimmerman, B. (1994). Investigation of Mixing in Jet Reactors Using Fast Competitive - Consecutive Reactions. Chemical Engineering Science, 49, 1937-1946.

Beek, J. M., R. S. (1959). Chem. Eng. Prog. Symp. Ser., 55(23).

Bierdel, M., & Piesche, M. (2001, 26-28, June). CFD - Simulation and Experimental Investigation of Impingement Mixing in Reaction Injection Molding (RIM). Paper presented at the 3rd European Congress of Chemical Engineering, Nuremberg.

Bourne, J. R. (1982). The Characterization of Micromixing Using Fast Multiple Reactions. Chemical Engineering Communications, 16(1-6), 79-90. doi: 10.1080/00986448208911087

Bourne, J. R. (1997). Mixing in Single-Phase Chemical Reactors. In A. W. Nienow, M. F. Edwards, & H. Harnby (Eds.), Mixing in the Process Industries. Oxford: Butterworth-Heinemann

Bourne, J. R., Kut, O. M., Lenzner, J., & Maire, H. (1990). Kinetics of the diazo coupling between 1-naphthol and diazotized sulfanilic acid. Industrial & Engineering Chemistry Research, 29(9), 1761-1765. doi: 10.1021/ie00105a004

Bourne, J. R., & Toor, H. L. (1977). Simple Criteria for Mixing Effects in Complex Reactions. AIChE Journal, 23(4), 602-604.

Bourne, J. R., & Yu, S. (1994). Investigation of micromixing in stirred tank reactors using parallel reactions. Industrial & Engineering Chemistry Research, 33(1), 41-55. doi: 10.1021/ie00025a007

Brodkey, R. S., & Lewalle, J. (1985). Reactor Selectivity Based on First-Order Closures of the Turbulent Concentration Equations. AIChE Journal, 31(1), 111-118.

Buchmann, M., & Mewes, D. (1998). Measurements of the Local Intensities of Segregation with the Tomographical Dual Wavelength Photometry. The Canadian Journal of Chemical Engineering, 76, 626-630.

Buchmann, M., & Mewes, D. (2000). Tomographic Measurements of Micro-and Macromixing Using the Dual Wavelenght Photometry. Chemical Engineering Science, 77, 3-9.

Byrde, O., & Sawley, M. L. (1999). Optimization of a Kenics Static Mixer for Non-Crreping Flow Conditions. Chemical Engineering Journal(72), 163-169.

Chella, R., & Ottino, J. M. (1984). Conversion and Selectivity Modifications due to Mixing in Unpremixed Reactors. Chemical Engineering Science, 39(3), 551-567.

Danckwerts, P. V. (1952). The Definition and Measurement of Some Characteristics of Mixtures. Applied Science Research, 3(Section A), 279-196.

Danckwerts, P. V. (1953). Continuous Flow Systems: Distribution of Residence Times. Chemical Engineering Science, 2(1), 1-13.

Danckwerts, P. V. (1958). The Effect of Incomplete Mixing on Homogeneous Reactions. Chemical Engineering Science, 8, 93-102.

deBruynKops, S. M., & Riley, J. J. (2001). Mixing Models for Large-Eddy Simulation of Nonpremixed Turbulent Combustion. Journal of Fluids Engineering, 123, 341-346.

Dutta, A., & Tarbell, J. M. (1989). Closure Models for Turbulent Reacting Flows. AIChE Journal, 35(12), 2013-2027.

El-Hamouz, A. M., & Mann, R. (1998). Effect of Micro-Mixing on the Yield of Intermediates in Triplet Consecutive/Competitive Reactions. The Canadian Journal of Chemical Engineering, 76, 650-656.

Fields, S. D., & Ottino, J. M. (1987). Effect of Striation Thickness Distribution on the Course on an Unpremixed Polymerization. Chemical Engineering Science, 42(3), 459-465.

Fonte, C. P. (2012). Mixing Studies with Impinging Jets PIV/PLIF Experiments and CFD Simulation. (PhD Thesis), FEUP - Faculdade de Engenharia da Universidade do Porto, Porto.

Fox, R. O. (1992). The Fokker-Planck Molecular Mixing Closure for PDF Modeling of Turbulent Flows. AIChE Symposium Series, 88(286), 83-87.

Fox, R. O. (1998). On the Relationship Between Lagrangian Micromixing Models and Computational Fluid Dynamics. Chemical Engineering and Processing, 37, 521-535.

Fox, R. O. G., M.R. (1993). Numerical Simulation of Turbulent Reacting Flows Using PDF Methods. AIChE Symposium Series, 89, 49-54.

Frouzakis, C. E., Tomboulides, A. G., Lee, J., & Boulouchos, K. (2002). From Diffusion to Premixed Flames in an H2/Air Opposed-Jet Burner: The Role of Edge Flames. Combustion and Flame, 130, 171-184.

Gerlinger, W., Schneider, K., Falk, L., & Bockhorn, H. (2000). Numerical Simulation of the Mixing of Passive and Reactive Scalars in Two-Dimensional Flows Dominated by Coherent Vortices. Chemical Engineering Science, 55, 4255-4269.

Ghosal, S., & Moin, P. (1995). The Basic Equations for the Large Eddy Simulation of Turbulent Flows in Complex Geometry. Journal of Computational Physics, 118(1), 24-37. doi: http://dx.doi.org/10.1006/jcph.1995.1077

Giona, M., Adrover, A., Muzzio, F. J., & Cerbelli, S. (2000). The Geometry of Mixing in 2-d Time-Periodic Chaotic Flows. Chemical Engineering Science, 55(2), 381-389. doi: 10.1016/S0009-2509(99)00333-4

Givi, P. (1989). Model-Free Simulations of Turbulent Reactive Flows. Progresse in Energy and Combustion Science, 15, 1-107.

Givi, P., & Mcmurtry, P. A. (1988). Nonpremixed Reaction in Homogeneous Turbulence: Direct Numerical Simulations. AIChE Journal, 34(6), 1039-1042.

Gomes, N. O. (2015). A new approach for RIM: from RIMCop technology to process design. (PhD Thesis), FEUP - Faculdade de Engenharia da Universidade do Porto, Porto.

Harris, R. F., Anderson, R. M., & Shannon, D. M. (1992). Speciality Polyurethane Soft Segments. II. Mixing Studies in Micro-RIM Using Polyether Diamine Oligomers Containing Backbone Urea Moieties. Journal of Applied Polymer Science, 46, 1547-1560.

Hobbs, D. M., & Muzzio, F. J. (1997). The Kenics Static Mixer: a three dimensional chaotic flow. Chemical Engineering Journal, 67, 153-166.

Howes, T., Mackley, M. R., & Roberts, E. P. L. (1991). The Simulation of Chaotic Mixing and Dispersion for Periodic Flows in Baffled Channels. Chemical Engineering Science, 46(7), 1669-1677.

Icardi, M., Gavi, E., Marchisio, D. L., Olsen, M. G., Fox, R. O., & Lakehal, D. (2011). Validation of LES predictions for turbulent flow in a Confined Impinging Jets Reactor. Applied Mathematical Modelling, 35(4), 1591-1602. doi: 10.1016/j.apm.2010.09.035

Johnson, D. A. (2000a). Experimental and Numerical Examination of Confined Laminar Opposed Jets. Part I Momentum Imbalance. International Communications in Heat and Mass Transfer, 27(4), 443-454.

Johnson, D. A. (2000d). Experimental and Numerical Examination of Confined Laminar Opposed Jets. Part II Momentum Balancing. International Communications in Heat and Mass Transfer, 27(4), 455-463.

Johnson, D. A., & Wood, P. (2000). Self-Sustained Oscillations in Opposed Impinging Jets in an Enclosure. Canadian Journal of Chemical Engineering, 78(5), 867-875.

Johnson, D. A., Wood, P., & Hrymak, A. N. (1996). The Effect of Geometrical Parameters on the Flow Field of an Opposed Jet RIM Mix Head: Equal Flow and Matched Fluids. Canadian Journal of Chemical Engineering, 74(1), 40-48.

Kling, K., & Mewes, D. (2004). Two-colour laser induced fluorescence for the quantification of micro- and macromixing in stirred vessels. Chemical Engineering Science, 59(7), 1523-1528.

Kolmogorov, A. (1991). The Local Structure of Turbulence in Incompressible Viscous Fluid for Very Large Reynolds Numbers. Proceedings of the Royal Society: Mathematical and Physical Sciences (1990-1995), 434(1890), 9-13.

Kolodziej, P. (1980). The Effect of Impingment Mixing on the Morphology of RIM Urethanes. (M.Sc. Dissertation), University of Minnesota.

Kolodziej, P., Macosko, C. W., & Ranz, W. E. (1982). The Influence of Impingement Mixing on Striation Thickness Distribution and Properties in Fast Polyurethane Polymerisation. Polymer Engineering and Science, 22(6), 388-392. doi: 10.1002/pen.760220611

Kolodziej, P., Yang, W. P., Macosko, C. W., & Wellinghoff, S. T. (1986). Impingement Mixing and its Effect on the Microstructure of RIM Polyurethanes. Journal of Polymer Science Part B: Polymer Physics, 25(10), 2359-2377. doi: 10.1002/polb.1986.090241017

Kosály, G. (1987). Non-Premixed Simple Reaction in Homogeneous Turbulence. AIChE Journal, 33(12), 1998-2002.

Kusch, H. A., & Ottino, J. M. (1992). Experiments on mixing in continuous chaotic flows. Journal of Fluid Mechanics, 236(1), 319-348.

Kusch, H. A., Ottino, J. M., & Shannon, D. M. (1989). Analysis of Impingement Mixing-Reaction Data: Use of a Lamellar Model to Generate Fluid Mixing Information. Industrial & Engineering Chemistry Research, 28, 302-315. doi: 10.1021/ie00087a009

Lamberto, D. J., Alvarez, M. M., & Muzzio, F. J. (2001). Computational Analysis of Regular and Chaotic Mixing in a Stirred Tank Reactor. Chemical Engineering Science, 56, 4887-4899.

Lee, B. S., Kang, I. S., & Lim, H. C. (1999). Chaotic mixing and mass transfer enhancement bypulsatile laminar flow in an axisymmetric wavy channel. International Journal of Heat and Mass Transfer, 42(14), 2571-2581.

Lee, D., & Chen, Y. T. (2011). Mixing in tangentially crossing microchannels. AIChE Journal, 57(3), 571-580. doi: 10.1002/aic.12299

Lee, J., Tripathi, A., & Chauhan, A. (2014). Taylor dispersion in oscillatory flow in rectangular channels. Chemical Engineering Science, 117, 183-197. doi: 10.1016/j.ces.2014.06.022

Lee, L. J., Ottino, J. M., Ranz, W. E., & Macosko, C. W. (1980). Impingement Mixing in Reaction Injection Molding. Polymer Engineering and Science, 20(13), 868-874. doi: 10.1002/pen.760201306

Lee, R. E., Finch, C. R., & Wooledge, J. D. (1957). Mixing of High Viscosity Newtonian and Non-Newtonian Fluids. Industrial and Engineering Chemistry, 49(11), 1849-1854.

Levenspiel, O. (1962). Chemical Reaction Engineering. New York: John Wiley & Sons.

Li, K. T., & Toor, H. L. (1986). Turbulent Reactive Mixing with a Series-Parallel Reaction: Effect of Mixing on Yield. AIChE Journal, 32(8), 1312-1320. doi: 10.1002/aic.690320809

Libby, P. A. (1996). Introduction to Turbulence. New York: Taylor & Francis.

Libby, P. A. W., F.A. (1994). Turbulent Reacting Flows. New York: Academic Press.

Mackley, M. R., & Saraiva, R. M. C. N. (1998). The Quantitative Description of Fluid Mixing Using Lagrangian - and concentration-based numerical approaches. Chemical Engineering Science, 54(2), 159-170.

Magde, D., Wong, R., & Seybold, P. G. (2002). Fluorescence quantum yields and their relation to lifetimes of rhodamine 6G and fluorescein in nine solvents: improved absolute standards for quantum yields. Photochem Photobiol, 75(4), 327-334.

Mahajan, A. J., & Kirwan, D. J. (1996). Micromixing Effects in a Two-Impinging-Jets Precipitator. AIChE Journal, 42(7), 1801-1814.

Malguarnera, S. C., & Suh, N. P. (1977). Liquid Injection Molding I. An Investigation of Impingement Mixing. Polymer Engineering and Science, 17(2), 111-115. doi: 10.1002/pen.760170209

Malguarnera, S. C., & Suh, N. P. (1977). Liquid injection molding II. Mechanical design and characterization of a RIM machine. Polymer Engineering and Science, 17(2), 116-121. doi: 10.1002/pen.760170210

Mickaily-Huber, E. S., Bertrand, F., Tanguy, P., Meyer, T., Renken, A., Rys, F. S., & Wehrli, M. (1996). Numerical Simulations of Mixing in an SMRX Static Mixer. The Chemical Engineering Journal, 63(2), 117-126.

Muzzio, F. J., & Liu, M. (1996). Chemical Reactions in Chaotic Flows. The Chemical Engineering Journal, 64, 117-127.

Nguyen, L. T., & Suh, N. P. (1985). Effect of High Reynolds Number on the Degree of Mixing in RIM Processing. Polymer Process Engineering, 3(1&2), 37-56.

Ottino, J. M., Ranz, W. E., & Macosko, C. W. (1979). A Lamellar Model for Analysis of Liquid-Liquid Mixing. Chemical Engineering Science, 34(6), 877-890. doi: 10.1016/0009-2509(79)85145-3

Pope, S. B. (1985). PDF Methods for Turbulent Reactive Flows. Progresse in Energy and Combustion Science, 11, 119-192.

Pope, S. B. (1994). Lagrangian PDF Methods for Turbulent Flows. Annual Reviews of Fluid Mechanics, 26, 23-63.

Pope, S. B. (2000). Turbulent Flows. Cambridge: Cambridge University Press.

Ranz, W. E. (1979). Applications of a Stretch Model to Mixing Diffusion, and Reaction in Laminar and Turbulent Flows. AIChE Journal, 25(1), 41-47. doi: 10.1002/aic.690250105

Roberts, E. P. L., & Mackley, M. R. (1995). The Simulation of Stretch Rates for the Quantitative Prediction and Mapping of Mixing Within a Channel flow. Chemical Engineering Science, 50(23), 3727-3746.

Sandell, D. J., Macosko, C. W., & Ranz, W. E. (1985). Visualization Technique for Studying Impingement Mixing at Representative Reynolds Numbers. Polymer Process Engineering, 3(1 & 2), 57-70.

Santos, R., Teixeira, A., Costa, M., & Lopes, J. (2002). Operational and design study of RIM machines. International Polymer Processing, 17(4), 387-394.

Santos, R. J. (2003). Mixing Mechanims in Reaction Injection Moulding - RIM. An LDS/PIV Experimental Study and CFD Simulation. (PhD Thesis), FEUP - Faculdade de Engenharia da Universidade do Porto, Porto.

Santos, R. J., Erkoc, E., Dias, M. A., Teixeira, A. M., & Lopes, J. C. B. (2008). Hydrodynamics of the mixing chamber in RIM: PIV flow-field characterization. AIChE Journal, 54(5), 1153-1163. doi: 10.1002/aic.11472

Santos, R. J., Teixeira, A. M., Costa, M. R. P. F. N., & Lopes, J. C. B. (2002). Operational and design study of RIM machines. International Polymer Processing, 17(4), 387-394.

Santos, R. J., Teixeira, A. M., Erkoc, E., Sultan, M., Karpinska, A. M., Dias, M. M., & Lopes, J. C. B. (2010). Validation of a 2D CFD Model for Hydrodynamics' Studies in CIJ Mixers. International Journal of Chemical Reactor Engineering, 8.

Santos, R. J., Teixeira, A. M., & Lopes, J. C. B. (2005). Study of mixing and chemical reaction in RIM. Chemical Engineering Science, 60(8-9), 2381-2398. doi: Doi 10.1016/J.Ces.2004.11.050

Santos, R. J. N. d. (2003). Mixing mechanisms in reaction injection moulding - RIM An LDA/PIV experimental study and CFD simulation. Porto: FEUP.

Sebastian, D. H., & Boukobbal, S. (1986). Mixhead Parameters Governing Impingement Mixing Effectiveness for Polyurethane Reactive Injection Molding Processes. Polymer Process Engineering, 4(1), 53-70.

Speziale, C. G. (1991). Analytical Methods for the Development of Reynolds-Stress Closures in Turbulence. Annual Reviews of Fluid Mechanics, 23, 107-157.

Teixeira, A. M. (2000). Escoamento na cabeça de mistura de uma máquina de RIM Caracterização experimental por LDA e simulação dinâmica por CFD. (PhD Thesis), FEUP - Faculdade de Engenharia da Universidade do Porto, Porto.

Teixeira, A. M., Santos, R. J., Costa, M. R. P. F. N., & Lopes, J. C. B. (2005). Hydrodynamics of the mixing head in RIM: LDA flow-field characterization. AIChE Journal, 51(6), 1608-1619. doi: 10.1002/aic.10454

Tennekes, H., & Lumley, J. L. (1997). A First Course in Turbulence. Cambridge: MIT Press.

Toor, H. L. (1969). Turbulent mixing of two species with and without chemical reactions. Industrial & Engineering Chemistry Fundamentals, 8(4), 655-659.

Tosun, G. (1987). A Study of Micromixing in Tee Mixers. Industrial & Engineering Chemistry Research, 26, 1184-1193.

Tropea, C., Yarin, A. L., & Foss, J. F. (2007). Springer Handbook of Experimental Fluid Mechanics Springer.

Tsai, K., & Fox, R. O. (1994). PDF Simulation of a Turbulent Series-Parallel Reaction in an Axismmetric Reactor. Chemical Engineering Science, 49(24B), 5141-5158.

Tucker, C. L., & Suh, N. P. (1980). Mixing for reaction injection molding. I. Impingement mixing of fiber suspensions. Polymer Engineering and Science, 20(13), 887-898. doi: 10.1002/pen.760201308

Tucker, C. L., & Suh, N. P. (1980). Mixing for Reaction Injection Molding. I. Impingement Mixing of Liquids. Polymer Engineering and Science, 20(13), 875-886. doi: 10.1002/pen.760201307

Unger, D. R., & Muzzio, F. J. (1999). Laser-induced Fluorescence Technique for the Quantification of Mixing in Impinging Jets. AIChE Journal, 45(12), 2477-2486. doi: 10.1002/aic.690451203

Unger, D. R., Muzzio, F. J., & Brodkey, R. S. (1998). Experimental and Numerical Characterization of Viscous Flow and Mixing in an Impinging Jet Contactor. The Canadian Journal of Chemical Engineering, 76, 546-555.

Vassilatos, G., & Toor, H. L. (1965). Second-Order Chemical Reactions in a Nonhomogeneous Turbulent Fluid. AIChE Journal, 11(4), 666-673. doi: 10.1002/aic.690110419

Villermaux, J., & David, R. (1983). RECENT ADVANCES IN THE UNDERSTANDING OF MICROMIXING PHENOMENA IN STIRRED REACTORS. Chemical Engineering Communications, 21(1-3), 105-122. doi: 10.1080/00986448308940280

Villermaux, J., Falk, L., Fournier, M.-C., & Detrez, C. (1992). Use of Parallel Competing Reactions to Characterize Miromixing Efficiency. Paper presented at the AIChE Symposium Series.

Wang, D. M., & Tarbell, J. M. (1993). Closure Models for Turbulent Reacting Flows with a Nonhomogeneous Concentration Field. Chemical Engineering Science, 48(23), 3907-3920.

Wehrmeyer, J. A., Cheng, Z., Mosbacher, D. M., Pitz, R. W., & Osborne, R. (2002). Opposed Jet Flames of Lean or Rich Premixed Propane-Air Reactants versus Hot Products. Combustion and Flame, 128, 232-241.

Weinstein, H., & Adler, R. J. (1967). Micromixing Effects in Continuous Chemical Reactors. 22, 65-75.

Wood, P., Hrymak, A. N., Yeo, R., Johnson, D. A., & Tyagi, A. (1991). Experimental and Computational Studies of the Fluid Mechanics in an Opposed Jet Mixing Head. Physics of Fluids A, 3(5), 1362-1368.

Zalc, J. M., & Muzzio, F. J. (1999). Parallel-Competitive Reactions in a Two-Dimensional Chaotic Flow. Chemical Engineering Science, 54, 1053-1069.

Zhao, Y., & Brodkey, R. S. (1998a). Averaged and Time-resolved Full-field (three-dimensional), Measurements of Unsteady Opposed Jets. The Canadian Journal of Chemical Engineering, 76, 536-545.

Zhao, Y., & Brodkey, R. S. (1998d). Particle Paths in Three-dimensional Flow Fields as a Means of Study: Opposing Jet Mixing System. Powder Technology, 100(2-3), 161-165. doi: 10.1016/S0032-5910(98)00136-3

Zwietering, N. (1959). The Degree of Mixing in Continuous Flow Systems. Chemical Engineering Science, 11(1), 1-15.

A Mathematical discretization techniques

The present appendix present the mathematical techniques used in the special and temporal discretization to evaluate the dependent and independent variables. Also the gradient discretization is presented. The intent of this chapter is provide to the reader background of the mathematical discretization implementation used in the CFD program.

A.1 Space discretization

A.1.1 MUSCL scheme

The MUSCL scheme uses the local cell averages values of the quantities in transport at time t to evaluate the value of such quantities in cell edges at $t + \Delta t/2$ and afterward to predict values at $t + \Delta t$. This process is done in four steps

I. Calculating the slopes: Local cell averages, for the desired quantity, can be represented as

$$W(x,t) = W_i + \frac{x - x_i}{\Delta x}\delta W_i \tag{A.1}$$

Where $x_{i-\frac{1}{2}} < x < x_{i-\frac{1}{2}}$, $x_i \equiv (x_{i+\frac{1}{2}} + x_{i-\frac{1}{2}})/2$, $\Delta x \equiv x_{i+\frac{1}{2}} + x_{i-\frac{1}{2}}$ and δW_i are the reconstructed slope calculated as

$$\delta W_i = ave\ (W_i - W_{i-1}, W_{i+1} - W_i) \tag{A.2}$$

Where ave is the desired averaging function, where $ave(a,b) = (a+b)/2$ lead to the central differences scheme and $ave(a,b) = 0$ leads to the zero slope

II. Predict solution ate half step: Using the sloples previously calculated the solution will be progressed half time-step $\Delta t/2$, where the predict values in the cell can be calculated as

$$\tilde{V}_j = V_j - \frac{\Delta t}{2\Delta x} A_p(V_j)\delta V_j \tag{A.3}$$

III. Predict values at cell edges: Using the predict solution, the values at cell edges will be calculated assuming a linear solution

$$W^+_{i-\frac{1}{2}} = \widetilde{W}_i - \ \delta W_i/2 \tag{A.4}$$

$$W^-_{i+\frac{1}{2}} = \widetilde{W}_i + \ \delta W_i/2 \tag{A.5}$$

IV. Calculate values at cell edges: Used Reimann solver to update desired variables at time t

$$V_i^{n+1} = V_i^n - \frac{\Delta t}{\Delta x}\left(F_{i+\frac{1}{2}} - F_{i-\frac{1}{2}}\right) \tag{A.6}$$

Where $F_{i\pm 1/2}$ correspond the numerical fluxes calculated form values predicted in III

$$F_{i-\frac{1}{2}} \equiv F(W^-_{i+\frac{1}{2}}, W^+_{i-\frac{1}{2}}) \tag{A.7}$$

A.1.2 Coupled scheme

Coupled scheme is an full implicit algorithm which solved the momentum equation and the pressure-based continuity equation in simultaneous. This process uses the implicit discretization of the pressure gradients using the momentum equation and an implicit discretization for the mass flux. The momentum equation is in the form

$$apu = \sum_{nb} a_{nb} u_{nb} + \sum_f p_f A \cdot \hat{\imath} + S \tag{A.8}$$

Where the pressure values at the faces is interpolated using the momentum equation

$$p_f = \frac{\frac{P_{c_0}}{a_{p,c_0}} + \frac{P_1}{a_{p,c_1}}}{\frac{1}{a_{p,c_0}} + \frac{1}{a_{p,c_1}}} \tag{A.9}$$

Resulting in a smooth variation of the pressure. This equation is also known as standard pressure scheme. From the momentum equation the pressure gradient for component k is calculated as

$$\sum_f p_f A_k = \sum_f a^{u_k} p_j \tag{A.10}$$

Where $a^{u_k} p_j$ is the coefficient provided from the Gauss divergence theorem and the coefficient of the pressure interpolation scheme. The momentum equation for a given cell i and for a component u_k is defined as

$$\sum_j a_{ij}^{u_k u_l} u_{kj} + \sum_j a_{ij}^{u_k} p_j = b_i^{u_k} \tag{A.11}$$

The value of the velocity in a cell face isn't linear average but instead a weighted method is used based on the coefficients of the momentum equation, therefore the flux over a face cell can be calculated as

$$\begin{aligned} J_f &= \rho_f \frac{a_{p,c_0} v_{n,c_0} + a_{p,c_1} v_{n,1}}{a_{p,c_0} + a_{p,c_1}} + d_f \left(\left(p_{c_0} + (\Delta p)_{c_0} \cdot \overrightarrow{r_0} \right) - \left(p_{c_1} + (\Delta p)_{c_1} \cdot \overrightarrow{r_1} \right) \right) \hat{J}_f \\ &+ d_f \left(p_{c_0} - p_{c_1} \right) \end{aligned} \tag{A.12}$$

Where p_{c_0}, p_{c_1} the pressure at two cells on the same side of the face and v_{n,c_0}, v_{n,c_1} are the normal velocity ate the same location. $\hat{J}_f$ is the influence of the velocity in this cells. d_f is function of average momentum equation coefficients. Substituting the flux formulation in the momentum equation results in

$$\sum_k \sum_j a_{ij}{}^{p u_k} u_{kj} + \sum_j a_{ij}^{pp} \, p_j = b_i^p \tag{A.13}$$

This equation is then transform into a matricial form in order to be calculated

$$\sum_j [A]_{ij}\bar{X}_j = \bar{B}_i \tag{A.14}$$

Where each matrix have the following form

$$A_{ij} = \begin{bmatrix} a_{ij}^{pp} & a_{ij}^{pu} & a_{ij}^{pv} & a_{ij}^{pw} \\ a_{ij}^{up} & a_{ij}^{uu} & a_{ij}^{uv} & a_{ij}^{uw} \\ a_{ij}^{vp} & a_{ij}^{vu} & a_{ij}^{vv} & a_{ij}^{vw} \\ a_{ij}^{wp} & a_{ij}^{wu} & a_{ij}^{wv} & a_{ij}^{ww} \end{bmatrix} \tag{A.15}$$

$$\bar{X}_j = \begin{bmatrix} p_i{}' \\ u_i{}' \\ v_i{}' \\ w_i{}' \end{bmatrix} \tag{A.16}$$

$$\bar{X}_j = \begin{bmatrix} -r_i^p \\ -r_i^u \\ -r_i^u \\ -r_i^w \end{bmatrix} \tag{A.17}$$

A.1.3 SIMPLE-C scheme

The SIMPLE-C algorithm is an adaptation of the SIMPLE scheme for velocity-pressure coupling. This method, introduced by Pantankar(), initially start to predict the velocity components and the pressure (u, v, w, p). After the guess is performed momentum equations is used to calculate the velocity component's (u^*, v^*, w^*) based on the momentum equation which afterwards is used to calculate the pressure p'.

$$a_e u'_e = \sum_{nb} a_{nb}\, u'_{nb} + \Delta y\left(p'_p - p'_e\right) \tag{A.18}$$

$$a_e v'_e = \sum_{nb} a_{nb}\, v'_{nb} + \Delta x\left(p'_s - p'_p\right) \tag{A.19}$$

$$a_e w'_e = \sum_{nb} a_{nb}\, w'_{nb} + \Delta x\left(p'_w - p'_p\right) \tag{A.20}$$

Where e, s, w, p correspond to the east, south, direction perpendicular to e,s plane and the position of the point respectively. Approximation of the velocity correction are made ignoring the first term of the momentum equation $\sum_{nb} a_{nb}\, u'_{nb}$, $\sum_{nb} a_{nb}\, v'_{nb}$, $\sum_{nb} a_{nb}\, w'_{nb}$. The

correct velocities are substituting the continuity equation yielding a discrete pressure correction equation

$$a_p p'_p = \sum_{nb} a_{nb}\, p_{nb} + b \tag{A.21}$$

After is obtain the corrected velocity and pressure p', u', v', w', the variables are updated using:

$$u = u^* + \alpha_p u' \quad v = v^* + \alpha_p v' \quad w = w^* + \alpha_p w' \quad p = p^* + \alpha_p p' \tag{A.22}$$

Where α_p is the under relaxation factor being necessary since the nonlinear nature of the equations. Whit all the variables corrected the face flux cell is then calculated using

$$J_f = J_f^* + d_f\left(p'_{c_0} - p'_{c_1}\right) \tag{A.23}$$

Where the coefficient d_f is defined as

$$d_f = \overline{\left(a_p - \sum_{nb} a_{nb}\right)} \tag{A.24}$$

A.2 Time discretization

Finite-difference method are a numerical method used to solve a differential equation based on the approximation into a finite space/time. Initial a function $\varphi = f(x)$ is pointed approximated using Taylor series expansion into a polynomial form in the space discretization

$$f(x,t) = f(a)|_{t=1} + \frac{f'(a)}{1!}(x-a)\Big|_{t=i} + \frac{f^{(2)}(a)}{2!}(x-a)^2\Big|_{t=i} + \cdots + \frac{f^{(n)}(a)}{n!}(x-a)^n\Big|_{t=i} \tag{A.25}$$

Where n is the order of the interpolation and a the point where the function is discretize. Solving $f(x,t)$, time dependent, can be done using three methodologies, full implicit, full explicit and Crank-Nicolson scheme (central differences).

$$\frac{x^{t+1} - x^t}{\Delta t} = k\,.\, f(x^{t+1}) + (1-k)\,.f(x^t) \tag{A.26}$$

Where $k = 0$ for full explicit scheme, $k = 1$ for full implicit scheme and $k = 0.5$ for central difference scheme. The function $f(x,t)$ will be then integrated over a discrete domain

$$\int_{t}^{t+\Delta t} f(x)dt = \left[k.f_x^{t+\Delta t} + (1-k).f_x^t\right]\Delta t \tag{A.27}$$

Explicit scheme the function is evaluated at the current time $(t+1)$ provided by previous values t and added the current increment value $\Delta t\, f(x^t)$, resulting in

$$x^{t+1} = x^t + \Delta t\, f(x^t) \tag{A.28}$$

This method is fast since only is necessary to add value, but conditionally stable, since the time step marching is limited by the Courant–Friedrichs–Lewy condition. Implicit scheme evaluate the current time x^{t+1} based on the previous values x^t and adding values correspondent to the current time values $\Delta t\, f(x^{t+1})$,. This methodology implies solving a linear system of equations resulting in a computational effort to invert the constant's matrix. Although this factor this method is unconditionally stable for any increment of time

$$x^{t+1} = x^t + \Delta t\, f(x^{t+1}) \tag{A.29}$$

This formulation is referred for a first order implicit, but can be extender for higher orders

$$f(x^t) = \sum_{K=0}^{r} \binom{t}{k} (-1)^{t-k} f(x+k) \tag{A.30}$$

Where $\binom{t}{k}$ is the binomial coefficient wheke the row of pascal triangle provide the coefficient for k.

A.3 Gradient discretization

A.3.1 Least Squares cell-Based Gradient evaluation

This method assume a linear variation of a propriety ϕ between a cell c_0 and adjacent cells C_i with the distance between the adjacent cell's center δr_i. The cell centroid evaluation can be expressed as

$$(\Delta\phi)_{c_0} \cdot \Delta r_i = \left(\phi_{c_i} - \phi_{c_0}\right) \tag{A.31}$$

Where the vectorial distance between the two center cells can be calculated as

$$\cdot\, \Delta r_i = \Delta x_i\, \mathbf{i} + \Delta y_i\, \mathbf{j} + \Delta z_i\, \mathbf{k} \tag{A.32}$$

Where the change of proprieties between the two center cells can be estimated as

$$\Delta x_i \left.\frac{\partial \phi}{\partial x}\right|_0 + \Delta y_i \left.\frac{\partial \phi}{\partial y}\right|_0 + \Delta z_i \left.\frac{\partial \phi}{\partial z}\right|_0 = \phi_i - \phi_0 \tag{A.33}$$

Which can be transform into an algebraic system of equations

$$\mathbf{M}\,\mathbf{d} = \Delta\phi \tag{A.34}$$

Being each one variable transform into matricial form

$$\Delta\phi = \begin{bmatrix} \phi_1 - \phi_0 \\ \phi_2 - \phi_0 \\ \vdots \\ \phi_i - \phi_0 \end{bmatrix} \qquad \boldsymbol{d} = \begin{bmatrix} \left.\frac{\partial \phi}{\partial x}\right|_0 \\ \left.\frac{\partial \phi}{\partial y}\right|_0 \\ \left.\frac{\partial \phi}{\partial z}\right|_0 \end{bmatrix} \qquad \mathbf{M} = \begin{bmatrix} \Delta x_1 & \Delta y_1 & \Delta z_1 \\ \Delta x_3 & \Delta y_3 & \Delta z_3 \\ \vdots & \vdots & \vdots \\ \Delta x_i & \Delta y_3 & \Delta z_3 \end{bmatrix} \tag{A.35}$$

Since the system is over-determinated, a weighted method, based on the Gram-Schmidt is used, where the decomposition of the matrix's yields a weight matrix for each cell, and therefore three individual weights, for each vector in the Cartesian reference frame will be calculated in order to produce values at each face of the cell C_0 ,

$$(\phi_x)_{c_0} = \sum_{i=1}^{n} W^x i_0 \cdot \left(\phi_{c_i} - \phi_{c_0}\right) \tag{A.36}$$

$$\left(\phi_y\right)_{c_0} = \sum_{i=1}^{n} W^y i_0 \cdot \left(\phi_{c_i} - \phi_{c_0}\right) \tag{A.37}$$

$$(\phi_z)_{c_0} = \sum_{i=1}^{n} W^z i_0 \cdot \left(\phi_{c_i} - \phi_{c_0}\right) \tag{A.38}$$

B Spatial Evolution of the flow along the relevant time domain in the probe points

B.1 Reynolds 150

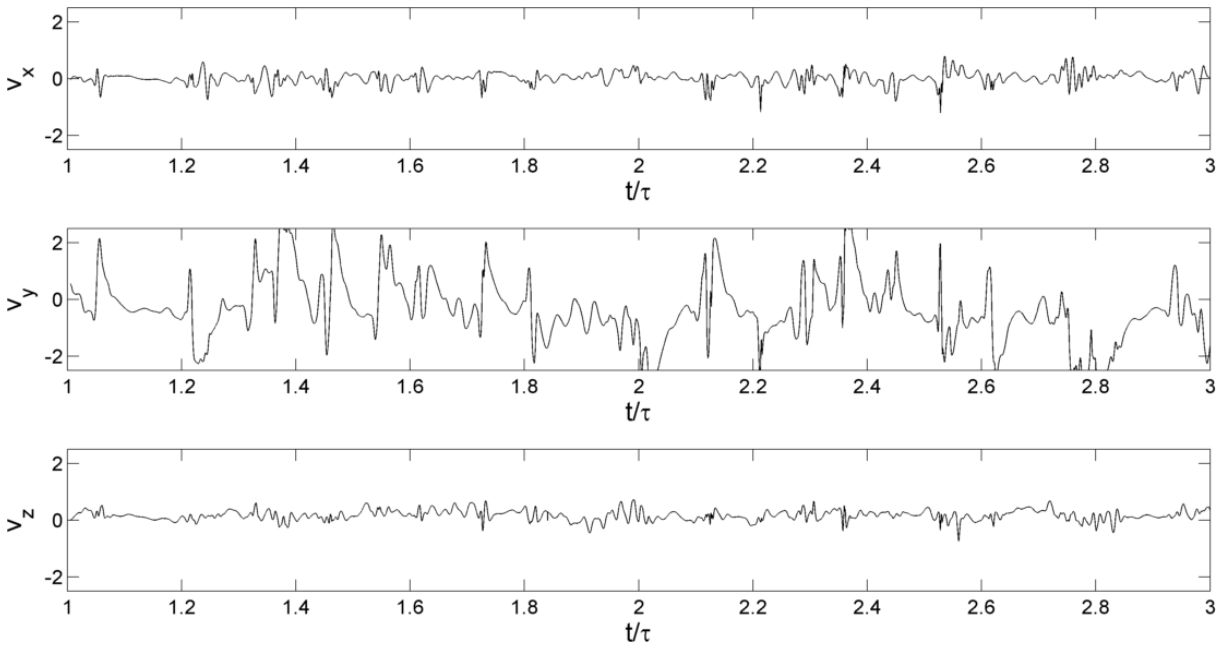

Figure B.1 – Temporal evolution for v_x, v_y and v_z at Reynolds 150 in p_0

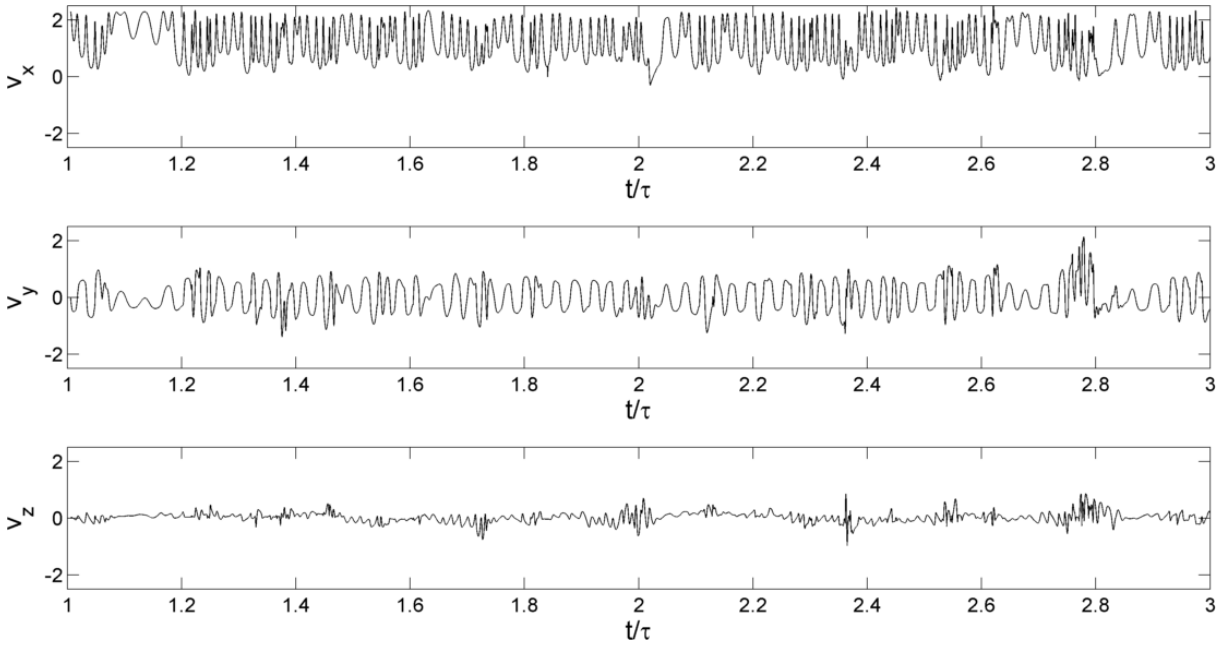

Figure B.2 – Temporal evolution for v_x, v_y and v_z at Reynolds 150 in p_1

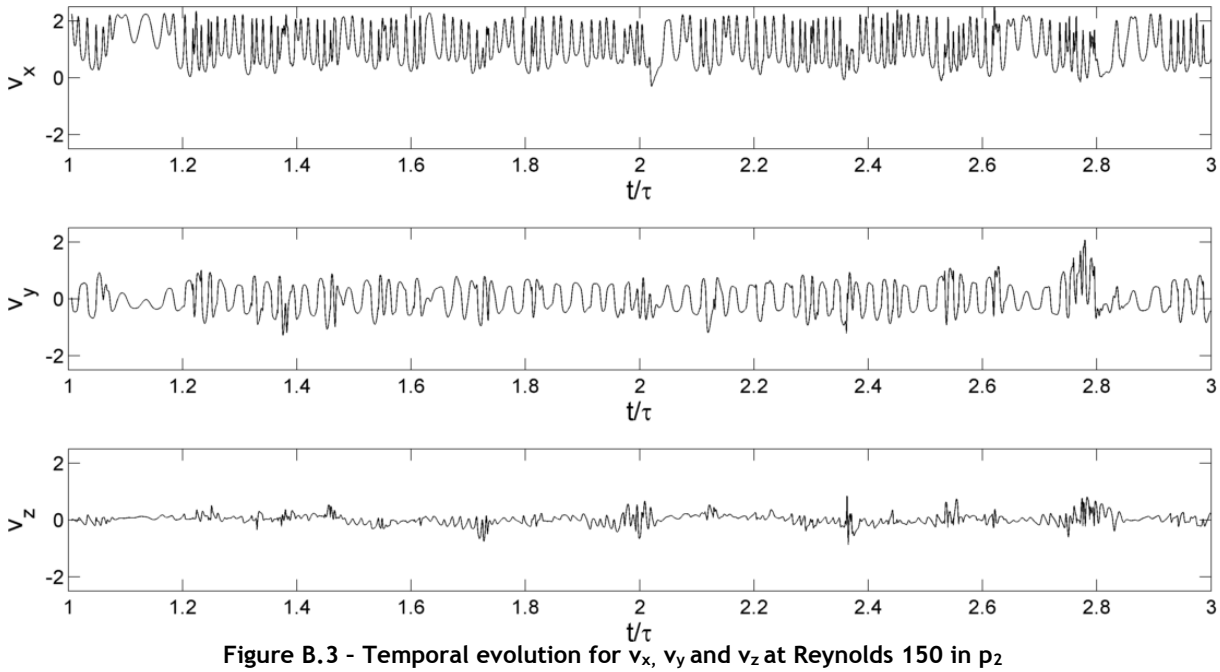

Figure B.3 – Temporal evolution for v_x, v_y and v_z at Reynolds 150 in p_2

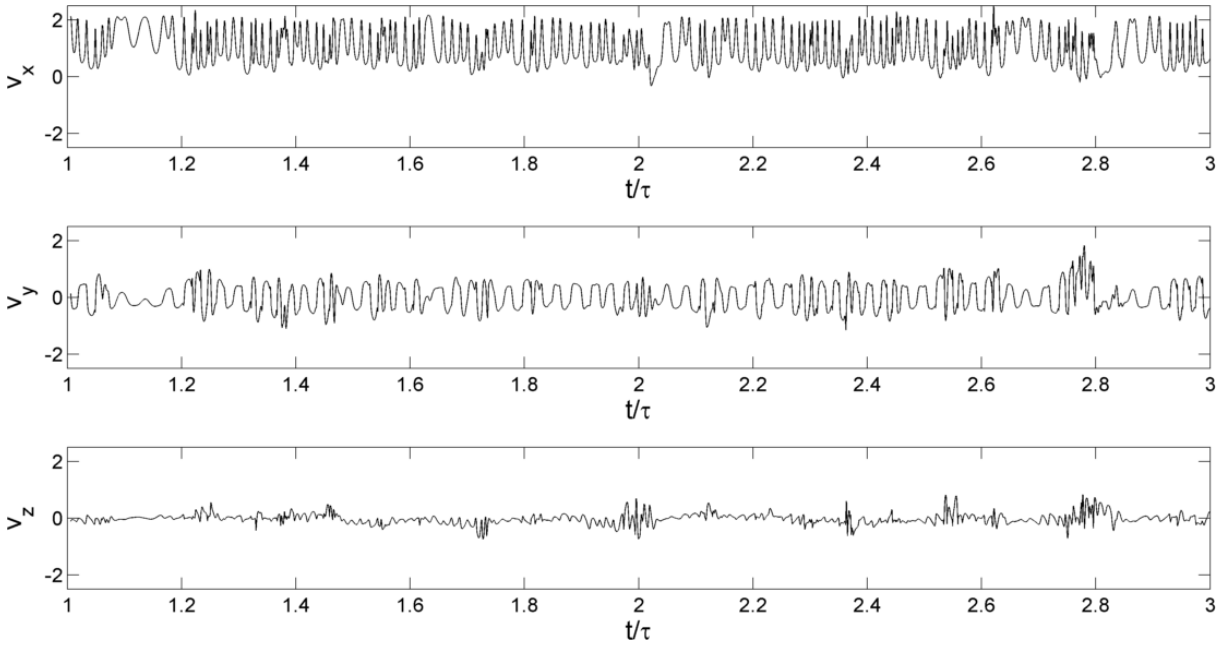

Figure B.4 – Temporal evolution for v_x, v_y and v_z at Reynolds 150 in p_3

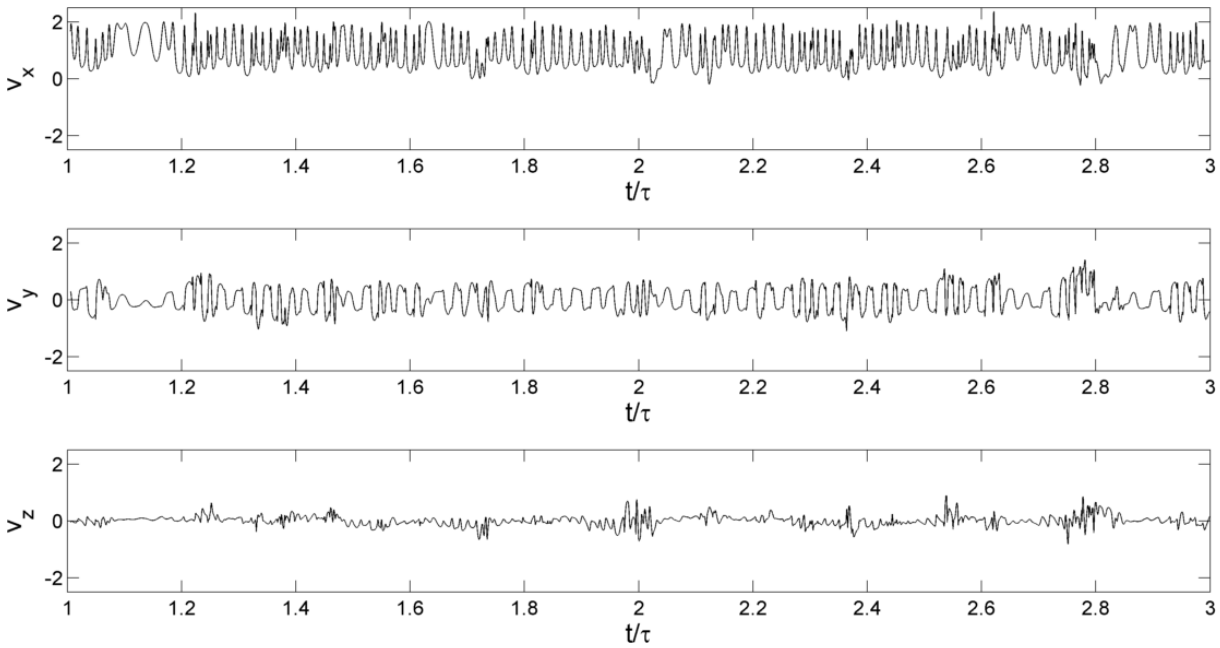

Figure B.5 – Temporal evolution for v_x, v_y and v_z at Reynolds 150 in p_4

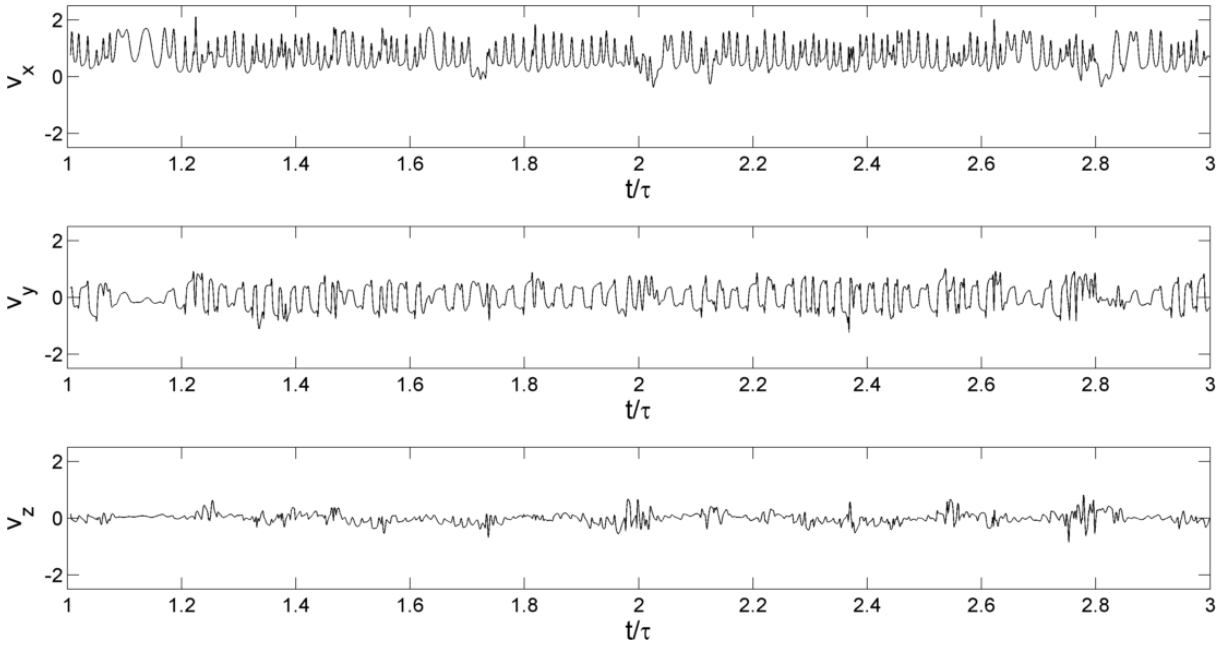

Figure B.6 – Temporal evolution for v_x, v_y and v_z at Reynolds 150 in p_5

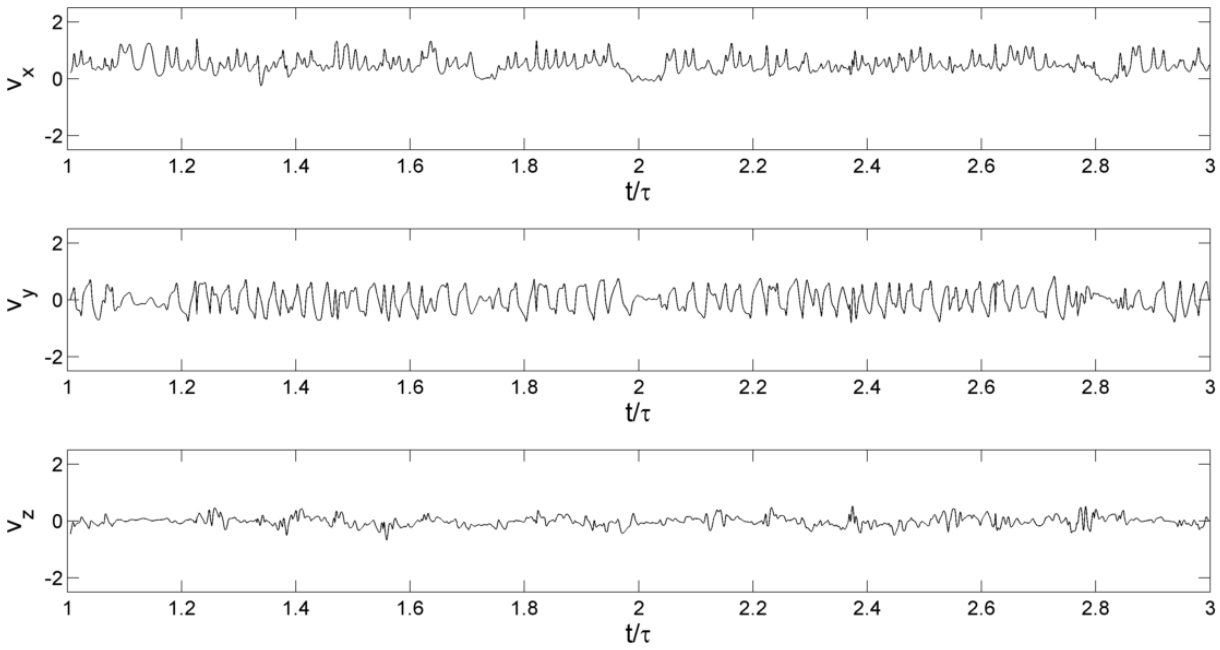

Figure B.7 – Temporal evolution for v_x, v_y and v_z at Reynolds 150 in p_6

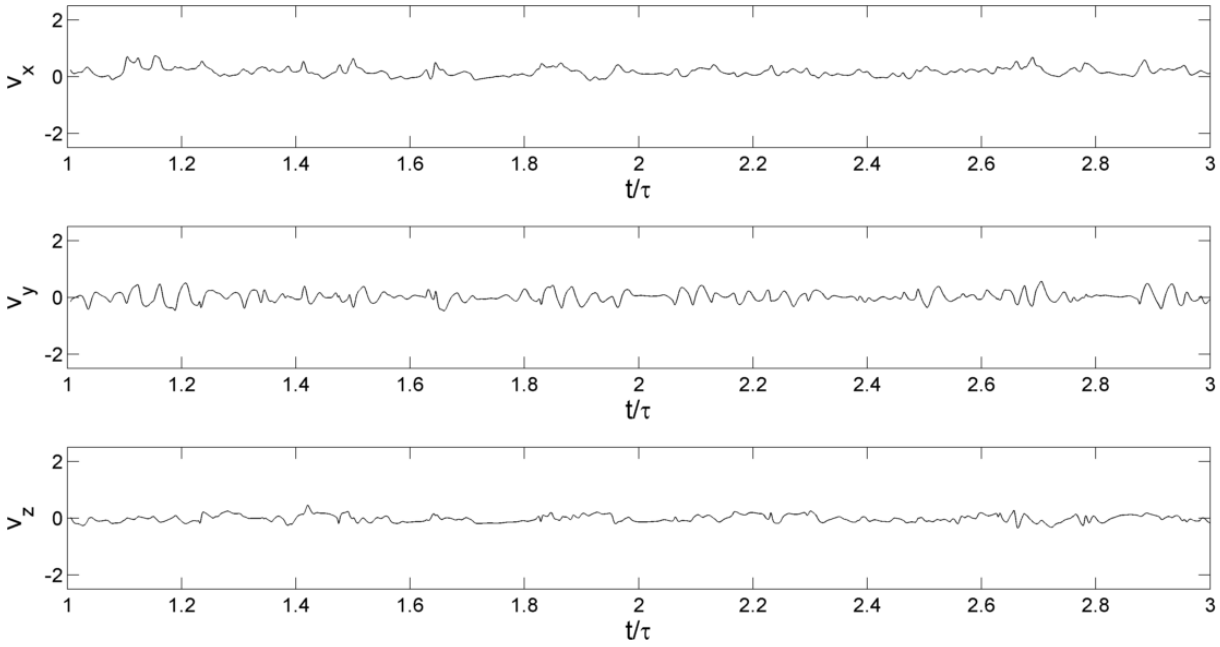

Figure B.8 – Temporal evolution for v_x, v_y and v_z at Reynolds 150 in p_7

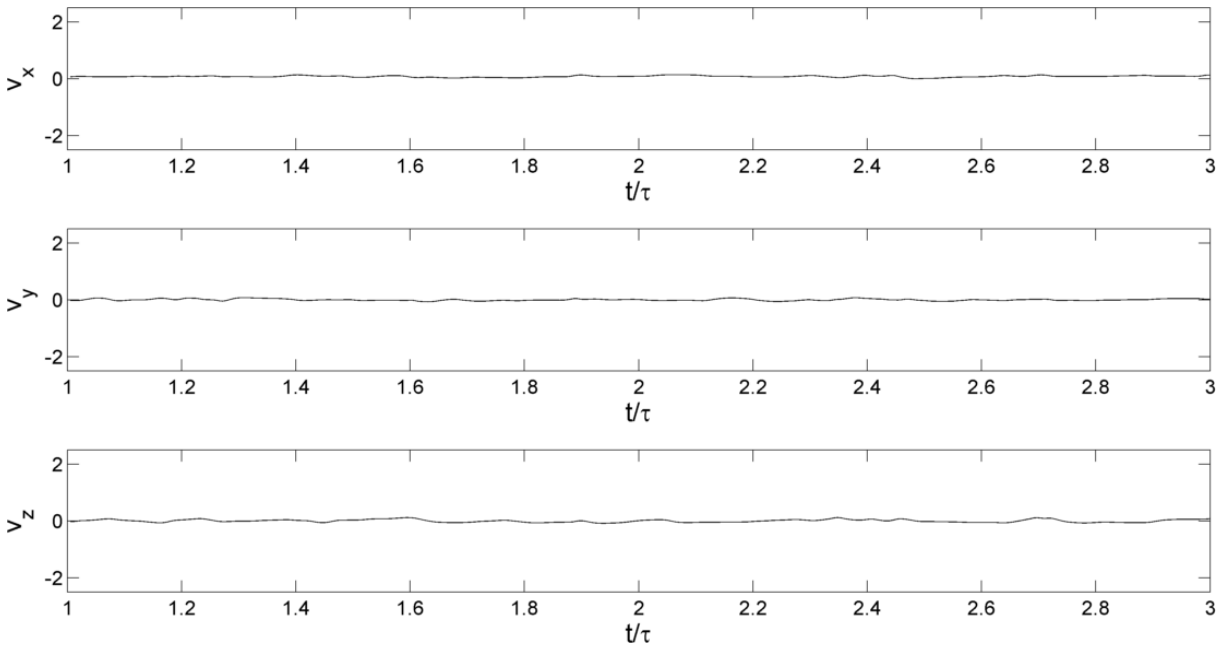

Figure B.9 – Temporal evolution for v_x, v_y and v_z at Reynolds 150 in p_8

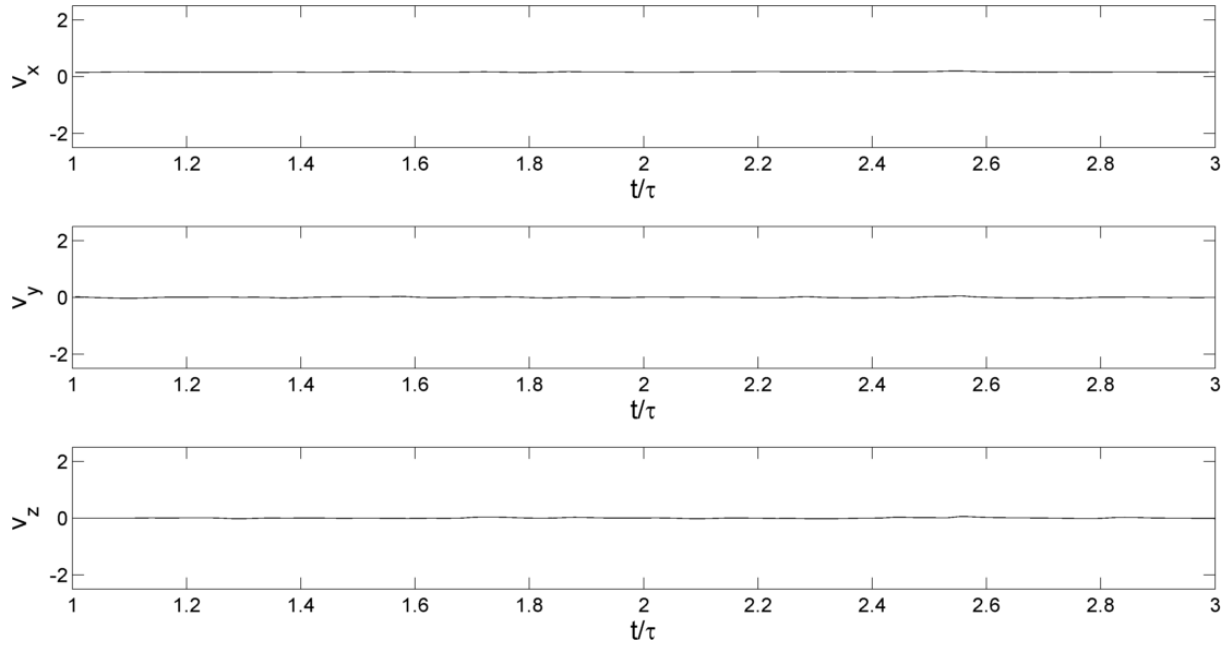

Figure B.10 – Temporal evolution for v_x, v_y and v_z at Reynolds 150 in p_9

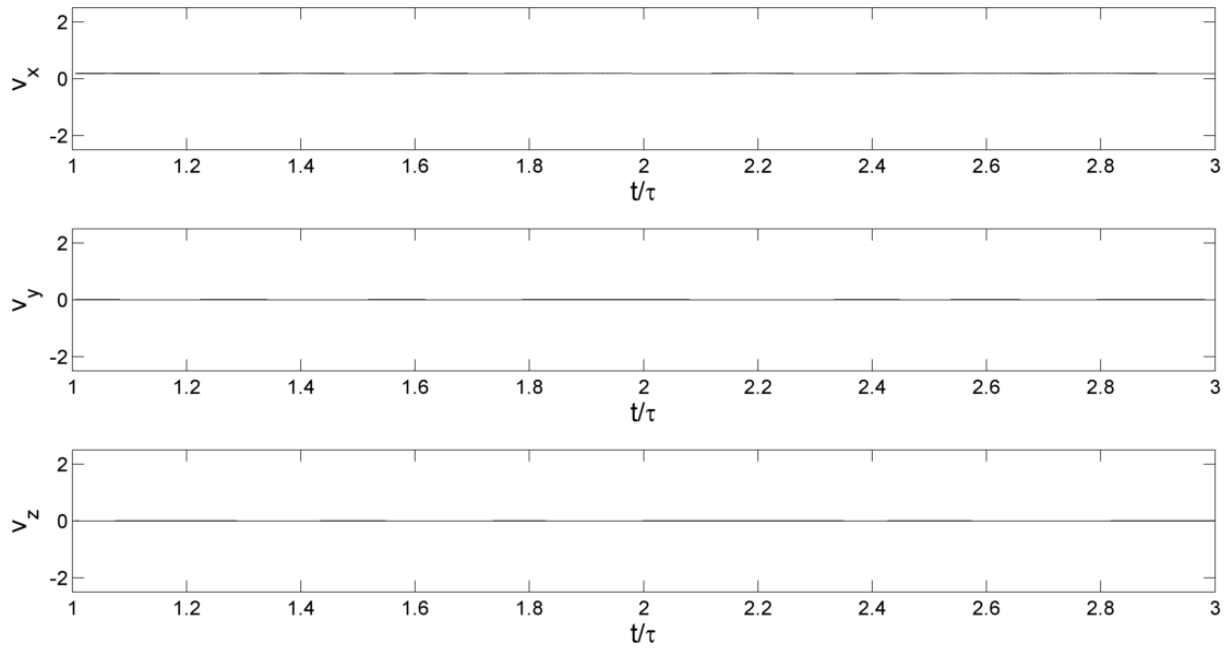

Figure B.11 – Temporal evolution for v_x, v_y and v_z at Reynolds 150 in p_{10}

B.2 Reynolds 200

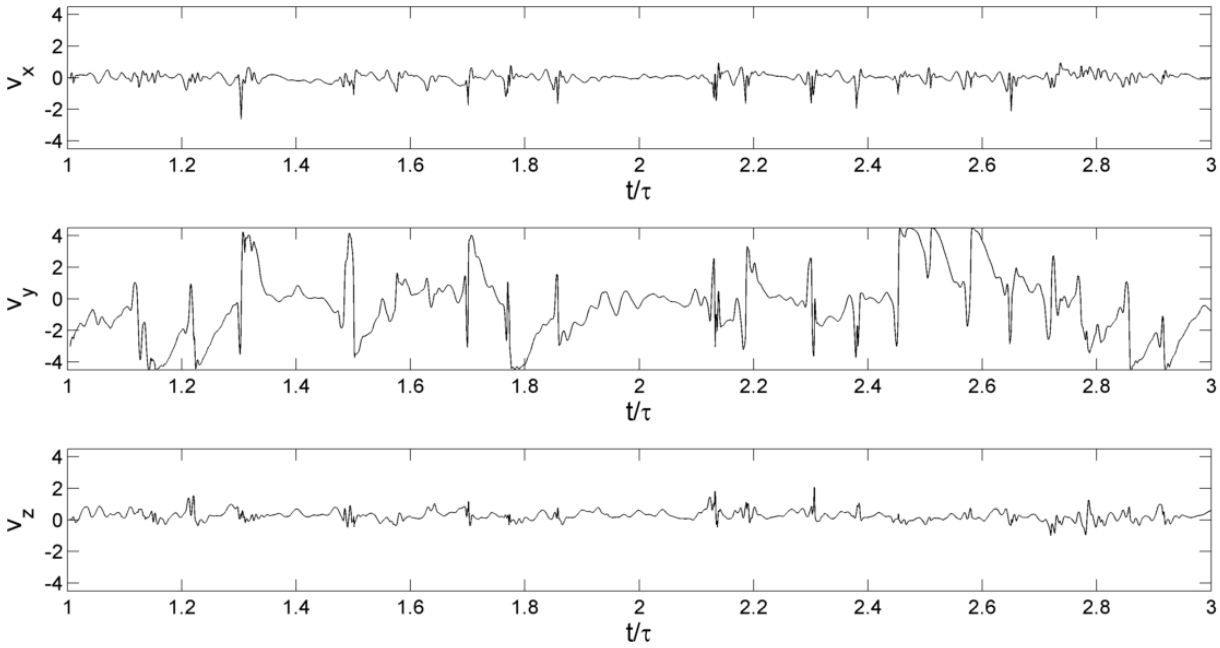

Figure B.12 – Temporal evolution for v_x, v_y and v_z at Reynolds 200 in p_0

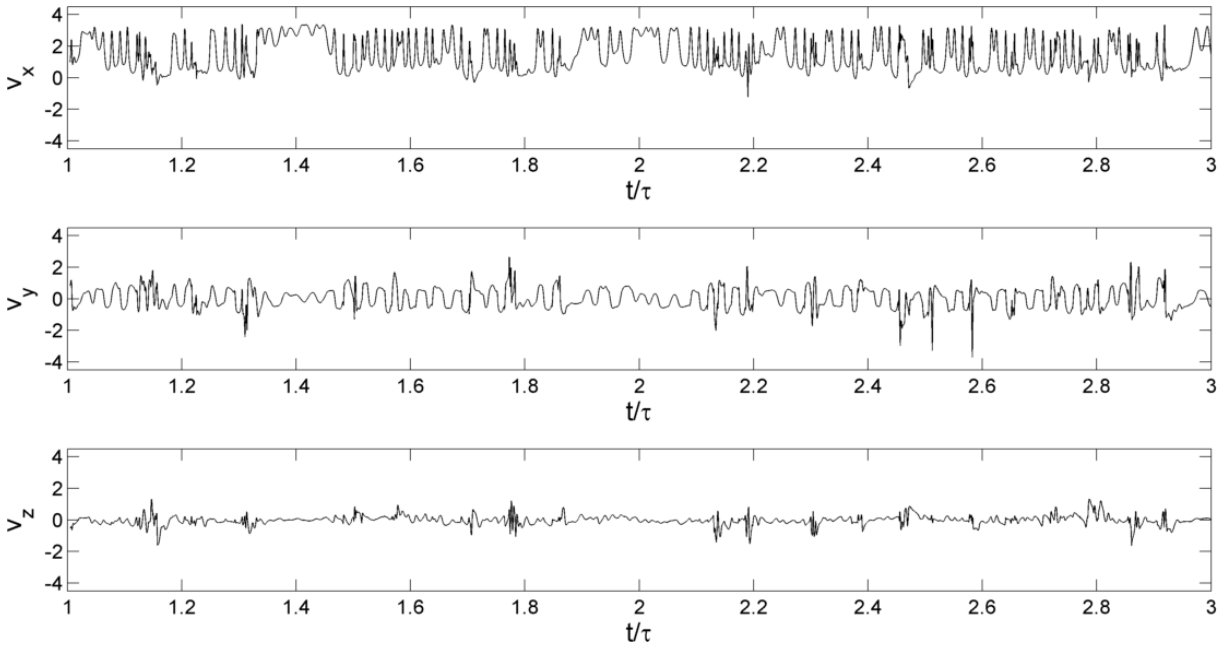

Figure B.13 – Temporal evolution for v_x, v_y and v_z at Reynolds 200 in p_1

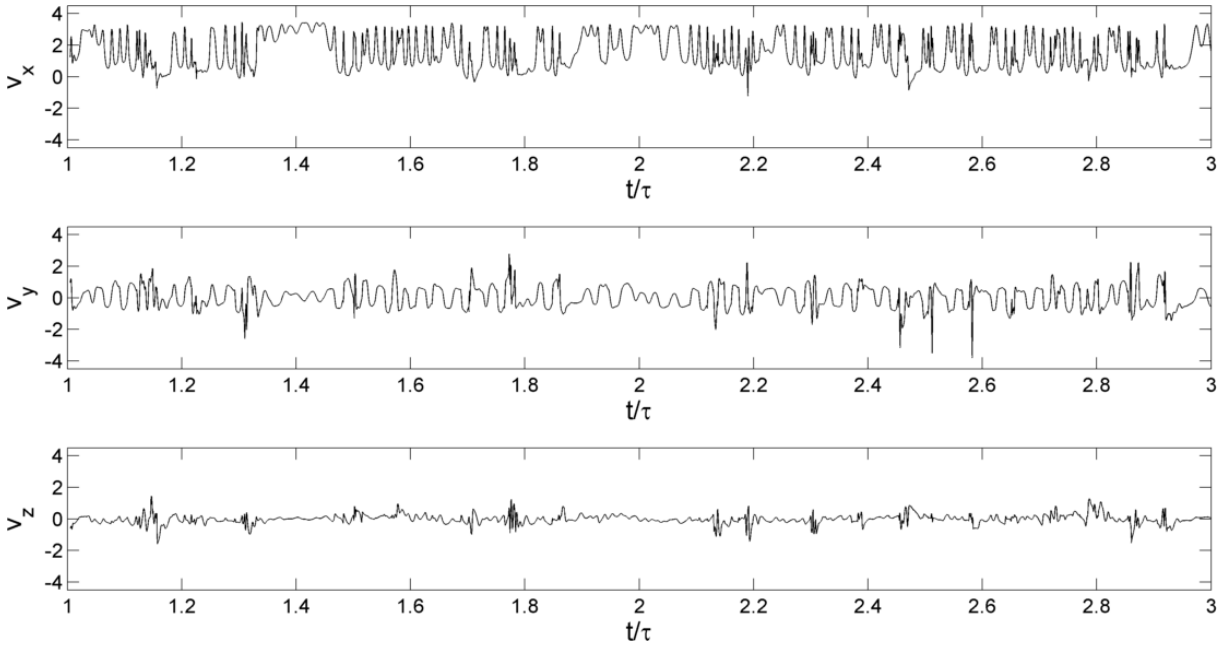

Figure B.14 – Temporal evolution for v_x, v_y and v_z at Reynolds 200 in p_2

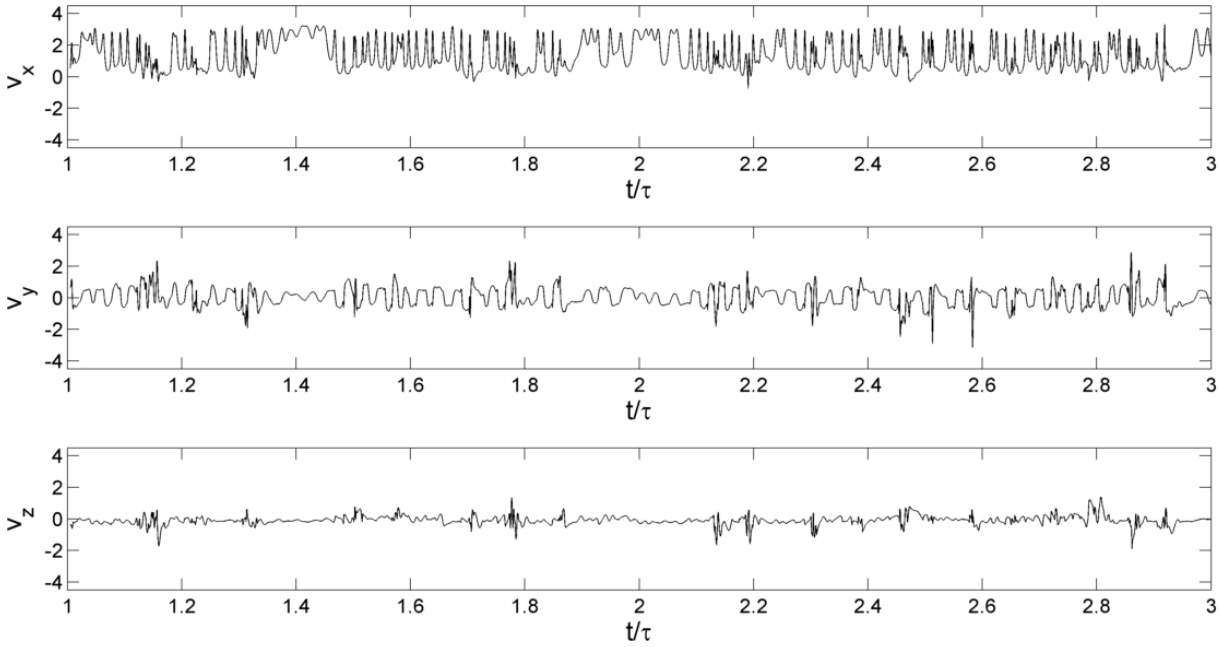

Figure B.15 – Temporal evolution for v_x, v_y and v_z at Reynolds 200 in p_3

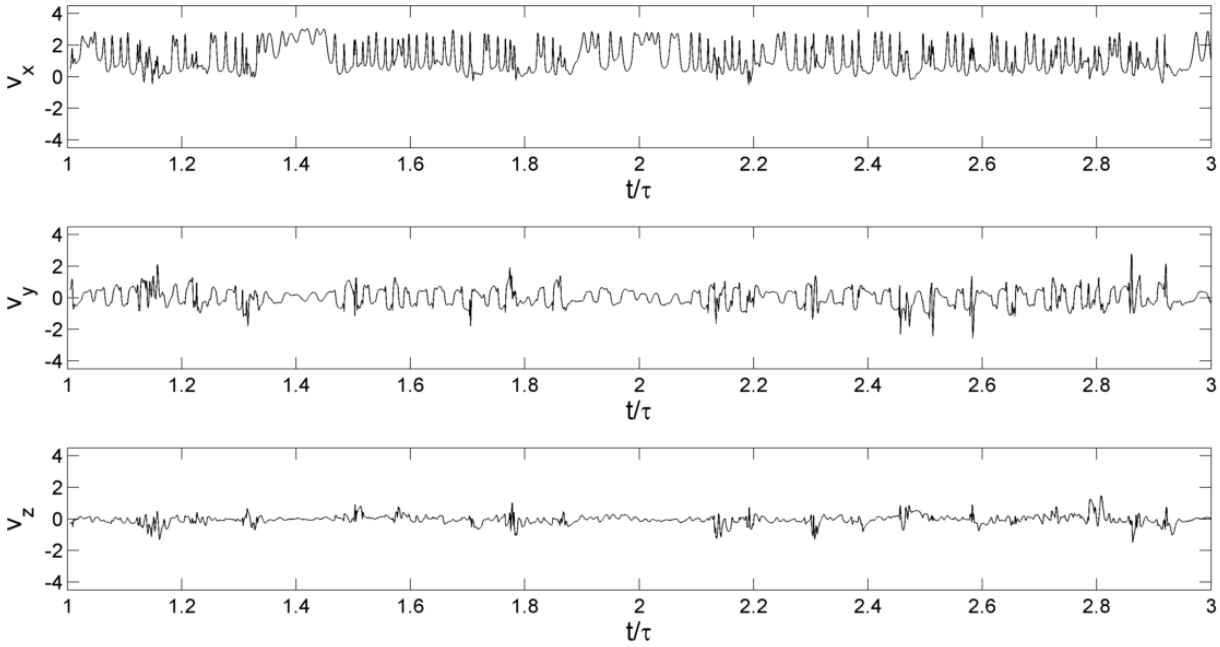

Figure B.16 – Temporal evolution for v_x, v_y and v_z at Reynolds 200 in p_4

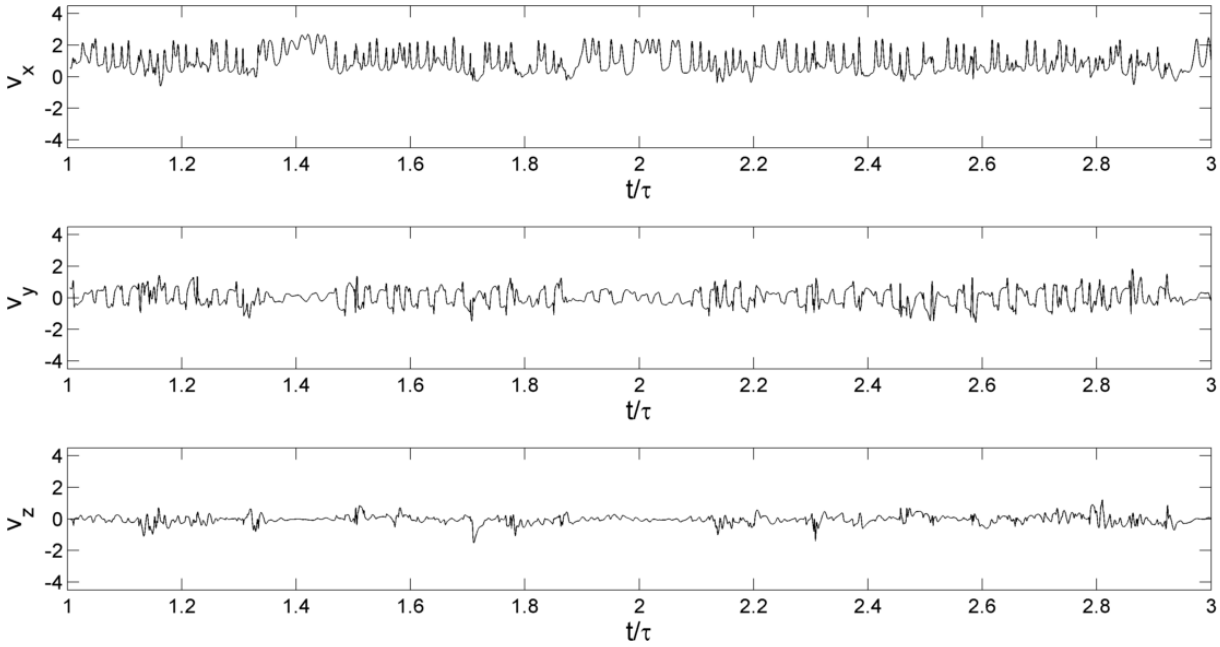

Figure B.17 – Temporal evolution for v_x, v_y and v_z at Reynolds 200 in p_5

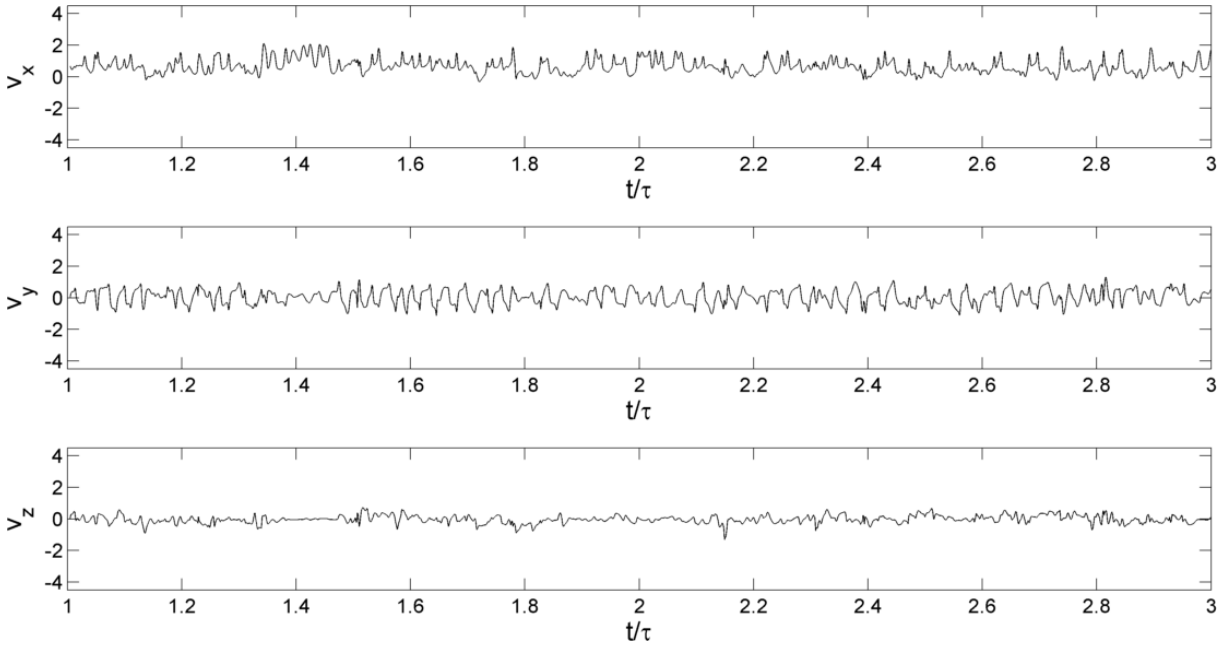

Figure B.18 – Temporal evolution for v_x, v_y and v_z at Reynolds 200 in p_6

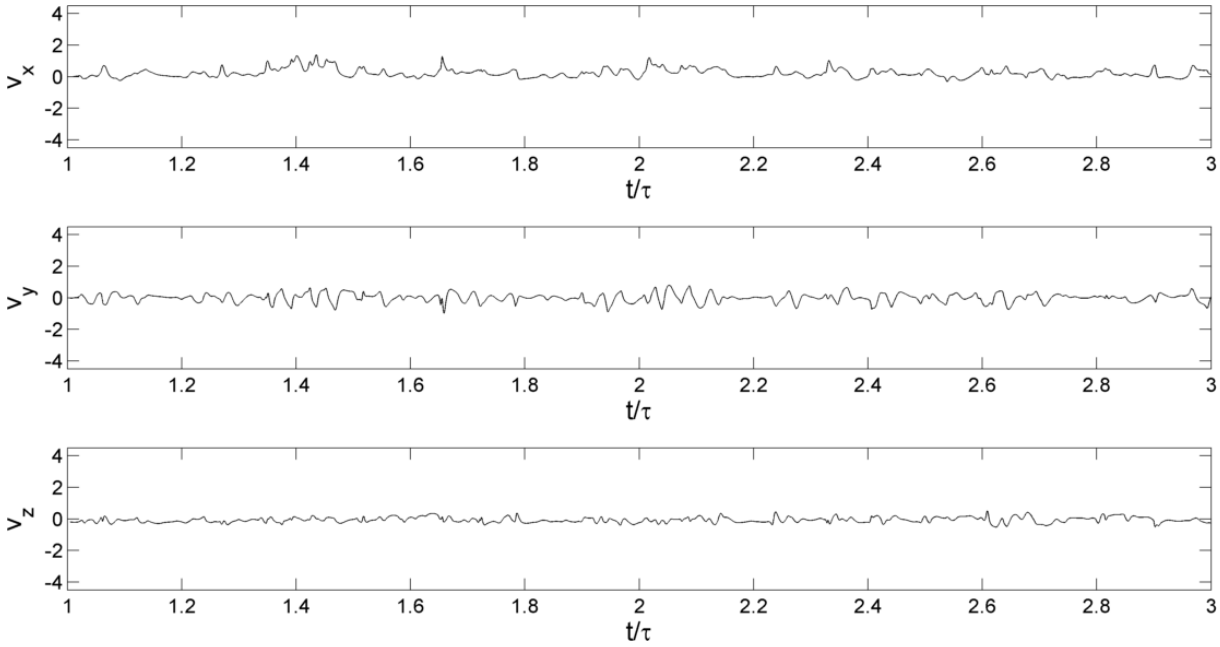

Figure B.19 – Temporal evolution for v_x, v_y and v_z at Reynolds 200 in p_7

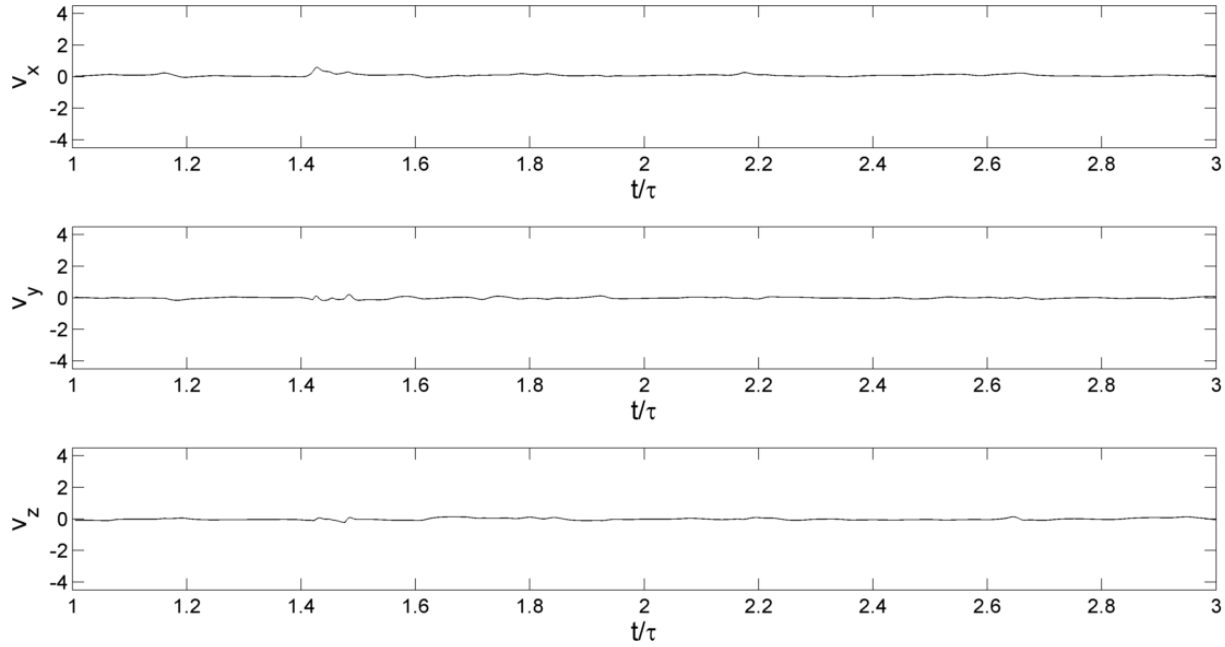

Figure B.20 – Temporal evolution for v_x, v_y and v_z at Reynolds 200 in p_8

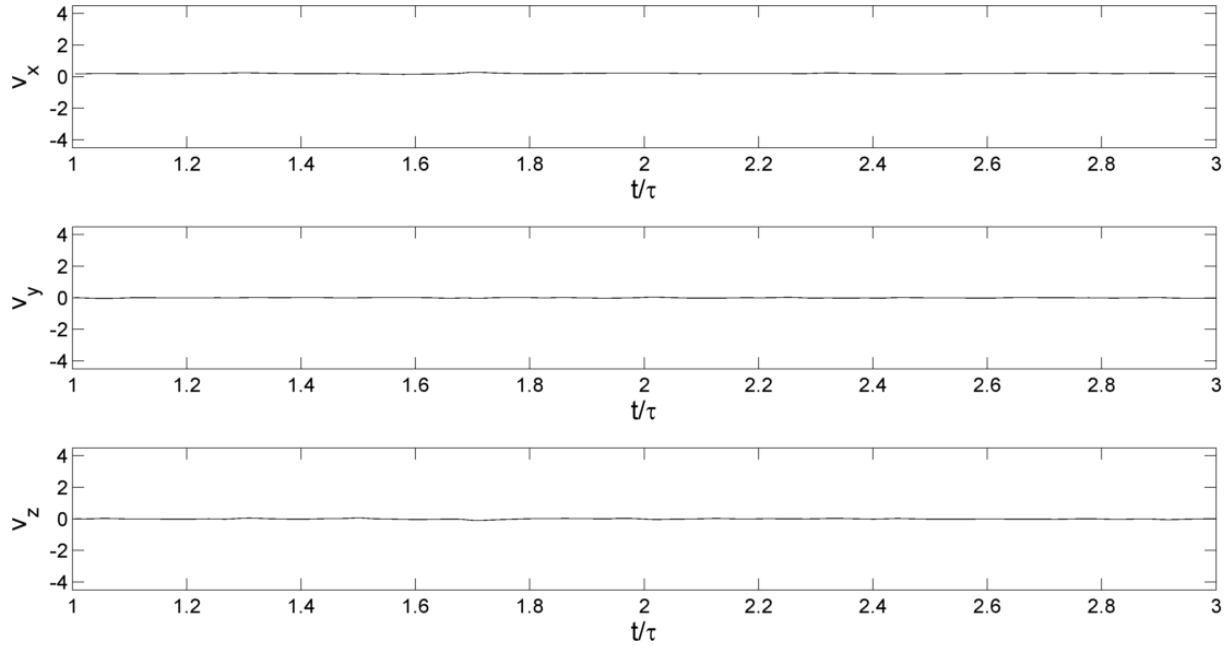

Figure B.21 – Temporal evolution for v_x, v_y and v_z at Reynolds 200 in p_9

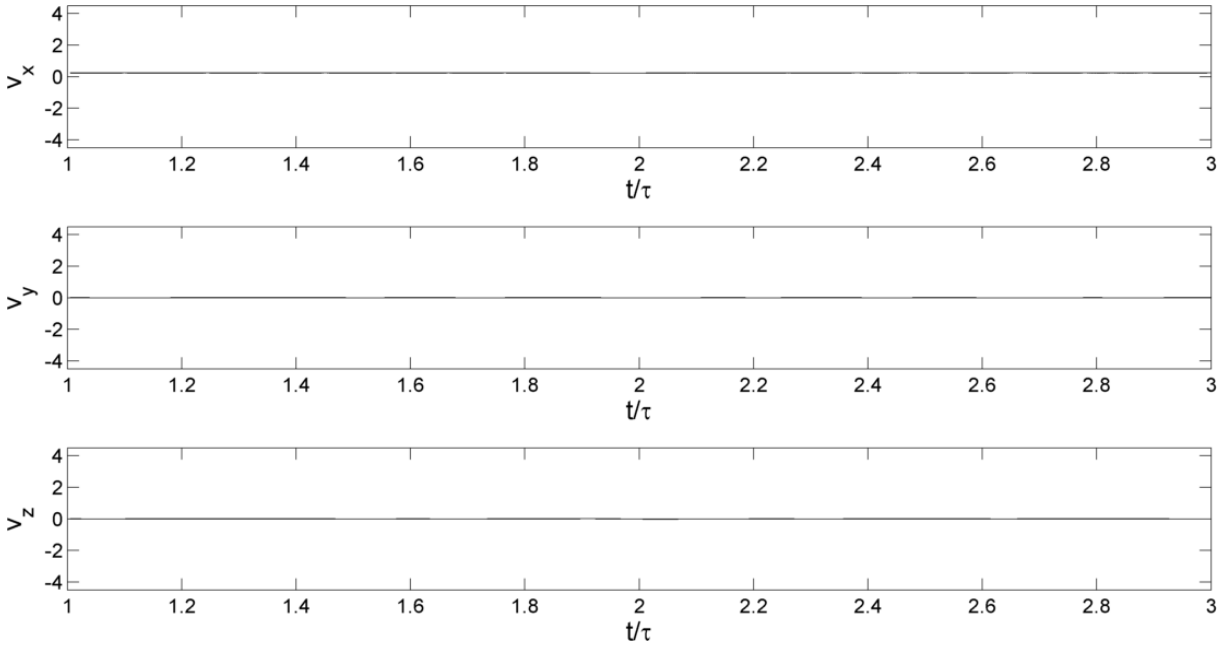

Figure B.22 – Temporal evolution for v_x, v_y and v_z at Reynolds 200 in p_{10}

B.3 Reynolds 250

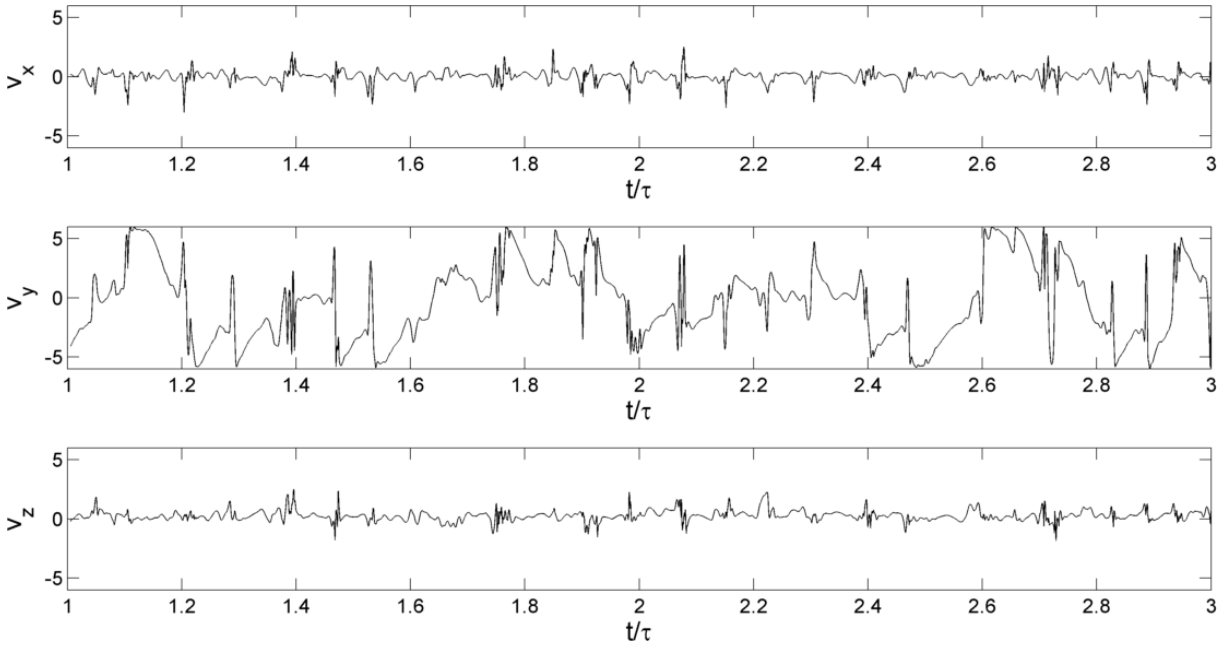

Figure B.23 – Temporal evolution for v_x, v_y and v_z at Reynolds 250 in p_0

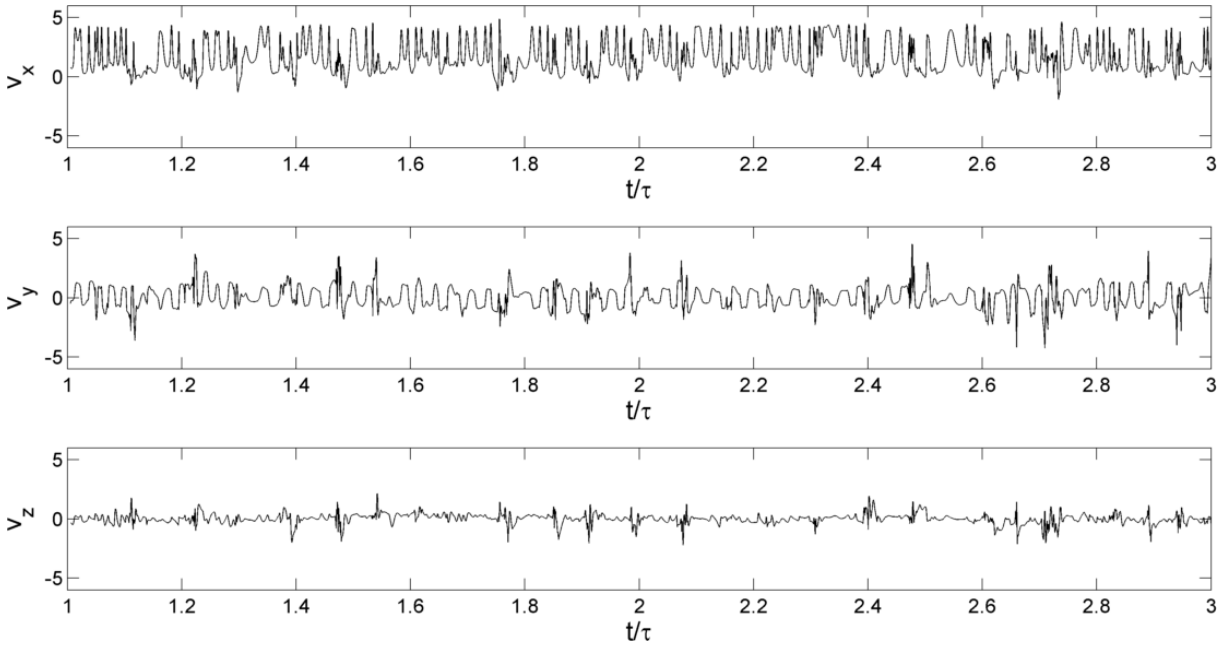

Figure B.24 – Temporal evolution for v_x, v_y and v_z at Reynolds 250 in p_1

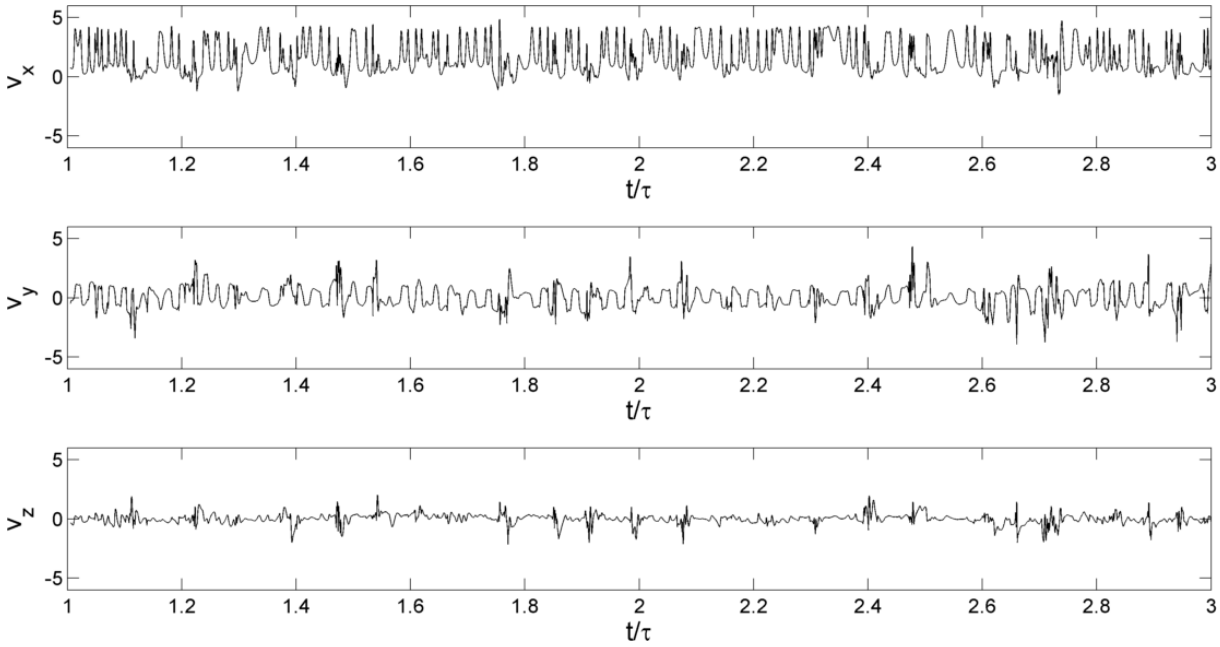

Figure B.25 – Temporal evolution for v_x, v_y and v_z at Reynolds 250 in p_2

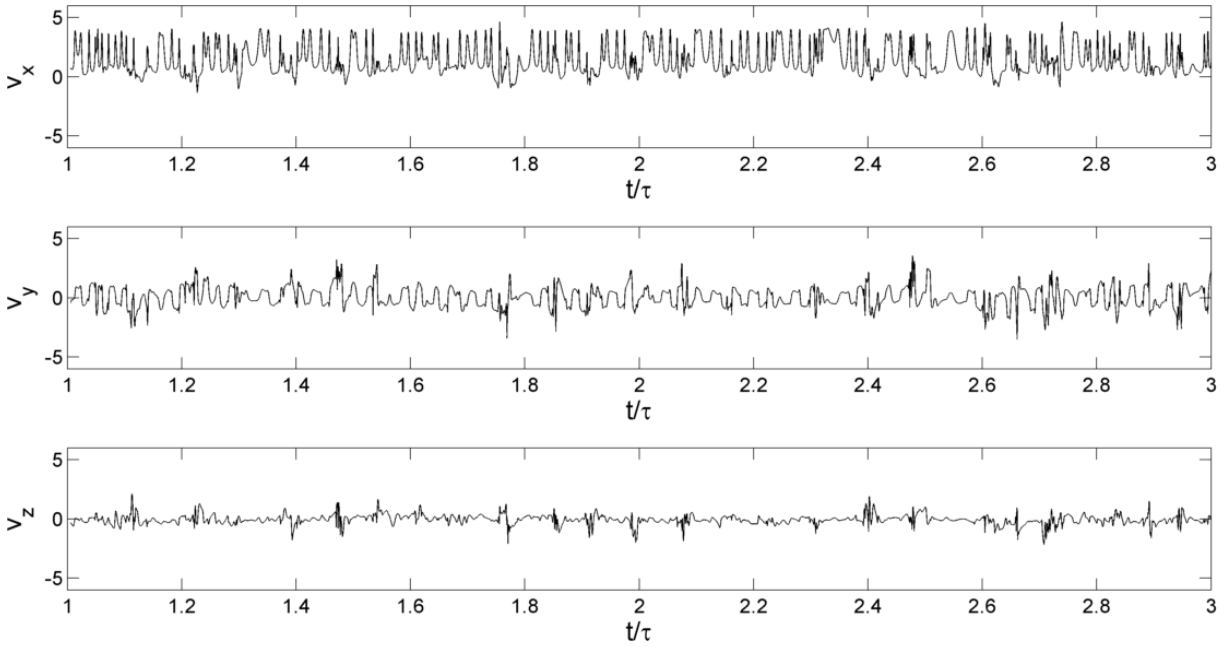

Figure B.26 – Temporal evolution for v_x, v_y and v_z at Reynolds 250 in p_3

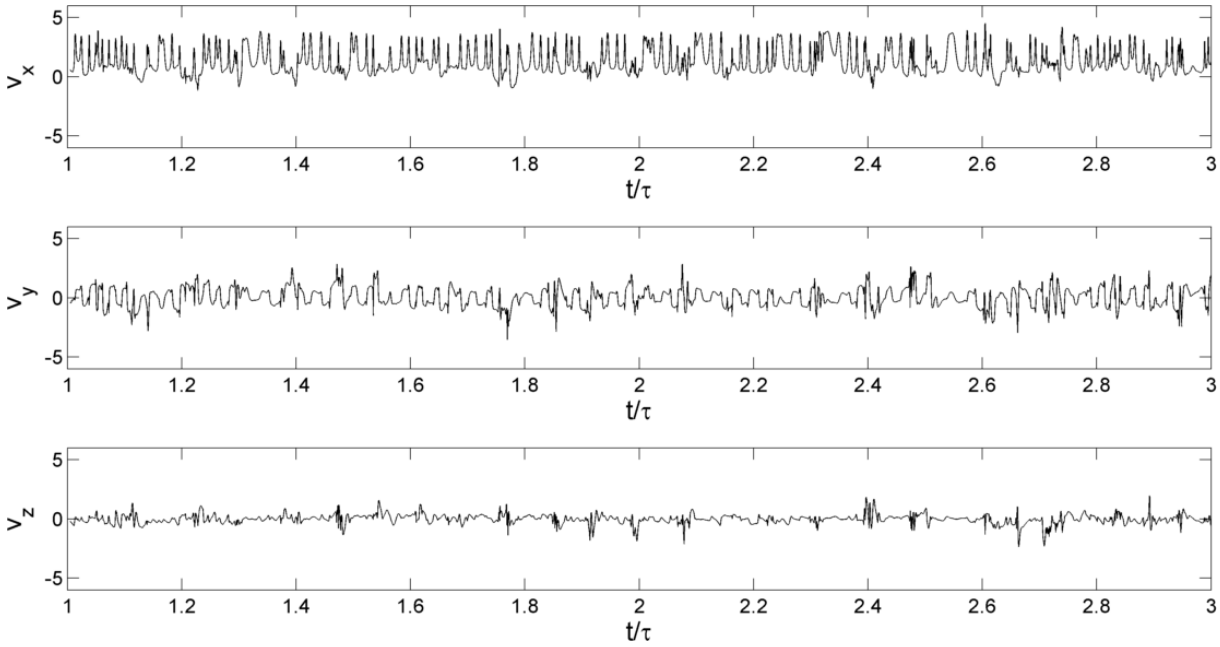

Figure B.27 – Temporal evolution for v_x, v_y and v_z at Reynolds 250 in p_4

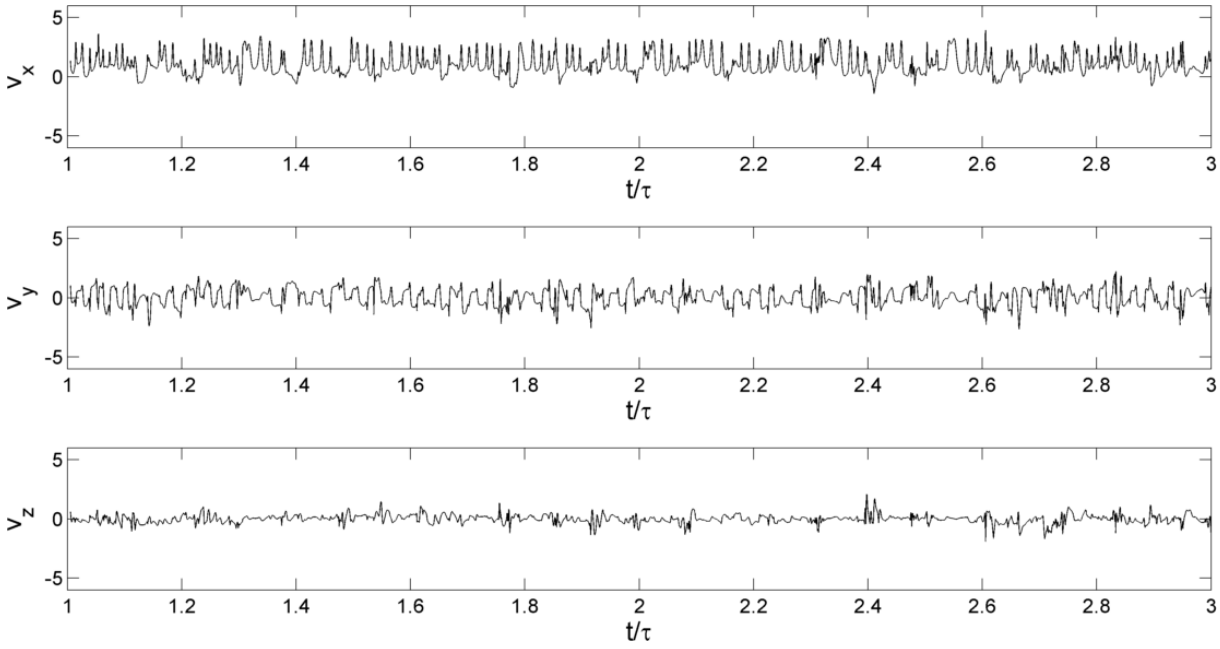

Figure B.28 – Temporal evolution for v_x, v_y and v_z at Reynolds 250 in p_5

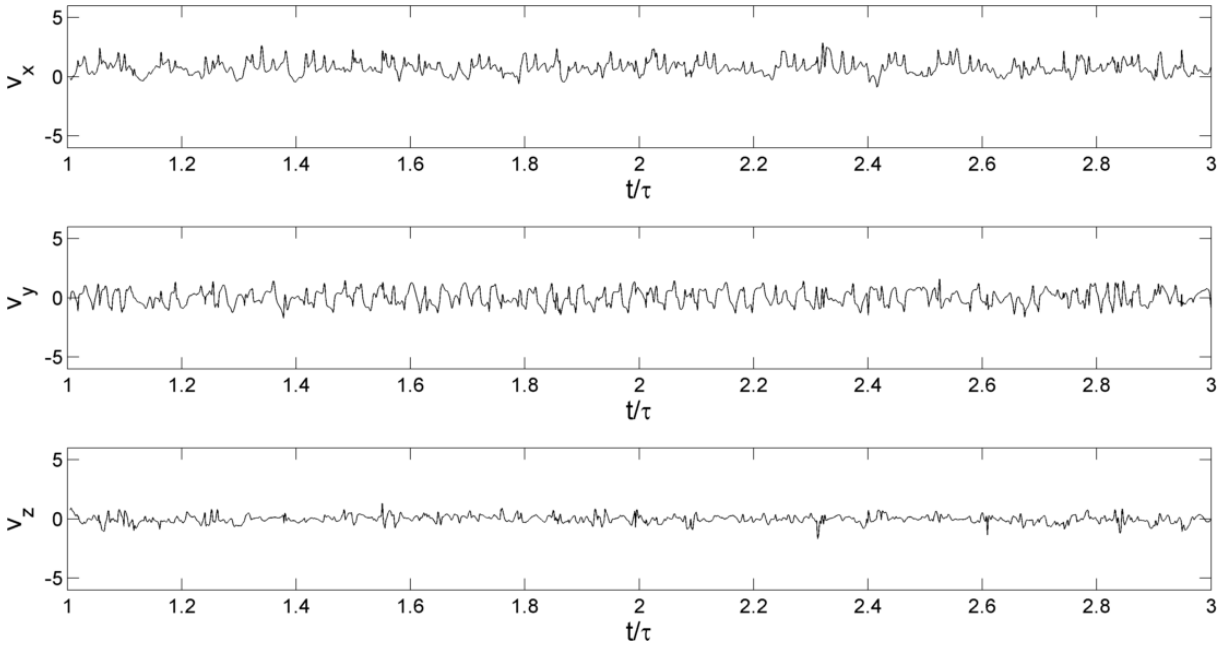

Figure B.29 – Temporal evolution for v_x, v_y and v_z at Reynolds 250 in p_6

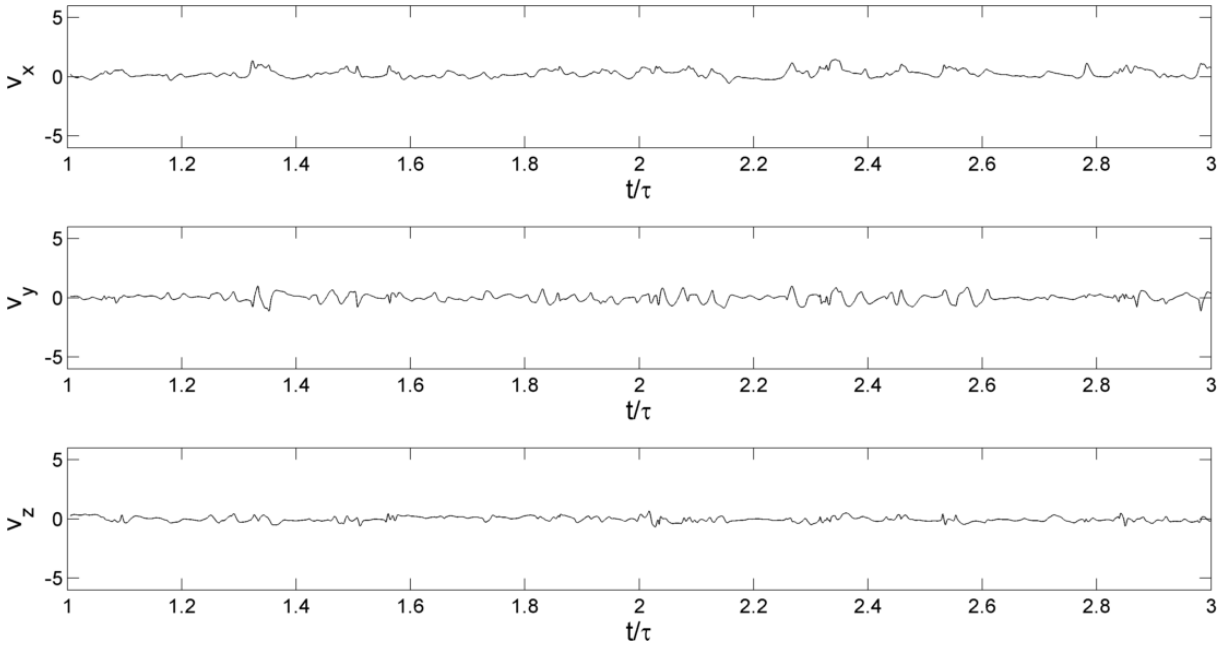

Figure B.30 – Temporal evolution for v_x, v_y and v_z at Reynolds 250 in p_7

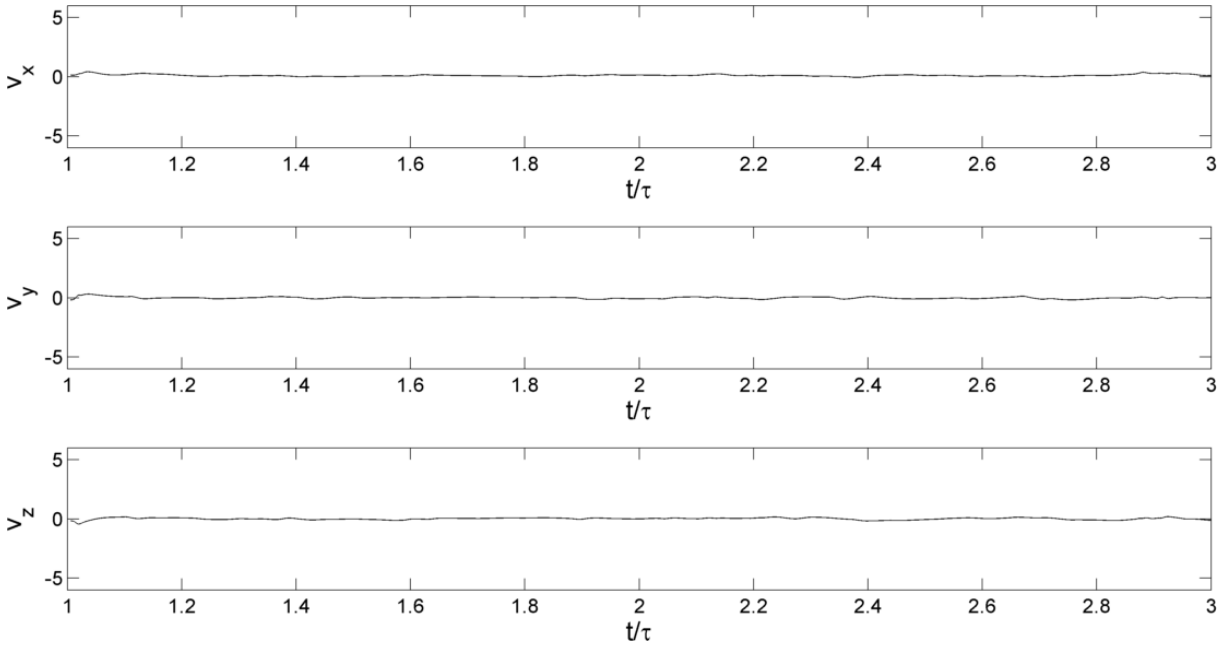

Figure B.31 – Temporal evolution for v_x, v_y and v_z at Reynolds 250 in p_8

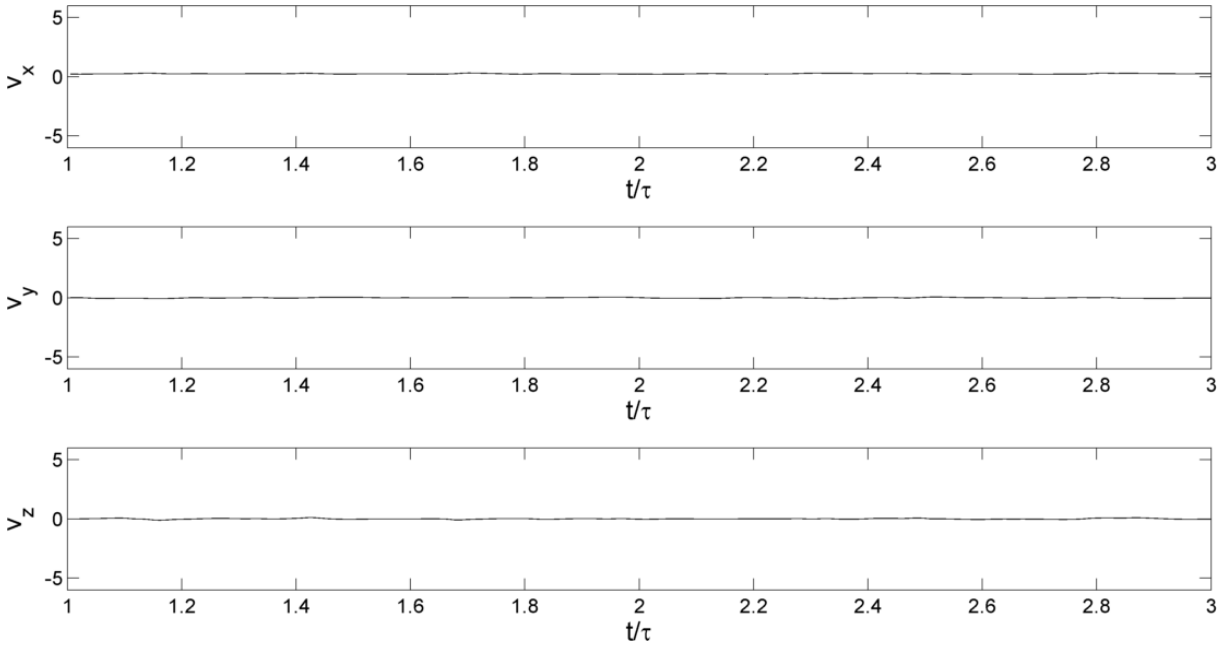

Figure B.32 – Temporal evolution for v_x, v_y and v_z at Reynolds 250 in p_9

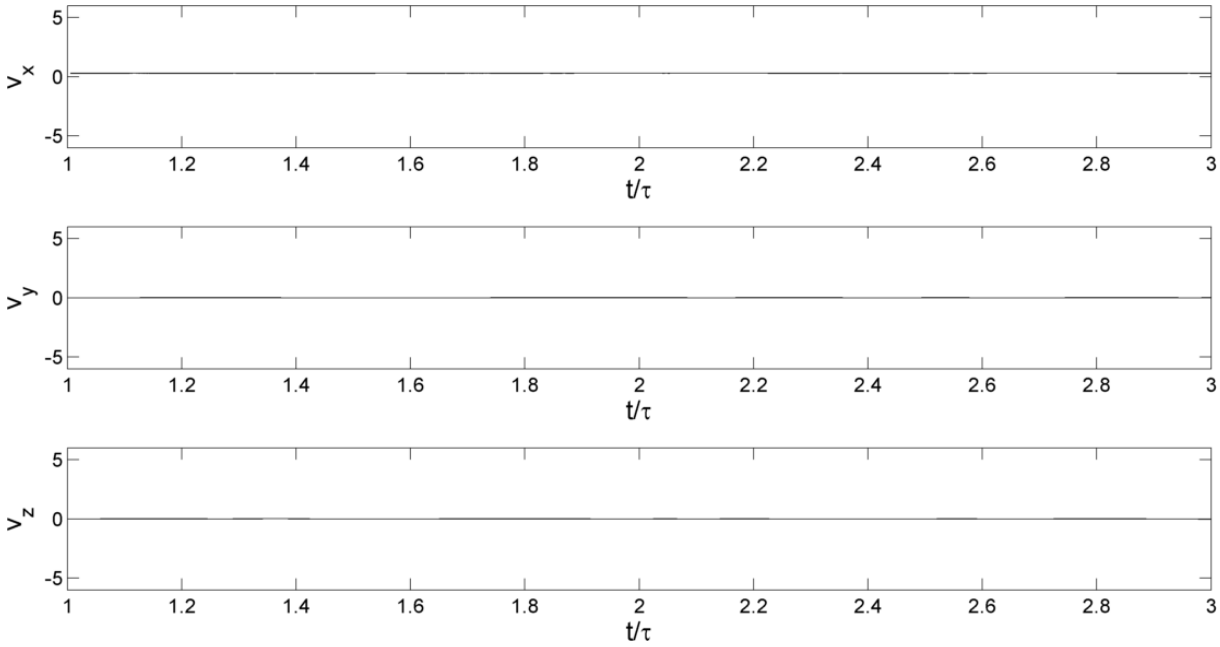

Figure B.33 – Temporal evolution for v_x, v_y and v_z at Reynolds 250 in p_{10}

B.4 Reynolds 300

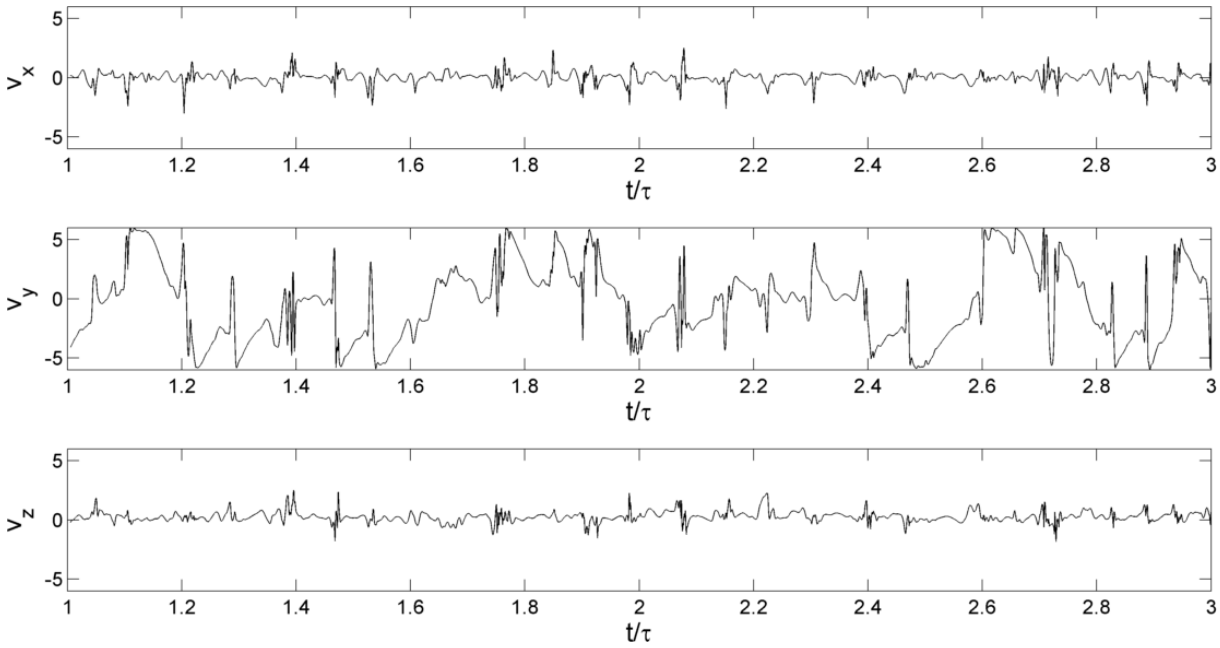

Figure B.34 – Temporal evolution for v_x, v_y and v_z at Reynolds 300 in p_0

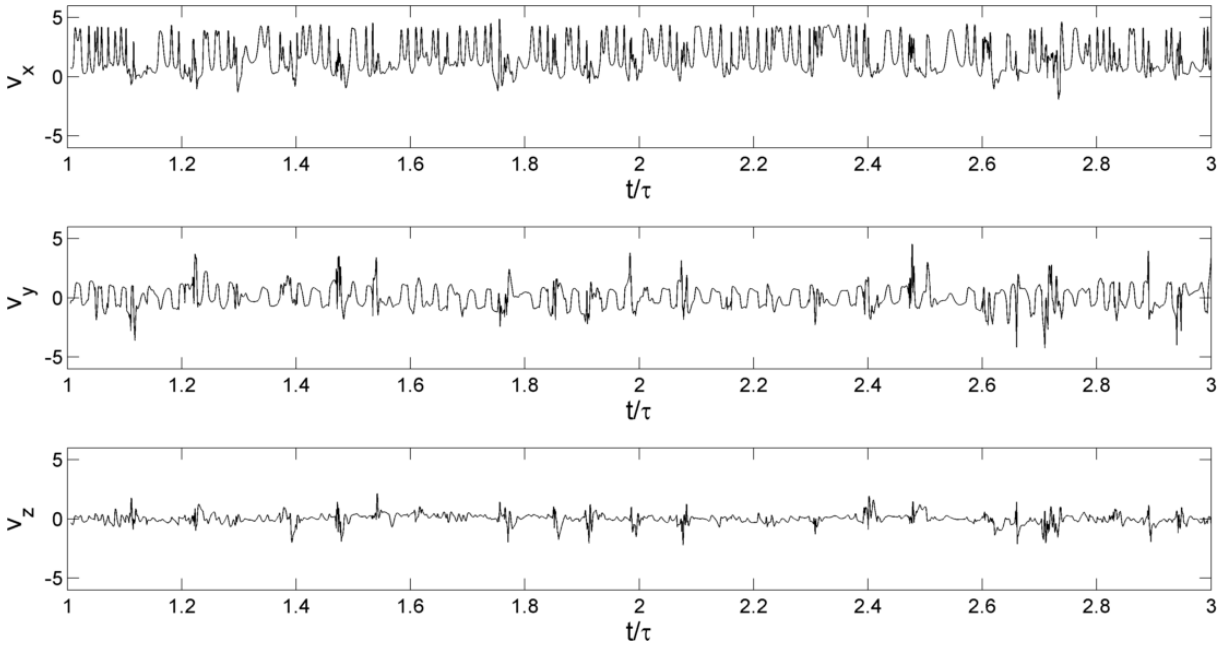

Figure B.35 – Temporal evolution for v_x, v_y and v_z at Reynolds 300 in p_1

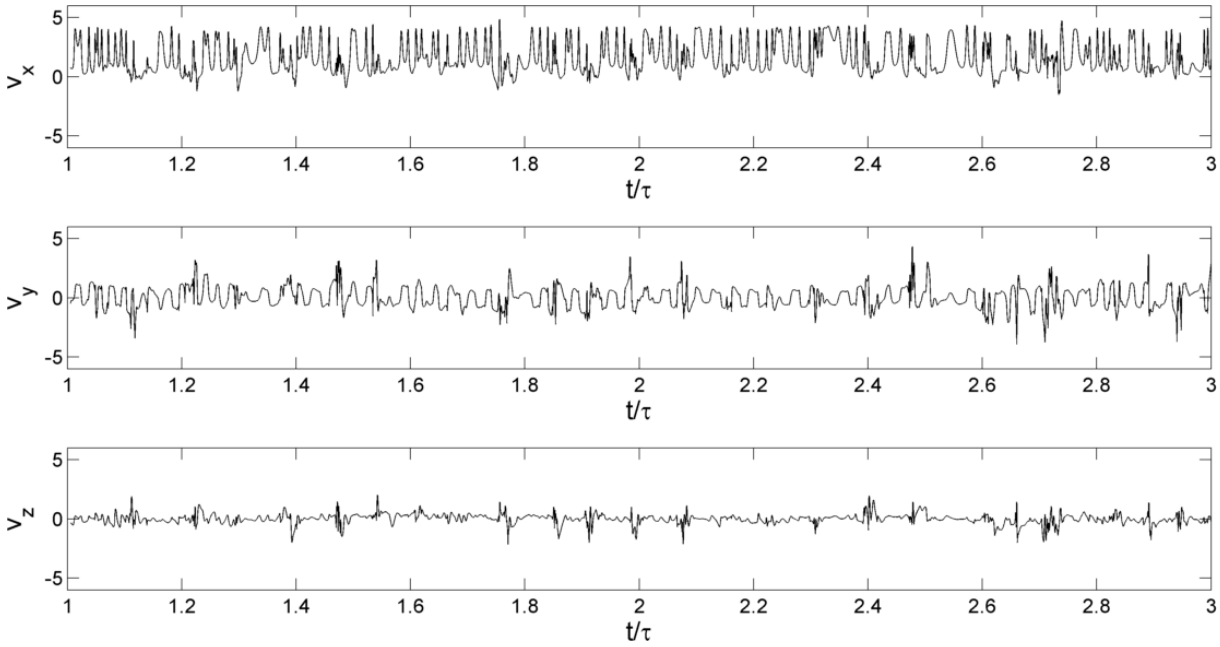

Figure B.36 – Temporal evolution for v_x, v_y and v_z at Reynolds 300 in p_2

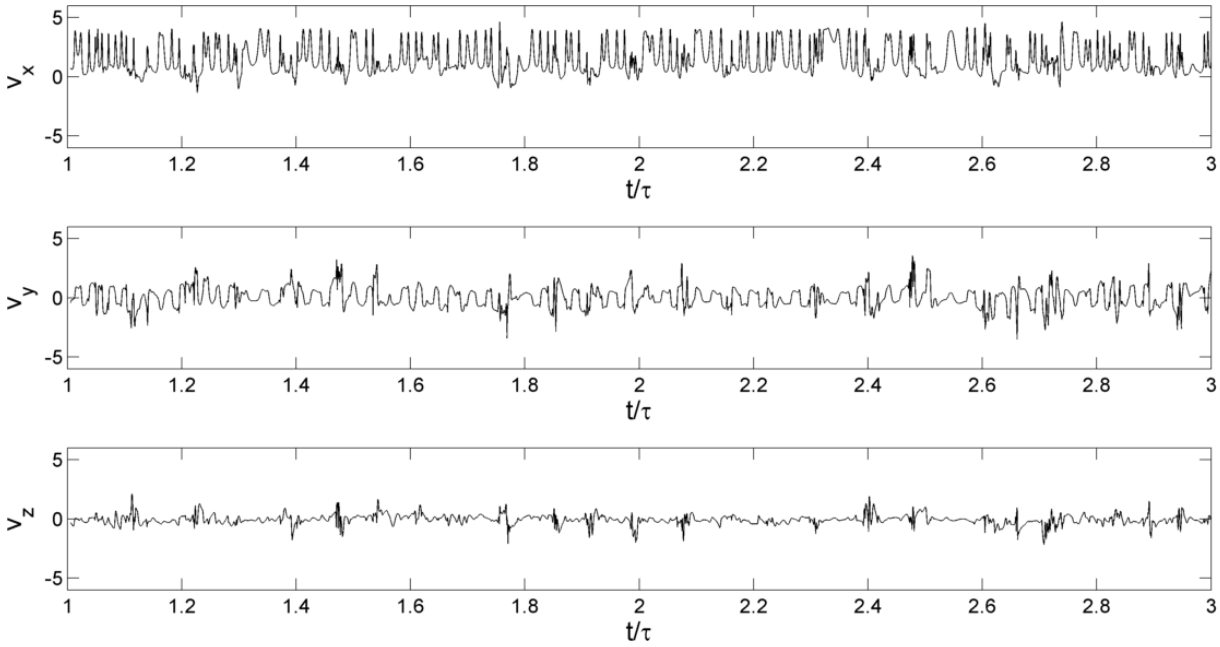

Figure B.37 – Temporal evolution for v_x, v_y and v_z at Reynolds 300 in p_3

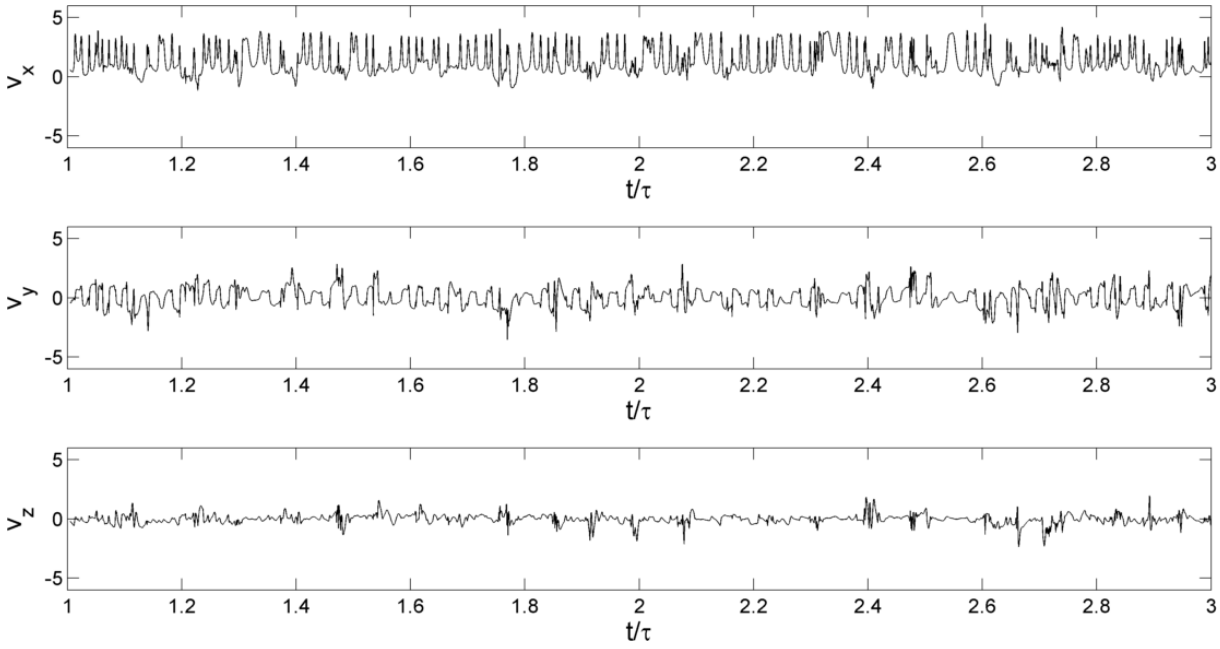

Figure B.38 – Temporal evolution for v_x, v_y and v_z at Reynolds 300 in p_4

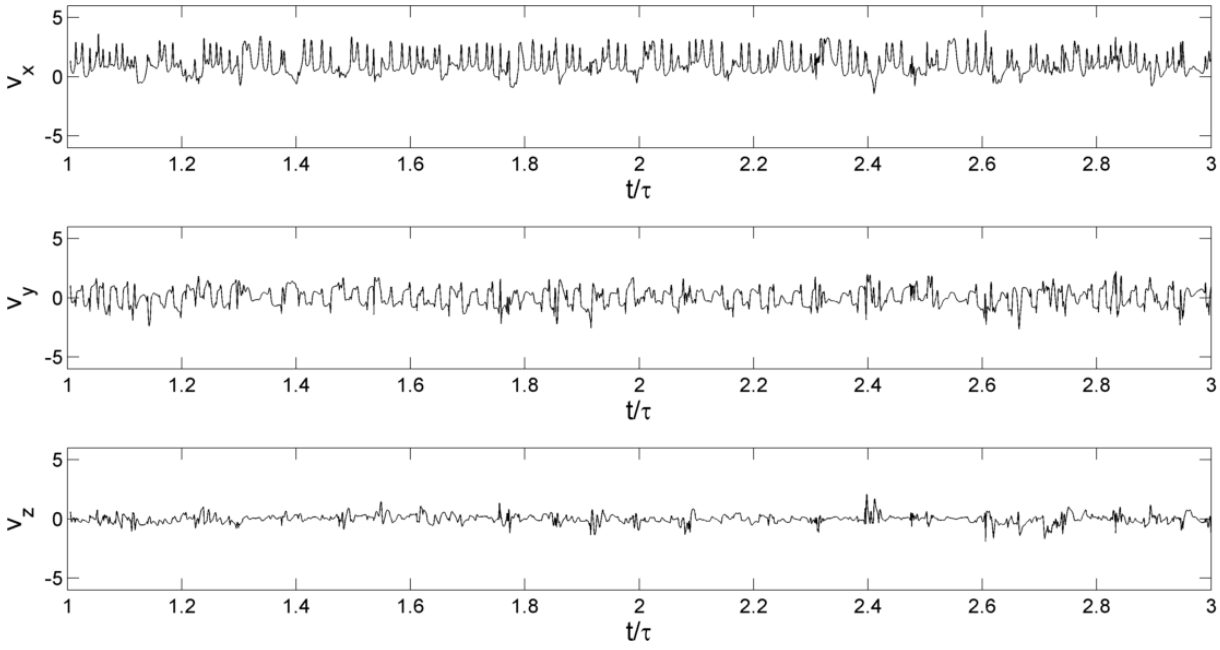

Figure B.39 – Temporal evolution for v_x, v_y and v_z at Reynolds 300 in p_5

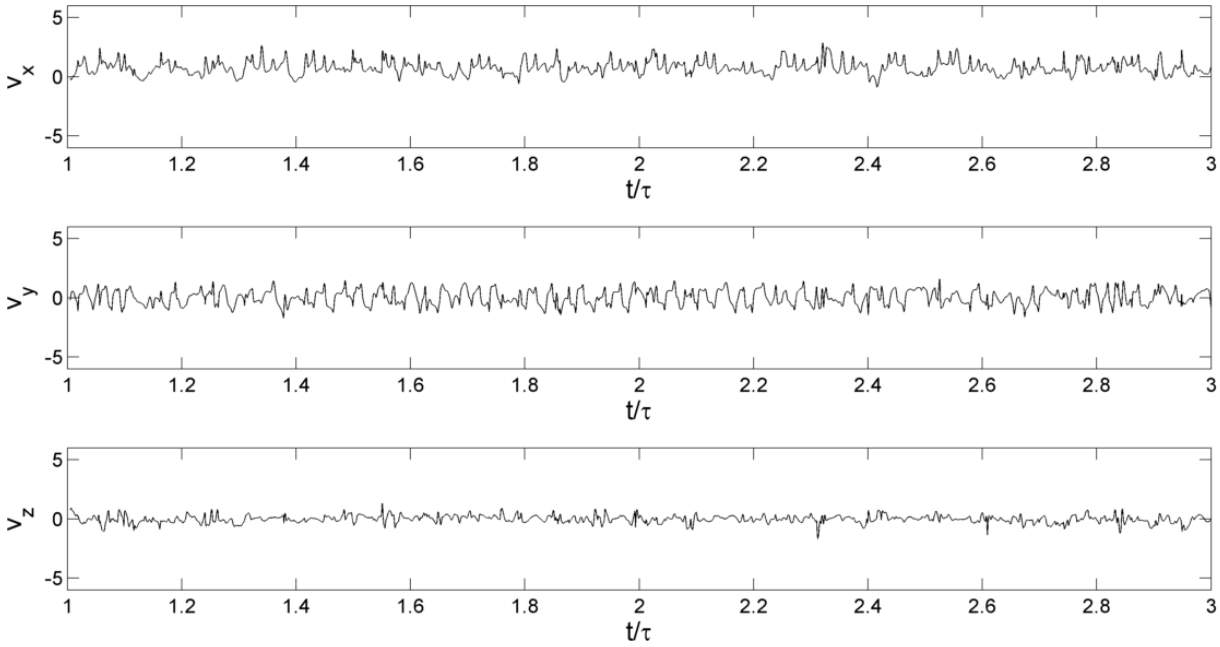

Figure B.40 – Temporal evolution for v_x, v_y and v_z at Reynolds 300 in p_6

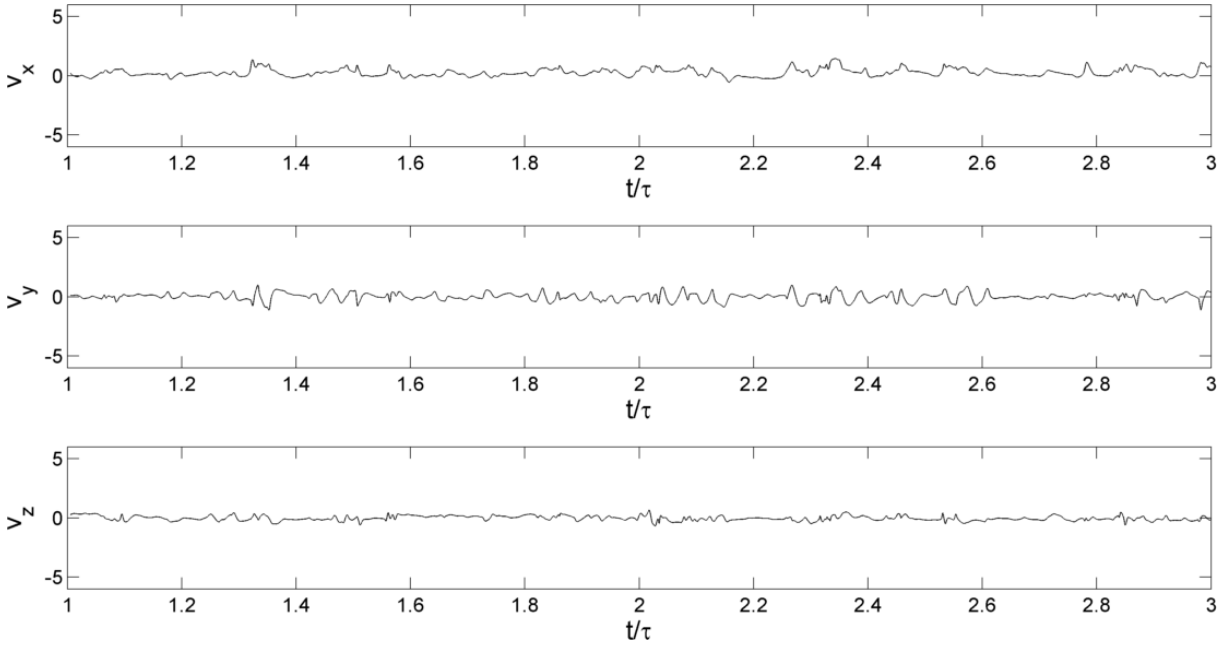

Figure B.41 – Temporal evolution for v_x, v_y and v_z at Reynolds 300 in p_7

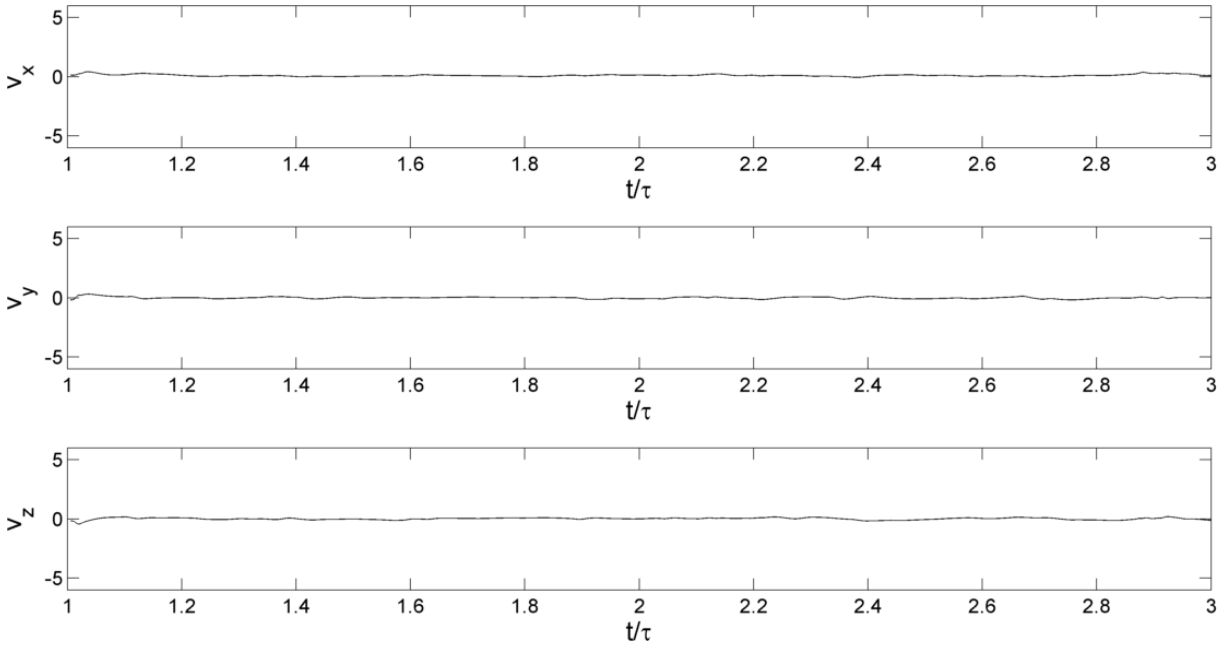

Figure B.42 – Temporal evolution for v_x, v_y and v_z at Reynolds 300 in p_8

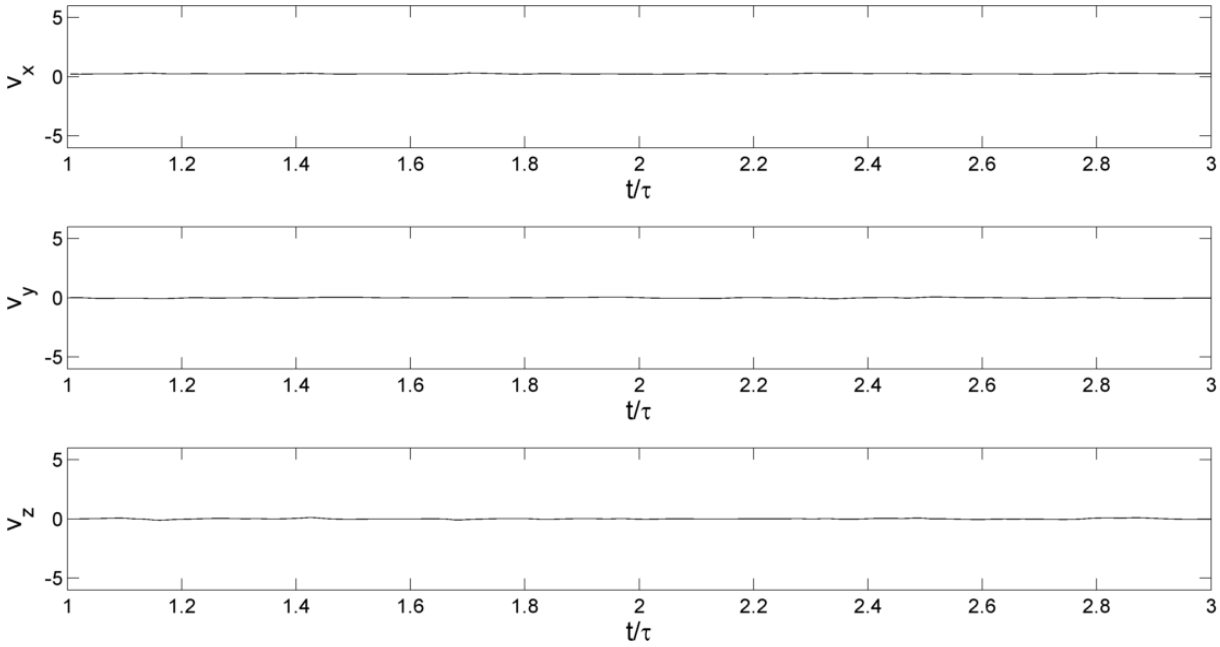

Figure B.43 – Temporal evolution for v_x, v_y and v_z at Reynolds 300 in p_9

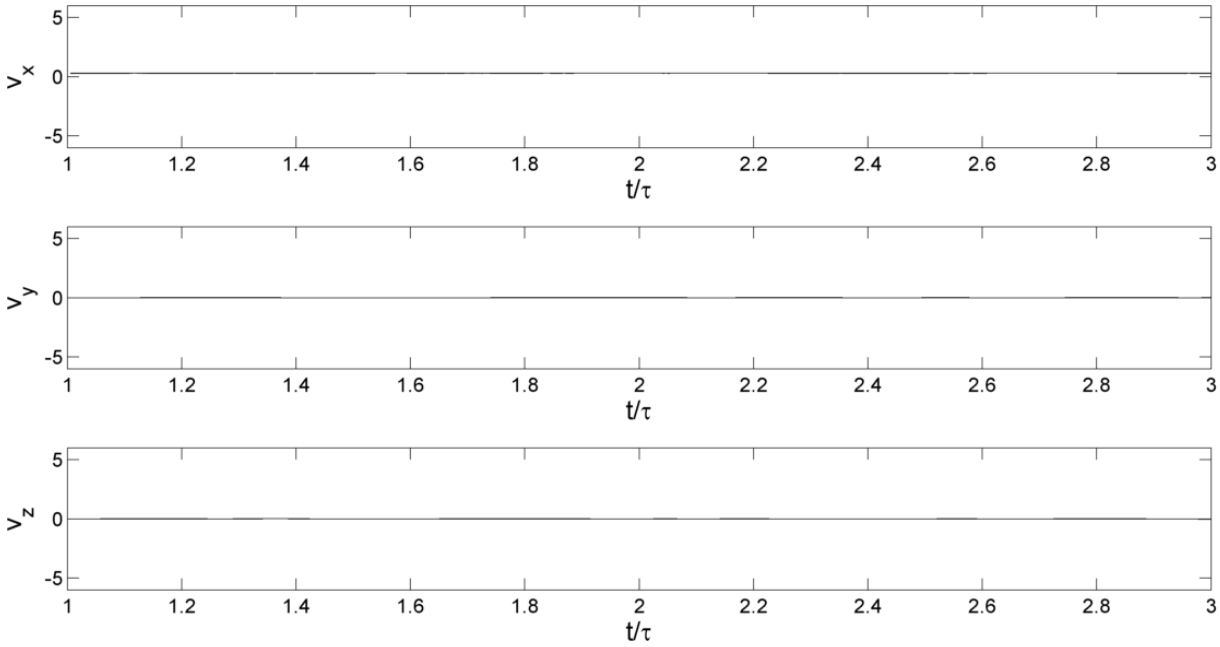

Figure B.44 – Temporal evolution for v_x, v_y and v_z at Reynolds 300 in p_{10}

C Power spectra for velocity components in probe points

C.1 Reynolds 150

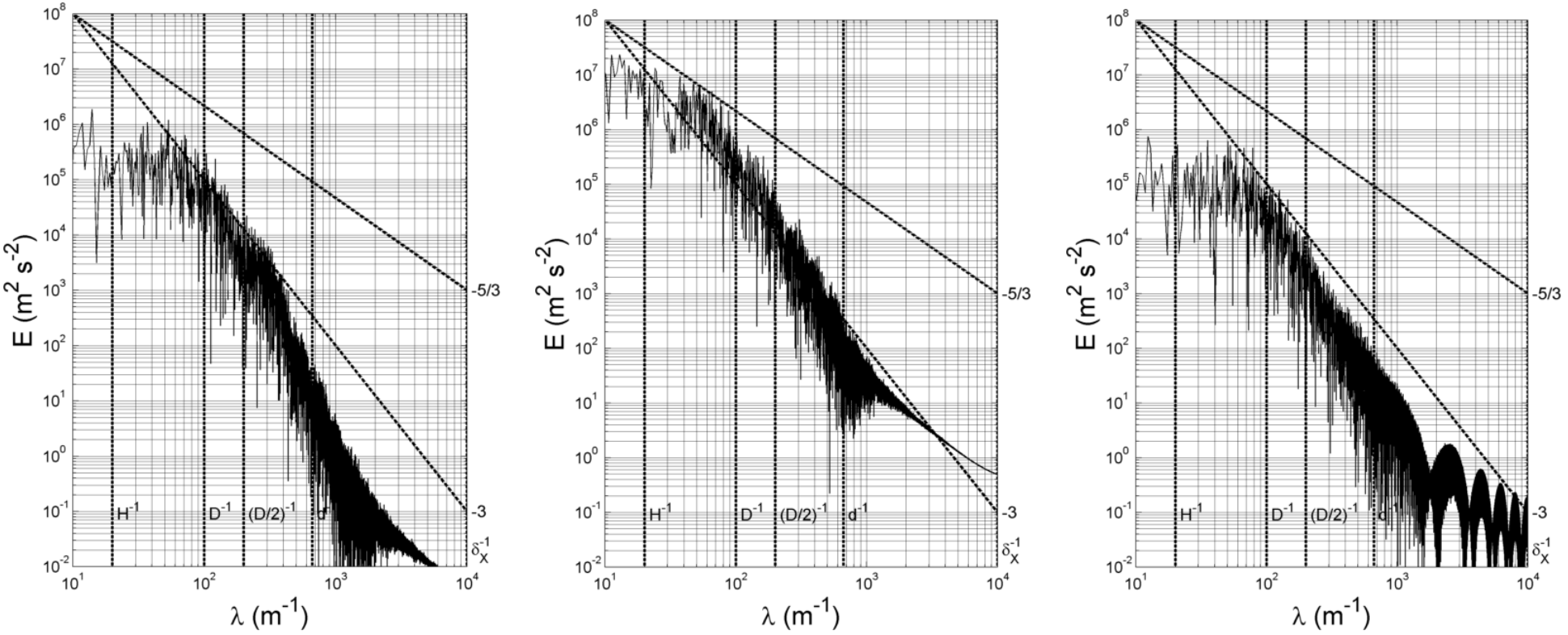

Figure C.1 – Power Spectra for v_x, v_y and v_z at Reynolds 150 in p_0

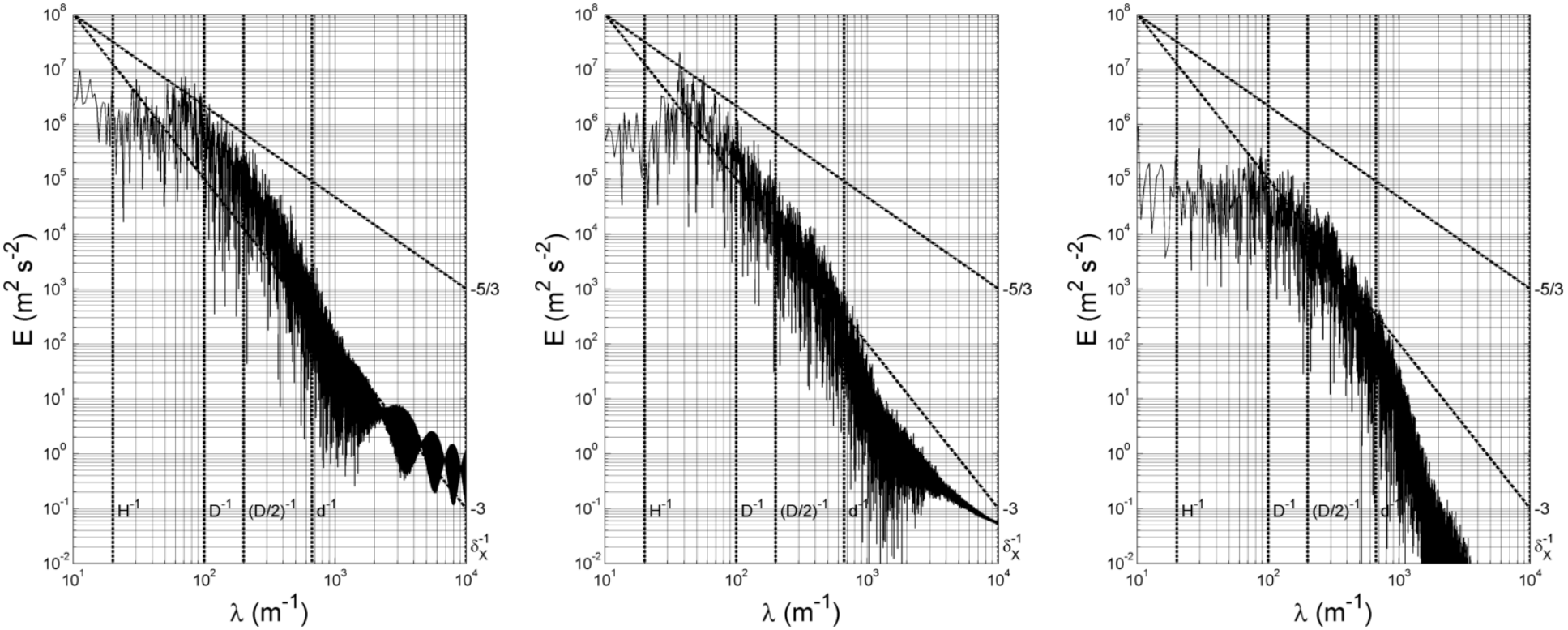

Figure C.2 – Power Spectra for v_x, v_y and v_z at Reynolds 150 in p_1

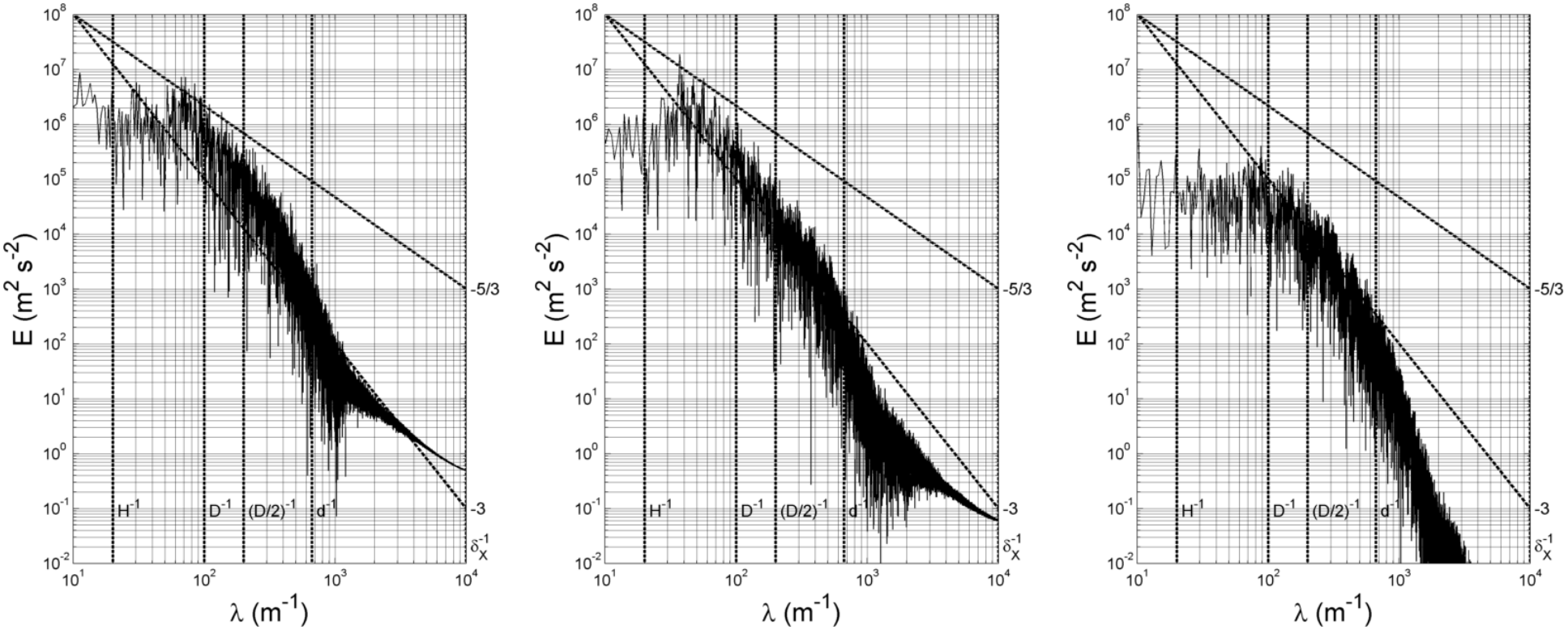

Figure C.3 – Power Spectra for v_x, v_y and v_z at Reynolds 150 in p_2

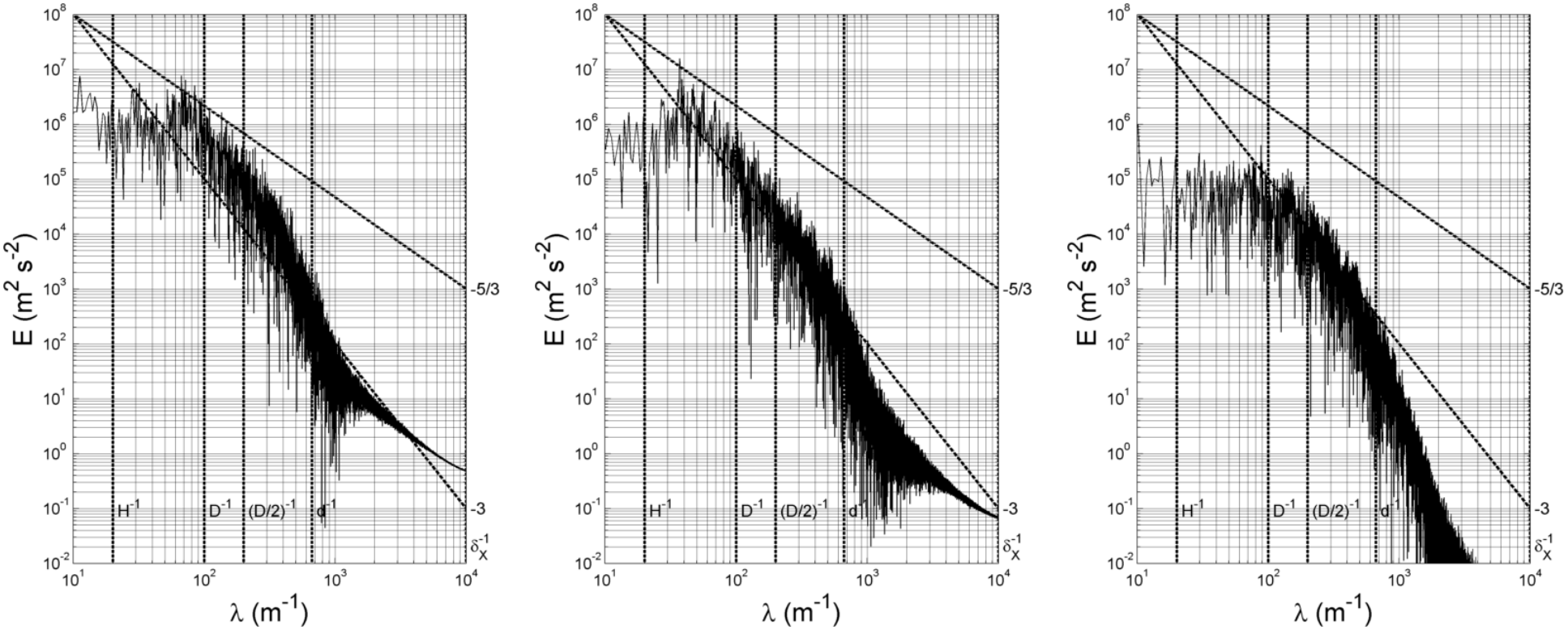

Figure C.4 – Power Spectra for v_x, v_y and v_z at Reynolds 150 in p_3

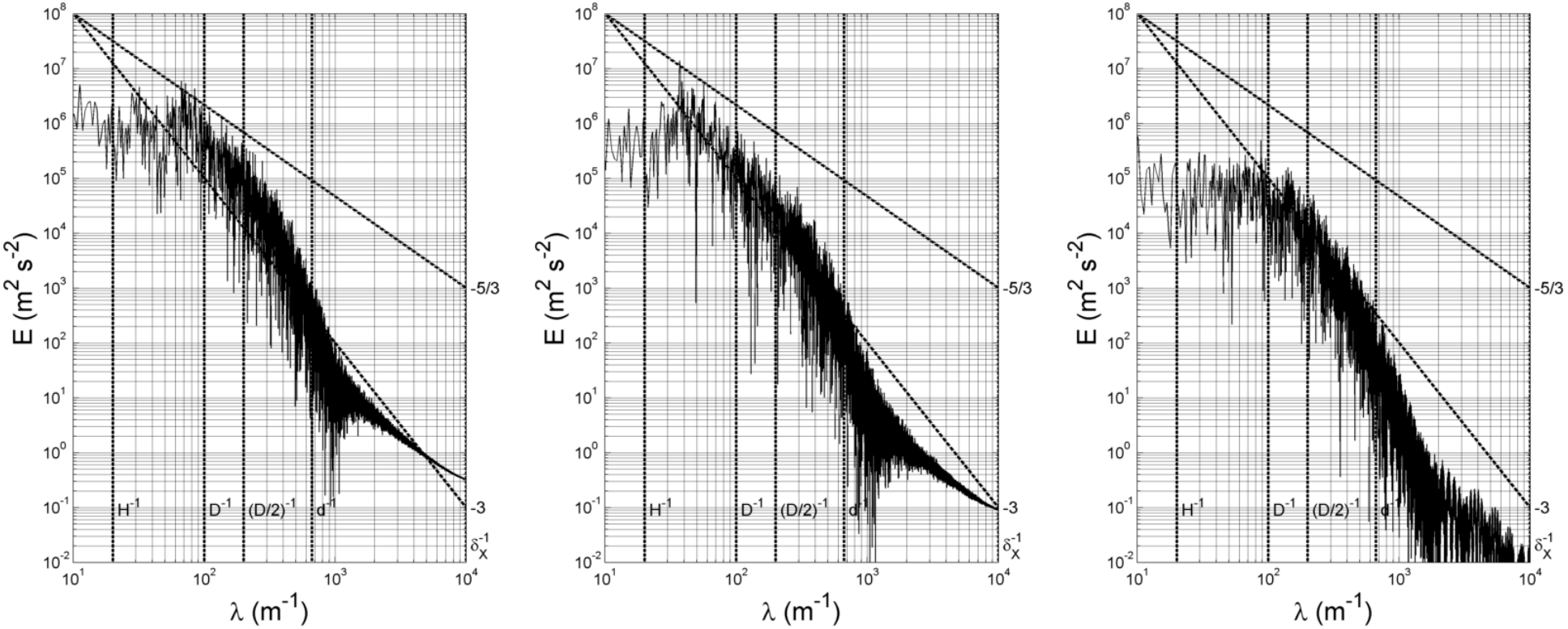

Figure C.5 – Power Spectra for v_x, v_y and v_z at Reynolds 150 in p_4

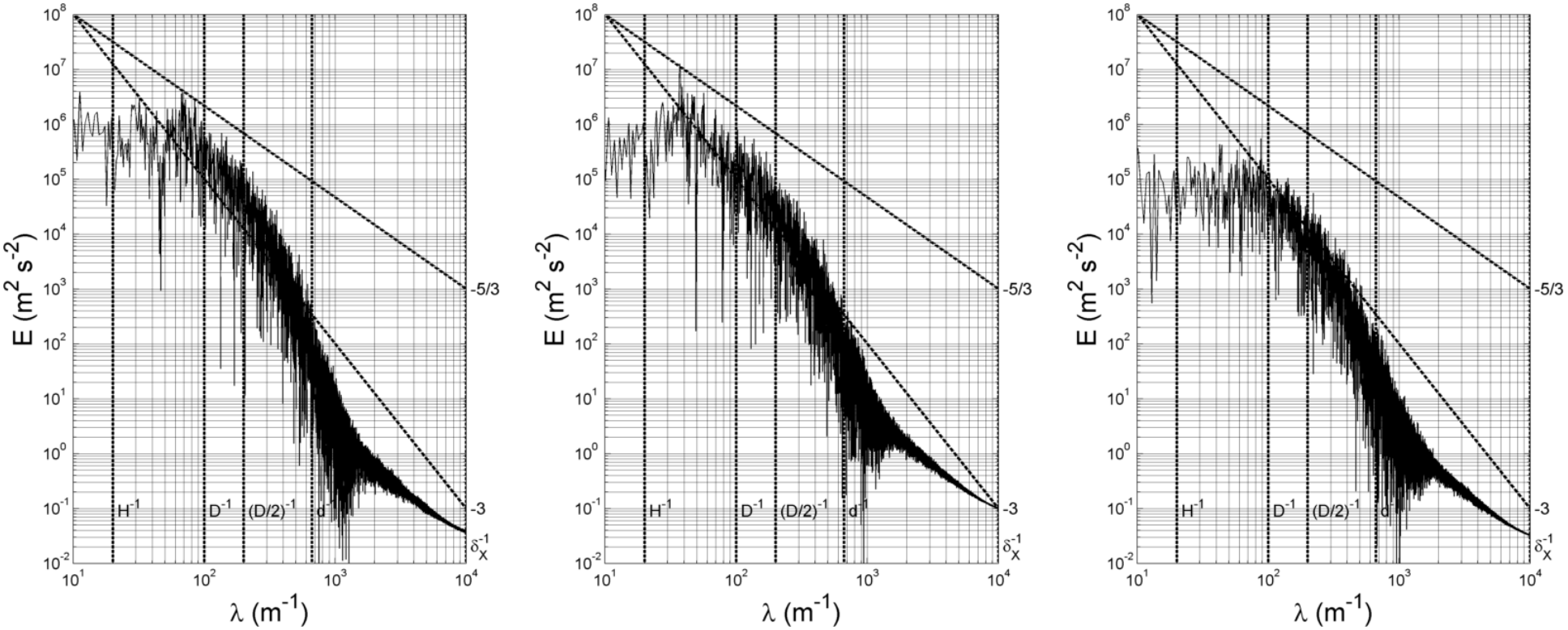

Figure C.6 – Power Spectra for v_x, v_y and v_z at Reynolds 150 in p_5

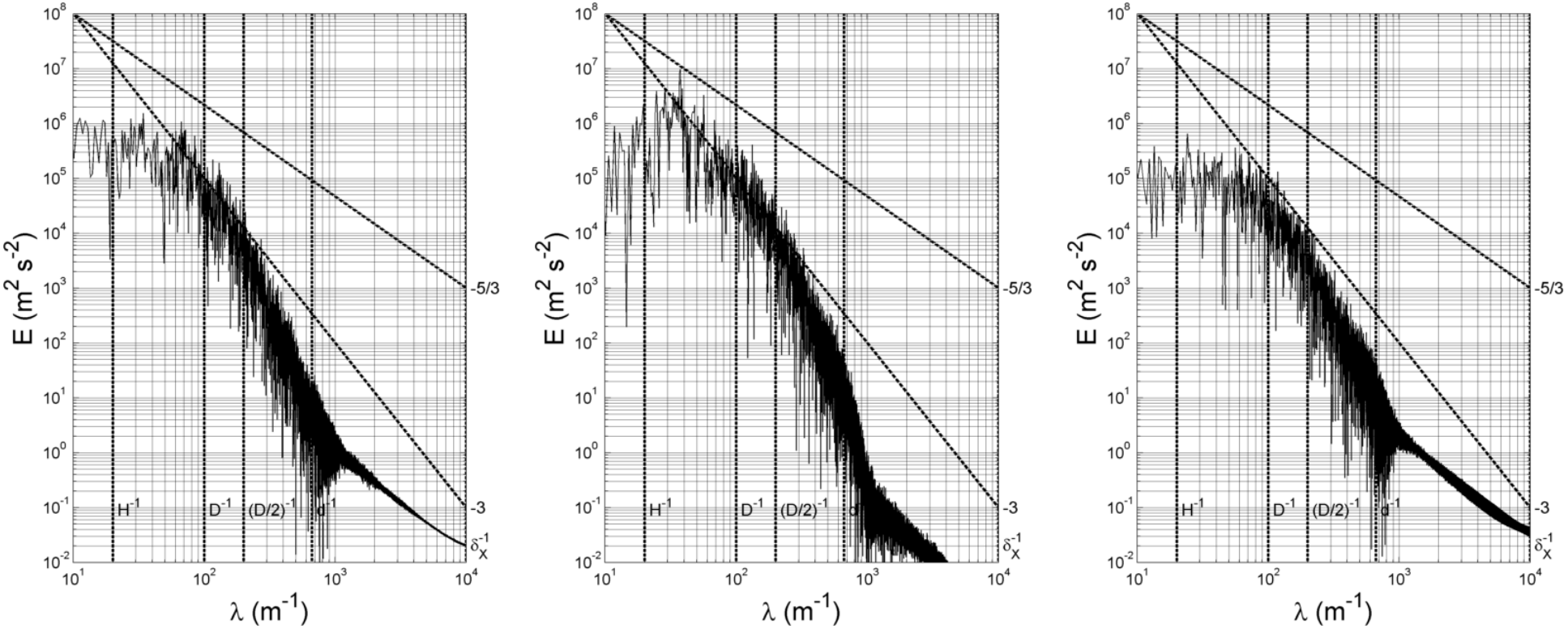

Figure C.7 – Power Spectra for v_x, v_y and v_z at Reynolds 150 in p_6

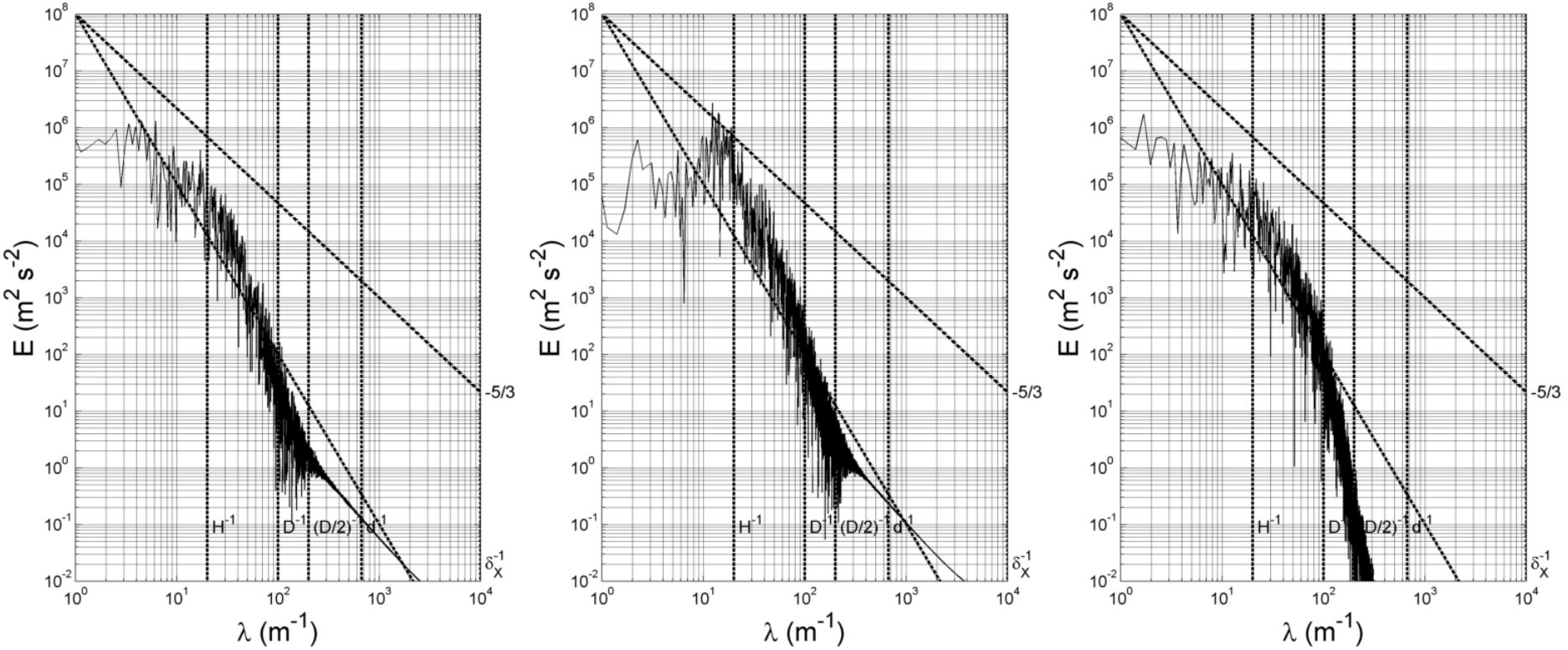

Figure C.8 – Power Spectra for v_x, v_y and v_z at Reynolds 150 in p_7

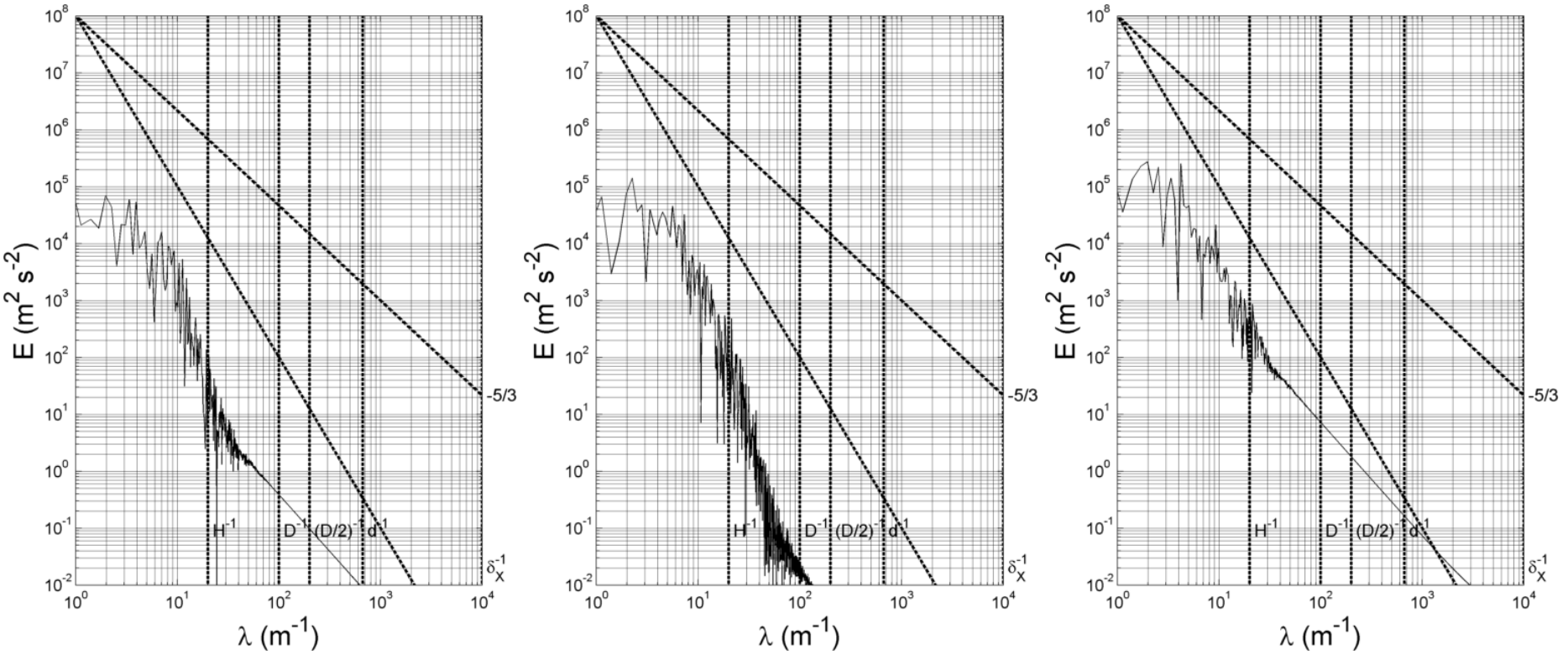

Figure C.9 – Power Spectra for v_x, v_y and v_z at Reynolds 150 in p_8

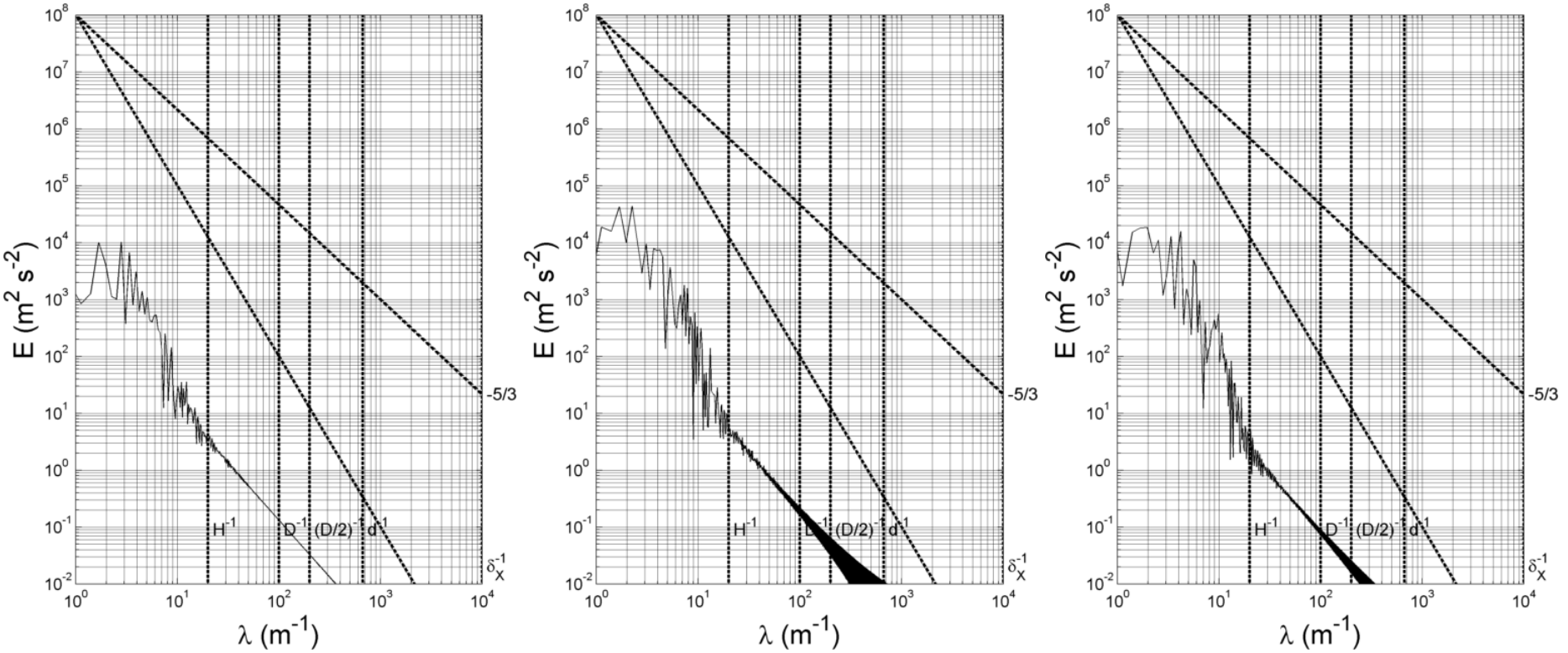

Figure C.10 – Power Spectra for v_x, v_y and v_z at Reynolds 150 in p_9

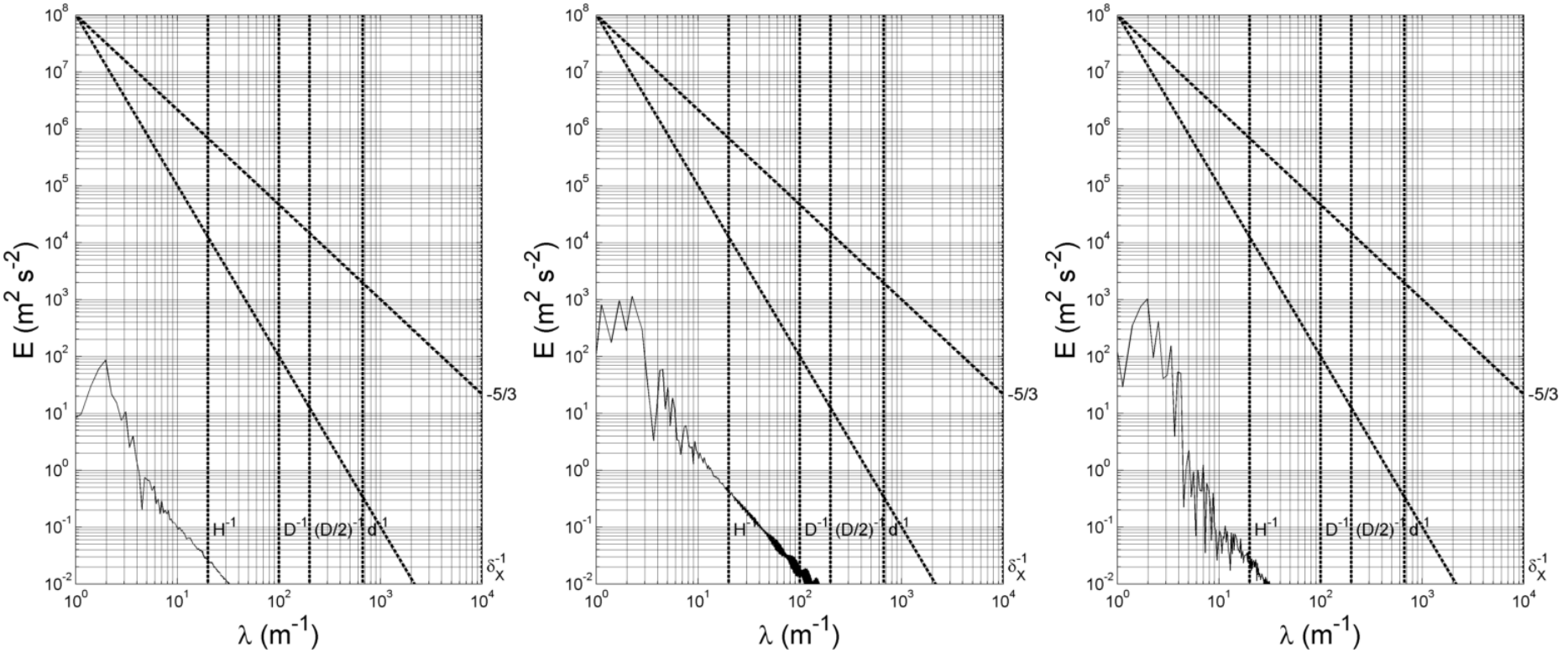

Figure C.11 – Power Spectra for v_x, v_y and v_z at Reynolds 150 in p_{10}

C.2 Reynolds 200

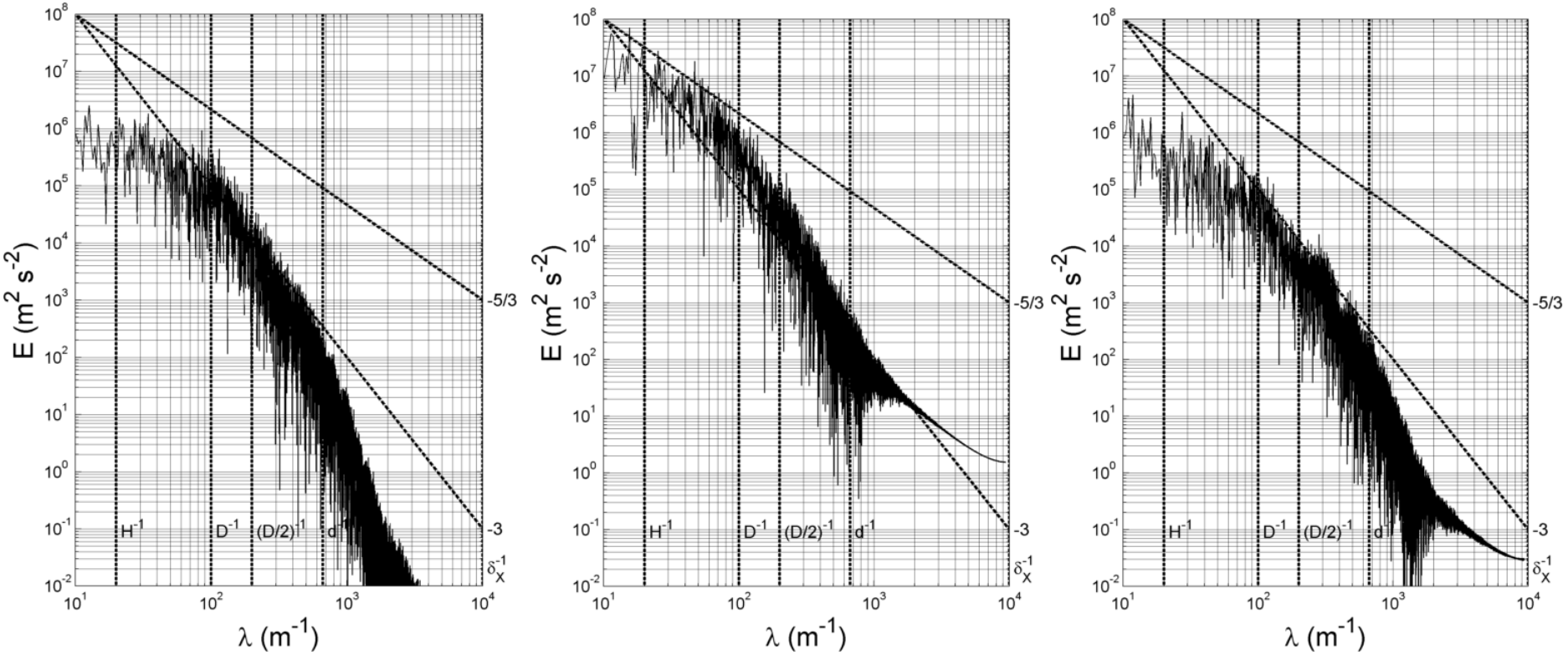

Figure C.12 – Power Spectra for v_x, v_y and v_z at Reynolds 200 in p_0

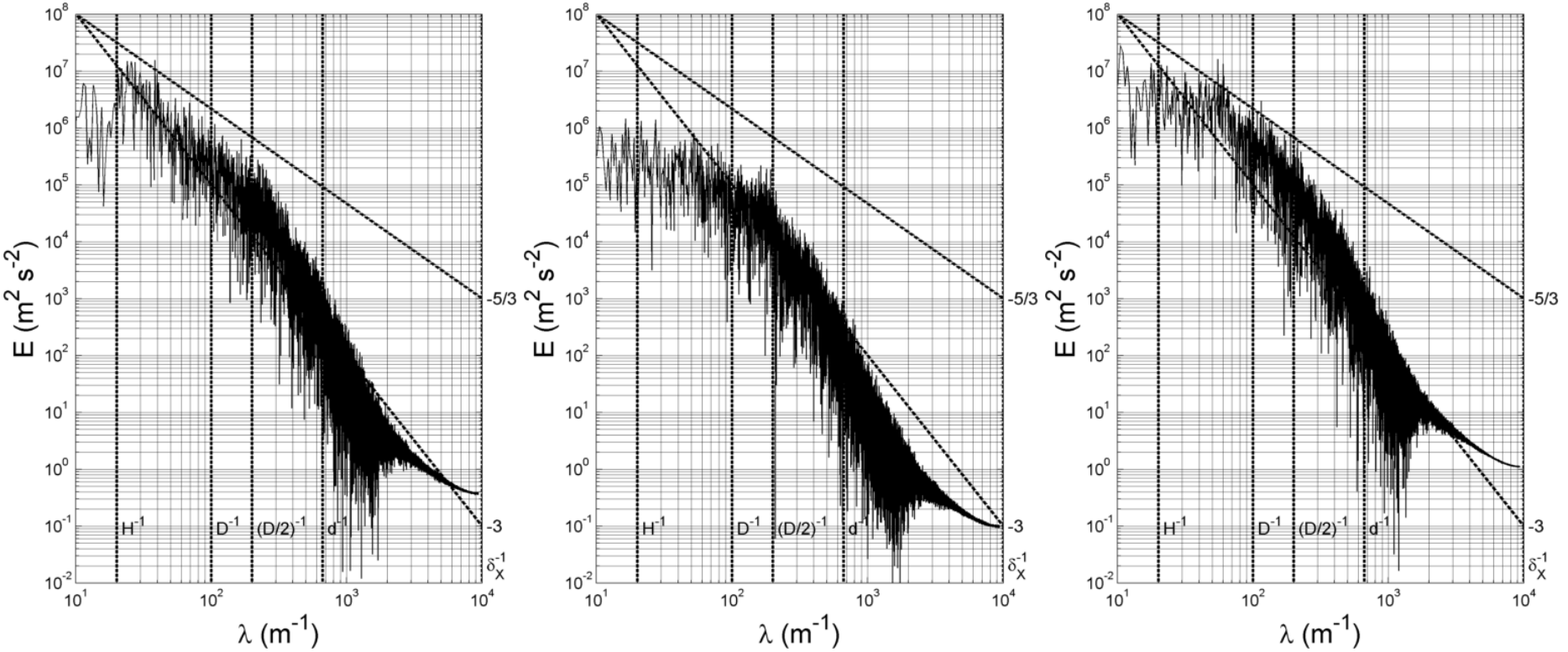

Figure C.13 – Power Spectra for v_x, v_y and v_z at Reynolds 200 in p_1

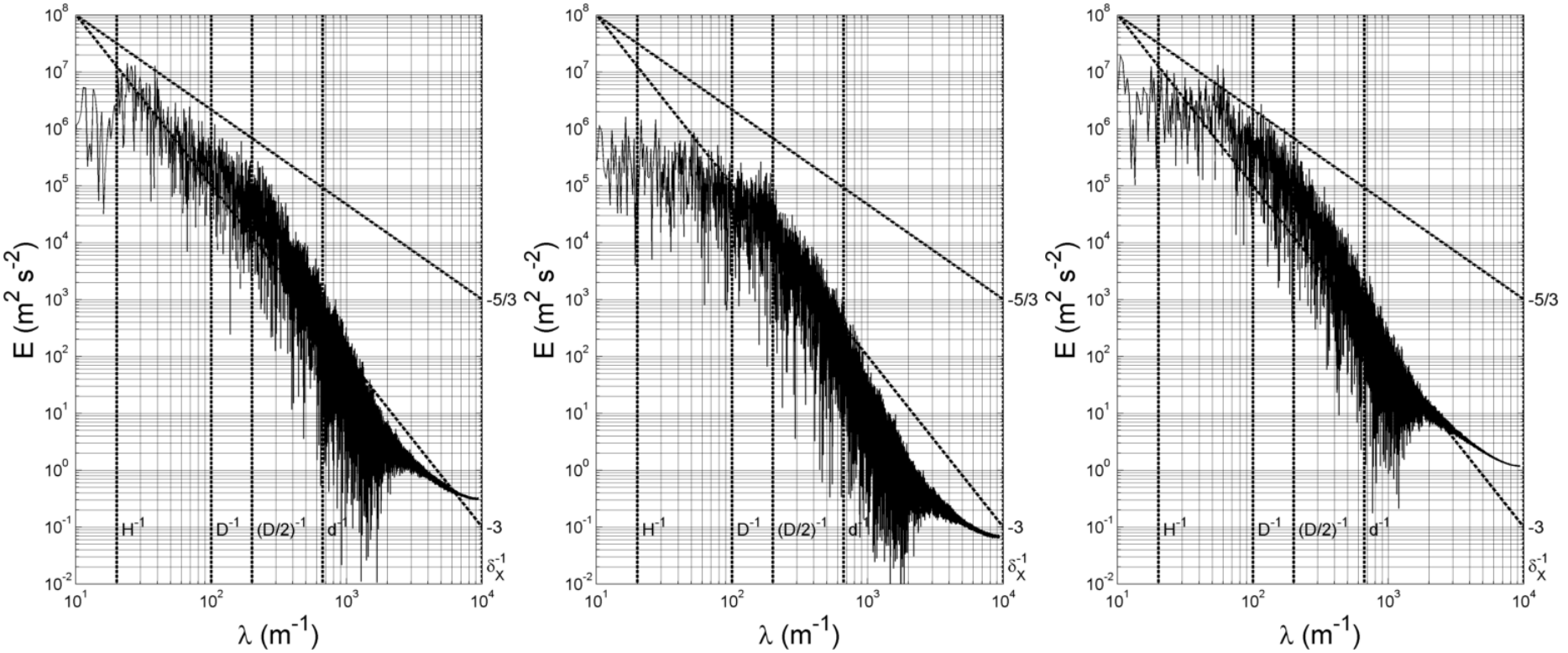

Figure C.14 – Power Spectra for v_x, v_y and v_z at Reynolds 200 in p2

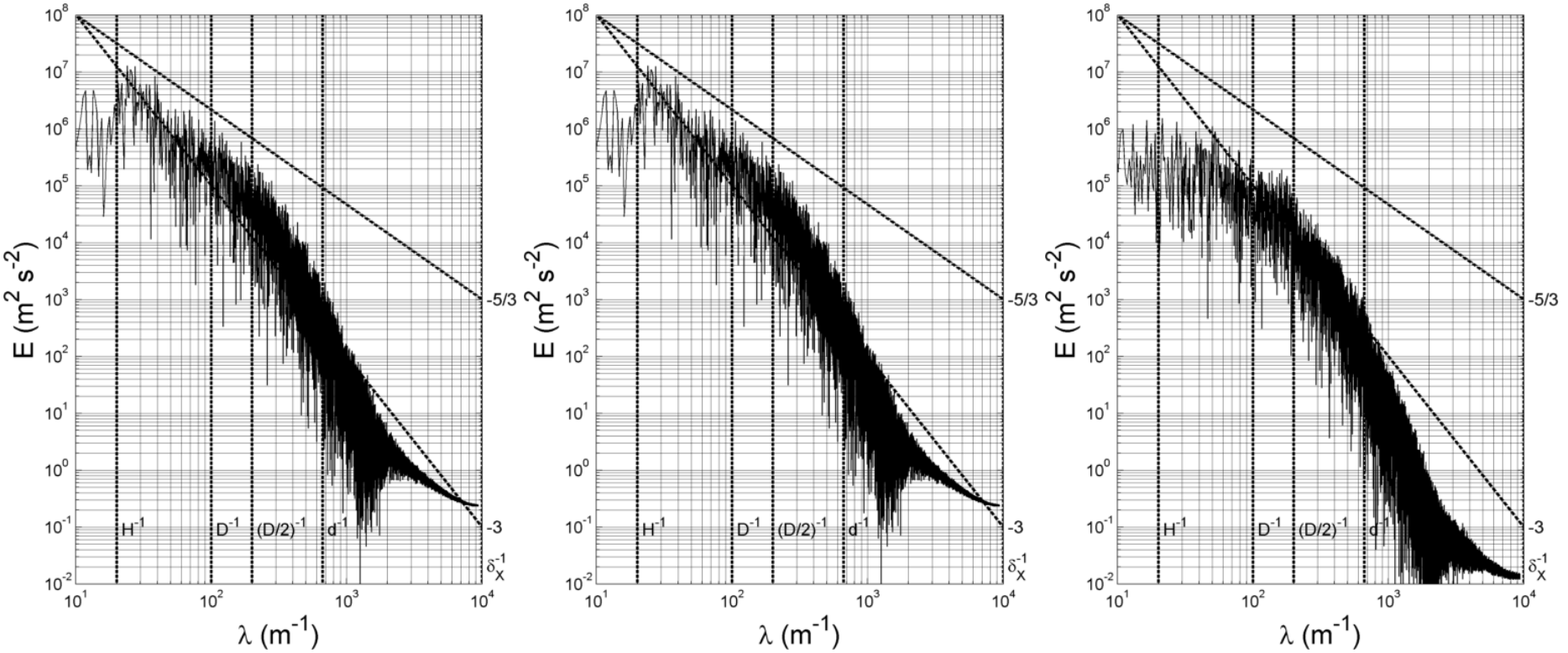

Figure C.15 – Power Spectra for v_x, v_y and v_z at Reynolds 200 in p_3

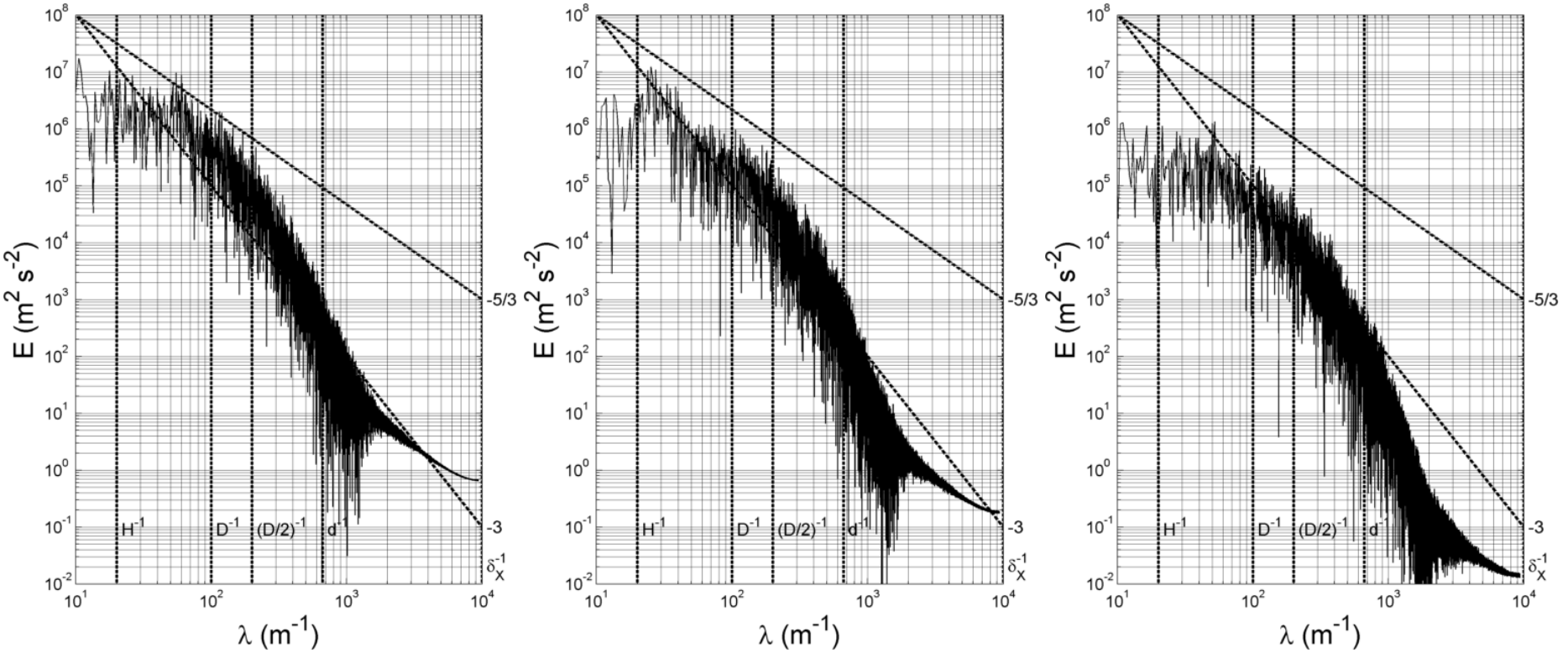

Figure C.16 – Power Spectra for v_x, v_y and v_z at Reynolds 200 in p_4

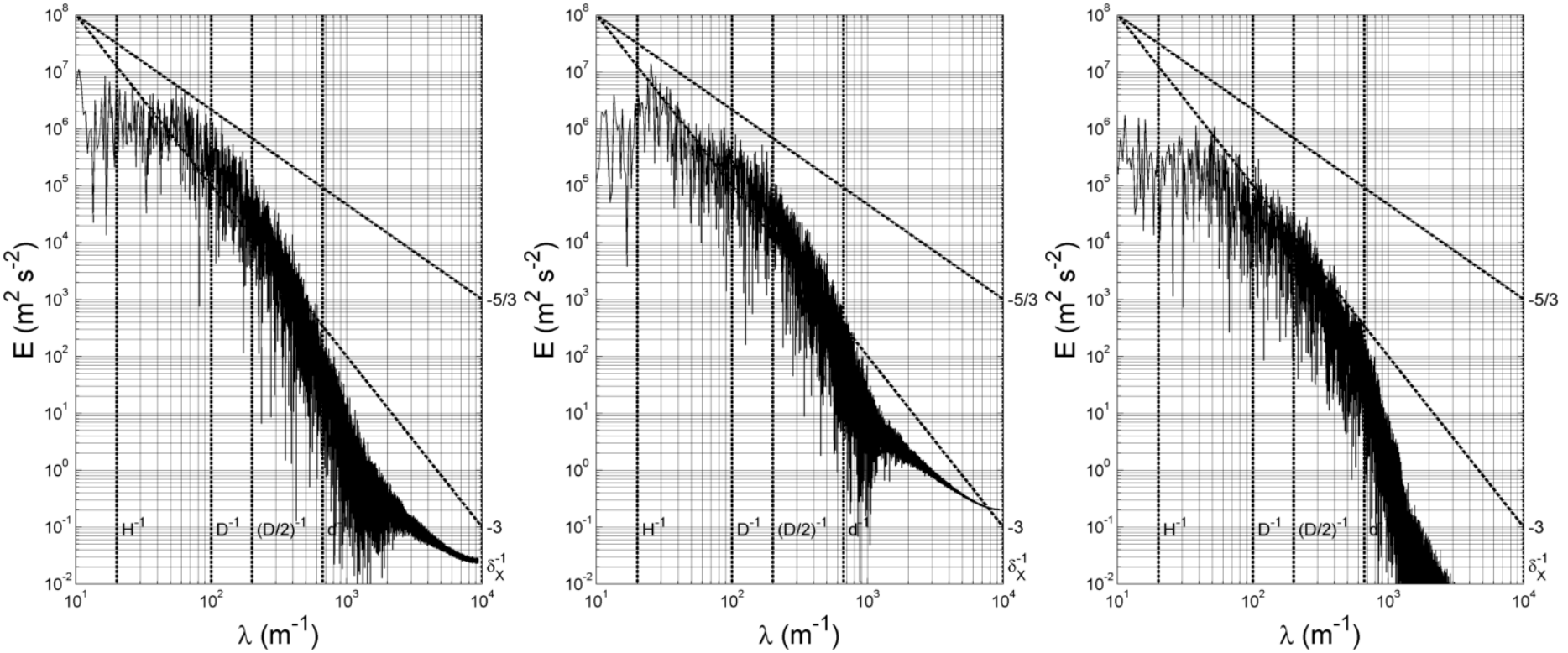

Figure C.17 – Power Spectra for v_x, v_y and v_z at Reynolds 200 in p_5

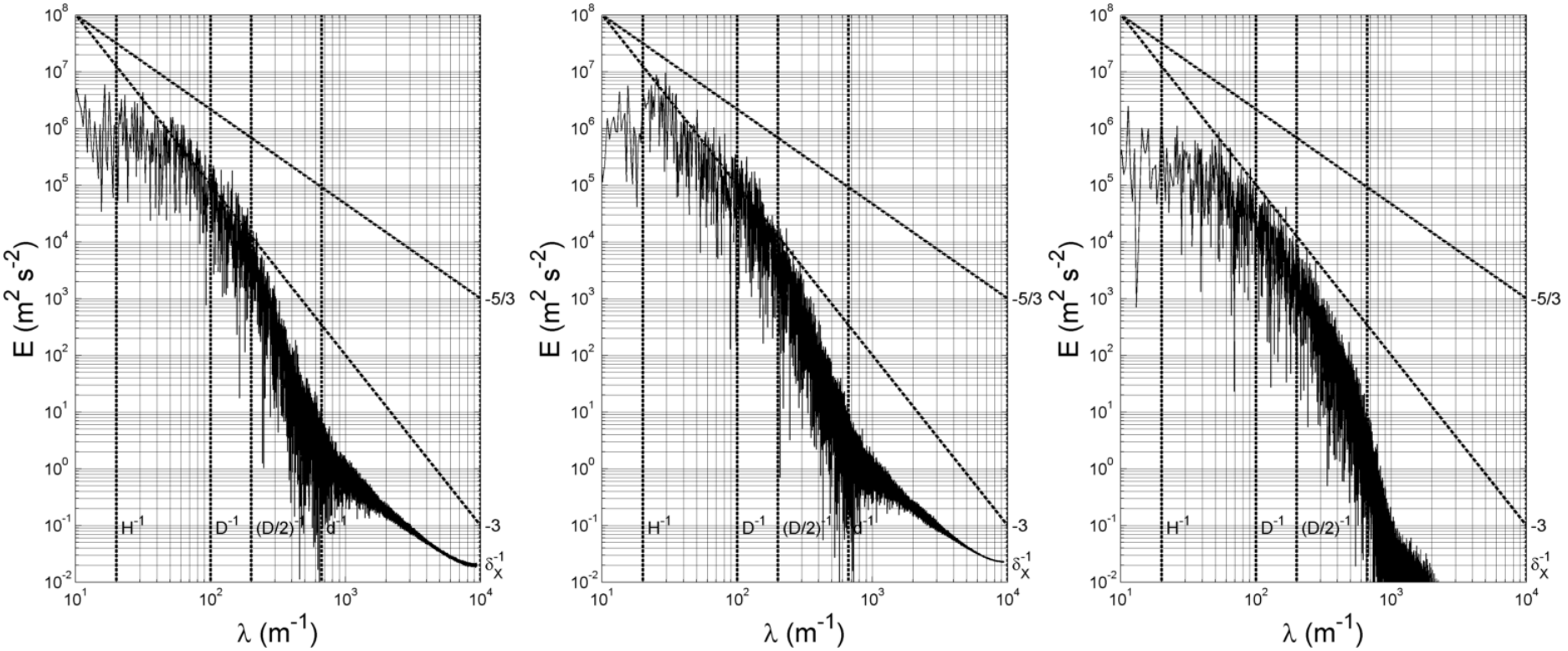

Figure C.18 – Power Spectra for v_x, v_y and v_z at Reynolds 200 in p_6

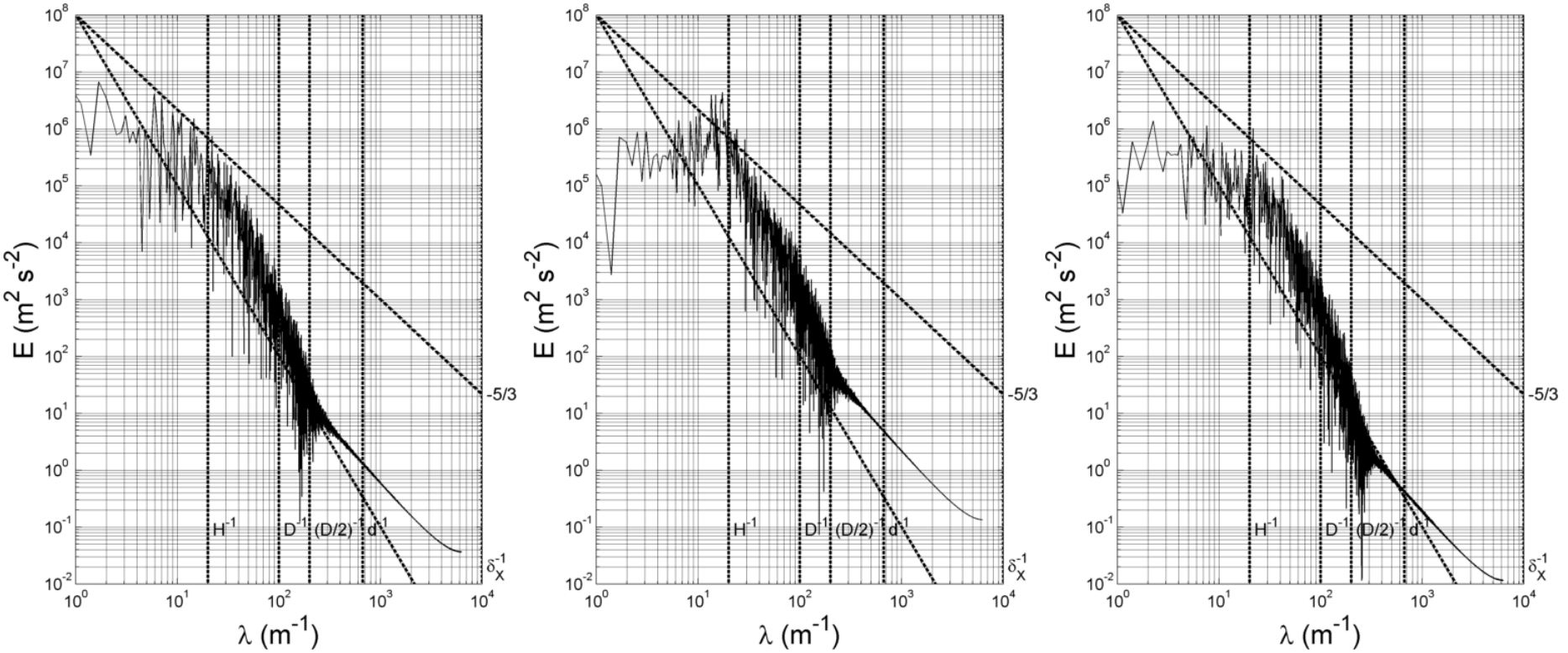

Figure C.19 – Power Spectra for v_x, v_y and v_z at Reynolds 200 in p_7

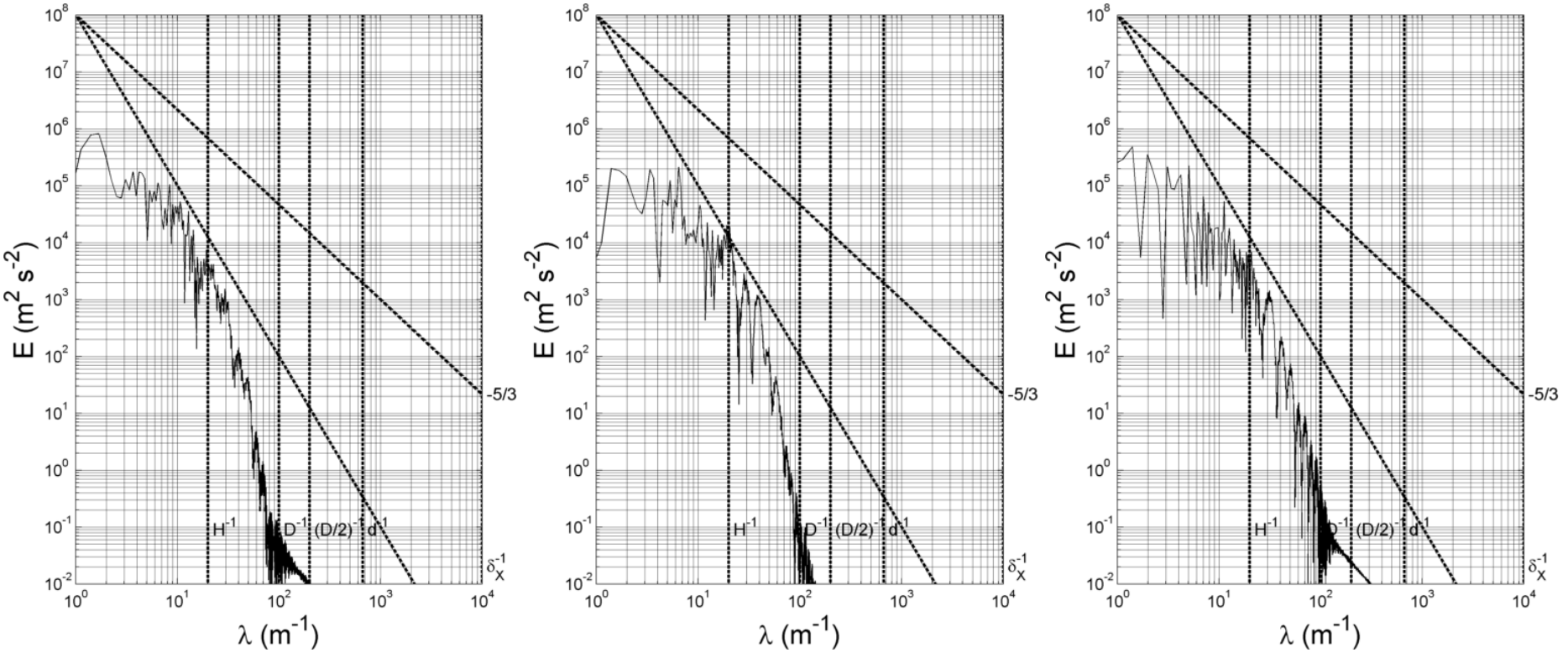

Figure C.20 – Power Spectra for v_x, v_y and v_z at Reynolds 200 in p_8

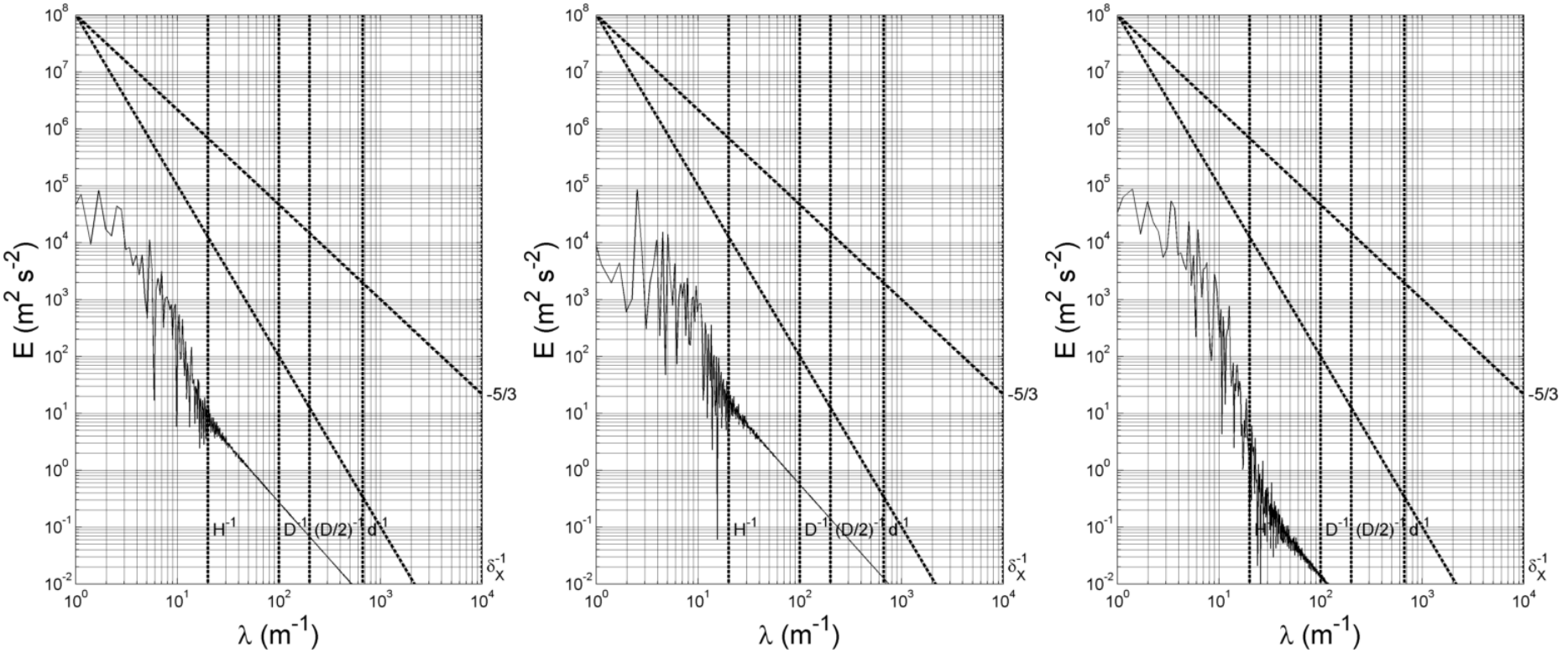

Figure C.21 – Power Spectra for v_x, v_y and v_z at Reynolds 200 in p_9

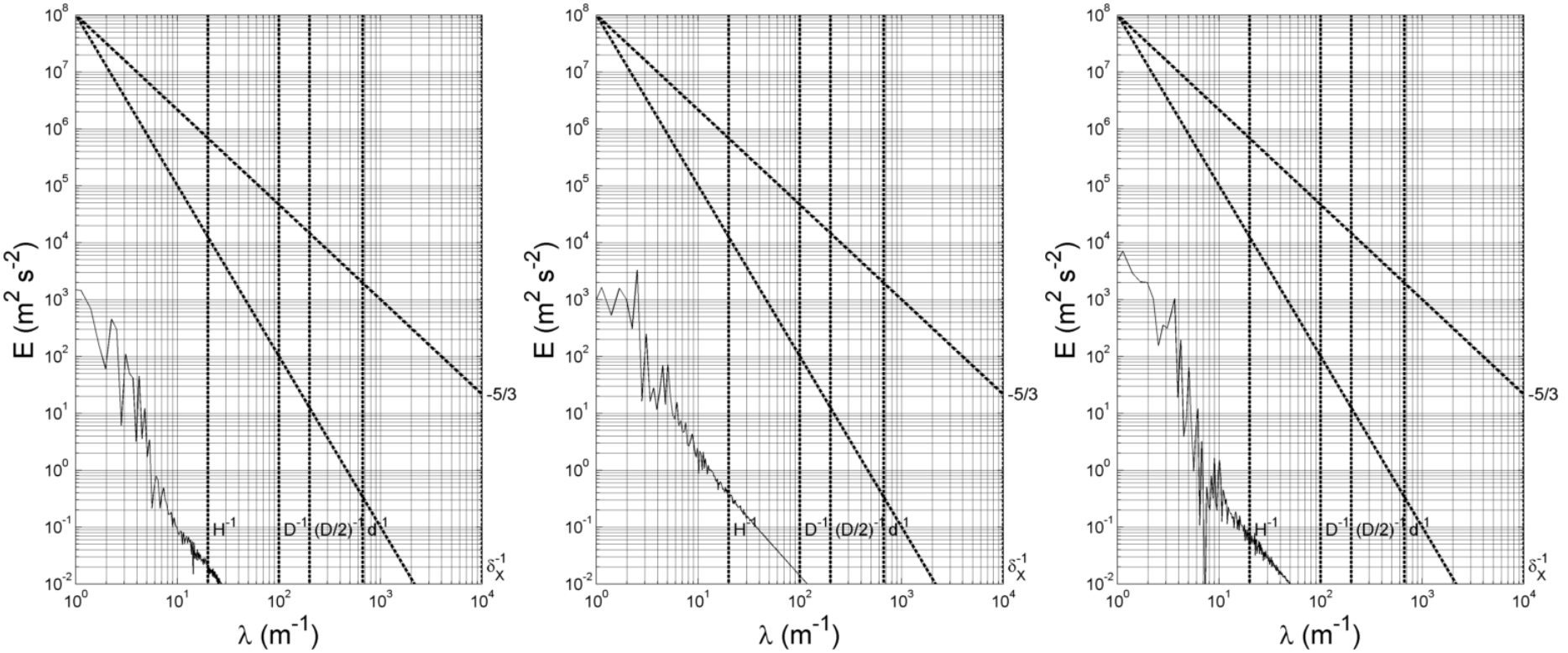

Figure C.22 – Power Spectra for v_x, v_y and v_z at Reynolds 200 in p_{10}

C.3 Reynolds 250

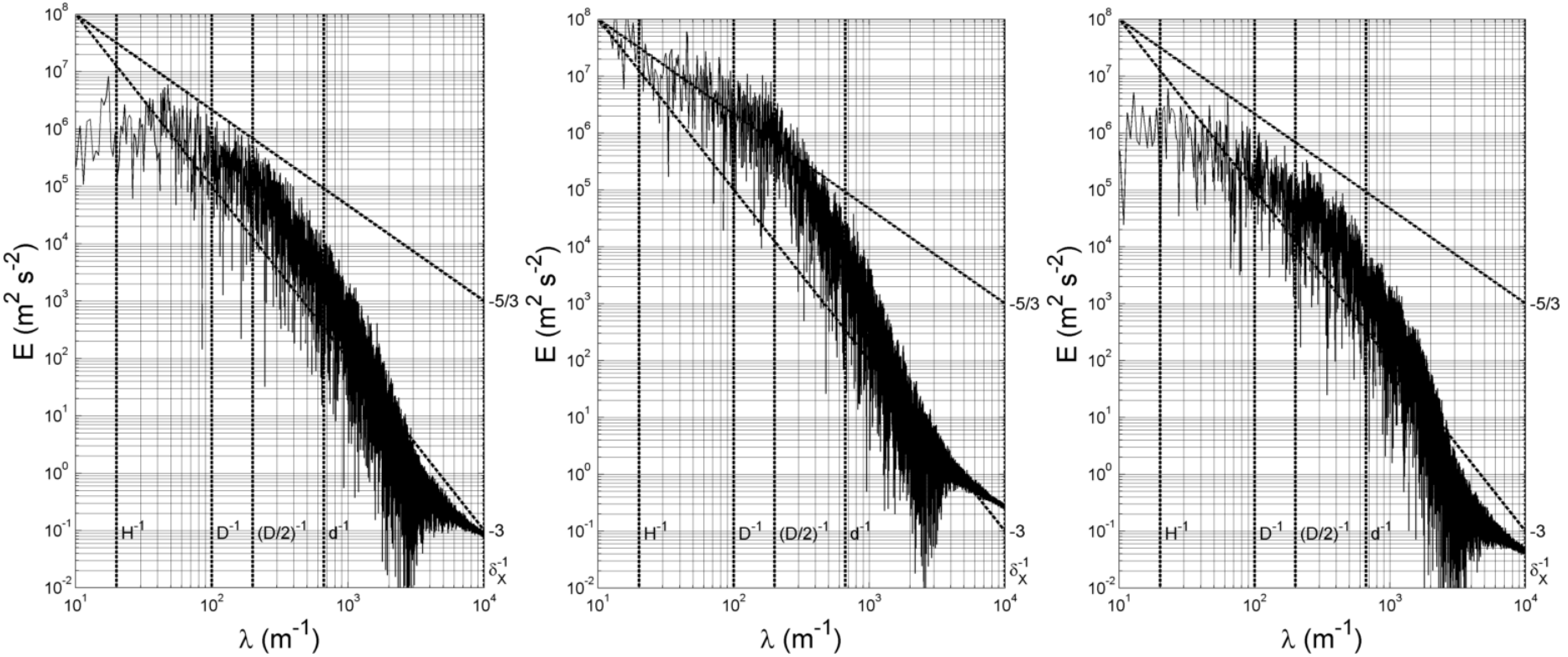

Figure C.23 – Power Spectra for v_x, v_y and v_z at Reynolds 250 in p_0

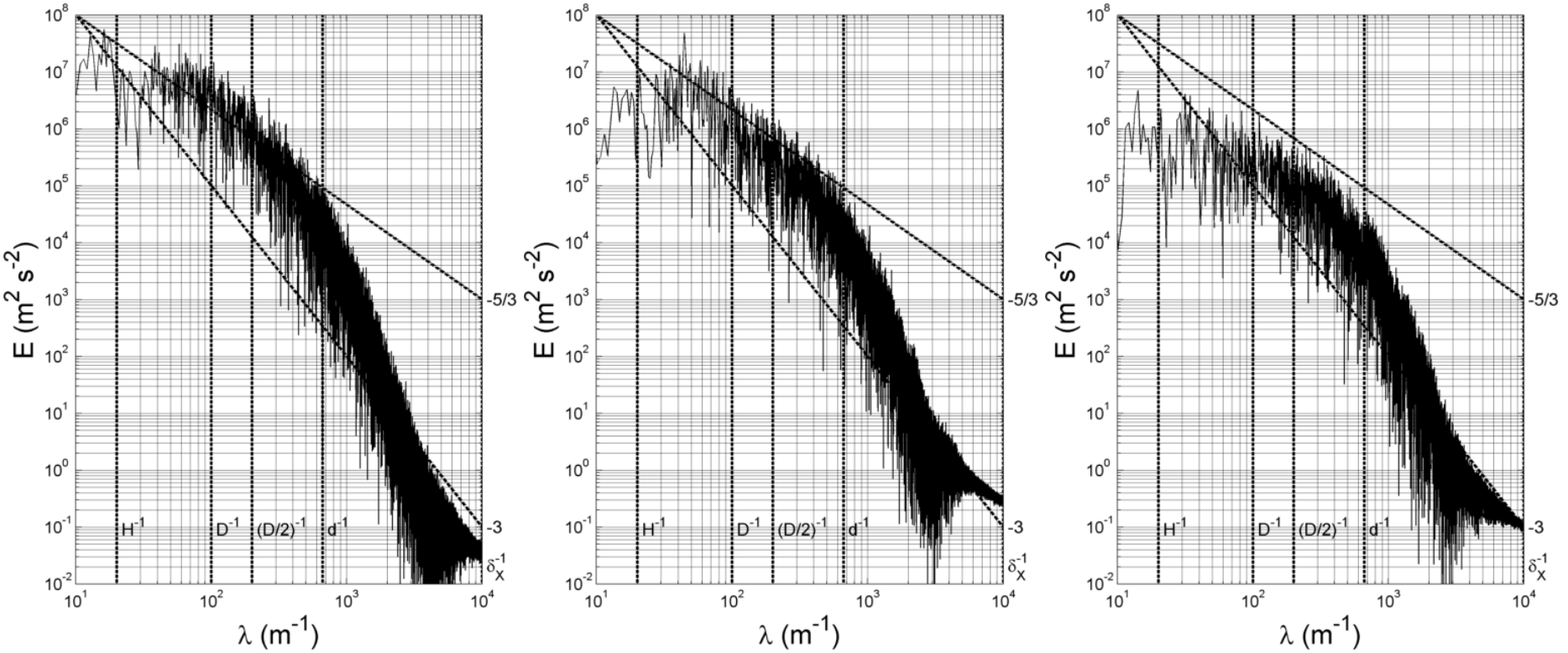

Figure C.24 – Power Spectra for v_x, v_y and v_z at Reynolds 250 in p_1

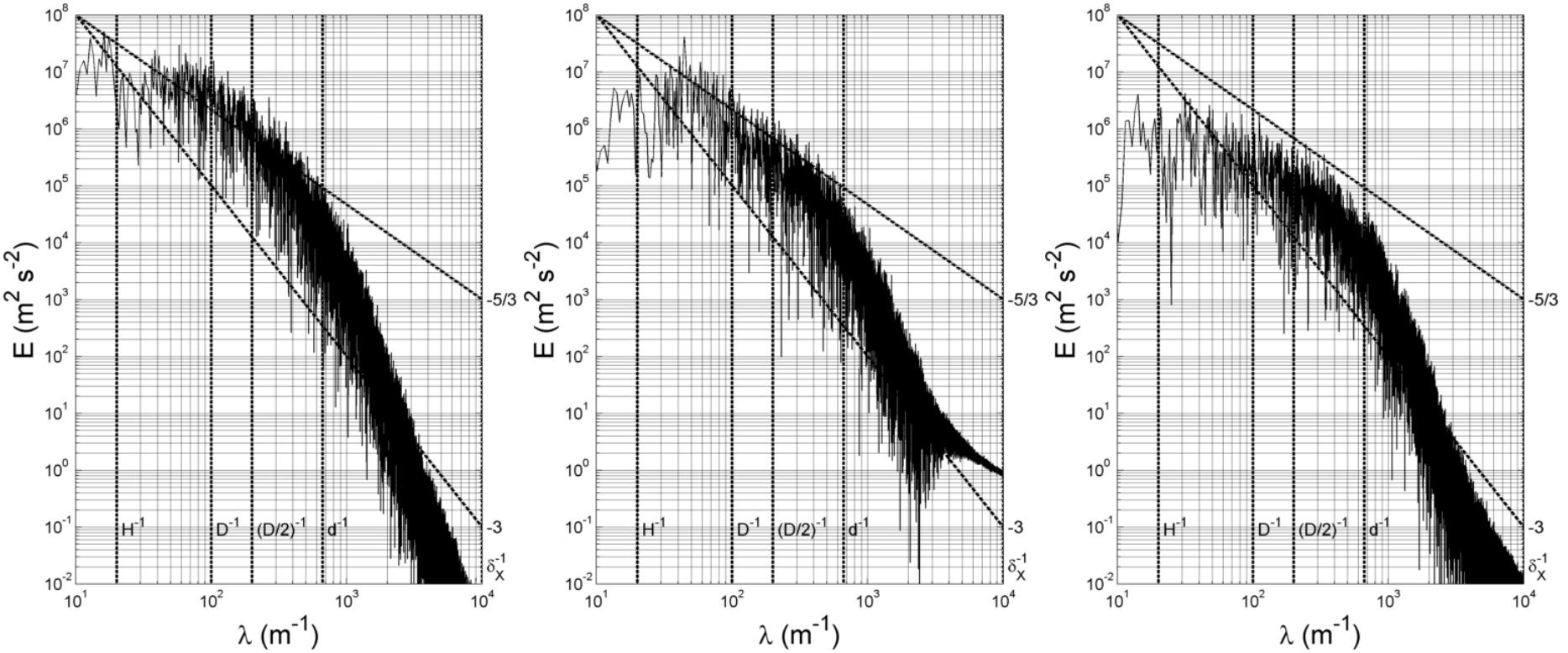

Figure C.25 – Power Spectra for v_x, v_y and v_z at Reynolds 250 in p_2

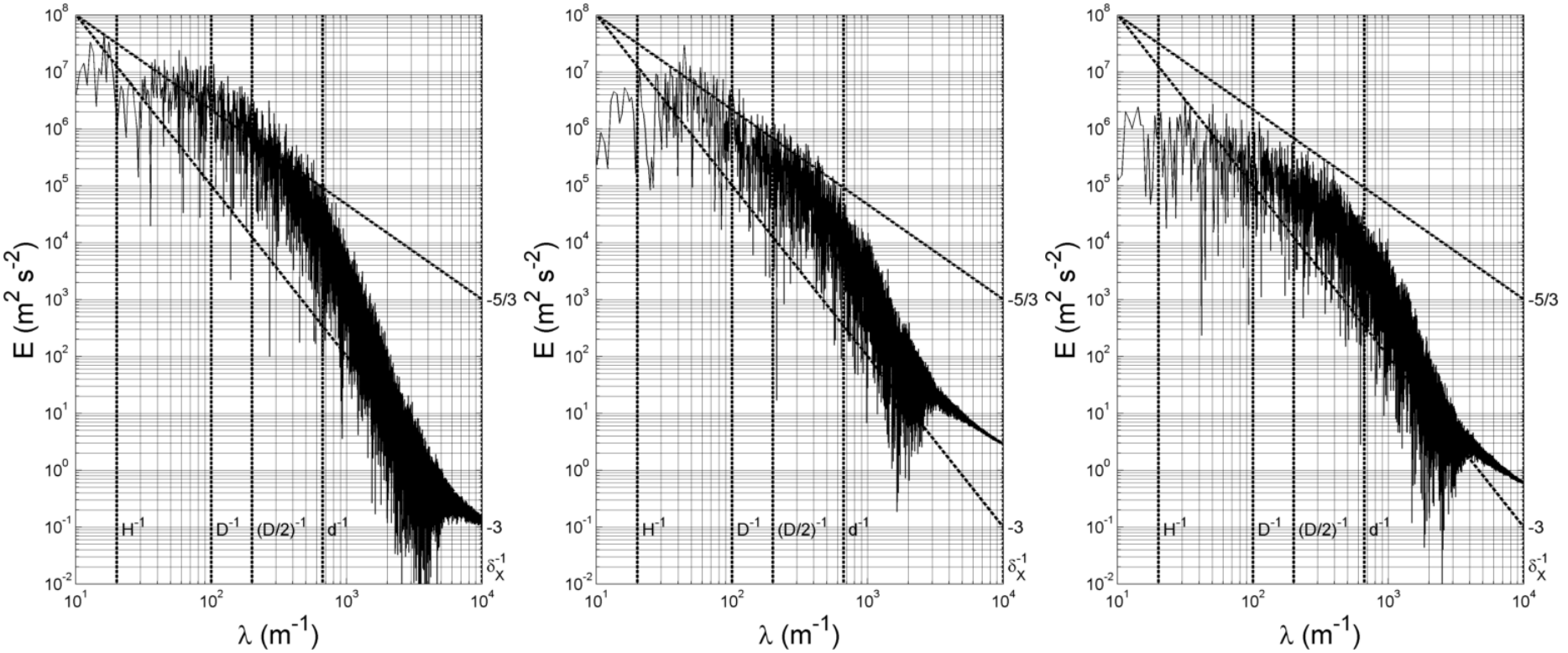

Figure C.26 – Power Spectra for v_x, v_y and v_z at Reynolds 250 in p_3

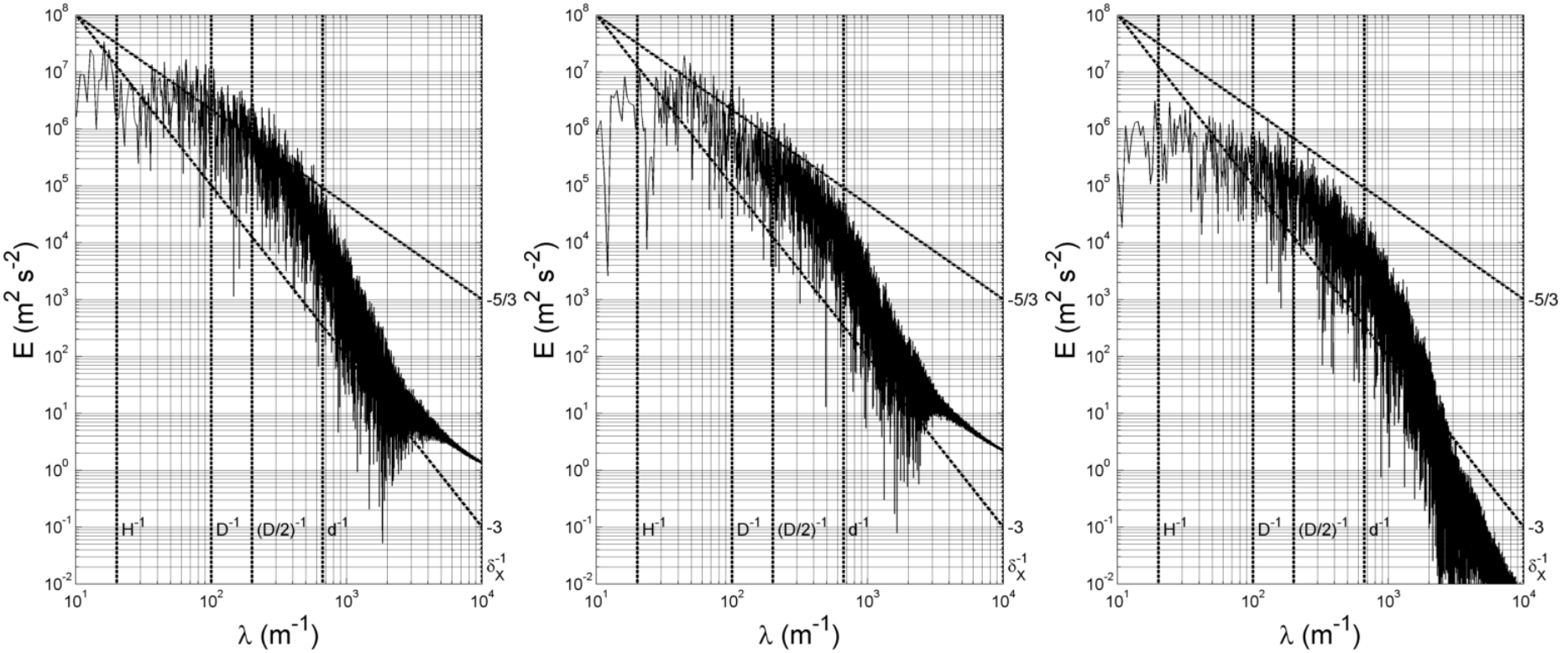

Figure C.27 – Power Spectra for v_x, v_y and v_z at Reynolds 250 in p_4

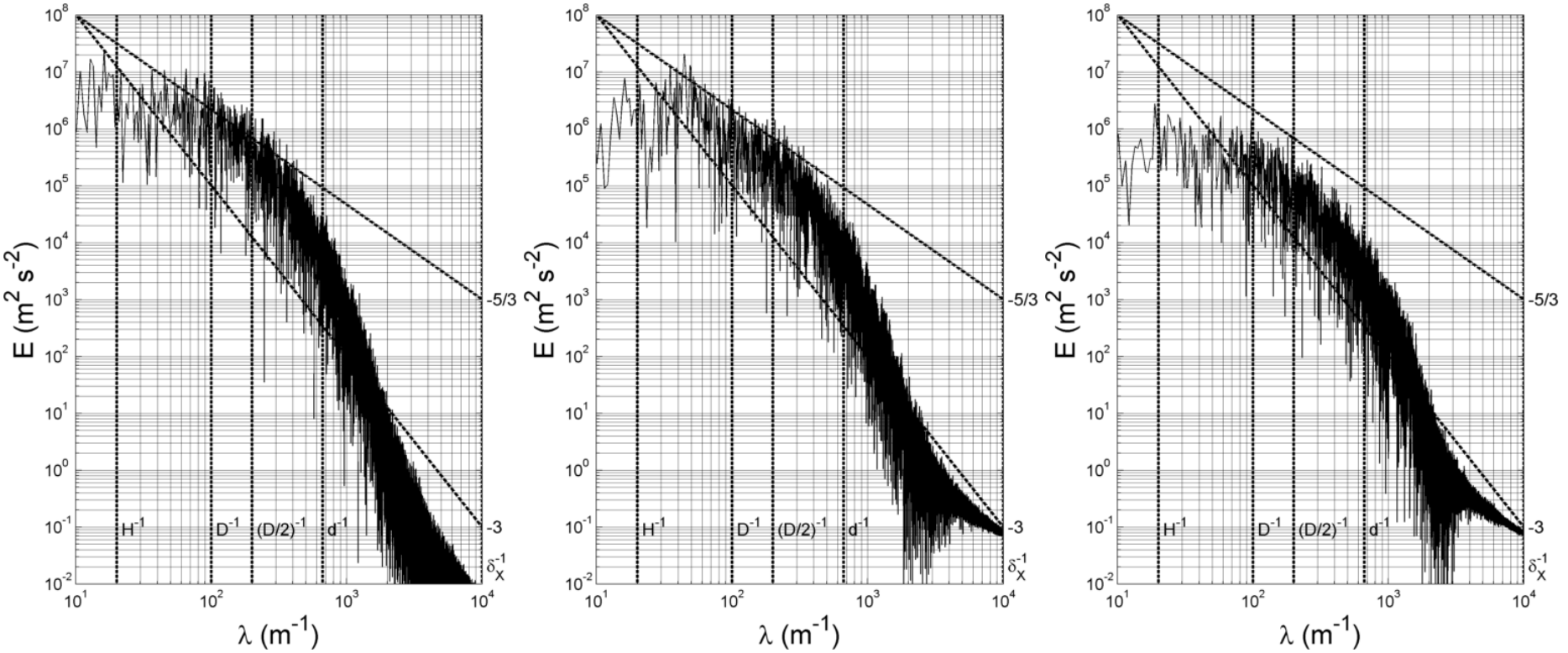

Figure C.28 – Power Spectra for v_x, v_y and v_z at Reynolds 250 in p_5

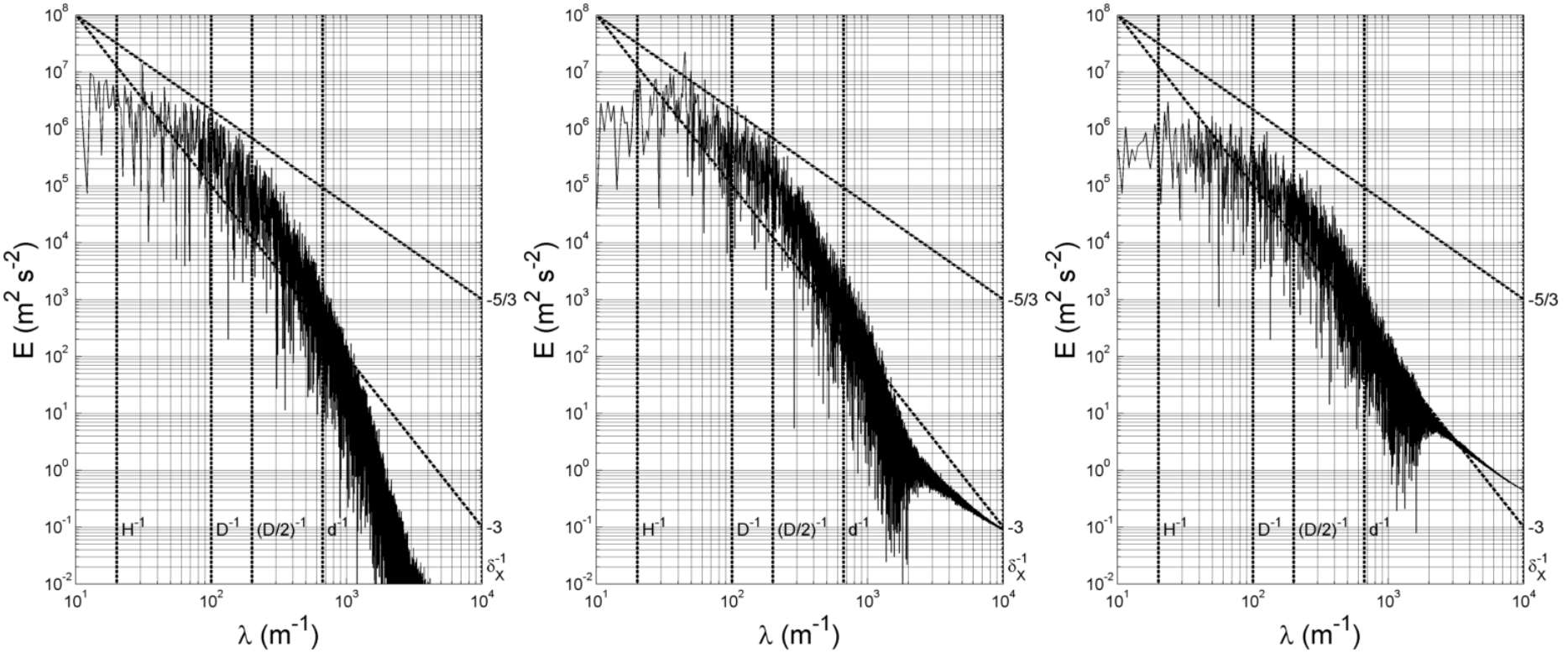

Figure C.29 – Power Spectra for v_x, v_y and v_z at Reynolds 250 in p_6

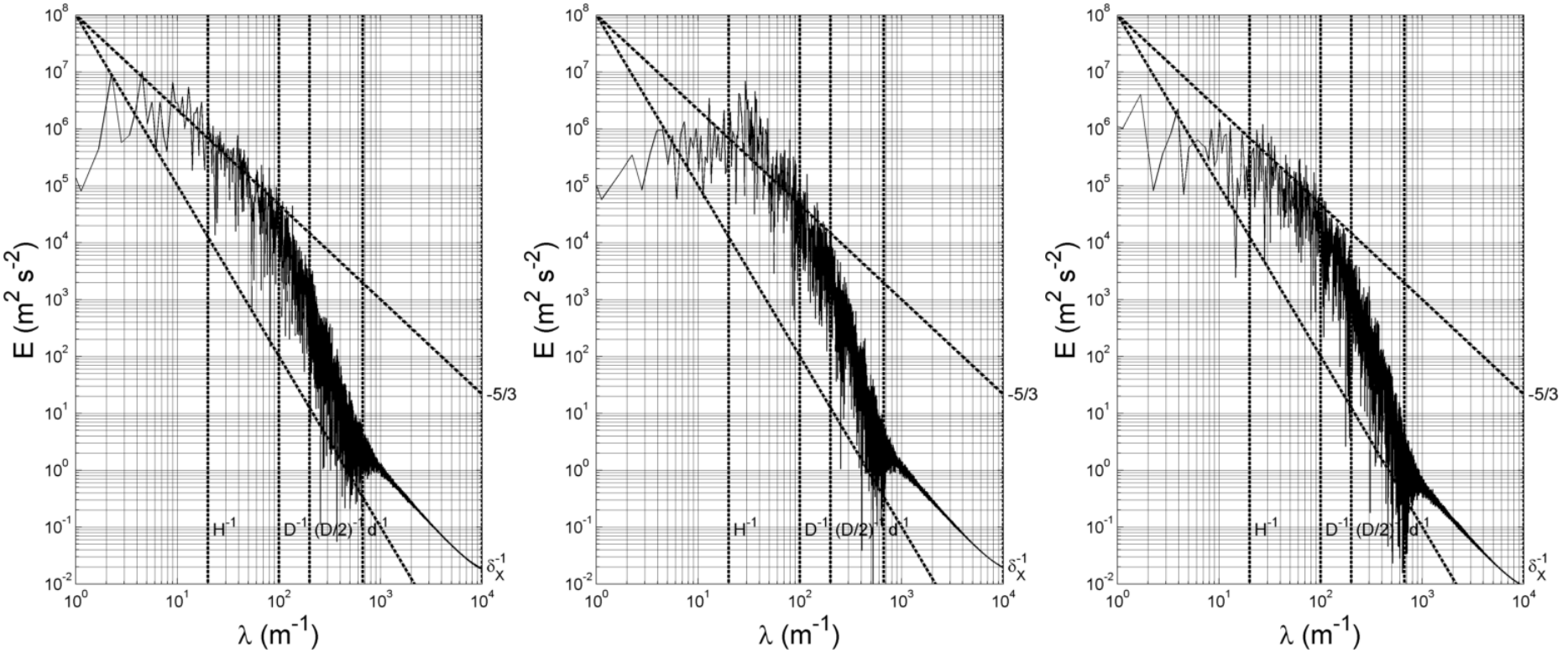

Figure C.30 – Power Spectra for v_x, v_y and v_z at Reynolds 250 in p_7

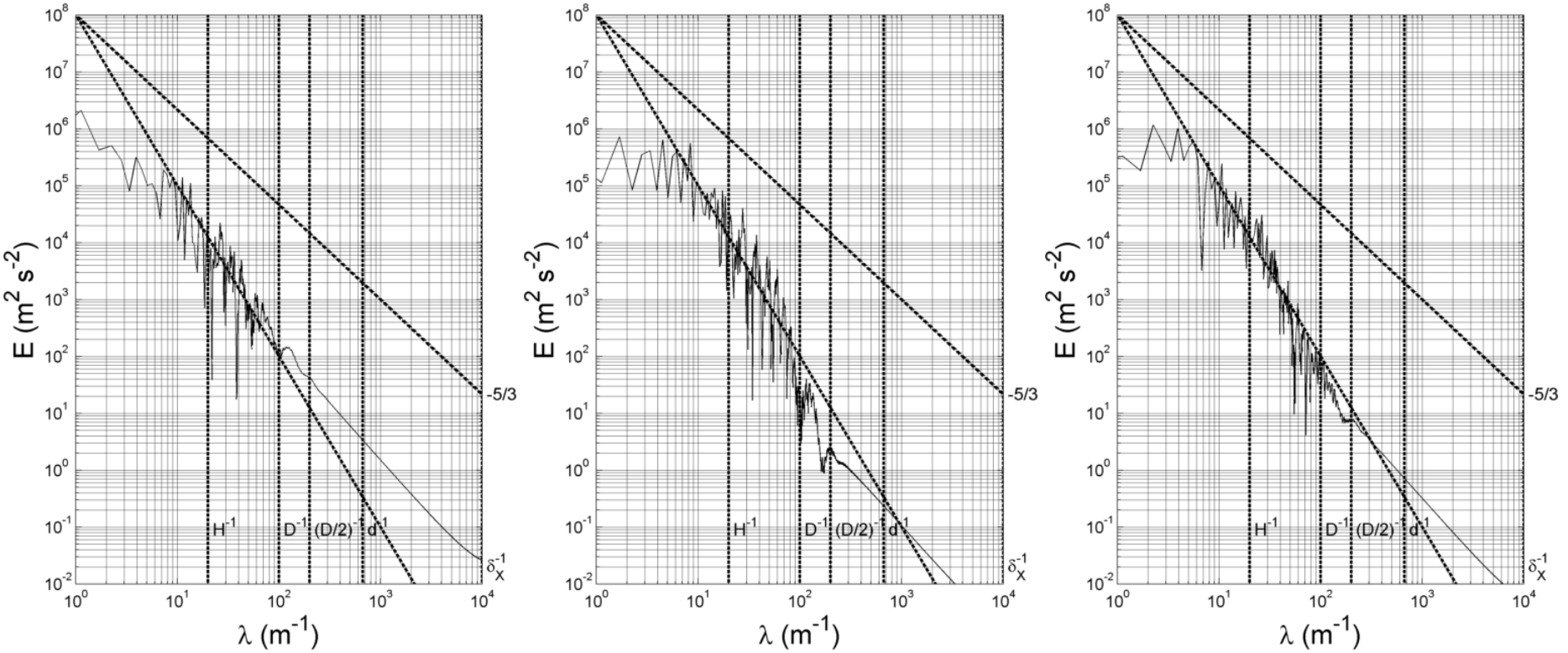

Figure C.31 – Power Spectra for v_x, v_y and v_z at Reynolds 250 in p_8

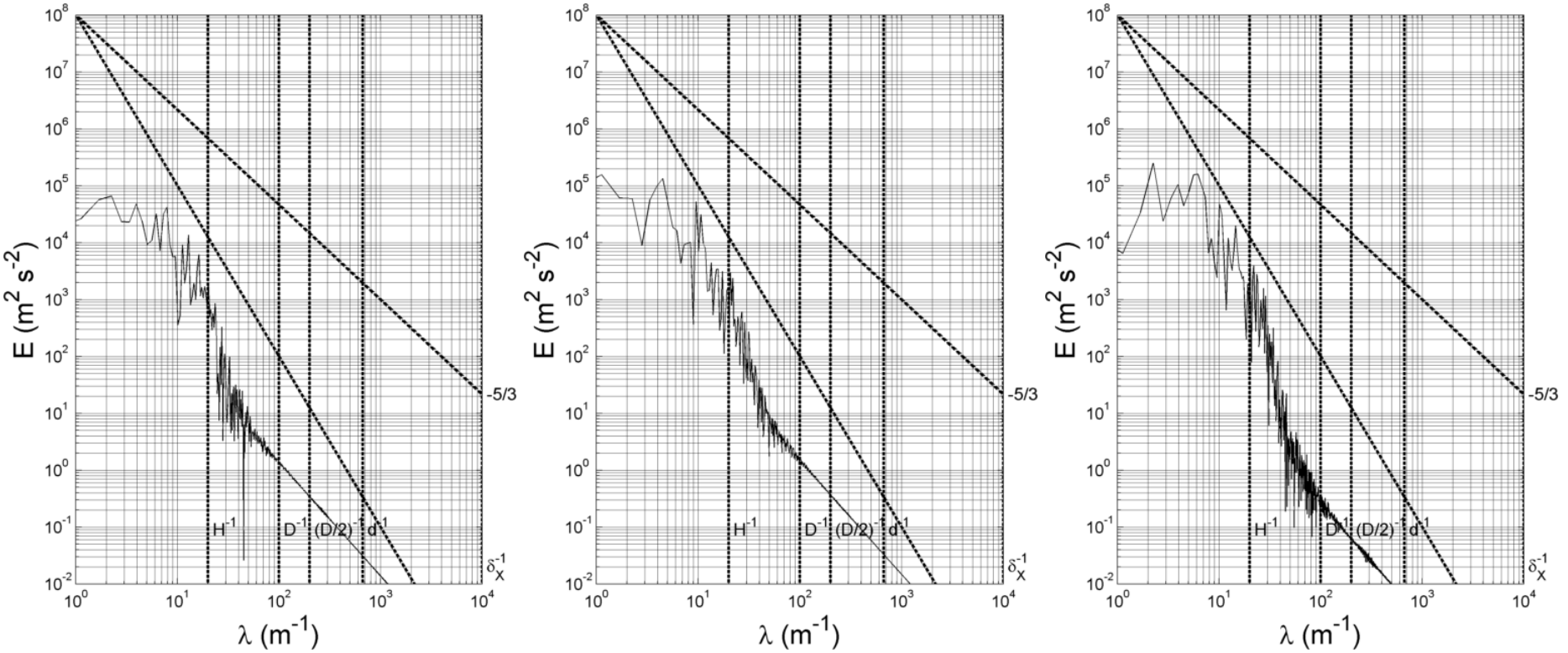

Figure C.32 – Power Spectra for v_x, v_y and v_z at Reynolds 250 in p_9

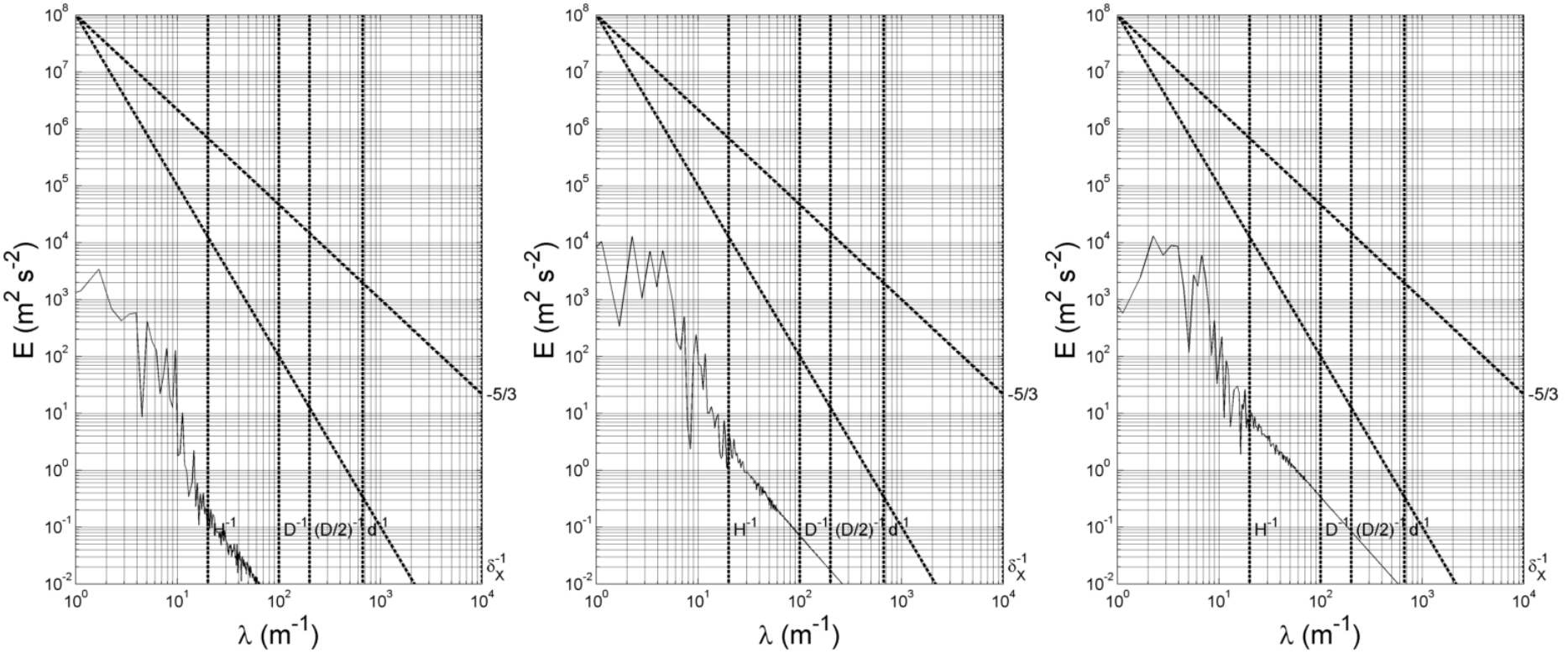

Figure C.33 – Power Spectra for v_x, v_y and v_z at Reynolds 250 in p_{10}

C.4 Reynolds 300

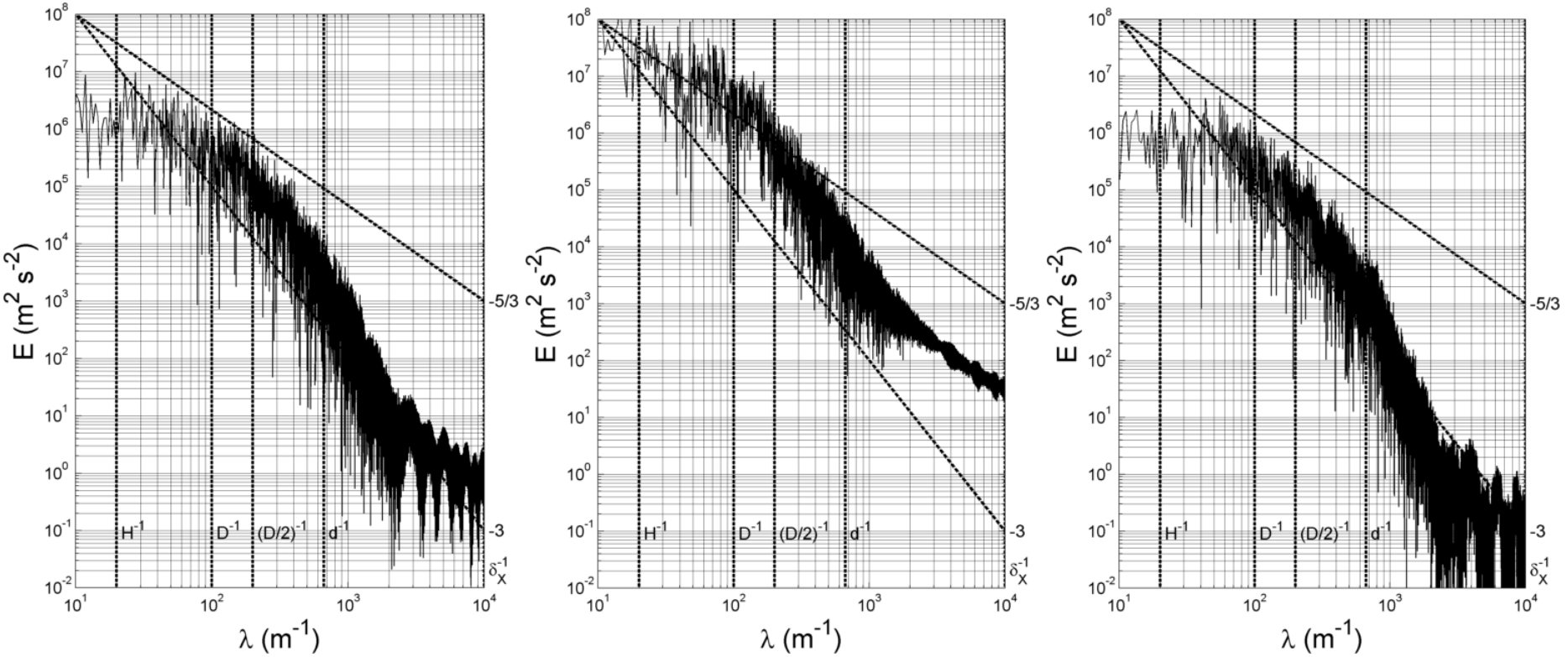

Figure C.34 – Power Spectra for v_x, v_y and v_z at Reynolds 300 in p_0

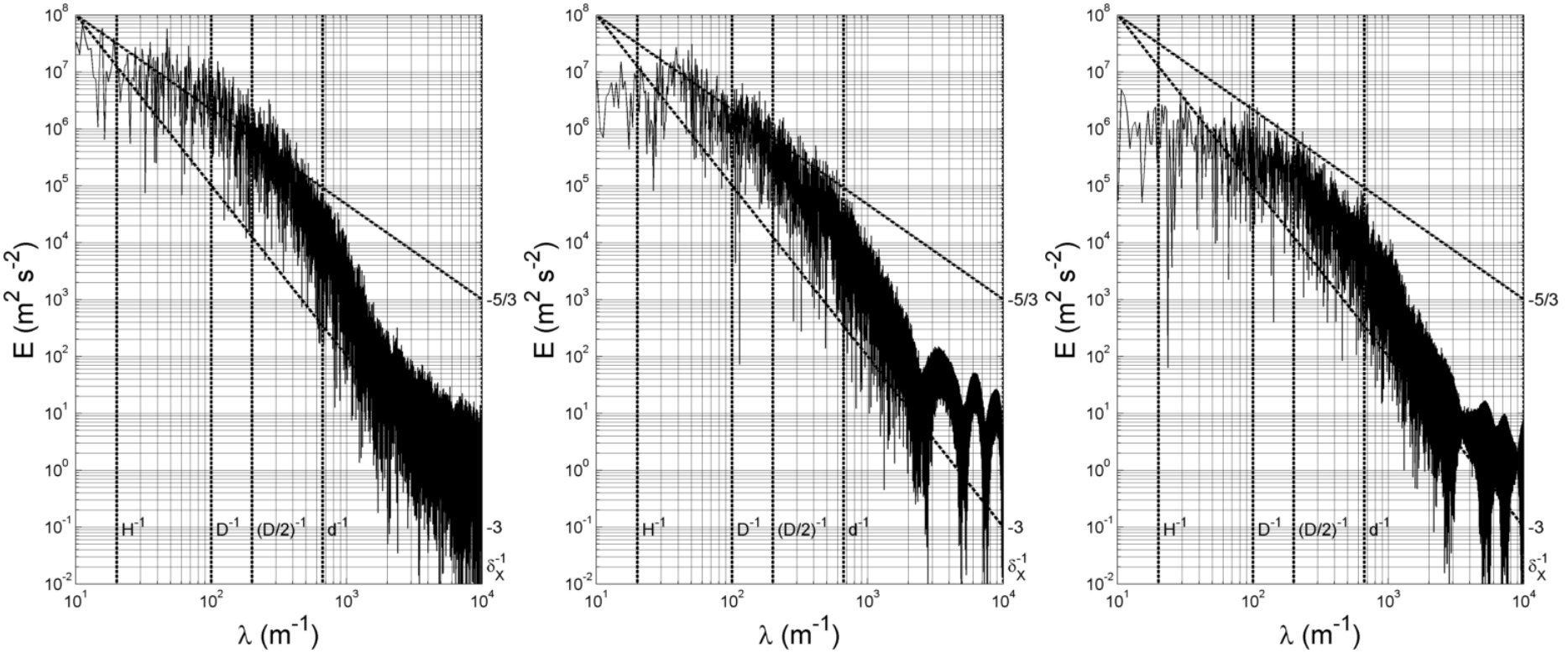

Figure C.35 – Power Spectra for v_x, v_y and v_z at Reynolds 300 in p_1

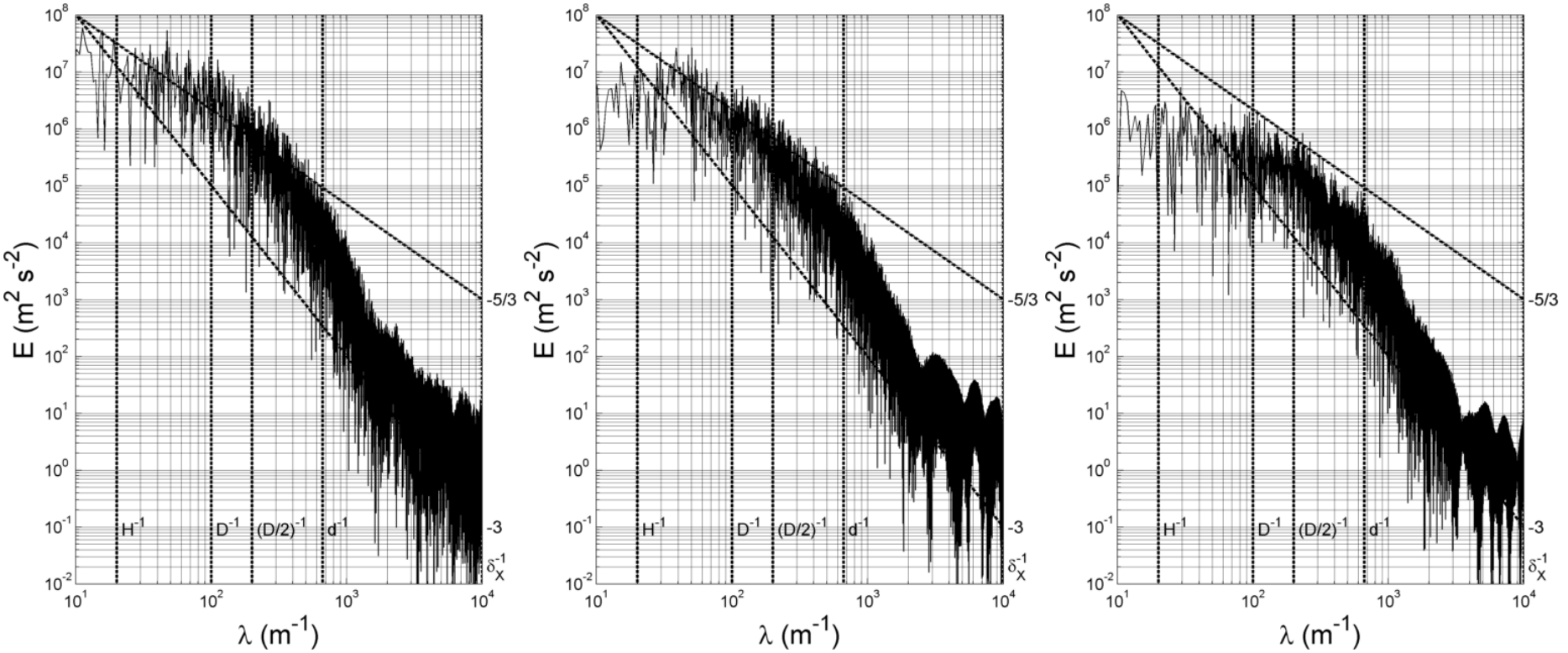

Figure C.36 – Power Spectra for v_x, v_y and v_z at Reynolds 300 in p_2

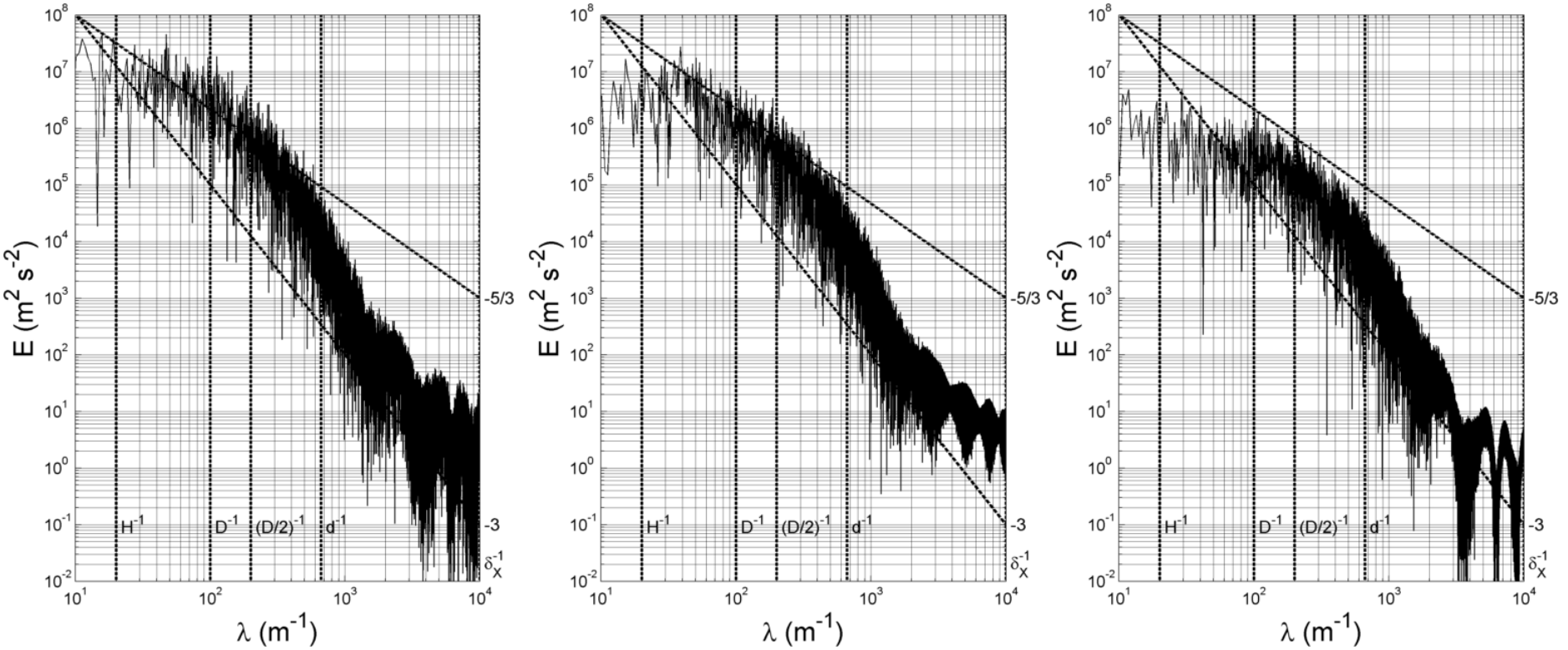

Figure C.37 – Power Spectra for v_x, v_y and v_z at Reynolds 300 in p_3

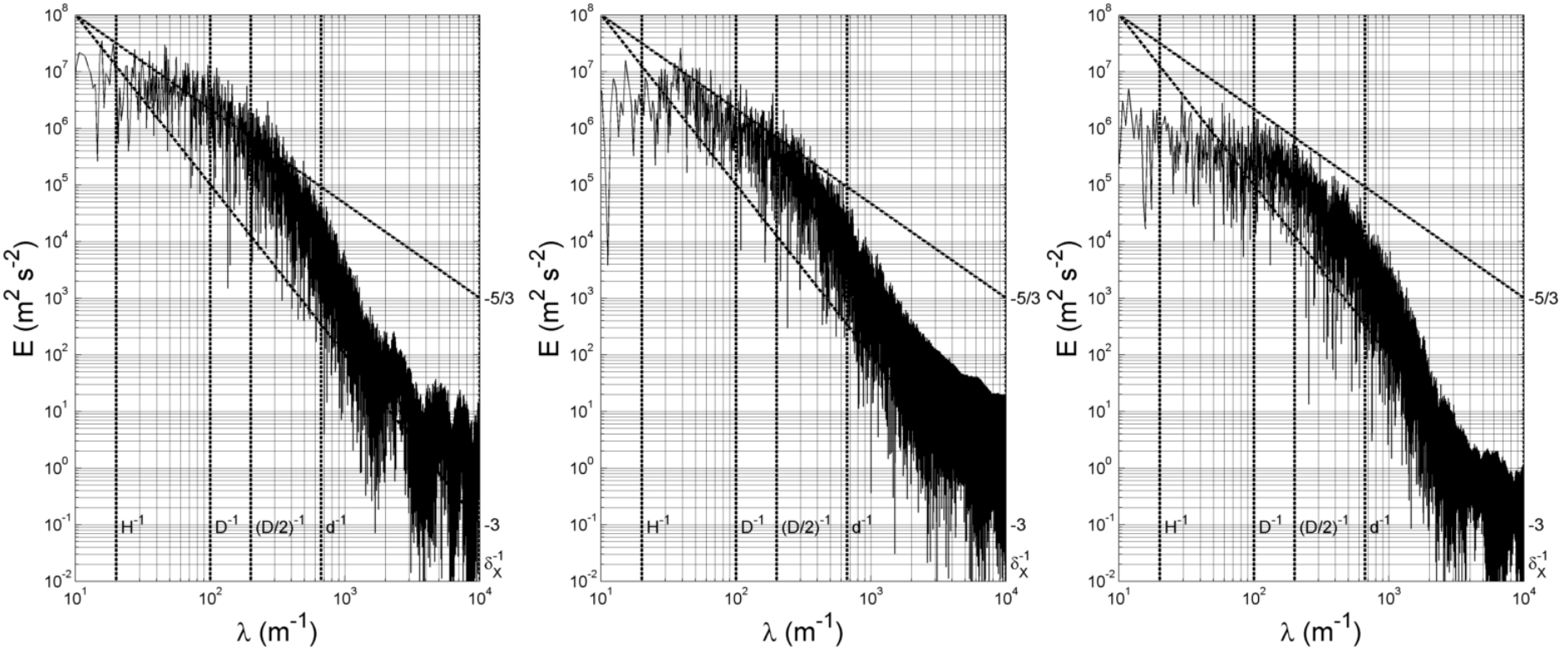

Figure C.38 – Power Spectra for v_x, v_y and v_z at Reynolds 300 in p_4

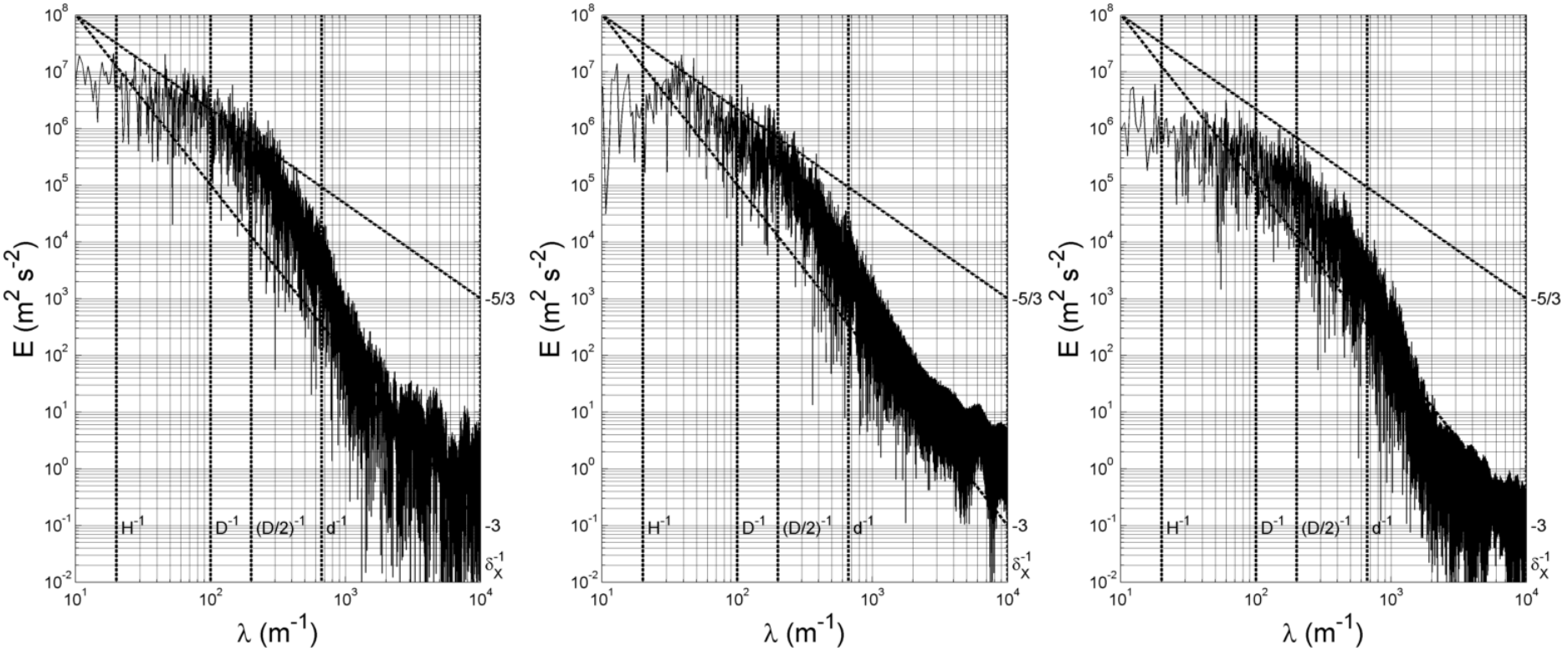

Figure C.39 – Power Spectra for v_x, v_y and v_z at Reynolds 300 in p_5

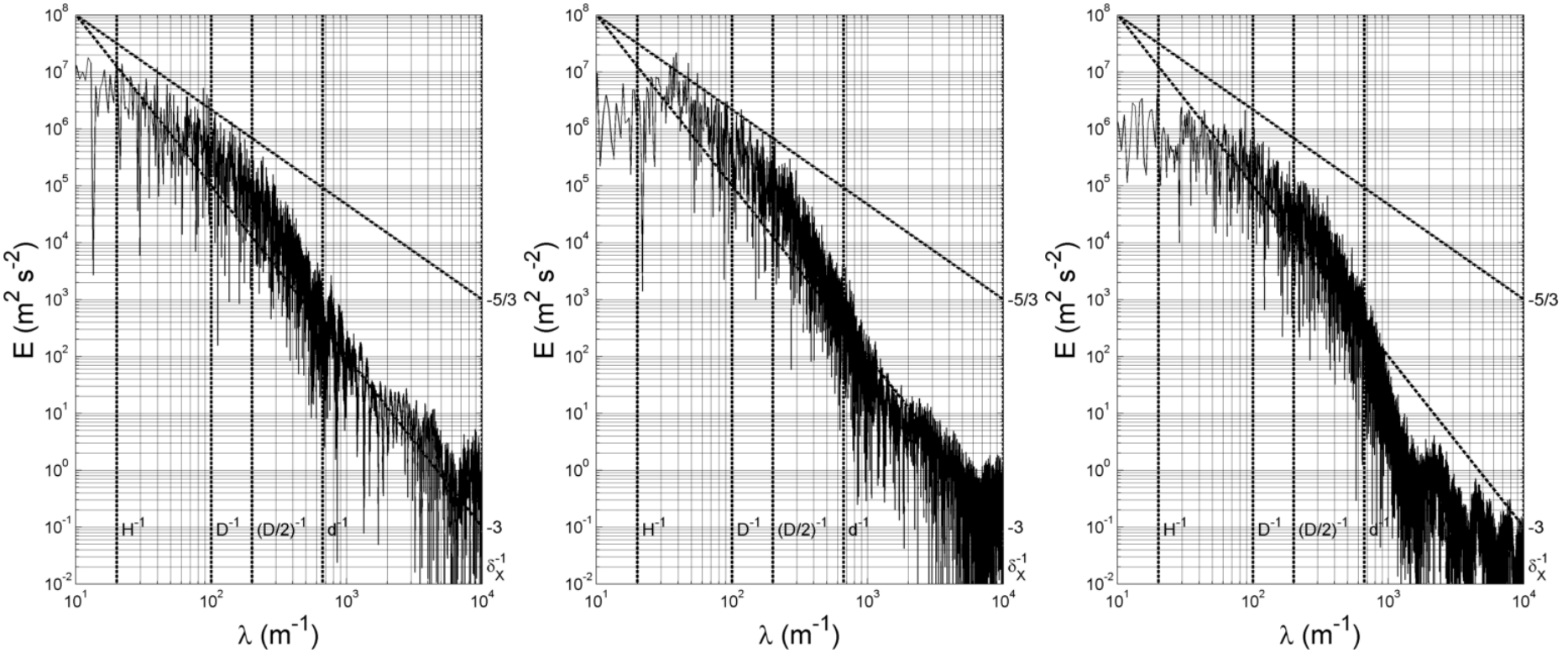

Figure C.40 – Power Spectra for v_x, v_y and v_z at Reynolds 300 in p_6

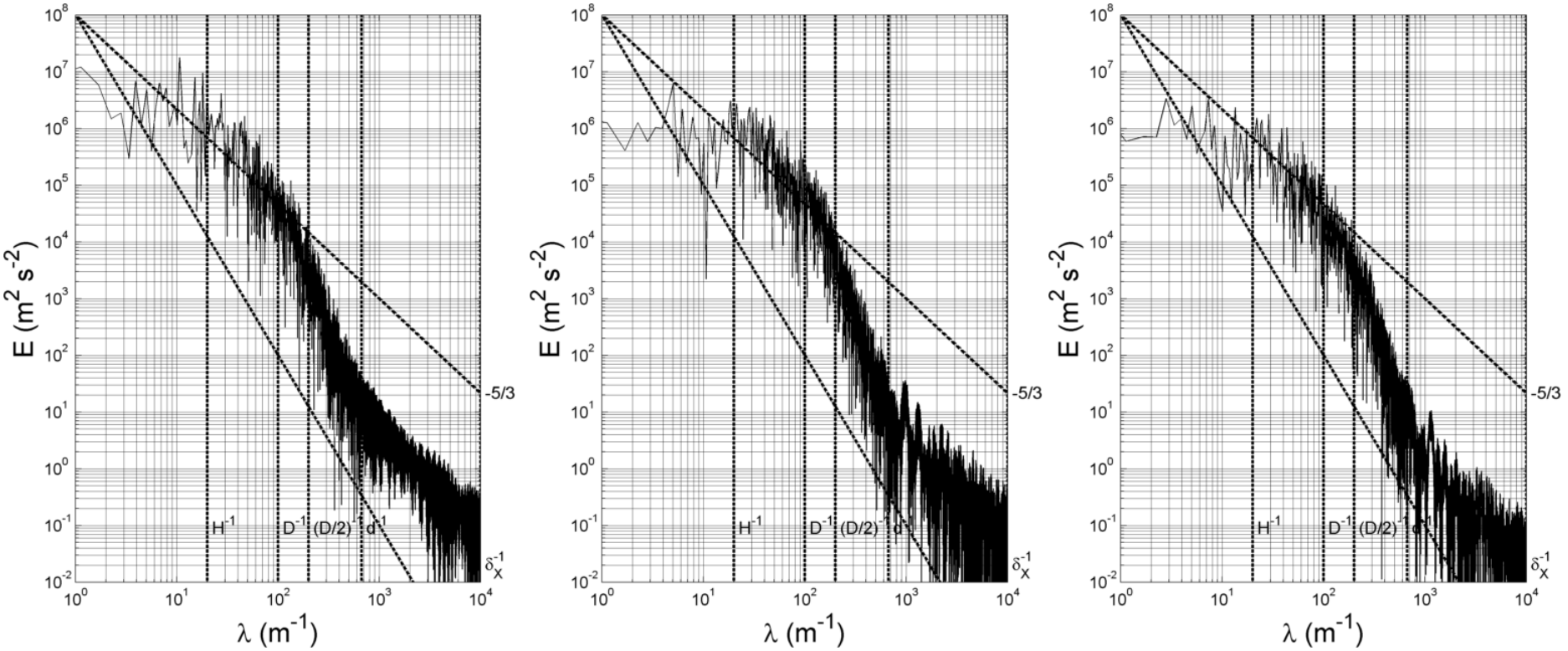

Figure C.41 – Power Spectra for v_x, v_y and v_z at Reynolds 300 in p_7

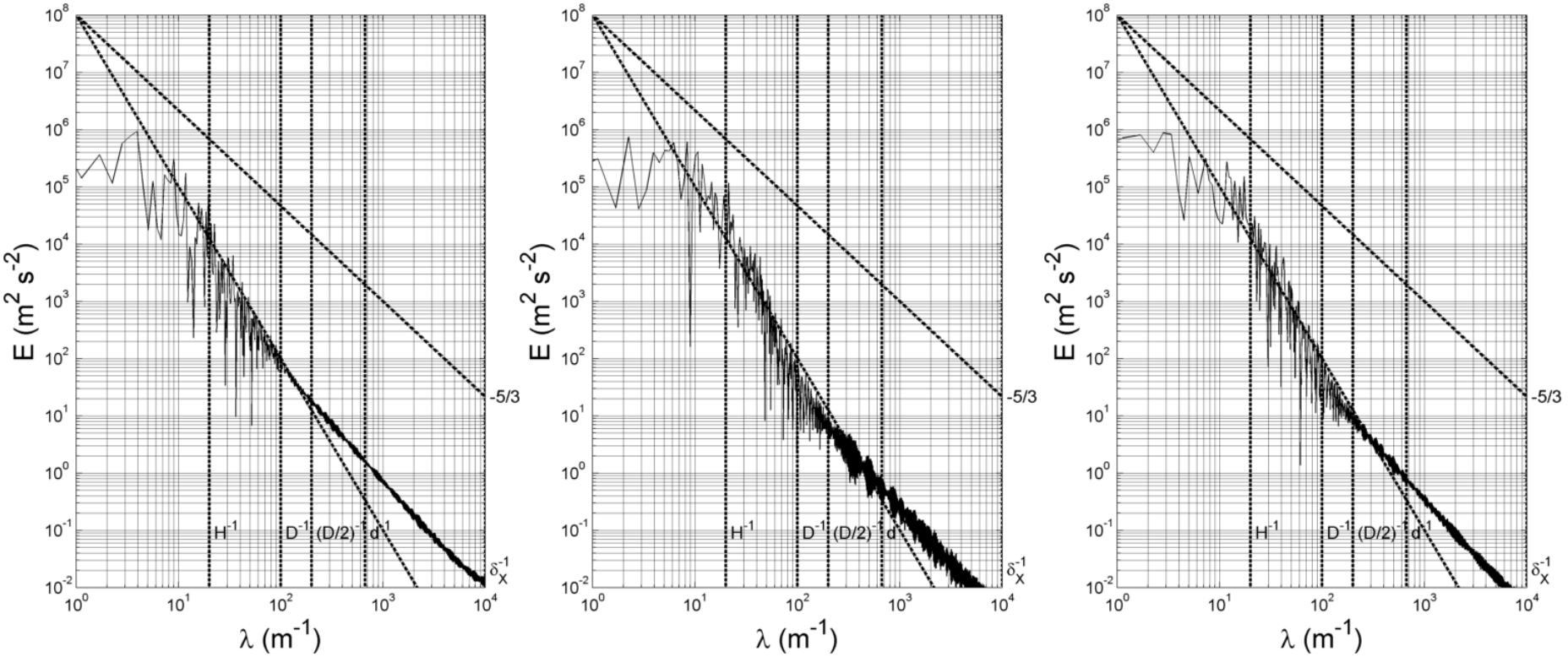

Figure C.42 – Power Spectra for v_x, v_y and v_z at Reynolds 300 in p_8

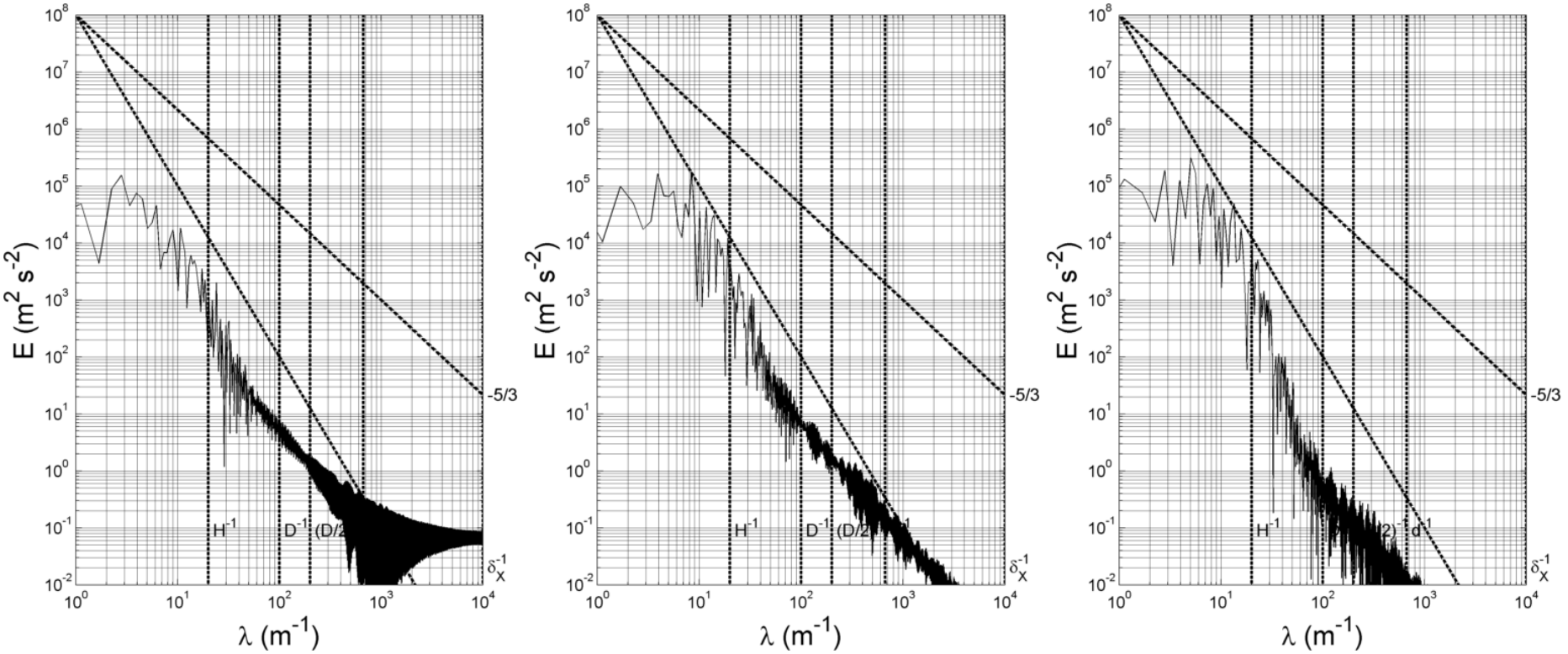

Figure C.43 – Power Spectra for v_x, v_y and v_z at Reynolds 300 in p_9

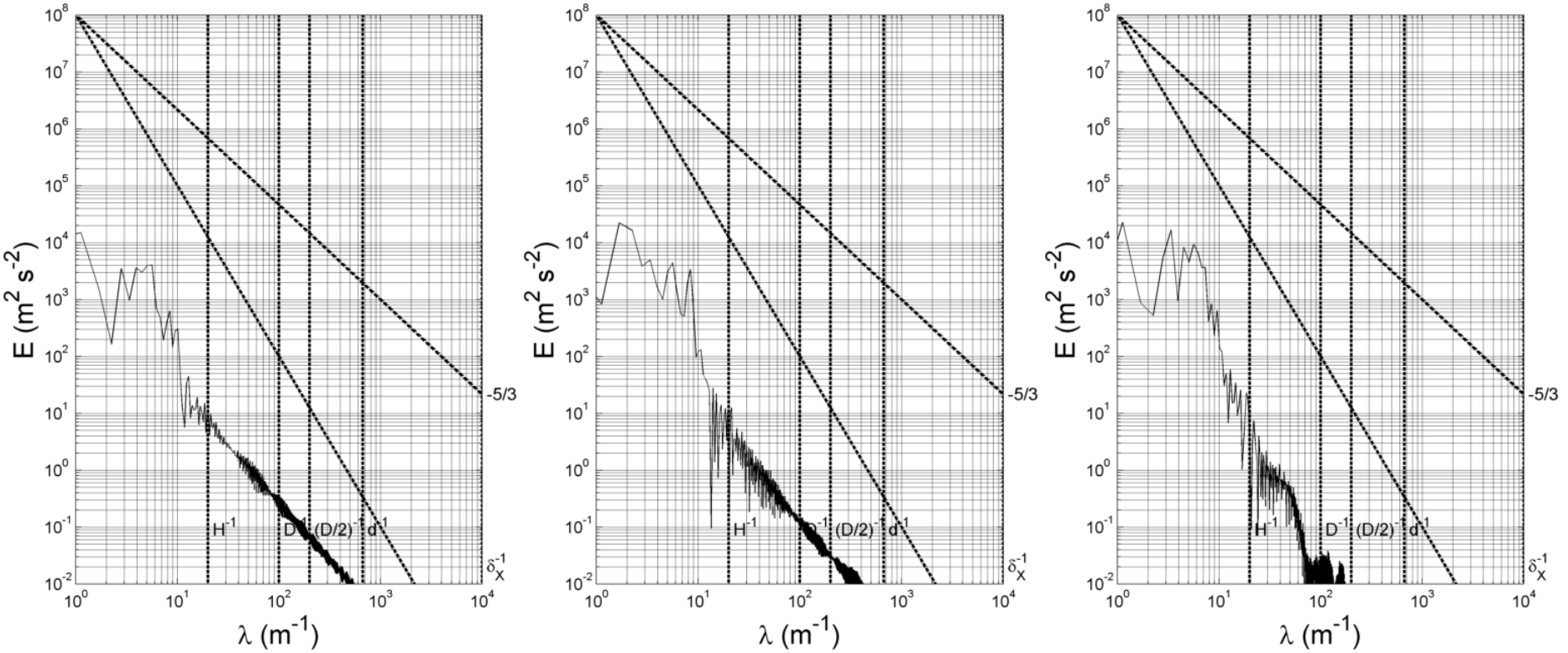

Figure C.44 – Power Spectra for v_x, v_y and v_z at Reynolds 300 in p_{10}

D Average flow field visualization for different viscosity ratios

D.1 Reynolds 72

$\phi_K = 0.0460$

$\phi_K = 0.0685$

$\phi_K = 0.1526$

$\phi_K = 0.3073$

Figure D.1-Average flow field visualization, using PLIF, for Reynolds 72

$\phi_K = 0.5741$

$\phi_K = 0.8201$

$\phi_K = 1.1294$

$\phi_K = 1.6707$

Figure D.2-Average flow field visualization, using PLIF, for Reynolds 72

$\phi_K = 1.9473$

$\phi_K = 2.4825$

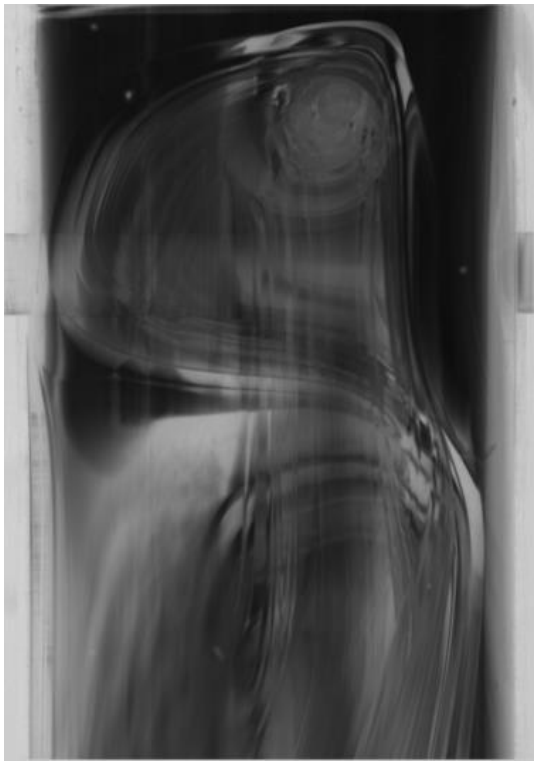

$\phi_K = 3.3024$

$\phi_K = 3.6071$

Figure D.3-Average flow field visualization, using PLIF, for Reynolds 72

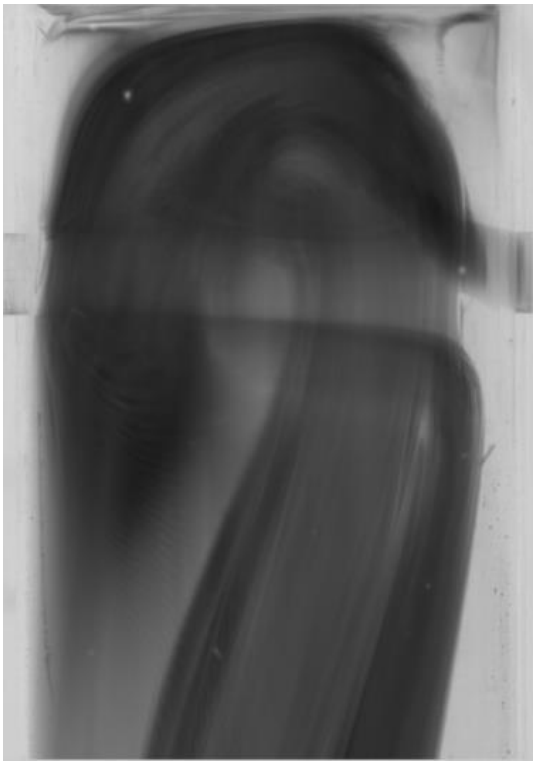

$\phi_K = 4.3171$

$\phi_K = 6.5673$

$\phi_K = 7.1909$

Figure D.4-Average flow field visualization, using PLIF, for Reynolds 72

D.2 Reynolds 81

$\phi_K = 0.0185$

$\phi_K = 0.0438$

$\phi_K = 0.1048$

$\phi_K = 0.1422$

Figure D.5-Average flow field visualization, using PLIF, for Reynolds 81

$\phi_K = 0.3358$

$\phi_K = 0.4181$

$\phi_K = 0.5954$

$\phi_K = 0.9136$

Figure D.6-Average flow field visualization, using PLIF, for Reynolds 81

$\phi_K = 1.0786$

$\phi_K = 1.3867$

$\phi_K = 1.7419$

$\phi_K = 2.3349$

Figure D.7-Average flow field visualization, using PLIF, for Reynolds 81

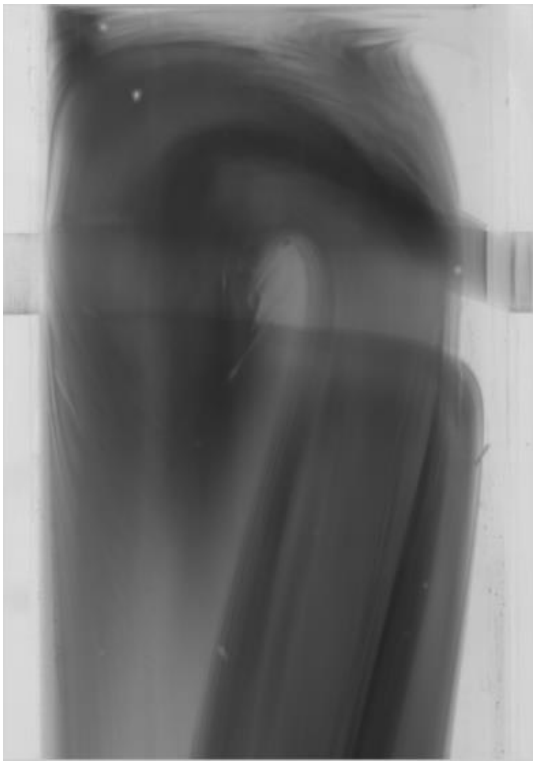

$\phi_K = 2.7144$

$\phi_K = 3.0808$

$\phi_K = 10.0679$

Figure D.8-Average flow field visualization, using PLIF, for Reynolds 81

D.3 Reynolds 118

$\phi_K = 0.0097$

$\phi_K = 0.0277$

$\phi_K = 0.0572$

$\phi_K = 0.1052$

Figure D.9-Average flow field visualization, using PLIF, for Reynolds 118

$\phi_K = 0.2027$

$\phi_K = 0.2502$

$\phi_K = 0.2830$

$\phi_K = 0.4255$

Figure D.10-Average flow field visualization, using PLIF, for Reynolds 118

$\phi_K = 0.6754$

$\phi_K = 0.6785$

$\phi_K = 0.8940$

$\phi_K = 1.3266$

Figure D.11-Average flow field visualization, using PLIF, for Reynolds 118

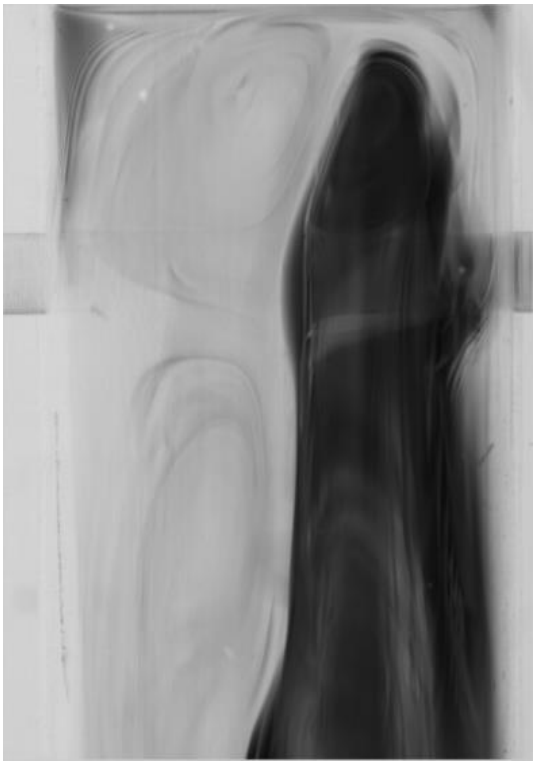

$\phi_K = 1.7358$

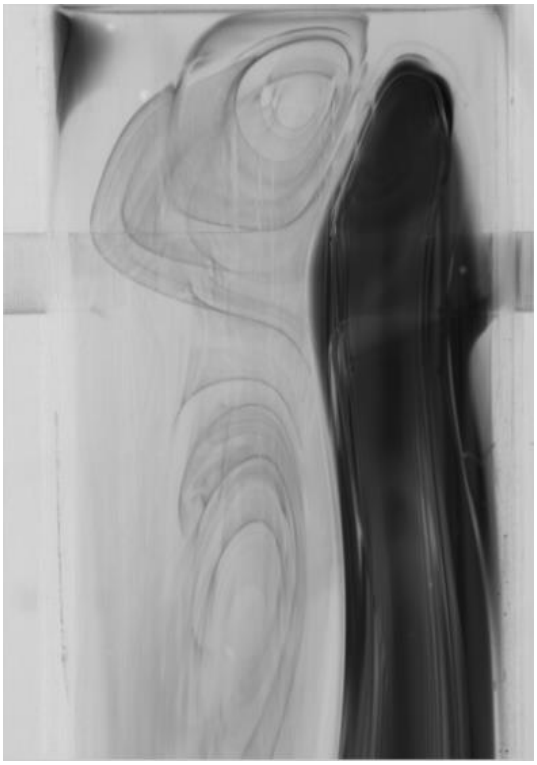

$\phi_K = 2.0207$

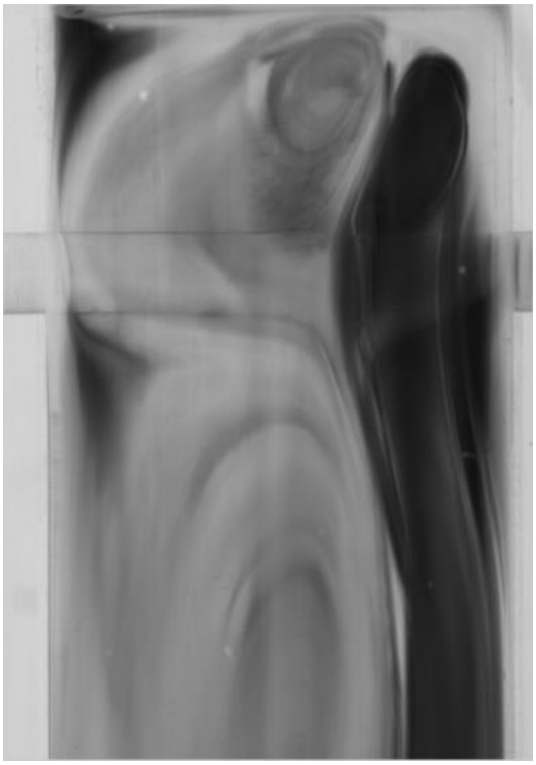

$\phi_K = 1.9620$

$\phi_K = 2.4638$

Figure D.12-Average flow field visualization, using PLIF, for Reynolds 118

$\phi_K = 3.3944$

Figure D.13-Average flow field visualization, using PLIF, for Reynolds 118

D.4 Reynolds 138

$\phi_K = 0.0669$

$\phi_K = 0.1092$

$\phi_K = 0.1815$

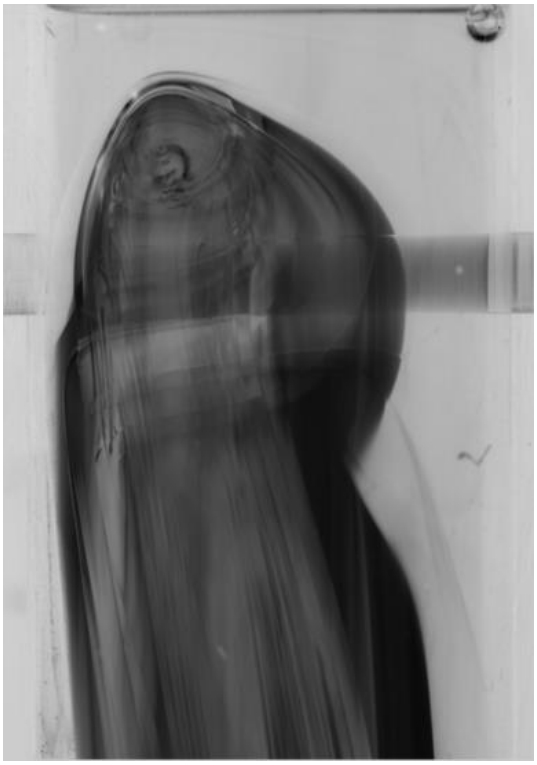

$\phi_K = 0.2391$

Figure D.14-Average flow field visualization, using PLIF, for Reynolds 138

$\phi_K = 0.3311$

$\phi_K = 0.4049$

$\phi_K = 0.4930$

$\phi_K = 0.7355$

Figure D.15-Average flow field visualization, using PLIF, for Reynolds 138

$\phi_K = 0.8783$

$\phi_K = 0.9295$

$\phi_K = 1.1449$

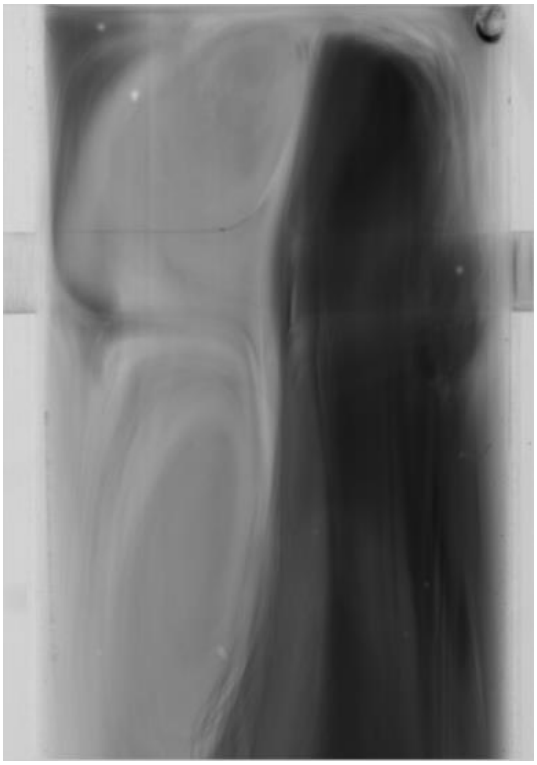

$\phi_K = 1.4497$

Figure D.16-Average flow field visualization, using PLIF, for Reynolds 138

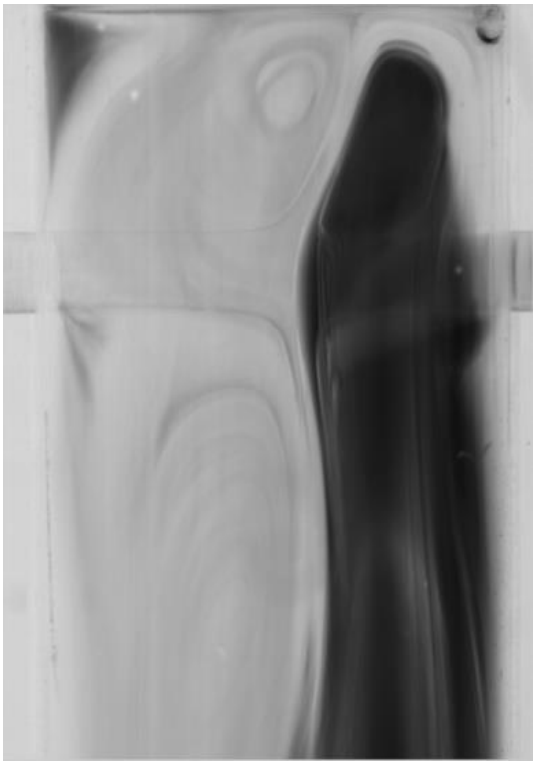

$\phi_K = 1.8520$

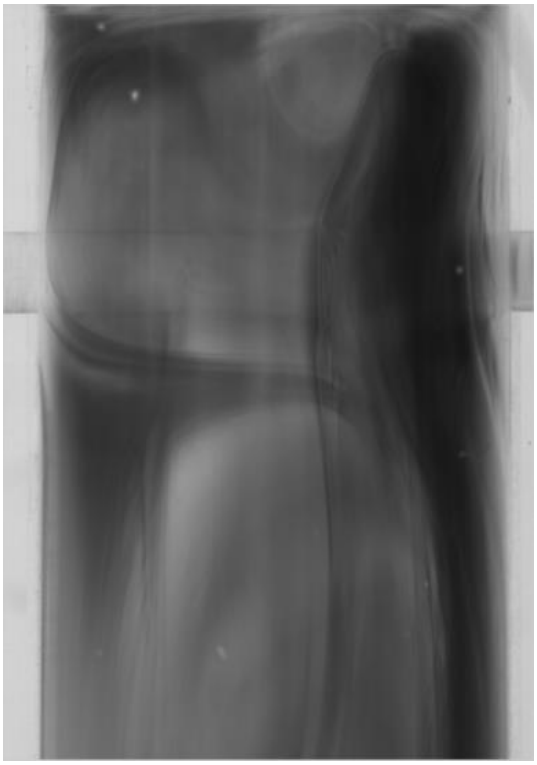

$\phi_K = 2.3517$

$\phi_K = 3.2775$

Figure D.17-Average flow field visualization, using PLIF, for Reynolds 138

D.5 Reynolds 162

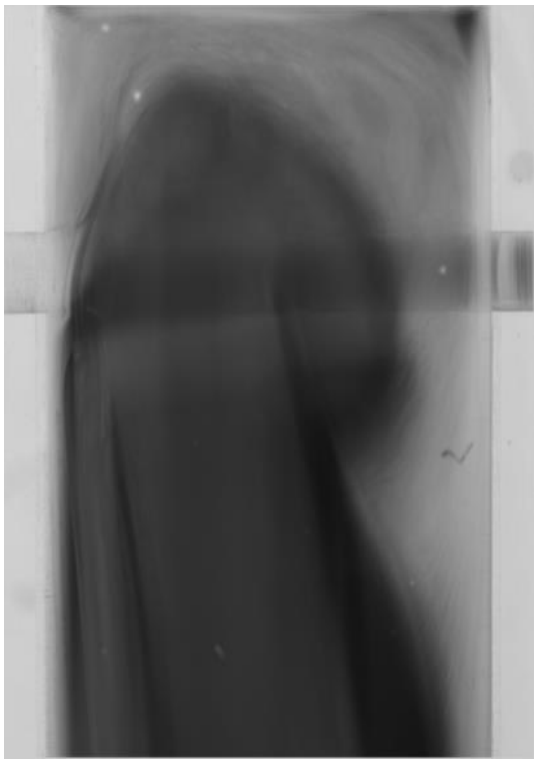

$\phi_K = 0.3117$

$\phi_K = 0.3928$

$\phi_K = 0.4508$

$\phi_K = 0.5198$

Figure D.18-Average flow field visualization, using PLIF, for Reynolds 162

$\phi_K = 0.5343$

$\phi_K = 0.6434$

$\phi_K = 0.6906$

$\phi_K = 0.8226$

Figure D.19-Average flow field visualization, using PLIF, for Reynolds 162

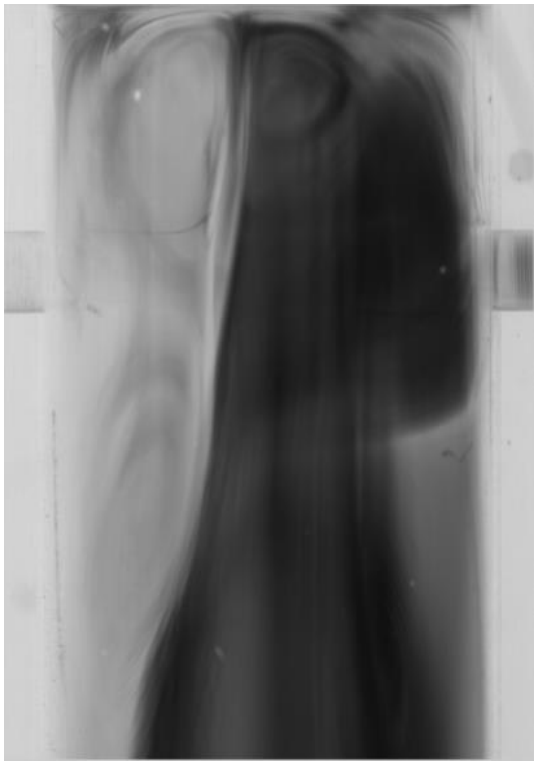

$\phi_K = 1.0854$

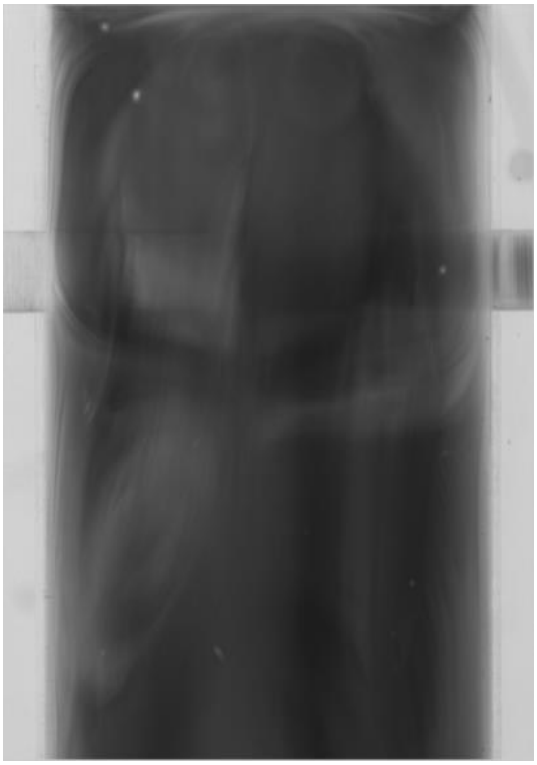

$\phi_K = 1.1841$

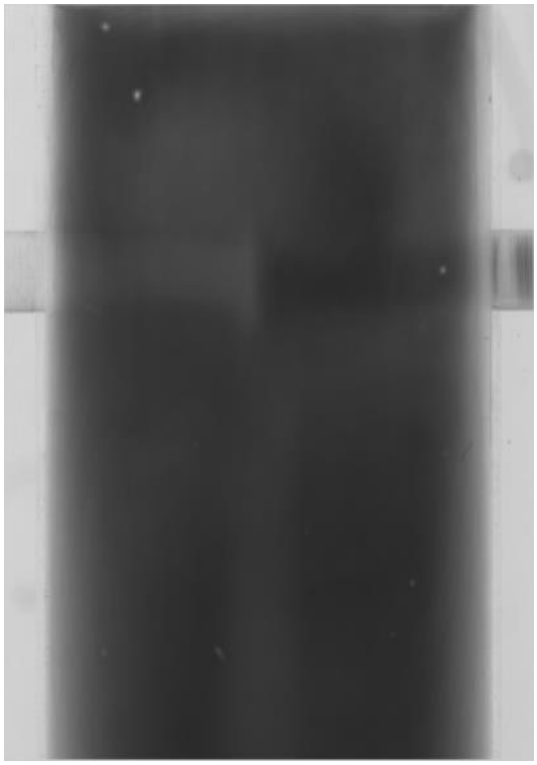

$\phi_K = 1.13912$

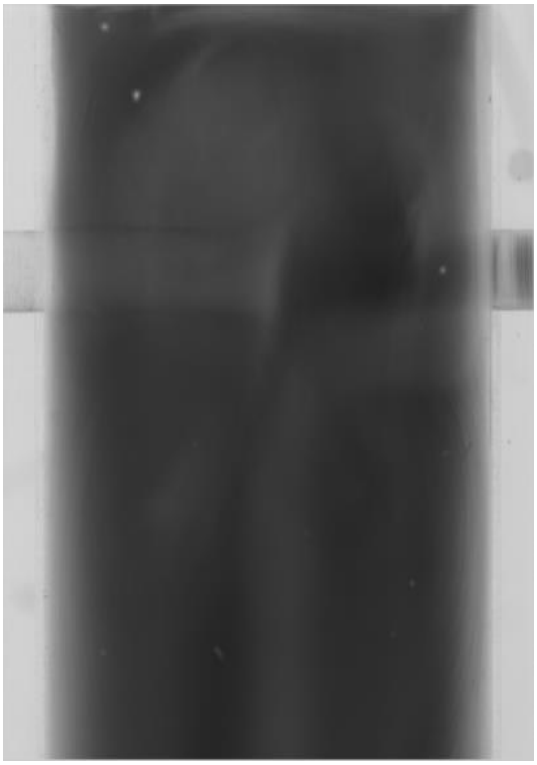

$\phi_K = 1.6631$

Figure D.20-Average flow field visualization, using PLIF, for Reynolds 162

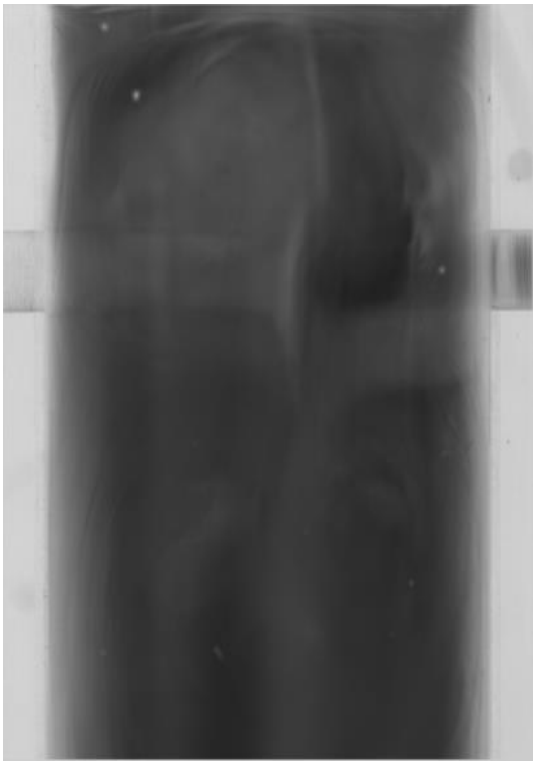

$\phi_K = 1.8038$

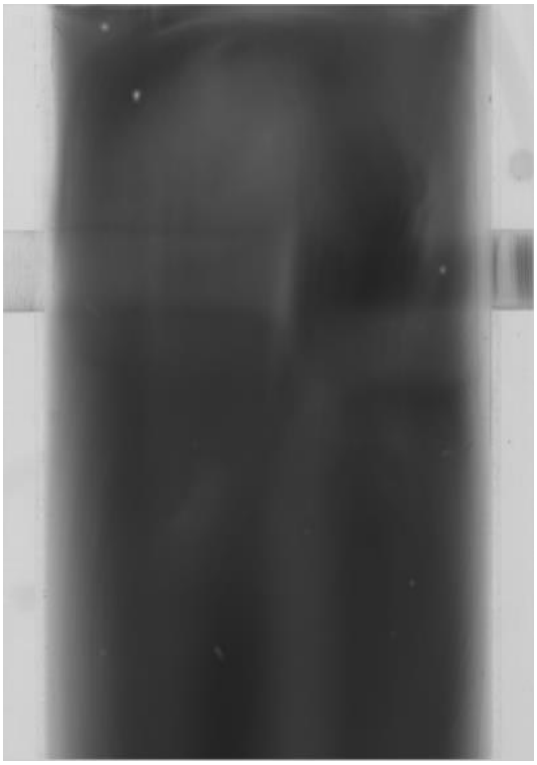

$\phi_K = 1.7639$

Figure D.21-Average flow field visualization, using PLIF, for Reynolds 162